

Tzyh-Jong Tarn  
Shan-Ben Chen  
Xiao-Qi Chen *Editors*

# Robotic Welding, Intelligence and Automation

RWIA'2014

# **Advances in Intelligent Systems and Computing**

Volume 363

## **Series editor**

Janusz Kacprzyk, Polish Academy of Sciences, Warsaw, Poland  
e-mail: [kacprzyk@ibspan.waw.pl](mailto:kacprzyk@ibspan.waw.pl)

### *About this Series*

The series “Advances in Intelligent Systems and Computing” contains publications on theory, applications, and design methods of Intelligent Systems and Intelligent Computing. Virtually all disciplines such as engineering, natural sciences, computer and information science, ICT, economics, business, e-commerce, environment, healthcare, life science are covered. The list of topics spans all the areas of modern intelligent systems and computing.

The publications within “Advances in Intelligent Systems and Computing” are primarily textbooks and proceedings of important conferences, symposia and congresses. They cover significant recent developments in the field, both of a foundational and applicable character. An important characteristic feature of the series is the short publication time and world-wide distribution. This permits a rapid and broad dissemination of research results.

### *Advisory Board*

#### Chairman

Nikhil R. Pal, Indian Statistical Institute, Kolkata, India  
e-mail: nikhil@isical.ac.in

#### Members

Rafael Bello, Universidad Central “Marta Abreu” de Las Villas, Santa Clara, Cuba  
e-mail: rbello@uclv.edu.cu

Emilio S. Corchado, University of Salamanca, Salamanca, Spain  
e-mail: escorchado@usal.es

Hani Hagras, University of Essex, Colchester, UK  
e-mail: hani@essex.ac.uk

László T. Kóczy, Széchenyi István University, Győr, Hungary  
e-mail: koczy@sze.hu

Vladik Kreinovich, University of Texas at El Paso, El Paso, USA  
e-mail: vladik@utep.edu

Chin-Teng Lin, National Chiao Tung University, Hsinchu, Taiwan  
e-mail: ctlin@mail.nctu.edu.tw

Jie Lu, University of Technology, Sydney, Australia  
e-mail: Jie.Lu@uts.edu.au

Patricia Melin, Tijuana Institute of Technology, Tijuana, Mexico  
e-mail: epmelin@hafsamx.org

Nadia Nedjah, State University of Rio de Janeiro, Rio de Janeiro, Brazil  
e-mail: nadia@eng.uerj.br

Ngoc Thanh Nguyen, Wroclaw University of Technology, Wroclaw, Poland  
e-mail: Ngoc-Thanh.Nguyen@pwr.edu.pl

Jun Wang, The Chinese University of Hong Kong, Shatin, Hong Kong  
e-mail: jwang@mae.cuhk.edu.hk

More information about this series at <http://www.springer.com/series/11156>

Tzyh-Jong Tarn · Shan-Ben Chen  
Xiao-Qi Chen  
Editors

# Robotic Welding, Intelligence and Automation

RWIA'2014

 Springer



*Editors*

Tzyh-Jong Tarn  
Washington University  
St. Louis, MO  
USA

Xiao-Qi Chen  
Department of Mechanical Engineering  
University of Canterbury  
Christchurch  
New Zealand

Shan-Ben Chen  
School of Materials Science and Engineering  
Shanghai Jiao Tong University  
Shanghai  
China

ISSN 2194-5357                      ISSN 2194-5365 (electronic)  
Advances in Intelligent Systems and Computing  
ISBN 978-3-319-18996-3              ISBN 978-3-319-18997-0 (eBook)  
DOI 10.1007/978-3-319-18997-0

Library of Congress Control Number: 2015941884

Springer Cham Heidelberg New York Dordrecht London  
© Springer International Publishing Switzerland 2015

This work is subject to copyright. All rights are reserved by the Publisher, whether the whole or part of the material is concerned, specifically the rights of translation, reprinting, reuse of illustrations, recitation, broadcasting, reproduction on microfilms or in any other physical way, and transmission or information storage and retrieval, electronic adaptation, computer software, or by similar or dissimilar methodology now known or hereafter developed.

The use of general descriptive names, registered names, trademarks, service marks, etc. in this publication does not imply, even in the absence of a specific statement, that such names are exempt from the relevant protective laws and regulations and therefore free for general use.

The publisher, the authors and the editors are safe to assume that the advice and information in this book are believed to be true and accurate at the date of publication. Neither the publisher nor the authors or the editors give a warranty, express or implied, with respect to the material contained herein or for any errors or omissions that may have been made.

Printed on acid-free paper

Springer International Publishing AG Switzerland is part of Springer Science+Business Media  
([www.springer.com](http://www.springer.com))

# Preface

The intelligentized welding manufacturing (IWM) is becoming an inevitable trend. The intelligentized robotic welding is the key technology in the IWM.

Welding handicraft is one of the most primordial and traditional technics, mainly by manpower and human experiences. Weld quality and efficiency are, therefore, straitly limited by the welder's skill.

Robotic welding can provide several benefits in welding applications. The most prominent advantages of robotic welding are precision and productivity. Another benefit is that labor costs can be reduced. Robotic welding also reduces risk by moving the human welder/operator away from hazardous fumes and molten metal close to the welding arc. The robotic welding system usually involves measuring and identifying the component to be welded, welding it in position, controlling the welding parameters and documenting the produced welds. To develop an intelligent robotic welding system that can accomplish useful tasks without human intervention and perform in the unmodified real-world situations that usually involve unstructured environments and large uncertainties, the robots should be capable of determining all the possible actions in an unpredictable dynamic environment using information from various sensors such as computer vision, tactile sensing, ultrasonic and sonar sensors, and other smart sensors. From the existing successful applications, it can be concluded that emerging intelligent techniques can enhance and extend traditional robotic welding.

In recent years, the intelligentized techniques for robotic welding have a great development. The current teaching play-back welding robot is not with real-time functions for sensing and adaptive control of weld dynamical process. Generally, the key technologies on Intelligentized welding robot and robotic welding process include computer visual and other information sensing, monitoring and real-time feedback control of Seam tracking, weld penetration, pool shape, seam forming and welding quality. Some applications on intelligentized robotic welding technology is also described in this book, it shows a great potential and promising prospect of artificial intelligent technologies in the IWM.

This volume is mainly based on the papers selected from the 2014 International Conference on Robotic Welding, Intelligence and Automation (RWIA'2014),

October 25–27, 2014, Shanghai, China. We have also invited some known authors as well as announced a formal Call for Papers to several research groups related to welding robotics and intelligent systems to contribute the latest progress and recent trends and research results in this field. The primary aim of this volume is to provide researchers and engineers from both academic and industry with up-to-date coverage of new results in the field of robotic welding, intelligent systems and automation.

The volume is divided into four logical parts containing 55 chapters. In Part I (17 chapters), the authors deal with some intelligent techniques for robotic welding. In Part II (18 chapters), the authors introduce the Sensing of Arc Welding Processing. Various applications such as vision sensing and control of welding process are discussed. In Part III (10 chapters), the authors describe their work on Modeling and Intelligent Control of Welding Processing. In Part IV (10 chapters), the authors exhibit their works on Intelligent Control and its Applications in Engineering.

We would like to thank Professors Jiluan Pan, Bo Zhang, Lin Wu, Qiang Chen, Yuming Zhang and Gu Fang for their kind advice and support to the organization of the RWIA'2014 and the publication of this book; to Dr. Na Lv, Huabin Chen, Xizhang Chen, Huanhuan Zhang, Yunxai Chen, Zhifen Zhang, Yuxi Chen, Ji-Yong Zhong, Cheng-dong Yang, Yiming Huang and Yin Shui He for their precious time to devote all RWIA'2014 correspondences and to reformat the most final submissions into the required format of the book, last but not least to Dr. Thomas Ditzinger for his advice and help during the production phases of this book.

October 2014

Tzyh-Jong Tarn  
Shan-Ben Chen  
Xiao-Qi Chen

# Contents

## Part I Intelligent Techniques for Robotic Welding

<b>On Intelligentized Welding Manufacturing</b> . . . . .	3
Shan-Ben Chen	
<b>Effects of Arc-Sidewall Distance on Arc Appearance in Narrow Gap MAG Welding</b> . . . . .	35
Hu Lan, Hua-Jun Zhang, De-Long Zhao, A-Jing Chen and Shang-Yang Lin	
<b>Tacked Weld Point Recognition from Geometrical Features</b> . . . . .	47
Fu-Qiang Liu, Zong-Yi Wang, Xing-Jian Wang and Yu Ji	
<b>Tracking on Right-Angle Weld with Drain Holes by Robot</b> . . . . .	57
Jian Le, Hua Zhang, Fei Wu and Feng-Yu Yuan	
<b>Welding Robot with Laser Tracking System Used in High-Mobility Off-road Vehicle Rack Girder</b> . . . . .	67
Xing-Wang Wen, Li-Qin Li, Ying Jing, Li-Hong Yan, Li-Bin Zhao and Jin-Liang Zhang	
<b>Partition Mutation PSO for Welding Robot Path Optimization</b> . . . . .	77
Xue-Wu Wang, Ying-Pan Shi, Xing-Sheng Gu and Dong-Yan Ding	
<b>Influence of Heat Input on the Performance of Joint with Filling Wire Laser Welding 5A06 Aluminum Alloy</b> . . . . .	87
Yangchun Yu, Yanling Xu, Guodong Xu, Ajing Chen and Shanben Chen	

<b>Feature Extraction from Arc Signal for Height Tracking System of P-MAG Welding . . . . .</b>	95
Zhen Ye, Hua-Bin Chen, Fang Gu and Shan-Ben Chen	
<b>Research of Laser Hybrid Welding for T-Joint in the Box Girder . . . . .</b>	109
Yang-Chun Yu, Kong Bao, Yan-Ling Xu, A-Jing Chen, Hua-Jun Zhang and Shan-Ben Chen	
<b>Development of Laser Processing Robot Integrated System Solution (LAPRISS) for Remote Laser Welding . . . . .</b>	119
Jing-Bo Wang, Tatsuyuki Nakagawa, Yasushi Mukai, Hitoshi Nishimura, Makoto Ryudo and Atsuhiko Kawamoto	
<b>On the Mechanism and Detection of Porosity During Pulsed TIG Welding of Aluminum Alloys . . . . .</b>	133
Yiming Huang, Zhifeng Zhang, Na Lv and Shanben Chen	
<b>Design of a Scalable Wall Climbing Robot for Inter-plane Traversing . . . . .</b>	145
Yuan Chang and Xiaoqi Chen	
<b>Handheld Device System Development for Video Camera Movement Control System . . . . .</b>	159
Jing-Jie He, Su Wang and Xin-Gang Miao	
<b>Research of One Torch Double-Wire Pipeline Welding Robot . . . . .</b>	167
Xin-Gang Miao, Feng Zhang, Zhi-Feng Ma and Yi Zhang	
<b>Optimal Motion Planning on 120° Broken Line Seam for a Mobile Welding Robot . . . . .</b>	175
Tao Zhang and Shan-Ben Chen	
<b>A Self-calibration Algorithm with Chaos Particle Swarm Optimization for Autonomous Visual Guidance of Welding Robot . . . . .</b>	185
Wei-Feng Ni, Shan-Chun Wei, Tao Lin and Shan-Ben Chen	
<b>Simultaneous Calibration of a Stereo Vision System and a Welding Robot-an Automated Approach . . . . .</b>	197
Mitchell Dinham and Gu Fang	

**Part II Sensing of Arc Welding Processing**

**Development of Metal Oxide Gas Sensors for Environmental Security Monitoring: An Overview** . . . . . 215  
 Xi-Zhang Chen and Jie Yu

**Temperature Field of Double-Sided Asymmetrical MAG Backing Welding for Thick Plates** . . . . . 229  
 Yu-Xi Chen, Yan-Ling Xu, Hua-Bin Chen, Hua-Jun Zhang, Shan-Ben Chen and Yu Han

**Research on Visual Weld Trace Detection Method Based on Invariant Moment Features** . . . . . 239  
 Jin-Le Zeng, Yi-Rong Zou, Dong Du, Bao-Hua Chang and Ji-Luan Pan

**Mechanism Analysis and Feature Extraction of Arc Sound Channel for Pulse GTAW Welding Dynamic Process** . . . . . 249  
 Na Lv, Yan-ling Xu, Gu Fang, Hui Zhao and Shan-ben Chen

**Online Diagnosis of Joints Quality in Resistance Spot Welding for Sedan Body** . . . . . 263  
 Peng-Xian Zhang, Zhi-Fen Zhang and Jian-Hong Chen

**A Low-Cost Vision System for Open Arc Welding Based on Multi-exposure** . . . . . 273  
 Xiang Luo, Zong-Yi Wang and Chun-Bo Jia

**Study on Vision-Based Dimensional Position Extraction of Plane Workpiece for Groove Automatic Cutting** . . . . . 283  
 Hui-Hui Chu, Yu Ji, Xing-Jian Wang and Zong-Yi Wang

**A Novel Center Line Extraction Algorithm on Structured Light Strip Based on Anisotropic Heat Diffusion** . . . . . 295  
 Xin-Tang Lin, Zong-Yi Wang and Yu Ji

**Image Feature Analysis of Weld Pool in Aluminium Alloy Twin Arc PMIG Welding Based on Snake Model** . . . . . 303  
 Jia-Jia Yang, Ke-Hong Wang, Tong-Li Wu and Ai-Min Wei

**A Detection Framework for Weld Seam Profiles Based on Visual Saliency** . . . . . 311  
 Yin-Shui He, Yu-Xi Chen, Di Wu, Yi-Ming Huang, Shan-Ben Chen and Yu Han

<b>The Effects of Arc Length on Welding Arc Characteristics in Al–Mg Alloy Pulsed Gas Tungsten Arc Welding . . . . .</b>	321
Huanwei Yu, Jinquan Song, Guoan Zhang, Jianzhong Pu, Huabin Chen and Shanben Chen	
<b>Review of Sensors and Its Applications in the Welding Robot . . . . .</b>	337
Xue-Qin Lu, Wen-Ming Liu and Yi-Xiong Wu	
<b>A Review and Preliminary Experiment on Application of Infrared Thermography in Welding . . . . .</b>	351
Chao Hu and Xi-Zhang Chen	
<b>Active Shape Model for Visual Detection and Localization of Variable Polarity PAW Weld Pool . . . . .</b>	361
Di Wu, Ming-Hua Hu, Lu-Lu Chen, Hau-Bin Chen, Tao Lin and Shan-Ben Chen	
<b>Information Fusion in Pulsed GTAW Using ANFIS and Fuzzy Integral . . . . .</b>	373
Bo Chen and Shan-Ben Chen	
<b>Study on the Relationship Between the Energy in Most Effective Frequency Range of Arc Sound Signal and the Change of Arc Height in Pulsed Al Alloy GTAW Process . . . . .</b>	385
Huan-Huan Zhang, Na Lv and Shan-Ben Chen	
<b>Data-Driven Feature Selection for Multisensory Quality Monitoring in Arc Welding . . . . .</b>	401
Zhifen Zhang and Shanben Chen	
<b>Sensing Technology for Intelligentized Robotic Welding in Arc Welding Processes. . . . .</b>	411
Yanling Xu, Na Lv, Gu Fang, Tao Lin, Huabin Chen, Shanben Chen and Yu Han	
<b>Part III Modeling and Intelligent Control of Welding Processing</b>	
<b>Fault Diagnosis of Inverter Power Supply Device Based on SVM . . . . .</b>	427
Fei Wang, Yue Wang, Xi-Xia Huang and Yong-Kui Zhang	

**Process Planning Strategy for Wire and Arc Additive Manufacturing** . . . . . 437  
 Dong-Hong Ding, Zeng-Xi Pan, Cuiuri Dominic and Hui-Jun Li

**Modeling of Human Welder Response Against 3D Weld Pool Surface Using Machine-Human Cooperative Virtualized Welding Platform** . . . . . 451  
 Yu-Kang Liu, Ning Huang and Yu-Ming Zhang

**Modeling Welding Deviation of Rotating Arc NGW Based on Support Vector Machine** . . . . . 459  
 Wen-Hang Li, Kai Gao, Jing Wu and Jia-You Wang

**Dynamics Modeling and Analysis of a Type of High Frequency 6-DOF Parallel Platform** . . . . . 469  
 Qi-Tao Huang, Zheng-Mao Ye and Zhi-zhong Tong

**The Application of Robotic Welding in the Shipbuilding** . . . . . 483  
 Hua-Bin Chen, Tao Lin and Shan-Ben Chen

**The Microstructure and Properties of S32750 Multipass Welds** . . . . . 493  
 Hua Huang, Jing-Hui Jin and Zhong-Ping Ding

**Microstructure, Mechanical Properties of Welded Joints of F22 and F91** . . . . . 503  
 Min-Li Ma and Xi-Zhang Chen

**Enhanced Active Control of Metal Transfer in GMAW** . . . . . 517  
 Jun Xiao, Shu-Jun Chen, Guang-Jun Zhang and Yu-Ming Zhang

**Research on Reconstruction of Weld Pool Surface Based on Shape from Shading During Robot Aluminum Alloy Pulse GTAW** . . . . . 525  
 Jiyong Zhong, Chengdong Yang, Yanling Xu, Huabin Chen and Shanben Chen

**Part IV Intelligent Control and Its Applications in Engineering**

**The Development of a Low Cost Autonomous Robotic Arc Welding System** . . . . . 541  
 Mitchell Dinham and Gu Fang



**Multi-pass Route Planning for Thick Steel Plate Using Laser Welding with Filler Wire** . . . . . 551  
Tian-Yu Huang, Li-Wen Fan, Yi-Ning Bao, Hao Shi and Ke Zhang

**Study of Mechanism and Kinetic About Low Frequency Piezoelectric Motor** . . . . . 561  
Rui Wang, Shu-Chen Yang, Xiao-Yang Jiao and Xiao-Tao Li

**Microstructures and Mechanical Properties of 30CrMnSiA Steel Joints Welded by Vacuum Electron Beam** . . . . . 571  
Shan-Lin Wang, Shan-Ben Chen, Xing Li and Li-Peng Wan

**Key Technologies and Automation System for Large-Scale Aerospace Component Welding** . . . . . 581  
Yirong Zou, Baohua Chang, Li Wang, Jiluan Pan and Dong Du

**Research of a Linear Switched Reluctance Motor** . . . . . 595  
Xiao-Yue Liang, Su Wang and Xin-Gang Miao

**The Stone Carving Reproduction for the Reservation of Chinese Ancient Architectures** . . . . . 603  
Zhuo Liu, Xin-Gang Miao and Su Wang

**Research and Analysis of Architectural Construction Safety Dynamic Infrasonic Network System Based on Acoustic Vector Sensor** . . . . . 609  
Hui-Chao Xu, Su Wang and Bao-Jun Zhao

**Design and Optimization of Magnetic Wheel for Wall Climbing Robot** . . . . . 619  
Zheng-Yi Xu, Ke Zhang, Xiao-Peng Zhu and Hao Shi

**Improved Cold Crack Resistance of Q690 Steel Weldments Using Double-Sided Arc Welding** . . . . . 631  
Cheng-dong Yang, Yu-xi Chen and Shan-ben Chen

**Part I**  
**Intelligent Techniques for Robotic Welding**

# On Intelligentized Welding Manufacturing

Shan-Ben Chen

**Abstract** This paper presents some concepts on intelligentized welding manufacturing, such as the ideas of intelligentized welding manufacturing technology/systems (IWMT/S), intelligentized robotic welding technology/systems (IRWT/S) and intelligentized welding manufacturing engineering (IWME), and investigates the framework and constitution of technologies and systems for intelligentized welding manufacturing. Furthermore, the paper also shows some new evolutions of research works in the IRWTL at SJTU on intelligentized welding manufacturing, which includes multi-information sensing and knowledge modeling of arc welding process; intelligent control methodology for welding dynamic process; intelligentized technologies for robotic welding and intelligentized autonomous welding robot system for the special environment. The author wishes to present a systematization of intending research framework and constitution on the IWMT/S in this paper. Some studies on intelligentized welding presented in this paper might introduce related essential research directions or fields of intelligentized technologies for modern welding manufacturing.

## 1 Introduction

With development of modern manufacturing, the intelligent manufacturing (IM), which is to simulate intelligent behaviors and functions of the human's sense, brain and body activity in manufacturing process of various industrial products by the Artificial Intelligence (AI) technology, is increasingly becoming an inevitable trend about in recent two decades [1–7], and the intelligentized welding manufacturing (IWM) undoubtedly is the most representative intelligent manufacturing in all IM processes.

---

S.-B. Chen (✉)

Intelligentized Robotic Welding Technology Laboratory, School of Materials Science and Engineering, Shanghai Jiao Tong University, Shanghai, People's Republic of China  
e-mail: sbchen@sjtu.edu.cn

As is known to all, welding handicraft was invented more than 3000 years, and traditional welding was implemented mainly by welder handwork and experiences. Manual welding operation is not only a burdensome and tedious labor for welder; moreover, reliability and consistency of welding quality depends on welder's skills and experiences, but efficiency of welding production is also limited straitly [1–3].

Studying and simulating intelligent action and function of welder's operations is very significant for the development of intelligentized robotic welding [4]. Much better than any welding robot, a professional welder is highly adaptive to practical situations through observing the position of welding joint, pool dynamics and appearance of the welding seam to identify the welding status; and regulating the parameters to produce high quality welding seam [5–7]. To realize automatic welding similar to welder, three essential technical approach are inevitable, the first is to sense and acquire information of the welding process in real time, similar to human sensing organs for detecting the interior and exterior welding conditions; the next is to identify characteristics of the welding process, i.e. modeling the welding process; the third is to develop the human-brain-like controller to reason the controlling strategy [8–10].

With requirements of modern welding manufacturing, it is become an inevitable trend to realize automatic, robotic, flexible and intelligentized welding technologies [11–14]. Modern welding manufacturing has developed and evolved from the original handworked craft to the modern systemic technical science, and it is related to material, mechanical, electrical, control, computer sciences and other extensive subject technical fields. As far as easing welder works, one of main functions in modern welding manufacturing systems is to substitute or partially replace the physical force and brains doings of a welder with machines. It is one of hot topics in advanced welding manufacturing technologies to simulate and realize a welder's actions by some intelligent machines [12].

Aiming at the bottleneck technological problem of effective control of weld quality during automatic and robotic arc welding process, this paper will present mainly researching works on intelligentized methodology for arc welding dynamical process in the Intelligentized Robotic Welding Technology Laboratory (IRWTL), Shanghai Jiao Tong University (SJTU), which involves multi-information sensing and feature acquiring, knowledge modeling and intelligent control of arc welding dynamical process [11, 12].

Since arc welding is one of the most representative welding techniques with wide application in modern welding manufacturing, no loss of generality, this paper discusses main intelligentized technical problems related to intelligentized welding manufacturing technology/systems (IWMT/S), intelligentized robotic welding technology/systems (IRWT/S) and intelligentized welding manufacturing engineering (IWME) combining with an arc welding technics, which could be also useful to other welding techniques.

## 2 The Concepts, Frameworks and Constitutions of the IWMT/S

In this paper, the intelligentized welding manufacturing (IWM) is preliminarily defined as for simulating intelligent behaviors and functions of welder’s sense, brain and body activity in welding process by the Artificial Intelligence technology, seeing Fig. 1 for composition parts of the IWM process. Furthermore, investigating the constitution of general intelligentized manufacturing, functions and systems, we present a pentabasic framework of the IWMS as Fig. 2.

Based on scientific and technical contents related to development of modern welding manufacturing technology [11–14], the concept on intelligentized welding manufacturing technology (WMT) as Fig. 3 is introduced in this paper, it shows for the key scientific and technical formwork of the IWMT, which contains three advanced manufacturing fields: The virtual and digital welding manufacturing and technology—V&DWMT including the virtual manufacturing; intelligentized Robotic Welding Technology—IRWT; and the flexible and agile welding manufacturing and technology—F&AWMT; and key technical elements and system techniques of the IWMT including the network manufacturing.

The IWMT is mainly related to key intelligent technical elements: sensing welding process for imitating welder’s sense organ function, knowledge extraction and modeling of welding process for imitating welder’s experience reasoning function, and intelligent control of welding process for imitating welder’s decision-making operation function. Figure 4 shows some key scientific methods and technologies of the IWM.

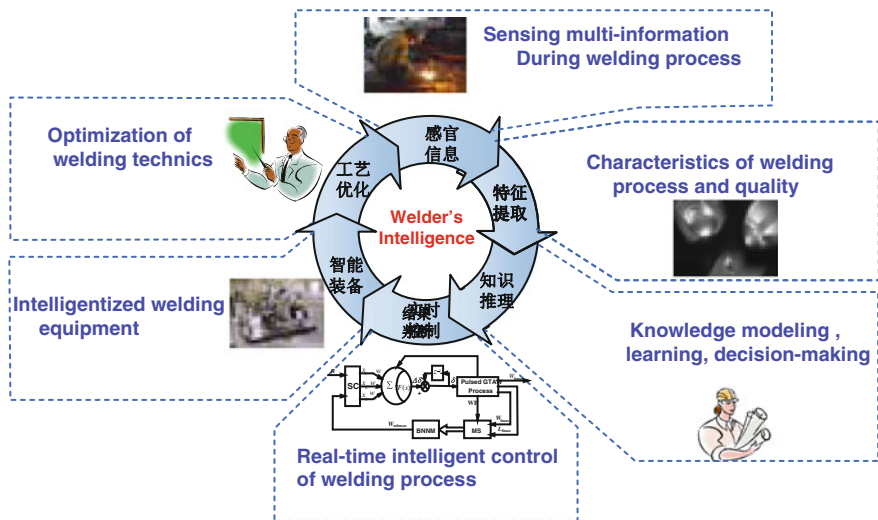


Fig. 1 Composition of IWM

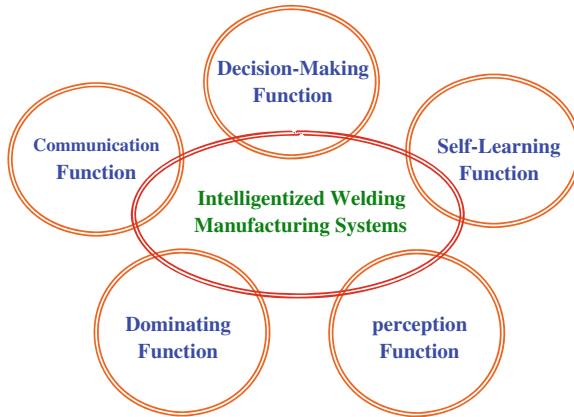


Fig. 2 A pentabasic framework of IWM

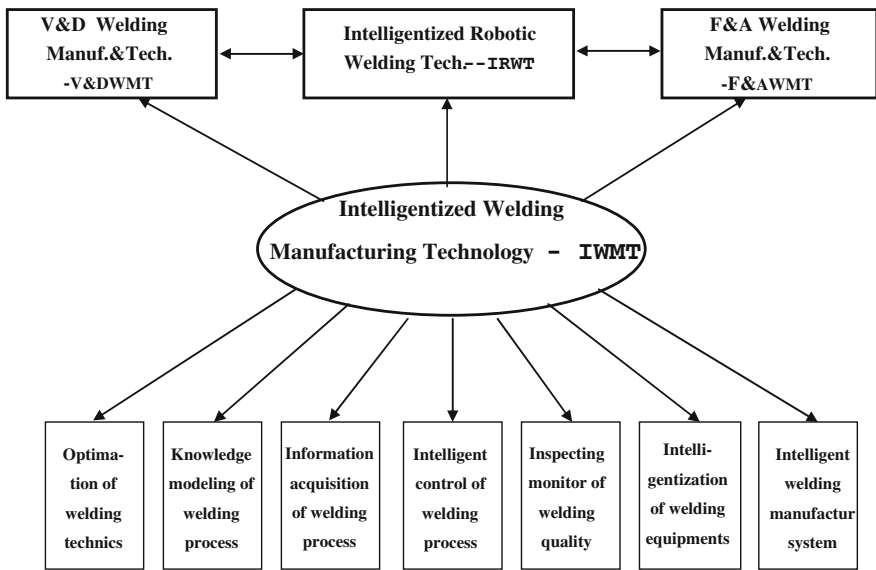


Fig. 3 The framework of the IWMT

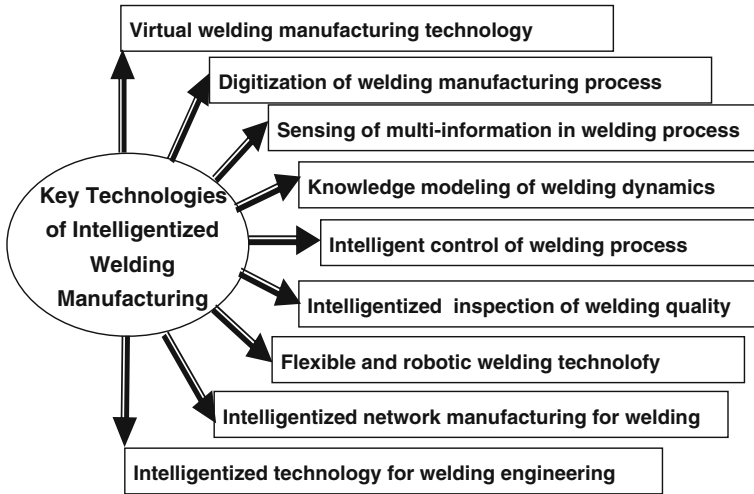


Fig. 4 The key technologies of the IWM

### 3 Intelligentized Welding Technologies and Systems

#### 3.1 *Multi-information Acquirement of Arc Welding Dynamical Process*

As is well known, monitoring and sensing of arc welding dynamic process is very important for real-time control of welding manufacturing process [15–18]. The arc welding dynamic process is extremely perplexing, which contains plentiful, complicated and uncertainty information during welding process. Many sensing methods for arc welding process have been used in consideration of the disturbance from arc, high temperature, vibration, electromagnetic fields and the features of the process, such as ultrasonic for penetration [16], arc pressure method and arc light for vibration information of the weld pool, infrared thermoscope for welding temperature field, X-ray for shape of welding pool [17], acoustic [18] and visual sensing [19–25] for penetration and seam, and so on.

In order to obtain the effectual characteristics of arc welding process for real-time control of weld quality, various signal processing methods have been used for information of arc welding process, such as processing algorithms for arc voltage, current, pool, acoustic, visual, spectrum, thermic, optical, mechanical informations [11]. Figure 5 is a schematic diagram of multi-information sources during arc welding dynamical process. In recent years, the multi-information fusion methods has been also introduced into extraction of characteristics of welding process [26, 27]. Figure 6 is a scheme of multi-information fusion for arc welding dynamical process, and further investigating research on has been developed in [28, 29].

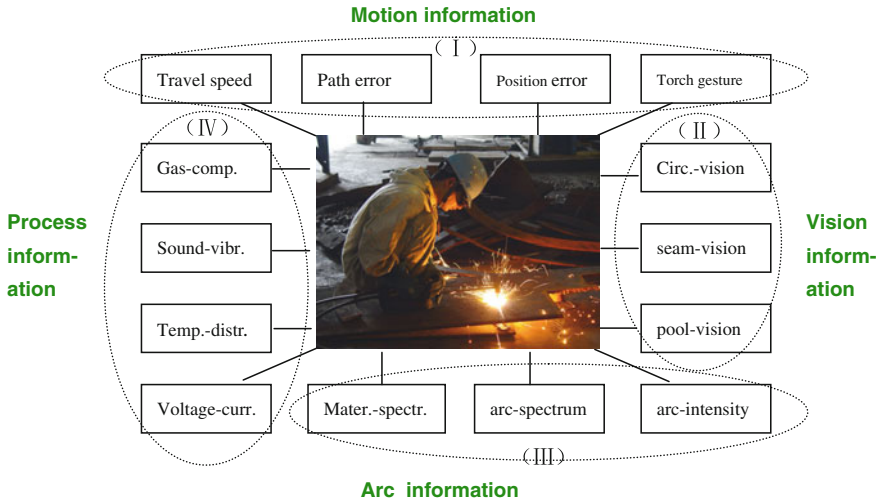


Fig. 5 Multi-information sources during arc welding dynamical process

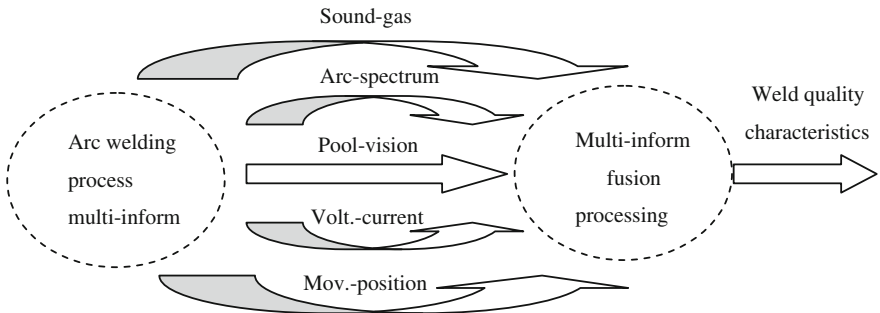


Fig. 6 Multi-information fusion for arc welding dynamical process

### 3.1.1 Visual Sensing and Monitoring of Weld Pool Dynamical Process

Vision is one of main functions of human sensing environment information. In manual welding process, the welder receives visual information from weld circumstance, especially weld pool region, and then proper operations are adopted for controlling good welding quality. Therefore, using the computer visual technology to realize human vision and image processing functions in welding process is one of the most important and basic technologies for the IWMT. With development of computer vision technology, using upside pool visual images to detect dynamical varieties of weld pool geometry figure and to predict weld fusing depth, penetration and seam forming has become a hot researching direction [19–24].

In the recent two decades research, we have developed the methodology of visual monitoring and processing of welding pool image [10, 11]. Recently, we

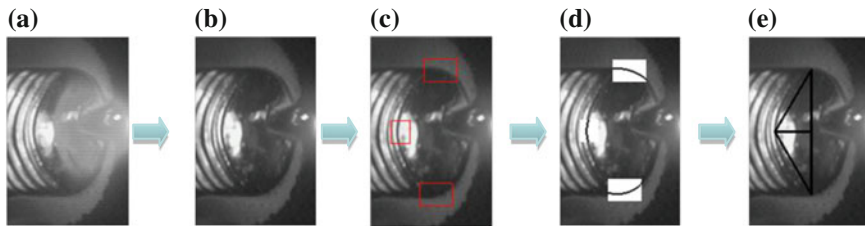


have presented a visual attention modeling method based on the characteristics of images obtained from the experiments, processed only the region of interest (ROI) [30–32]. The visual characteristics of the pool are effectively extracted and fused to obtain the ROI parameters of the welding dynamic process, and established a flowchart of related image processing algorithms. Since only a small visual attention is processed using the visual attention method, the ROI algorithms of the image processing are used to detect some welding defects occurring during the welding process, such as the feature characteristics of non-penetration, weld leak porosity, slag, and linear misalignment pool images. Figure 7 shows an image processing of a general Al alloy GTAW pool by the ROI detection [31], and Fig. 8 shows an image processing of Al alloy GTAW pool in the three-path images with linear misalignment by the ROI detection in real-time [32].

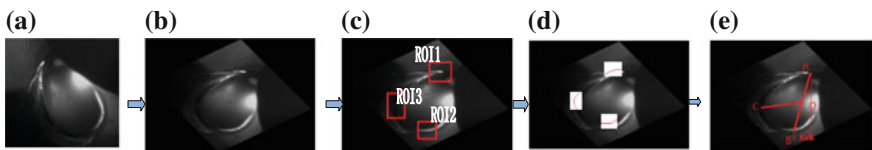
Compared with other sensing methods, the visual sensing is the most prospective sensing technology since it is not in tough with the welding circuit and workpiece, thus visual signal detection does not affect the welding process so that the visual sensing can provide with sufficient information, such as type of joint, welding edges, type of arc, position of wire and the shape of solidified welding seam.

### 3.1.2 Audio Sensing and Characteristic Extraction of Arc Sound Information

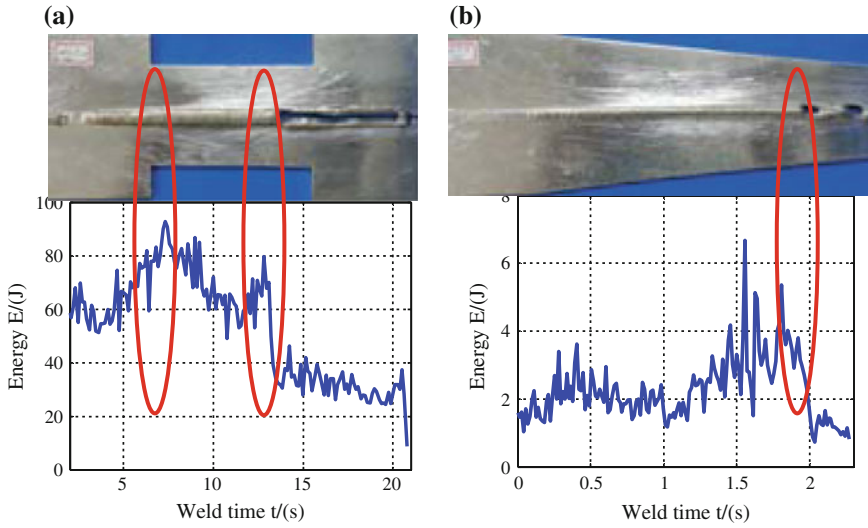
Some investigations show that the arc sound signal is an important information for monitoring of welding dynamics and quality characteristics [33–35], which show



**Fig. 7** Image processing of a general GTAW pool by ROI detection. **a** The original, **b** re-processing, **c** ROI detection, **d** ROI processing, **e** final results



**Fig. 8** Image processing of Al alloy GTAW weld pool with linear misalignment by ROI detection. **a** The original, **b** re-processing, **c** ROI detection, **d** ROI processing, **e** final results



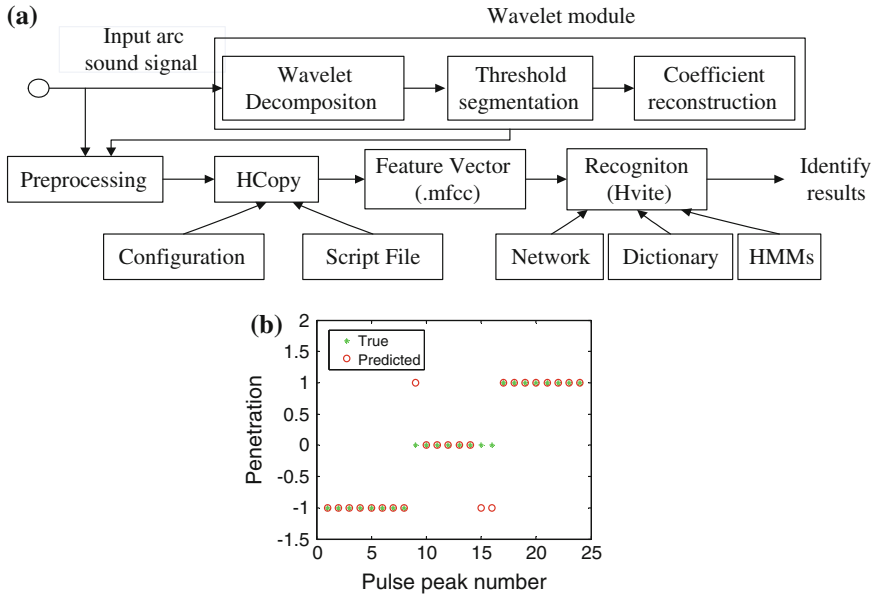
**Fig. 9** The penetration features of arc sound signals. **a** dumbbell plate, **b** trapezoid plate

that the arc sound intensity is used as the variable reflecting changes of welding status. The time domain, frequency domain and wavelet features were extracted at different frequency band under different penetration states like partial penetration, full penetration and excessive penetration. Figure 9 shows different features of weld penetration states [36]. Also some other algorithms were developed for extraction of welding status, e.g. penetration characteristics in [35–37].

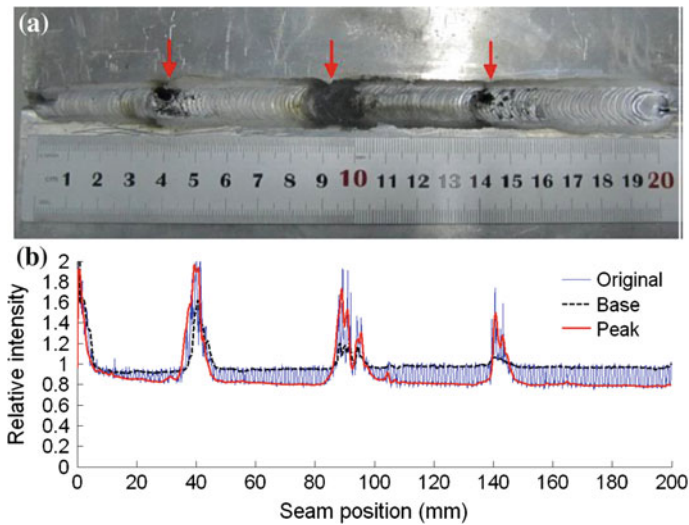
The Hidden Markov Model with the wavelet analysis algorithms was developed for predicting different penetration status based on all the features of arc sound signal. Figure 10 shows the prediction results of weld penetration based on arc sound features by the Hidden Markov Model and wavelet model. The features of arc sound signal in time domain and frequency domain are essential factors for setting up a prediction model of welding quality control. Further investigations are shown in [37].

### 3.1.3 Spectrum Characteristic Extraction of Welding Dynamical Process

Arc plasma transfers energy from power source to the work-piece and emits large amount of spectra to the surrounding space [38]. The arc spectra contains the abundant information related to welding dynamic characteristics and quality status. The arc spectra during Al Mg alloy pulsed GTAW have been acquired and investigated [39–42]. Some arc spectra processing algorithms were developed for characteristic signals extraction from the original spectral information. The relationships among these extracted signals and the defects caused by wire feed have



**Fig. 10** Prediction penetration based on arc sound features by Wavelet and Hidden Morkov models. **a** The schematic diagram of recognition model, **b** a prediction results of weld penetration



**Fig. 11** Spectral characteristic signals of seam with porosities. **a** Welding seam with porosities, **b**  $I/H/Ar$  profile as well as the base and the peak profiles

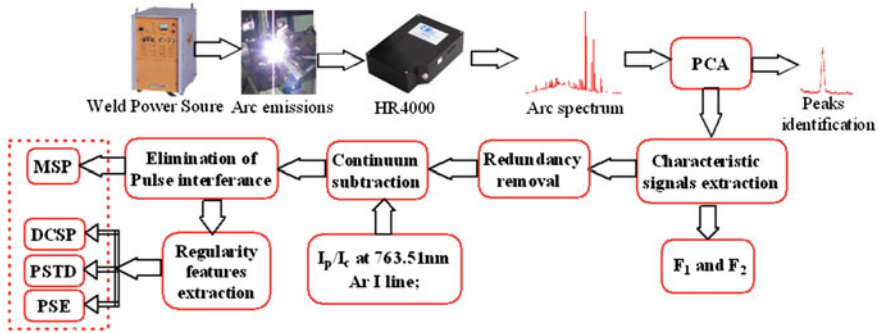


Fig. 12 Procedure of spectral characteristic signals extraction of arc welding

been studied. Figure 11 shows spectral characteristic signals of the seam with porosities [39, 40]. The defects of seam oxidation are produced by different disturbances, i.e., the oil painted on the surface of the plate and the non-removed insoluble oxide film of aluminum alloy. And Fig. 12 is the processing procedure of spectral characteristic signals extraction of arc welding [41, 42].

### 3.1.4 Multi-information Acquisition and Fusion Extraction of Characteristics During Arc Welding Process

Reference [26] developed the experimental system with multi-sensor for acquisition of multi-information of welding dynamical process, combining the three collecting modules, weld pool image, welding current, arc voltage, welding sound and spectral features could be collected at the same time. Figure 13 shows the collected weld pool, current, voltage and sound information in five pulses. From the current, voltage and sound waveforms, it is apparent that the welding process can be divided into weld pulse peak period and weld pulse base period.

The multi-sensor fusion model of the three sensors is developed in [27]. The information obtained from each of the sensors was first processed by back-propagation (BP) neural networks individually. Because welding process was influenced by heat inertia, responded to welding parameters with a time delay, the historical information should also be included to obtain more precise prediction results for the back-side bead width. The D-S evidence theory was used to combine the BPAs and obtain the final fusion BPA and obtain the prediction results [28], as Fig. 14.

The experiment and analysis results shows that the multi-sensors could obtain better results than a single sensor. The prediction results by fusing three sensors are better than that by fusing two sensors. It shows that multi-sensor information fusion could obtain more information about the welding process and therefore describe the process more roundly and precisely [26–29].

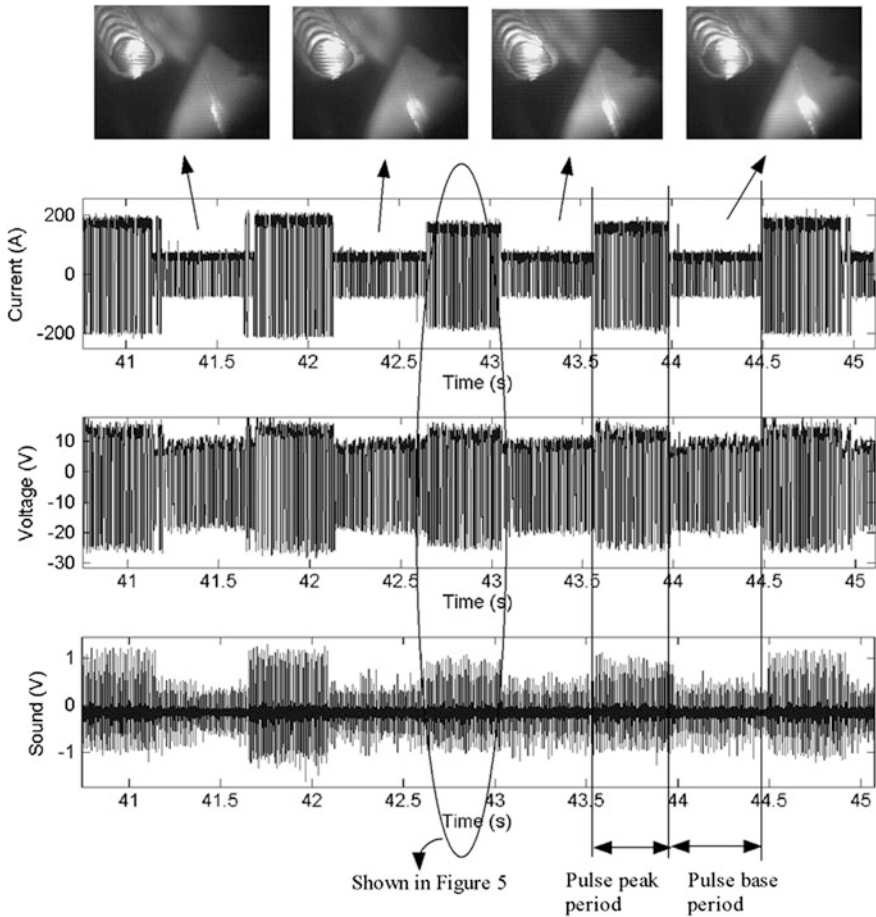
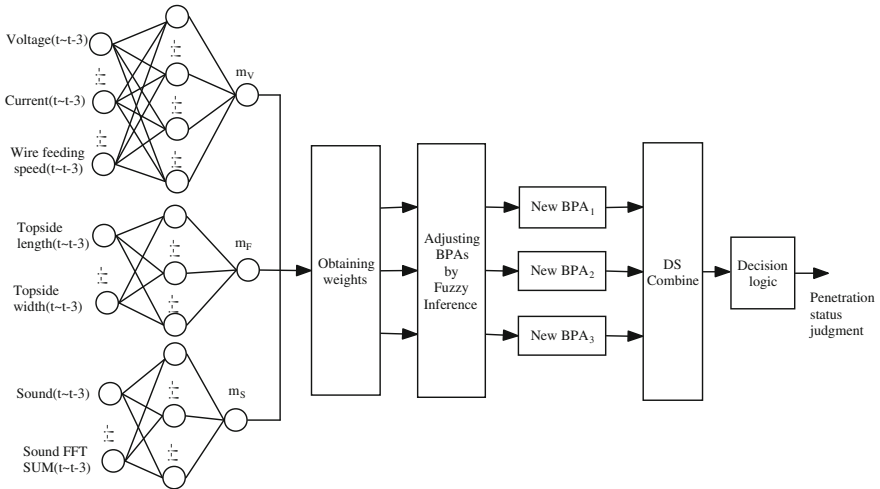


Fig. 13 Visual, current, voltage and sound during GTAW welding

### 3.2 Modeling of Welding Dynamical Process

Another function of welder’s brainpower behaviors is to estimate and manage welding process, it requires welder to be able to understand welding process, handle experience knowledge and make inference and judgement for manipulating welding process [10, 11]. As one of intelligent technical elements, developing model of welding process by maths and knowledge methods is an essential technology for the IWMT. Such as identification modeling method [8–11, 43, 44] by modern control theory, artificial neural network (ANN) modeling [8–10, 45] and knowledge modeling methods [46–51] are used to welding pool process.



**Fig. 14** Multi-information fusion model based on neural network and D-S evidence theory

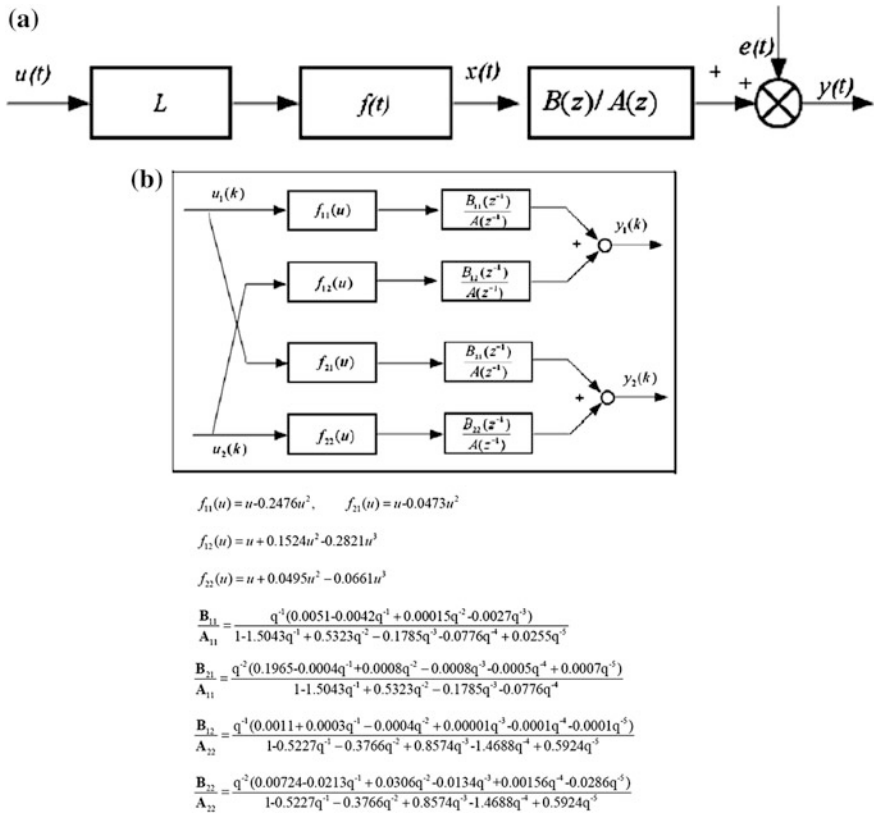
### 3.2.1 Identification of the Non-linear Hammerstein Model of Welding Dynamic Process

We investigate the dynamical characteristics of arc welding dynamic process, and presented and developed a non-linear dynamical model structure for describing heat resource of welding arc as a static nonlinearity and heat conduction as a linear dynamics, i.e., so-called the non-linear Hammerstein model (Ham) for arc welding dynamic process. Figure 15a gives a model schematic diagram of the arc welding dynamic process [43]. The further study developed a MIMO non-linear Ham model for Al alloy GTAW dynamic process [44], shown as Fig. 15b.

### 3.2.2 Knowledge Modeling of Welding Dynamic Process

Intelligentized welding requires knowledge description of human welding manipulating experiences. One of key intelligent technologies is to establish knowledge model from extracting welder manipulations so that the computer or robotic systems could play back human knowledge and intelligent decision-making function.

Because of the differences of human describing himself experience capability and uncertainty in welding process, it is very difficult or almost impossible for one to directly get enough expert knowledge from welder's experiences [46–51]. A feasible way is extracting knowledge from measured experimental data by fuzzy computing, rough set theory and other soft-computing methods. References [8, 9] obtains a fuzzy rule model of weld pool dynamics in the pulsed GTAW process by fuzzy identification algorithms. Refs. [46, 47] investigated knowledge modeling methods for welding process from collected data by the basic rough set (RS) theory, Refs. [48, 49] developed an improved knowledge model for Al alloy pulsed GTAW



**Fig. 15** a The Ham model schematic diagram of arc welding dynamic process. b Non-linear MIMO Ham models for Al alloy GTAW dynamic process

process by the variable precision rough set (VPRS) theory. Figure 16 shows a principle of the VPRS theory and the schematic diagram of modeling welding process by the VPRS method. Furthermore, we have developed the VPRS modeling software for welding process, and obtained knowledge models of the low carbon steel and Al alloy GTAW dynamical process [49].

Here is a knowledge model of Al alloy GTAW process by the VPRS algorithm software.

- A3 is 1 and I is 0 and WB3 is 2 and A is 2 and I2 is 2 then WB is 6.75
- WB1 is 1 and I2 is 0 and TL3 is 0 and WT2 is 0 and A is 1 then WB is 6.75
- WB1 is 2 and TL3 is 0 and I is 0 and WB2 is 1 then WB is 6.75
- I is 2 and WT3 is 2 and WT is 0 and A1 is 1 then WB is 9.75
- A3 is 1 and I is 0 and TL is 2 and WB1 is 1 and TL2 is 2 and I2 is 2 then WB is 6.75
- A3 is 0 and WB3 is 2 and A is 1 and A2 is 1 then WB is 6.75
- WB2 is 2 and TL2 is 2 and WB3 is 1 and i2 is 0 and A3 is 1 then WB is 8.25

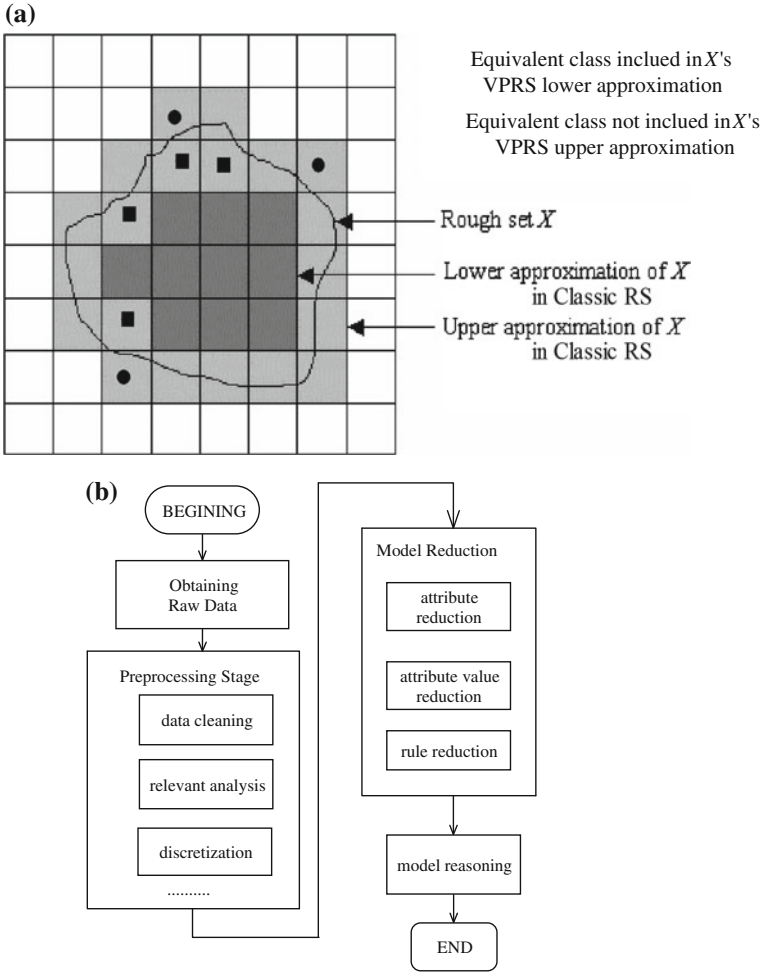
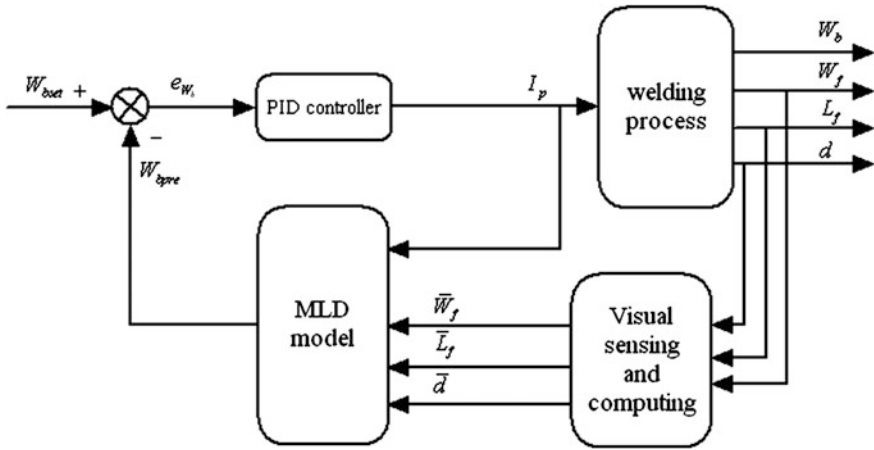


Fig. 16 Knowledge modeling welding process by the VPRS method

### 3.2.3 Mixed Logical Dynamical (MLD) Modeling of Pulsed GTAW Process

In the control theory research field, a hot topic is the so-called mixed logical dynamical (MLD) modeling and control method for the complex system, which is useful to model and control the so-called hybrid systems with interacting physical laws, logical rules, continuous and discrete variables, and operating constraints [52]. Our investigation shows the MLD method is highly suitable for welding dynamical process, particularly, automatic and robotic welding systems [53–56]. Our study in [53] presented a novel MLD modeling framework for robotic welding process and systems, In Fig. 17, the MLD model is then established and gives a





**Fig. 17** Schematic diagram of closed PID control system with MLD model

good prediction quality of the back bead width of pulsed GTAW process with misalignment joint during robotic welding. The study in [52] shows that the MLD framework is a good modeling method for pulsed GTAW process and robotic welding systems.

The general MLD model is described as:

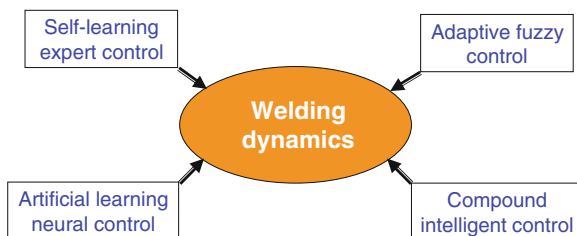
$$\begin{cases} W_f(k) = f_1(W_f(k-1) \dots W_f(k-n_{W_f}), I_p(k) \dots I_p(k-n_{I_p})) \\ L_f(k) = f_2(L_f(k-1) \dots L_f(k-n_{L_f}), I_p(k) \dots I_p(k-n_{I_p})) \\ W_b(k) = f_3(W_b(k-1) \dots W_b(k-n_{W_b}), W_f(k) \dots W_f(k-n_{W_f}), \\ L_f(k) \dots L_f(k-n_{L_f}), I_p(k) \dots I_p(k-n_{I_p})) \end{cases}$$

A MLD model with gap variation (WPG-MLD) is described as:

$$\begin{cases} W_f(k) = 0.6328W_f(k-1) + 0.02596I_p(k) - 0.01143I_p(k-1) \\ L_f(k) = 0.9542L_f(k-1) + 0.007477I_p(k) - 0.005348I_p(k-1) \\ W_b(k) = 0.01666I_p(k) - 0.001824I_p(k-1) - 0.3246W_f(k) \\ \quad + 0.09963W_f(k-1) + 0.5567L_f(k) - 0.1341L_f(k-1) \end{cases}$$

### 3.3 Intelligent Control Methods for Welding Dynamical Process

The technical approach imitating welder’s decision-making functions is to develop intelligent controller for welding process. Intelligent control strategy is mainly aiming at the objective or process with complex uncertainty. Because of especial complexity in welding dynamical process, such as strong nonlinear and



**Fig. 18** Intelligent control methods for welding process

multivariable coupling process, time-variety, randomness and involving many uncertain phenomena, it is specially suitable to adopt intelligent control strategy for it [10–12]. At present, intelligent control methods mainly include fuzzy logical, artificial neural networks, expert system and their combination control schemes [9–12, 57–61], showing as Fig. 18.

Under different welding technical conditions, such as based-on plate welding, butt welding, with filler, with gap variety and uncertainty in welding process, many intelligent control methods, Such as a self-learning fuzzy neural control, adaptive fuzzy neural control, compound intelligent controller with feed-forward compensating control methods for gap variety [61], and so on, have been developed for the penetration, the width of the upside and backside pool and seam, face reinforcement and fine forming of the weld seam during arc welding process.

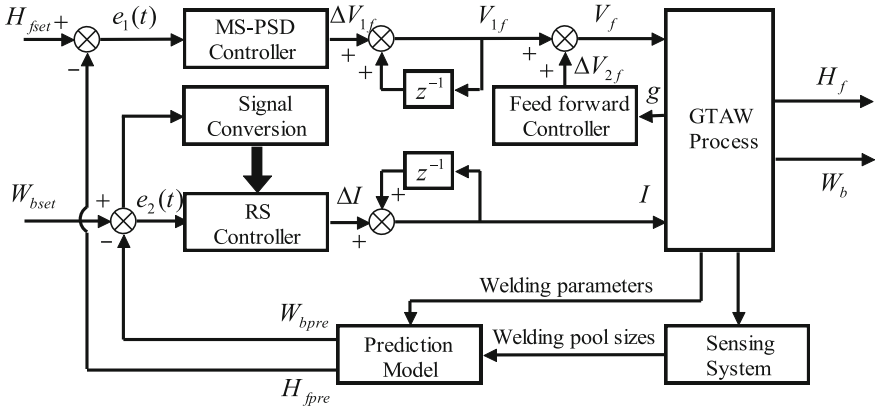
The expert system for real-time control of welding process is another important part in intelligentized welding systems. Although some single technical expert system has been applied in welding production, advanced autonomous expert system for control of welding dynamical process should be still investigated for mode recognition of weld workpiece, environment and seam type; autonomous programming robotic welding path and technics, intelligent control of welding process in the IWMT [11, 12].

### 3.3.1 Closed-Loop Control Schemes Based-on the Knowledge Model by the RS Theory

Based on the obtained knowledge rule models for weld pool dynamics of aluminum alloy GTAW by RS methods, a composited intelligent adaptive control scheme with fuzzy monitor, RS model and MS-PSD controllers was developed for Al alloy welding penetration; seam forming quality and pool dynamics during Al alloy pulsed GTAW [62], shown as in Fig. 19.

### 3.3.2 The Model-Free Adaptive Control of Pulsed GTAW

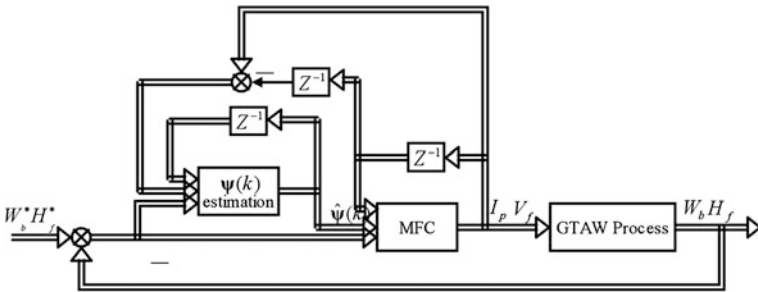
Arc welding is characterized as inherently multi-variable, nonlinear, time varying and having a coupling among parameters. In addition the variations in welding



**Fig. 19** The compound control systems with RS and MS-PSD controllers for Al alloy pulsed GTAW

conditions cause uncertainties in welding dynamics [10]. Therefore, it is very difficult to design an effective control scheme by conventional modeling and control methods. A model-free adaptive control algorithm has been developed to control the welding process [63–65], as Fig. 20, which only needs the measured input output data and no modeling requirement for controlled welding process. Thus, the developed model-free adaptive control provides a promising technology for GTAW quality control as detailed in [64]

$$\begin{aligned}
 \mathbf{U}(t) &= \mathbf{U}(t-1) + \left( \mathbf{R} + \boldsymbol{\psi}(t)^T \boldsymbol{\psi}(t) \right)^{-1} \boldsymbol{\psi}(t)^T \Delta \mathbf{Y}(t+1) \\
 \varphi_i(t) &= \varphi_i(t-1) + \frac{\eta_i \Delta \mathbf{U}(t-1)}{\mu_i + \|\Delta \mathbf{U}(t-1)\|^2} \\
 &\quad \times \left( \Delta y_i(t+1) - \Delta \mathbf{U}(t-1)^T \boldsymbol{\varphi}_i(t-1) \right)
 \end{aligned}$$



**Fig. 20** The closed-loop MIMO model-free adaptive control of GTAW process

The above systematized investigation provides effective and realizable technical approaches for intelligent control of welding pool width, penetration, seam forming quality and pool dynamics during pulsed GTAW process under various conditions [11, 12]. It is a key and essential technology for the IWMT to realize intelligent control of arc welding dynamics.

### 3.3.3 The Adaptive Control of GTAW Process as a Nonlinear Dynamics

Based on the non-linear Ham model for arc welding dynamic process as Fig. 15 [43], The nonlinear self-tuning control systems with the Ham model of welding process have been developed for adaptive control of penetration and seam formation [43, 44]. Figure 21a is the principal of a single-input and single-output (SISO) control system, and Fig. 21b is the a double-input and double-output (DIDO) control system for the backside width and topside reinforced height of the weld seam with welding current regulation and feed-forward compensation [44].

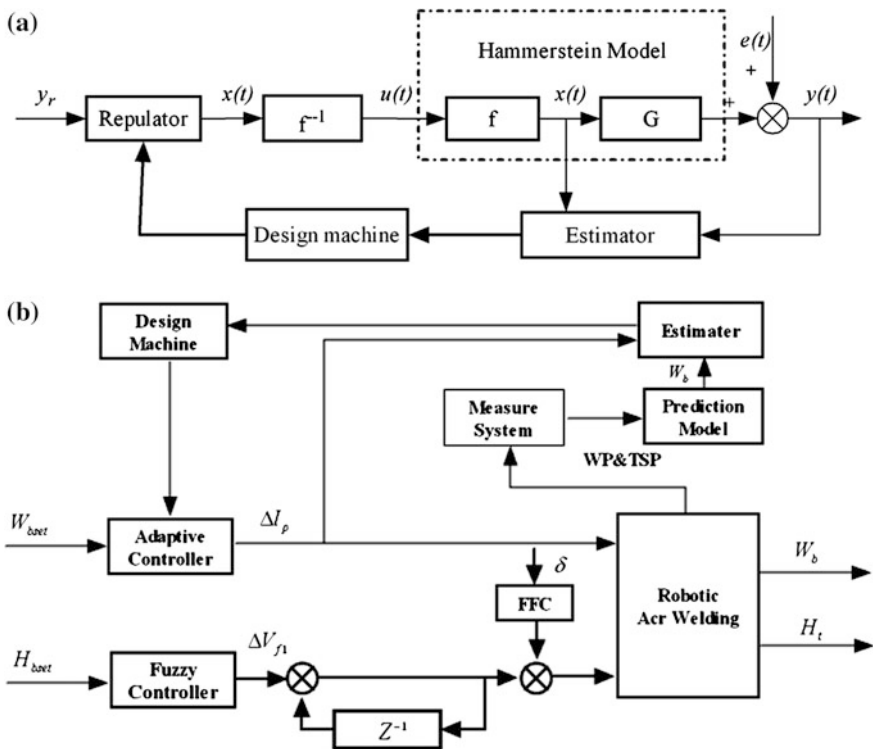


Fig. 21 The nonlinear self-tuning control system with Ham model of welding dynamical process. **a** Principal of SISO control system, **b** DIDO control system for seam formation

### 3.4 Intelligentized Robotic Welding Technology

Developing the intelligent welding robot (IWR) is crucial and necessary for realization of IWMT, generally, the function of IWR system involves visual sensing welding environment, recognising weld workpiece, seam type, guiding weld starting, tracking seam, instructing technics, programming paths and parameters, dominating welding pool dynamical characters, control seam forming and quality, diagnosing failures, and so on, shown as Fig. 22, i.e., the IWR is “an atom” in IWMT systems, a platform integrated by intelligentized welding technologies. Based on single intelligent welding robot with collaborating positioner, an intelligentized welding flexible manufacturing cell (IWFMC) could be established [13, 14]. The IWFMC could be considered as “a molecule” in the IWMT systems, which could autonomously complete a certain welding task and process [11, 12, 66].

#### 3.4.1 The Seam Tracking During Robotic Welding by Visual Sensing

Intelligent welding robots should have some intelligent functions like welder, such as finding start welding position (SWP), adjusting the welding path and parameters according to the changing work environment [67–75]. Refs. [68, 69] developed an welding robot systems with binocular vision calculating three-dimensional (3D) coordinates of the SWP for autonomous detection and guiding of robotic welding torch motion, as Fig. 23.

The seam tracking technique and on-line quality control for the curve weld during robotic pulsed GTAW process was developed based on passive visual

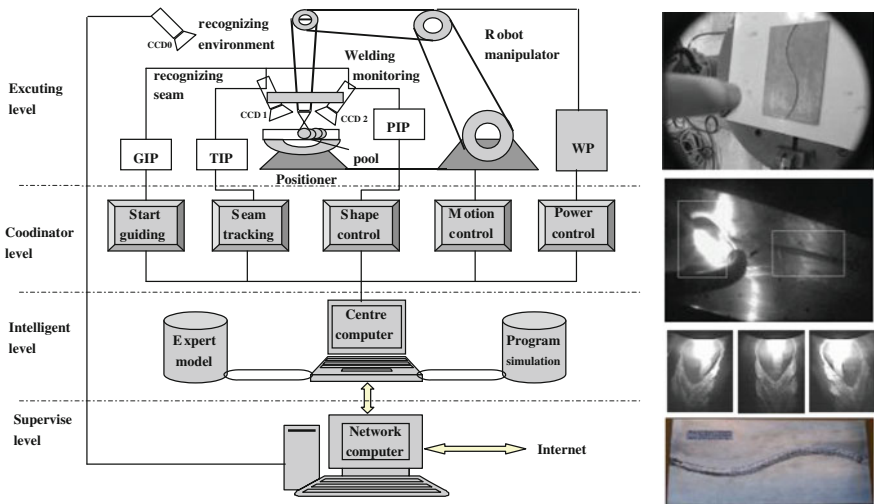


Fig. 22 The IWR technology in IWFMC

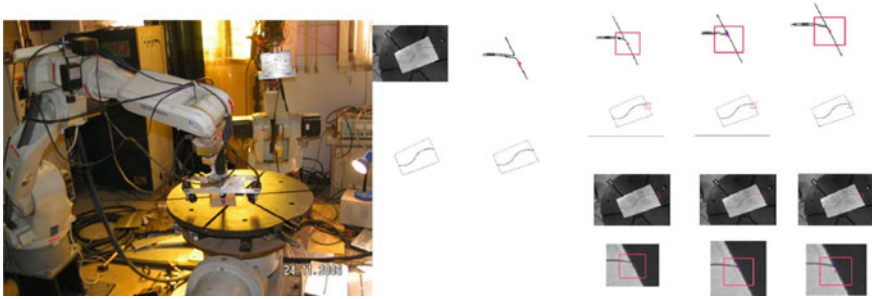


Fig. 23 The autonomous detection and guiding of start welding position for arc welding robot

sensing system [72]. And Fig. 24 shows a robotic welding systems with the visual sensor for monitoring welding pool and tracking seam during robotic GMAW process [69, 70].

### 3.4.2 The 3-D Seam Tracking During Robotic Welding by Combining Arc Sensing and Visual Sensing

The guiding and tracking seam technique for three dimension (3-D) curve during robotic pulsed GTAW process was developed by the combination of arc sensing for torch height or arc length with passive visual sensing for correcting the error of seam or torch deflexion [76–80]. Figure 25 shows a robotic welding systems for 3D seam tracking by arc and visual sensing during robotic GTAW process [77].

The arc voltage signals of AC pulsed GTAW in one cycle contain base value and peak value voltage. The base value voltage is produced during piloting arc process, which can not be used to characterize the arc length. Whether the quality of welding is good largely depends on peak currents, while the corresponding peak voltage is strongly related to the arc length. Another 3D seam tracking welding example completed by robotic welding system is shown as Fig. 26 [79, 80].



Fig. 24 Welding robot system with visual sensor for monitoring welding pool and tracking seam

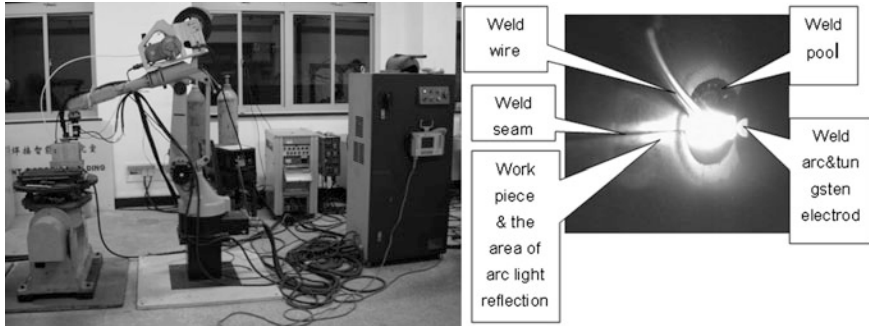


Fig. 25 Robotic welding systems for 3D seam tracking during robotic GTAW process



Fig. 26 3D seam tracking results by robotic GTAW system

### 3.4.3 Application of Real-Time Control of Pool and Penetration During Robotic Welding by Visual and Arc Sensing

The real-time control of pool and penetration during robotic welding is very important for achieving intelligentized welding. The visual information and arc signal could be used for on-line monitoring of the welding quality [81–85]. Figure 27 shows the application experiment by the robotic welding system with arc and visual sensing for a complicated workpiece [82].

### 3.4.4 Development of Autonomous Welding Robot System for Special Environment

In many practical welding manufacturing sites, such as welding for ship structures and large tanks, there is a need for the autonomous moving welding in a long distance and complicated space position [11, 12]. It also requires the welding robot with adsorbent and climbing functions for all position motion and flexible pose





Fig. 27 Application of robotic welding system for real-time control of penetration

changes for various joints, such as the fillet, lap, vertical, inclined welding, and so on. Hence, a primary autonomous moving welding robot system with a combination of wheels and foot for adsorbent climbing and getting across obstacle was developed [86, 87], shown as in Fig. 28. This robot system can realize some welder’s intelligent functions, such as detecting and recognizing weld surroundings by visual sensing technology, identifying the initial position of weld seam, autonomously guiding weld torch to the weld starting and tracking the seam, real-time control of arc weld pool dynamics. In order to ensure the obstacle-crossing and the welding process are conducted in the same time, The programming tracks of robot obstacle-crossing motion has been studied in [88].

### 3.4.5 The Complicated Modeling and Control Methodology for the Intelligentized Welding Manufacturing Systems (IWMS)

The intelligentized welding manufacturing systems (IWMS) is a highly complicated systems, which contains not only the complex welding equipments, such as welding robot, welding machine, fixtures and chucking appliance and so on; a large mixed information variables, such as continuous and discrete variables, logical rules and operating constraints; and various sensors, information processing units, computing

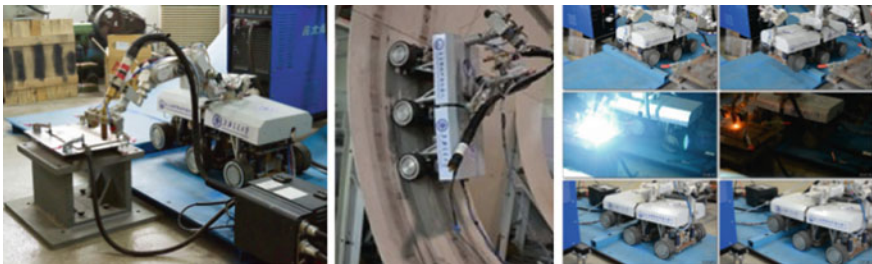


Fig. 28 An autonomous wall-climbing welding robot system



and intelligent units, and so on [10–12]. The IWMS can be classified as a typical hybrid system in advanced control theory [52]. One can see that the modeling and dominating of the IWMS is extremely difficult.

### 1. A MLD Model for Robotic Welding Systems

Aiming at the hybrid characteristics in the IWMS, mixed with the continuous and discrete variables, logical rules and operating constraints, Ref. [54] presented the so-called mixed logical mixed logical dynamical (MLD) models for the robotic welding systems as following:

$$\begin{aligned} \begin{bmatrix} x_r(t+1) \\ x_b(t+1) \end{bmatrix} &= \begin{bmatrix} A_{rr} & A_{rb} \\ A_{br} & A_{bb} \end{bmatrix} \begin{bmatrix} x_r(t) \\ x_b(t) \end{bmatrix} + \begin{bmatrix} B_{1rr} & B_{1rb} \\ B_{1br} & B_{1bb} \end{bmatrix} \begin{bmatrix} u_r(t) \\ u_b(t) \end{bmatrix} + \begin{bmatrix} B_{2rb} \\ B_{2bb} \end{bmatrix} d(t) \\ &\quad + \begin{bmatrix} B_{3rr} \\ B_{3rb} \end{bmatrix} z(t) + \begin{bmatrix} B_{5r} \\ B_{5b} \end{bmatrix} \\ \begin{bmatrix} Y_r(t) \\ y_b(t) \end{bmatrix} &= \begin{bmatrix} C_{rr} & C_{rb} \\ C_{br} & C_{bb} \end{bmatrix} \begin{bmatrix} x_r(t) \\ x_b(t) \end{bmatrix} + \begin{bmatrix} D_{1rr} & D_{1rb} \\ D_{1br} & D_{1bb} \end{bmatrix} \begin{bmatrix} u_r(t) \\ u_b(t) \end{bmatrix} + \begin{bmatrix} D_{2rb} \\ D_{2bb} \end{bmatrix} d(t) \\ &\quad + \begin{bmatrix} D_{3rr} \\ D_{3br} \end{bmatrix} z(t) + \begin{bmatrix} D_{5r} \\ D_{5b} \end{bmatrix} \\ E_2 d(t) + E_3 z(t) &\leq E_1 \begin{bmatrix} u_r(t) \\ u_b(t) \end{bmatrix} + E_4 \begin{bmatrix} x_r(t) \\ x_b(t) \end{bmatrix} + E_5 \end{aligned}$$

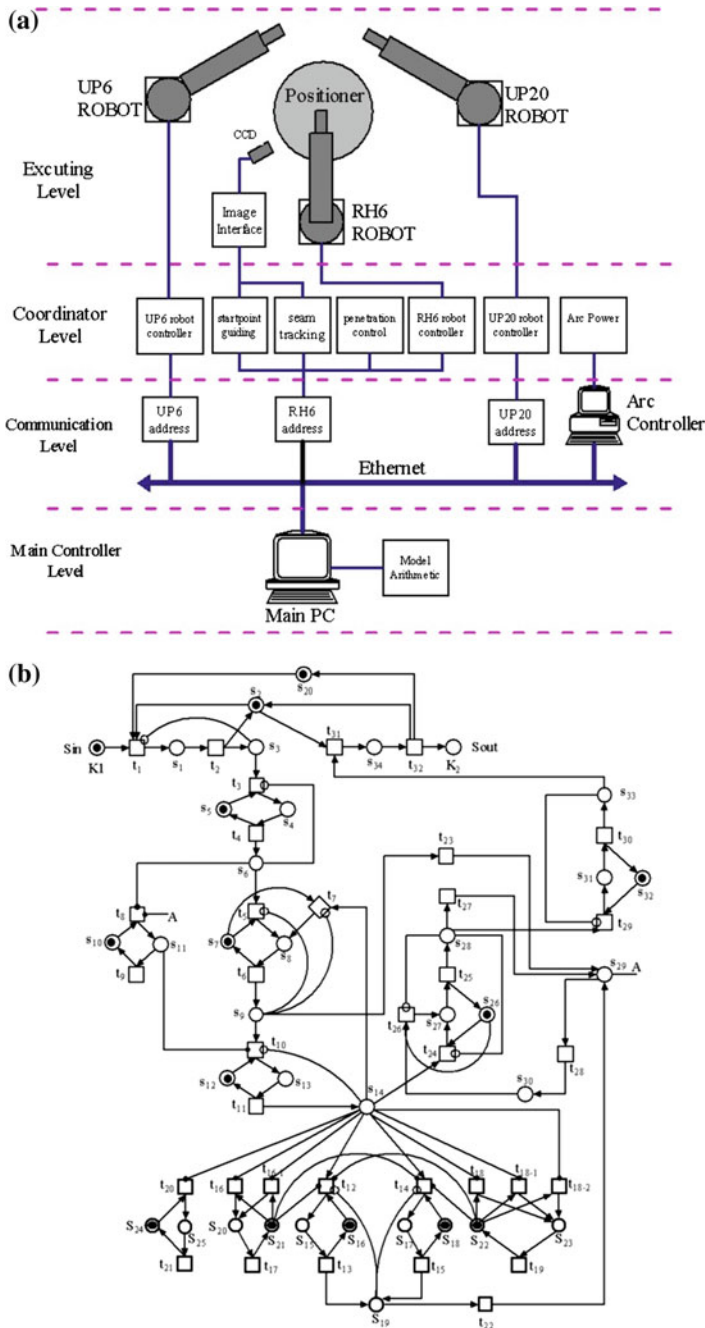
and with 65 inequality constraints.

### 2. A Petri Net Model for Three-robot Welding Systems

Aiming at the information concurrency in the IWMS, e.g., synchronous conflicts between information flow and materials flow, Refs. [89–91] presented some improved Petri net models for multi-robot welding system and welding production line, the Petri net modeling method is very suitable for discrete-event property in the IWMS. Here Fig. 29 shows an improved PN model with sensing information for three robotic welding systems.

### 3. A MAS Model for Multi-robot Welding Flexible Production Line Systems

Considering to the intelligent processing functions in multi-robot welding flexible production line systems with distributed multi-sensors, information exchange and communications, Refs. [92–96] presented some Multi-Agents (MAS) models for complicated multi-robot welding system and welding production line, the MAS theory and technology has become an important approach for modeling and control of complex manufacturing systems. Here Fig. 30 shows an improved MAS models with sensing information for complicated multi-robot welding systems or welding production line.



**Fig. 29** An improved PN modeling of multi-robot welding systems. **a** Schematic diagram of 3-robot welding systems, **b** the PN model of 3-robot welding systems

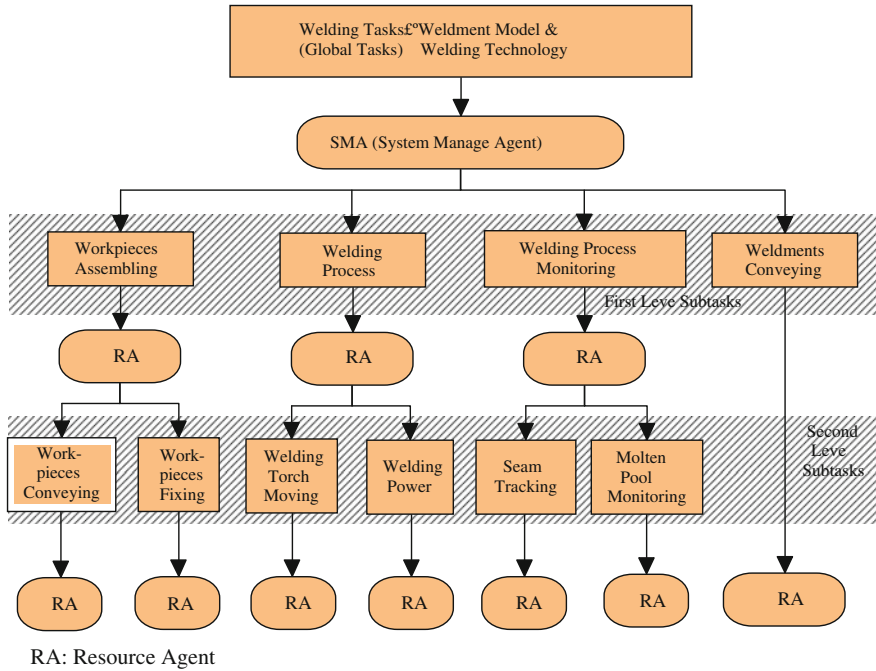


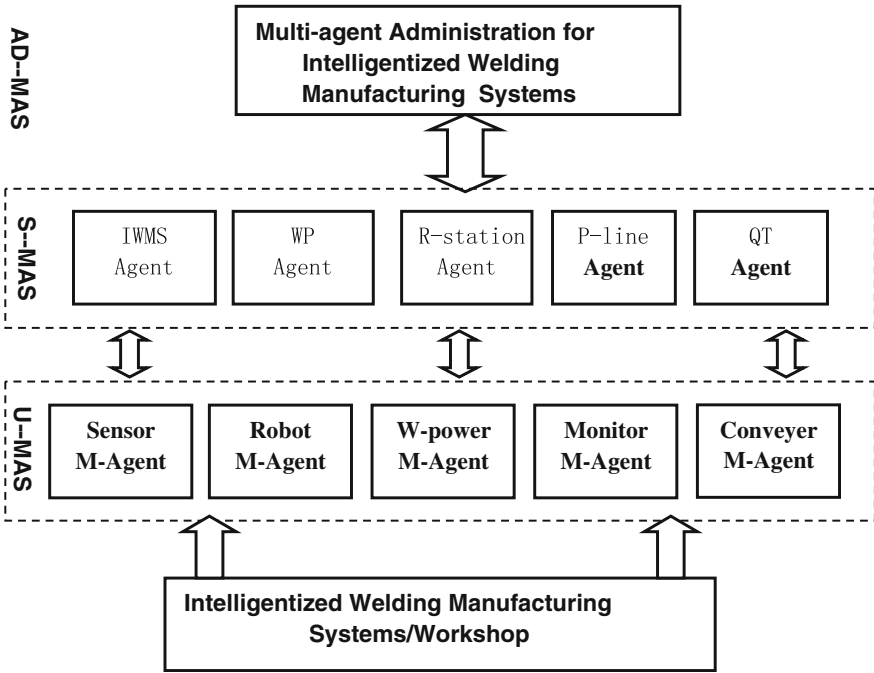
Fig. 30 Multi-agents model for distributed intelligent robotic welding line/systems

4. A multi-agents method for IWMS

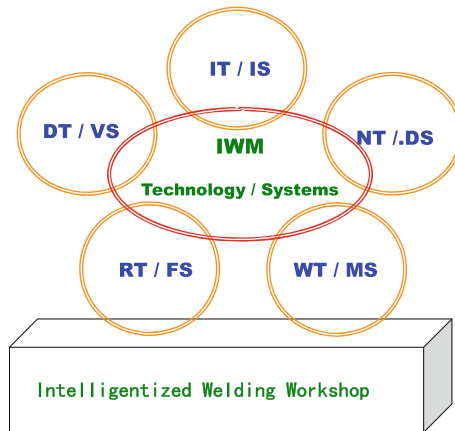
The MAS modeling and control method, are highly suitable for the IWMS, we developed an improved MAS model for the IWMS in this paper, as Fig. 31.

**3.5 On Intelligentized Welding Manufacturing Engineering**

Based on the IWMT related to scientific and technical researching contents, a concept on intelligentized welding manufacturing engineering (IWME) is introduced for a systematized research and application engineering of the IWMT/S. Figure 32 shows for a simple subject compositions of the pentabasic IWMT/S schematic diagram for an intelligentized welding manufacturing workshop (IWMW), which briefly reveals the main scientific and technical elements of the IWME [97–100]. And Fig. 33 is an example application of the IWME for the IWMW of the oceanic drill platform.



**Fig. 31** The MAS model for IWMS. **Abbreviations:** *IWMS* intelligentized welding manufacturing systems; *WP* welding process; *R* robot; *P* production; *QT* quality test; *W* welding; *AD* administration; *S* system; *U* unit



**Fig. 32** The pentabasic IWMT/S schematic diagram for the IWMW. *IT* informatization technology; *IS* intelligent System; *DT* digitization technology; *VS* virtuality system; *NT* networking technology; *DS* distributed systems; *RT* robot technology; *FS* flexible systems; *WT* welding technology; *MS* manufacturing systems

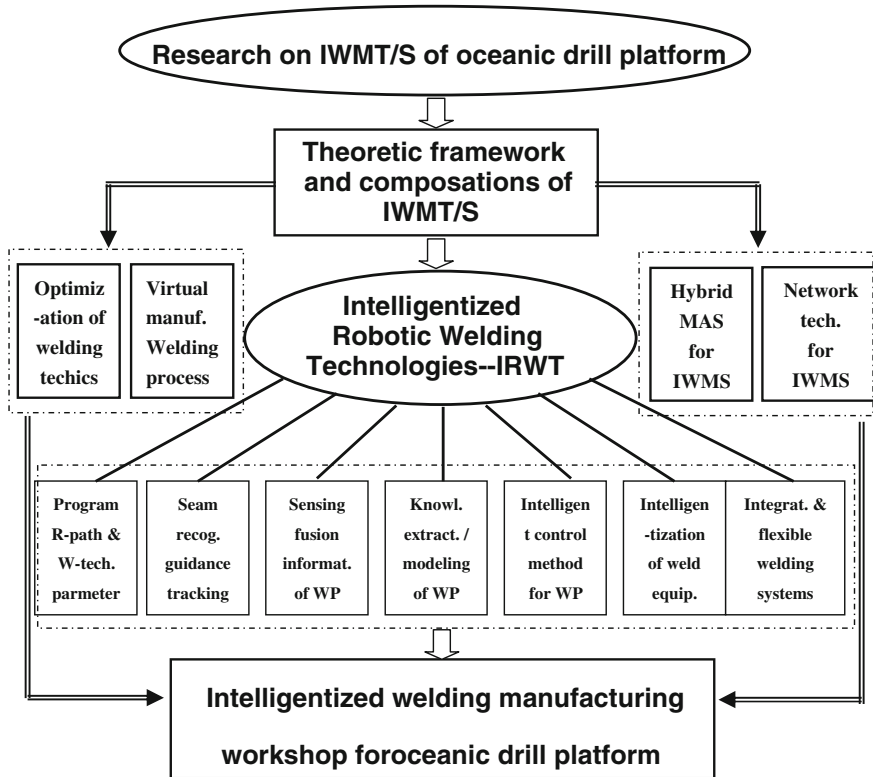


Fig. 33 The IWME schematic diagram for the IWMW of oceanic drill platform

## 4 Conclusion

In this paper, we have presented some concepts on intelligentized welding manufacturing (IWM), and the framework and constitution of technologies and systems for the IWM, such as the intelligentized welding manufacturing technology/systems (IWMT/S), intelligentized robotic welding technology/systems (IRWT/S) and intelligentized welding manufacturing engineering (IWME). The author hopes that it is instructive to investigate the IWM as a systematization of intending research framework and constitution on the IWMT/S. This paper has also shown some new evolutions of research results on the IWMT/S in the IRWTL at SJTU.

At present, there is an evident trend that artificial intelligent technology is widely used into almost manufacturing and engineering processes. The motivation of introducing the concepts, IWMT/S, IRWT/S, and IWME, research framework and constitution of intelligentized welding manufacturing in this paper, is to promote systematization research for forming an organic combination of modern welding manufacturing and artificial intelligent technology.

**Acknowledgments** This work was supported by National Natural Science Foundation of China, No. 61374071; Shanghai Sci. & Tech. Commit., No. 11111100302, P. R. China. The author thanks his all Ph.D. students who made in the contribution to this paper.

## References

1. Drews P, Starke G (1994) Welding in the century of information technology. *Weld World* 34:1–20
2. Dilthey U, Stein L (1992) Robot system for arc welding—current position and future trends. *Weld Cutting* 8:E150–E152
3. Pan JL (1999) A survey of welding sciences in 21st century. In: *Proceeding of 9th Chinese welding conference*, vol 1. Tianjun, China, pp D-001–D-017
4. Trailer (1995) Manufacturer depends on robotic welding to boost production. *Weld J* 74 (7):49–51
5. Tarn TJ, Chen SB, Zhou CJ (2004) *Robotic welding, intelligence and automation*. Springer, Berlin, (LNCIS 299)
6. Tarn TJ, Chen SB, Zhou CJ (2007) *Robotic welding, intelligence and automation*. Springer, Berlin, (LNCIS 362)
7. Tarn TJ, Chen SB, Fang G (2011) *Robotic welding, intelligence and automation*. Springer, Berlin, (LNEE 88)
8. Chen SB, Lou YJ, Wu L, Zhao DB (2000) Intelligent methodology for measuring, modeling, control of dynamic process during pulsed GTAW—part I bead-on-plate welding. *Weld J* 79:151s–163s
9. Chen SB, Zhao DB, Wu L, Lou YJ (2000) Intelligent methodology for measuring, modeling, control of dynamic process during pulsed GTAW—part II butt welding. *Weld J* 79:164s–174s
10. Chen SB, Wu J (2009) *Intelligentized technology for arc welding dynamic process*. Springer, Berlin, (LNEE 29)
11. Chen SB, Lv N (2014) Research evolution on intelligentized technologies for arc welding process. *J Manuf Process* 16:109–122. Available online 21 Sept 2013 15(4):45–65 (Invited paper)
12. Chen SB (2011) Research evolution on intelligentized technologies for robotic welding at SJTU. *Lecture notes in electrical engineering*, vol 88, pp 3–14
13. Chen S (2003) On intelligentized technologies for modern welding manufacturing. *Chin J Mech Eng* 16:367–370
14. Chen S (2004) The concept and technologies on intelligentized welding manufacturing engineering. *Trans China Weld Inst* 25:124–128
15. Masumoto L, Araya T, Iochi A, Normura H (1983) Development and application of sensors and sensor system for arc welding. *J Jpn Weld Soc* 52:39–47
16. Carlson NM, Johnson JA (1988) Ultrasonic sensing of weld pool penetration. *Weld J* 67:239s–246s
17. Guu AC, Rokhlin SI (1992) Arc weld process control using radiographic sensing. *Mater Eval* 11:1344–1348
18. Futamata M (1983) Application of arc sound for detection of welding process. *Q J JWS* 1:11–16
19. Zhang YM, Kovacevic R, Li L (1996) Characterization and real-time measurement of geometrical appearance of weld pool. *Int J Mach Tool Manufact* 36(7):799–816
20. Wang JJ, Lin T, Chen SB (2005) Obtaining of weld pool vision information during aluminum alloy TIG welding. *Int J Adv Manuf Tech* 26:219–227
21. Laiping L, Shanben C, Tao L (2005) The modeling of welding pool surface reflectance of aluminum alloy pulse GTAW. *Mater Sci Eng A* 394:320–326

22. Du QY, Chen SB, Lin T (2006) Inspection of weld shape based on the shape from shading. *Int J Adv Manuf Technol* 27(7–8):667–671
23. Chen SB (2007) Visual information acquirement and real-time control methodologies for weld pool dynamics during pulsed GTAW. *J Mater Sci Forum* 539:3996–4001
24. Fan C, Lv F, Chen S (2009) Visual sensing and penetration control in aluminum alloy pulsed GTA welding. *Int J Adv Manuf Technol* 42:126–137
25. Wu J, Chen SB (2007) Software system designs of real-time image processing of weld pool dynamic characteristics. *Lecture notes in control and information sciences, robotic welding, intelligence and automation, LNCIS 362*. Springer, pp 303–310
26. Chen B, Wang J, Chen S (2010) A study on applications of multi-sensor fusion in pulsed GTAW. *Ind Robot Int J* 37(2):168–176
27. Chen B, Chen SB (2011) A study on applications of multi-sensor information fusion in pulsed-GTAW. *Lecture notes in electrical engineering, robotic welding, intelligence and automation, LNEE, vol 88*. Springer, pp 245–252
28. Chen B, Wang J, Chen S (2010) Prediction of pulsed GTAW penetration status based on BP neural network and D-S evidence theory information fusion. *Int J Adv Manuf Technol* 48(1–4):83–94
29. Chen B, Chen S (2010) Multi-sensor information fusion in pulsed GTAW based on fuzzy measure and fuzzy integral. *Assembly Autom* 30(3):276–285
30. Itti L, Koch C, Niebur E (1998) A model of saliency-based visual attention for rapid scene analysis. *IEEE Trans Pattern Anal Mach Intell* 20(11):1254–1259
31. Cai M, Lv N, Zhong J, Lin T, Chen S (2012) Image process for aluminium alloy weld pool based on ROI detection. *J Shanghai Jiao Tong Univ* 46:103–105
32. Zhang Y, Lv N, Huang Y-M, Chen S-B (2014) Feature characters extraction with visual attention method based on three-path vision sensing of Al alloy GTAW welding. *Transactions of the China Welding Institution*
33. Cudina M, Prezelj J, Polajnar I (2008) Use of audible sound for on-line monitoring of gas metal arc welding process. *Metalurgija* 47(2):81–85
34. Wang JF, Lv F, Chen SB (2009) Analysis of arc sound characteristics for gas tungsten argon welding. *Sens Rev* 29(3):240–249
35. Z Ye, Chen SB et al (2011) Feature selection of arc acoustic signals used for penetration monitoring. *Lecture notes in electrical engineering, robotic welding, intelligence and automation, LNEE, vol 88*. Springer, pp 203–210
36. Lv N, Xu Y, Zhong J, Chen H, Wang J, Chen S (2013) Research on detection of welding penetration state during robotic GTAW process based on audible arc sound. *Ind Robot: Int J* 40(5):474–493
37. Lv N, Xu Y, Zhang Z, Wang J, Chen B, Chen S (2013) Audio sensing and modeling of arc dynamic characteristic during pulsed Al alloy GTAW process. *Sens Rev* 33(2):141–156
38. Mirapeix J, Cobo A, Fernandez S et al (2008) Spectroscopic analysis of the plasma continuum radiation for on-line arc-welding defect detection. *J Phys D Appl Phys* 41(13):1–8
39. Yu H, Xu Y, Lv N, Chen H, Chen S (2013) Arc spectral processing technique with its application to wire feed monitoring in Al-Mg alloy pulsed gas tungsten arc welding. *J Mater Process Technol* 213(5):707–716
40. Yu H, Chen H, Xu Y, Zhang Z, Chen S (2013) Spectroscopic diagnostics of pulsed gas tungsten arc welding plasma and its effect on weld formation of Al-Mg alloy. *Spectrosc Lett* 46(5):350–363
41. Yu H, Ye Z, Chen S (2013) Application of arc plasma spectral information in the monitor of Al-Mg alloy pulsed GTAW penetration status based on fuzzy logic system. *Int J Adv Manuf Technol* 68(9–12):2713–2727
42. Zhang Z, Yu H, Lv N, Chen S (2013) Real-time defect detection in pulsed GTAW of Al alloys through on-line spectroscopy. *J Mater Process Technol* 213(7):1146–1156
43. Chen SB, Wu J, Du QY (2011) Non-linear modelling and compound intelligent control of pulsed gas tungsten arc welding dynamics. *Proc Inst Mech Eng Part I J Syst Control Eng* 225 (11):113–124

44. Chen H (2009) The development of robotic GTAW quality control system for the five-port connector. Ph.D. dissertation of Shanghai Jiao Tong University
45. Kovacevic R, Zhang YM (1997) Neuro-fuzzy model-based weld fusion state estimation. *IEEE Trans Control Syst Technol* 5(4):30–42
46. Wang B, Chen SB, Wang JJ (2005) Rough set based knowledge modeling for the aluminum alloy pulsed GTAW process. *Int J Adv Manuf Technol* 25(9–10):902–908
47. Wang WY, Chen SB et al (2011) Rough set-based model for penetration control of GTAW. *Lecture notes in electrical engineering, robotic welding, intelligence and automation, LNEE*, vol 88. Springer, pp 211–218
48. Li WH, Chen SB, Lin T (2007) Discretization in rough set modeling method for welding process. *Lecture notes in control and information sciences, robotic welding, intelligence and automation, LNCIS 362*. Springer, pp 325–332
49. Li WH, Chen SB, Wang B (2008) A variable precision rough set based modeling method for pulsed GTAW. *Int J Adv Manuf Technol* 36(11–12):1072–1079
50. Huang XX, Chen SB (2006) SVM-based fuzzy modeling for the arc welding process. *Mater Sci Eng A* 427(1–2):181–187
51. Huang X, Shi F, Gu W, Chen S (2009) SVM-based fuzzy rules acquisition system for pulsed GTAW process. *Eng Appl Artif Intell* 22(8):1245–1255
52. Ma H (2010) Research on mixed logical dynamical modeling method of robotic Al alloy pulsed TIG welding process based in vision sensing. Ph.D. dissertation of Shanghai Jiao Tong University
53. Ma H, Wei S, Li L, Lin T, Chen S (2011) Mixed logical dynamical model of the pulsed gas tungsten arc welding process with varied gap. *Proc Inst Mech Eng Part I-J Syst Control Eng* 225(3):270–280
54. Ma HB, Chen SB (2011) Mixed logical dynamical model for robotic welding system. *Lecture notes in electrical engineering, robotic welding, intelligence and automation, LNEE*, vol 88. Springer, pp 123–128
55. Ma H, Wei S, Lin T, Chen S (2010) Mixed logical dynamical model for back bead width prediction of pulsed GTAW process with misalignment. *J Mater Process Technol* 210(14):2036–2044
56. Ma HB, Chen SB (2011) Study on the MLD modeling method of pulsed GTAW process for varied welding speed. *Lecture notes in electrical engineering, robotic welding, intelligence and automation, LNEE*, vol 88. Springer, pp 271–278
57. Cook GE (1995) Weld modeling and control using artificial neural networks. *IEEE Trans Ind Appl* 31:1484–1491
58. Zhang YM, Kovacevic R, Li L (1996) Adaptive control of full penetration GTA welding. *IEEE Trans Control Syst Technol* 4(4):394–403
59. Chen SB, Wu L, Wang QL (1997) Self-learning fuzzy neural networks for control of uncertain systems with time delays. *IEEE Trans Syst Man Cyb Part B* 27:142–148
60. Zhao DB, Chen SB, Wu L, Chen Q (2001) Intelligent control for the double-sided shape of the weld pool in pulsed GTAW with wire filler. *Weld J*. 80:253s–260s
61. Zhang GJ, Chen SB, Wu L (2005) Intelligent control of pulsed GTAW with filler metal. *Weld J*. 80(1):9s–16s
62. Fan C (2008) Weld pool characters extraction and intelligent control during varied gap Al alloy pulsed GTAW process. Ph.D. dissertation of Shanghai Jiao Tong University
63. Lv FL, Chen SB, Dai SW (2007) A model-free adaptive control of pulsed GTAW. *Lecture notes in control and information sciences, robotic welding, intelligence and automation, LNCIS*, vol 362. Springer, pp 333–339
64. Lv FL, Wang JF, Fan CJ, Chen SB (2008) An improved model-free adaptive control with G function fuzzy reasoning regulation design and its applications. *Proc Inst Mech Eng Part I-J Syst Control Eng* 222(18):817–828
65. Lv F, Chen H, Fan C, Chen S (2010) A novel control algorithm for weld pool control. *Ind Robot: Int J* 37(1):89–96



66. Chen SB (2007) On the key intelligentized technologies of welding robot. Lecture notes in control and information sciences, LNCIS, vol 362. pp 105–116
67. Chen XZ, Chen SB, Lin T et al (2006) Practical method to locate the initial weld position using visual technology. *Int J Adv Manuf Technol* 30(7–8):663–668
68. Chen XZ, Chen SB (2010) The autonomous detection and guiding of start welding position for arc welding robot. *Ind Robot: Int J* 37(1):70–78
69. Ye Z, Fang G, Chen S, Dinham M (2013) A robust algorithm for weld seam extraction based on prior knowledge of weld seam. *Sens Rev* 33(2):125–133
70. Ye Z, Fang G, Chen S, Zou JJ (2013) Passive vision based seam tracking system for pulse-MAG welding. *Int J Adv Manuf Technol* 67(9–12):1987–1996
71. Zhou L, Lin T, Chen SB (2006) Autonomous acquisition of seam coordinates for arc welding robot based on visual servoing. *J Intell Rob Syst* 47(3):239–255
72. Shen H, Wu J, Lin T, Chen S (2008) Arc welding robot system with seam tracking and weld pool control based on passive vision. *Int J Adv Manuf Technol* 39(7–8):669–678
73. Shen H, Lin T, Chen S et al (2010) Real-time seam tracking technology of welding robot with visual sensing. *J Int Rob Syst* 59:283–298
74. Wei S, Ma H, Lin T, Chen S (2010) Autonomous guidance of initial welding position with single camera and double positions method. *Sens Rev* 30(1):62–68
75. Ma H, Wei S, Sheng Z, Lin T, Chen S (2010) Robot welding seam tracking method based on passive vision for thin plate closed-gap butt welding. *Int J Adv Manuf Technol* 48(9):945–953
76. Chen SB, Chen XZ, Li JQ, Lin T (2005) Acquisition of welding seam space position information for arc welding robot based on vision. *J Intell Rob Syst* 43(1):77–97
77. Wei S, Kong M, Lin T, Chen S (2011) Three-dimensional weld seam tracking for robotic welding by composite sensing technology. *Ind Robot: Int J* 38(5):500–508
78. Chen X-Z, Huang Y-M, Chen S-b (2012) Model analysis and experimental technique on computing accuracy of seam spatial position information based on stereo vision for welding robot. *Ind Robot: Int J* 39(4):349–356
79. Xu Y, Lv N, Zhong J, Chen H, Chen S (2012) Research on the real-time tracking information of three-dimension welding seam in robotic GTAW process based on composite sensor technology. *J Intell Rob Syst* 68(2):89–103
80. Xu Y, Zhong J, Ding M, Chen H, Chen S (2013) The acquisition and processing of real-time information for height tracking of robotic GTAW process by arc sensor. *Int J Adv Manuf Technol* 65(5–8):1031–1043
81. Chen SB, Wang WY, Ma HB (2010) Intelligent control of arc welding dynamics during robotic welding process. *J Mater Sci Forum* 638:3751–3756 (The invited paper of the THERMEC 2009)
82. Chen H, Lv F, Lin T, Chen S (2009) Closed-loop control of robotic arc welding system with full-penetration monitoring. *J Intell Rob Syst* 56:565–578
83. Ma H, Wei S, Lin T, Chen S, Li L (2010) Binocular vision system for both weld pool and root gap in robot welding process. *Sens Rev* 30(2):116–123
84. Shen HY, Ma HB, Lin T, Chen SB (2007) Research on weld pool control of welding robot with computer vision. *Ind Robot* 34(6):467–475
85. Kong M, Chen S-B (2008) Al alloy weld pool control of welding robot with passive vision. *Sens Rev* 29(1):28–37
86. Wu M, Gao X, Yan WX, Fu Z, Zhao Y, Chen S (2011) New mechanism to pass obstacles for magnetic climbing robots with high payload, using only one motor for force-changing and wheel-lifting. *Ind Robot: Int J* 38(4):372–380
87. Wu M, Pan G, Zhang T, Chen S, Zhuang F, Zhao Y-Z (2013) Design and optimal research of a non-contact adjustable magnetic adhesion mechanism for a wall-climbing welding robot. *Int J Adv Rob Syst* 10(63)
88. Zhang T, Chen S, Wu M, Zhao Y, Chen X (2013) Optimal motion planning of all position autonomous mobile welding robot system for fillet seams. *IEEE Trans Autom Sci Eng* 10(4):1147–1151

89. Ma G (2005) Research on model and control of robotic welding flexible manufacturing system with petri net. Ph.D. dissertation of Shanghai Jiao Tong University
90. Ma GH, Chen SB, Lin T (2007) Modeling and controlling the FMS of a welding robot. *Int J Adv Manuf Tech* 34(11–12):1214–1223
91. Ma GH, Chen SB (2007) Model on simplified condition of welding robot system. *Int J Adv Manuf Tech* 33(9–10):1056–1064
92. Piao Y-J, Tao L, Tao Q, Chen S (2002) Application of multi-agent systems in welding flexible manufacturing system. *Trans China Weld Inst* 23(5):87–90
93. Piao Y, Zhu Z, Chen S (2004) Multi-agent collaboration control for multi-manipulator WFMS. *J Syst Simul* 16(11):2571–2574
94. Piao Y (2004) Study on multi-agent collaboration controlling for welding flexible manufacturing cell. Ph.D. dissertation of Shanghai Jiao Tong University
95. Yang CD, Chen SB (2011) Survey on modeling and controlling of welding robot systems based on multi-agent. Lecture notes in electrical engineering, robotic welding, intelligence and automation, LNEE, vol 88. Springer, pp 107–113
96. Chen W, Chen S (2013) Web based motion simulation and control of arc welding robot. In: “Award of Excellent Paper”, 2013 international symposium on advanced intelligent manufacturing technology. Beijing, China, 27 June 2013
97. Zhong JY, Chen SB et al (2011) Research on the robotic arc welding of a five-port connector. Lecture notes in electrical engineering, robotic welding, intelligence and automation, LNEE, vol 88. Springer, pp 115–122
98. Zhang HJ, Chen SB et al (2011) Robot path planning in multi-pass weaving welding for thick plates. Lecture notes in electrical engineering, robotic welding, intelligence and automation, LNEE, vol 88. Springer, pp 351–359
99. Zhang HJ, Cai CB, Yu ZS, Chen SB (2013) Control of root pass stress by two-side arc welding for thick plate of high strength steel. *Rev Adv Mater Sci* 33:298–304
100. Yang C, Zhang H, Chen Y, Zhong J, Chen S(2013) The effect of DSAW on preheating temperature in welding thick plate of low alloy high strength steel. *Int J Adv Manuf Technol* 1–8. doi:[10.1007/s00170-013-5287-0](https://doi.org/10.1007/s00170-013-5287-0)

# Effects of Arc-Sidewall Distance on Arc Appearance in Narrow Gap MAG Welding

Hu Lan, Hua-Jun Zhang, De-Long Zhao, A-Jing Chen  
and Shang-Yang Lin

**Abstract** Arc appearance is a key factor to sidewall fusion in narrow gap MAG welding (NG-MAG). By observing arc images with high-speed video and weld cross-sections at different arc-sidewall distances in NG-MAG vertical welding, it was discovered that the arc ascended along the groove sidewalls and arc appearance changed from cone to olive when the arc-sidewall distance was relatively small, which contributed to large weld concavity and significant “bead separation” phenomenon. On the other hand, arc length and arc appearance were stable as the arc-sidewall distance was relatively large. Due to not being heated directly and effectively by the arc high temperature zone, the sidewall penetration was low and weld was convex. Only when the arc-sidewall distance was controlled in the range of 2.0 to 3.0 mm, the arc was stable and the weld appearance was concave. Also, the penetration of groove sidewalls was deep. Thus, the sidewall fusion in NG-MAG vertical welding is highly sensitive to process parameters under the low heat input conditions. The laws being discovered above will make a good preparation for the realization of thick high strength low alloy steel (HSLA) plates with NG-MAG automatic welding technology in ocean engineering.

---

H. Lan (✉)

Rongcheng Campus, Harbin University of Science and Technology,  
Rongcheng 264300, China  
e-mail: lanhucx@163.com

H.-J. Zhang · D.-L. Zhao · A.-J. Chen  
Welding Institute, Shanghai Zhenhua Heavy Industries Co., Ltd,  
Shanghai 200125, China

S.-Y. Lin  
Harbin Welding Institute, Mechanical Engineering Research Institute,  
Harbin 150080, China

## 1 Introduction

In recent years, with increasing on the size of welded structures and the thickness of steel plates, high production efficiency and quality, and excellent joint mechanical properties are required, which conventional welding methods can not meet [1]. However, Narrow gap MAG welding (NG-MAG) is an energy-saving technology of welding joints of large wall thickness in a narrow gap with minimum groove dimensions. Correspondingly, such gaps should result in a decrease in the cross-section areas of the welding gap, and a decrease in the consumption of welding consumables, welding time, electric energy, deformation and stresses in welding structures [2].

NG-MAG, as a special industrial technology, needs to solve a key technical problem of improving the stability of double sidewall penetration. Studies have shown that the most direct factor, influencing sidewall fusion, is the heat effect of arc on the sidewalls [3]. Currently, the main approach to enhance this heat effect is changing the arc appearance near groove sidewalls, such as bending the wire [4–6], oscillating the electrode [7–10], moving the arc up and down in the gap [11], swing the arc transversely and periodically in groove with applied magnetic field [12], constraining the arc with flux [13] and so on. But it was discovered that sidewall fusion is sensitive to NG-MAG welding process parameters under low heat input conditions in practical applications. If the arc-sidewall distance (the distance between wire tip i.e. the center of arc and the sidewall) is not controlled properly, short arc-sidewall distance will lead to arc climbing up along the groove sidewalls and destroy the arc appearance, while long arc-sidewall distance will contribute to no effective heating to the sidewalls with arc high energy zone. Both conditions above will result in poor sidewall fusion. Therefore, controlling a reasonable arc-sidewall distance is the basic premise to maintain a desirable arc heating shape and the basic guarantee to achieve uniform sidewall fusion.

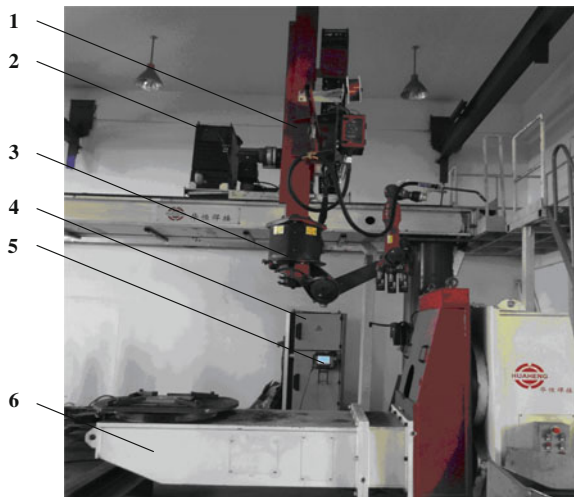
Reference [14] employed deposition experiments to research two typical visual arc appearances (conical and wispy) and the characteristics of heating on the weld pool in pulsed metal arc welding. Reference [15] adopted mathematical derivation and numerical calculation methods to analyze the heat input distributions in traditional V-shaped and U-shaped grooves in swing arc welding. Reference [3] analyzed the errors of the arc-work position in the process of narrow gap welding, and studied the influence of the arc-work position on the continuous fusion of the thick wall with corresponding experimental. Reference [16] combined the structure characteristics of small-diameter thick-walled pipe and the properties of 40CrMnMo steel, applied narrow gap pulsed MAG welding technique to the oil drill collars and investigated the gas protection, arc morphology, arc stability, and weld appearance in narrow groove. However, the influence of arc-sidewall distance on arc appearance and sidewall fusion in NG-MAG welding has not been reported. Therefore, in order to get the optimal arc-sidewall distance for heat effect of arc on the wall sidewalls, a large number of experiments about the influence of arc-sidewall distance on arc appearance in robot NG-MAG pulsed welding were

conducted in this paper. This would contribute to define the adaptive ranges of welding process parameters to the errors of groove width and assembly, and provide technology support for thick plates with NG-MAG automatic welding.

## 2 Experimental Procedure

In Fig. 1 is seen the robot NG-MAG pulsed vertical welding system with 11 degrees of freedom (DOF). The whole workstation consists of 6-DOF robot system cooperated with KUKA-KR16, 3-DOF gantry HLV03-13, 2-DOF L-type positioner HDS50 and power source EWM PHOENIX 521 ForceArc. The arc-sidewall distance (described by  $d$ ) experiments were carried out with segmented vertical up welding, and the base metal is Q345B with a groove of 20 mm in width and 12 mm in depth and 3 mm in fillet radius. Shielding gas is Ar mixed with 20 % CO<sub>2</sub> with flow rate in the range of 15–18 L/min. The other detailed welding process parameters are shown in Table 1. The processes of arc-dynamic changes are recorded by a high-speed video in different arc-sidewall distance experiments.

**Fig. 1** Experiment Device of Robot NG-MAG Welding. 1 3-DOF gantry, 2 welding power, 3 robot, 4 controller, 5 teach pendant, 6 L-type 2-DOF positioner



**Table 1** Process parameters of NG-MAG welding

Pulse current (A)	Background current (A)	Arc voltage (V)	Pulse frequency (Hz)	Welding speed (m/min)	<sup>a</sup> Weaving amplitude (mm)	Weaving frequency (Hz)	Dwell time (s)
400–405	50	21.3–22.2	84–108	0.13	6.0–8.8	0.5–0.6	0.2–0.3

<sup>a</sup>Corresponding arc-sidewall distance  $d = 1.2–4.0$  mm

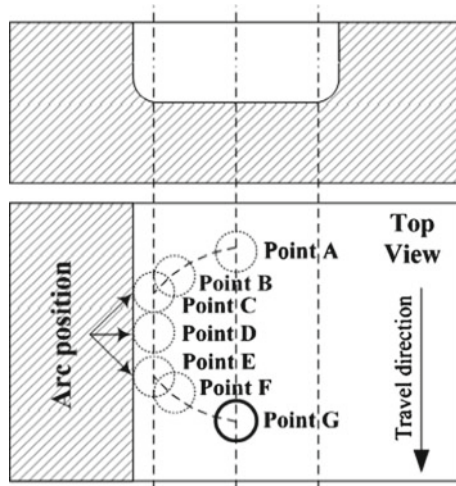


Fig. 2 Torch oscillation positions for measuring arc images

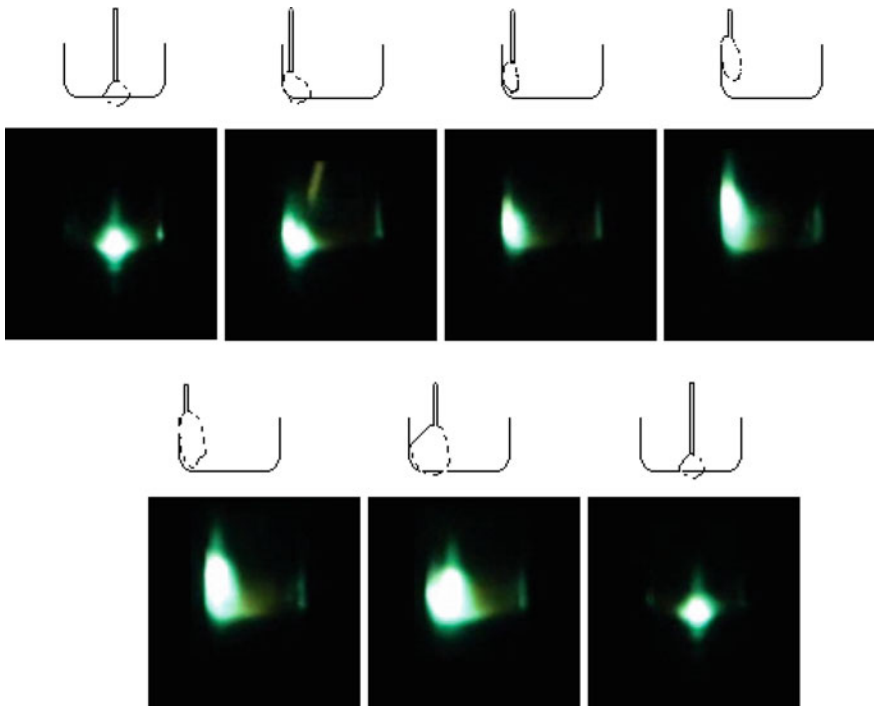
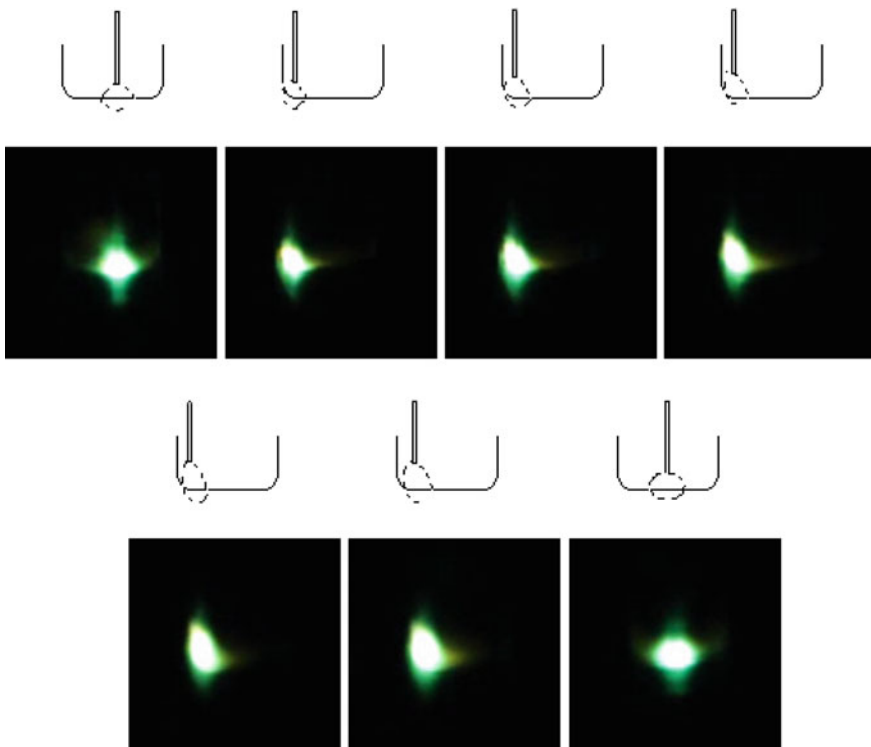


Fig. 3 Arc appearance variation at each torch position for half oscillation cycle of arc-sidewall distance  $d = 1.2$  mm

### 3 Results and Discussion

#### 3.1 Effects of Arc-Sidewall Distance on Arc Appearance

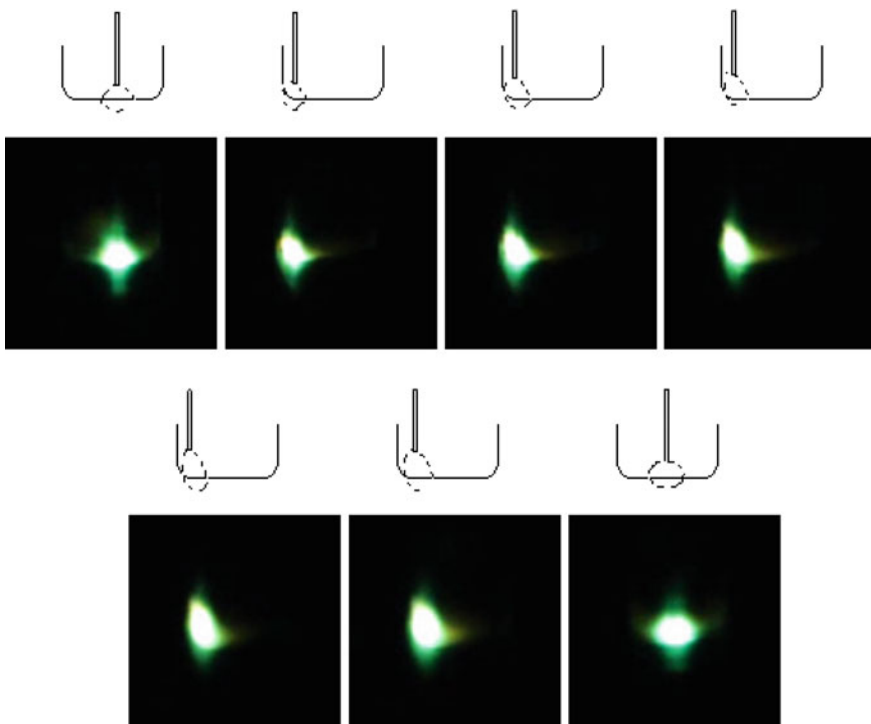
It can be found that the different visual arc appearances are dependent on the changing process of the instantaneous arc appearances in NG-MAG vertical pulsed welding by analyzing the photos taken by high-speed video. As illustrated in the Ref. [14], if the duration of pulse current is long enough, in the vicinity of the weld center, the bright zone of arc (arc appearance) has a dynamic process of changing from wispy to conical. Moreover, after the wispy arc appearance changing into conical, the arc appearance shall keep conical even the role of the pulse current continues until the pulse current stopped. In order to facilitate the analysis of the influence of arc-sidewall distance on the arc appearance in NG-MAG vertical welding, photographs taken in experiments were chosen in accordance with the arc positions shown in Fig. 2. Among the positions shown in Fig. 2, Point A and Point G are at the weld center. Point B and Point F are the positions where arc and sidewall are contacting and detaching with each other in a half cycle of arc swing. While Point C, Point D



**Fig. 4** Arc appearance variation at each torch position for half oscillation cycle of arc-sidewall distance  $d = 1.6$  mm

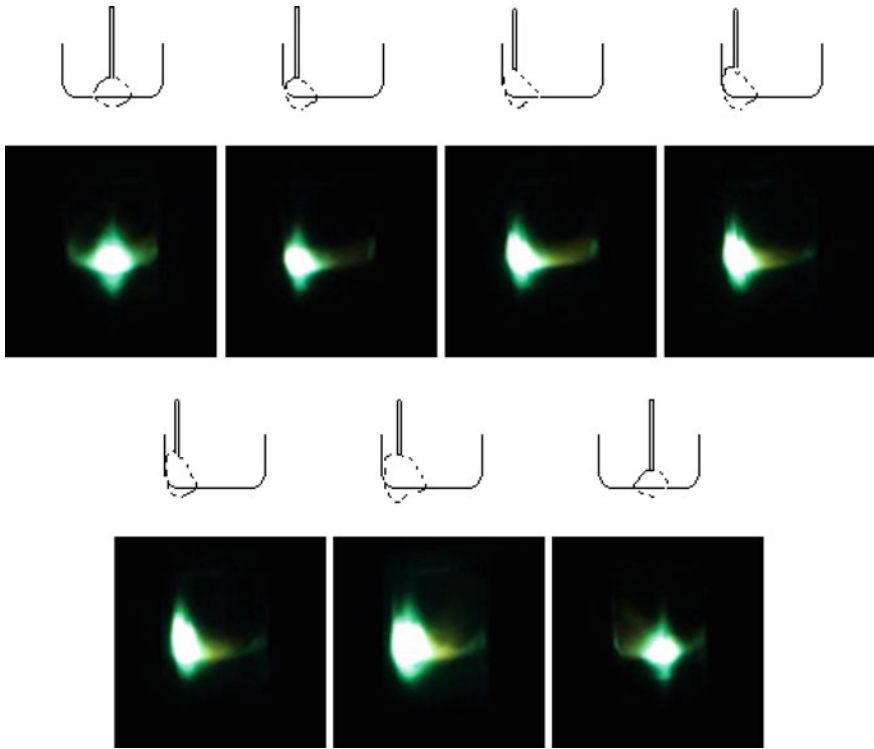
and Point E respectively are at the initial, middle, and end position where arc moved to the edge of weld (maximum swing point). Figures 3, 4, 5, 6, 7 and 8 show the instantaneous arc appearances when the arc is approaching to and departing from the sidewall in the range of arc-sidewall distance of  $d = 1.2\text{--}4.0$  mm.

As can be seen from Figs. 3 and 4, the phenomenon of arc climbing up was obvious when the arc-sidewall distance is small ( $d = 1.2$  or  $1.6$  mm). The arc was lengthening and changing from conical to olive. Also, the wire tip was ascending with the arc approximating to the sidewall successively. While the arc length and arc appearance recovered as the arc was detaching from the sidewall. Generally speaking, the arc length can be maintained stable by inherent self-regulation with constant speed wire feeding in gas metal arc welding (GMAW). That means the arc length can be adjusted by the wire melting rate. In other words, when the arc length is shortened by some factors, the welding current will increase to accelerate the wire melting speed immediately to restore the arc length. According to the principle of minimum voltage, if the arc-sidewall distance was shorter than arc length in the process of NG-MAG welding, the arc would burn between wire and sidewall. Although welding current was increasing rapidly, the cathode spot was climbing up along the sidewall. The ability of self-regulation of arc was lost with the arc



**Fig. 5** Arc appearance variation at each torch position for half oscillation cycle of arc-sidewall distance  $d = 2.0$  mm



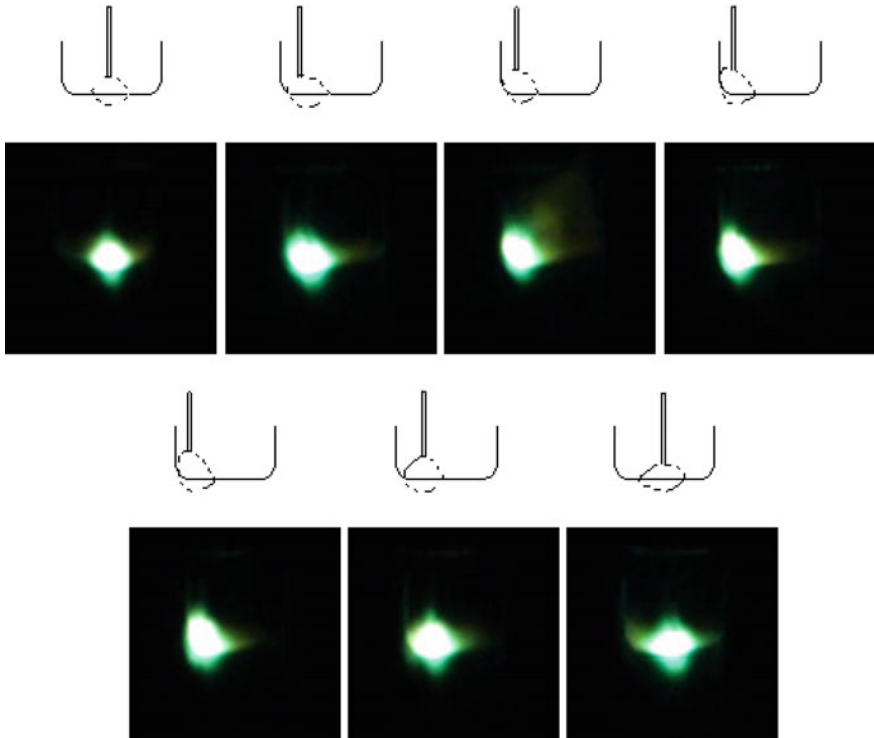


**Fig. 6** Arc appearance variation at each torch position for half oscillation cycle of arc-sidewall distance  $d = 2.4$  mm

ascending. However, the arc length could be shortened by reducing the wire melting speed with its inherent self-regulation in the subsequent departure from the sidewall.

See Figs. 5, 6 and 7, it is clear that the arc was stable with good sidewall fusion, in the whole process of arc approaching to and departing from the sidewall successively, when the arc-sidewall distance  $d = 2.0\text{--}3.0$  mm. And the change of wire extension, arc length and arc appearance was smaller than that of arc-sidewall distance  $d = 1.2$  or  $1.6$  mm.

With increasing the arc-sidewall distance  $d$ , the arc almost remained conical shape. However, the heat effect of arc on the sidewalls was weakened. When  $d = 4.0$  mm, as shown in Fig. 8, the arc edge could just touch the sidewall. In this case, the sidewall was mainly heated by the arc heat radiation and heat conduction of weld pool. Comparing to the occasion that the sidewall was heated by the arc directly (see Figs. 5, 6 and 7), there was a greater chance of emerging poor fusion at the sidewall due to insufficient heat. That's because when the arc-sidewall distance is becoming larger, the high energy zone can not heat the sidewall effectively under low heat input conditions.

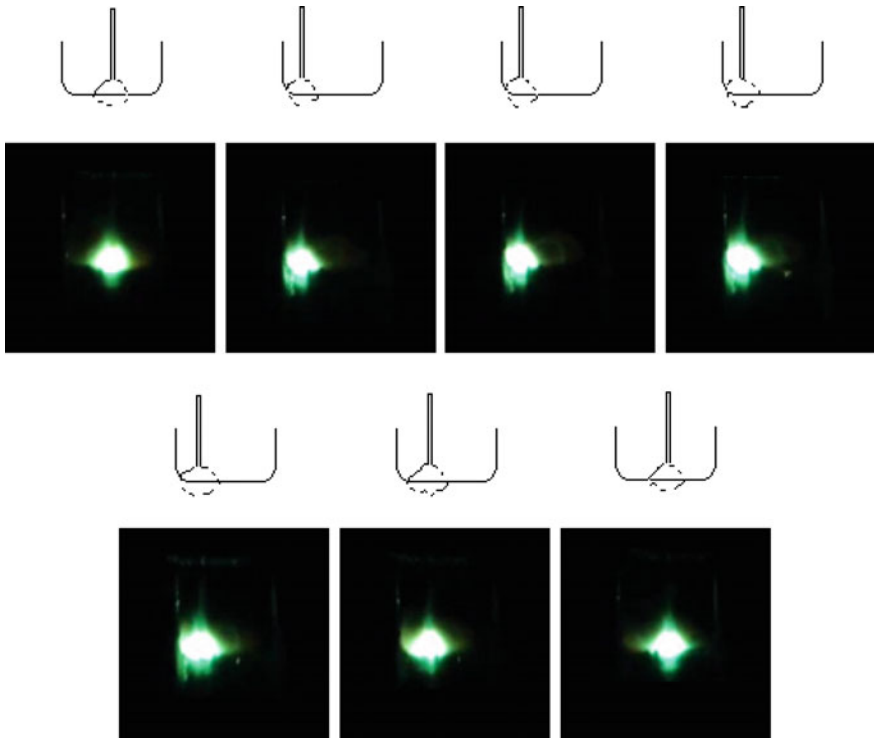


**Fig. 7** Arc appearance variation at each torch position for half oscillation cycle of arc-sidewall distance  $d = 3.0$  mm

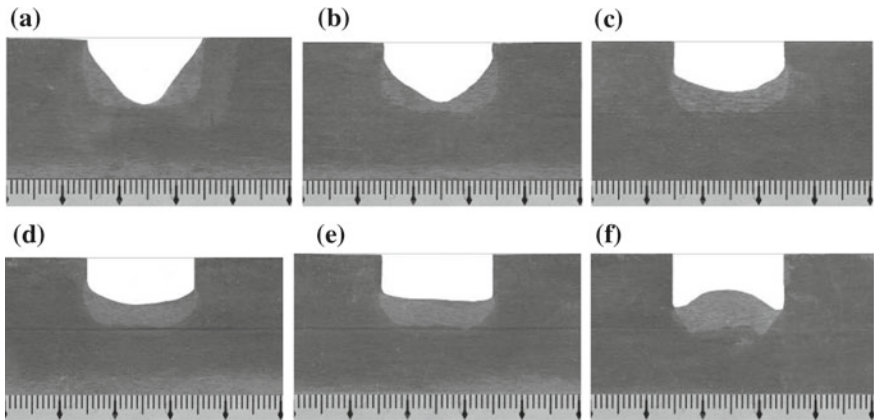
In short, the sidewall fusion has higher sensitivity to process parameters under low heat input conditions in NG-MAG welding, which also confirms the statements above. The arc can maintain a relatively stable shape and heat the sidewall effectively and directly when arc-sidewall distance  $d$  is controlled in the range of 2.0–3.0 mm.

### ***3.2 Effects of Arc-Sidewall Distance on Weld Cross Section***

By observing the cross section of specimens, see Fig. 9, it's easy to find that the arc ascended when the arc-sidewall distance was short ( $d = 1.2$  or  $1.6$  mm), which contributed to too much filler metal on sidewall and too little in center, and significant “bead separation” phenomenon. While heating the sidewall was limited and the welding pool could not dissipate timely with long arc-sidewall distance ( $d = 4.0$  mm), which resulted in high temperature at weld center, the liquid flowing to the center, weld raised significantly and not being conducive to the subsequent

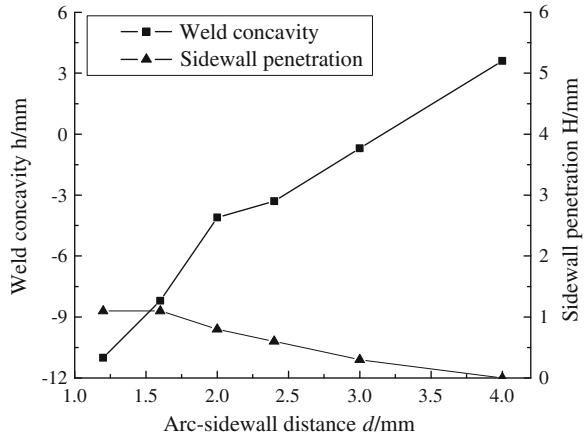


**Fig. 8** Arc appearance variation at each torch position for half oscillation cycle of arc-sidewall distance  $d = 4.0$  mm



**Fig. 9** Weld cross section shape of arc-sidewall distance test: **a**  $d = 1.2$  mm, **b**  $d = 1.6$  mm, **c**  $d = 2.0$  mm, **d**  $d = 2.4$  mm, **e**  $d = 3.0$  mm, **f**  $d = 4.0$  mm

**Fig. 10** Curve of weld cross section shape coefficient



welding. Only when the arc-sidewall distance  $d = 2.0\text{--}3.0$  mm, the weld could be of good sidewall fusion and slightly concave weld appearance.

The curve of shape coefficient of the weld cross sections is shown in Fig. 10. As shown in the figure, the concavity of weld was gradually reduced, and weld appearance finally transformed from slightly concave ( $d = 2.0\text{--}3.0$  mm) to convex ( $d = 4.0$  mm) with the increasing of arc-sidewall distance  $d$ . While the sidewall penetration kept decreasing with the increasing of arc-sidewall distance  $d$ . There was almost no sidewall penetration when the distance  $d = 4$  mm. The laws are consistent with the above analysis of influence of arc-sidewall distance on arc appearance in NG-MAG welding. That is when the arc-sidewall distance  $d = 2.0\text{--}3.0$  mm, continuous and uniform sidewall fusion can be got in NG-MAG welding under low heat input conditions.

## 4 Conclusion

1. The process of NG-MAG pulse welding has a high sensitivity to the welding process parameters under low heat input conditions.
2. The influence of arc-sidewall distance on arc appearance in NG-MAG vertical welding is significant. If arc-sidewall distance is small, arc will climb up along sidewall of the groove quickly to the surface. While the sidewall can not be heated sufficiently as the distance is large, which contributes to large probability of emerging defects.
3. With the increasing of arc-sidewall distance, the weld appearance gradually transforms from concave to slightly concave and convex finally. While the sidewall penetration always shows a tendency of decreasing until it is zero.
4. The welding process is stable and good sidewall fusion can be maintained when the arc-sidewall distance is in the range of 2.0–3.0 mm.

**Acknowledgments** The authors would like to thank the supports of NDRC Major Funded Projects (High-Tech No. [2012]2144 of NDRC Office) and National Natural Science Foundation (51105252).

## References

1. Ellis DJ (1991) Narrow gap welding of steel. *Welding & Metal Fabrication*, vol 59, p 118
2. Zhang FJ, Luo CHH (2000) Narrow gap welding and its new progress. *Weld Technol* 29 (6):33–35
3. Hu CY, Liu GX, Xiao Y et al (2000) The influence of the arc-work position on the continuous fusion of the thick wall. *J South China Univ Technol (Nat Sci Ed)* 30(2):91–93
4. Kawahara M, Asano I (1986) BHK type narrow gap GMA welding process. *Narrow Gap Welding (NGW), The State-of-the-Art in Japan*, 39–45
5. Shono S, Matsumoto O, Kamei H (1986) Development and application of narrow-gap GMA welding process with corrugated wire. *Narrow Gap Welding (NGW), The State-of-the-Art in Japan*, 54–59
6. Kanbe Y, Suda K (1986) Narrow gap welding process with oscillating arc Loopnap. *Narrow Gap Welding (NGW), The State-of-the-Art in Japan*, 60–64
7. Wang JY, Zhu J, Fu P et al (2012) A swing arc system for narrow gap GMA welding. *ISIJ Int* 1:110–114
8. Ding M, Tang XH, Lu FG et al (2011) Welding of quenched and tempered steels with high-spin arc narrow gap MAG system. *Int J Adv Manuf Technol* 55:527–533
9. Nomura H, Sugitani Y, Kobayashi Y (1986) Narrow gap welding process with high speed rotating arc. *Narrow Gap Welding (NGW), The State-of-the-Art in Japan*, 74–80
10. Nakajima H, Nagai A, Minehisa S (1986) Rotating arc narrow gap MIG welding process. *Narrow Gap Welding (NGW), The State-of-the-Art in Japan*, 65–73
11. Araya T (1986) General review—the state-of-the-art of narrow gap welding in Japan. *Narrow Gap Welding (NGW), The State-of-the-Art in Japan*, 13–33
12. Kang YH, Na SJ (2003) Characteristics of welding and arc signal in narrow groove gas metal arc welding using electromagnetic arc oscillation. *Weld J* 82(S):92–99
13. Zheng SHX, Zhu L, Huang BW et al (2009) Constricted arc by flux strips applied to ultra-narrow gap welding. *J Mech Eng* 45(2):119–223
14. Wang QL, Yin SHY, Zhang JH et al (1980) The controllability of the arc appearance and its relation to the metal transfer modes in the pulse MIG welding process. *J Harbin Inst Technol* 4:103–115
15. Yongjae K, Seun R (2005) A study of heat input distribution on the surface during torch weaving in gas metal arc welding. *JSME Int J* 48(3):144–150
16. Ba LJ, Ma CX, Zhang TJ et al (2013) Narrow gap pulsed MAG welding of 40CrMnMo thick-walled pipe. *Trans China Weld Inst* 34(6):101–104

# Tacked Weld Point Recognition from Geometrical Features

Fu-Qiang Liu, Zong-Yi Wang, Xing-Jian Wang and Yu Ji

**Abstract** In order to guarantee that a workpiece is securely fixed during a welding process, some areas of the workpiece should be tack welded before the formal welding process starts. Weld seam images captured at these tacked weld points, however, will be different from normal weld seam images. These differences present a difficulty when trying to obtain accurate feature points from an image. Tacked weld point recognition is the key factor of the robustness and stability in the tracking process of welding. It is easy to distinguish tacked weld points on regular fillet weld seam images, rather than irregular fillet and overlapped weld seam images. This paper analyzes the geometrical features of tacked weld points and introduces the methods to recognize these tacked weld points. Experimental results show that the methods proposed by this paper are robust and the weld point recognition is accurate.

## 1 Introduction

In the welding process, heat accumulates in the workpiece and can't spread out in a short time, resulting in possible deformation of the workpiece. In some instances, these deformations can make workpieces unusable. In other instances deformed workpieces may need to be tack welded to prevent their dropping out in the hoisting process.

---

F.-Q. Liu · Z.-Y. Wang (✉) · Y. Ji  
Department of Automation, Harbin Engineering University (HEU), Harbin 150001,  
People's Republic of China  
e-mail: hirobot@163.com

F.-Q. Liu · Z.-Y. Wang  
Harbin XiRobot Co., Ltd, Harbin 150060, People's Republic of China

X.-J. Wang  
University of Wisconsin-Madison, Madison 53706-1481, USA

Therefore, tack welding is necessary before the formal welding process. Some additional tacked weld points may be created after the formal welding process. In captured images, the geometrical features of these tacked weld points will be different from those of the normal weld seams [1]. When the normal weld seam is covered by tacked weld points, the feature point may not be found at all. This presents difficulties for the vision tracking process.

There are two ways to address these issues:

1. Ignore the result of image processing at the areas where there are tacked weld points, or do not adjust based on the error.
2. Make use of the a priori knowledge of the weld seam. For example, if the type of the weld seam is a line-type or circular-type, then fit the adjustment values of the weld gun by using the feature point information captured before and after meeting the tacked weld points.

There are only a few papers and research projects which address tacked weld point recognition. This paper introduces the geometrical features and recognition methods for the tacked weld points on the fillet weld seams.

## 2 Geometrical Features and Recognition Methods of Tacked Weld Points

In general, there are differences of geometrical features between the images with and without tacked weld points, including the differences of the slope and position of the laser light.

This paper analyzes the geometrical features of two types of tacked weld points on the fillet weld seams.

1. Tacked weld points on the fillet weld seams with regular shapes

We can use a priori knowledge of the weld seam while recognizing the tacked weld points on fillet weld seams with regular shapes. The structured light image can be processed with the template matching method, and then be compared with the template of the matched part in the image. We can recognize the tacked weld point with the geometrical feature differences between the template and the matched part.

Figure 1 is a picture of a saddle-shape fillet weld seam. This picture was captured at China International Marine Containers (Group) Ltd., NanTong. The welding robot designed by Harbin XiRobot Co., Ltd. successfully completed the welding experiments.

Figure 2a, b are images of weld seams, respectively, without and with tacked weld point. As can be seen, the middle segment of structured light is especially short, consequently it is difficult to find the feature point while structured light encounters the tacked weld point.

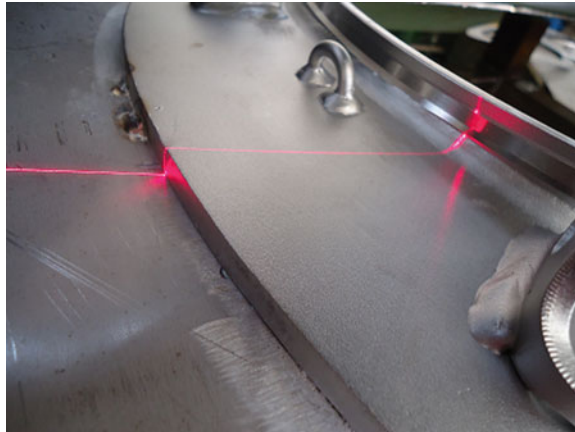


Fig. 1 Saddle-shape fillet weld seam

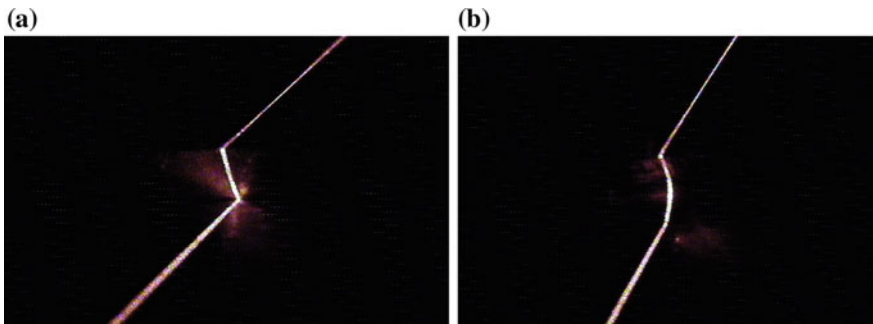


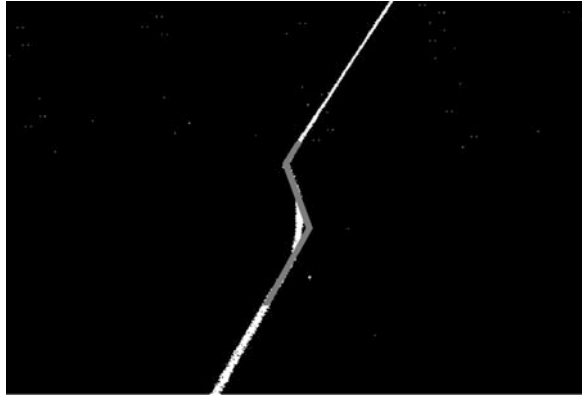
Fig. 2 a Weld seam without tacked weld point. b Weld seam with tacked weld point

From the two pictures above it can be seen that the structured light is composed of three line segments. Where there is a tacked weld point, the transition of the two line segments below becomes smooth. At the same time, the inflection point of the two line segments below is covered by the tacked weld point, consequently the inflection point cannot be found by using sliding window method [2]. Because the shapes of this type of weld seams are regular, the information given by the line segments in the figure can also be used. This paper finds the feature point using the template matching method. Figure 3 shows the result of the template matching.

The gray part of Fig. 3 is the template, and the white part is the structured light after threshold process. From the result of Fig. 3 we can conclude that, because of the consideration of the global matching degree, the template matching method is not sensitive to the irregular bend caused by the tacked weld point. After the template matching process, tacked weld points can be recognized according to the differences of the feature points on the template and the source image.



**Fig. 3** The result of template matching

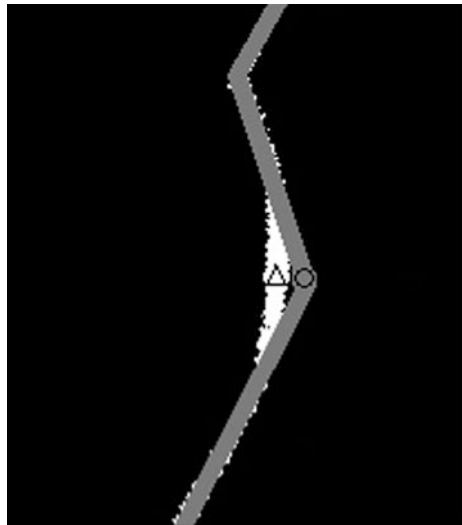


**Algorithm 1** Tacked weld point recognition according to the template and the matched part in the image

1. Get the coordinate of the feature point on the source image  $(x_t, y_t)$ .
2. Find the area where the sum of gray value is the maximum between line  $(y_t - y_{\text{delta}})$  and line  $(y_t + y_{\text{delta}})$ , and this area determines the feature point position  $(x_r, y_r)$  changed because of the existence tacked weld point.

The circle in Fig. 4 represents the area of feature point after template matching, and the triangle represents the area of feature point changed because of the existence tacked weld point.

**Fig. 4** Feature point and its offset



1. Judge the distance between the circle and the triangle in Fig. 4. If the absolute value of  $(x_t - x_r)$  is larger than  $Dis\_thresh$ , there is a tacked weld point, otherwise there isn't a tacked weld point.

From Fig. 4 it can be seen that because of the drift of the structured light, there are few white pixels at the position of template's feature point. Whether there is tacked weld point or not can be judged by this geometrical feature.

**Algorithm 2** Tacked weld point recognition through the template matching result and the source image

1. Get the coordinate of the feature point  $(x_t, y_t)$  after template matching process.
2. In the rectangle range determined by point  $(x_t - x_{delta}, y_t - y_{delta})$  and point  $(x_t + x_{delta}, y_t + y_{delta})$ , count the number of pixels whose gray value are larger than the gray threshold value, namely Num.
3. If Num is smaller than NumThresh, there is tacked weld point. Otherwise, there isn't tacked weld point. NumThresh was set in advance.

Figure 5 shows the welding result by using the algorithm proposed by this paper.

2. Fillet weld seam with irregular shape

The image of the weld seam with irregular shape will change at different places, so that this kind of image cannot be processed by template matching method. In this case, the recognition method using geometrical features of the weld seam image needs to be performed.

Figure 6 is the picture with spiral board heat exchanger and the welding robot designed by Harbin XiRobot Co., Ltd. Figure 7 is the picture of weld seams of spiral board heat exchanger. The algorithm proposed by this paper has been applied on the robot and successfully made the robot robust.

**Fig. 5** Welding result



**Fig. 6** Spiral board heat exchanger



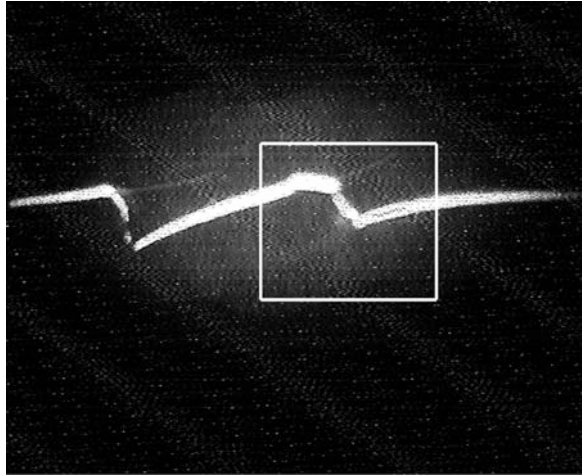
**Fig. 7** Overlapped weld seams of spiral board heat exchanger



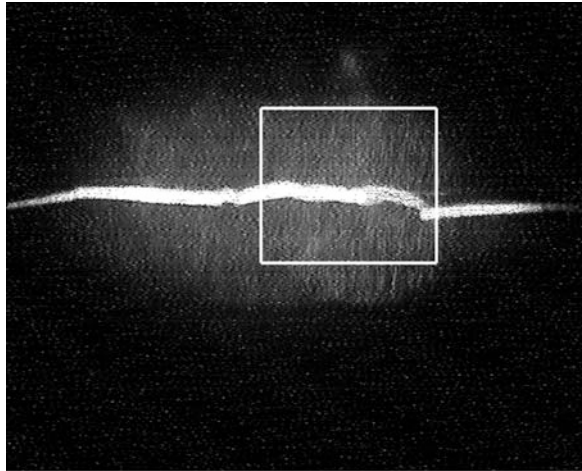
Figures 8 and 9 are the images of structured light projected onto the overlapped weld seams, one with no tacked weld point and one with tacked weld points.

When there isn't a tacked weld point, the geometrical feature of the structured light's position is: up, down, and up again. When there is a tacked weld point, the structured light almost changes into one straight line, because the weld seam is filled with the tacked weld point. Tacked weld point can be recognized based on the change of the structured light's geometrical feature.

**Fig. 8** Weld seam image without tacked weld point

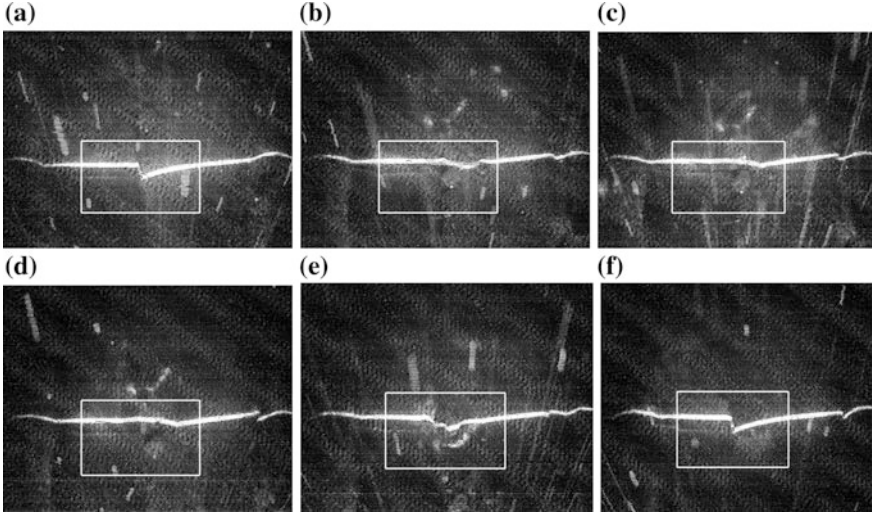


**Fig. 9** Weld seam image with tacked weld point



**Algorithm 3** Recognize the tacked weld point according to the structured light's geometrical feature

1. Set up the region of interest of the image, and find the position of the weld seam to be tracked.
2. Break the structured light line in the region of interest down into  $N$  segments, then calculate the slope of every single structured light's segment, finally save them into array  $k[]$ .
3. Compare two adjacent elements in array  $k[]$ . If two of the elements  $k[i]$  and  $k[i + 1]$  satisfy that the absolute value of  $(k[i] - k[i + 1])$  is larger than  $k\_thresh$ , there is no tacked weld point in the image. Else, if there are no such two adjacent slopes, there will be tacked weld point in the image.



**Fig. 10** Welding image captured from the experiment process

Six pictures are randomly chosen from the experimental process, and the experimental result is listed in this paper.

Figure 10a–f are the images captured in the real welding process.

The experiment is done with  $N = 9$ , and calculates  $N$  slopes for every picture in the real-time tracking process, shown in Table 1.

$k\_thresh$  is 1.0. Substituting the data in Table 2 into algorithm 3, we can get the recognition result of the tacked weld point, shown in Table 3.

The result shown above proves the robustness and accuracy of this algorithm.

In the real tracking process, sometimes the recognition result is wrong. When this occurs we can set  $k\_thresh$  to be higher, so that the probability of the false positives can be higher than that of the false negatives.

In reality, when encountering the tacked weld point [3], keeping away from the positions where there are tacked weld points is a good method, that is, to confirm whether there is a tacked weld point or not. If there is a tacked weld point, then two

**Table 1** Structured light's slopes

No.	k[1]	k[2]	k[3]	k[4]	k[5]	k[6]	k[7]	k[8]
Figure 10a	0.208	0.1806	0.1828	0.1948	0.187	-1.0137	-0.0923	-0.032
Figure 10b	-0.2478	-0.0017	0.3786	-0.2858	-0.2609	0.1007	-0.0669	0.012
Figure 10c	-0.1519	0.0985	0.0124	-0.1579	0.0442	-0.0527	0.0409	-0.018
Figure 10d	-0.2458	0.1268	-0.1394	-0.2622	-0.0135	-0.0126	0.1001	-0.0344
Figure 10e	0.0818	0.101	0.0249	0.5813	0.1543	-0.0743	-0.5717	0.0456
Figure 10f	-0.2473	0.1813	0.1572	0.2373	0.3252	-1.3924	0.0144	0.0177

**Table 2** Differences of structured light's slopes

No.	$\Delta k[1]$	$\Delta k[2]$	$\Delta k[3]$	$\Delta k[4]$	$\Delta k[5]$	$\Delta k[6]$	$\Delta k[7]$	$\Delta k[8]$
Figure 10a	-0.0274	0.0022	0.012	-0.0078	-1.2007	0.9214	0.0603	0.0402
Figure 10b	0.2461	0.3803	-0.6644	0.0249	0.3616	-0.1676	0.0789	-0.0246
Figure 10c	0.2504	-0.0861	-0.1703	0.2021	-0.0969	0.0936	-0.0589	0.0056
Figure 10d	0.3726	-0.2662	-0.1228	0.2487	0.0009	0.1127	-0.1345	0.0095
Figure 10e	0.0192	-0.0761	0.5564	-0.427	-0.2286	-0.4974	0.6173	-0.0448
Figure 10f	0.4286	-0.0241	0.0801	0.0879	-1.7176	1.4068	0.0033	-0.0459

**Table 3** Recognition result

No.	Figure 10a	Figure 10b	Figure 10c	Figure 10d	Figure 10e	Figure 10f
Tacked weld point	No	Yes	Yes	Yes	Yes	No

images can be captured before and after this position. Generally, the length of the tacked weld point is particularly short [4], so that there won't be tacked weld points again in the images captured before and after the tacked weld point's position [5]. While planning a robot's path, using the coordinates of the points newly captured will help to prevent the robot from encountering the tacked weld point.

If the tracking mode is real-time tracking, capturing images without tacked weld points before and after the tacked weld point is impossible. In this case, getting the feature point's coordinate using template matching method [6] would be a good choice. If the real weld seam image is irregular and accurate feature point coordinates cannot be obtained through template matching, then the weld gun may not be adjusted at this time. In a robotics system operating in a real-time tracking mode, the time interval is short between two images processed, so that, even though the weld gun is not being adjusted at the current position, it will not tend to be away far from the weld seam and will be able to reach it in a short time [7]. However, if a wrong feature point is accepted, and the robot adjusts the weld gun according to this wrong feature point, the consequence may be very destructive.

### 3 Conclusion

This paper addresses tacked weld point recognition in the real welding process. The geometrical features of tacked weld points differ according to the shapes of the weld seams. To recognize the tacked weld point, the images in which there are tacked weld points need to be analyzed, and the geometrical features of tacked weld point and the normal weld seam need to be compared.

The typical weld seam types include angle weld, fillet weld, butt weld, V-groove weld, and U-groove weld, etc. This paper mainly introduces the analysis and

recognition of the tacked weld point's geometrical features on the fillet weld. The geometrical features of the tacked weld point on other kinds of weld seams need to be summarized in the near future.

**Acknowledgement** The author would like to express his appreciation for the help provided by Harbin XiRobot Co., Ltd. while doing research for this paper.

## References

1. Yu J-Y, Na S-J (1997) A study on vision sensors for seam tracking of height-varying weldment, part 1: mathematical model. *Mechatronics* 7(7):599–612
2. Kawahara M (1983) Tracking control system using image sensor for arc welding. *Automation* 19:357–363
3. Lee SK, Na SJ (2002) A study on automatic seam tracking in pulsed laser edge welding by using a vision sensor without an auxiliary light source. *J Manuf Syst* 21(4):302–315
4. Kim JS, Son YT, Cho HS, Koh KI (1996) A robust method for vision-based seam tracking in robotic arc welding. *Mechatronics* 6(2):141–163
5. Zhou FQ, Zhang GJ (2006) Fast extraction method for sub-pixel center of structured-light. *Chin J Sci Instrum* 27(10):1326–1329
6. White RA, Smith JS, Lucas J (1994) Vision-based gauge for online weld profile metrology. *IEE Proc—Sci Measur Technol* 141(6): 521–526
7. Geiger M, Christian K, Michael S (2008) High-power laser welding of contaminated steel sheets. *Prod Eng-Res Develop* 2(3):235–240

# Tracking on Right-Angle Weld with Drain Holes by Robot

Jian Le, Hua Zhang, Fei Wu and Feng-Yu Yuan

**Abstract** In order to complete the automatic tracking on the grate weld by robot, it is necessary to track the right-angle weld with drain holes accurately. To track the welding seam, the welding current which is collected should be filtered and identified the deviation. Then the stretch and the indent of the horizontal slider or the left-and-right-wheels differential movement of the robot should be controlled. When the robot hasn't entered the stage of quarter turn, it is based on the tracking fillet welding of left and right wheels differential movement. When at the stage of quarter turn, the welding is completed through path planning and tracking fillet welding based on the horizontal slider stretch. Extinguish the arc when the starting point of a drain hole has been detected. Ignite the arc after passing through drain holes with path planning. The accurate identification of intersection is very important when the robot is in the quarter turn stage. Finally, the correctness of the algorithm is proved by the experiments of tracking on right-angle weld.

## 1 Introduction

With the rapid development of shipbuilding industry, high requirements of welding quality and efficiency are put forward. Poor working conditions and strong arc are not conducive to workers' health when welding, so developing a new type of sensor to track welding seam accurately is essential.

---

J. Le (✉) · H. Zhang

Key Laboratory of Robot and Welding Automation of Jiangxi, School of Mechanical and Electrical Engineering, Nanchang University, Nanchang 330031, People's Republic of China  
e-mail: lejian\_ncu@163.com

F. Wu · F.-Y. Yuan

School of Foreign Languages, Nanchang University, Nanchang 330031, People's Republic of China



At present, welding seam is mainly tracked through visual sensor and arc sensor [1, 2]. However, the visual sensor lags behind and the welding points are not the testing points so that the tracking of welding seam is not so accurate. On the contrary, the rotating arc sensor is extraordinarily real-time [3, 4] because it is not subject to the interference of arc, spatter or electromagnetic field. Grate weld usually has drain holes, so designing a robot that can track right-angle weld with drain holes accurately is a necessity.

## 2 Tracking Weld

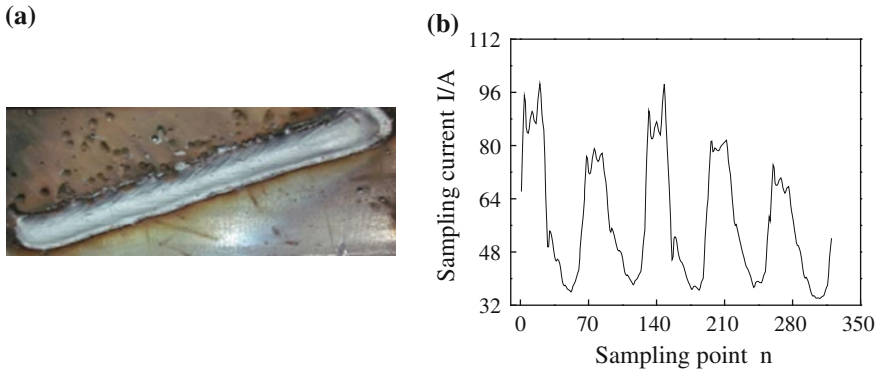
### 2.1 Filtering

The information at the weld groove ought to be converted into the change of the welding current by rotating arc sensor. Then the hall sensor collects the welding current and gets 768 continuous current values for each circle. Due to the fluctuations of welding voltage and the instability of the wire feeding speed, there is a lot of noise in the sampling current both in low frequency and high frequency. Unless the method of combination filter, it is impossible to remove most of the noise. First of all, average the sampling current in the four consecutive circles correspondingly by the means of the spatial averaging filter, to change the four-circle sampling current into one circle and filter the sampling current in space. Then average the three adjacent sampling current for each circle and filter the sampling current in time to make the sampling current with the size of  $4 \times 768$  into  $1 \times 256$ . Next, decompose the sampling current with the size of  $1 \times 256$  by use of wavelet soft threshold de-noising [5], and deal with the approximation and detail components in different dimensions respectively. Set the component to 0 when it is less than the threshold value. Otherwise, set the difference between the component and threshold value as the component value. This ensures the continuity of the sampling current. Then is the process of wavelet reconstruction, which can remove most of the noise. In order to further smooth the waveform of the sampling current, finally is the median filter, making the sampling current with the size of  $1 \times 256$  to  $1 \times 64$ .

Figure 1a is the plate welding experiment which uses the welding robot to weld the plate.

Figure 1b is the waveform of sampling current for five continuous circles after combination filter corresponding to the plate welding experiment.

From the diagram, the waveform of the sampling current after filtering is relatively smooth without most of the noise. The cycle of the sampling current is 64 sampling points in the plate welding experiment.



**Fig. 1** a Plate welding experiment; b waveform of the welding current for five circles after filtering

## 2.2 Deviation Identification

At present, there are a lot of recognition algorithms of deviation, but they are short of complexity and poor reliability. The method that identifies the deviation by using linear fitting has the advantages of high accuracy and a small amount of calculation. The “absolute difference algorithm” and “least squares” are always used to carry on the linear regression from the 17th to 48th sampling points of the waveform after combined filter. The slope of the regression straight line shows the deviation. The absolute value of the deviation expresses the distance between the welding torch and the welding seam and the plus or minus of deviation respectively expresses the deviation direction of the welding torch, left or right.

## 2.3 Control Algorithm

The control algorithms used to track welding seam mainly include, fuzzy control algorithm [6], neural network control algorithm and so on. A large number of experiments find that the fuzzy control algorithm has the merits of relatively little calculation, easy program and tremendous reliability. Set the deviation and the change rate of deviation as the input of the fuzzy controller. Then, through the fuzzification of input, fuzzy reasoning and the clearness of the output, making numbers of stepper motor pulse as the output of fuzzy controller, so the design of the fuzzy controller is finished.

### 3 Path Planning

The turning radius is set as  $S_0$ . When the ultrasonic sensor detects that the distance between the center of the robot and the steel plate is  $S_0$ , the robot begins to turn around.

As Fig. 2 shows, EC section of welding seam is divided into  $m$  segments on average by using the method of numerical analysis. Since the welding speed is constant, the time that the robot spends on welding each small section of welding seam is the same, namely  $\Delta t$ .

In order to simplify the process of calculation, it is presumed that when the robot welds every segments of welding seam, the horizontal slider outstretches or indents at the same rate, and the angular velocity of the robot is the same. Through controlling the angular velocity of the robot when it is turning, and the speed that the horizontal slider stretches out or indents, as a result, the orbit of the extremity of the welding wire is right-angle. The path planning designed for trajectory of EC section satisfies the following formula:

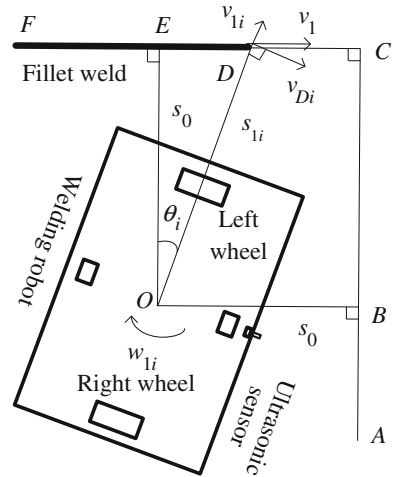
$$v_{Di} = w_{1i}s_{1i} = v_1 \cos \theta_i \quad (1)$$

$$v_{1i} = v_1 \sin \theta_i \quad (2)$$

$$s_{1i} = s_0 + \sum_{i=1}^k v_{1i} \Delta t \quad (3)$$

$$\theta_i = \sum_{i=1}^k w_{1i} \Delta t \quad (4)$$

Fig. 2 Path planning



In this formula,  $v_1$  stands for the speed of welding. When welding the  $i$ th segment of EC,  $v_{1i}$  is the speed when the horizontal slider stretches out.  $v_{Di}$  is the speed of tangential line when the point D which is at the end of welding wire turns around center point O of the robot.  $\theta_i$  refers to the angle the robot turns.  $w_{1i}$  represents the angular velocity when the robot turns.  $s_{1i}$  is the distance between the welding points and the center point O of the robot and  $\Delta t$  is the time the robot spends on welding each section of welding seam.  $s_0$  stands for the turning radius of the robot.  $m$  is the number of EC segments.  $k$  is the serial number of the welding seam which is being welded whose values range from 1 to  $m$ .

By simultaneous equations of formula (1) to (4) through using C++ programming, the outstretch speed of the horizontal slider and the rotating angular velocity of the robot are worked out and the path planning of EC welding seam is completed. Similarly, this method can be used to carry out the path planning of CB welding seam. Finally, it will lead to the accomplishment of the path planning for right-angle turning of the robot.

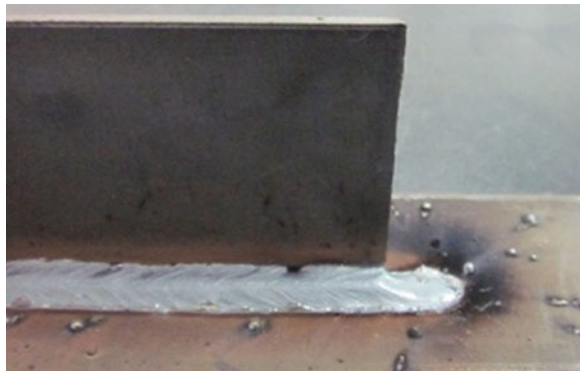
#### 4 Detection of Welding Seam Endpoint

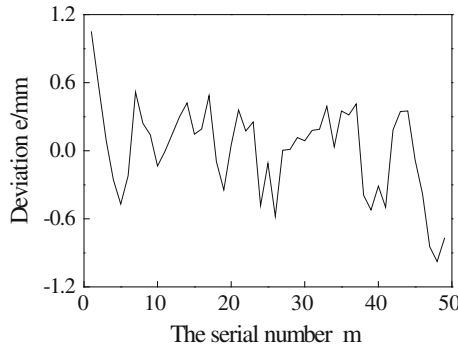
There will be several welding seam endpoints in the actual welding process, such as the starting point of the drain hole. So it needs to identify the welding seam endpoint accurately to make the robot stop welding automatically.

Figure 3 is a detection experiment of welding seam endpoint. The figure shows that it is the equivalent of welding on a flat plate when the robot is welding to the welding seam endpoint. It has already been discussed in the case of welding flat plate in which the deviation of the absolute value is larger than 0.6.

Figure 4 is the deviation curve corresponding to the detection of the welding seam endpoint. It can be seen from the figure that the welding torch, relatively to the welding seam, becomes fully left compared to the direction of welding at the beginning of welding. With the contraction of horizontal slider, the deviation is

**Fig. 3** Detection of welding seam endpoint



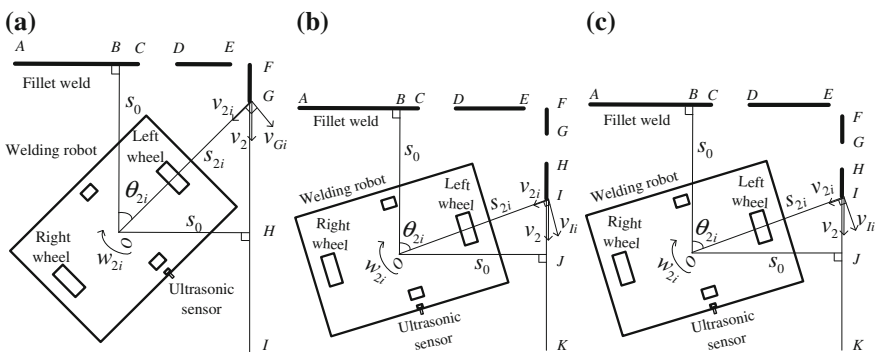


**Fig. 4** Deviation curve corresponding to the detection of the welding seam endpoint

smaller slowly than before. Finally, the deviation is slightly amplitude fluctuated between  $-0.6$  and  $0.6$  mm, which shows that the accuracy of tracking on the welding seam. The deviation value is less than  $-0.6$  when welding the welding seam endpoint. In order to increase the reliability of program, when the three values of deviation are all less than  $-0.6$ , suggest that the robot has arrived at the welding seam endpoint. The last three deviation values in Fig. 4 are less than  $-0.6$ , which suggests that the robot should extinguish arc and stop welding at the welding seam endpoint.

### 5 Implementation

Figure 5 is the implementation of tracking right-angle weld with drain holes. Figure 5 shows that there are two types of drain holes. One is a hole on the side of the right angle, and the other is the intersection of the right-angle. According to Fig. 5a, AB section is the tracking of the welding seam based on two rounds of



**Fig. 5** a No drain hole on the second side of the right angle; b one drain hole on the second side of the right angle; c two drain holes on the second side of the right angle

differential movement. The distance ultrasonic sensors measured from the center of the robot to the welding seam FI is  $s_0$ , which is the quarter turn radius of the robot. When the robot is welding to point B, weld BC section of the welding seam through the trajectory planning and tracking on the welding seam that based on the horizontal slider telescopic. When welding to point C, the welding seam endpoint, the arc should be extinguished. Adopt the method of trajectory planning and using timer through CD section. Igniting the arc when arrives at the point D. DE section should be welded through trajectory planning and the tracking on the welding seam based on the horizontal slider telescopic. Extinguish the arc when the robot welds to point E, the welding seam endpoint. The method of trajectory planning and using timer should be used in getting through EF section. Ignite the arc when arrives at the intersection point F. Weld FH section of the welding seam by trajectory planning and the tracking on the welding seam based on horizontal slider telescopic. The welding seam of HI section is welded by the method based on two wheels of differential movement. When the robot welds to the I-spot, the endpoint, extinguish the arc and stop the robot. Finally complete the tracking on the right-angle weld with drain holes.

Figure 5b shows that there is one drain hole on the second side of the right angle, one more drain hole than Fig. 5a. When the robot welds to the G-spot, extinguish the arc. The path planning and timer are used for passing GH period and ignite the arc when arrives at the H point. Other process are the same as those in Fig. 5a.

Figure 5c shows that there are two drain holes on the second side of the right angle. The distance between point E and the straight line FG equals that between point F and DE straight line. When the robot is welding to point E, the endpoint, extinguish the arc. Then use the timer and path planning to go through the EF part. When the end of the wire reaches point F, Ignite the arc. Other parts of the process are the same as Fig. 5b.

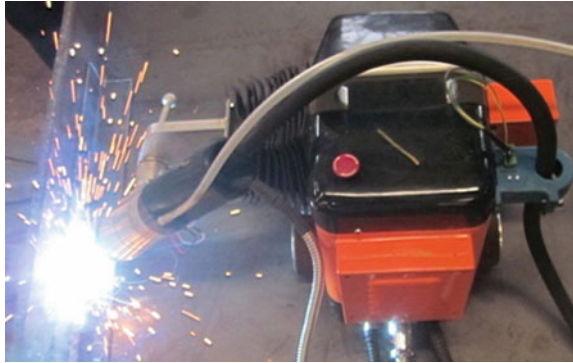
According to the form of right-angle weld with drain holes in the factory, choose a different tracking program. The tracking on right-angle weld with drain holes is finally achieved.

## 6 Experiments

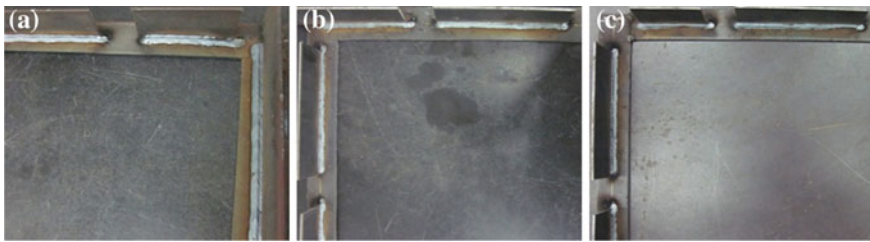
The following are welding conditions. The diameter of the welding wire is 1.2 mm, and the welding voltage is 24.8 V. The welding current is 198 A. Shielding gas is made up of 80 % Ar + 20 % CO<sub>2</sub>. The gas flow is 16 L/min. The welding material is Q235 whose thickness is 5 mm without overheating processing.

Figure 6 shows the scene of the robot tracking the fillet weld.

Figure 7 is the experiment of tracking right-angle weld with drain holes. The size of the drain hole on the side of the right angle is 60 mm, and the size of the drain hole on the intersection of right-angle is 30 mm.



**Fig. 6** Real figure of the robot



**Fig. 7** **a** No drain hole on the second side of the right angle; **b** one drain hole on the second side of the right angle; **c** two drain holes on the second side of the right angle

Figure 7 shows that the welding robot can well track right-angle weld with drain holes, The welding robot can accurately identify the starting point of drain holes, the endpoint of drain holes and the intersection point of right-angle weld. The effect of tracking on the welding seam is better.

## 7 Conclusion

1. Use the combined filter of the sampling current, after which the result is used to identify the deviation. Set the deviation and deviation change rate as input and the speed of the movement of the horizontal slider as output based on the stretch of the horizontal slider after a fuzzy controller. Set the speed differential as the output based on the left and right wheel differential motion tracking weld.
2. When the robot makes a turn, complete the track on the right-angle weld by controlling the horizontal slider speed and rotating angular velocity. Otherwise, the robot track the weld based on the two wheels differential movement.

3. Finally, finish the tracking on the right-angle weld with drain holes. It is based on the tracking on the welding seam by controlling the stretch of the horizontal slider, the two wheels differential movement of the robot, path planning and the detection of the welding seam endpoint. The results of the experiment show that the tracking on the right-angle weld with drain holes by the welding robot has high accuracy and reliability.

**Acknowledgments** This work is supported by National High Technology Research and Development Program of China (863 Program), No. 2013AA041003, P.R. China and Key Technology R&D Program of Jiang Xi, No. 20133BBE50030, P.R. China.

## References

1. Xu YL, Zhang JY et al (2013) The acquisition and processing of real time information for height tracking of robotic GTAW process by arc sensor. *Int J Adv Manuf Technol* 65 (5):1031–1043
2. Jeong SK, Lee GY, et al (2001) Development of high speed rotating arc sensor and seam tracking controller for welding robots. In: *Proceedings of international symposium on industrial electronics*, pp 845–850
3. Ye JX, Wei H, Wei MF (2008) Detection of welding torch inclination based on rotating arc sensor. In: *Proceedings of international conference on intelligent computation technology and automation*, pp 1025–1028
4. Shi YH, Zeng SS, Wang GR (2009) Signal pattern analysis of high speed rotational arc sensor in GMAW. In: *Proceedings of international conference on information and automation*, pp 1156–1160
5. Gonzalez RC, Woods RE (2010) *Digital image processing*, 3rd edn
6. Jia JP, Zhang H, Xiong ZY (2006) A fuzzy tracking control system for arc welding robot based on rotating arc sensor. In: *Proceedings of international conference on information acquisition*, pp 967–971



# Welding Robot with Laser Tracking System Used in High-Mobility Off-road Vehicle Rack Girder

Xing-Wang Wen, Li-Qin Li, Ying Jing, Li-Hong Yan, Li-Bin Zhao and Jin-Liang Zhang

**Abstract** By using a laser tracking system on an arc welding robot workstation, irregular welding, misalignment, and undercut etc. problems could be solved due to contour size deviation of the truck rack girder on the high mobility off-road vehicle, without a very precise trajectory teach. And the welding joint quality is with good consistency. The ability to control the production process of welding is enhanced, too. By using an arc welding robot workstation with laser tracking system, instead of manual welding, welding quality and efficiency are significantly improved, while labor intensity is reduced, and product quality and reliability are enhanced.

## 1 Introduction

With the rapid development of welding automation and intelligence, the traditional teaching playback welding robot has been difficult to meet the high-tech welding quality, accuracy and efficiency. Due to accuracy error of the welding workpiece, assembly error, the operating environment and mixed-model assembly line requirements, the important role of intelligent robot with visual function has become increasingly prominent in welding.

By means of a laser tracking system, a welding robot could own the following abilities: real-time sensing to the welding environment, weld seam tracking, automatic identification of the welding joint type, real-time path planning and real-time adjustment of welding parameters. According to the above functions, welding quality can be controlled in real-time, and the welding productivity is improved. In addition, a welding robot with visual function can replace workers in harsh environments, reduce the difficulty and danger of workers, and ensure stability and reliability of the weld quality in special occasions [1].

---

X.-W. Wen (✉) · L.-Q. Li · Y. Jing · L.-H. Yan · L.-B. Zhao · J.-L. Zhang  
FAW Jiefang Automotive Company Ltd., Changchun 130400, China  
e-mail: wen-sevenyy@163.com

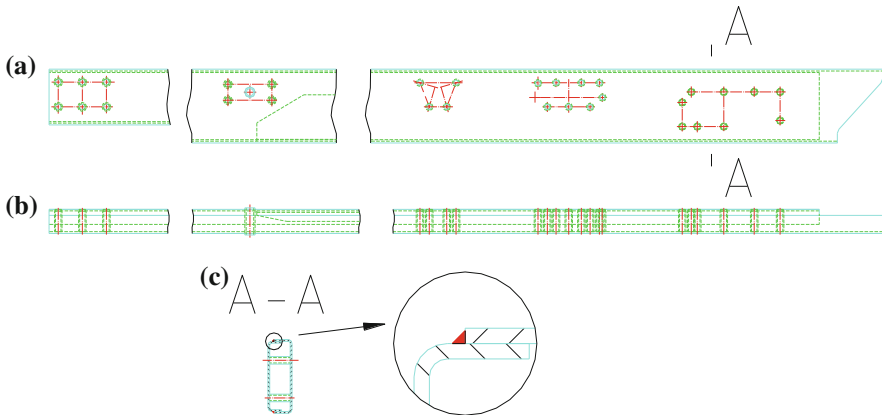
## 2 Features of High-Mobility Off-road Vehicle Rack Girder

### 2.1 Requirements of Product Process

There are four series of high-mobility off-road vehicles produced in our company high totally. It is expected to 2000 vehicles/year, and production cycle is 3600 s. The type of production is mixed-model assembly line. The four series are consistent with the size of tip contour, only different in the trailing lengths, and the longest rack girder outside dimensions is 7285 mm  $\times$  245 mm  $\times$  80 mm. Two U-shaped Stamping girders are snapped together with the thickness of 6 mm. The two girders are welded together as a long box structure, and they are shaped by supporting plates shown in Fig. 1.

### 2.2 Requirements of Product Quality

The straightness of the rack girder after welding should be controlled within 4 mm, and the straightness of any section straightness is less than 1/1000. According to process design requirements, the two straight seam of rack girder is assembly of total length  $2 \times 7285$  mm. Due to the long weld, heat, it is necessary to use anti distortion control when welding the rack girder to control deformation. Flexible structure are used when clamping and fixing the fixture. The rack girder is rigidly fixed by clamping unit every 500 mm. The position a rack girder fixed is



**Fig. 1** Sketch of the rack girder. **a** The front view. **b** The top view. **c** The magnified section diagram of A-A

three-dimensional adjustable. According to the rack girder deformation trend when commissioning the equipment, the spatial position of clamping unit is adjusted. By changing the corresponding position anti-deformation, the rack girder straightness would finally meet the design requirements.

### ***2.3 Production Problems***

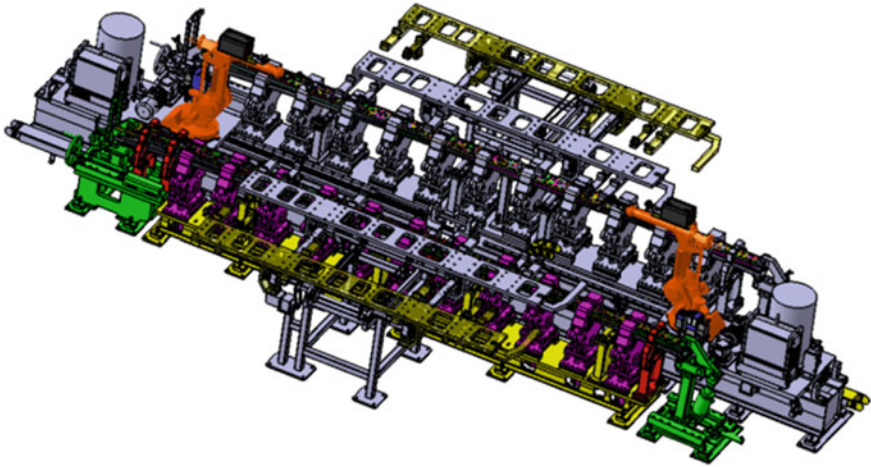
1. Due to the structure of the inner and outer plates and the precision of existing equipment, the wing surface height deviation is large and unstable after molding. The maximum deviation is up to  $\pm 5$  mm. The playback robot can not adapt to such a large deviation.
2. Welding seam quality is not stable under manual welding. The same posture during continuous welding make the operator fatigue easily and the stability of the welding technique is affected, resulting in welding defects. It is not conducive to the process control of the product.
3. Due to the low productivity of manual welding, the production takt is unable to meet annual needs of 2000 copies of the program.

## **3 Configuration and Application of the Rack Girder Automatic Welding System**

The rack girder automatic welding system is mainly composed of two ABB welding robot, Fronius MAG welding machine and related accessories, SLPi laser tracking system, the robot traverse table and rail mounting base, hydraulic welding fixtures, PLC controller and touch operator panels.

### ***3.1 Robot Welding Station***

The work of Robot welding station is welding after the rack girder point and anti-distortion. In order to improve efficiency and reduce the cost of equipment investment, using a duplex station arrangement, shown in Fig. 2. The robot is disposed at both side of the traverse table. One station is used to manual loading and unloading, the other is used for welding. The robot keeps working, saving loading and unloading time, and the utilization efficiency of the robot is fully enhanced. Hydraulic welding fixtures and robot are linkage controlled. The jaws could request signals from the robot to open or clamping in accordance.



**Fig. 2** Layout of the welding station

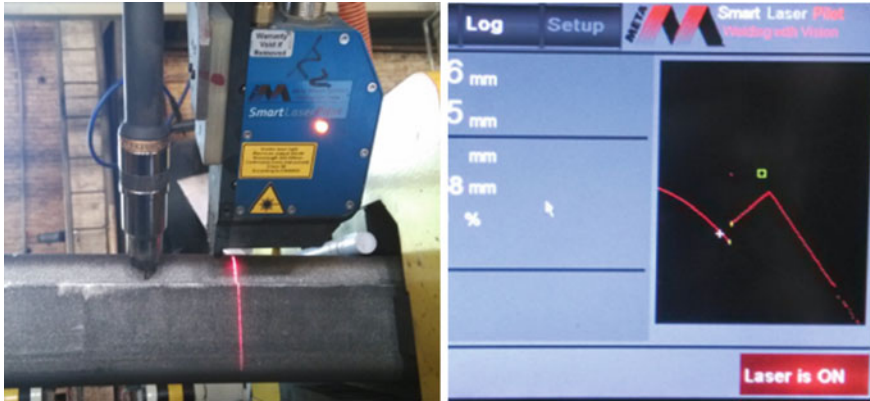
### **3.2 *SLPi Laser Tracking System***

Due to welding misalignment and undercut may appeared when the deviation of the win is too large while welding the rack girder, laser weld automatic tracking system made by META company is equipped for the robot workstation. The position of laser sensor tracking and welding torch is shown in Fig. 3. Calibration is needed after the sensor is installed stably and reliably. After calibration, the sensor could be able to exercise with six-axis coordinately.

Laser tracking systems have the following advantages:

1. Large amount of information and high precision. The joint cross-sectional precise geometry and spatial position attitude information can be obtained.
2. Due to the detection space range and error tolerance are large, it is possible to find the joint in a wide range prior to welding.
3. With intelligent features that can automatically detect and select the start and end of welding, fitting the positioning spot and joint characteristics and so on.
4. Good universality, and it could tracking and control parameters for a variety of joint types, furthermore, it could also be used for automatic planning multi-layer welding bead, adaptive control parameters and visual inspection of solder joints after.
5. Real-time performance is good [2].

It is very important to make a correct choice of sensor field of view only to achieve good tracking results according to the actual situation of the weld seam. Selection of the viewing field of the sensor depends on the size of the weld seam, the tracking accuracy and weld lines move. The sensor with a smaller field of view is more accurate, it is possible to see a small weld seam [3]. While a sensor with a



**Fig. 3** Laser tracking sensor and the weld information collected

larger field of view a field of sensor is capable to measure a large weld seam, which can handle a large change in position of the weld seam. META standard weld types includes: Left lap, Right lap, Butt, Butt LT, Butt GM Fillet, V-groove, External fillet, Left edge, Right edge, and Height only. It is possible to select the weld seam type on the Settings menu directly, or build the weld seam model based on the actual situation [4, 5]. The laser tracking sensor and the weld information collected is shown in Fig. 3. It is necessary to make sure the torch trace explicitly and the joint position, so that to make the weld seam characteristics clear and the object type the sensor is going to track.

### 3.3 PLC Controller Design

Siemens PLC is chosen as the automatic welding system master controller to collect and process the peripheral signal, and driver programs correspondingly according to the requirements. The system architecture is shown in Fig. 4.

The system controller controls the L/R station, including: unloading motor's forward and backward movements, the carriage, opening and closing of all hydraulic jaws, movement of the robot car, robot program's starting and stopping. PLC communicates with the touch screen, while the state of the robot and the hydraulic cylinders are shown in real time on the touch screen. Because there are four different length models of high-mobility off-road vehicle, it is necessary to manually change the tackle position at the end of fixture when producing different varieties. PLC will select a corresponding welding process based on the tackle position at the end of fixture and the actual length from the fixture to the rack girder. When the position of the workpiece and the tackle position do not match, the system will automatically alarm, prompting the operator to make changes.

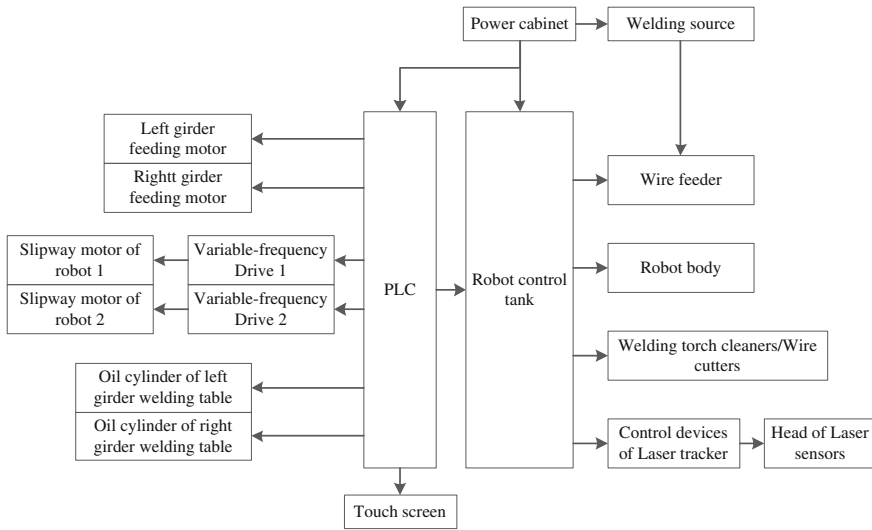


Fig. 4 System structure

### 3.4 Offline Programming and Teaching of the Robot Welding System

The welding sequence should be firstly decided according to process requirements, and then determine the robot, the robot tackle, each hydraulic cylinder of the fixture action sequence. These programs can be achieved through the offline programming. Points used in the program can be calibrated through online teaching.

After the off-line programming, the robot can teach. The teaching-reproduction mode requires a stable state of the workpiece, while the clamping fixture must be accurate. No matter what changes occur to the workpiece, the robot always act repetitively according to the track of teaching, without taking an initiative adjustment. The process of teaching of a robot equipped with a laser tracking device are essentially different from the traditional teaching and playback mode. Start and end of the weld by laser tracker sensor active search. The laser tracking sensor can find the beginning and end of any welding seam on its own initiative.

First, move the welding torch to the starting point and insert point A, point A is in the visual field of the laser tracking system, and open the laser tracking device can detect the welding seam characteristics. Move the welding torch to the starting point again and insert point B, point B is out of the visual field of the laser tracking system, then open the laser tracking device can not detect the weld properties. Call a subroutine function “search” to search the welding beam, the weld properties in the viewing field of the laser tracking system is from nothing to emerge when the torch moved from point B to point A. At this point the laser tracking system records point C spatial location automatically as the welding beam starting point. The robot can

use the same methods to find point D as the welding beam end. When welding from point C to point D, the laser tracking system can call a “track” command to real-time control weld quality according to the actual shape of the workpiece between C and D. When repairing in the position between two welding seams, the laser tracking system can also call “search” command to find the start and end points initiatively. But there are differences of the laser tracking sensor movement pattern: it moves from the welded place to the un-welded place, instead of the movement from far to near. After the system finding the point with the weld beam characteristics, the torch may offset to a certain distance as the arc beginning point. The shift is to make sure the arc starting point could cover the adjacent arc crater or the arc ignition and obtain a good joint. The torch attitude and the laser gun stripes are adjusted according to the shape of the workpiece, and the teaching process is continued until the end of the weld.

Anti-deformation amount should be adjusted constantly according to the welding, if teaching and reappearing is adopted, the teaching track will be changed continually. While the teaching method using a laser tracking system can allow C point vary within a certain range, without repeat teaching, and the debug time will be greatly reduced.

Since there are small differences among the four types of the rack girder, teaching program can directly be copied at the same location with a change to the different place. It could reduce the commissioning time.

### 3.5 *Welding Parameters Commissioning*

Fronius TS5000 welder can preset groups of Job, each Job group contains: different welding power, wire feed speed, arc current, arc current duration, closing arc current, arc duration closing, pre-ventilation time, stop gas lagging time and other parameters. Different Jobs stored in the welder could be called according to different needs. After several tests, the rack girder after welding is shown in Fig. 5.

**Fig. 5** The rack girder after welding





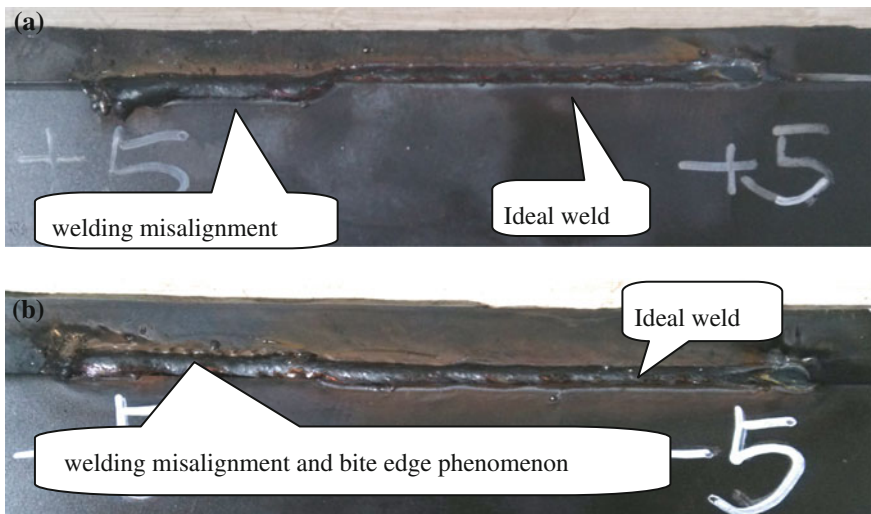
## 4 Advantages of Laser Tracking System

### 4.1 Improvement of the Adaptability to Workpiece Deviation

The demand for the precision of the workpiece in the traditional teach-repeat model robot arc welding was very high. For a wire with a diameter of 1.2 mm, when the weld position and teach position deviation exceeds 1.5 mm, welding misalignment and bite edge phenomenon will be happened. Laser tracking device can effectively solve the problem, laser tracking system can find the weld in  $\pm 5$  mm or even greater scope of the teaching position and guideline the torch to adjust automatically. As shown in Fig. 6a, b, the deviation between the actual position and teaching position of the two weld was  $+5$  mm and  $-5$  mm, respectively, welding misalignment and bite edge phenomenon was obvious in the left of the two welds without laser tracking system, while the right of the two welds exhibit ideal weld state with the laser tracking system.

### 4.2 Reduction of Commissioning Time

In order to obtain ideal straightness after welding, anti distortion structure was adopted in the welding jig. The space position of clamping unit should adjust continuously according to the deflection of the girder in the process of commissioning, so the location of the weld will change. The robot without laser tracking



**Fig. 6** The comparison of welding state with and without laser tracking system when the deviation between welding position and teaching position is  $+5$  mm (a) and  $-5$  mm (b)



system cannot adapt to the change and a new teaching was need. However, robot with laser tracking device can found the weld within a certain range actively, and guide the welding torch to adjust the trace accordingly. Repeat teaching was saved and the commissioning time was reduced effectively.

## **5 Problems of Laser Tracking System in Application**

### ***5.1 Mistaken Fixture as Workpiece***

Because of the processing accuracy of the inner and outer sheet, a seam tracking and automatic recognition function is needed on a robot. It is found during the debugging process that sometimes the laser tracker may mistakenly identify the seam between the rack girder and the fixture as welding seam. This can lead to a serious result that the rack girder may scrap and the fixture be damaged. After several changes to the track, the laser tracking system can be away from the fixture when finding the welding seam. Furthermore, a more precise welding seam modeling has been built to avoid the problem mentioned above.

### ***5.2 Collision Between Robot and Fixture Due to Large Workpiece Deviation***

Since the outer plate wing of the rack girder deviation is too large, robotic welding may exceed the safety scope of torch according to the welding seam, resulting in a collision laser tracking sensor hitting the fixture. Thanks to the bumpers equipped on the torch, welding process stopped in time and serious damage did not occur to break the equipment. Although the laser tracking system could overcome the workpiece size deviation, track the welding seam characteristics, and guide the torch, it can not accept the deviations of the piror process workpiece unboundedly. Parts on order deviations should remain within a reasonable range to ensure the system safe and stable.

## **6 Conclusion**

1. Using a robot equipped with a laser tracking system workstation could solve the problems such as welding misalignment and undercut caused by large deviations of the workpiece when welding the high-mobility off-road vehicle rack girder, while the consistency and product stability are ensured, too.

2. Since the automatic rack girder welding system is equipped the function of automatic looking for welding seam without accurate teaching, it meets the requirements of highly flexible production. Rack girder automatic welding system with a laser tracking system improves the working conditions of workers and improves the efficiency and quality of welding, with popularization.

**Acknowledgement** This work is supported by FAW Jiefang Automotive Company Ltd., P.R. China.

## References

1. Liu S (2005) Application and prospect of vision sensing system in robot welding. *Mech Sci Technol* 11:1296–1300
2. Zhou L, Chen S, Lin T (2005) The study of arc welding robot tracking method. In: The eleventh national welding conference proceedings, pp 531–534
3. Huang J et al (2008) Research on the seam positioning system of laser tracking style rail-free welding robot. *Electr Weld Mach* 6:13–17
4. Lin T, Chen H et al (2012) The application of laser welding seam tracking system in automobile sheet robot GTAW. *Welding* 5:62–65 (production theme)
5. Zhao J, Lin S (2010) Introduction to laser sensors for automated welding. *Electr Weld Mach* 11:40–43

# Partition Mutation PSO for Welding Robot Path Optimization

Xue-Wu Wang, Ying-Pan Shi, Xing-Sheng Gu and Dong-Yan Ding

**Abstract** Many solder joints usually have to be traversed for spot welding robots, and reasonable welding sequence will improve welding efficiency. Intelligent optimization algorithms have been used to study path optimization problems in these years because of their effective optimization abilities. Due to its simplicity, high search accuracy and fast convergence rate, the particle swarm optimization (PSO) algorithm was used to study welding robot path planning. A novel hybrid discrete PSO algorithm was proposed to improve the basic PSO after the partition operation, mutation strategy were combined. Then, the optimization performance of the algorithm was used to solve 3-dimensional welding path planning problem.

## 1 Introduction

Reasonable path planning can reduce working time of welding robot, improve production efficiency and reduce production costs. Mostly, the welding path planning is mainly based on the experiences of workers and the product design documentation, and it was used to guide on-site path planning. This path planning method is hard to ensure a reasonable planning result. Hence, many researches have been conducted to realize robot path optimization. Intelligent optimization algorithms were applied for robot path optimization in many cases, and desired effects were obtained [1–3].

Inspired by the social behavior of animals such as bird flocking, fish schooling and swarm theory, PSO algorithm was first proposed as a stochastic search

---

X.-W. Wang (✉) · Y.-P. Shi · X.-S. Gu

Key Laboratory of Advanced Control and Optimization for Chemical Processes of Ministry of Education, East China University of Science and Technology, Shanghai 200237, China  
e-mail: wangxuew@ecust.edu.cn

D.-Y. Ding

Institute of Microelectronic Materials and Technology, School of Materials Science and Engineering, Shanghai Jiao Tong University, Shanghai 200240, China

approach by Kennedy and Eberhart in 1995 [4]. PSO is a kind of heuristic algorithms based on swarm intelligent, and its idea roots in artificial life and evolutionary computation theory. PSO drew much attention in decades due to its simple computation and rapid convergence capability. It was also used in welding and assembly fields [5, 6].

To this end, the PSO algorithm is applied to study welding robot path planning in this paper. Description of welding robot path planning is first given in Sect. 2. Then, a hybrid PSO based on mutation and partition strategies is given in Sect. 3. Besides, the hybrid PSO is applied for welding robot path planning in Sect. 4. At last, the conclusion is given in Sect. 5.

## 2 Description of Welding Robot Path Planning

Besides improve the productivity, effective path planning can improve the ability of OLP and accelerate the development of welding automation. How to find an optimal path to go through all the solder joints is the most concern. Welding robot path planning problem can be described as finding a reasonable solder joints sequence for welding robot under some criteria. In general, there are many solutions for solder joints sequence, and one optimal path has to be selected based on the certain criteria. The criteria may be the shortest path, the least time-consuming, the minimum welding deformation, or the minimum energy consumption and so on. Therefore, the robot path planning is a constrained optimization problem. When two or more robots exist in the system, the problem will be more complicated because the cooperation and influence between robots have to be considered.

The optimization problem for one spot welding robot can be described as follows:

$$\text{Minimize } F(P) = (f_l(P), f_d(P), f_e(P)) \quad (1)$$

where  $P$  represents the welding path.  $f_l(P)$  denotes the length of the welding path,  $f_d(P)$  denotes welding deformation,  $f_e(P)$  denotes energy consumption. The total length of the welding path can be described as:

$$f_l(P) = \sum_{i=1}^N (S_i) \quad (2)$$

where  $S_i$  represents the distance between two solder joints. Energy consumption mainly includes two parts, one is for welding operation, and the other is for robot travel. The energy consumed for welding operation is up to the welding parameters, and the energy consumed for robot travel is proportional to the length of welding path. Welding distortion is affected by change of temperature fields, and welding

sequence is also an important factor for it. It can be seen that optimized path will affect above three objectives in Eq. (1).

The welding robot path optimization will be studied as a single objective optimization problem in this paper. Here the shortest path is used as the criteria to optimize the welding path, and only one robot exist. After the effectiveness of intelligent optimization algorithm was verified, multi-objective optimization of welding robot path will be studied then. Hence, the optimization problem is described as follows.

Considering a solder joints welding task  $C = (c_1, c_2, \dots, c_N)$ , the distance between two solder joints can be described as  $d(c_i, c_j) \geq 0$ , where  $c_i, c_j \in C$  ( $1 \leq i, j \leq N$ ),  $c_i$  stands for one solder joint. The task in this paper is to find the best solder joints sequence  $\{c_{i\pi(1)}, c_{i\pi(2)}, \dots, c_{i\pi(N)}\}$ , where  $\pi(1), \pi(2), \dots, \pi(N)$  is the full array of  $1, 2, \dots, N$ , to make sure the total path length of the welding robot is minimum.

$$S = \sum_{i=1}^{N-1} d(c_{\pi(i)}, c_{\pi(i+1)}) + d(c_{\pi(N)}, c_{\pi(1)}) \quad (3)$$

Based on above optimization problem analysis, intelligent optimization algorithm will be studied in the following section, and it will be applied to realize welding robot path optimization.

### 3 Hybrid PSO Algorithm

#### 3.1 Basic PSO Algorithm

In basic PSO algorithm, a swarm of individuals is utilized, which is called particles. Assume that there are  $N$  particles searching in a  $D$ -dimensional space, and they respectively represent a feasible solution of problems to be optimized. All these particles are evaluated by the fitness function to be optimized. Initially, particles are assigned a group of random velocities and positions. They are updated from one generation to the next. To achieve the optimum, each particle is directed toward the personal best position, called *pbest*, found by its own so far, and the global best position, called *gbest*, found by all particles in the whole swarm.

In  $n$ th generation, the position of the  $i$ th particle, which represents the candidate solution, is characterized as  $x_i^t = (x_{i1}^t, x_{i2}^t, \dots, x_{iD}^t)$ ,  $i = 1, 2, \dots, n$ .

The position of every particle is a solution, the fitness could be obtained after the function was calculated through  $x_i$ , and the  $x_i$  can be evaluated based on the fitness.

The velocity of the  $i$ th particle is represented as  $v_i^t = (v_{i1}^t, v_{i2}^t, \dots, v_{iD}^t)$ ,  $i = 1, 2, \dots, n$ . Let  $p_i^t = (p_{i1}^t, p_{i2}^t, \dots, p_{iD}^t)$  represents *pbest* of  $i$ th particle, and  $p_g^t = (p_{g1}^t, p_{g2}^t, \dots, p_{gD}^t)$  denotes *gbest*.

After  $pbest$  and  $gbest$  were obtained, the  $i$ th particle update its velocity and position in  $(t + 1)$  generation as follows:

$$v_i(t + 1) = wv_i(t) + c_1r_1(p_i(t) - x_i(t)) + c_2r_2(p_g(t) - x_i(t)) \quad (4)$$

$$x_i(t + 1) = x_i(t) + v_i(t + 1) \quad (5)$$

where  $w$  is inertia weight. It introduces the weight of the current velocity on the next generation velocity. Inertia weight usually declines with the iteration.  $c_1$  and  $c_2$ , namely acceleration factors, are two positive constants. They can accelerate the searching speed of the particle, and usually are assigned as 2.  $r_1$  and  $r_2$  are random numbers uniformly distributed in  $[0, 1]$ .  $c_1r_1$  and  $c_2r_2$  provide stochastic effects of  $(p_i(t) - x_i(t))$  and  $(p_g(t) - x_i(t))$ , respectively. In the searching process, all these particles cooperate and compete with each other, and finally the optimal solution was achieved while the fitness function is optimized [4].

### 3.2 Discrete PSO

Above conventional PSO algorithm has fast convergence, strong optimization capability to solve continuous optimization problems, but it cannot be used for welding robot path planning directly because it is a discrete optimization problems. Therefore, in order to make use of PSO to solve discrete optimization problems, appropriate discrete transformation of PSO is necessary. Kennedy and Eberhart proposed a binary particle swarm optimization (BPSO) based on the basic PSO for discrete space [7]. In Ref. [8], Clerc proposed a discrete PSO specifically for the TSP problem by introducing the swap operator, swap sequence, and redefinition of the PSO operation rules.

When discrete PSO algorithm is applied to the welding robot path planning, one solder joints in sequences is represented as one element in a particle. For example, there are  $N$  solder joints in a welding task, particle  $i$  can be expressed as  $C = (c_1, c_2, \dots, c_N)$ . If  $N = 5$ , the particle  $i$  would be  $C_i = (1, 2, 3, 4, 5)$ , which means that the welding path is 1–2–3–4–5.

The main idea of the PSO algorithm is that every particle in the swarm will be affected by  $pbest$  and  $gbest$ . Since the discrete particle swarm cannot use Eqs. (4) and (5) to update particles, cross method is used here to realize the discrete PSO. The impact of  $pbest$  can be expressed as the crossover between the particle and  $pbest$ . When  $n = 5$ , particle  $i$  is  $C_i = (1, 2, 3, 4, 5)$ , its history optimum  $pbest_i = (4, 2, 1, 5, 3)$ , if the crossover code is 3–5, that means exchange the element 3, 4, 5 of  $C_i = (1, 2, 3, 4, 5)$  and  $pbest_i = (4, 2, 1, 5, 3)$ , the result should be  $C_i = (2, 4, 1, 5, 3)$ . Make a comparison of its current fitness value and the last fitness value, if the current fitness value is better, then the particle's position will be replaced by its current position. Similarly, the global optimization crossover results can be obtained.

Based on the above discrete particle swarm optimization, mutation and partition strategies will be introduced to improve the algorithm optimization ability in following sections.

### 3.3 Effective Mutation Operation

In order to improve the global optimization ability of particle swarm optimization algorithm, mutation operator is applied in the algorithm to make the algorithm jump out of local optimal solutions. Most mutation methods can improve PSO algorithm more or less, but these mutation methods are based on random operation. Sometimes mutation will decrease the fitness of particles, and reduce the quality of the swarm. Hence, an effective mutation strategy is proposed to ensure better fitness. This mutation operation gives proximity solder joints more chance to be together. For a welding task which includes  $N$  solder joints, solder joint  $k$  is selected in the random selection process, and the shortest solder joint to  $k$  is solder joint  $j$ . Before mutation operation the particle is

$$C_i = (c_{\pi(1)}, c_{\pi(2)}, \dots, c_{\pi(a)}, c_{\pi(j)}, c_{\pi(b)}, \dots, c_{\pi(c)}, c_{\pi(k)}, c_{\pi(d)}, \dots, c_{\pi(N)}),$$

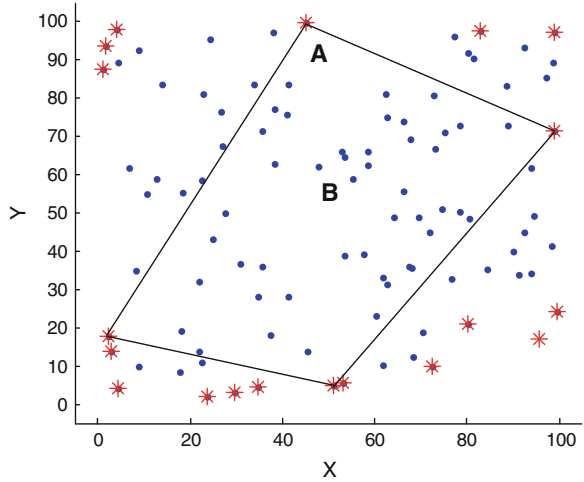
where  $\pi(1), \pi(2), \dots, \pi(N)$  is the full array of  $1, 2, \dots, N$ . In the mutation operation, we need to compare the distance between  $d(c_{\pi(k)}, c_{\pi(a)})$  and  $d(c_{\pi(k)}, c_{\pi(b)})$ , if  $d(c_{\pi(k)}, c_{\pi(a)}) \leq d(c_{\pi(k)}, c_{\pi(b)})$ , then  $c_{\pi(k)}$  will be inserted to the place between  $c_{\pi(a)}$  and  $c_{\pi(j)}$ , and particle  $i$  will become  $C_i = (c_{\pi(1)}, c_{\pi(2)}, \dots, c_{\pi(a)}, c_{\pi(k)}, c_{\pi(j)}, c_{\pi(b)}, \dots, c_{\pi(c)}, c_{\pi(d)}, \dots, c_{\pi(N)})$ , otherwise  $C_i = (c_{\pi(1)}, c_{\pi(2)}, \dots, c_{\pi(a)}, c_{\pi(j)}, c_{\pi(k)}, c_{\pi(b)}, \dots, c_{\pi(c)}, c_{\pi(d)}, \dots, c_{\pi(N)})$ .

### 3.4 Partition Strategy

The basic discrete PSO has a good ability to find optimal solution for small scale problem, but it is hard to get the optimal solution when a lot of solder joints exist. Hence, the partition PSO will be used to solve large scale solder joints path planning problem.

For  $N$ -dimensional welding path optimization problem, the number of the possible solutions is  $(N - 1)!/2$ , when  $N = 20$ , there will be more than  $10^{16}$  possible solutions. For larger scale, the number will grow explosively. If the  $N$ -dimensional problem is divided into several small scale problem, which are described as  $n_1, n_2, \dots, n_k$ , the number of the possible solutions will be  $\frac{(n_1-1)!}{2} + \frac{(n_2-1)!}{2} + \dots + \frac{(n_k-1)!}{2}$ , the search space will be reduced greatly. Hence, partitioning is an effective way for large solder joints path planning problem.

**Fig. 1** Reference points of 4 partition



Partitioning principle for particles is based on the distance between different particles. Particle  $X_i = (x_{i1}, x_{i2}, \dots, x_{iD})$  will be divided into  $k$  zones as  $X_i = ([x_{i1_1}, x_{i1_2}, \dots], [x_{i2_1}, x_{i2_2}, \dots], \dots, [x_{ik_1}, x_{ik_2}, \dots])$  according to the partition principle. The first step of partition is to find the boundary points, and define  $k$  reference points from the boundary points. In order to ensure that the solder joint can get a reasonable allocation, these  $k$  reference points should be defined as decentralized as possible.

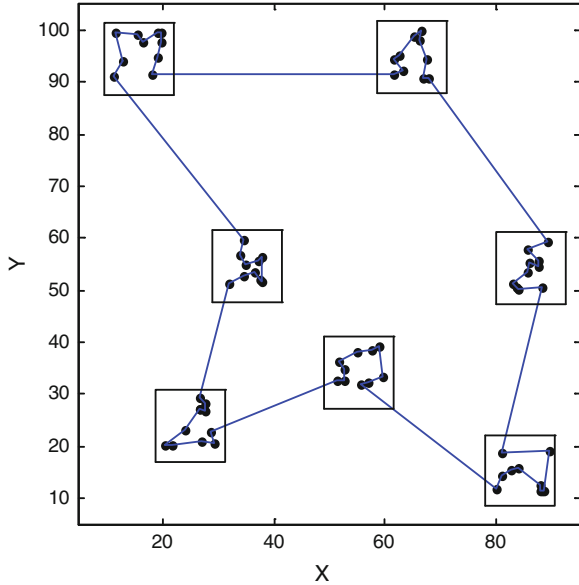
In Fig. 1, A is a boundary point and B is not a boundary point. If there are  $m$  boundary points, we need to find  $k$  reference points, in order to make it easier to divide all points, and the distance of loop of the  $k$  reference points should be as long as possible. There are 4 reference points in Fig. 1 and it means this is a four partition problem. Every point should be divided along with the nearest reference point. Evenly divided points will be useful for us to find optimal solution.

Based on the above operation, all the element in particle  $i$  can be divided into  $k$  zones. Then, PSO algorithm is used to obtain optimal solder joints sequence for different zones separately. In order to ensure the global optimal, the distance of adjacent areas in the zones should be shortest, it means that the last element in a zone and the first element in the next zone should be the nearest.

The process of partition PSO is described as follows. The partition operation is conducted to divide the large scale solder joints first. Then, the connection solder joints are determined to ensure the distance of adjacent areas in the zones is shortest. At last, the PSO is used to get the optimal sequence of every zone, and the optimal solutions in every single zone are obtained. Figure 2 shows the result of partition-PSO algorithm, all points are obviously divided.



**Fig. 2** Result of partition-PSO algorithm



## 4 Path Planning Based on Hybrid PSO

### 4.1 Algorithm Strategy

Welding robot path planning here is to find a solder joints sequence to ensure path length is shortest or near shortest. For a welding tasks of  $D$  solder joints, particle  $i$  can be represented as  $X_i = (x_{i1}, x_{i2}, \dots, x_{iD})$ ,  $x_{ij}$  means this solder joint will be welded by welding robot in the  $j$ -th time. All the elements in  $X_i$  are different positive integer between 1 and  $D$ , hence each particle is a closed loop path. The steps of optimization process for one zone are given as follows:

1. Initializing the particle swarm, including random position and population size of the particles.  $X_1 = (x_{11}, x_{12}, \dots, x_{1D})$  is defined, and it represents a possible path sequence of the solder joints. According to the partitioning method discussed above,  $X_1 = ([x_{11_1}, x_{11_2}, \dots], [x_{12_1}, x_{12_2}, \dots], \dots, [x_{1k_1}, x_{1k_2}, \dots])$ .  $X_i$  can be got after all welding joints were randomized in each zone, and every zone holds an identical serial number.
2. Obtaining the connection points of two adjacent zones which are the nearest welding points in the two adjacent zones.
3. Using PSO algorithm to search optimal zone sequence.
4. Evaluating the fitness, the total welding path length is defined as the fitness function, and the shorter length means better fitness.
5. Calculating  $pbest$  and  $gbest$ .

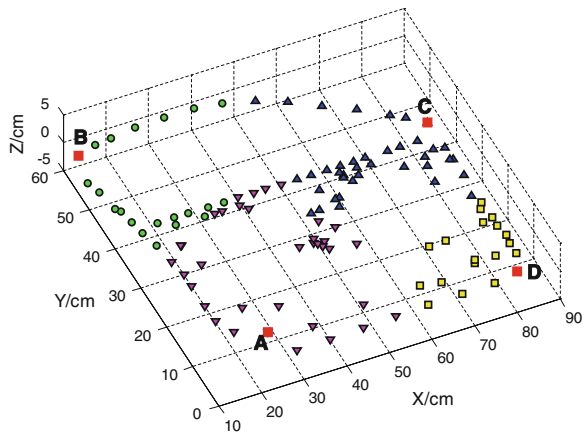
6. Conducting crossover operation with *pbest*. If the fitness became better, the crossover would be accepted.
7. Conducting crossover operation with *gbest*. If the fitness became better, the crossover would be accepted.
8. Conducting mutation operator. If the fitness became better, the mutation would be accepted.
9. Optimization operation will end if it reaches the maximum number of iterations. Otherwise, return to step (4).

## 4.2 Welding Path Planning

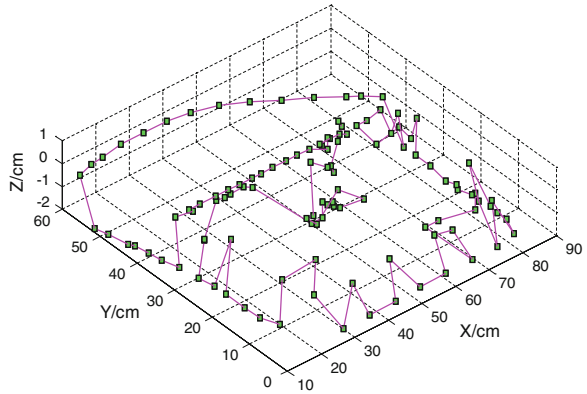
A car door with 115 solder joints is used for older joints sequences optimization in this paper. Figure 3 shows partition result of welding joints and four red points in the picture are reference points. Figure 4 is the path planning result of the path planning result of PM-PSO, the final total path length is 466.9176. Comparison of the three algorithms is given in Table 1, the simulation results show that the PM-PSO is better than the basic PSO algorithm and P-PSO for welding joints sequence optimization. It also shows that the convergence speed of PM-PSO is faster obviously.

PM-PSO converts massive solder joints path optimization into several small-scale computing, simplify the search space, and can quickly converge at the optimal solution. Besides, the optimal solution is easier to be found after the effective mutation operation was combined. Hence, the final result shows that the result of PM-PSO is greatly improved compared to the basic PSO.

**Fig. 3** Partition result of welding joints



**Fig. 4** Optimization result of PM-PSO



**Table 1** Performance comparison of PSO and hybrid PSO

	Optimal solution (cm)	Convergence rate
PSO	512.4208	Roughly 1400 generation
P-PSO	479.8333	Roughly 220 generation
PM-PSO	466.9176	Roughly 20 generation

## 5 Conclusion

A hybrid PSO algorithm was presented for welding robot path planning. After the effective mutation operation was combined with the basic PSO in PM-PSO, the diversity of the particles was increased, and the overall fitness of the particles was improved. Partition strategy converts massive solder joints path optimization into several small scale computations, which greatly reduces the computational complexity and improves search accuracy. The simulation results show that the improved hybrid PSO algorithm is effective for welding robot path optimization, capable for solving large scale optimization problem especially.

**Acknowledgment** This work is supported by Shanghai Natural Science Foundation under Grant No. 14ZR1409900, and National Major Scientific Instruments Equipment Development Project under Grant No. 2012YQ15000105.

## References

1. Chong JWS, Ong SK, Nee AYC, Youcef-Youmi K (2009) Robot programming using augmented reality: an interactive method for planning collision-free paths. *Robotics Comput Integr Manuf* 25:689–701
2. Givehchi M, Ng A, Wang LH (2011) Spot-welding sequence planning and optimization using a hybrid rule-based approach and genetic algorithm. *Robotics Comput Integr Manuf* 27:714–722

3. Yang H, Shao H (2009) Distortion-oriented welding path optimization based on elastic net method and GA. *J Mater Process Technol* 209:4407–4412
4. Kennedy J, Eberhart RC (1995) Particle swarm optimization. *IEEE Int Conf Neural Netw* 1942–1948
5. Wang XW, Li RR (2013) Intelligent modelling of back-side weld bead geometry using weld pool surface characteristic parameters. *J Intell Manuf* doi:[10.1007/s10845-013-0731-4](https://doi.org/10.1007/s10845-013-0731-4)
6. Wang Y, Liu JH (2010) Chaotic particle swarm optimization for assembly sequence planning. *Robotics Comput Integr Manuf* 26:212–222
7. Kennedy J, Eberhart RC (1997) A discrete binary version of the particle swarm algorithm. *IEEE Int Conf Comput Cybern Simul* 4104–4108
8. Clerc M (2004) Discrete particle swarm optimization, illustrated by the traveling salesman problem. *New Optim Tech Eng* 141:219–239

# Influence of Heat Input on the Performance of Joint with Filling Wire Laser Welding 5A06 Aluminum Alloy

Yangchun Yu, Yanling Xu, Guodong Xu, Ajing Chen  
and Shanben Chen

**Abstract** 5A06 aluminum alloy sheets were welded using a 4 kW fiber laser with SA1-Mg5 filler. Processing parameters such as laser power, welding speed and wire filler speed were optimized with the objective of producing a welded joint with complete penetration and smooth welding profile. Influence of heat input on microstructures and mechanical properties of butt joints have been studied. The results show that the microstructure of the welding seam was dense columnar crystals near to the fusion area and fine dendrites in the center. The crystal of heat affected zone (HAZ) was coarsening and increased slightly with increasing heat input, but the width of HAZ was only about 80  $\mu\text{m}$ . With increasing heat input, the mechanical properties of butt joints were improvement and the damage position was migrating from HAZ to base metal. Scanning electron microscope (SEM) observation on the fracture surface of welded joint showed that the pores exerted a great influence on the reduction in strength and elongation, but the microstructure of the welding seam hardly affected the tensile properties.

## 1 Introduction

5A06 aluminum alloy belongs to Al–Mg alloy, which is one of the most widely used aluminum alloy in the welded structure because of its good corrosion resistance, high specific strength, and good weld ability. It has been widely used in

---

Y. Yu (✉) · A. Chen

Institute of Welding Application, Shanghai Zhenhua Heavy Industries Co., Ltd (ZPMC),  
Shanghai, People's Republic of China  
e-mail: yuyangchun@zpmc.net

Y. Yu · Y. Xu · S. Chen

School of Materials Science and Engineering, Shanghai Jiao Tong University, Shanghai,  
People's Republic of China

Y. Yu · G. Xu

School of Mechanical and Electrical Engineering, Nanchang Institute of Technology,  
Nanchang, People's Republic of China

many industrial fields such as aerospace, automotive, machinery manufacturing, electrical and chemical industry. Until now, the welding of this alloy is mainly using the conventional arc welding methods such as metal-arc inert-gas (MIG), tungsten inert-gas (TIG) and so on. However, due to the low melting point, high heat conduction coefficient, low density, large linear expansion coefficient and other characteristics of the 5A06 aluminum alloy, it is very easy to formation the pores, cracks, heat distortion, and other welding defects in the weld and heat affected zone. In particular, the softening of heat-affected zone after going through arc welding thermal cycle lead to the joint strength of arc welding is often much lower than the base material strength, which seriously restricted its application in industry [1].

Use high-energy laser beam to welding the aluminum alloy can greatly improve the performance of joints because of its high energy density, but it can also lead to the evaporation of high-temperature volatile alloying elements (such as Mg), which greatly reduce the performance of weld joints. In addition, the burning of alloying elements in laser welding can result in some weld shape defects such as undercut, crack and porosity, which further lead to a decline in mechanical properties of joints [2, 3]. Added the filling wire in laser welding can eliminate the above problems, and many studies about it have been carried out [4–7]. However, the relationship between laser welding heat input and performance of joints are still lack of systematic research.

In this paper, 5A06 aluminum alloy sheets with thickness of 2.0 mm were welded using a 4 kW fiber laser with SAl-Mg5 filler. The relationship between laser welding heat input and performance of joints were studied through the tensile test and microstructure observation of weld joint.

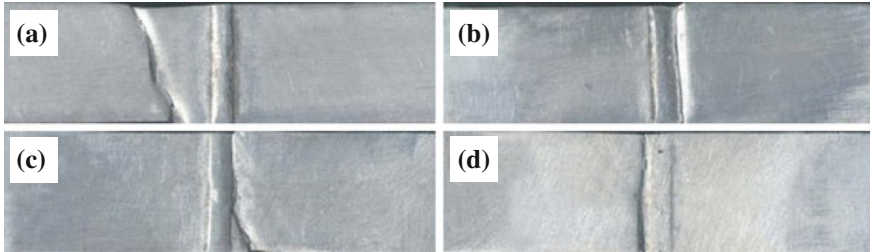
## 2 Experimentations

The base material used in this study was 5A06 aluminum alloy with thickness of 2.0 mm. SAl-Mg5 aluminum wire (1.0 mm in diameter) was used as filler wire. The chemical compositions of base material and filler wire are exhibited in Table 1. The welding direction is along the rolling direction of the aluminum alloy plate (150 mm × 100 mm). Argon gas was used as shielding gas and the flow rate was 16 l/min.

Experiments were carried out by using a 4 kW YLR4000 IPG fiber laser and a VR7000 fronius wire feeder. The filler wire was supplied just ahead the laser beam at an angle of 30° with respect to the surface normal, which can avoid laser leaking

**Table 1** Composition of 5A06 and SAl-Mg5 (%)

Alloy	$\omega$ (Si)	$\omega$ (Fe)	$\omega$ (Cu)	$\omega$ (Mn)	$\omega$ (Mg)	$\omega$ (Zn)	$\omega$ (Ti)	$\omega$ (Al)
5A06	0.4	0.4	0.1	0.5–0.8	5.8–6.8	0.2	0.02–0.1	Bal.
SAl-Mg5	0.4	0.4	–	0.2–0.6	4.7–5.7	–	0.05–0.2	Bal.



**Fig. 1** Fracture position of tensile specimen (a, b in base metal and c, d in HAZ)

**Table 2** Laser welding parameters

No.	Laser power P/W	Wire feed speed $V_f/\text{mm s}^{-1}$	Welding speed $V_w/\text{mm s}^{-1}$	Heat input $\text{K/J mm}^{-1}$
1	2700	100	33	81.8
2	3800	130	50	76
3	3400	120	58	58
4	2700	120	50	54

through the gap of the butt joint. The focus point of the laser beam was set at the substrate surface, as shown in Fig. 1. The parameters of the laser welding experiments are shown in Table 2.

### 3 Results and Discussions



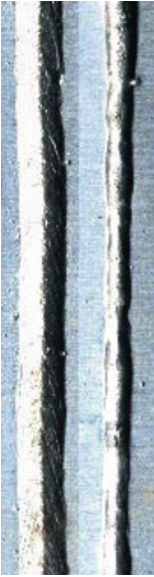

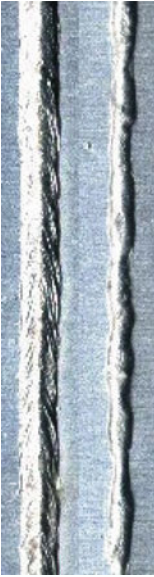



Laser power and welding speed are two main factors that affect the quality of the joints in laser welding. The matching relationship between them has a directly affection on the geometric morphology, microstructure and mechanical properties of the joints. In order to better understand the synergistic effect of laser power and welding speed on the quality of welded joints. The ratio of laser power and welding speed has been defined as  $K$ . when the unit of laser power ( $P$ ) is watts ( $W$ ) and the unit of welding speed ( $VW$ ) is  $\text{mm s}^{-1}$ , the unit of  $K$  is  $\text{J mm}^{-1}$ .

The geometric shape and mechanical properties of the weld joint with different heat input is respectively shown in Tables 3 and 4.

The fracture location of tensile specimen with different heat input is shown in Fig. 1.

The geometric shape of joints and the fracture location are both changed with the decrease of heat input. The geometric shape of joints is similar “I” type when the heat input ( $K$ ) is higher or equal to  $76 \text{ J mm}^{-1}$  and the fracture occur in base metal, therefore, it is safe to think that the mechanics properties of weld joint is equivalent to the base materials. When the heat input decrease down to  $58 \text{ J mm}^{-1}$ , the

**Table 3** The geometric shape of the weld joint with different heat input

No.	Heat input K/J mm <sup>-1</sup>	Surface of weld	Cross section
1	81.8		
2	76		
3	58		
4	54		

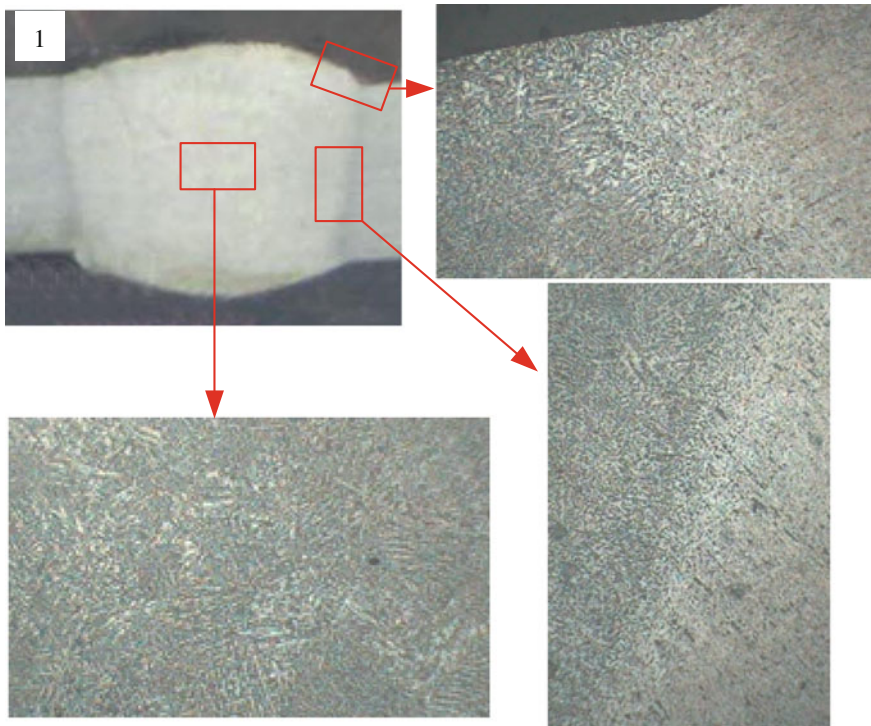


**Table 4** The mechanical properties of the weld joint with different heat input

No.	Heat input K/J mm <sup>-1</sup>	Tensile strength $\sigma_b$ /MPa	Elongation $\delta$ /%	Break location
1	81.8	310.75	25.27	Base metal
2	76	303.46	23.41	Base metal
3	58	286.76	17.47	HAZ
4	54	280.42	15.29	HAZ

geometric shape of joints change into a “T” type, and the fracture location is also migrating to HAZ, then, the joints tensile strength and elongation is lower than the base materials.

Based on the above results, it can be say that the geometric shape of joints, mechanical properties and fracture location are all closely related to the heat input. The increase of heat input is beneficial to the formation of the geometric shape of “T” type. Its upper weld width is approximately equal to the lower and the transition between the seam and base material is relatively smooth in the joint of “T” type, therefore, the stress concentration in the joint is relatively small, which is the reason for fracture occurred in the base metal rather than the weld metal (see Fig. 2). With the decrease of heat input, the joint of “T” type shall be get. Its upper weld width is



**Fig. 2** Microstructures of typical joint of “T” type

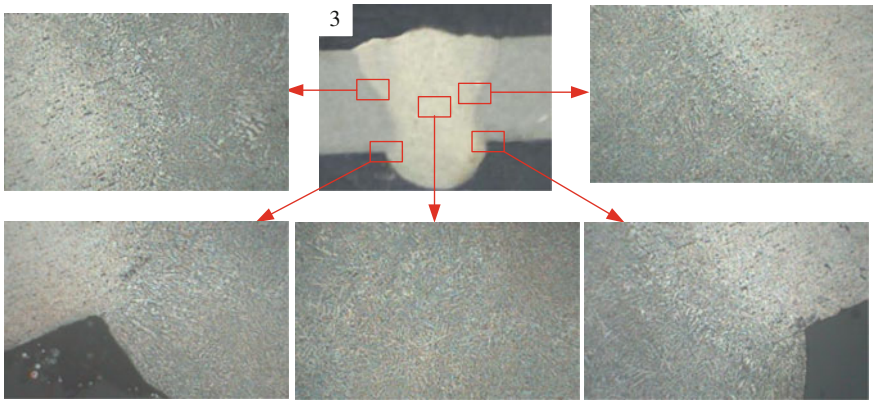


Fig. 3 Microstructures of typical joint of “T” type

bigger than the lower and a mutation between the seam and base material lead to a very high stress concentration in the joint, which is the cause of that the fracture occurred in the HAZ (see Fig. 3).

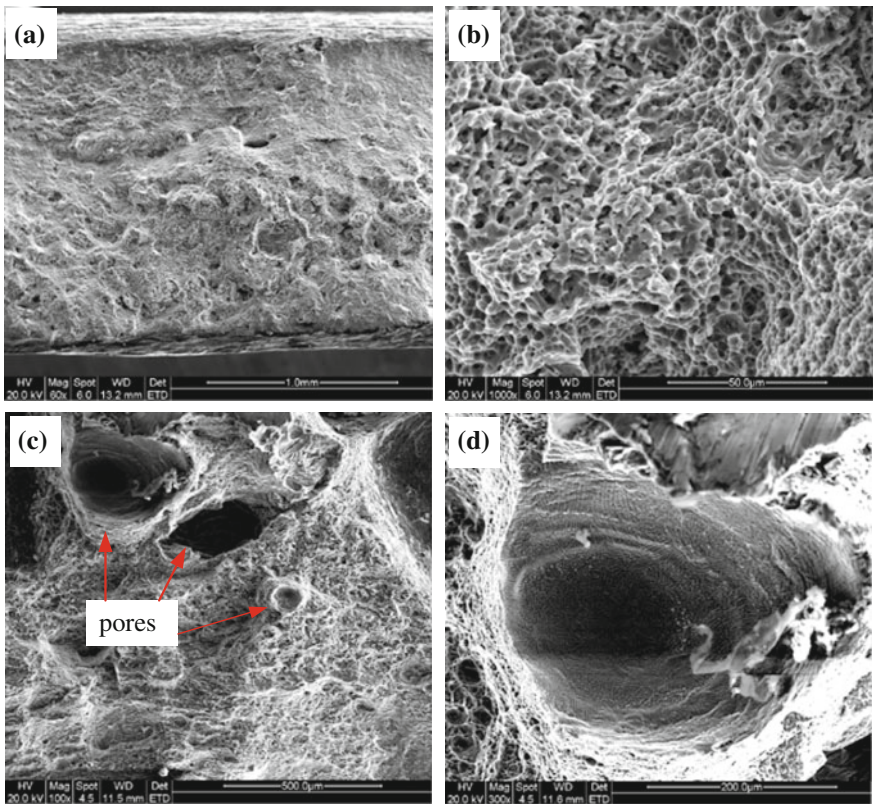


Fig. 4 Fracture SEM images of No. 1 (a, b) and No. 3 (c, d)

As for the joint of “T” type, the fracture location in the HAZ, both its strength and elongation are decreased, the strength reduced less than 10 %, while the elongation is reduced to about 40 %.

In order to further analyze the effect of heat input on the performance of the joints, the SEM of tensile fracture surface for sample No. 1 and No. 3 (see Fig. 4) has been made to further analysis of the fracture properties of joint. According to Fig. 4, it can be see that the uniform distribution of dimples (see a, b in Fig. 4) is the dominating character of the fracture surface except for scattered porosity in No. 3 (see c, d in Fig. 4).

The uniform distribution of dimples in the fracture surface indicating the fault belongs to plastic fracture; therefore a higher strength and elongation have been getting for No. 1. The scattered porosity (see c, d in Fig. 4) may be the reason for the decrease of strength and elongation in No. 3.

## 4 Conclusion

1. Heat input have an important influence on the geometric shape and mechanical properties of joints. When the heat input ( $K$ ) is higher or equal to  $76 \text{ J mm}^{-1}$ , the geometric shape of joints is similar “I” type which has the low stress concentration due to the smooth transition between the weld seam and base metal, and the fracture occur in the base metal with a high tensile strength. On the contrary, when the heat input ( $K$ ) is less than or equal to  $58 \text{ J mm}^{-1}$ , the geometric shape of joints change into a “T” type which has severe stress concentration due to the cross-section mutation for the joint, and the fracture location is also migrating to HAZ with a low tensile strength.
2. With the decrease of heat input, the escape of hydrogen bubbles become difficult due to rapid solidification of weld pool during the laser welding 5A06 aluminum alloy with filling wire, the formation of pores in the joint lead to significantly reduced in the joint elongation.

**Acknowledgements** This work is supported by the Intelligent Welding Workshop Project for Offshore Drilling Platform Equipment Manufacturing (2012) (No. 2144) and the National Natural Science Foundation of China under the Grant No. 51405298.

## References

1. Dickerson PB (1986) Welding of aluminum and aluminum alloys. *Encycl Mater Sci Eng* 5:108–121
2. Mayer C, Fouquet F, Robin M (1996) Laser welding of aluminium–magnesium alloys sheets process optimization and welds characterization. *Mater Sci Forum* 217–222:1679–1684
3. Zhao H, Debroy T (2001) Weld metal composition changes during conduction mode laser welding of aluminum alloy 5182. *Metall Mater Trans* 32B(1):163–172

4. Haboudou A, Peyre P, Vannes AB, Peix G (2003) Reduction of porosity content generated during Nd:YAG laser welding of A356 and AA5083 aluminium alloys. *Mater Sci Eng A* 363:40–52
5. Kutsuna M, Yan Q, Study on porosity formation in laser welds of aluminium alloys, IIW-doc IV-683-97
6. Yoon JW, Lee YS, Lee KD, Park KY (2005) Effect of filler wire composition on Nd:YAG laser weld ability of 6061 aluminum alloy. *Mater Sci Forum* 475–479:2591–2594
7. Schinzelt C, Hohenberger B, Dausinger F, Hugel H (2000) Laser welding of aluminum extended processing potential by different wire positions. *High-Power Lasers Manufact Proc SPIE* 3888:380–391

# Feature Extraction from Arc Signal for Height Tracking System of P-MAG Welding

Zhen Ye, Hua-Bin Chen, Fang Gu and Shan-Ben Chen

**Abstract** An experimental system is established to acquire and process the arc signal. Possible Features and a signal process method are proposed by analyzing the characteristics of the pulse power supply. The best feature is selected by applying the feature selection method and the relational model between the feature and the torch height is established. Experiments are conducted to confirm the accuracy of the model and its application in height tracking system.

## 1 Introduction

Nowadays, fewer and fewer people want to be welders because of the hostile nature of the welding environment and extreme physical demands of the welding process. To address the shortage of welders, welding robots have been widely used and proves to be a good substitute. However, most of current welding robots can only follow predefined actions and have no ability to deal with variations in the weld seam positions caused by natural welding factors [2]. Therefore they may not meet the requirement of high welding quality.

To solve the problem, many intelligent welding systems have been proposed by researchers [8, 12]. In these systems, passive vision method becomes the focus because of its low cost, non-contact to the weld pool and rich information of the welding process it collects. Most research on passive vision based seam tracking

---

Z. Ye (✉)

Shanghai Electric Group Co., Ltd. Central Academe, Shanghai, People's Republic of China  
e-mail: zhye1985@aliyun.com

H.-B. Chen · S.-B. Chen

School of Materials Science and Engineering, Shanghai Jiao Tong University,  
Shanghai 200240, People's Republic of China

F. Gu

School of Computing, Engineering and Mathematics, University of Western Sydney,  
Sydney, NSW 2751, Australia

technology only focused on acquiring the 2-dimensional planar information while ignoring the third dimension (height) information [9, 10]. However, in some conditions, the height variation exists and it should be considered because it can affect the weld pool formation and the weld bead geometry.

Arc sensors have been designed for detecting the electrical signal during the welding process as the arc electrical signal has been found to have a certain relationship with the welding torch height. For example, [3] found that arc voltage can be modeled as a linear function of the arc length in GTAW. Kim et al. [5–7] developed a mathematical model to predict the welding current change in response to variation of tip-to-workpiece distance in GMAW. Then Kim et al. [5–7] proposed an empirical model to represent the relationship between the welding current and tip-to-workpiece distance under different welding voltage and wire feed speed. Based on these relational models, the weaving arc sensors [4–7] and the rotating arc sensors [11] are designed to realize the seam tracking for groove shape joint and fillet weld joint. Bao et al. [1] and Zhu [13] designed a method to detect the torch height via measuring the wire electrode extensions during the metaphase of short-circuit according to the characteristic of CO<sub>2</sub> welding.

However, existing research focused only on the standard arc welding. The power supply of pulse welding, which has less heat while providing stable arc and superior welding quality, is quite different. Thus, the method to realize the torch height tracking for pulsed MAG welding needs to be further studied. The main contribution of this paper is to study the relationship between the electrical features of the pulse welding and the welding torch height, and find the best feature to represent the torch height based on the feature selection method.

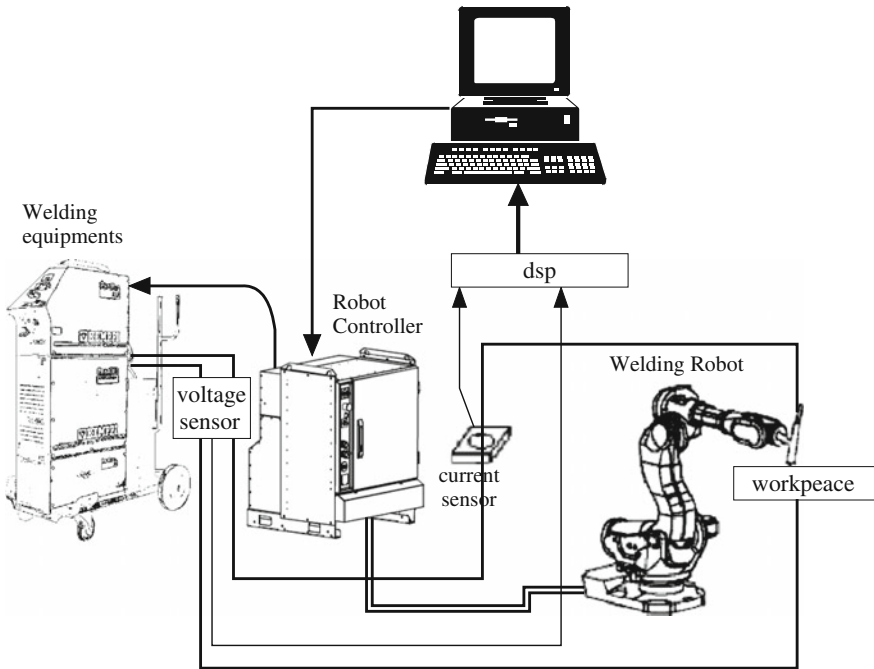
The rest of this paper is organized as follows. In Sect. 2, a height tracking system is introduced based on the arc sensor, which can effectively acquire arc current and arc voltage signals. In Sect. 3, several electrical features and a signal processing method are proposed by analyzing characteristics of the pulse power supply. Then best feature is selected by applying the feature selection method. The relational model between the feature and the torch height is established. In Sect. 4, experiments are conducted to confirm the feasibility of the method.

## 2 System Descriptions

Our experimental system includes a “teach and play back robot”, a current sensor and a voltage sensor, welding equipments, a digital signal processor (DSP) and an industrial computer. The schematic diagram is shown in Fig. 1. Firstly, the sensors generate signals proportional to the welding current and the welding voltage. Then the signals are read by the A/D converter module of the digital signal processor. Finally, the signals are transferred to the computer for saving or further processing via serial communication.

This research focuses on the low carbon steel-Pulse MAG welding. In order to acquire and process the data in real time, the sampling frequency is set at 1800 Hz.





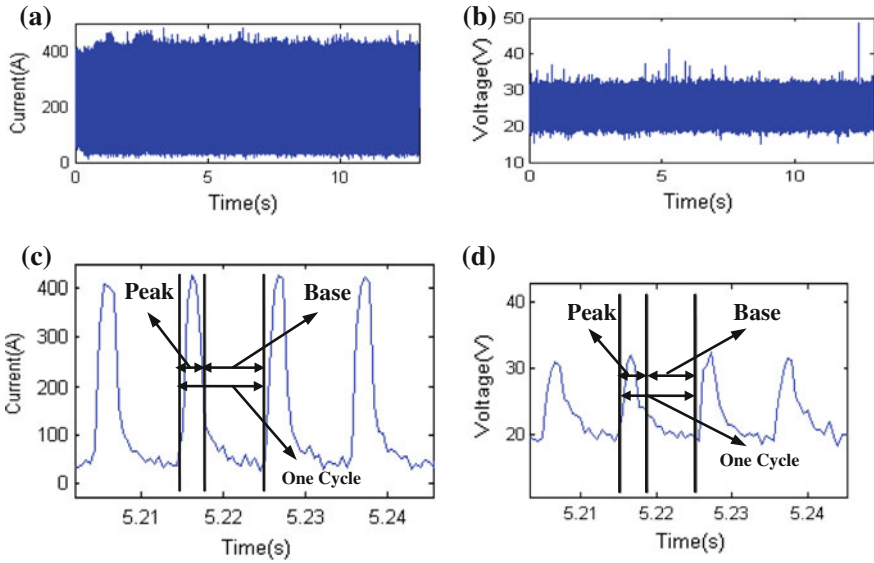
**Fig. 1** Schematic diagram of the system

Figure 2a, b show the electrical signals collected during the welding process when the welding torch height is constant. Figure 2c, d are the local enlargements of Fig. 2a, b and show the waveform of the signals. From Fig. 2, we can see that even when the torch height is constant, the current and the voltage still change with time. The current ranges from 50 to 450 A, the voltage ranges from 20 to 30 V. The original electrical signal cannot represent the torch height directly. Therefore, the signals must be processed to extract the features which can accurately represent the torch height.

### 3 Feature Extraction from the Arc Signal

#### 3.1 Feature Expression

In this paper, pulse MAG power supply uses the Constant Current (CC) mode during the pulse peak duration and the Constant Voltage (CV) mode during the base duration. The CC mode is characterized by large change in voltage for small current change while CV mode is characterized by large change in current for small voltage change. Such characteristics of the power supply produce the peak voltage change and the base current change in response to the variation of the welding torch height.



**Fig. 2** The electrical signal of the welding process. **a** Original current, **b** original voltage, **c** current wave form, **d** voltage waveform

Additionally, any variation in welding torch height will result in the change of the arc length. To ensure the stability of the welding process, the power source needs to regulate the arc by modifying pulse frequency, which in turn modifies the average current. Therefore, the average current can also represent the welding torch height.

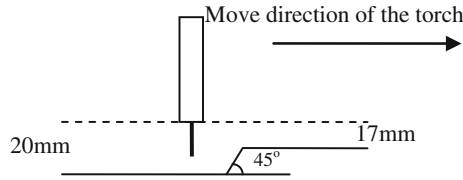
From the above analysis, the base current, the peak voltage, and the average current are selected to be possible features in determining the torch height. Besides, the ratio of the voltage to the current is also considered. The equations of these features are given in Table 1.

In Table 1, I is the current, U is the voltage, t is the time, R is the ratio between voltage and current, subscript b, p, a are for base, peak, and average, respectively.

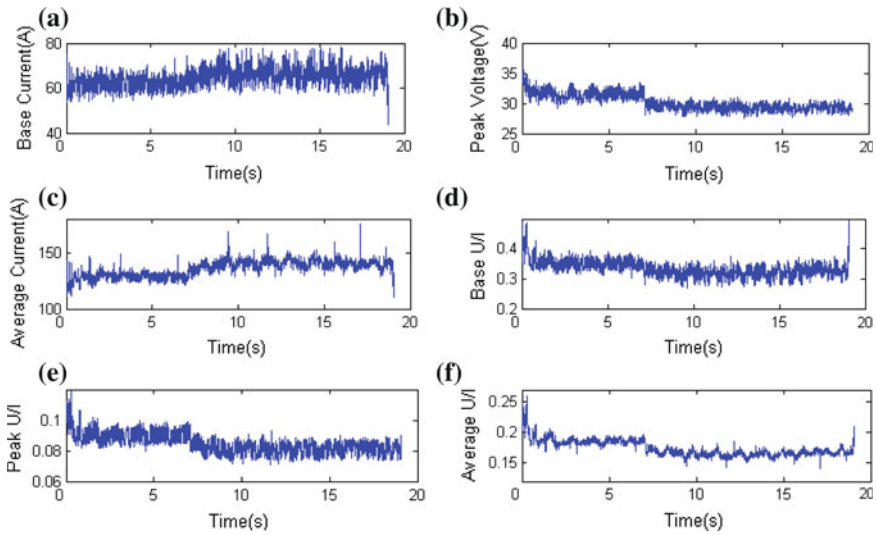
**Table 1** The equations of features

Base current	$I_b = \frac{1}{t_b} \int_{t_b} I dt$	Base voltage	$U_b = \frac{1}{t_b} \int_{t_b} U dt$
Peak current	$I_p = \frac{1}{t_p} \int_{t_p} I dt$	Peak voltage	$U_p = \frac{1}{t_p} \int_{t_p} U dt$
Average current	$I_a = \frac{I_p \cdot t_p + I_b \cdot t_b}{t_p + t_b}$	Average voltage	$U_a = \frac{U_p \cdot t_p + U_b \cdot t_b}{t_p + t_b}$
Base U/I	$R_b = \frac{U_b}{I_b}$	Peak U/I	$R_p = \frac{U_p}{I_p}$
Average U/I	$R_a = \frac{U_a}{I_a}$		





**Fig. 3** The schematic diagram of step response



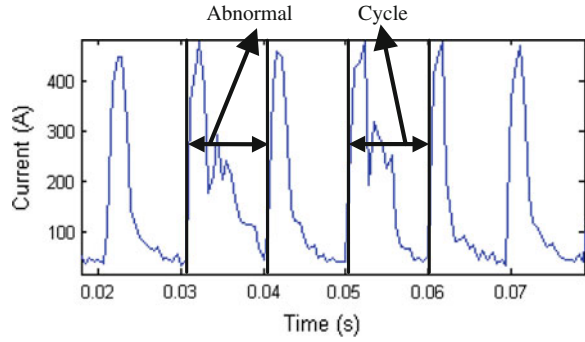
**Fig. 4** The processing results using equations in Table 1. **a** Base current, **b** peak voltage, **c** average current, **d** base U/I, **e** peak U/I, **f** average U/I

In order to testify the relationship between the torch height and possible features, an experiment is conducted, in which the robot is strictly taught along the contour line and the welding torch height changes from 20 to 17 mm, as shown in Fig. 3. Features of the signal are calculated according to the equations in Table 1 and the results are shown in Fig. 4. From Fig. 4, it can be found that all features have a significant change when the torch height decreases from 20 to 17 mm. Such results confirm the feasibility of possible features.

### 3.2 Filtering

From Fig. 4 it can be seen that in addition to the information of welding torch height, the collected signals contain significant amount of noise. The noise is due to welding environment, like surface conditions of the workpiece, unstable airflow and

**Fig. 5** Schematic diagram of the abnormal cycle



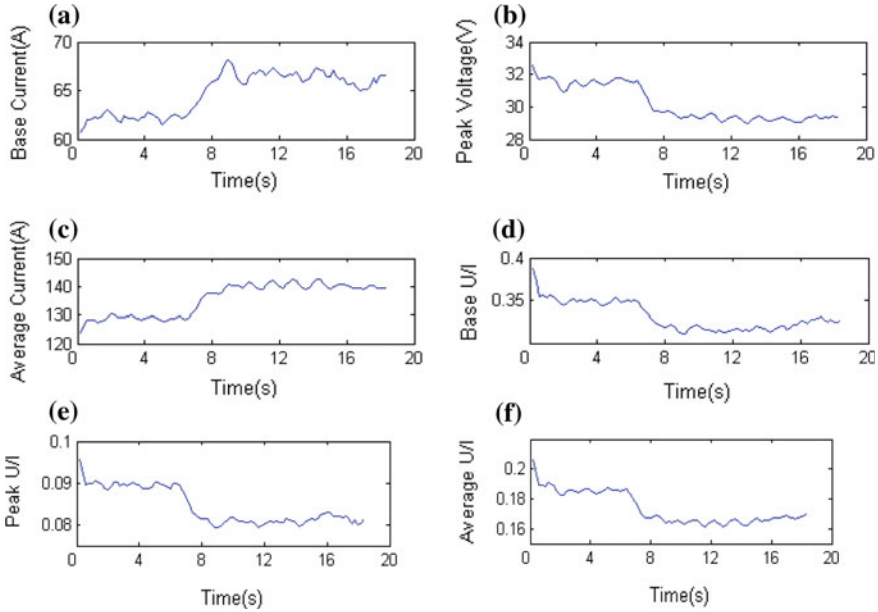
changing speeds of the wire feeding. It is also caused by the characteristic of the welding, like the change of the arc length and wire extensions happening with the droplet transfer. All these factors may lead to the fluctuation of the signal even under constant torch height, and therefore interfere with the precision of tracking. In order to reduce such interference, the collected signals are analyzed and it is found that some variations of feature values are results of the abnormal cycles, which are caused by the unsatisfied droplet transfer but not the change of welding torch height, as shown in Fig. 5. Experiments show that the peak duration during the normal welding process should range from 2 to 3 ms, and the base duration from 7 to 10 ms. Therefore, some abnormal feature values can be eliminated first by eliminating abnormal cycles.

Additionally, a moving average filter is applied to process the signal to further reduce the noise. The moving average filter operates by averaging a number of points from the input signal to produce each point in the output signal, the equation of which is given by Eq. 1. The smoothing action of the moving average filter decreases the amplitude of the noise, but also reduces the sharpness of the edges.

$$y(i) = \frac{1}{M} \sum_{j=0}^{M-1} x[i-j] \quad \forall i = M, M+1, \dots \quad (1)$$

where  $x[i-j]$  is the  $(i-j)$ th input signal,  $y(i)$  is the  $i$ th output signal, and  $M$  is the number of points in the moving average window.

Figure 6 shows the processing results of the feature value in Fig. 4 after abnormal cycle elimination and moving average filter. From Fig. 6, it can be found that the fluctuation of the processed feature value is much smaller while the change of the feature value in response to the variation of torch height is persisted.



**Fig. 6** The processing results of Fig. 4 by a moving average filter: **a** base current, **b** peak voltage, **c** average current, **d** base U/I, **e** peak U/I, **f** average U/I

### 3.3 Feature Selection and Parameter Optimization

Since the features introduced in Sect. 3.1 are redundant and the time allowed to process the signal is limited, a proper feature selection method is required to find the best feature. In addition, the moving average window size,  $M$ , also needs to be determined properly.

To select the best feature for the torch height, a series of experiments are conducted to acquire the electrical signals under different height from 13 to 23 mm, which cover the main range of allowed welding torch heights. Meanwhile, we define the  $i$ th type of signal as the signal collected when the torch height is at  $(12 + i)$  mm, where  $i = 1, 2, \dots, 11$ .

#### 3.3.1 Evaluation Function

A good feature for the welding torch height should be as stable as possible when the height is constant and change as large as possible when the height is different. Therefore, the evaluation function we design is as Eq. 2.

$$J(F_k, M) = \min \left( \frac{d^{(i)(i+1)}(F_k, M)}{S^i(F_k, M) + S^{i+1}(F_k, M)} \right) \quad (2)$$

where  $F_k$  is the feature in Table 1;  $M$  is the number of points in the moving average window;  $J(F_k, M)$  is the criterion value;  $d^{ij}(F_k, M)$  is the Euclidean distance between the  $i$ th type of signal and the  $j$ th type of signal, which is used to describe the sensitivity of the feature to the change of the height, and is given by Eq. 3;  $S^i(F_k, M)$  is the inside distance of the  $i$ th type of data, which is used to describe the degree of fluctuation of the feature under the constant height, and is given by Eq. 4. In order to distinguish the height change, a larger  $d^{i(i+1)}/(S^i + S^{i+1})$  is required. Therefore, to ensure that all heights can be distinguished, the minimum value of  $d^{i(i+1)}/(S^i + S^{i+1})$  is chosen to be the criterion value,  $J$ .

$$d^{ij}(F_k, M) = \left| \bar{X}^i(F_k, M) - \bar{X}^j(F_k, M) \right| \quad (3)$$

where  $d^{ij}(F_k, M)$  is the same as that in Eq. 2;  $\bar{X}^i(F_k, M)$  is the average value of the  $i$ th type of signal when the feature  $F_k$  is selected and the number of points in the average is set as  $M$ .

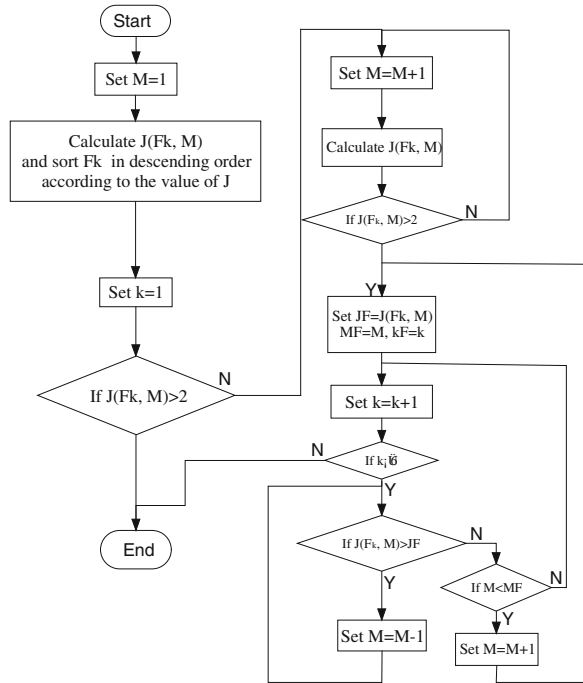
$$S^i(F_k, M) = \sqrt{\frac{\sum_{l=1}^n \left( X_l^i(F_k, M) - \bar{X}^i(F_k, M) \right)^2}{n}} \quad (4)$$

where  $S^i(F_k, M)$  is the same as that in Eq. 2;  $\bar{X}^i(F_k, M)$  is the same as Eq. 3;  $X_l^i(F_k, M)$  is the  $l$ th data of the  $i$ th signal when the feature  $F_k$  is selected and the numbers of points in the average is set as  $M$ ;  $n$  is the number of the data of the  $i$ th signal.

### 3.3.2 Search Algorithm

On one hand, the feature and the number of points in the average should make the criterion value ( $J$ ) as large as possible so that different heights can be distinguished more clearly. On the other hand, the number of points in the average window ( $M$ ) should be as small as possible to make the signal more responsive to real time change. However, the above two targets can not be reached at the same time because  $J$  increases with the increase of  $M$ . Therefore, the compromise is to find the smallest  $M$  under the condition that signals at different heights can be distinguished. In order to distinguish signals at different heights,  $J$  should be no less than 2. This threshold value is chosen as it is the minimum requirement to make a clear discrimination between different heights. A search algorithm is developed to select the proper  $M$  and  $F_k$ . The flow chart of the searching method is shown in Fig. 7.

**Fig. 7** The flowchart of the searching method



**Table 2** The result of feature selection

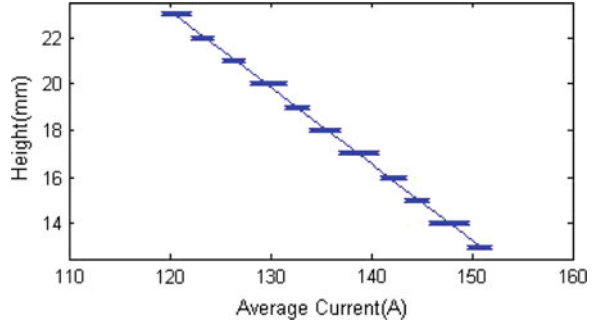
Selected feature	M	J
Average current ( $I_a$ )	82	2.0021

Using this method, the optimal feature and the best moving average window size, M, are determined and presented in Table 2. Also presented in the table is the selection criteria value J obtained using these selections.

### 3.4 Linear Fitting

To establish a model between the welding current and the welding torch height, Fig. 8 is constructed to show the distribution of the average current under different heights. From Fig. 8, it can be found that the average current reduces with the increase of the torch height, and there is a linear relationship between the height and the average current. Additionally, it should also be noted that the average current has certain variation under a constant height. The main reason for such variations is the characteristic of the welding process, such as the change of stick-out length caused by droplet transfer, where the variation is within a small range and can be a

**Fig. 8** The distribution of the average current under different heights



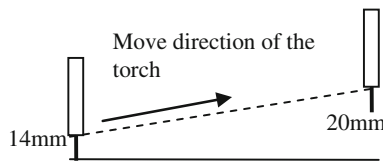
part of the model. Consequently, the relational model between the welding current and the torch height can be fitted by straight line and the model is given by Eq. 5.

$$H = -0.3291 \times I + 62.6539 \pm 0.6 \quad (13 \leq H \leq 23) \tag{5}$$

## 4 Experiments and Results

### 4.1 Verification of the Model

In order to test the accuracy of the proposed model relating to the welding torch height, an experiment is designed as shown in Fig. 9. The robot was strictly taught to move along the contour line in the experiment without any adjustments. In particular, the torch height changed gradually from 14 to 20 mm. Table 3 shows the welding condition and Fig. 10 shows the collected original signal. Figure 11 shows the results obtained using the proposed method. Figure 12 shows the real height and the calculated results using the model proposed in this paper. From results, it can be seen that the model represents the relationship accurately between the welding torch height and the average current. It is also worth noting that there is a large fluctuation at the beginning of the welding. This is expected as at the beginning of the welding, the current is determined by the welding equipment and cannot be modified.

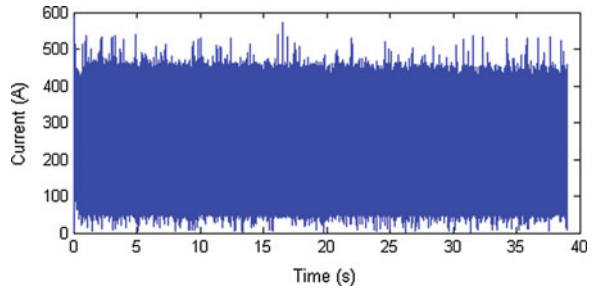


**Fig. 9** The schematic diagram of the verification test

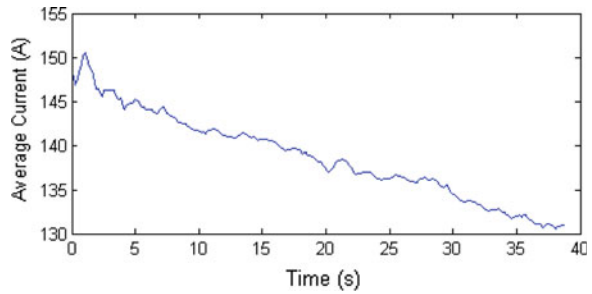
**Table 3** The welding condition

Material	Low carbon steel
Wire feed speed (m/min)	3.7
Current (A)	140
Voltage (V)	24
Welding speed (m/min)	0.3

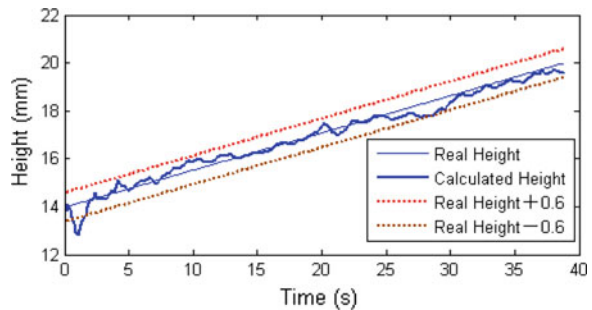
**Fig. 10** The original current



**Fig. 11** Processing results of the signals in Fig. 10



**Fig. 12** The calculated results of Fig. 11 using the proposed relational model



### 4.2 Tracking Experiments

Using the proposed model, we implemented a control algorithm for automatic seam height tracking in P-MAG welding of low carbon steel. The algorithm uses the arc sensor signal to infer the current welding height and drive the robot to adjust the position of the welding torch to maintain a constant height of the torch. In order to avoid the interference of the large current of arc at the beginning of the welding, we only begin seam tracking 1 s after the welding has started. Besides, in order to keep the welding process stable, the height is only corrected when the difference between the detected and the set heights is larger than 0.6 mm. We calculate the height difference once every 20 cycles (approximately 200 ms).

The taught path, desired path and tracked path is shown in Fig. 13 and the welding result is shown in Fig. 14. From Fig. 13, it can be found that the largest error is 1.2 mm, and the average error is 0.545 mm, which is adequate to meet the requirement of the welding.

Fig. 13 The schematic diagram of the robot path

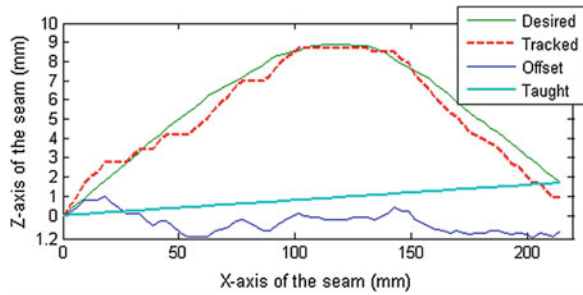
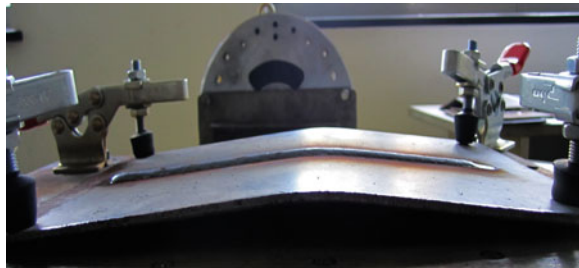


Fig. 14 The welding result





## 5 Conclusion

1. An arc sensing system was established, which can acquire the electrical signal during welding process.
2. Several features related with the welding torch height were proposed, and a method to reduce the noise was introduced in this paper.
3. The best feature was selected to represent the torch height, and the relational model was established between them.
4. The verification experiment confirmed the feasibility of the model, and the tracking experiment showed that the developed system can realize the seam tracking function.

**Acknowledgments** This work is supported by the National Natural Science Foundation of China under the Grant No. 51075268 and Shanghai Sciences & Technology Committee under Grant No. 11111100302, P.R. China.

## References

1. Bao Y, Zhu Z, Wu W (2001) Through-the-wire sensor of short-circuit CO<sub>2</sub> welding. *Trans China Weld Inst* 22(3):55–58
2. Chen SB, Qiu T (2004) Intelligent technologies for robotic welding. *Lect Notes Control Inf Sci* 299:123–143
3. Cook GE (1983) Robotic arc welding: research in sensory feedback control. *IEEE Trans Ind Electron IE* 30(3):252–268
4. Gan Y, Dai X (2009) Deviation extraction for through-arc sensor with sinusoidal weave motion. *Trans China Weld Inst* 30(9):89–92
5. Kim JW, Na SJ (1991) A study on prediction of welding current in gas metal arc welding part 1. *Proc Inst Mech Eng B* 205:59–63
6. Kim JW, Na SJ (1991) A study on prediction of welding current in gas metal arc welding part 2. *Proc Inst Mech Eng B* 205:64–69
7. Kim JW, Na SJ (1991) A study on arc sensor algorithm for weld seam tracking in gas metal arc welding of butt joints. *Proc Inst Mech Eng Part B J Eng Manuf* 205(B4):247–255
8. Li LP, Lin T, Chen SB (2005) Light intensity analysis of a passive visual sensing system in GTAW. *Int J Adv Manuf Technol* 27(1–2):106–111
9. Ma HB, Wei SC, Sheng ZX (2010) Robot weld seam tracking method based on passive vision for thin plate closed-gap butt welding. *Int J Adv Manuf Technol* 48(9–12):945–953
10. Shen HY, Li LP, Lin T, Chen SB (2010) Real-time seam tracking technology of welding robot with visual sensing. *J Intell Rob Syst* 59(3–4):283–298
11. Shi YH, Yoo WS, Na SJ (2006) Mathematical modelling of rotational arc sensor in GMAW and its applications to seam tracking and endpoint detection. *Sci Technol Weld Joining* 11(6):723–730
12. Xu PQ, Xu GX, Tang XH, Yao S (2008) A visual seam tracking system for robotic arc welding. *Int J Adv Manuf Technol* 37(1–2):70–75
13. Zhu ZM (2008) Real-time detection and control of torch-height in waveform controlled short-circuit CO<sub>2</sub> arc welding. *Mater Sci Forum* 580–582:427–430

# Research of Laser Hybrid Welding for T-Joint in the Box Girder

Yang-Chun Yu, Kong Bao, Yan-Ling Xu, A-Jing Chen,  
Hua-Jun Zhang and Shan-Ben Chen

**Abstract** T-joint is widely used in box girder structure of lifting machinery and bridges. The welding of T-joint by use of manual arc welding has many problems, such as large deformation, operational difficulties inside the box, low productivity and so on. To solve these problems, the technical feasibility of welding for T-joint by use laser hybrid welding has been study. The results show that the single face welding-double face forming of T-joint for box girder structure can be achieved by use laser hybrid welding, and the weld quality and productivity is greatly improved.

## 1 Introduction

Lifting machinery play an important role in the construction of shipping, metallurgy, chemical industry, power plants, bridges, and so on. As the main parts of lifting machinery, box girders have to withstand a variety of complex loads during the working, so its manufacturing quality is critical to the security. Welding is the key to the box girders manufacturing, more than 90 % of welding is related to T-joint. The welding of T-joint is usually with manual arc welding which has many problems, such as large deformation, operational difficulties inside the box, low productivity and so on. Laser beam welding technology may be a promising solution to these problems because of its high welding speed, low distortion, and

---

Y.-C. Yu (✉) · Y.-L. Xu · S.-B. Chen

School of Materials Science and Engineering, Shanghai Jiao Tong University,  
Shanghai, People's Republic of China  
e-mail: yuyangchun@zpmc.net

Y.-C. Yu

School of Mechanical and Electrical Engineering, Nanchang Institute of Technology,  
Nanchang, People's Republic of China

Y.-C. Yu · K. Bao · A.-J. Chen · H.-J. Zhang

Institute of Welding Application, Shanghai Zhenhua Heavy Industries Co., Ltd. (ZPMC),  
Shanghai, People's Republic of China

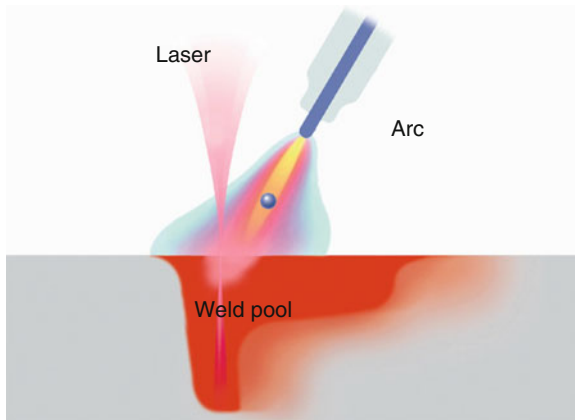
easy automation, but the high cost of processing and harsh demand of beveling hindered its industrial application in the welding of plate. As a highly efficient, energy-saving, high-quality, economical welding method, laser hybrid welding shows great potential in the welding of lifting machinery.

Figure 1 is the schematic of laser-arc hybrid welding. In the laser-arc hybrid welding, the energy of laser beam source and arc has been work together to form a welding pool. Both laser beam welding and arc welding have long been used for industrial production and each of them has its specific areas of application and advantages. The laser radiation can lead to a very narrow heat-affected zone with a large ratio of welding depth to joint width (deep-weld effect) and reach a high welding speed, but the gap bridging ability is very low due to its small focus diameter. The arc welding process has a much lower energy density and a slower speed of processing, but the gap bridging ability is good because of a bigger focal spot on the surface of the work piece. By merging both these processes, useful synergies can be achieved. Ultimately, this makes it possible to achieve both quality advantages and production engineering benefits, as well as improved cost efficiency. The merged process offers interesting and economically attractive applications in the shipbuilding industry, not least because higher tolerances are permitted on the weldments, higher joining rates are possible, and very good mechanical/technological values can be achieved [1–3].

A large number of research about laser hybrid welding for thick plate have been carry out in the Europe [4–8], such as Switzerland, Germany, France, Denmark and so on. The single penetration of laser-arc hybrid welding is up to 30 mm and the weldable steel yield strength is from 180 to 690 MPa. Laser hybrid welding have been report to partially replace arc welding in the shipbuilding by the Werft Shipyard, U.S. Naval Institute, Bender Shipbuilding and General Electric Boat Equipment.

However, until now, industrial applications of laser-arc hybrid welding for lifting machinery, marine engineering had hardly been reported in the literature. In

**Fig. 1** Schematic of laser-arc hybrid welding



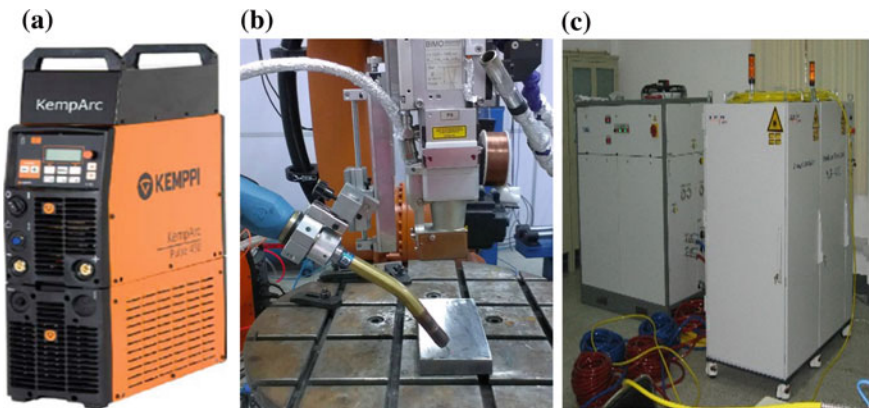
order to promote the industrial applications of laser hybrid welding in the lifting machinery manufacturing, the single face welding-double face forming of T-joint for box girder structure has been study in this paper.

## 2 Experimentations

The base material used in this study was A709-50-2 low-alloy steel with a thickness of 8.0 and 10.0 mm. JM-56 low-alloy steel wires (1.2 mm in diameter) was used as filler wire. The chemical compositions of the base material and filler wire are listed in Table 1. Argon gas was used as shielding gas with a flow rate of 25 l/min. Experiments were carried out by YLR-8000 CW Ytterbium Fiber Laser and a digital arc welding power for robot. The filler wire of arc welding was supplied just ahead of the laser beam, the angle can be free adjustment between 45° and 75° with respect to the normal surface. The focus point of the laser beam was set at the substrate surface (Fig. 2). The parameters of the laser welding experiments are shown in Table 2.

**Table 1** Composition of A709-50-2 and JM-56 (%)

Alloy	C	S	Si	Mn	P	Ni	V	Mo	Nb	Cr	Ti	Cu	Al
A709-50-2	0.15	<0.002	0.3	1.42	0.19	0.01	0.008	<0.01	0.018	0.02	0.01	0.02	0.028
JM-56	0.08	0.018	0.9	1.48	0.014	0.01	0.002	0.002	–	–	–	0.09	–



**Fig. 2** Laser hybrid welding equipment. **a** Digital arc welding power. **b** Hybrid welding head. **c** Fiber laser

**Table 2** Parameters of laser hybrid welding condition

$D_f$ (mm)	$\alpha_L$ ( $^\circ$ )	$D_A$ (mm)	$\alpha_A$ ( $^\circ$ )	$D_{L-A}$ (mm)
-2 to +2	0-5	15-20	45-75	2-6

### 3 Results and Discussion

#### 3.1 The Matching of Laser and Arc Power

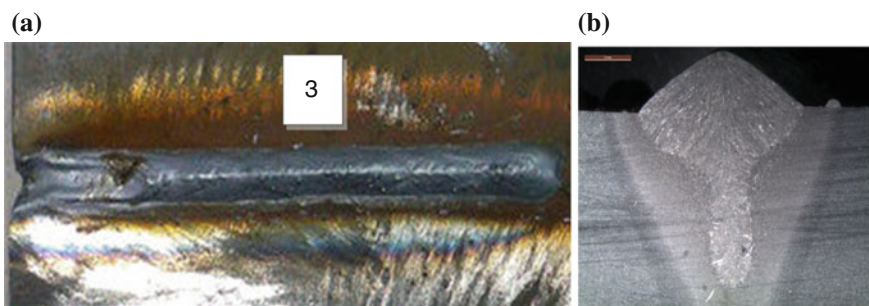
In order to study the optimal matching between the laser and arc power, the laser hybrid welding of butt joints with a thickness of 8.0 mm has been carrying out. The changes in weld penetration have been comparing with the single laser welding and arc welding. The parameters of laser hybrid welding condition have been used is within the ranges that shown in Table 2, the details of welding parameters is shown in Table 3.

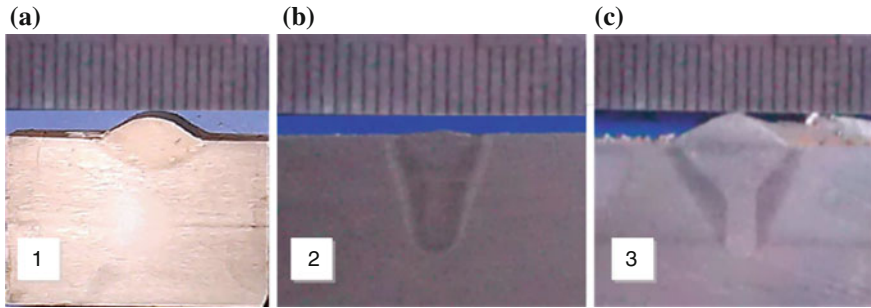
The appearance morphology and cross-sectional shape of laser hybrid welding of butt joint is shown in Fig. 3. The contrast of joint's cross-sectional shape between the laser hybrid welding and single source welding is shown in Fig. 4.

According to Figs. 3 and 4, under the optimization parameters, the joint of laser-arc hybrid welding has a smooth surface and a deep penetration. The cross-sectional of the laser-arc hybrid welding joint can be divided into two parts, the upper half has a shape of bowl as same as the characteristics of arc welding, the

**Table 3** Welding procedures

No.	Laser power P (kW)	Wire feed speed $V_F$ (m/min)	Welding speed $V_W$ (m/min)	Sheet thickness (mm)	Gap (mm)
1	0	4	0.4	8	0
2	4.5	0	0.8	8	0
3	4.5	4	1.0	8	0

**Fig. 3** Weld appearance of laser hybrid welding of butt joint



**Fig. 4** The contrast of joint’s cross-sectional shape. **a** Arc welding. **b** Laser welding. **c** Laser hybrid welding

lower half has the shape of finger as same as the characteristics of laser welding. So, the characteristics of laser-arc hybrid welding can be think a synthesis of laser welding and arc welding. It is show that the good energy coupling of laser and arc source has been getting in the laser-arc hybrid welding. Combines the advantages of the laser and arc, the laser hybrid heat source can achieve the high-speed welding of the thick plate with lower beveling requirements.

### 3.2 Laser Hybrid Welding of T-Joint

With the optimization parameters, two laser hybrid welding tests of T-joint were carried out, the details of welding parameters are shown in Table 4, the inclination degrees of hybrid welding head with respect to the normal surface of webs is respectively 10° and 30°. The weld appearance morphology is shown in Figs. 5 and 7.

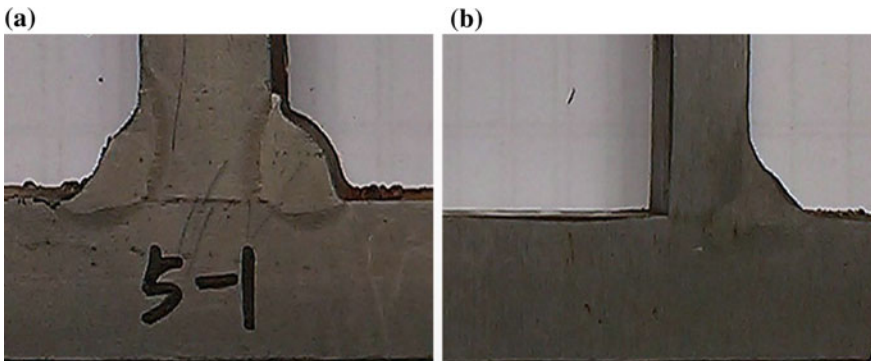
According to Table 4 and Fig. 5, when the inclination degrees of hybrid welding head with respect to the normal surface of webs is 30°, the weld surface forming is smooth and the cross-sectional of joint is the typical morphology of the laser-arc hybrid welding, the weld penetration is greater than the carbon dioxide gas shielded arc welding. As shown in Fig. 6, because of the shallow penetration of single arc weld, the middle part of webs is difficult to form an effective connector even with symmetrical weld on both sides. The lack of fusion defects in the webs equivalent to a pre-penetration crack in the joint which have a great damage to the joint performance. On the other hand, due to the deep penetration of laser welding, the not

**Table 4** Laser hybrid welding parameters for T-joint

No.	Laser power P (kW)	Wire feed speed $V_F$ (m/min)	Welding speed $V_W$ (m/min)	Sheet thickness (mm)	Inclination degrees of hybrid head (°)
TH-1	4.5	4	0.8	8/14	30
TH-2	7.6	6	0.8	8/14	10



**Fig. 5** Macroscopic morphology of laser hybrid welding T-joints (TH-1)



**Fig. 6** The contrast of cross-section morphology. **a** Carbon dioxide gas shielded arc welding. **b** Laser/arc hybrid welding

connected part of laser-arc hybrid welding joint is greatly reduced which is beneficial to the mechanical properties of joints. But, the weld penetration of laser-arc hybrid welding has not been fully utilized because of the angle between the axis weld and the normal surface of webs is about  $30^\circ$  which is depending on the inclination degrees of hybrid welding head, so the webs of T-joint cannot achieve full penetration.

In order to high-efficient utilization of the welding penetration for the connecting of T-joint, the inclination degrees of hybrid welding head with respect to the normal surface of webs is reduced from  $30^\circ$  to  $10^\circ$ . On the other hand, the laser power and arc energy matched is also increased to ensure the full penetration of the web. When the laser power is increased from 4.5 to 7.6 kW and the wire feed speed is increased from 4.0 to 6.0 m/min, the full penetration of the web is achieved (see in Fig. 7).





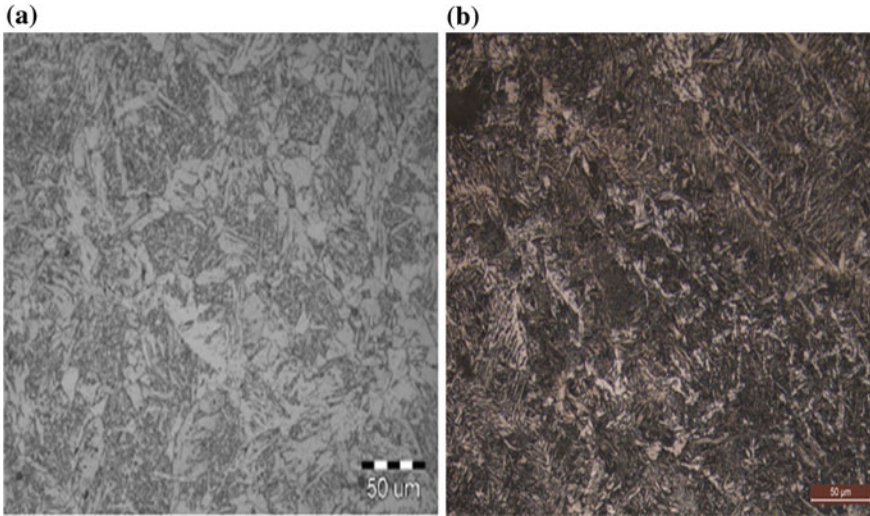
**Fig. 7** Macroscopic morphology of laser hybrid welding T-joints (TH-2)

According to Fig. 7, both sides of the weld surface is smooth which means the connection of T-joint can be achieved from one side by use of laser hybrid welding rather than from two side by use of arc welding. On the other hand, due to the high penetration of laser, the large groove which is need in the arc welding can be avoided or can be replaced by a small groove. The decrease of bevel area means the decrease of weld filler metal and the energy savings. By use laser-arc hybrid welding instead of arc welding, the single face welding-double face forming of T-joint can be achieved, with which the inside welding of box girder structure can be reduced or even completely avoid.

### 3.3 *Microstructure*

The microstructure of the heat affected zone (HAZ) for the arc welding joint and laser hybrid welding joint is respectively shown in Fig. 8a, b. The microstructure of the HAZ is mainly uniform distribution of ferrite side-plate and acicular ferrite. As

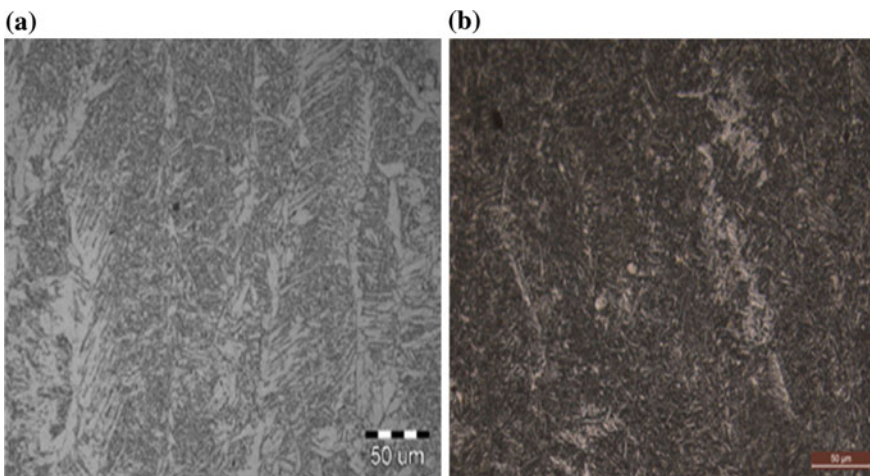




**Fig. 8** Microstructure of heat-affected zone for **a** arc welding and **b** laser hybrid welding

shown in Fig. 8, the geometric dimensions and percentage of ferrite side-plate in the HAZ of laser hybrid welding joint (see Fig. 8b) is less than the arc welding joint (see Fig. 8a). On the contrary, the percentage of acicular ferrite in the HAZ of laser hybrid welding joint is greater than the arc welding joint. So the mechanical properties of laser hybrid welding joint is higher than the arc welding joint because of the good mechanical properties of acicular ferrite.

As shown in Fig. 9a, the microstructure of weld zone for arc welding joint is mainly ferrite side-plate and a small amount of acicular ferrite, so it can be



**Fig. 9** Microstructure of weld zone for **a** arc welding and **b** laser hybrid welding

considered ferrite side-plate-based. On the contrary, in the weld zone of laser hybrid welding joint (see Fig. 9b), the microstructure can be regard as acicular ferrite-based. The microstructure of acicular ferrite-based can resulting in greatly improved to the mechanical properties of joints, especially the impact toughness of joints. That is mean the quality of joint which is get by use of laser hybrid welding can be better than the joint which is get by use of traditional arc welding because of the high welding speed and low heat input of laser hybrid welding.

## 4 Conclusion

According to the laser hybrid welding of low alloy steel A709-50-2 with T-joint, following conclusions can be obtained.

1. Due to the deep penetration of laser hybrid welding, the single face welding-double face forming for a T-joint with 8 mm thick in the webs have been achieved, with which the inside welding of box girder structure can be reduced or even completely avoid.
2. The microstructure of laser arc hybrid low alloy steel A709-50-2 is mainly fine acicular ferrite and ferrite side-plate, the fine acicular ferrite can resulting in a good mechanical properties, especially the excellent impact toughness.

## References

1. Olsen FO (ed) (2009) Hybrid laser-arc welding. Elsevier, Amsterdam
2. Bagger C, Olsen FO (2005) Review of laser hybrid welding. *J Laser Appl* 17(1):2–14
3. Kutsuna M, Chen L (2003) Interaction of both plasmas in CO<sub>2</sub> Laser-MAG hybrid welding of carbon steel. In: LAMP 2002: international congress on laser advanced materials processing. International Society for Optics and Photonics, pp 341–346
4. Kristensen K (2001) Laser welding in shipbuilding—a challenge to research and development for more than a decade. In: 7th international Aachen welding conference
5. Roepke C, Liu S, Kelly S et al (2010) Hybrid laser arc welding process evaluation on DH36 and EH36 steel. *Welding J* 89(7):140–149
6. Roland F, Manzon L, Kujala P et al (2004) Advanced joining techniques in European shipbuilding. *J Ship Prod* 20(3):200–210
7. Cao X, Wanjara P, Huang J et al (2011) Hybrid fiber laser—arc welding of thick section high strength low alloy steel. *Mater Des* 32(6):3399–3413
8. Webster S, Kristensen JK, Petring D (2008) Joining of thick section steels using hybrid laser welding. *Ironmaking Steelmaking* 35(7):496–504

# Development of Laser Processing Robot Integrated System Solution (LAPRISS) for Remote Laser Welding

Jing-Bo Wang, Tatsuyuki Nakagawa, Yasushi Mukai,  
Hitoshi Nishimura, Makoto Ryudo and Atsuhiko Kawamoto

**Abstract** A newly developed laser processing robot integrated system solution (LAPRISS) is reported. LAPRISS is comprised of a next generation of high brilliance direct diode laser (DDL), a novel laser scanning head directly mounted on robot manipulator and a light load robot. The motion of robot manipulator, laser oscillation including its output power and irradiated laser pattern on work piece are fully controlled by the robot controller. The optics in the laser scanning head is specially designed to form any shapes of irradiated laser pattern on work piece, for example a circle, a spiral, a C-shape, a line or etc. With a circle or a line shape of weld bead, LAPRISS could replace conventional resistance spot welding (RSW) or arc welding (AW) both of which are widely used in automotive manufacturing industry. A laser welding (LW) navigation function is built in LAPRISS for helping operators select welding conditions automatically, which makes LAPRISS more competitive as a next generation of remote laser welding (RLW) system.

## 1 Introduction

Due to the emergence of high power, high beam quality and high efficiency solid state lasers (SSLs) like fiber laser (FBL) and thin disk laser (TDL) about ten years ago [1, 2], laser welding (LW) becomes more and more popular in manufacturing industries such as automotive, shipbuilding, heavy industry and etc. The excellent beam quality of these state-of-the-art SSLs makes them more attractive from the view point of both application and optics design. During welding, laser with a high beam quality could be focused to a smaller spot on work piece, which makes a welding more efficient because of its high coupling rate by a narrow and deep keyhole [3]. For designing optics, it is possible to deliver a high beam quality laser with a small core diameter of optical fiber and, to select a small collimating or

---

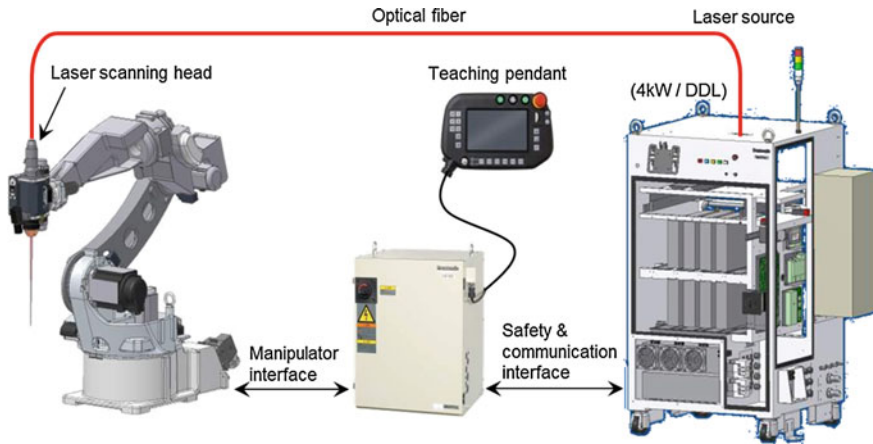
J.-B. Wang (✉) · T. Nakagawa · Y. Mukai · H. Nishimura · M. Ryudo · A. Kawamoto  
Panasonic Welding Systems Co., Ltd., 3-1-1 Inazuchou, Toyonaka, Osaka 561-0854, Japan  
e-mail: wang.jingbo@jp.panasonic.com

focusing optics, or to use a long focal length optics with a same size of optics [4, 5]. Eventually, a laser head becomes more accessible to a welding point even in a small space like the case of car assembly and, the optics in the laser head becomes more difficult to be contaminated by fumes or spatters. By using a long focal length laser head, it is also possible to undergo remote laser welding (RLW) whose focal length is generally said to be above 300 mm [6].

RLW was introduced by combining a long focal length with a laser spot refraction on work piece with mirrors, generally called scanner, from 1990s [7]. In a typical scanner, the laser beam is scanned with a pair of fast moving galvano-mirror to form any shapes of pattern on work piece [6, 8, 9]. During welding period, traveling speed of laser spot is characterized by welding phenomena itself and nearly the same as a conventional LW. But during moving period from one welding point to another, laser spot can move very fast. Up to now, work distance of this type of RLW is approximately 500–1000 mm for a SSL system and about 1500 mm for a CO<sub>2</sub> laser system [9, 10]. For increasing the usage and flexibility of scanner a robot based RLW system was introduced by using SSLs which could be delivered with an optical fiber [6]. A more complex but efficient RLW, welding on-the-fly is in progress [6, 11]. In all of these cases, weight of the scanner is generally over 30 kg [9], which makes it necessary to use a heavy load robot.

A little later after the appearance of FBL or TDL, kilowatts class of direct diode laser (DDL) becomes available in commercial base whose beam quality is even competitive to FBL or TDL and, whose powers are increasing with the progress of development and production technology [12, 13]. Before the emergence of this DDL, concepts for scaling diode laser (DL) beams by polarization or wavelength combining technologies had been proposed [14, 15]. Up to now, lasers designed with these ideas have been available in commercial base [16]. But their application to industry is being mainly limited to surface treatment [15, 17], and sometimes for welding thin sheet materials [18]. This is because their beam quality is even poorer than conventional Nd:YAG laser, which makes it difficult to become a competitor to other existing SSLs [15]. Recently, conventional DL is at first time reported to be applicable to RLW [16]. Even though this, its beam quality is nearly equal to Nd:YAG laser and still poorer than FBL, TDL or DDL. Comparing with conventional DL, high beam quality DDL is mainly contributed to a novel laser beam combining method called wavelength beam combining (WBC) by which there are no degradation of beam quality when scaling laser power [12, 13]. It is this WBC technology that makes it possible for DDL to be used in high speed RLW [19].

In this paper, concerning with the above mentioned issue of conventional RLW, the authors report a newly developed laser processing robot integrated system solution (LAPRISS). LAPRISS is a wholly robot based RLW system in which both the laser oscillation including its output power and irradiated laser pattern on work piece are fully controlled by robot.



**Fig. 1** Outline of LAPRISS (components and connection)

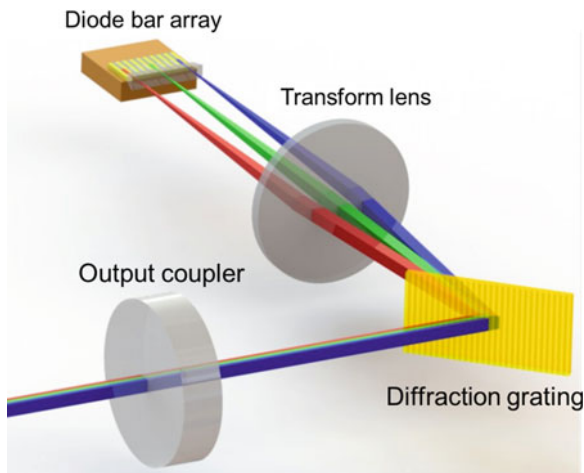
## 2 Outline of LAPRISS

The outline of LAPRISS is shown in Fig. 1. It is comprised of a high brilliance DDL, a novel laser scanning head mounted directly on robot manipulator and a light load robot. The robot motion, laser oscillation including its output power and irradiated laser pattern on work piece are all controlled by robot controller.

### 2.1 Laser Source, DDL

A 4 kW DDL is used in LAPRISS. As a next generation of high power laser for LW or cutting, DDL has a high beam quality even competitive to FBL or TDL and higher wall-plug efficiency than FBL or TDL which were all achieved by a newly developed WBC technology [12, 13]. The schematic of WBC is shown in Fig. 2. The elements of WBC are a diode bar array, a transform lens, a diffraction grating and an output coupler. The resonator cavity is comprised of a reflector on the back facet of the diode bar arrays and an output coupler. Transform lens collimates the laser beams from each diode bars and focuses the diffracted laser beams from diffraction grating onto output coupler. These 4 elements construct an external resonator cavity partially out of the diode bar array. The resonation wavelength is characterized by the diffraction grating and focal length of the transform lens. Because all of the laser beams from diode bar array are diffracted to a same direction according to Bragg's diffraction condition [20], laser beams can be scaled without degrading their beam qualities which is different from other conventional DL.

**Fig. 2** Schematic of WBC technology [12]



## 2.2 Laser Scanning Head

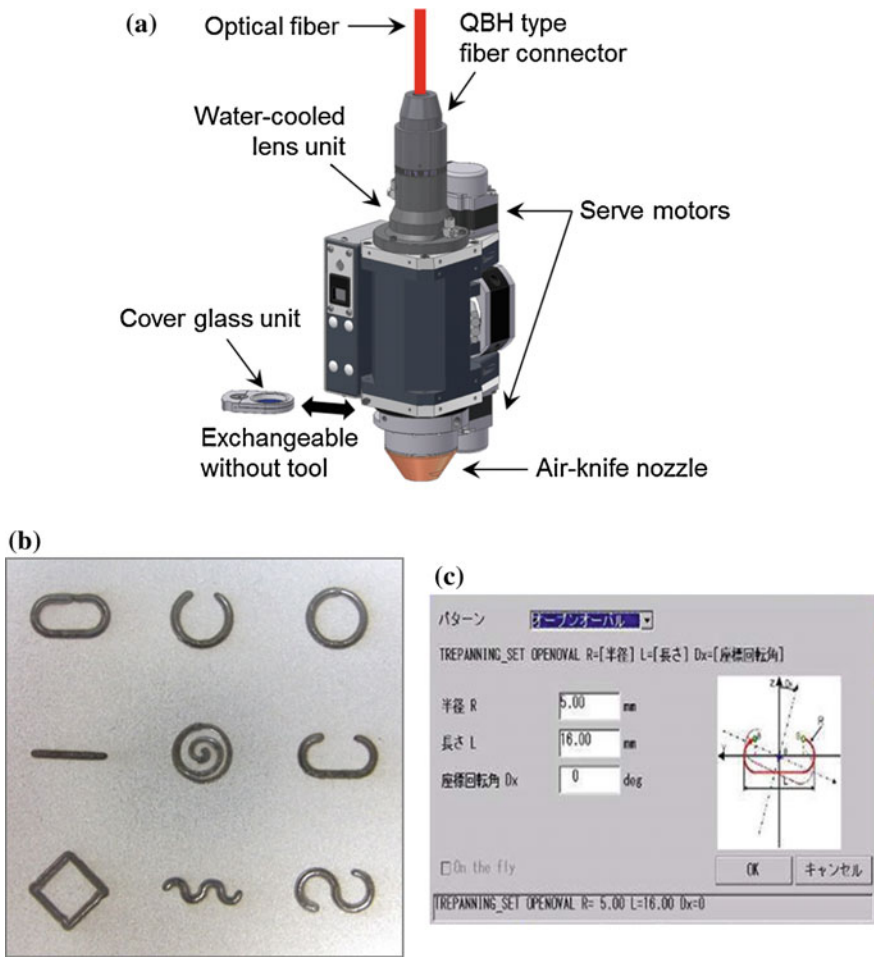
The laser scanning head is specially designed to irradiate laser beam on work piece to form any shapes of pattern. The schematic of laser scanning head and irradiated laser pattern are shown in Fig. 3. In Fig. 3a, a fiber connector is supported with a QBH type one. A specially designed optics is driven by two AC servo motors which are all controlled by robot controller. In Fig. 3b, all of these irradiated laser patterns could be programmed from a teaching pendant as shown in Fig. 3c. A lens unit is water-cooled one so that it could be used with a heavy duty cycle. A cover glass unit and an air-knife nozzle using pressure air are both mounted near the outlet of laser beam for preventing the optics from contamination. The cover glass unit is changeable without any special tools.

## 2.3 Laser Welding Robot

In conventional RLW, a laser head generally weighs over 30 kg [9]. It is necessary to carry it with a heavy load robot manipulator. Concerning with the control of laser source and RLW head, the situation is more complicated. In most commercial RLW robot system, not only are the robot, laser source and LW head made by different manufacturers, but also are the interfaces different. It is difficult for users to construct a system by themselves without the knowledge of interfaces. In many case, this is done by a system integrator.

In LAPRISS, the robot, laser source and laser scanning head are all made by Panasonic. The laser scanning head is designed less than 5 kg. It is possible to carry it with a light load robot manipulator. As Panasonic robot, a load capacity of 6 kg





**Fig. 3** Laser scanning head, typical irradiated patterns. **a** Image of laser scanning head. **b** Several typical patterns formed on work piece. **c** Programming a irradiated pattern from teaching pendant

one called TM-1400 could be used in this system. During welding in production line, many troubles concerning with electrical cable, cooling water or air hoses may occur. In LAPRISS, all the electrical cable, cooling water or air hoses are built in robot arm. The robot controller designed for LAPRISS is based on AW robot system, TAWERS from Panasonic. Users could operate it easily like running an AW robot. The laser resonation including its output power and irradiated laser pattern on work piece are fully controlled by the robot controller. The irradiated laser pattern could be programmed to form any shapes like a circle, a spiral, a C-shape, a line or etc. as shown in Fig. 3c.

A LW navigation function is supported in LAPRISS. Its schematic is shown in Fig. 4. This function could be selected from a teaching pendant and easily operated

**Fig. 4** Image of LW navigation function

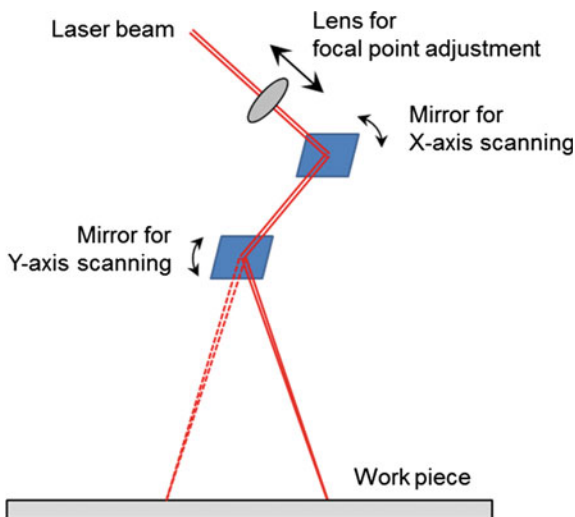


as running an AW robot. By this function, operators could input a plate thickness and a joint shape to obtain welding conditions like laser power, welding speed, etc.

### 2.4 Comparison with Conventional RLW Scanner

In conventional RLW scanner [6] as shown in Fig. 5 and mentioned above, a laser beam is reflected by a pair of galvano-mirrors very quickly not only during welding period but also during moving period from one welding point to another. In LAPRISS, the scanning speed during welding period is characterized by LW phenomena itself and is the same as conventional RLW scanner. But the traveling speed between two welding points is determined by the maximum traveling speed

**Fig. 5** Schematic of a conventional RML scanner [6]





of a robot and is generally slower than the one in conventional RLW scanner. From the view point of reducing cycle time, conventional RLW scanner is superior to LAPRISS. On the other hand, from the view point of equipment and running costs, LAPRISS is superior to conventional RLW scanner. This is because both the galvano-mirrors and expensive cover glass are not necessary in LAPRISS.

### 3 Experiment Results and Discussions

As shown in Fig. 3, any shapes of irradiated laser pattern on work piece can be obtained by controlling laser scanning head from robot controller. It is easily to consider that with a circle or line shape of welding bead, LAPRISS could replace conventional RSW or arc welding (AW) both of which are widely used in automotive manufacturing industry. Replacing RSW with LW has been applied to automotive manufacturing industry, for example to the roof welding from about 2000 years [21]. Among the many merits of RLW, how LAPRISS could reduce cycle time is discussed by comparing with conventional RSW.

On the other hand, in LW without filler addition the most difficult thing is how to increase its gap tolerance especially when using a high beam quality laser because of its small laser spot. This becomes more important in a production line, for example in automotive manufacturing industry. How LAPRISS could increase gap tolerance is discussed by comparing with conventional LW.

#### 3.1 Decreasing Cycle Time

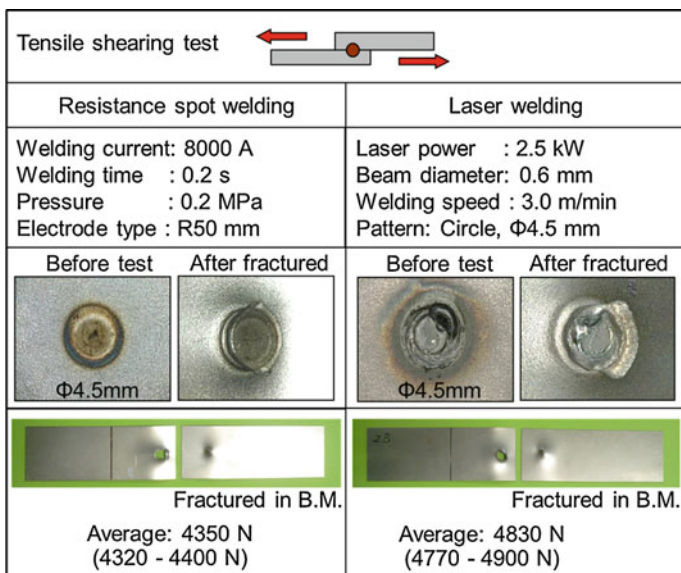
Cycle times by RSW and LAPRISS were evaluated with a mild steel of 0.8 mm in thickness. The nugget diameters of RSW and circle diameter in LAPRISS are both set to 4 mm. Welding times of each action in both processes were measured and shown in Table 1. The average times for one welding are 2.85 and 0.675 s respectively in RSW and LAPRISS. The cycle time by LAPRISS is only 1/4 of RSW. Supposing the total number of welding spots in one car body is 3500–7000, the total welding time could be saved from 10,000–20,000 s to 2400–4800 s.

The tensile shearing strengths of a lap spot joint by RSW and LAPRISS with mild steel of 0.8 mm in thickness were evaluated. The results are shown in Fig. 6. Both in RSW and LAPRISS, the joints fractured in base metal near the heat affected zone (HAZ). There are no difference in tensile shearing strength between RSW and LAPRISS.

In conventional RSW the distance between two spots is mainly determined by a so-called a shunt effect from pre-welded spot [22]. In LAPRISS there are no any limits, which is very important in automotive manufacturing industry. By replacing RSW with LAPRISS it is possible to increase the total number of welding spots so that the stiffness of a car body can be increased.

**Table 1** Cycle times of conventional RSW and LAPRISS

(a) Conventional RSW	
Resistance spot welding material: mild steel/t 0.8 mm (lap joint)	
Nugget diameter: 4 mm	
Action	Time (s)
Robot moving	1.00
Gun moving	0.50
Pressurizing and holding	0.20
Welding current ON	0.15
Pressure holding (cooling)	0.50
Gun moving	0.50
Total	2.85
(b) LW by LAPRISS	
Laser welding material: mild steel/t 0.8 mm (lap joint)	
Circle diameter: 4 mm	
Action	Time (s)
Robot moving	0.425
Laser irradiation	0.25
Total	0.675



**Fig. 6** Tensile shearing test results of lap spot joint by RSW and LAPRISS

## 3.2 Increasing Gap Tolerance

When applying LW to automotive manufacturing industry, many thin sheet work pieces are produced by shearing or press. Especially in the case of parts made from high strength steel, how to maintain a gap between two work pieces as small as possible becomes important because the spring back in high strength steel is generally larger than in mild steels [23]. This is because that even though a LW can easily be done from one side of a work piece, the work pieces could not be clamped like an electrode gun in conventional RSW.

Concerning with the above mentioned issue of gap tolerance, LAPRISS has prepared two standard scanning functions to increase gap tolerance.

### 3.2.1 Increasing Gap Tolerance by a Spiral Scanning

Spiral scanning welding is a method that laser is irradiated on work piece from one point and then scanned to draw a circle but the circle diameter increases gradually. During the spiral scanning, robot itself stops at one welding point. The optics in laser scanning head is controlled by robot to run the scanning. After finishing one welding, the robot moves to another welding point. The welding results with a circle scanning and a spiral scanning both by LAPRISS are shown in Fig. 7. The pre-gaps are all set to 0.5 mm. In the case with a circle scanning, burn-through occurred because of the shortage of molten metal. The maximum gap tolerance by a circle scanning was only 0.3 mm. On the other hand, in the case of spiral scanning even though the pre-set gap was 0.5 mm a sound bead was obtained. The maximum gap tolerance by a spiral scanning was 0.5 mm.

The spiral scanning welding is mainly used to replace RSW. By replacing RSW with a spiral scanning welding the cycle time can be reduced to 1/4.

### 3.2.2 Increasing Gap Tolerance by a Spin Scanning

Spin scanning welding is a method that laser is irradiated on work piece and scanned to draw a circle with a same diameter during robot motion. The irradiated laser track on work piece is like a projection of spring on a plane. The molten pool size is determined by the scanning circle diameter. By changing this scanning circle diameter, many weld beads with different bead widths (molten pool size) can be obtained. The effect of spin scanning welding was evaluated in a butt joint with mild steel of 0.8 mm in thickness by comparing with conventional LW. The laser spot on work piece was set to the contact surface of two plates, or with an offset of 0.2 mm perpendicular to the welding direction. The pre-gaps were all set to 0 or 0.2 mm. The welding conditions are shown in Table 2. When a pre-gap = 0 mm, the

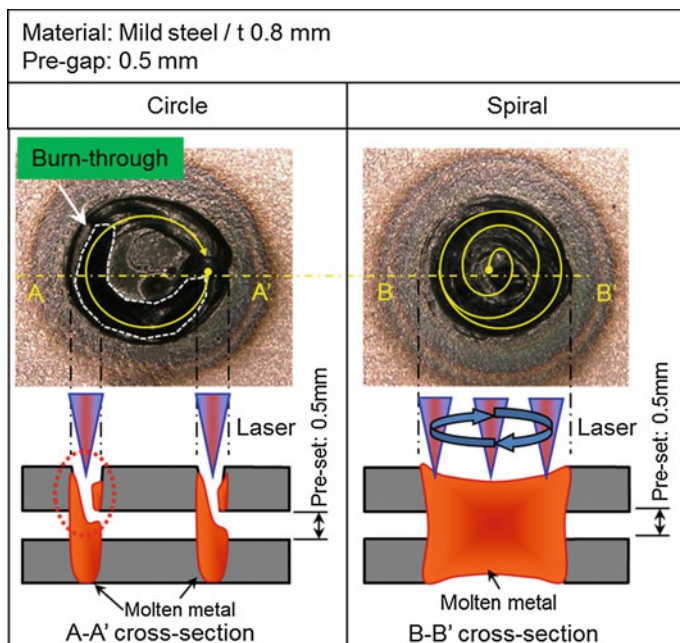


Fig. 7 Joints by conventional circular LW and spiral scanning welding

Table 2 Welding conditions used in spin scanning test

	Conventional laser welding	Spin scanning welding
Plate thickness (mm)	0.8	0.8
Pre-gap (mm)	0 and 0.2	0 and 0.2
Welding speed (m/min)	2.0	2.0
Laser power (kW)	1.25	1.25
Circle diameter (mm)	–	0.5

permitted offset was only 0.2 mm by the conventional LW, but increased up to 0.5 mm by the spin scanning welding. When a pre-gap = 0.2 mm, the permitted offsets was 0.45 mm by the spin scanning welding which is 9 times of the conventional LW of 0.05 mm. The bead appearances at the conditions of pre-gap = 0.2 mm, offset = 0.4 mm are shown in Fig. 8.

The spin scanning welding is mainly used to replace conventional AW. By replacing AW with a spin scanning welding the welding speed can be increased up to 2–3 times.

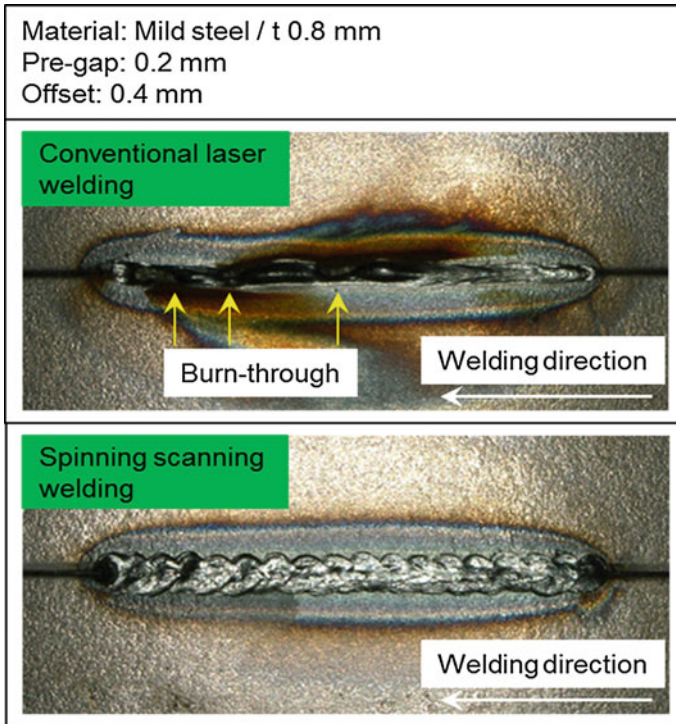


Fig. 8 Joints by conventional LW and spin scanning

## 4 Summary

A newly developed laser processing robot integrated system solution, LAPRISS was reported. The outline of LAPRISS and the evaluated welding results are summarized as followings.

1. LAPRISS is comprised of a next generation of brilliant direct diode laser (DDL) whose beam quality is even competitive to the existing state-of-the-art solid state lasers (SSLs) like fiber laser (FBL) and thin disk laser (TDL), a novel laser scanning head mounted directly on a robot manipulator and a robot. The laser source, laser scanning head and robot are all manufactured by Panasonic itself, and their control is fully conducted by robot controller. This makes it possible for users to connect them easily without taking care of any interfaces.
2. In LAPRISS, it is possible to form any shapes of irradiated laser pattern on work piece like a circle, a spiral, a C-shape, a line or etc. by controlling the specially designed optics in laser scanning head. With a circle or a line shape of welding bead, LAPRISS could replace conventional resistance spot welding (RSW) or arc welding (AW). By replacing RSW with a spiral scanning welding the cycle

time can be reduced to 1/4, and by replacing AW with a spin scanning welding the welding speed can be increased up to 2–3 times.

3. In LAPRISS, a laser welding (LW) navigation function is supported. By this function, the operator is only needed to input a plate thickness and a joint shape so that he or she could obtain a series of proposed welding conditions like laser power, welding speed or etc. This function could be selected and operated easily from a teaching pendant just like running an AW robot.

## References

1. Gapontsev V, Krupke W (2012) Fiber lasers grow in power. *Laser Focus World* 8:83–87
2. Giesen A (2005) Thin disk lasers, power scalability and beam quality. *Laser Tech J* 2(2):42–45
3. Katayama S, Kawahito Y, Mizutani M (2012) Latest progress in performance and understanding of laser welding. *Phys Proc* 39:8–16
4. Hugel H (2001) Laser beam welding—recent developments in process technology and lasers. In: *Proceedings of the 7th international symposium, Japan Welding Society*, pp 547–554
5. O’Neill W, Sparkes M, Varnham M, Horley R, Birch M, Woods S, Harker A (2004) High power high brightness industrial fiber laser technology. In: *ICALEO 2004, fiber and disc lasers*, pp 1–7
6. Schwoerer T (2008) Robot-guided remote laser scanner welding for highly-productive welding applications. In: *ICALEO 2008*, pp 392–398
7. Machen J (1996) Remote laser welding. In: *Proceedings of the IBEC’96, advanced technologies and processes*, pp 11–15
8. Lu JH, Kujanpaa V (2013) Review study on remote laser welding with fiber lasers. *J Laser Appl* 25(5):052008
9. Higuchi T (2008) Remote laser welding-development and applications in American automotive industries. *J Jpn Weld Soc* 77(3):25–28 (in Japanese)
10. Bemnek M (2006) Welding from a distance. *Ind Laser Solutions* 3:19–23
11. Zaeh MF, Moesl J, Musiol J, Oefele F (2010) Material processing with remote technology-revolution or evolution? *Phys Proc Part A* 5:19–33
12. Huang RK, Chann B, Burgess J, Kaiman M, Overman R, Glenn JD, Tayebati P (2012) Direct diode lasers with comparable beam quality to fiber, CO<sub>2</sub>, and solid state lasers. *Proc SPIE* 8241:824102
13. Hecht J (2012) Beam combining cranks up the power. *Laser Focus World* 6:50–53
14. Bachmann F (2003) Introduction to high power diode laser technology. *LIM* 2003:7–12
15. Bachmann F (2001) Present status and future prospects of high power diode and diode-pumped solid-state-laser technology and applications in Germany. In: *53rd meeting of the Japan laser processing society*, pp 55–62
16. Stittgen T, Luft A, Todt W (2014) Diode lasers for remote welding. *Ind Laser Solutions* 7/8:18–20
17. Riedelsberger H (2012) Heat treating with high power direct-diode lasers. *Laser User* 68:9
18. Howard K, Lawson S, Zhou Y (2006) Welding aluminum sheet using a high-power diode laser. *Weld J* 85(5):101s–110s
19. Nakagawa T, Mukai Y, Nishimura H, Ryudou M, Wang JB, Kawamoto A (2014) Development of a remote laser welding robot system with high power direct diode laser “LAPRISS”. *Weld Technol* 62(7):84–88 (in Japanese)
20. Thorlabs material. Introduction to diffraction grating. <http://www.thorlabs.com/catalogpages/802.pdf>

21. Mori K, Tarui T, Hasegawa T, Yoshikawa N (2008) Remote laser welding application for car body. *J Jpn Weld Soc* 77(3):11–15
22. Chang HS, Cho HS (1990) A study on the shunt effect in resistance spot welding. *Weld J* 69(8):308s–317s
23. Yoshida T, Isogai E, Sato K, Hashimoto K (2013) Springback problems in forming of high-strength steel sheets and countermeasures. *Nippon Steel technical report*, no. 103, pp 4–10

# On the Mechanism and Detection of Porosity During Pulsed TIG Welding of Aluminum Alloys

Yiming Huang, Zhifeng Zhang, Na Lv and Shanben Chen

**Abstract** Porosity is the remarkable barrier to realize the high efficient automatic welding of aluminum alloy. The paper provides new insights into the nucleation mechanism of porosity formation during pulsed TIG welding of aluminum alloys. Firstly, the model of bubble's nucleation based on inclusions is proposed. The calculated pore minimum radius shows large sensitivity to pulse duty cycle as well as welding current. Then a novel method based on spectral analysis to detect porosity is developed. The relationships among the extracted signals and porosity deflection are discussed, and the results show that Ar and HI spectral lines can be used as an aid to determine the most likely position of the porosity.

## 1 Introduction

Aluminum alloy is widely used to make low density and high strength structures in aerospace, military-industrial sectors due to its high comprehensive mechanical properties and good conductive heat conduction [1, 2]. These structures are of great significance, which require higher welding quality. But as a result of big thermal expansion coefficient, strong oxidizing, easy to inhale, a weld is inclined to deformation, crack, oxidation as well as porosity. And porosity is most likely to occur among those common defects in aluminum alloy welding process [3, 4], the morphology and distribution of which is one of the important factors that affect the material performance and microstructure.

Porosity widely exists in all kinds of welding methods, including MIG welding, laser welding, TIG welding and so on. Therefore, in the past several decades the study of porosity has been the hot spot in welding researches.

---

Y. Huang · Z. Zhang · N. Lv · S. Chen (✉)

Intelligentized Robotic Welding Technology Laboratory, School of Materials Science and Engineering, Shanghai Jiao Tong University, Shanghai, People's Republic of China  
e-mail: sbchen@sjtu.edu.cn



Haboudou et al. [5] studied the influence of mechanical surface preparation as well as dual spot on porosity formation during Nd:YAG laser welding of A356 and AA5083 aluminum alloys. It is recognized that cleanliness of base metal is extremely important for reaching aluminum sound welds. Matsunawa et al. [6] found the type of shielding gas employed in high power CW CO<sub>2</sub> laser welding causes large differences in penetration and the formation of porosity defects. That is to say, the penetration depth of base metal is the deepest and a number of characteristic pores are formed with an inert shielding gas. Morais [7] evaluated the influence of different GMAW metal transfer modes on porosity generation in an AA5052 alloy using the gravimetric method. He concluded that pulsed GMAW leads to lesser porosity than welds carried out with the standard transfer modes. Da Silva and Scotti [8] proposed that the double pulsed GMAW technique does not increase the porosity susceptibility in aluminum welding in spite of having theoretically higher potential for porosity generation.

As to the detection of porosity, the main methods are acoustic emission testing and radiographic inspection. Aboali et al. [9] and Tao et al. [10] respectively determined several kinds of weld deflections, including lack of penetration, porosity and slag, by using acoustic emission testing technology. The results show that the distribution range of AE parameter value caused by porosity is bigger, but the amount of AE signals caused by welding porosity and other defects is roughly in the same order of magnitude. Sun et al. [11] and Valavanis and Kosmopoulos [12] respectively presented a method based on real-time X-ray image for detecting and discriminating discontinuities that may correspond to false alarms or defects such as porosity, linear slag inclusion, gas pores, lack of fusion or crack. However, the detection methods mentioned above both have some limitations. The result of ultrasonic testing is often judged by experience; X-ray inspection has a higher requirement to equipment. So it urgently needs a new NDT technology which can quickly inspect inside porosity deflection.

The key to reduce porosity lies in understanding the mechanism of the porosity formation and how the welding parameters affect the forming of porosity quantitatively. However, the researches on the mechanism are relatively few. Seto et al. [13] explored the influence of keyhole and pulse on porosity formation, but the reason is expounded.

The objective of this work is to explore the mechanism of porosity initial formation during pulsed TIG welding of aluminum alloys and to discuss the relationship between porosity and spectrum signals.

## 2 Porosity Formation Mechanism

As the initial stage of solidification of welding pool, bubble nucleation determines the distribution and size of pores, especially the minimum size of porosity. Therefore, factors influencing on porosity can be found by studying the bubble nucleation.

### 2.1 Nucleation Model

Liquid metal solidification of welding molten pool is similar to casting solidification process. But it has some unique characteristics, which consist of small size, fast cooling speed, solidifying with the moving heat source. Solidification of welding molten pool starts from the boundary to weld center in columnar crystal form. In view of the fact that cooling speed of aluminum alloy is very fast, non-equilibrium crystallizing process happens. Hydrogen precipitated during the welding process is not likely to be diffused evenly to the molten pool but to attach to high melting point inclusions. In the molten pool bubble heterogeneous nucleation is facilitated by inclusions, such as  $Al_2O_3$  high melting point oxide, which reduced resistance of bubble nucleation because of its not wetting or partially wetting.

It is assumed that nucleation is conducted on the plane surface of inclusions, schematic diagram shown in Fig. 1.

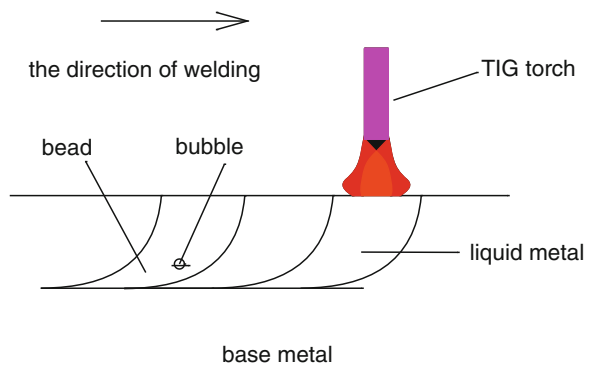
### 2.2 Theoretical Calculations

Bubble is presumed to be spherical with radius  $R$ . The Gibbs free energy  $\Delta G$  of whole system is composed of two parts, including the reduction of volume free energy  $-4\pi R^3 \Delta G_v / 3$  and the increment of interfacial free energy  $4\pi R^2 \sigma_{LG}$  (Fig. 2).  $\Delta G_v$  is described to be the work by draining away per unit volume of liquid metal. Therefore, formula (1) is obtained:

$$\Delta G = 4\pi R^2 \sigma_{LG} - \frac{4}{3} \pi R^3 P_b \tag{1}$$

According to Henry’s law, the gas-liquid interface keeps thermal dynamic equilibrium. When in balance state, in consideration of capillary pressure and arc force, relationship between internal pressure and external pressure of bubble can be gotten as formula (2):

**Fig. 1** Schematic of nucleation based on the plane surface of inclusions



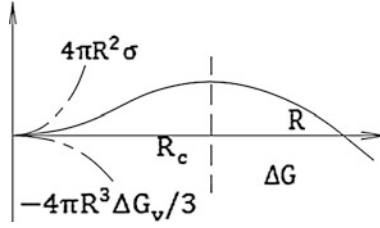


Fig. 2 Relationship between bubble radius and  $\Delta G$

$$P_b = P_{at} + P_s + P_C + P_{ar} \quad (2)$$

The static pressure of the bubble from the melt:

$$P_s = \rho_{al} \cdot g \cdot h \quad (3)$$

$\rho_{al}$  is  $2400 \text{ kg/m}^3$ ,  $g$  is  $9.8 \text{ N/kg}$ ,  $h$  is considered to be constant ( $3 \text{ mm}$ ) in contrast to the height of base metal ( $5 \text{ mm}$ ).

As it's known that capillary pressure is caused by surface tension, so

$$\begin{aligned} P_C dV &= \sigma_{LG} dS \\ P_C &= \frac{2\sigma_{LG}}{R} \end{aligned} \quad (4)$$

$P_{ar}$  is caused by arc force, which consists of electromagnetic force, plasma flow force and gas evaporation force. However, the last force is usually neglected because it is far smaller than the first two forces. Therefore, it is expressed as formula (5).

$$P_{ar} = \frac{F_e + F_p}{S} \quad (5)$$

It is presumed that the projection on the pool is approximate to a circle with radius  $R_b$ ,  $R_a$  is regarded as the radius of tungsten electrode.

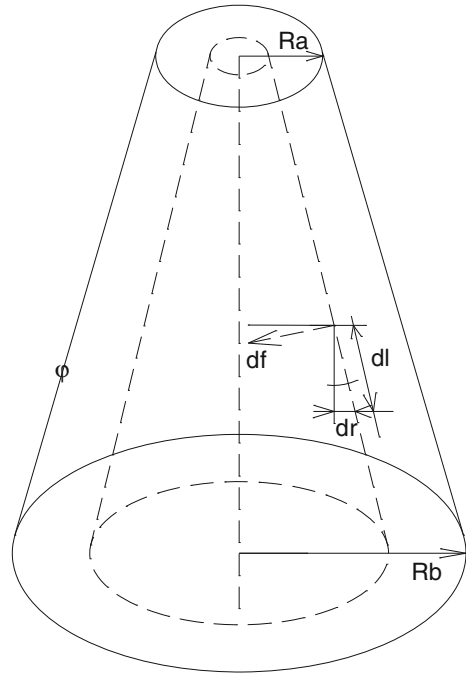
$$S = \pi R_b^2 \quad (6)$$

The arc shape is simplified to circular truncated cone, as shown in Fig. 3. And the assumption is made that current  $I$  goes evenly through each section of the arc. Therefore, magnetic induction intensity is  $B$

$$B = \mu_0 H = \frac{\mu_0 i}{2\pi r_i} \quad (7)$$

$i$  is the current going through the circle with radius  $r_i$ .

**Fig. 3** Schematic diagram of simplified arc shape



The component of electromagnetic force per unit length  $dl$  in the direction from tungsten electrode to the molten pool is  $df_{\perp}$ , with the following expression:

$$df_{\perp} = \sin \varphi \cdot df = \frac{dr}{dl} \cdot B \cdot di \cdot dl = \frac{\mu_0 i di dr_i}{2\pi r_i} \tag{8}$$

The integration of  $df_{\perp}$  in radial direction:

$$dF = \int_{R_a}^{R_b} df_{\perp} = \frac{\mu_0 i di}{2\pi} \ln \frac{R_b}{R_a} \tag{9}$$

Then  $F_e$  is obtained by integrating  $dF$ :

$$F_e = \int_0^I dF = \frac{\mu_0 I^2}{4\pi} \ln \frac{R_b}{R_a} \tag{10}$$

For TIG welding, when arc length is more than 2 mm, radial distribution of plasma flow force is in concordance with the hyperbolic curve. That is to say:

$$f_p = F_{\max} \exp(-a|r|) \tag{11}$$

$F_{\max}$  is arc force in central axis, proportional to the square of the current;  $a$  is concentration factor of the distribution curve as well as constant;  $r$  is the radial coordinate value

$$F_p = \int_0^{2\pi} \int_0^{R_b} \frac{1}{2r} f_p dr d\theta = \frac{\pi a^2 F_{\max}}{2R_b^2} \int_0^{R_b} \frac{r^3 e^{-ar} dr}{1 - e^{-ar}(1 + ar)} \quad (12)$$

$$F_{\max} = \varepsilon I^2 \quad (13)$$

$\varepsilon$  is proportionality coefficient as well as constant.

Alternating current pulse TIG welding process is chosen in the experiment,  $T_p$  and  $T_b$  are period of peak value and base value current respectively.

$$I = \begin{cases} I_p n(T_p + T_b) \leq t \leq n(T_p + T_b) + T_p \\ I_b n(T_p + T_b) + T_p \leq t \leq (n+1)(T_p + T_b) \end{cases} \quad (14)$$

From the classical solidification nucleation theory, it's known that the maximum of  $\Delta G$  corresponds to the critical embryo.

$$\frac{D(\Delta G)}{dR} = 8\pi R \sigma_{LG} - 4\pi R^2 P_b - \frac{4}{3} \pi R^3 \frac{dP_b}{dR} = 0 \Big|_{R=R_c} \quad (15)$$

By solving the above equation set, the critical radius of bubble is obtained as following expression:

$$R_o = \frac{2\sigma_{LG}}{3(P_{at} + \rho_{al}gh + P_{ar})}$$

When current is equal to base value  $I_b$ ,  $R_b = 1.5R_a$

$$P_{ar} = \frac{F_e + F_p}{S} = \frac{1}{\pi R_b^2} \left[ \frac{\mu_0 I_b^2}{4\pi} \ln \frac{R_b}{R_a} + \frac{\pi \varepsilon a^2 I_b^2}{2R_b^2} \int_0^{R_b} \frac{r^3 e^{-ar} dr}{1 - e^{-ar}(1 + ar)} \right]$$

When current is equal to peak value  $I_p$ ,  $R_b = 3R_a$

$$P_{ar} = \frac{F_e + F_p}{S} = \frac{1}{\pi R_b^2} \left[ \frac{\mu_0 I_p^2}{4\pi} \ln \frac{R_b}{R_a} + \frac{\pi \varepsilon a^2 I_p^2}{2R_b^2} \int_0^{R_b} \frac{r^3 e^{-ar} dr}{1 - e^{-ar}(1 + ar)} \right]$$

### 3 Results and Discussions

#### 3.1 Experimental System

The diagram of the experimental system is shown in Fig. 4, which consists of two subsystems. The welding subsystem is worked with an OTC INVERTER ELESON 500P-type TIG welding power, a fixed water-cooled gas tungsten arc (GTA) torch. The data collection subsystem can obtain image, sound and spectrum information. The latter is studied in our research and acquired by a 3648 linear CCD spectrometer HR4000 UV-NIR, with spectral resolution of 0.02 nm (FWHM). Table 1 shows the chemical compositions (wt%) of 5A06 aluminum alloy and ER5183 welding wire.

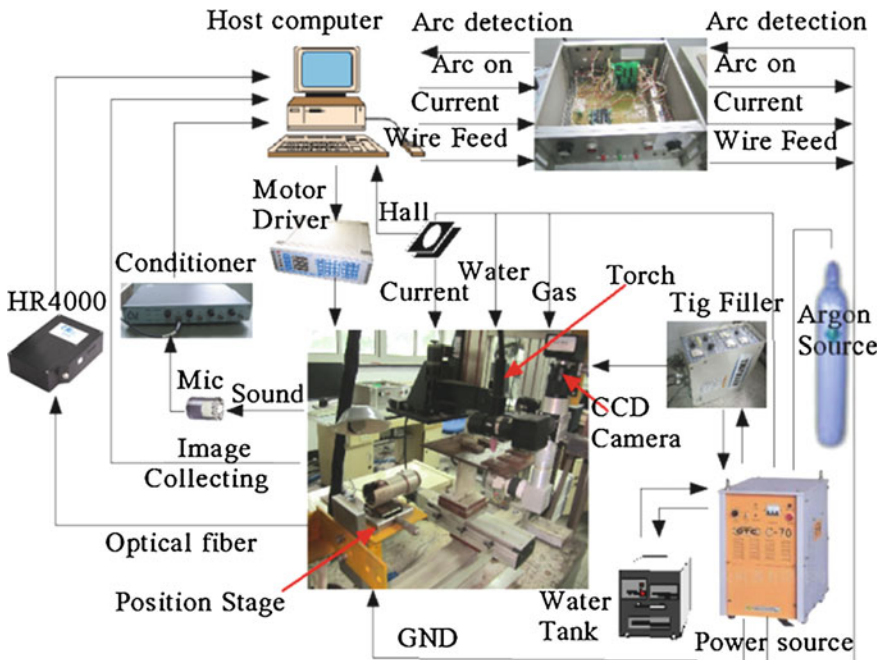


Fig. 4 Schematic diagram of the experiment system

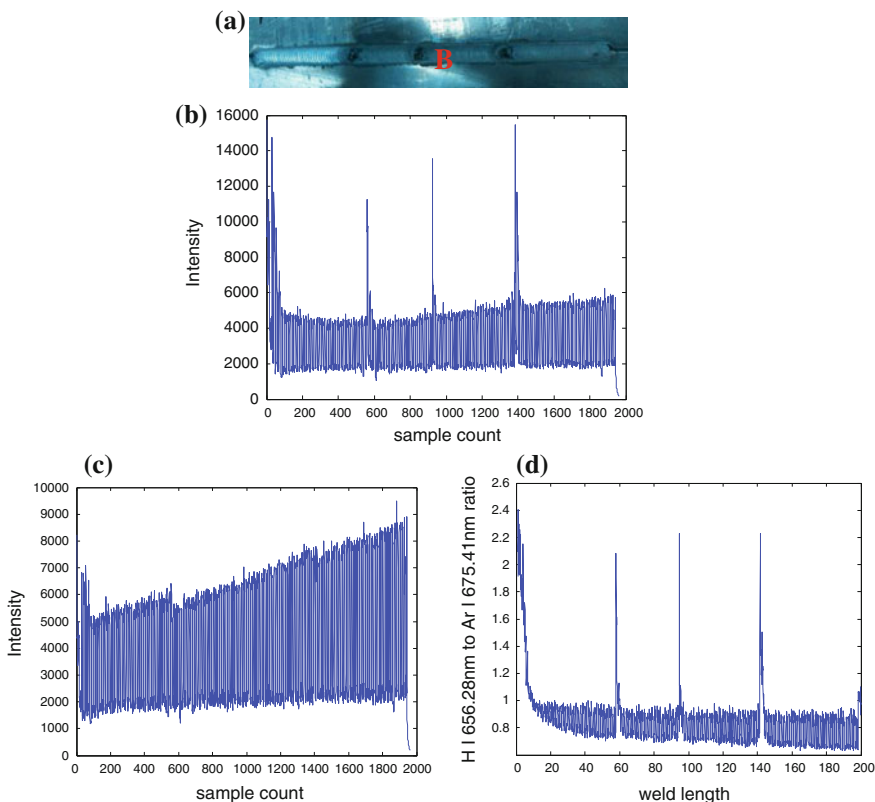
Table 1 Chemical compositions of 5A06 Al alloy

Element	Mg	Mn	Fe	Si	Zn	Cu	Al
5A06	5.8–6.8	0.5–0.8	≤0.4	≤0.4	≤0.2	≤0.1	Bal.
ER5183	4.3–5.2	0.5–1.0	0.4	0.4	0.25	0.1	Bal.

A commercial 5A06 sheet was sheared into sample sizes of  $260 \times 50 \times 4 \text{ mm}^3$ . 99.999 % pure argon gas with a flow rate of 12 L/min was selected as the shielding gas. In order to remove oxide film on the surface of the aluminum alloy, reduce the loss of tungsten electrode, control energy, experiments of 5A06 aluminum alloy are done by AC pulse TIG welding method. Through the test, the welding parameter is gotten shown in Table 2.

**Table 2** Normal welding parameters

Pulse frequency (Hz)	Peak current (A)	Base current (A)	Welding speed (mm/s)	Electrode diameter (mm)	Ar flow (L/min)	Pulse duty ratio (%)
1	170	50	3	3.2	12	50

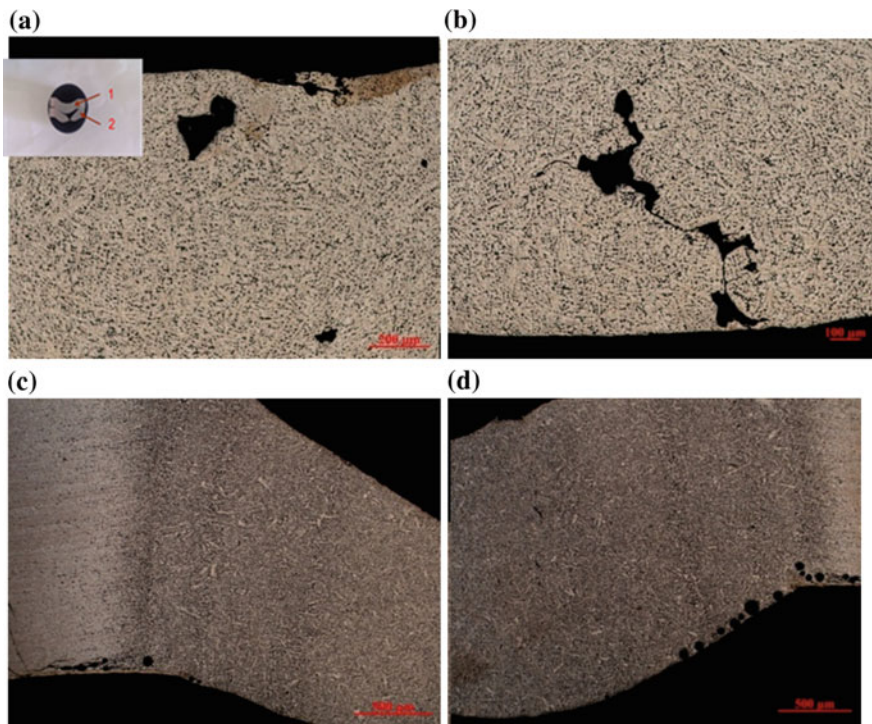


**Fig. 5** a Welding seam, b intensity of HI 656.28 nm, c intensity of Ar I 675.41 nm, d ratio of HI 656.28 nm and Ar I 675.41 nm

### 3.2 Detection of Porosity Based on Spectral Analysis

Under normal atmospheric pressure, hydrogen partial pressure of arc atmosphere is determined by hydrogen content of arc atmosphere. Hydrogen of arc atmosphere generates radiation spectrum under the effect of electric arc heat, and the content of hydrogen is positively related to the intensity of the spectrum. Given that hydrogen of arc atmosphere is in dynamic equilibrium with hydrogen in the molten pool, the detection of porosity can be achieved by the measurement of hydrogen spectral intensity.

To obtain apparent porosity defection, artificial boreholes are made and hydrocarbons are added in Fig. 5a. The spectral signals of HI 656.28 nm and Ar I 675.41 nm are collected by spectrometer, shown in Fig. 5b, c. It's obvious that the intensity of spectrum line becomes greater and greater through the welding process. And the intensity of HI 656.28 nm has a steep rise in the position where defection happens, while Ar I 675.41 nm is completely on the contrary to HI 656.28 nm. To eliminate the effect of welding heat input on the intensity of H spectrum line and avoid wrong judgment, the ratio of intensity of HI 656.28 nm and Ar I 675.41 nm is used to determine the defection.



**Fig. 6** a The upper of section 1, b the bottom of section 1, c the left side of section 2, d the right side of section 2



### 3.3 Observation of Internal Surfaces of Porosity

Transaction is selected along the vertical welding direction of specimen from the welding deflection B (shown in Fig. 5a) every 2 mm. Microstructure and morphology are investigated by means of the optical microscopy, shown in Fig. 6. The upper of section 1 exists several porosity deflections, one of which is bigger because of the combination of multiple holes. There is crack deflection in the bottom of the welding seam. And pores distribute intensively in the both left and right sides of the root in section 2.

## 4 Conclusions

The principal conclusions obtained from this study may be summarized as follows:

1. New insights into the nucleation mechanism of porosity formation during pulsed TIG welding of aluminum alloys are proposed. As parameters are constant or in accordance with specific welding conditions, the relationship between critical radius and current is acquired by theoretical deduction. The critical radius can be regarded as the minimum radius of porosity, which shows large sensitivity to pulse duty cycle as well as welding current.
2. The content of hydrogen in the arc atmosphere can be monitored by H spectrum line. To eliminate the effect of welding heat input on the intensity of H spectrum line and avoid wrong judgment, the ratio of intensity of H I 656.28 nm and Ar I 675.41 nm is used to determine the content of hydrogen. It indicates serious porosity deflection when the ratio is greater than 1.

**Acknowledgment** This work is supported by the National Natural Science Foundation of China under the Grant No. 61401275

## References

1. Liu G, Sun J, Nan CW et al (2005) Experiment and multiscale modeling of the coupled influence of constituents and precipitates on the ductile fracture of heat-treatable aluminum alloys. *Acta Mater* 53(12):3459–3468
2. Nanninga N, White C, Furu T et al (2008) Effect of orientation and extrusion welds on the fatigue life of an Al–Mg–Si–Mn alloy. *Int J Fatigue* 30(9):1569–1578
3. Malin V (1991) Efficient welding fabrication of extruded aluminum mat panels. ELECTROCOM GARD NILES IL
4. Mathers G (2002) *The welding of aluminium and its alloys*. Woodhead publishing, Cambridge
5. Haboudou A, Peyre P, Vannes AB et al (2003) Reduction of porosity content generated during Nd: YAG laser welding of A356 and AA5083 aluminum alloys. *Mater Sci Eng A* 363(1):40–52

6. Matsunawa A, Mizutani M, Katayama S et al (2003) Porosity formation mechanism and its prevention in laser welding. *Weld Int* 17(6):431–437
7. Morais FC (2001) Influence of operational factors on porosity formation in aluminum MIG welding. Federal University of Uberlandia, Brazil
8. Da Silva CLM, Scotti A (2006) The influence of double pulse on porosity formation in aluminum GMAW. *J Mater Process Technol* 171(3):366–372
9. Aboali A, El-Shaib M, Sharara A et al (2014) Screening for welding defects using acoustic emission technique. *Adv Mater Res* 1025:7–12
10. Tao Y, Wang W, Sun B (2014) Nondestructive online detection of welding defects in track crane boom using acoustic emission technique. *Adv Mech Eng* 2014
11. Sun Y, Bai P, Sun H et al (2005) Real-time automatic detection of weld defects in steel pipe. *NDT & E Int* 38(7):522–528
12. Valavanis I, Kosmopoulos D (2010) Multiclass defect detection and classification in weld radiographic images using geometric and texture features. *Expert Syst Appl* 37(12):7606–7614
13. Seto N, Katayama S, Matsunawa A (2001) Porosity formation mechanism and suppression procedure in laser welding of aluminum alloys. *Weld Int* 15(3):191–202

# Design of a Scalable Wall Climbing Robot for Inter-plane Traversing

Yuan Chang and Xiaoqi Chen

**Abstract** This paper describes a new concept of scalable wall-climbing robot which integrates wheeled locomotion and Vacuum adhesion mechanism. The robot consists of two modules connected by an active joint. The joint is equipped with a motor, which can drive the joint to the desired direction. The robot also adopts a balance tail to avoid rolling over. These mechanisms enable the robot to make transition between walls. The mechanical analysis and kinematic calculation based on the proposed concept are presented. The robotic device will have a wide range of industrial applications, such as inspection in narrow duct, bridge, and storage tank.

## 1 Introduction

Wall-climbing robots, which have been developed in the last few decades, are mainly employed for the tasks which are hazardous and/or costly when performed by humans due to the harsh environment. These tasks include remote maintenance of large storage tanks [1], inspection of large concrete structures such as bridge pylons, cooling towers or dams [2] and inspection in narrow spaces [3, 4].

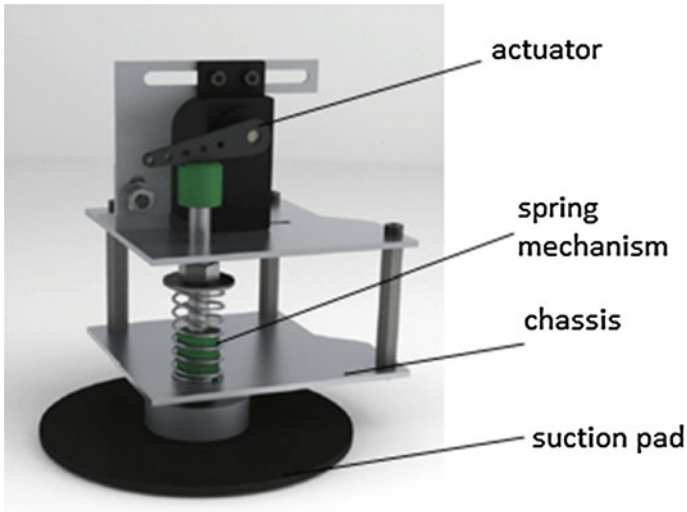
One essential element of wall-climbing robot is the adhesion mechanism, which decides the adhesion capability of the device on the vertical wall or ceiling. The adhesion mechanism of present wall-climbing robots can mainly be categorized into magnetic adhesion [5, 6], Van Der Waals force adhesion [7], electrostatic adhesion [8, 9] and vacuum adhesion [10]. An overall survey for adhesion mechanism is provided in [9].

Vacuum adhesion is widely employed in the wall-climbing robot technology, as it has advantages such as simple structure and the ability to adapt to various types of surfaces. However, vacuum adhesion mechanism is limited in safety because the

---

Y. Chang · X. Chen (✉)

Department of Mechanical Engineering, University of Canterbury, Private Bag 4800,  
Christchurch 8041, New Zealand  
e-mail: xiaoqi.chen@canterbury.ac.nz



**Fig. 1** The adhesion mechanism [7]

suction pads are usually stiff and may not attach well to a rough surface, thus causing air leakage [7, 9]. In this study, the proposed climbing robot adopts a vacuum adhesion mechanism as shown in Fig. 1 [7], which includes actuators, spring mechanisms and suction pads, supported on a chassis. This adhesion mechanism introduces a control system to re-prime pads when necessary by sensing the level of air leakage for each pad.

Another crucial element of wall climbing robot is locomotion mechanism, as it decides the motion capability. The current locomotion mechanisms of the wall-climbing robot include tracked locomotion [6, 11], legged locomotion [10, 12] and wheeled locomotion mechanism [2, 5].

Among these mechanisms, robots with wheeled locomotion are more flexible in changing direction. In comparison with legged locomotion robot [10, 12], they do not need to be designed with multi-degree-of-freedom and gaits controlling, which results in a simple structure and control.

However, wall climbing robot technology has a challenge in making transition between walls. Few studies have focused on wheeled locomotion robot which can transit from one surface to another.

The object of this research is to address the problem of the current wheeled locomotion robot in making transition, and develop a new robotic system that can travel between two angled surfaces. A concept of wall-climbing robot, which consists of several re-configurable modules, has been studied.

The paper is organized as follows. Section 2 introduces the modeling and presents its motion planning. Section 3 analyzes the factors influencing the performance of the device, and demonstrates the feasibility. Finally, the conclusion of this study is made in Sect. 4.

## 2 Concept Design

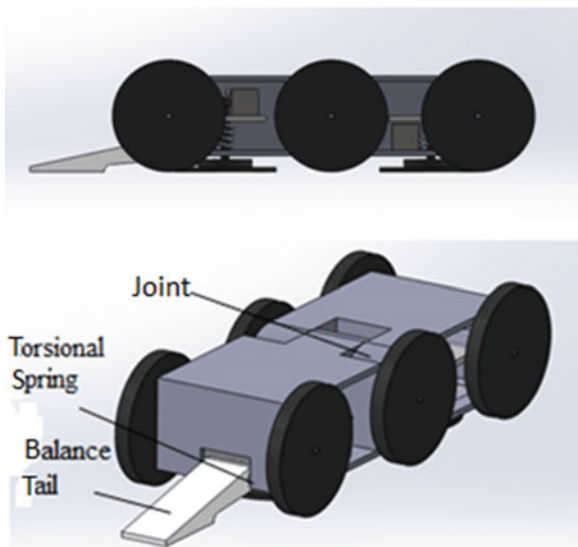
### 2.1 Basic Mechanical Structure

Figure 2 shows the 3D CAD model of a scalable robot, which consists of two small modules connected by a motor-driven active joint. Each module has one suction pad for adhesion. The two compact modules will not only increase the flexibility, but also reduce the weight of the device. As a result, the device will have wide range of applications, such as narrow duct inspection and bridge maintenance.

The wheeled locomotion robot has three pairs of wheels, two of which (front wheels and rear wheels) are driven by two separated motors. The third pair of free wheel is mounted on the middle active joint.

The robot adopts a balance tail, which is connected with the rear module by a joint (Fig. 2). The joint utilizes a torsion spring which can prevent the robot from rolling over.

Fig. 2 CAD model of scalar robot



## 2.2 Typical Operation Scenarios

For inter-plane traversing, two typical operation scenarios are studied, as shown in Fig. 3.

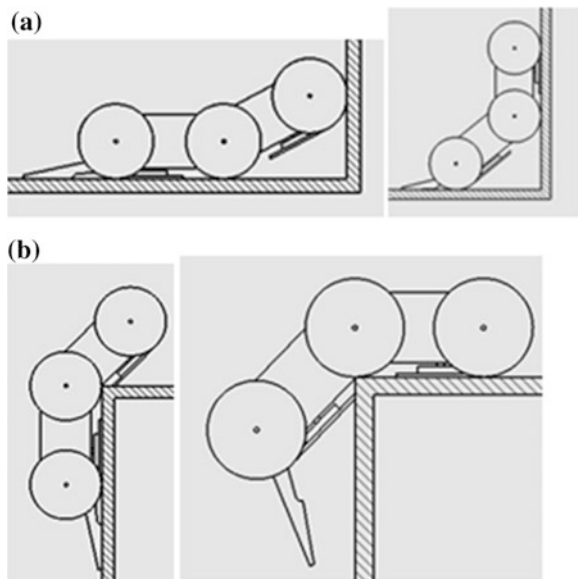
(a) Traversing an Inner Corner

When the device traverse an inner corner, the front wheels will climb up the wall and the front suction pad will lose its adhesion to the wall. Meanwhile, the motor of the middle joint drives the joint to rotate. During this process, the rear module keeps moving ahead and the front module folds continuously around the joint. The front module will lose its adhesion until it folds to the desired angle (i.e. the angle of two climbing surfaces), and then the suction pad under it adheres to the next surface. After this folding action, the motor of the middle joint rotates in the opposite direction, thus allowing the front module to keep moving ahead and the rear module rotate to touch the next surface. During this rotation, the suction pad under the rear module loses its adhesion, and the whole device will rely on the front module to adhere to the climbing surface.

(b) Traversing an External Corner

When the device traverse an external corner, the driving wheel on the rear module pushes the device to move ahead; meanwhile the motor of the middle joint will drive the front module to rotate and touch the next surface. After this rotating process, the front module adheres to the next wall, and the front wheel will drive the device moving ahead. Then the rear modules will lose its suction force, and the middle joint will enable the device to rotate the rear module to touch the next surface.

**Fig. 3** **a** Traversing an inner corner; **b** traversing an external corner



### 3 Mechanical Analysis and Calculation

#### 3.1 Adhesion Mechanism

As shown in Fig. 1, the robot adopts a vacuum adhesion mechanism [7]. This mechanism includes actuators, spring mechanisms and suction pads, supported on a chassis. The actuators are capable of exerting forces on the suction pads towards the climbing surface in order to force out the air between the pads and the climbing surface. The spring mechanism provides a force on the pads in the direction opposite to the climbing surface. As a result, the mechanism is able to supply a vacuum adhesion between the suction pads and the climbing surface by forcing out the air and then pulling the pads.

This adhesion mechanism introduces a control system to re-prime pads only when necessary by sensing the level of air leakage for each pad. The control system, using a servo and spring mechanism, is able to minimize the power requirement for adhesion mechanism, thus enabling the device be actuated by a battery. This control system also makes the adhesion mechanism more efficient and reliable. This adhesion can maintain a required suction force on various types of surfaces, such as steel, glass and concrete.

In this device, each module has one suction pad, and the front pad and rear pad provide suction force  $F_1$  and  $F_2$ , respectively. Figure 4 shows the scenario of the robot transiting from ceiling to wall. When the rear pad begins to lose the suction force, to make the device stay at the wall, it should have:

$$\mu F_1 > M \quad (\mu < 1) \tag{1}$$

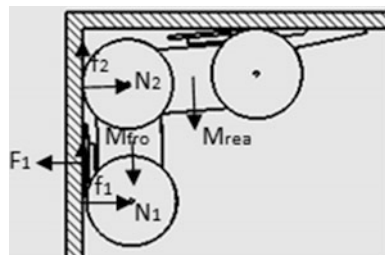
where  $\mu$  is the sliding friction coefficient between the wheel and the wall.

#### 3.2 Motor Torque Analysis

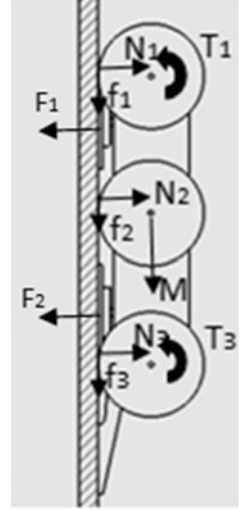
A rubber wheel is considered. Its friction force of rolling on a surface is:

$$f = \delta N \tag{2}$$

Fig. 4 Transition from ceiling to wall



**Fig. 5** Climb up the wall



where  $\delta$  is the coefficient of rolling friction of the wheel and wall, and  $N$  is the force on the wheel and perpendicular to the contact surface.

When the robot climbs up the wall, it has the maximum resistance, as shown in Fig. 5. The rolling friction is:

$$f = \delta(F_1 + F_2) \quad (3)$$

To drive the robot with payload of  $M$ , the motors of the wheels need to provide torque:

$$T_1 + T_3 \geq r[\delta(F_1 + F_2) + M] \quad (4)$$

where  $r$  is the wheel radius, and  $T_1$ ,  $T_3$  are the torque of front motor and rear motor, respectively.

Before the front pad begins to lose the suction force at an external corner, as shown in Fig. 6, the rolling friction is:

$$f_2 + f_3 = \delta(F_1 + F_2) \quad (5)$$

To drive the robot, it requires

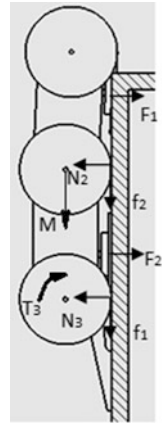
$$T_3 \geq r[(f_2 + f_3) + M] = r[\delta(F_1 + F_2) + M] \quad (6)$$

During the transition from floor to wall, when the front module adheres to the front surface, as shown in the Fig. 7, we have:

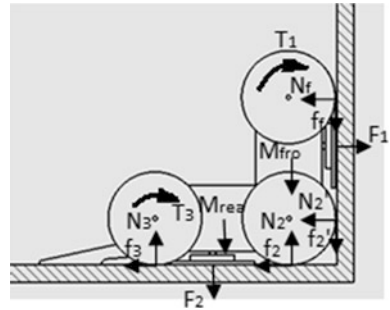
$$f'_2 + f_f = \delta(N'_2 + N_f) = \delta[T_3/r - (f_2 + f_3) + F_1] \quad (7)$$



**Fig. 6** Climb up to an external corner



**Fig. 7** Rear module transition from floor to wall



To lift the rear module, the following condition should be satisfied:

$$T_1/r - (f_f + f'_2) - M - F_2 > 0 \tag{8}$$

By substituting Eq. (7) into Eq. (8), it can be obtained:

$$T_1 > r\{[\delta(T_3/r + F_1) - \delta^2(M + F_2)]/(1 + \delta^2) + M + F_2\} \tag{9}$$

### 3.3 Joint Analysis

As shown in Figs. 8 and 9, a motor mounted on the middle joint allows the joint to rotate, enabling the front module to fold to the desired direction at corners. The torque of the joint motor is a constant  $T_r$ , and the angular displacement  $\theta$  are:

$$\theta = \alpha t^2/2 \tag{10}$$

Fig. 8 Section view of joint

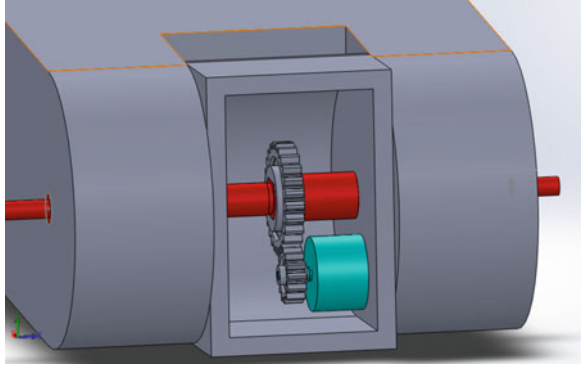
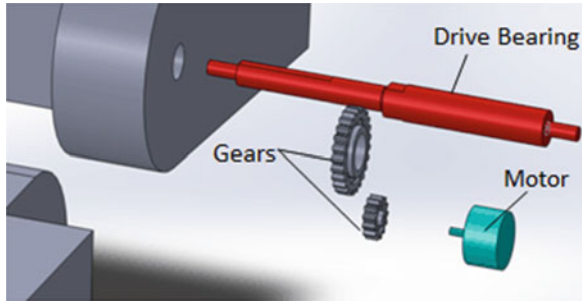


Fig. 9 Parts of the joint



$$\alpha = T_r / I_{fro} \quad (11)$$

where  $\alpha$  is angular acceleration,  $I_{fro}$  is the moment of inertia of the front module. By substituting Eq. (11) into Eq. (12), it can be obtained:

$$T_r = 2I_{fro}\theta/t^2 \quad (12)$$

As shown in Fig. 10a,  $\beta$  is the angle of the front module need to rotate when the robot raises a distance of  $r$ ;  $c$  is the radius of the suction pad; and  $b$  is the distance from middle wheel to the front suction pad. It can be expressed as:

$$\beta = \sin^{-1} \left( \frac{\sqrt{r^2 + c^2}}{b} \right) = \theta \quad (13)$$

If the speed of the robot is 0.1 m/s, then

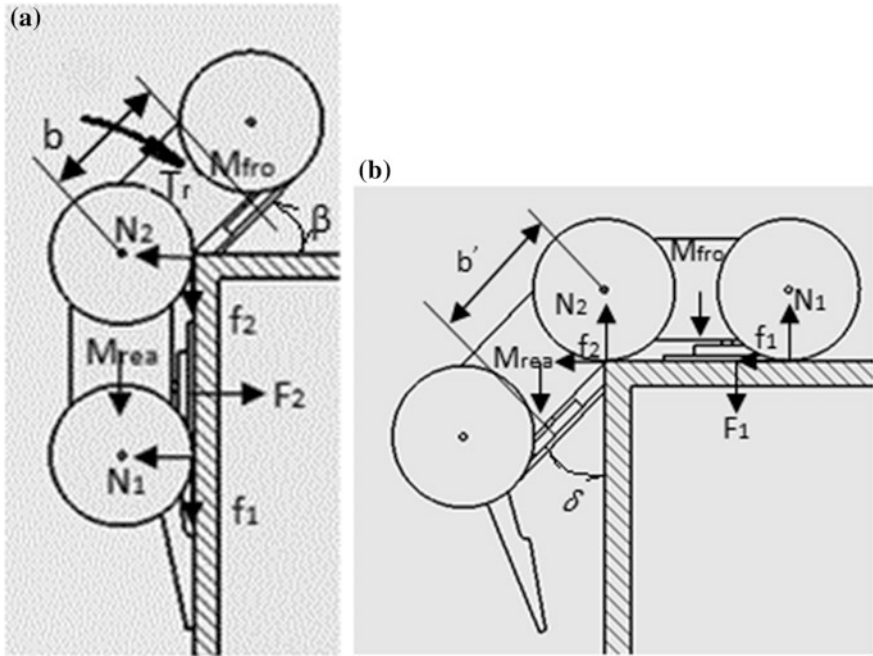


Fig. 10 a Front pad loses suction force; b rear pad loses suction force

$$t = r/0.1 \tag{14}$$

Substitute (13) and (14) into (12), the torque of the joint motor is:

$$T_r \geq \left[ 0.02 I_{fro} \sin^{-1} \left( \frac{\sqrt{r^2 + c^2}}{b} \right) \right] / r^2 \tag{15}$$

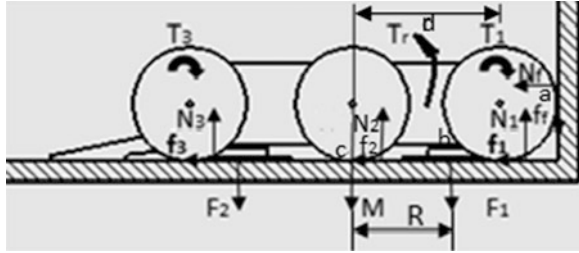
When the rotate speed of the motor is n, then

$$n = \frac{\beta}{t} \frac{60}{2\pi} = 3 \sin^{-1} \left( \frac{\sqrt{r^2 + c^2}}{b} \right) / (\pi r) \tag{16}$$

The case of Fig. 10b is similar to the case of Fig. 10a.

Figure 11 illustrates the force analysis of the robot on an inner corner. The friction force and the driving force of the motors  $F_m$  are:

**Fig. 11** Transition at an inner corner



$$\begin{aligned} f &= \delta(M + F_1 + F_2) \\ F_m &= (T_1 + T_3)/r \end{aligned} \quad (17)$$

Then at point “a”, we have

$$N_f = F_m - f = (T_1 + T_3)/r - \delta(M + F_1 + F_2) \quad (18)$$

$$f_f = \delta N_f = \delta[(T_1 + T_3)/r - \delta(M + F_1 + F_2)] \quad (19)$$

Then the motive force at point “a” is:

$$F_a = T_1/r - f_f = T_1/r - \delta[(T_1 + T_3)/r - \delta(M + F_1 + F_2)] \quad (20)$$

When “c” is the pivot, the torque caused by  $F_a$  is:

$$T_a = F_a(d + r) = (d + r)\{T_1/r - \delta[(T_1 + T_3)/r - \delta(M + F_1 + F_2)]\} \quad (21)$$

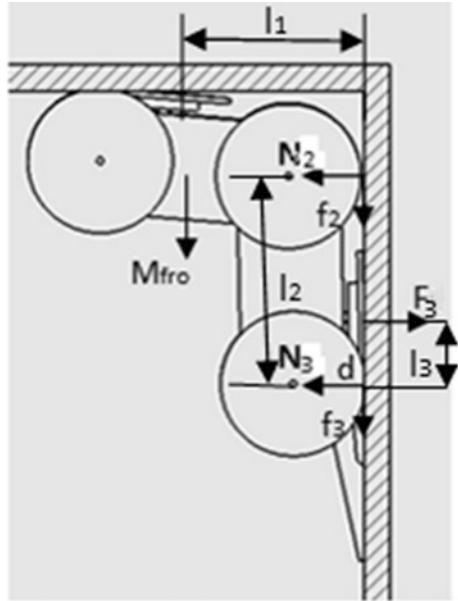
Assume the suction force and the gravity of the front module has the same moment arm “R”, the torque  $T_b$  is

$$T_b = R(F_1 + M_{fro}) \quad (22)$$

To raise the front module, the torque  $T_r$  of the joint motor, should satisfy

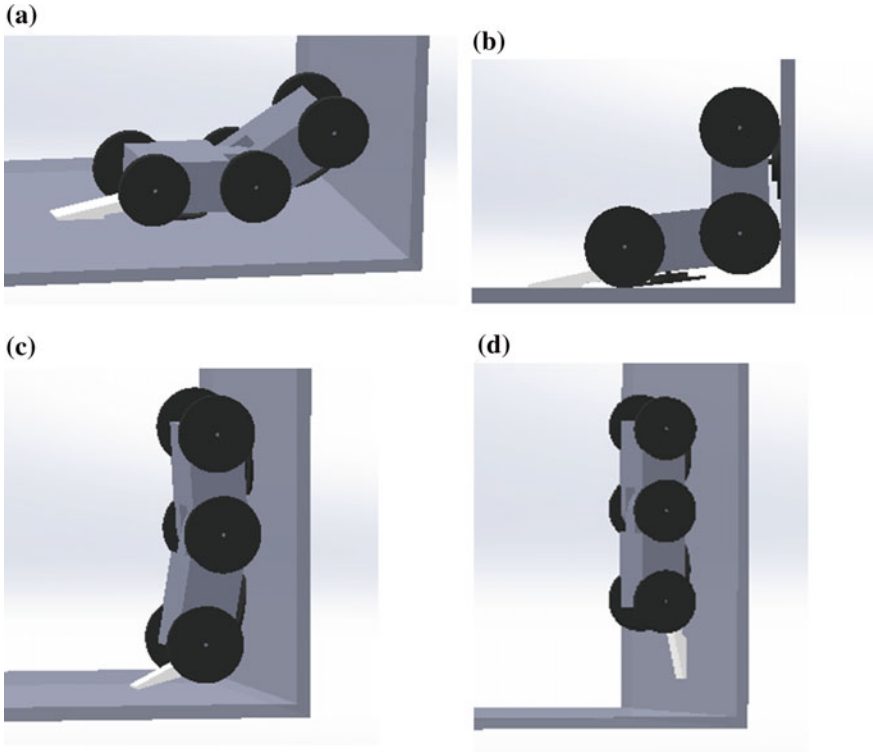
$$T_r > T_b - T_a \quad (23)$$

**Fig. 12** Transition from wall to ceiling



**Table 1** Technical specifications

Parameter	Value
Payload	1 kg
Climbing speed of the robot	$s = 0.1 \text{ m/s}$
Front module	50 mm (width) $\times$ 75 mm (length)
Rear module	50 mm (width) $\times$ 80 mm (length)
Wheel radius size	$r = 21 \text{ mm}$
Coefficient of rolling friction	$\delta = 0.6$
Coefficient of sliding friction	$\mu = 0.8$
Suction force	$F_1 = F_2 = 11 \text{ N}$
Motor of wheels	$T_3 = 0.6 \text{ N m}$
	$T_1 = 1 \text{ N m}$
	$n_1 = n_2 = 46 \text{ rpm}$
	$p_1 = 5 \text{ W}$
	$p_2 = 5 \text{ W}$
Motor of joint	$T_r = 0.1$
	$n_r = 31 \text{ rpm}$
	$p_r = 1 \text{ W}$
Balance tail spring	$F_p = 8 \text{ N}$



**Fig. 13** A right-angle inner corner traversing. **a** Step I: front module rotates; **b** Step II: rear module is lifted; **c** Step III: rear module rotates; **d** Step IV: completes traversing

### 3.4 Balance Tail Analysis

In the case of Fig. 12, during the transition from wall to ceiling, when the front suction pad does not contact to the up surface, the torque caused by the payload  $M_{fro}$  of the front module reaches its maximum value

$$F_3 l_3 = M_{fro} l_1 + N_2 l_2 \quad (24)$$

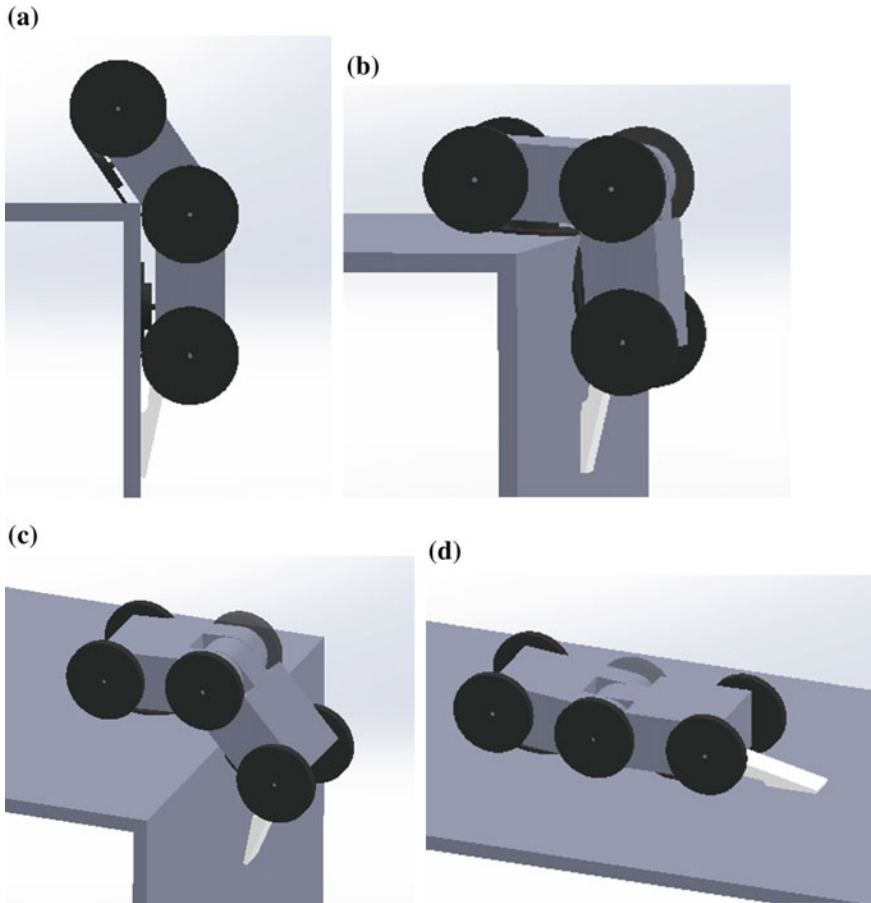
Since  $N_2 = 0$  in this case, then

$$F_3 = M_{fro} l_1 / l_3 \quad (25)$$

The force  $F_s$  provide by spring of the tail is

$$F_s = F_3 - F_p = M_{fro} l_1 / l_3 - F_1 \quad (26)$$

where  $F_p$  is the suction force of the pad.



**Fig. 14** A right-angle external corner traversing. **a** Step I: front module rotates; **b** Step II: front module adheres; **c** Step III: rear module rotates; **d** Step IV: completed traversing

## 4 Case Studies

To validate above concept design, a prototyping robot with technical specifications being listed in Table 1 is developed by using Solidworks.

Figures 13 and 14 illustrate how the prototype robot successfully traverses a right-angle inner corner and a right-angle external corner step by step as expected, respectively.

The simulation results clearly indicate the feasibility of the proposed design of a scalable wall-climbing robot for inter-plane traversing. Such a robot can be used for duct inspection. Its 1 kg payload may include video camera, wireless communication apparatus, and etc.

## 5 Conclusion

In this paper, a scalable wall-climbing robot consisting of two small modules is presented. This device is capable of traversing from one surface to the next at a right-angle corner. The mechanical analysis of the device is provided to determine the technical specifications of the motors, the payload, the balance tail and the suction force.

Simulation results preliminarily verify the feasibility of the proposed robot design. The future work is to physically build a prototype robot based on the proposed concept for validation. The proposed robot can be employed in extensive industry applications, such as inspection in narrow duct, bridge, and storage tank.

## References

1. Kalra LP et al (2006) A wall climbing robot for oil tank inspection. In: 2006 IEEE international conference on robotics and biomimetics, ROBIO 2006, Kunming, China, 17–20 Dec 2006, pp 1523–1528
2. Schmidt D et al (2011) Omni-directional locomotion and traction control of the wheel-driven, wall-climbing robot. *CROMSCI Robotica* 29:991–1003
3. Fischer W et al (2009) Compact magnetic wheeled robot for inspecting complex shaped structures in generator housings and similar environments. In: 2009 IEEE/RSJ international conference on intelligent robots and systems, IROS 2009, St. Louis, 11–15 Oct 2009, pp 4116–4121
4. Sakamoto S et al (2005) Parallel-link robot for pipe inspection. In: IECON 2005: 31st annual conference of IEEE industrial electronics society, Rayleigh, 6–10 Nov 2005, pp 345–350
5. Wu M et al (2013) Design and optimal research of a non-contact adjustable magnetic adhesion mechanism for a wall-climbing welding robot. *Int J Adv Robot Syst* 10
6. Shao J et al (2012) A wall-climbing robot with gecko features. In: 2012 9th IEEE international conference on mechatronics and automation, ICMA 2012, Chengdu, 5–8 Aug 2012, pp 942–947
7. Tom D, Ben S, Andrew T, Tichadou S, Liam S, (2011) Wall climbing robot. University of Canterbury, New Zealand: Project Report. October 2011
8. Bi Z et al (2012) A miniature biped wall-climbing robot for inspection of magnetic metal surfaces. In: 2012 IEEE international conference on robotics and biomimetics, ROBIO 2012, Guangzhou, 11–14 Dec 2012, pp 324–329
9. Koh KH et al (2011) Modeling and simulation of electrostatic adhesion for wall climbing robot. In: 2011 IEEE international conference on robotics and biomimetics, ROBIO 2011, Phuket, 7–11 Dec 2011, pp 2031–2036
10. Guo W et al (2008) Design of a six legged wall-climbing robot. In: IEEE international conference on advanced robotics and its social impacts, ARSO 2008, Taipei, 23–28 Aug 2008
11. Liu R et al (2013) Wall climbing robot using electrostatic adhesion force generated by flexible interdigital electrodes. *Int J Adv Robot Syst* 10
12. Xiao J et al (2009) Intelligent control for wall climbing robot. In: 2009 Chinese control and decision conference, CCDC 2009, Guilin, 17–19 June 2009, pp 1336–1341



# Handheld Device System Development for Video Camera Movement Control System

Jing-Jie He, Su Wang and Xin-Gang Miao

**Abstract** Film production has been in the digital age, dynamic control of video camera is one of the key technologies. This paper introduces the exploitation of handwheel for the motion control system. The handwheel development should match to the control system. This paper explores the handwheel control memory configuration of the UMAC motion control cards and achieves the rocker and buttons two basic functions. Manufacture the SCM system with analog signal and switch signal processing capability. And it communicates with UMAC via RS232 serial port. By settings the related register and writing PLC programs, the motor is moving in different rate proportional to the swing amplitude of rocker. The result shows that the signal transmission are sensitive and stable, the data processing works properly, the motor moving as expected. At last, propose the conceptual design of handwheel for the video camera movement control system.

## 1 Background

The development of photography technology is promoting the film industry. Digital technology has become a necessary means of filmmaking. The trajectory control of the camera is an important technique to achieve a variety of movie special effect [1]. In the “Lord of the Rings · Twin Towers”, the digital characters—tolu (Serkis ornaments) must shooting twice every scene in the same locus with camera motion control system. The first time, shoot Serkis with other actors to get other actors performing and tolu’s location. The second time, shoot background separately for compounding the erase screen [2]. Cameraman manipulates camera motion control

---

J.-J. He (✉) · S. Wang · X.-G. Miao  
School of Mechanical Engineering and Automation, Beihang University,  
100191 Beijing, China  
e-mail: 670411163@qq.com

S. Wang · X.-G. Miao  
Beijing University of Civil Engineering and Architecture, 100044 Beijing, China

system to get shoot path, the substance is key point selected and connected with different path.

Selecting the key points has the following characteristics:

1. The cameraman isn't a motor motion control professor. Control should be simple and convenient to make the photographer to concentrate on image.
2. The motion control system can record and reproduce the path.
3. The track mode and velocity within two key points are determined by the photographer.

## 2 System Introduction

This paper develops the handheld device for the UMAC (Universal Motion and Automation Controller, as Fig. 1) control system. There has not been related discourse. This paper is about function development. UMAC following system includes UMAC PLC signal processing and reproducing the locus. SCM handheld system includes switching and analog signal receiving and processing, RS232 communication. At last, the result of using the rocking bar to control the movement of the motor at different rates is presented.

## 3 System Structure

The system structure diagram is shown as Fig. 2 and the physical objects are shown as Fig. 3. The MCU system is shown as Fig. 4. The important hardware are Japan Matsushita AC servo motors, Delta Tau UMAC motion controller and Atmega64 SCM.

**Fig. 1** UMAC controller



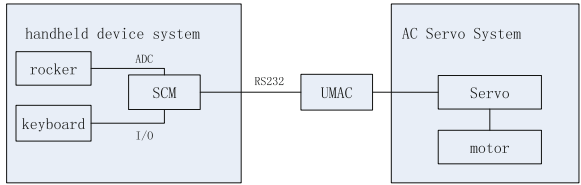


Fig. 2 System structure diagram

Fig. 3 Motion control system

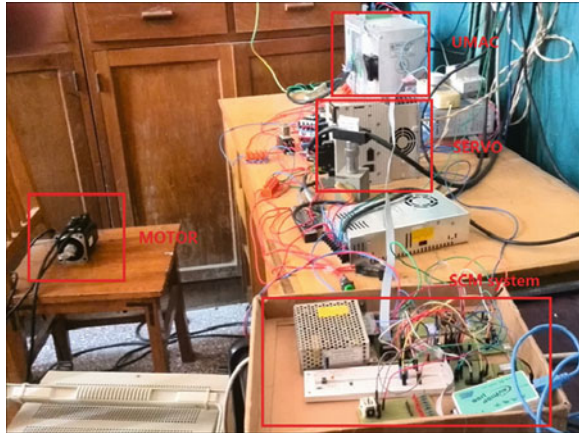
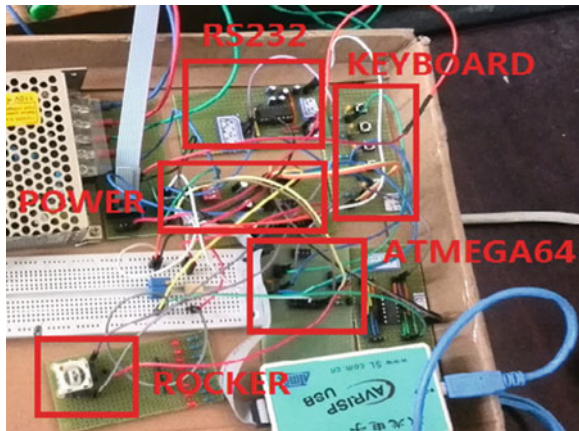


Fig. 4 SCM system



### 4 System Workflow

The SCM system access to analog signals and switch signals in real-time. The signals which are processed by A/D converter and encoding are sent to the UMAC controller. The UMAC change the incremental variable of the corresponding motor in PLC program to realize the synchronization of the motor motion and the handle signals. The SCM send the command to make the UMAC record the position of the motor and the path between the two points when the motor moves in the target position. At last, reproduce the movement with PMAC Executive Pro2 Suite software.

### 5 Synchronization Movement Control System

The target is controlling the motor position by handheld device. Set the motor in position following mode in UMAC. The user moves the camera in right position and shooting view by handheld device, send the command to UMAC to record the present position of the motor. The substance of the position following mode is sending the digital signal of handwheel (master axle) encoder to the corresponding UMAC encoder input register. The internal storage structure of UMAC position following module is shown as Fig. 5 [3].

The switch variable of position following function is the 0-bit of Ixx06 in UMAC. The user can specify the master position address of the No. xx motor by Ixx05 variable. Note, xx represent the number of motor. This address is the result of the encoder conversion table which is used to process the motor encoder digital

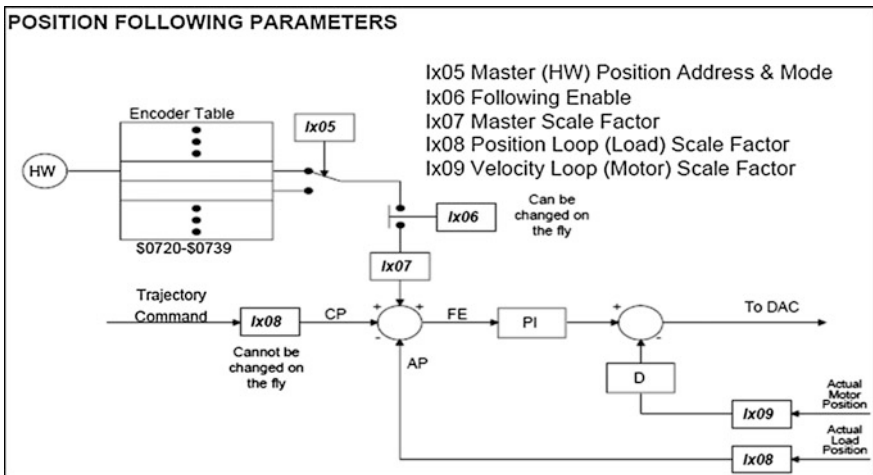
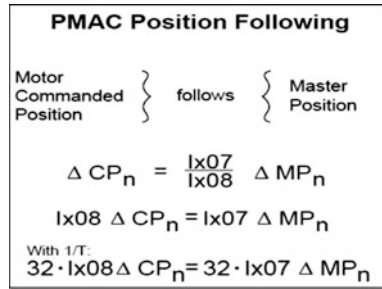
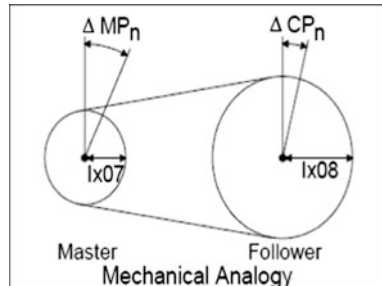


Fig. 5 The internal storage structure of UMAC position following module

**Fig. 6** Position following equation



**Fig. 7** Electronic gear ratio



signal. The position command of handwheel is sent as interpolating points to drive the following axle. The electronic gear ratio is set by Ixx07 and Ixx08 variable. User can change the ratio with Ixx07 variable in the air. This is shown as Figs. 6 and 7 [3].

```

Giving the 3th motor (xx = 3) as an example.
I0305 = X:$30000 //specify the master position address of the 3th motor
I0307 = 1
I0308 = 1 // setting the electronic gear ratio as 1:1
I0306 = 1 // Enable Position Following
    
```

## 6 Experiment

The workflows of functional experiment are shown as Fig. 8 for the SCM system and Fig. 9 for the UMAC.

The SCM system’s chip is Atmega64 which is used to receive the rocker analog. Then convert the analog into digital signal. The analog ranging from 0–5 V is corresponding to digital 0–20. The middle of the range, 2.5 V (digital 10) means the speed of motor is 0. The voltage upon 2.5 V means the motor rotates in forward direction. The greater the voltage, the faster the speed. And it is similarly for

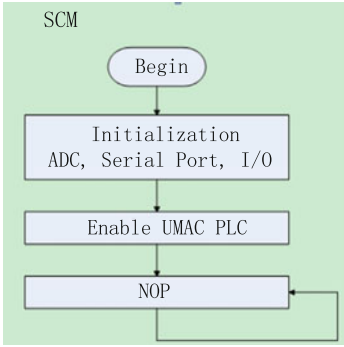


Fig. 8 SCM workflow

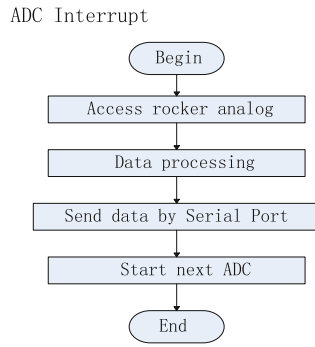
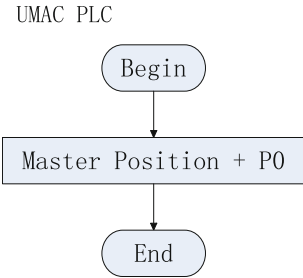


Fig. 9 UMAC workflow



voltage below 2.5 V. For example, the analog is 4 V, which means the speed of motor should be  $4 - 2.5 = 1.5$ ,  $1.5 \times (10/2.5) = 6$ . The final digital value means the feed step for the motor. The SCM send the speed with  $\langle + \backslash - \rangle$  to the UMAC in ASCII format end with  $\langle \text{carry} \rangle$  by RS232 serial port. UMAC store the value in  $P0$  variable as feed step.

Setting the speed identify interval. When the AD conversion result in absolute value is less than the threshold, MCU specify the speed as jamming signal, preventing rocker cannot be fully back to zero position for mechanical friction. Specify the UMAC pointer variable  $M11$  pointed to the register of 3th motor Encoder Conversion Table Result. UMAC PLC executes the incremental command in period:  $M11 = M11 + P0$ .

Realize the synchronization of handwheel and motor through the two steps above.

## 7 Effectiveness Analysis of Signals

For the SCM system signal processing, the most affecting factor for the processing time is serial transmission speed. In this system, the baud rate is 9600, about 4 ms/byte. Other tasks execution time is at least an order of magnitude.



Fig. 10 Handheld device control motor movement at different rates

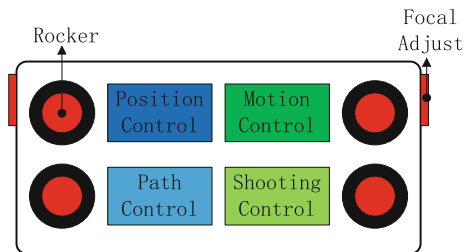
UMAC PLC executes in the frequency of 0.753 kHz, the cycle is 1.3 ms. In this way, the state of each handle signal sent by a MCU is read at least two times, meeting the design requirements. By monitoring the UMAC motor location register, draw signal curve as shown in Fig. 10.

### 8 Handheld Device Shape Concept Design

The shape design is shown as Fig. 11. 4 rockers distribute on both side of front handheld. Set focal length manual adjustment button on the two sides of handheld.

Position control module includes key points record and delete, speed selection; Path control module includes the path type selection and delete; Motion control

Fig. 11 Shape design



module includes return-to-zero, single step (forward/backward) and continuous movement (start/pause); Export control module includes start-stop, path deriving, focal length condition deriving.

In the process of path simulation, user can adjust the focal length and record manually.

## 9 Conclusion

This paper introduces the synchronization control technology of handheld device and motor based on UMAC. Elaborate the configuration of handwheel control in UMAC in detail. Make the handheld device control system and control the motor in different movement rate. The experimental results show that handheld device system implements basic functions and the performances meet the request for utilization. At last, this paper gives the shape concept design of the handheld.

## References

1. Liu J (2004) The advanced camera motion control system. *Motion Picture Video Technol* 5:7–11 (in Chinese)
2. Liu J (2005) Interpret wonderful film digital special effects. *Entertainment Technol* 5:58–61 (in Chinese)
3. TURBO PMAC User Manual (2008) Delta Tau Data Systems Inc



# Research of One Torch Double-Wire Pipeline Welding Robot

Xin-Gang Miao, Feng Zhang, Zhi-Feng Ma and Yi Zhang

**Abstract** One torch double-wire pipeline all-position welding robot is mounted on a small vehicle with two wires, which can work simultaneously, and this approach can significantly improve the welding efficiency and welding quality. In this paper, double-wire pipeline all-position welding robot has been studied, and its mechanical structure includes the walking part, the swing part of torch, and the up-and-down adjusting part of the torch, and its mathematical model is established. Its control system includes the main control unit PMAC, the embedded system for the auxiliary interface, the touch screen for the interactive interface, and the hand-held remote control unit for welding command, coordinated with control system software. So the welding parameter can be edited and modified, and the robotics servo motion can be controlled.

## 1 Introduction

In recent years, long-distance oil and gas pipeline construction has developed to use the high-grade and large-diameter steel, such as X80 steel with the diameter of 1219 mm and the pipe wall thickness of 18.4 mm, used in the second and third west-east national gas pipeline project, which will obviously increase the difficulty and workload in welding processes. So there is an emergent need for the pipeline welding equipment which could meet the higher requirements, not only in the welding quality, but also in the welding speed. To this end we have developed a double-torch pipeline all-position welding robot, mounted on a small vehicle

---

X.-G. Miao (✉) · F. Zhang · Z.-F. Ma · Y. Zhang  
Pipeline Research Institute of CNPC, Langfang 065001, China  
e-mail: 670411163@qq.com

X.-G. Miao  
Beijing Engineering Research Center of Monitoring for Construction Safety, Beijing  
University of Civil Engineering and Architecture, Beijing 100044, China

equipped with two welding torches to work simultaneously, which can weld fast and efficiently, with little defects. In this paper, double-torch pipeline all-position welding robot will be studied.

## 2 Design of Mechanical Structure

### 2.1 Structural Design

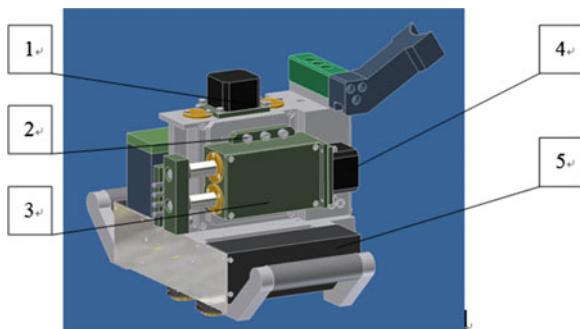
The robot mechanical structure is consisted of torch attitude adjusting part, torch swing part, and welding vehicle driving part. See Fig. 1. The torch attitude adjusting part mainly complete the adjustments of the torch to meet the requirement of the welded seam in the welding process, which is achieved by the movements of skateboard 2 driven by the motor 1; the torch swing part controls the torch swing distance, swing frequency, the swing mode, and the residence time at both ends of a location, which is achieved by the movements of skateboard 3 driven by the motor 4; the movement of the torch along the pipeline is achieved by the welding vehicle driving part, and during the welding process, the welding speed is just the welding vehicle running speed, thus the welding vehicle is required to run very smoothly, which is driven by the motor 5.

### 2.2 Mathematical Model Analysis

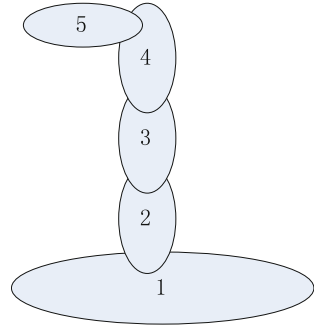
During the welding process, the welding vehicle with double-wire is clamped and running on a circular track to achieve the all-position pipe welding. The multi-body system theory is applied to the structure of the welding vehicle, whose topology is shown in Fig. 2.

First, the various components of the welding vehicle are numbered. Provided the circular track is numbered 0, the topology of welding vehicle consists of two parts,

**Fig. 1** The mechanical structure of the welding vehicle



**Fig. 2** The topology of the welding vehicle



which can be seen in Fig. 2. The left part is consisted of circular track 0, positioning guide wheel 1, vehicle cross slide 2, left and right ball screw 3, upper and lower ball screw 4, and torch holder 5. Coordinate system  $O_0-x_0y_0z_0$  is established at one point of the circular welding track, coordinate system  $O_1-x_1y_1z_1$  is established at the positioning guide wheel 1, and  $O_5-x_5y_5z_5$  coordinate system is established at the torch holder, where the left and right moving direction of the welding vehicle is set as x direction, the upper and lower moving direction of the welding torch is set as y direction, and the direction vertical to x and y direction is set as z direction. According to the multi-body system theory, we can calculate each transformation matrix between adjacent elements of the multi-body system within the welding vehicle.

Take the left part of the topology for example, between the positioning guide wheel 1 and the torch holder 5, provided the coordinate system  $O_5-x_5y_5z_5$  is obtained through the translations of the coordinate system  $O_1-x_1y_1z_1$  through the first translation of u along the X axis, then translation of v along the Y-axis, and finally translation w along the Z-axis, then the transformation matrix between the two coordinate systems is as follows:

$$T_{15}(M) = T_{15}(u) T_{15}(v) T_{15}(w) = \begin{bmatrix} 1 & 0 & 0 & u \\ 0 & 1 & 0 & v \\ 0 & 0 & 1 & w \\ 0 & 0 & 0 & 1 \end{bmatrix} \tag{1}$$

The matrix  $T_{15}(M)$  above is an ideal translational movement characteristic matrix between the positioning guide wheel and welding torch holder A, namely,  $T_{15}(u), T_{15}(v), T_{15}(w)$  are the ideal translational movement characteristic matrixes between the positioning guide wheel and welding torch holder A along X, Y, Z-axis respectively. The right part of the topology can be analyzed by the similar method.

If the coordinates of the position in the earth coordinate system where the circular track coordinate  $O_0-x_0y_0z_0$  is established have been known, the final coordinates of the welding torch holder can also be calculated according to the

homogeneous coordinate transformation, and so as the coordinates of the joint between the welding wire and the welded pipe. Therefore, the kinematic model of the welding vehicle is established, which can work under the control system.

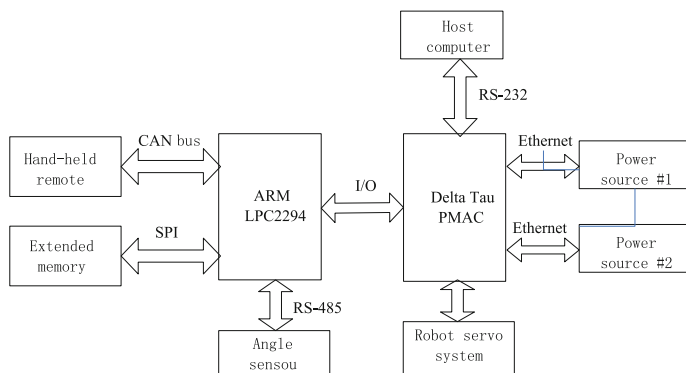
### 3 Hardware Design of the Control System

The hardware structure of the control system in the welding robot is shown in Fig. 3. In order to reduce the burden on the host controller, the system uses dual-controller architecture. The host controller is a PMAC motion controller made by Delta Tau Ltd., which can achieve a variety of welding robot control algorithms through the work of the servo systems. The host computer uses a touch screen, which offers the interface to edit the welding parameters and greatly improve its practicality; it is also communicated with the welding power via Industrial Ethernet to achieve the real-time control on modifying the welding power parameters.

The supplementary controller, using ARM chip made by Philips Ltd., is mainly responsible for the control of peripheral interface circuit, which is connected to a handheld remote control box via the CAN bus interface and accept a variety of welding control commands; it is also connected to the angle sensor via RS-485, which collects the spatial position data of the welding vehicle timely acquisition to call the corresponding welding parameters in the position.

Throughout the system, PMAC exchanges data directly with ARM through I/O interface, which can ensure timeliness and reliability in transferring data between the two processors.

The power source is TPS3200 from Fronius, Its ethernet port communication use Modbus/UDP protocol. Modbus/UDP is a protocol which is based on modbus fieldbus and ethernet-based TCP/IP protocol, the transport layer use UDP connection-oriented protocol and application layer use Modbus/RTU protocol. All Modbus/UDP ADU are sent via UDP on registered port 502. For example, the



**Fig. 3** Block diagram of hardware system

Request		Response	
Field Name	(Hex)	Field Name	(Hex)
Transaction Identifier Hi	00	Transaction Identifier Hi	00
Transaction Identifier Lo	01	Transaction Identifier Lo	01
Protocol Identifier Hi	00	Protocol Identifier Hi	00
Protocol Identifier Lo	00	Protocol Identifier Lo	00
Length Hi	00	Length Hi	00
Length Lo	06	Length Lo	06
Unit Identifier	00	Unit Identifier	00
Function code	06	Function code	06
Register Address Hi	E0	Register Address Hi	E0
Register Address Lo	11	Register Address Lo	11
Register Value Hi	08	Register Value Hi	08
Register Value Lo	98	Register Value Lo	98

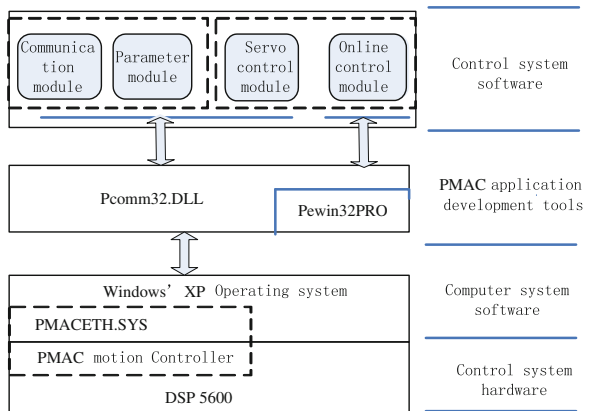
Fig. 4 Fronius gas preflow control

function 0x06 code is used to write a single holding register in a remote device. When we want to control “gas preflow”, it request to write register 0xE011 with the value 0x898, see Fig. 4.

### 4 Software Design of the Control System

According to the hardware architecture of the control system, software development process has adopted a modular approach in order to make operations more conveniently, whose architecture is shown in Fig. 5. The software includes four major functional modules, which are communication connection module, parameter modification module, servo control module and online control module. Among the

Fig. 5 Software design of the control system



位置 clock	焊接速度 mm/min (P322-334)	送丝速度1 m/min (P325-347)	送丝速度2 m/min (P348-360)	摆动宽度 mm (Q551-563)	摆动时间 ms (Q564-576)	边缘停留 ms (Q577-589)
0点	0.0	0.0	0.0	0.0	0.0	0.0
0.5	0.0	0.0	0.0	0.0	0.0	0.0
1点	0.0	0.0	0.0	0.0	0.0	0.0
1.5	0.0	0.0	0.0	0.0	0.0	0.0
2点	0.0	0.0	0.0	0.0	0.0	0.0
2.5	0.0	0.0	0.0	0.0	0.0	0.0
3点	0.0	0.0	0.0	0.0	0.0	0.0
3.5	0.0	0.0	0.0	0.0	0.0	0.0
4点	0.0	0.0	0.0	0.0	0.0	0.0
4.5	0.0	0.0	0.0	0.0	0.0	0.0
5点	0.0	0.0	0.0	0.0	0.0	0.0
5.5	0.0	0.0	0.0	0.0	0.0	0.0
6点	0.0	0.0	0.0	0.0	0.0	0.0

Fig. 6 Parameters modification interface

four modules, the communication connection module and parameter modification module consist of host computer software to implement communication settings and edit, modify and save welding parameters; online control module and servo control module are achieved by PMAC software to implement servo control algorithms and on-line monitoring.

#### 4.1 PC Touch Screen Software

The edit and modification of the welding parameters include welding speed, wire feed speed, swing width, swing time, edge retention time and voltage trimming etc., which is shown in Fig. 6. After setting the various parameters, the file can either be saved to the host machine or be downloaded via Ethernet to the PMAC Flash memory to enable offline operation.

## 5 Conclusion

The paper has presented a design of the one torch double-wire pipeline welding robot, whose mechanical structure includes welding torch attitude adjustment part, welding torch swing part, and welding vehicle driving part, furthermore, mathematical model is also established. The hardware control system uses PMAC as the

host controller, which is responsible for connecting the servo motors, and uses ARM as supplementary controller, which is responsible for the peripheral interface connection; the software control system consists of PC and the PMAC divisions, while the PC is responsible for edit and modification of welding parameters, and PMAC is responsible for achieving the motion algorithms of each axis of the robot, so this design gives full play to the advantages of both parts. The robot has been successfully used in the second and third part of National West-East Gas Pipeline Project, and the results have shown its reasonable structure, stable operation, and improved weld quality and efficiency.

## References

1. Yan Z, Liang J, Chen J (2005) Research on high-efficient pipeline double-torch all-position auto-welding machine by DSP. *Electr Welding Mach* 35(4):38–43
2. Miao X, Wang S et al (2009) Software research of double-torch pipeline welding robot. *Comput Sci* 36(4A):294–296
3. Miao X, Wang S et al (2009) Research of welding robot controlled by PMAC and ARM two processors. In: 2009 International Asia conference on informatics in control, automation, and robotics. 2(1–2):111–113
4. Zhang F, Miao X, Ma Z et al Software research of single arc and double wire pipeline welding robot. *J Shanghai Jiaotong Univ*
5. Zhang L, Gao H, Zhang G et al (2007) Development of control software for open architecture arc welding robot. *Welding J* 28(1):25–28
6. Miao X, Wang S, Zhang F et al (2013) Research of double-torch pipeline all-position welding robot. In: 5th international conference on welding science and engineering, vol 10, pp 348–349
7. Fronius Corp. (2012) Implementation guide gateway Modbus UDP extended. Fronius 1

# Optimal Motion Planning on 120° Broken Line Seam for a Mobile Welding Robot

Tao Zhang and Shan-Ben Chen

**Abstract** This paper analyses the motion planning of a custom-built all position autonomous mobile welding robot. It proposes a motion planning method that allows the robot to complete 120° broken line seam welding while the vehicle turns simultaneously. It is applied to the welding experiments.

## 1 Introduction

Mobile welding robots broad application prospects in the shipbuilding and welding of large spherical tanks. In welding situation where two linear seams are formed at an angle, general-purpose wheeled mobile robots have difficulty to track the seams. It is a challenge for a mobile platform to turn smoothly while the welding torch moves along a right angle or broken line seam. Advanced robotic welding control is required to overcome this technical difficulty.

In the study of special shape weld, many researchers have focused the research on robot welding about fillet weld [1], rectangular weld [2], curve weld [3] and saddle-shaped weld [4]. Novel algorithms are proposed to reflect the advanced nature of intelligent welding robot [5–8]. In robot motion planning, there are a lot of research results [9–14], most of which has made high progress in the path planning [12] and trajectory planning [13, 14].

For broken line seams, the robot vehicle in this paper turns itself, and the torch moves along the seams at the same time. Broken line motion planning has a certain particularity. The torch does not move entirely in accordance with the straight path, but moves from one straight line to another through a mid-point transition. The work aims to develop optimal planning algorithm to optimize the turning and welding model of all-position mobile robot for broken line welding.

---

T. Zhang (✉) · S.-B. Chen

Intelligentized Robotic Welding Technology Laboratory, Shanghai Jiao Tong University, Shanghai 200240, China

e-mail: taurus509@163.com



The purpose of broken line motion planning is to achieve optimal co-ordination between the respective movement of the robot vehicle and the torch, and optimal control of the mechanical joints and spatial position. Therefore it lays a theoretical foundation for broken line motion planning and serves a valuable reference for experimental validation.

## 2 Wheeled Mobile Welding Robot System

The wheeled welding mobile robot system developed in this work is shown in Fig. 1.

The prototype is shown in Fig. 2. The robot system consists of a vehicle at the bottom and a manipulator arm mounted on the vehicle, and the welding torch is clamped onto the manipulator. The kinematic model of the robot system is divided into manipulator kinematics model and vehicle kinematics model.

## 3 Kinematics of Robot

### 3.1 Manipulator Kinematics

The manipulator arm has 5 degrees of freedom (DOF). According to the Denavit-Hartenberg rules, the robot kinematics equation can be obtained easily:

$${}^0_5T = {}^0_1T_1 {}^1_2T_2 {}^2_3T_3 {}^3_4T_4 {}^4_5T_5 T = \begin{bmatrix} r_{11} & r_{12} & r_{13} & p_x \\ r_{21} & r_{22} & r_{23} & p_y \\ r_{31} & r_{32} & r_{33} & p_z \\ 0 & 0 & 0 & 1 \end{bmatrix} \quad (1)$$

**Fig. 1** Designed model of robot system

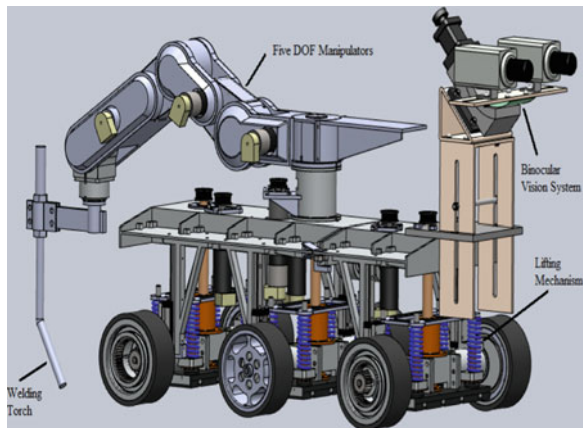
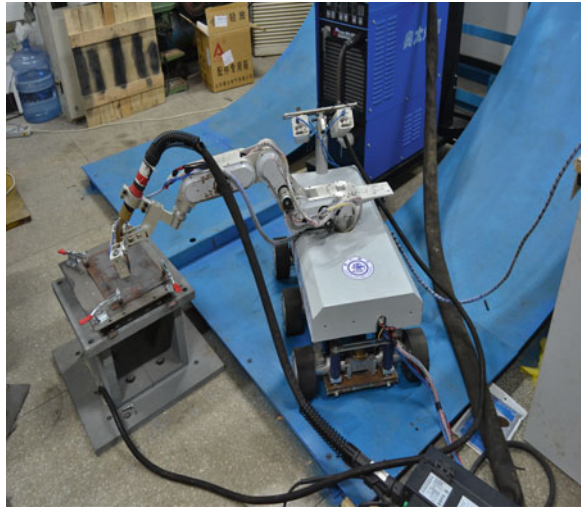


Fig. 2 Prototype of robot



### 3.2 Vehicle Kinematics

For broken line seams, turning kinematic model of the vehicle needs to be derived to achieve transition from one linear seam to the next. The vehicle turning process is shown in Fig. 3.

Firstly, the robot vehicle is aligned to be parallel to the seam AB, and then the torch moves to the initial position A. The distance between the robot center in the initial position and point A is  $L_y$ , while the distance between point A and point B is  $L_x$ . Point B is intersection point of the two seams. Then the torch moves along the two seams, while the vehicle turns simultaneously. When the forward direction of the vehicle is parallel to the second seam, the turning process is completed. Finally the torch reaches point C. The manipulator should be perpendicular to the second seam.

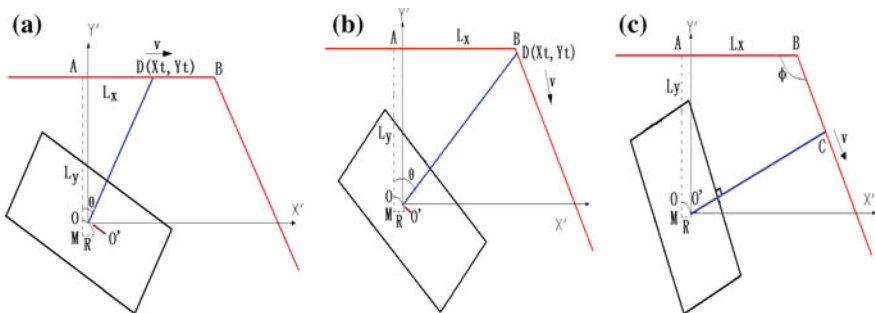


Fig. 3 Vehicle turning process

The angle of the two seams is  $\phi = 120^\circ$ . The vehicle center turns with point M as the turning center. A dynamic coordinate system  $X'O'Z'$  is created. Point  $O'$  is the dynamic origin of the vehicle center. The trajectory of dynamic center  $O'$  is just a circular arc with R as the radius. The dotted lines in Fig. 3 represent the distance from the initial position of the vehicle center to the first seam. The arm turns the angle  $\theta$  which is relative to the initial position at the time t. The maximum  $\theta$  is  $60^\circ$ . The coordinates and relations of these points can be obtained.

For  $0 \leq \theta \leq \angle AMB$  ( $\angle AMB = \arctan L_x / (L_y + R)$ ) shown in Fig. 3a:

$$\cos \theta = \frac{L_y + R}{\sqrt{(L_y + R)^2 + v^2 t^2}} \quad (2)$$

$$\omega = \frac{-2v \cos^2(\theta + 120^\circ)}{L_y + R + \sqrt{3}L_x} \quad (3)$$

For  $\angle AMB < \theta \leq 60^\circ$  shown in Fig. 3b:

$$\cos \theta = \frac{2(L_y + R) - \sqrt{3}(vt - L_x)}{\sqrt{[2(L_y + R) - \sqrt{3}(vt - L_x)]^2 + [2L_x + (vt - L_x)]^2}} \quad (4)$$

$$\omega = \frac{v[\sqrt{3}L_x + (L_y + R)]}{2L_x^2 + 2(L_y + R)^2 + 2(vt - L_x)^2 - 2(vt - L_x)[\sqrt{3}(L_y + R) - L_x]} \quad (5)$$

$\omega$  is the rotating angular velocity of the manipulator relative to the initial position, which has important research significance.

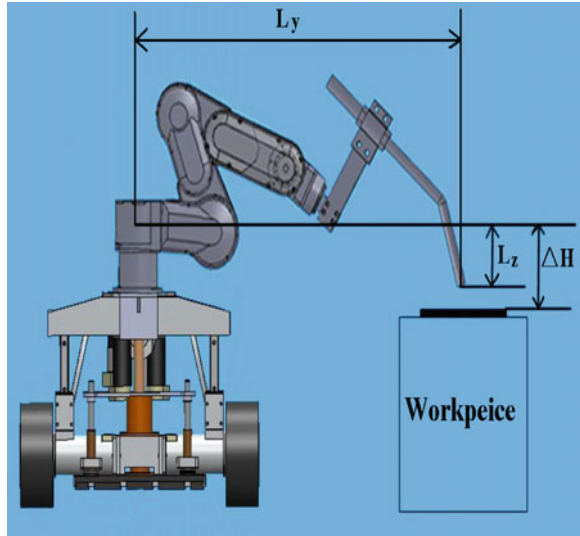
## 4 Pose Calculation of Robot

The coordinates of the torch at the end of manipulator are determined by five joint angles. Change of each joint angle will affect the final coordinates of the torch. As the direction of manipulator arm is always perpendicular to the vehicle direction, the first joint angle is  $90^\circ$ . The 5th joint angle affects the moving angle of the torch. In order to ensure the torch perpendicular to the surface of the workpiece, the 5th joint angle should remain at  $0^\circ$ . Therefore in this case, the 2nd, 3rd and 4th joint angles will be the key to determining the coordinates of welding torch.

In order to simulate the fillet weld environment, the working angle of the torch is  $-15^\circ$ , while the moving angle is  $0^\circ$ . The height difference between the welding platform and the base coordinate center is adjustable. For example, the difference is  $-135$  mm in Fig. 4. During welding, the distance between the torch and the seam must be 15–20 mm, so  $L_z$  marked in Fig. 4 should be  $-120$  to  $-115$  mm.

Based on coordinate transformation and changing the 2nd, 3rd and 4th joint angle, the range of calculated  $L_y$  can be got, which is from 545.01 to 850.36 mm.

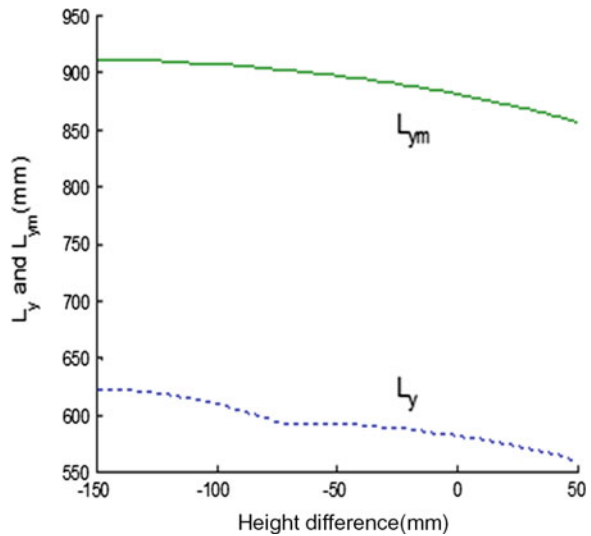
Fig. 4 Robot pose



In order to ensure that the manipulator can obtain larger stretching space, the optimal  $L_y$  in the initial position is selected as the minimum value of the corresponding range. Meanwhile, the maximum value of the range should be the maximum limit of y-coordinate, which is defined as  $L_{ym}$ .

For different height difference between the welding platform and the base coordinate center, which ranges from  $-150$  to  $50$  mm, the variation curve of  $L_y$  and  $L_{ym}$  can be obtained, as shown in Fig. 5. The height difference will affect the entire model.

Fig. 5 Variation curve of  $L_y$  and  $L_{ym}$



The equations after fitting the two curves in Fig. 5 are:

$$\begin{aligned} L_y &= 579.1204 - 0.2685\Delta H + 0.0003\Delta H^2 \\ L_{ym} &= 880.217 - 0.3985\Delta H - 0.0013\Delta H^2 \end{aligned} \quad (6)$$

## 5 Optimization Calculation

In the entire turning process, the most important point is to ensure that the extended length of the manipulator falls in the range of  $[L_y, L_{ym}]$ .

The manipulator length in mid stage and final stage should meet the following conditions:

$$\begin{aligned} L_y &\leq \overline{O'B} \leq L_{ym} \\ L_y &\leq \overline{O'C} \leq L_{ym} \end{aligned} \quad (7)$$

Because  $L_y \leq \overline{O'B}$  and  $\overline{O'C} \leq \overline{O'B}$ , inequality (7) can be simplified. In addition,  $\overline{MB} = \sqrt{L_x^2 + (L_y + R)^2}$ ,  $\overline{MC} = \frac{\sqrt{3}}{2}L_x + \frac{1}{2}(L_y + R)$ . Through arrangement, it can be obtained:

$$\begin{cases} R \geq \frac{1}{2(L_{ym} - L_y)}L_x^2 - \frac{L_y + L_{ym}}{2} \\ R \leq \sqrt{3}L_x - L_y \end{cases} \quad (8)$$

The solutions of R and Lx can be obtained through the analytical method:

$$0 \leq R \leq (3 + \sqrt{3 + 3\sqrt{3}})(L_{ym} - L_y) - L_y \quad (9)$$

$$\frac{\sqrt{3}}{3}(R + L_y) \leq L_x \leq \sqrt{2\left(R + \frac{L_{ym} + L_y}{2}\right)(L_{ym} - L_y)} \quad (10)$$

Since the scope of height difference is  $[-150, 50 \text{ mm}]$ , it can be obtained that:

$$\Delta H_q = -150 + q \quad (0 \leq q \leq 200, q \in Z) \quad (11)$$

According to (6), they will be:

$$L_{y,q} = 490.9908 - 0.7962\Delta H_q - 0.003\Delta H_q^2 \quad (12)$$

$$L_{ym,q} = 789.5755 - 0.6798\Delta H_q - 0.0017\Delta H_q^2 \quad (13)$$

The ranges of R and Lx can be obtained from inequalities (9) and (10), which are divided equally into 10 segments. Therefore, there are 11 × 11 parameter pairs. They will be:

$$R_i = \frac{i}{10} (3 + \sqrt{3 + \sqrt{3}}) [(L_{ym,q} - L_{y,q}) - L_{y,q}] \quad (0 \leq i \leq 10, i \in Z) \quad (14)$$

$$\frac{\sqrt{3}(R_i + L_{y,q})}{3} \leq L_{x,j} \leq \sqrt{2 \left( R_i + \frac{L_{ym,q} + L_{y,q}}{2} \right) (L_{ym,q} - L_{y,q})} \quad (0 \leq j \leq 10, j \in Z) \quad (15)$$

The extended length of manipulator at the different moment can be calculated. Three moments when the torch moves to point A, B and C are chosen. Point A is the moment to start turning; point B is the moment of half turning; point C is the moment of completing turning. Through comparison, when R is fixed, the extend length is increasing with the incremental Lx. When R and Lx are both smallest, the fluctuation of the extend length from moment A to moment B then to moment C is the smallest.

Therefore, the relationship between the pair of {R, Lx} and the height difference can be obtained, shown in Fig. 6.

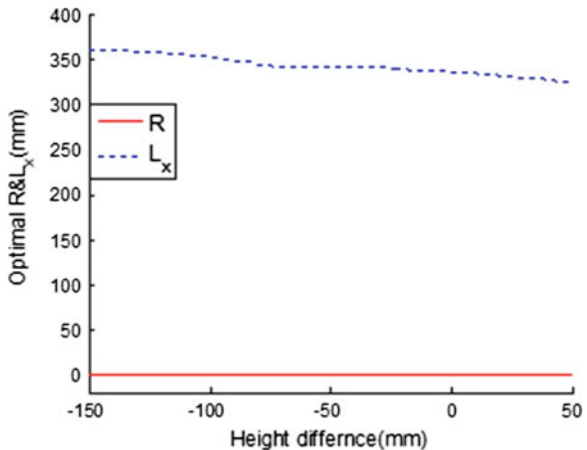
The following conclusions can be obtained: the optimal turning radius R remains at zero, and the optimal Lx decreases with increased ΔH. The fitting function is:

$$L_x = -0.0017\Delta H^2 - 0.4597\Delta H + 283.4737 \quad (16)$$

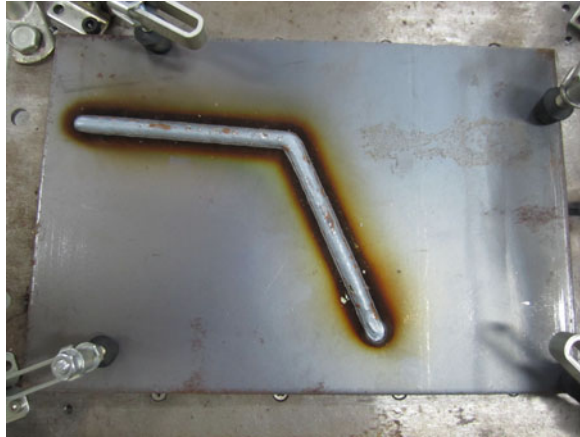
## 6 Welding Experiments

In the experiment using the method which have been introduced, the height difference between the welding platform and the vehicle center is taken as -135 mm. In addition,  $L_y = 545$  mm,  $R = 0$  mm,  $L_x = 313.2258$  mm for  $\phi = 120^\circ$ .

**Fig. 6** Calculation result under different height difference



**Fig. 7** Welding experiments for  $120^\circ$  broken line angle



The welding method is flat welding under mixed protective gas of  $\text{CO}_2$  and Ar. The speed is 300 mm/min. Due to the limit of metal plate length, when start turning, the torch only moves without welding. Until the torch reaches the surface of the plate, the weld starts. When the torch will leave the surface, the welding is finished. The torch keeps moving until the target position. Figure 7 shows the results.

## 7 Conclusion

This paper describes optimal motion planning of an all position autonomous welding mobile robot system. For  $120^\circ$  broken line seam, the vehicle at the bottom of robot turns itself while the torch held at the end of the arm completes welding. This paper has carried out a detailed analysis of the kinematic model as the base of the motion planning. Through the results, welding experiments are conducted to prove the feasibility and correctness of the proposed method.

## References

1. Fang Z, Xu D, Tan M (2011) A vision-based self-tuning fuzzy controller for fillet weld seam tracking. *IEEE/ASME Trans Mechatron* 16(3):540–550
2. Ngo MD, Duy VH, Phuong NT, Kim SB (2006) Robust control of welding robot for tracking a rectangular welding line. *Int J Adv Rob Syst* 3(3):239–248
3. Chung TL, Bui TH, Nguyen TT, Kim SB, Oh MS (2007) Two-wheeled welding mobile robot for tracking a smooth curved welding path using adaptive sliding-mode control technique. *Int J Control Autom Syst* 5(3):283–294
4. Chen H, Meng Y, Wang X (2011) Combined planning between welding pose and welding parameters for an arc welding robot. *Robot Weld Intell Autom* 88:73–80

5. Chang D, Son D, Lee J, Lee D, Kim T, Lee KY, Kim SJ (2011) A new seam-tracking algorithm through characteristic-point detection for a portable welding robot. *Robot Comput Integr Manuf* 28(1):1–13
6. Xiao Y, Du Z, Dong W (2012) Smooth and near time-optimal trajectory planning of industrial robots for online applications. *Indus Robot Int J* 39(2):169–177
7. Jeon YB, Kim SB, Park SS (2002) Modeling and motion control of mobile robot for lattice type welding. *KSME Int J* 16(1):83–93
8. Dinham M, Fang G, Zou J (2011) Experiments on automatic seam detection for a MIG welding robot. *Artif Int Comput Intell* 7003:390–391
9. Liu Z, Bu W, Tan J (2010) Motion navigation for arc welding robots based on feature mapping in a simulation environment. *Robot Comp Integr Manuf* 26(2):137–144
10. Chen XZ, Huang YM, Chen SB (2012) Model analysis and experimental technique on computing accuracy of seam spatial position information based on stereo vision for welding robot". *Indus Robot Int J* 39(4):349–356
11. Chen SB, Chen XZ, Li JQ (2005) Acquisition of weld seam dimensional position information for arc welding robot based on vision computing. *J Intell Rob Syst* 43(1):77–97
12. Chakraborty N, Akella S, Wen JT (2010) Coverage of a planar point set with multiple robots subject to geometric constraints. *IEEE Trans Autom Sci Eng* 7(1):111–122
13. Ngo MD, Phuong NT, Duy VH, Kim HK, Kim SB (2007) Control of two wheeled welding mobile manipulator. *Int J Adv Rob Syst* 4(3):293–302
14. Kim J, Kim SR, Kim SJ, Kim DH (2010) A practical approach for minimum-time trajectory planning for industrial robots. *Indus Robot Int J* 37(1):51–61



# A Self-calibration Algorithm with Chaos Particle Swarm Optimization for Autonomous Visual Guidance of Welding Robot

Wei-Feng Ni, Shan-Chun Wei, Tao Lin and Shan-Ben Chen

**Abstract** Camera calibration is the process of finding the true parameters of a camera. In this article, we study the application of improved particle swarm optimization (PSO) algorithm in camera calibration. Then proposes a new algorithm CPSO, combining PSO with chaos optimization algorithm, to optimize camera's intrinsic parameters based on absolute conics. Finally we carry out experiments to test its performance. Re-projection errors show that the method used in this paper is flexible and feasible, and the re-projection error is small enough to meet the accuracy demand of welding guidance.

## 1 Introduction

The widely use of welding robots has made great contributions to promote the development of welding automation. Nowadays welding robots are equipped with sensors to obtain external information to increase its intelligence and flexibility. However recognition of key points of welding seam is significant to realize intelligentized welding. With the rapid development of artificial intelligence and image processing technology, as well as its advantages that large amounts of information and high precision, vision sensing is feasible for guidance of the initial point of welding seam. However, the precondition of visual guidance for welding seam is camera calibration.

Camera calibration is the process of finding the true parameters of a camera. It is the key to obtain three-dimensional information from two-dimensional images, as well as to obtain stereo vision. Recently, camera calibration is widely used in three-dimensional reconstruction, navigation, and visual surveillance. Many

---

W.-F. Ni · S.-C. Wei · T. Lin · S.-B. Chen (✉)

Intelligentized Robotic Welding Technology Laboratory, School of Materials Science and Engineering Shanghai Jiao Tong University (SJTU), Shanghai 200240, People's Republic of China  
e-mail: sbchen@sjtu.edu.cn

methods have been proposed for camera calibration so far. In a broad sense, camera calibration can be divided into three categories: traditional calibration, calibration based on active vision and self-calibration. The traditional one computes camera parameters based on the relationship between coordinates in the corresponding image and the coordinates of special points in calibration block, whose geometric dimension is known in advance. This kind of method mainly contains DLT [1], Tsai's two-step method [2] and planar calibration method [3]. The second requires camera to do some specific motions and then computes parameters by using the particularity of movement. When using the two methods above for calibration, some factors must be known in advance. Therefore they are not feasible if coordinates of points or camera's motions are unknown. Whereas, self-calibration is much more flexible as it only utilizes restriction of camera's internal parameters. Thus it has a better prospect of application. Camera self-calibration technique was firstly proposed by Faugeras [4, 5] in 1990s, which mainly applies to calibrate in unknown scenes. Since proposed, it has been remarkably improved to branch out many new calibration methods, including Kruppa's equations method [6], methods based on absolute quadric or absolute conic [7], methods based on active vision [8–10].

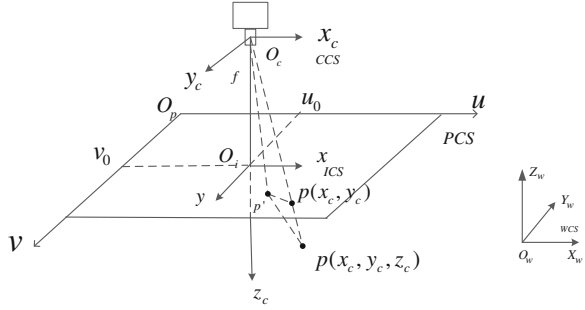
Considering the easy implementation and effectiveness of PSO, much attempt has been to improve its performance and it is widely used to solve global optimization problems. Zhang [11] used an improved adaptive PSO (IAPSO) for reservoir operation optimization. Compared with other methods, the IAPSO provides a better operational result with greater effectiveness and robustness. Furthermore it appears better in power generation benefit and convergence performance. Wang [12] presents a new Chaos PSO method for resource allocation problem in the container terminal system. This method enhances the allocation efficiency observably.

Consequently, in this article, we focus on the study of camera self-calibration, utilizing the method of hierarchical step-by-step to obtain the initial parameters, and then presents an improved particle swarm optimization (CPSO) to optimize initial parameters. CPSO combines PSO with chaos optimization algorithm. It can improve the quality of initial swarms observably, and avoids becoming premature when searching the optimal solution.

## 2 Problem Description

The pinhole camera model in perspective projection is the classical and most commonly used model, as showed in Fig. 1. In the model,  $O_c-X_cY_cZ_c$  stands for the camera coordinate,  $O_w-X_wY_wZ_w$  world coordinate and  $O_p-uv$  image plane. In the model, it assumes that all camera rays pass through the optical center and the relationship between coordinates of image points and the ones of points in camera coordinate system is linear. And object distance  $u$ , image distance  $v$  and focal length  $f$  follow the following equation.

**Fig. 1** Pinhole model and coordinates



$$\frac{1}{u} + \frac{1}{v} = \frac{1}{f} \tag{1}$$

Mostly  $u$  is much larger than  $f$ , thus  $v$  is nearly equal to  $f$ . Supposing that  $M$  is a point in world coordinates system and  $m$  is a point in the image plane, both of them are expressed in homogeneous coordinates.  $M = (x, y, z, 1)^T$ ,  $m = (u, v, 1)^T$ . The perspective projection of  $M$  onto  $m$  can be given by the following formula:

$$\lambda m = PM \tag{2}$$

$$K = \begin{bmatrix} f_x & \gamma & u_0 \\ 0 & f_y & v_0 \\ 0 & 0 & 1 \end{bmatrix}, \quad P = K[R - Rt] \tag{3}$$

And elements in matrix  $K$  are the intrinsic parameters of camera. The  $f_x$  and  $f_y$  are the focal length measured in pixel dimensions horizontally and vertically respectively;  $(u_0, v_0)$  is the coordinate of the principle point, which is the intersection of camera optical axis and image plane. The symbol  $\gamma$  stands for skew term which equals zero when pixel is square. In this paper we regard it as zero, and  $P$  is a  $3 \times 4$  matrix,  $R$  and  $t$  are the rotation matrix and translation vector from world coordinate system to camera coordinate system respectively. Thus calibration of camera is the processing to find values of  $K$ .

### 3 Particle Swarm Optimization Algorithm

Particle Swarm Optimization (PSO), first proposed by James Kennedy and Russ Eberhart [13], is a classical swarm intelligence algorithm. Due to the easy implementation and effectiveness, it is used to solve global optimization problems. It solves numerical optimization problems by imitating birds foraging. Each particle or member represents a potential solution, and they fly through a multidimensional solution space to search for the optimal one. In standard PSO algorithm, each

member contains two elements: position and velocity. The basic framework of PSO can be described as the follows: First, initialize a group of particles in solution space. Then each particle updates its position and velocity according to Eq. (4), and meanwhile uses a function, called cost function, to measure it, so as to record the best previous position of a singular particle and the best one among all the particles. Take the D-dimensional optimization problem for example, the particle group consists n members. The position of ith member is presented as  $X_i = (x_{i1}, x_{i2}, \dots, x_{iD})$ , the velocity presented as  $V_i = (v_{i1}, v_{i2}, \dots, v_{iD})$ , and its best previous position, giving the best fitness value, is recorded as  $P_{ibest} = (p_{i1}, p_{i2}, \dots, p_{iD})$ . The best one among all particles is presented as  $P_{gbest} = (p_{g1}, p_{g2}, \dots, p_{gD})$ . And each generation of the particle can be update through the following equations.

$$\begin{aligned} v_{id}^{t+1} &= wv_{id}^t + c_1r_1(p_{id} - x_{id}^t) + c_2r_2(p_{gd} - x_{id}^t) \\ x_{id}^{t+1} &= x_{id}^t + v_{id}^t \end{aligned} \quad (4)$$

In the equation,  $w$  is the inertia weight,  $c_1$  and  $c_2$  are study factors, and both  $r_1$  and  $r_2$  are random numbers ranging from 0 to 1. However, during the iteration, the best particle is inclined to be trapped into local optimal solution. That is to say, what we finally get may not be the best solution to a problem. Considering of this, scholars have proposed many methods to avoid the phenomenon [14–16].

## 4 Camera Calibration Based on Chaos Particle Swarm Optimization

When dealing with complex the problem, PSO may be trapped into local convergence. Furthermore, to some extent, the quality of initial particles will influence optimization results. To improve PSO algorithm, we combine it with chaos optimization algorithm and linearly decreasing inertia weight. We utilize chaotic system's properties, randomness, regularity and ergodicity, and linearly decreasing inertia weight to enhance its search ability.

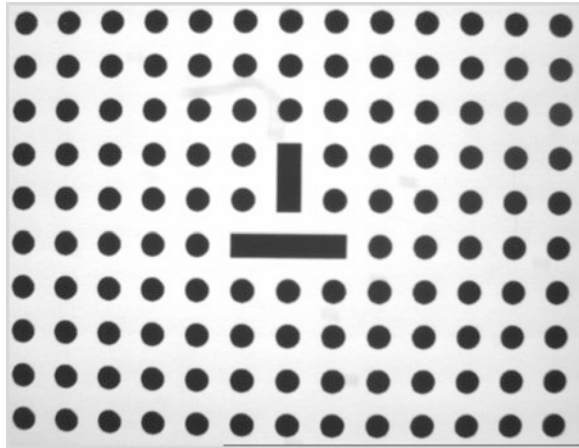
### 4.1 Calculation of the Initial Values

In this section, we manage to obtain intrinsic parameters of camera using hierarchical calibration. This kind of methods can be divided into three steps: projective reconstruction, affine reconstruction and Euclidean reconstruction [17].

We use equally spaced circular lattice as calibration plate. The radius of circle dots is 4 mm, and the distance between each dot is 8 mm, shown as Fig. 2.

Firstly we use the un-calibrated camera to obtain image sequence and carry out projective alignment operation, regarding the first image as the reference. Then

**Fig. 2** Calibration plate



ensuring the location of plane at infinity, in this operation projective space will be transformed into affine space. Finally we compute the degenerated curve based on the plane at infinity ensured in the previous step, and thus we could compute camera intrinsic parameters from degenerated curve. Computing process of  $K$  is shown in Fig. 3.

### 4.2 Definition of Cost Function

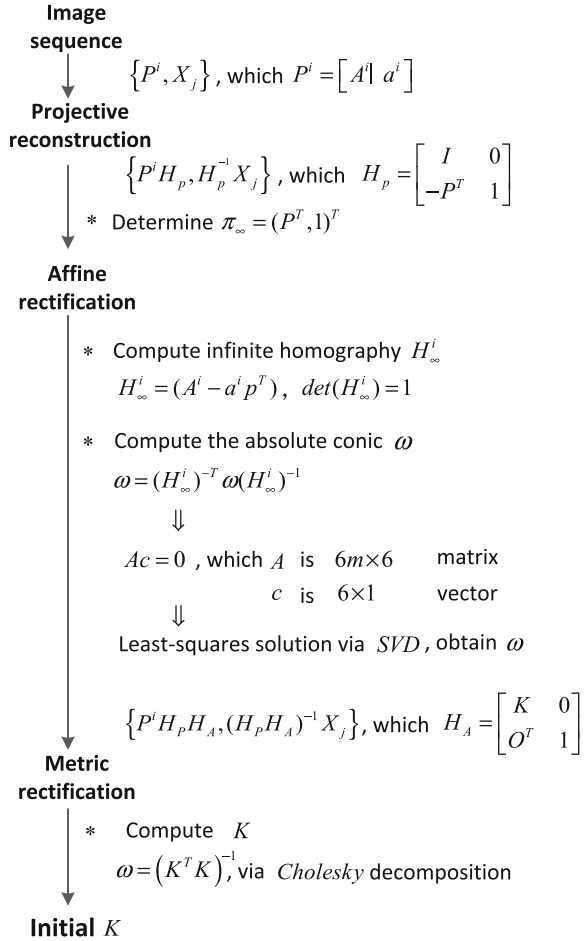
We assume that  $m_1, m_2$  and  $m_3$  are a set of matching points, projection points of the point  $M$  in world space, extracted from  $I_1, I_2$  and  $I_3$  image respectively. According to pinhole camera model, we use  $m_1$  and  $m_2$  to evaluate the coordinates of their corresponding points  $M$ . Then we compute the estimated value of  $m_3$ , recorded as  $m'_3$ . This process is called re-projection. And we define re-projection error as the next formula.

$$error(m) = |m - m'| = \frac{|u - u'| + |v - v'|}{2} \tag{5}$$

The symbol  $m$  represents a known image point,  $m = (u, v)$  and  $m' = (u', v')$  is the estimated value. In this case, the problem of optimizing camera's intrinsic parameters can be transformed into minimizing the mean of all points re-projection, shown as the formula (6).

$$fitness(x) = \sum_{i=1}^n error(m_i) \tag{6}$$

**Fig. 3** Determining  $K$  using the IAC



The parameter  $x$ , a particle of the group, in the formula above represents a potential solution of the problem. And the function *fitness* is called cost function.

### 4.3 Effects of Chaos Algorithm in Calibration

In this paper we use typical Logistic equation to produce chaotic sequence.

$$z_{n+1} = \mu z_n(1 - z_n), \quad n = 0, 1, 2, \dots \tag{7}$$

where  $z_0$  ranges from 0 to 1 and  $\mu$  equals 4.

Chaotic mutation mainly functions in the following two aspects:

1. Enhance the quality of initial particles. As mentioned above, the chaotic system has the properties of randomness, regularity and ergodicity, thus particles will be representative in search solution space if we use it in initialization.
2. Help to avoid local convergence. According to document [14], when local convergence occurs, we will carry out chaotic mutation operation. In this step, we use the scale of decrease of the best solution's fitness value, recorded as Rate, showed in Eq. (8), to judge whether the premature stagnation phenomenon occurs or not. If  $Rate < \Phi$ , change positions of members according to Eqs. (9) and (10).  $\Phi$  is a threshold value.

$$Rate = \frac{fitness(p_{ibest}(t))}{fitness(p_{ibest}(t-20))} \quad (8)$$

where  $p_{ibest}(t)$  and  $p_{ibest}(t-20)$  stands for the best position after iterating  $t$  and  $(t-20)$  times respectively. In the paper  $\alpha$  is a constant.

$$z = \mu z(1 - z), \quad z \in (0, 1), \quad \mu = 4 \quad (9)$$

$$x_{id} = (1 + \alpha(2 \cdot z - 1))P_{gbest}d, \quad d = 1, 2, 3, 4, 5 \quad (10)$$

#### 4.4 Algorithm Description

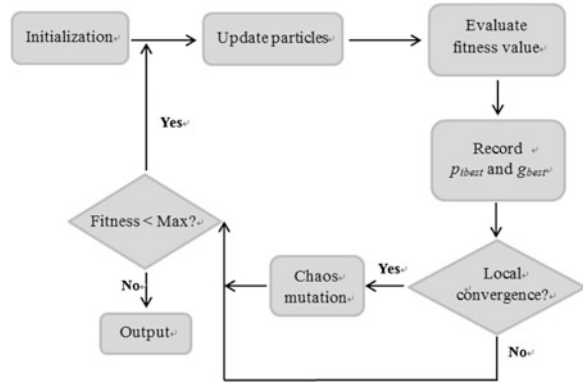
- Step 1 Initialize particle group and set parameters, such as number of particle, maximum iterations.
- Step 2 Compute the fitness value of initial members, and take it as the best previous position of particles. Then find the best one among current generation.
- Step 3 Update the  $d$ th-dimension of its velocity and position of particle  $i$  according to the following equations:

$$\begin{aligned} v_{id}^{t+1} &= (w_1 - (w_1 - w_2) \cdot t/T)v_{id}^t + c_1r_1(p_{id} - x_{id}^t) + c_2r_2(p_{gd} - x_{id}^t) \\ x_{id}^{t+1} &= x_{id}^t + v_{id}^t \end{aligned} \quad (11)$$

where stands for the times of iteration, and  $T$  is the maximum times of iteration. And  $w_1$  and  $w_2$  is maximum and minimum of inertia weight respectively. Here  $w_1 = 0.9$ ,  $w_2 = 0.4$ .

- Step 4 Evaluate the fitness value of each member, and then compare it with  $P_{ibest}$ . If current value is better than the fitness value of  $P_{ibest}$ , then set current location as the best location.

**Fig. 4** Flow diagram of CPSO



Step 5 Evaluate the scale of decrease of the best solution's fitness value, RATE, to judge whether local convergence has occurred or not. If it has, change positions of part of the members randomly according to Eqs. (9) and (10). Otherwise go to the next step.

Step 6 Return the camera intrinsic parameters (Fig. 4).

## 5 Experiment and Analysis

In this section, accuracy and feasibility of the method are demonstrated through experiments on estimated and real data. First we use 20 sets of matching points for optimization. Then we compute estimated coordinates of 10 points, selected from an image randomly. Finally compare the estimated value with the real one.

Table 1 shows the results: the average error is 0.73704 and 1.06472 pixels in X direction and Y direction respectively, which meets the requirement of wielding guidance.

Furthermore, we compare PSO and CPSO in optimization to confirm that chaos mutation plays an important role in breaking local convergence and accelerating convergence velocity. Figures 5 and 6 demonstrates that the optimal solution's fitness value changes along with iteration in both PSO and CPSO algorithm. Apparently convergence rate of CPSO is much higher than that of PSO, as same as the accuracy.

Table 2 shows the change of optimal solution during iteration. It demonstrates that the best solution tends to be stable in spite of small turbulence after 150 iteration operation.

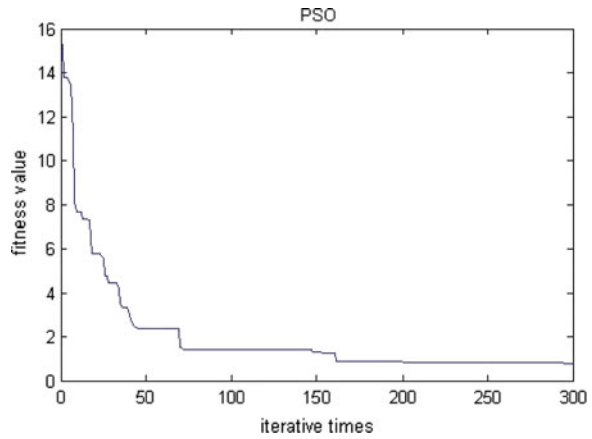
Table 3 gives calibration results of different methods. We can conclude from the results that optimal solution generated from CPSO is close to the result of planar calibration method. However, results of PSO are much different from the two other forms. The reason is that that PSO is readily to be trapped into local optimal solution.



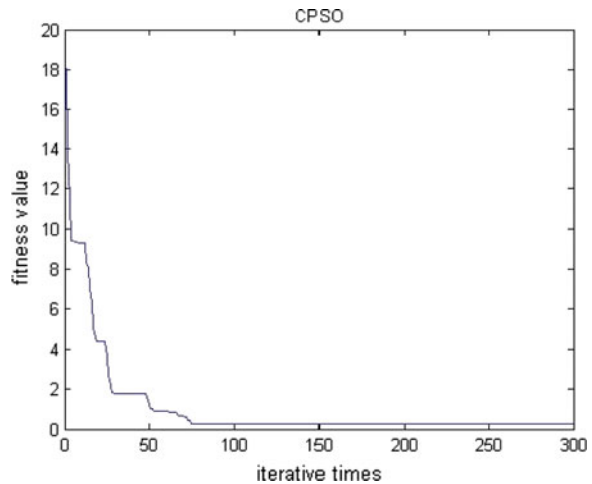
**Table 1** Re-projection error on CPSO

	X			Y		
	$u$	$u$	$ u - u' $	$v$	$v'$	$ v - v' $
CPSO	435	433.9525	1.0475	58.3	59.5985	1.2985
	582	581.5473	0.4527	198.3	199.0132	0.7132
	434.7	435.3152	0.6152	209.8	210.4723	0.6723
	260.1	258.0377	2.0623	322.2	320.5666	1.6334
	71.1	70.6731	0.4269	260.1	261.6591	1.5591
	132.1	132.4581	0.3581	348.6	349.3498	0.7498
	316.9	316.1927	0.7073	380.2	378.96	1.24
	193	192.5962	0.4038	177	178.3479	1.3479
	195.2	195.6931	0.4931	441.6	442.9824	1.3824
	414.1	414.9035	0.8035	518.2	518.1494	0.0506
	Mean value			0.73704	Mean value	

**Fig. 5** PSO algorithm



**Fig. 6** CPSO algorithm



**Table 2** Change of optimal solution during iteration

Number of iterations	$\alpha_x$	$\alpha_y$	$u_0$	$v_0$	$\gamma$
0	795.0356	790.2556	386.2654	260.5565	0
20	814.0322	808.9432	388.6154	259.5238	0
40	820.2107	817.3585	389.1659	258.7413	0
60	830.2206	827.3673	389.1555	258.7412	0
80	829.2207	831.3685	389.1457	258.7453	0
100	833.0669	832.0046	388.5452	258.7611	0
150	833.2094	832.9342	388.5713	258.7579	0
200	833.7588	833.3423	388.6576	258.9713	0
250	834.3544	833.6695	388.6843	258.9630	0
300	834.3381	833.5602	388.7137	258.9627	0

**Table 3** Calibration result of different methods

Parameter\method	CPSO	PSO	Planar calibration
$\alpha_x$	834.3381	839.6348	838.6920
$\alpha_y$	833.5602	820.6451	835.6899
$u_0$	388.7137	387.5941	388.1153
$v_0$	258.9627	259.4682	258.1889
$\gamma$	0	0	0
$k_1$	-0.2927	-0.0325	-0.32935
$k_2$	0.0405	0.1846	0.07035

## 6 Conclusion

In this paper, we propose a new method for camera calibration based on chaos particle swarm optimization. To enhance search ability of PSO in solution space, we combine it with chaos optimization algorithm and linearly decreasing weight. Results show that CPSO algorithm has a better performance in terms of convergence and accuracy. The optimal solution is close to that of traditional method, and re-projection errors are 0.73704 and 1.06472 pixels in X direction and Y direction respectively, which meets the requirement of wielding guidance. Therefore, results of experiment are encouraging, and the method proposed in the article is flexible and feasible.

**Acknowledgments** This work is supported by the National Natural Science Foundation of China under the Grant No. 61374071, No. 51275301 and Shanghai Sciences & Technology Committee under Grant No. 11111100302.

## References

1. Abdel-Aziz Y, Karara H (1971) Direct linear transformation into object space coordinates in close-range photogrammetry. In: The symposium on close-range photogrammetry. University of Illinois, Illinois, pp 1–18
2. Tsai RY (1986) An efficient and accurate camera calibration technique for 3D machine vision. In: Proceedings of IEEE conference on computer vision and pattern recognition
3. Zhang Z (2000) A flexible new technique for camera calibration. *IEEE Trans Pattern Anal Mach Intell* 22(11):1330–1334
4. Faugeras OD, Luong Q-T, Maybank SJ (1992) Camera self-calibration: theory and experiments. In: *Computer vision—ECCV'92[C]*, pp 321–334
5. Maybank SJ, Faugeras OD (1992) A theory of self-calibration of a moving camera. *Int J Comput Vision* 8(2):123–151
6. Hartley R (1997) Kruppa's equations derived from the fundamental matrix. *IEEE Trans Pattern Anal Mach Intell* 19(2):133–135
7. Triggs B (1997) Autocalibration and the absolute quadric. In: *Computer vision and pattern recognition, 1997. Proceedings, 1997 conference on IEEE computer society*, pp 609–614
8. Zhan-Yi HU, Fu-Chao WU (2002) A review on some active vision based camera calibration techniques. *Chin J Comput* 25(11):1149–1156
9. Hua LI, Fu-Chao WU, Zhan-Yi HU (2000) A new linear camera self-calibration technique. *Chin J Comput* 23(11):1121–1129
10. Chang-Jiang YANG, Wei WANG, Zhan-Yi HU (1998) An active vision based camera intrinsic parameters self-calibration technique. *Chin J Comput* 21(5):428–435
11. Zhang Z (2014) An adaptive particle swarm optimization algorithm for reservoir operation optimization. *Appl Soft Comput* 18:167–177
12. Wang S, Meng B (2007) Chaos particle swarm optimization for resource allocation problem. In: *Proceedings of the IEEE international conference on automation and logistics*. Jinan, China, 18–21 August 2007
13. Kennedy J, Eberhart R (1995) Particle swarm optimization. In: *Proceedings of IEEE international conference on neural networks*, 1995, pp 1942–1948
14. Zhu H, Yang C, Gui W, Li Y (2010) Particle swarm optimization with chaotic mutation. *Comput Sci* 37(3):215–217
15. Fan P, Zhang X, Yang T (2009) Particle swarm optimization for breaching local convergence. *J Comput Appl* 29:122–124
16. Shi Y, Eberhart RC (1999) Empirical study of particle swarm optimization. In: *Proceedings of congress on computational intelligence*, Washington DC, USA, pp 1945–1950
17. Meng X-Q, Hu Z-Y (2003) Recent progress in camera self-calibration. *Acta Automatica Sinica* 29(1):110–123

# Simultaneous Calibration of a Stereo Vision System and a Welding Robot-an Automated Approach

Mitchell Dinham and Gu Fang

**Abstract** For a vision guided industrial robot to be used in a production environment effectively and efficiently, it is important that such a system can be quickly and accurately calibrated. The work presented in this paper aims to develop a new method for calibrating a vision guided arc welding robot. This is achieved through automated calibration of the cameras and the optimised simultaneous calibration of a robot arm and robot mounted stereo vision system. The developed method can be implemented in practice and with minimum human intervention. The automatic calibration algorithm not only allows for a faster initial calibration, but also reduces the machine down-time for any subsequent calibrations after an accidental collision or if the camera fixture is relocated. Experimental results show that the proposed method can achieve the required accuracy for robotic arc welding applications.

## 1 Introduction

In an industrial production environment, the key factors for measuring the success of a robotic system are: reliability, accuracy and productivity. To achieve reliability and accuracy, vision systems are introduced to the robot based manufacturing system. In vision controlled robotic systems, the process of establishing the geometrical relationship between the camera and the robot, known as the calibration process, is frequently required.

Once the calibration is achieved, the relationship between the acquired object image and its physical location in space can be calculated. However, this geometric relationship will change if the relative location between the robot and the camera is changed. When such change occurs, a re-calibration is required.

---

M. Dinham (✉) · G. Fang  
School of Computing, Engineering and Mathematics, University of Western Sydney,  
Kingswood, Australia  
e-mail: Mitchell.dinham@gmail.com

Due to the working conditions of industrial robots, it is inevitable that the vision systems will need to be recalibrated at some stage. This could be due to a collision, routine maintenance or if the camera fixture is relocated. During the calibration, the robot has to be taken off-line. Therefore, it is critical that the calibration can be completed as soon as possible so the robot can be put back into production with minimum down time, as loss of productivity is undesirable and costly.

## 2 Related Work

### 2.1 Camera Calibration

One of the most time consuming stages of calibrating a vision system is the calibration of the individual cameras. Camera calibration refers to the calculation of the intrinsic and extrinsic parameters of the camera model. There are several well-known methods for camera calibration, most notable are Zhang's and Tsai's methods [1, 2]. The common approach to camera calibration algorithms is the use of a calibration pattern. Calibration patterns are typically a checkerboard grid, coded markers, or circles in grid form. Whichever pattern is used, the aim is to provide a set of feature points with known 3D positions. By obtaining the correspondences between the feature points in the 2D image plane and the 3D real world, the camera parameters can be determined.

The calculation of the camera parameters is a straight forward process; however one of the challenges of camera calibration is the automatic detection of feature points on the calibration board. Environmental conditions such as varying lighting (i.e. shadows and bright spots) and background objects can make it difficult for a computer vision system to detect the feature points. The simple solution is to manually select the feature points [3] but this is very time consuming and is not ideal for an automated production system.

The extrinsic parameters of a camera are defined by a homogenous transformation matrix between the camera frame and the world co-ordinate. The world frame is defined by the calibration process and is typically attached to the calibration board [4, 5]. In stereo vision calibration, it is important to calibrate each camera using the same world co-ordinate system in order to determine the relative position between the cameras. The relative position of the cameras is required for the calculation of the epipolar geometry during triangulation [6]. Therefore the calibration grid feature point detection method must be able to determine the order of correspondence points to maintain a consistent world frame reference system for all calibration images. Typically, during camera calibration multiple images are taken of the calibration board from various positions and angles. Using a generic grid pattern it is difficult to identify individual corners, especially once the image is rotated greater than 90°.

In this paper, a colour coded checkerboard pattern is proposed. The coloured grid squares are used to distinguish the calibration pattern from the background and to identify the world co-ordinate system for reliable stereo vision calibration.

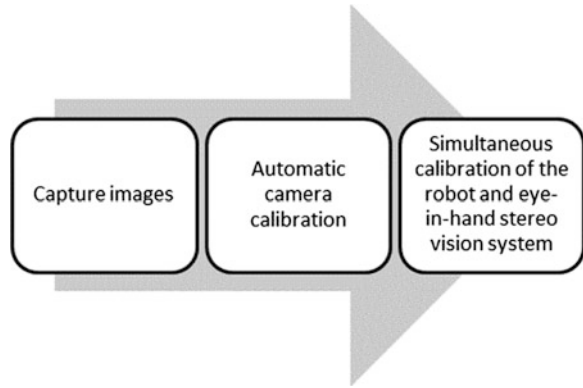
## ***2.2 Robot Manipulator Calibration***

The calculation of the relationship between the robot and eye-in-hand vision system is referred to as Hand-Eye calibration. Hand-Eye calibration relies heavily on an accurate kinematic model of the robotic manipulator, however manufacturing tolerances result in differences between the actual physical dimensions of the robot and the nominal dimensions. To determine the actual dimensions, robot calibration is required. In [7–9] external measurement sensors are used to calculate the error between the actual robot pose and the estimated pose (using the nominal kinematic model). By accurately calculating these errors, the actual robot dimensions can be obtained by non-linear optimisation. In this paper the robot kinematics, Robot-World and Hand-Eye transformations are combined into a single objective function known as “simultaneous calibration”. Non-linear optimisation is used to minimise the absolute positioning errors between the robot and the world reference frame.

## ***2.3 Contribution of the Paper***

The main contribution of this paper is the introduction of an automated calibration method which is designed for economical and practical implementation. The automatic calibration not only allows for a faster initial calibration, but also reduces the machine down-time for any subsequent calibrations after an accidental collision or if the camera fixture is relocated. Unlike existing methods which require expensive 3D co-ordinate measuring devices or laser scanners, the optimised calibration method developed in this paper is capable of achieving the sub-millimetre accuracy required for robotic arc welding using only the robot mounted stereo cameras, a mechanical pointer and a calibration board. This makes the proposed calibration method very practical, economical and easy to implement, hence making it highly desirable for industrial applications.

The rest of the paper is organised as follows: Sect. 3 details the methodology used in the automatic camera calibration with the experimental results given in Sect. 4. The conclusions are then given in Sect. 5.

**Fig. 1** Calibration overview

### 3 Methodology

#### 3.1 Calibration Method Overview

The overall calibration method in this paper is outlined in the flow chart in Fig. 1. The first step is capturing a set of calibration board images using the camera system. The images are then used by the automatic camera calibration algorithm to determine the intrinsic and extrinsic parameters of the cameras. This data is then used as to estimate the Hand-Eye and Robot-World transformations using the method in [10]. Finally the actual Hand-Eye and Robot-World transformations as well as the calibration of the robot are solved simultaneously using a non-linear optimisation method [11].

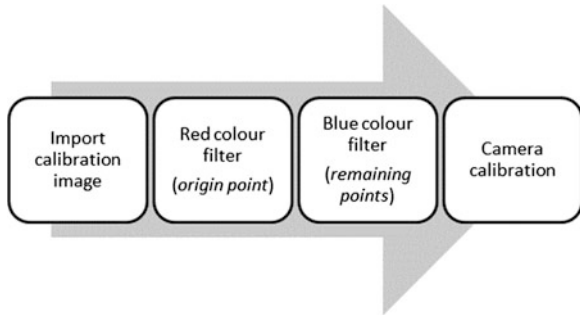
#### 3.2 An Automated Camera Calibration Method

The process of camera calibration can involve processing up to 30 images or more per camera and is arguably the most important step in the overall calibration of a vision system. It is also one of the most repetitive and time consuming stages. From this perspective, it makes sense to automate the camera calibration process. The flowchart in Fig. 2 shows the automatic camera calibration process developed in this paper. The grid area is selected based on the boundaries defined by coloured markers. The origin point of the World Frame is identified by using red markers.

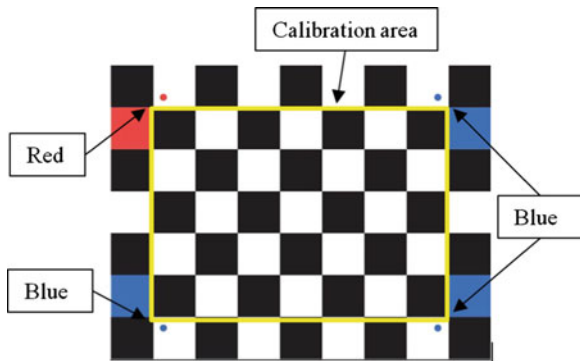
#### 3.3 The Proposed Calibration Grid

The proposed calibration grid pattern is shown in Fig. 3. The red markers comprising of a red square and a red dot indicate the origin of the World frame. The

**Fig. 2** Automatic camera calibration flowchart



**Fig. 3** Calibration grid (each square is 30 mm × 30 mm)



blue markers comprising of blue squares and blue dots indicate the remaining boundary points that define the calibration area. Defining the calibration area with coloured squares allows for image segmentation and removes interference from background objects. It is important to differentiate the origin from the other points, as this origin will be used as the world frame reference system in the calculation of the geometrical relationship between the stereo cameras. The red markers also allow for the origin point to be recognised regardless of the image orientation. The dots are used to determine which corners of the squares are used to define the boundary of calibration area.

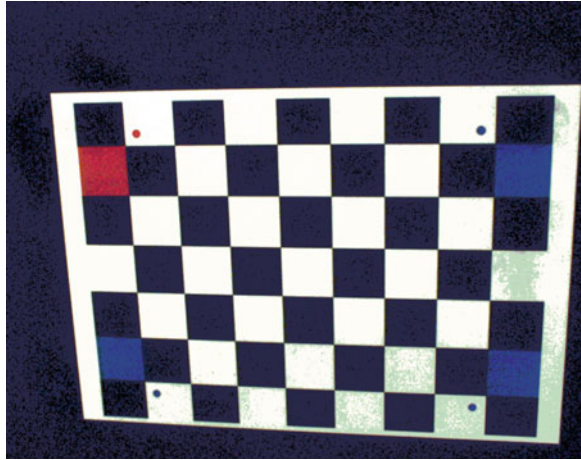
### 3.3.1 Rigin Point Recognition

From the original colour image (Fig. 4), the red square and circle are segmented by a red filter so that only the red pixels of the image remain by using (1) [12].

$$I_{RF}(u, v) = \begin{cases} I_{RGB}\{R\}(u, v), & C1 \wedge C2 = TRUE \\ I_{GRAY}(u, v), & otherwise \end{cases} \quad (1)$$



**Fig. 4** Original RGB image of calibration grid



where

$$C1 : I_{RGB}\{R\}(u, v) > \max(I_{RGB}) \times 0.1$$

$$C2 : I_{RGB}\{R\}(u, v) == \max[I_{RGB}\{R\}(u, v), \{G\}(u, v), \{B\}(u, v)]$$

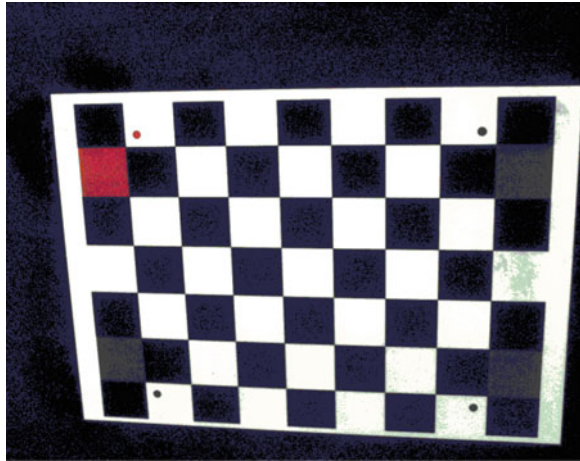
where,  $I_{RF}(u, v)$  is the output from the red filter of the pixel at coordinate location of  $u$  and  $v$ ,  $I_{RGB}$  is the original RGB colour image,  $I_{RGB}\{R\}$ ,  $I_{RGB}\{G\}$  and  $I_{RGB}\{B\}$  are the red, green and blue components of the RGB image respectively. Due to the image digitisation process, it is possible for the composition of the RGB values for individual pixels in the black squares to contain a higher blue intensity level. A scaling factor of 0.1 is used to suppress the blue pixels in the black squares. This value was chosen for this particular calibration board and CCD cameras through experimentation. The “ $\wedge$ ” is the logic ‘AND’ operation, “TRUE” is the logical ‘TRUE’, ‘==’ is the logical equal, i.e., C2 is only true when both sides of C2 is equal,  $I_{GRAY}$  is the gray level image converted from the colour image using the well-known equation.

$$I_{GRAY}(u, v) = [0.3 \quad 0.59 \quad 0.11] \begin{bmatrix} I_{RGB}\{R\}(u, v) \\ I_{RGB}\{G\}(u, v) \\ I_{RGB}\{B\}(u, v) \end{bmatrix} \quad (2)$$

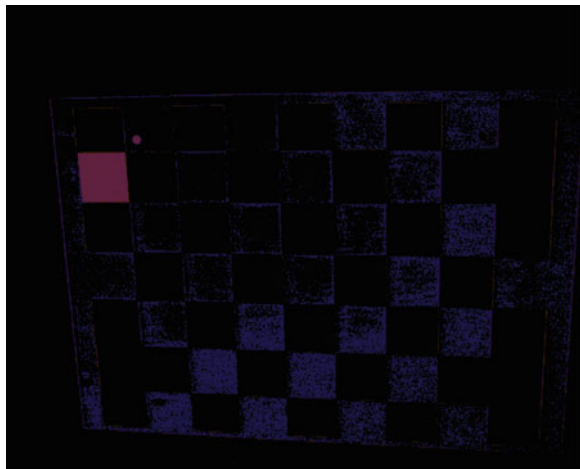
When (1) is applied to Fig. 4, the red image in Fig. 5 is obtained. It is then subtracted from the original RGB image (Fig. 4) using (3), leaving the red square and circle clearly visible, making further segmentation easier. The result is shown Fig. 6.

$$I_R = |I_{RF} - I_{RGB}| \quad (3)$$

**Fig. 5** Original RGB image after the red filter



**Fig. 6** Red square and circle after image subtraction

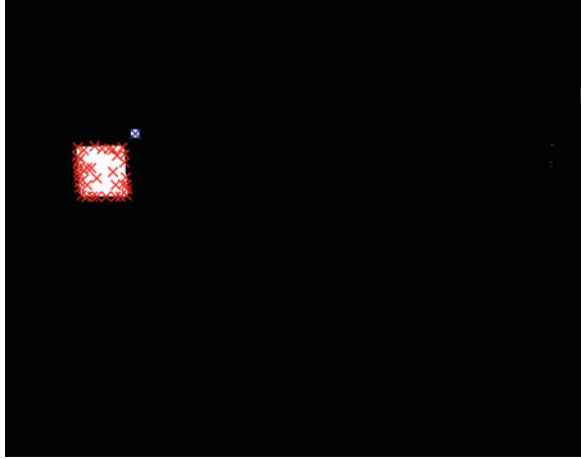


The image (IR) is then converted to a black and white binary image using adaptive thresholding [13]. Equation (4) is then used to remove all erroneous pixel clusters with an area smaller than a set threshold leaving only the red square.

$$I_{square} = \begin{cases} 1 & Area > T_{square} \\ 0 & otherwise \end{cases} \quad (4)$$

where  $T_{square}$  is the threshold used to remove any noise after the red filtering, Area is the number of connected red pixels (the white pixels in the binary image). The Harris corner detector [14] is used to find the corners of the square. The correct corner is determined by calculating the Euclidean distance from each Harris corner to the centre of the red circle. The corner with the smallest distance to the circle is

**Fig. 7** Red square harris corners and circle



then used as the origin point. The red circle is detected by converting the red filtered image to a black and white binary image and using Eq. (5).

$$I_{circle} = \begin{cases} 1 & (Area > T_{dot\_min}) \wedge (Area < T_{dot\_max}) = TRUE \\ 0 & otherwise \end{cases} \quad (5)$$

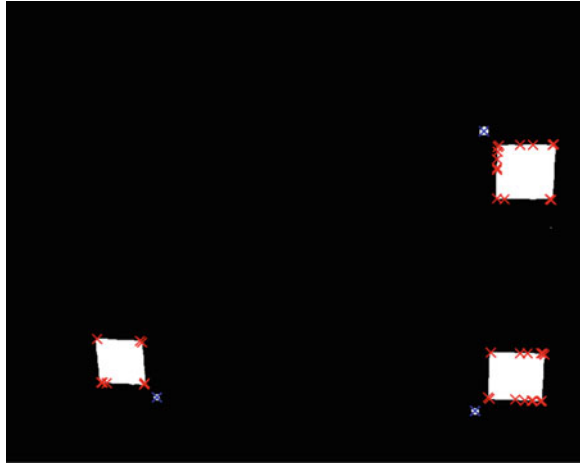
where “TRUE” is the logical ‘TRUE’ and  $T_{dot\_min}$  and  $T_{dot\_max}$  are set to ignore any erroneous areas left after binary conversion. The Harris corners and the centroid of the red dot are shown in Fig. 7. Since the dimensions of the coloured squares and dots are known from the setup, the thresholds can be estimated from the known working range of the camera. In this paper, the maximum working range of the camera is around 400–500 mm above the table. It was found that within this camera range that the pixel area of the squares is always greater than 5000 pixels and the area of the dots is within 30 to 600 pixels. Therefore it was found that  $T_{square} = 5000$ ,  $T_{dot\_min} = 30$  and  $T_{dot\_max} = 600$  was sufficient for the setup in this paper.

### 3.3.2 Remaining Boundary Points

After the red markers are identified, the remaining 3 boundary points of the calibration board can be determined by using the blue markers. To achieve this, a blue filter similar to that of the red filter is introduced.

$$I_{BF}(u, v) = \begin{cases} I_{RGB}\{B\}(u, v), & C3 \wedge C4 = TRUE \\ I_{GRAY}(u, v), & otherwise \end{cases} \quad (6)$$

**Fig. 8** Blue square harris corners and circles



where

$$C3 : I_{RGB}\{B\}(u, v) > \max(I_{RGB}) \times 0.1$$

$$C4 : I_{RGB}\{B\}(u, v) == \max[I_{RGB}\{R\}(u, v), \{G\}(u, v), \{B\}(u, v)]$$

where  $I_{BF}$  is the output from the blue filter (blue filtered pixel), other notions are similar to those in (1). The blue filtered image is then subtracted from the original RGB image, leaving only the blue squares and circles in the similar manner that the red square and circle were segmented using Eqs. (4) and (5).

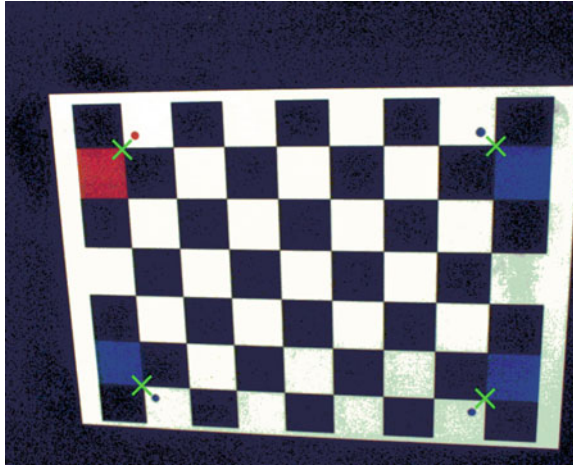
$$I_B = |I_{BF} - I_{RGB}| \tag{7}$$

The Harris corner detector is then used to find the corners of the blue squares. In the same manner as the red squares, the smallest Euclidian distance from each blue square corner to the centre of its blue circle is used to determine the correct corner. The Harris corners and blue circle centroids are shown in Fig. 8, and the final resulting corners are shown in Fig. 9. The four boundary points are then used in the existing method [3].

## 4 Results

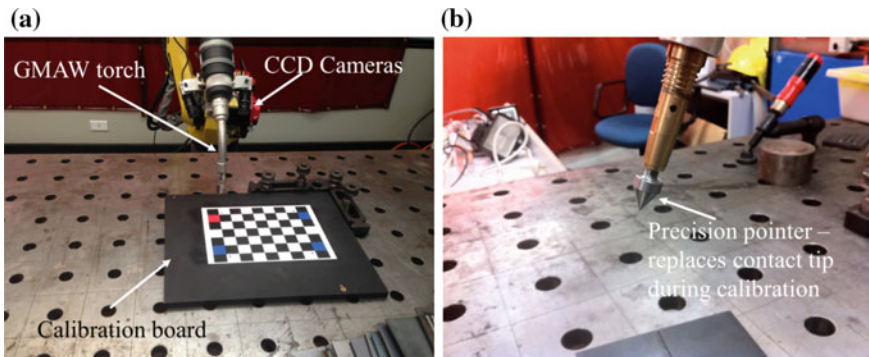
### 4.1 Experimental Setup

The experiments were conducted using a Fanuc ArcMate 100iC, a six axis industrial robot with a repeatability of  $\pm 0.08$  mm. It is fitted with a Binzel welding torch and Lincoln Electric PowerWave welder. The stereo vision system consists of



**Fig. 9** Final detected boundary points

two off the shelf uEye USB color CCD cameras (resolution  $1280 \times 1024$ ). The cameras are attached to the welding torch as shown in Fig. 10a. The calibration board was placed on the steel workbench in front of the robot. The welding torch tool centre point (TCP) was setup using the six-point method instructed by the robot manufacturer [15]. To ensure accuracy, the mechanical pointer shown in Fig. 10b was used instead of the welding wire to guarantee a consistent reference point during the TCP setup. By using the mechanical pointer instead of the welding wire, the TCP accuracy is kept to within the  $\pm 0.5$  mm recommended in [16]. The images captured during the calibration stage are taken from approximately 300–400 mm above the calibration board in various positions within the robots working envelope. As the cameras are calibrated within this range, all subsequent images of the welding work pieces are taken from within the same range. The Hand-Eye, Robot-World and robot calibration are solved using [11].



**Fig. 10** a Calibration board and b Precision pointer

**Table 1** Camera calibration comparison

Parameter	Standard		Automatic	
	Left	Right	Left	Right
Fu, Fv	1778.85	1792.60	1783.85	1792.65
	1779.10	1792.16	1783.90	1793.48
u0, v0	604.23, 493.53	644.37, 507.29	599.86, 494.33	642.12, 506.32
c	0.00112	0.00181	0.00111	0.00119
K1, K2	-0.14, 0.36	-0.13, 0.36	-0.13, 0.30	-0.14, 0.38
Pixel error	0.22, 0.30	0.29, 0.36	0.14, 0.16	0.23, 0.29
Avg. time	23.11 s/image		15.47 s/image	
Total time	23.11 min (60 images)		Minutes (60 images)	

### 4.2 Automated Camera Calibration Results

The left and right camera parameters were calculated using the Matlab calibration toolbox [3] integrated with the proposed automatic grid detection algorithm. Each camera was calibrated using a set of 30 images, therefore 60 images in total. The calibration images for the left and right cameras are captured simultaneously. It was found by experimentation that using 30 images for each camera allowed for the calibration board to cover most of image plane. This allowed for more accurate estimations of the distortion co-efficients and improved mapping between the image plane and camera frame.

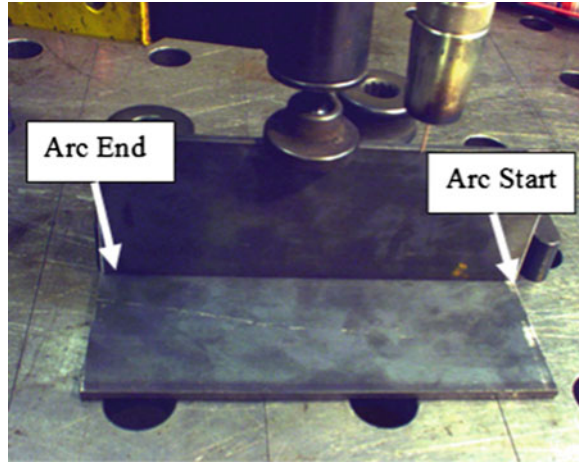
The experiment was conducted using MATLAB 2007b on a 2 GHz Intel Duo Core Processor. The results in Table 1 show a small difference in the camera parameters between the two cameras; however it is apparent that the automatic method has a much faster computation time than the standard method. Over the full set of 60 images the automatic method reduced the calibration time by 33 %. Also the automatic method results show a reduced pixel error. The pixel error represents the average reprojection error for u and v for all the calibration images. This suggests that automatically detecting the corner points is more accurate than clicking on them manually by the operator.

It is also important to note that manually selecting the four corners using the standard method is dependent on the speed and competence of the operator. In an industrial environment, if a manual calibration is required it would add further expense as a trained operator would be required to carry out the procedure. Even then the time and quality of the calibration will vary depending on the competence of the operator.

### 4.3 3D Cartesian Position Error

To confirm the accuracy of the proposed method proposed, many experiments were conducted to measure the actual 3D position of objects against their ‘computer vision’

**Fig. 11** A 3D fillet weld test piece

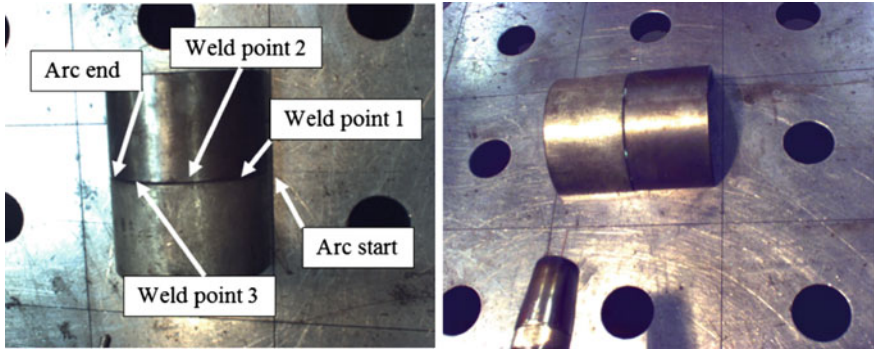


inferred positions. In particular, two examples are presented in this paper to show the effectiveness of this method. The first example is a typical fillet weld shown in Fig. 11. The second is a simulated pipe joint shown in Fig. 12. The inferred locations from the cameras are calculated in the robot base frame using the method in [11]. The work pieces were placed arbitrarily on the bench. The teach pendant was used to move the robot for image capture. The pixel co-ordinates were manually extracted from the image and the final positions were calculated using triangulation.

The calculated results for these examples were compared to the measured readings from the robot controller after moving the robot to each of the points manually with the mechanical pointer fitted to the welding torch. The 3D Cartesian errors for each example are given in Tables 2 and 3.

The results for both examples given in Tables 2 and 3 show that the automatic stereo vision and hand-eye calibration algorithm presented in this paper is able to achieve a 3D positional accuracy which is acceptable in most arc welding applications. In industry, it is generally accepted that the programmed position of the robot must be within  $\pm 1$  mm. The results for the X and Y errors are within this tolerance, however the Z measurement, which represents the contact tip to work distance (CTWD) is just over 1 mm in some instances. For modern inverter welding power sources, slight variations in the CTWD can be accounted for during operation using the inbuilt adaptive welding waveforms. Large variations in CTWD can affect the welding arc characteristics and results in a poor weld finish; however deviations by 1 or 2 mm in CTWD would not greatly affect the quality of the result as shown by the consistent finish of the welding results in Fig. 13. The welding results in Fig. 13 were obtained using a pulse waveform on a Lincoln Electric PowerWave which utilises such an adaptive control loop to cope with small changes in CTWD [17].





**Fig. 12** A 3D pipe joint test piece

**Table 2** Positional errors for the fillet weld

	Error (mm)		
	X	Y	Z
Arc start	0.55	0.68	0.61
Arc end	0.62	0.45	1.05

**Table 3** Positional errors for the pipe joint

	Error (mm)		
	X	Y	Z
Arc start	0.10	0.68	1.21
Weld point 1	0.50	0.71	0.92
Weld point 2	0.13	0.18	0.45
Weld point 3	0.17	0.77	1.02
Arc end	0.23	0.79	0.92



**Fig. 13** Fillet weld results



## 5 Conclusion

In this paper an automatic camera calibration algorithm is presented. The automatic calibration of the CCD cameras can be used as a platform for the simultaneous calibration of the stereo vision system and eye-in-hand configuration on an arc welding robot. The results in Tables 1, 2 and 3 have shown that the automatic calibration algorithm improves accuracy and reduces the time required to calibrate the cameras by 33 %. In addition to speed, the results have shown that this method is capable of achieving the required accuracy without the use of expensive external measurement devices making it affordable to implement.

Although the camera calibration is an off-line process, the method presented in this paper is particularly useful in a production environment as it reduces the system down time and requires no special skills of the operator.

**Acknowledgment** This work is supported by the Australian Research Council under project ID LP0991108 and the Lincoln Electric Company Australia.

## References

1. Zhang Z (1998) A flexible new technique for camera calibration. Microsoft research technical report MSR-TR-98-71
2. Tsai R (1987) A versatile camera calibration technique for high-accuracy 3D machine vision metrology using off-the-shelf TV cameras and lenses. *IEEE J Robot Autom* RA-3:323–344
3. Bouguet J (2008, 9/4/2013) Camera calibration toolbox for Matlab. Available [http://www.vision.caltech.edu/bouguetj/calib\\_doc/](http://www.vision.caltech.edu/bouguetj/calib_doc/)
4. Xu GY, Chen LP, Gai F (2011) Study on binocular stereo calibration method. In: 2011 international conference on image analysis and signal processing (IASP), pp 133–137
5. Zhao P, Li Y, Chen L, Bai X (2011) Camera calibration technology based on circular points for binocular stereovision system. In: Yu Y et al (eds) *Communications in computer and information science*, vol 158(1). Springer, Berlin, pp 356–363
6. Hartley RI, Zisserman A (2003) *Multiple view geometry in computer vision*, 2nd edn. Cambridge University Press, Cambridge
7. Kang HJ, Jeong J, Shin S, Suh Y, Ro Y (2007) Autonomous kinematic calibration of the robot manipulator with a linear laser-vision sensor. In: Huang DS, Heutte L, Loog M (eds) *Advanced intelligent computing theories and applications. Lecture notes in computer science*, vol 4682. Springer, Berlin, pp 1102–1109
8. Li A, Wu D, Ma Z (2008) Robot calibration based on multi-thread particle swarm optimization. In: 6th IEEE international conference on industrial informatics, pp 454–457
9. Gatla C, Lumia R, Wood J, Starr G (2007) An automated method to calibrate industrial robots using a virtual closed kinematic chain. *IEEE Trans Rob* 23:1105–1116
10. Dinham M, Fang G (2009) A low cost hand-eye calibration method for arc welding robots. In: 2009 IEEE international conference on robotics and biomimetics (ROBIO), pp 1889–1893
11. Dinham M, Fang G (2010) Simultaneous calibration method of a stereo vision system and a welding robot. In: IEEE international conference on robotics and biomimetics (ROBIO), pp 1452–1456
12. Keizer K (2008, 01/02/2012) Color filter. Available <http://www.mathworks.com/matlabcentral/fileexchange/20477-color-filtering>

13. Otsu NA (1979) A threshold selection based on gray-level histograms. *IEEE Trans Syst Man Cybern* 9:62–66
14. Harris C, Stephens M (1988) A combined corner and edge detection. In: 4th Alvey vision conference, pp 147–151
15. Fanuc (2003) Fanuc robot series R-30iA controller ARC tool operators manual B-82594EN-3/03: Fanuc Robots Japan
16. Chen XZ, Huang YM, Chen SB (2012) Model analysis and experimental technique on computing accuracy of seam spatial position information based on stereo vision for welding robot. *Ind Robot Int J* 39:349–356
17. Nadzam J (2004) Waveform control technology and the pulse fundamentals of pulsed spray metal transfer. Technical report No. 40511006, The Lincoln Electric Company, The Lincoln Electric Company, Cleveland, Ohio, USA

**Part II**  
**Sensing of Arc Welding Processing**

# Development of Metal Oxide Gas Sensors for Environmental Security Monitoring: An Overview

Xi-Zhang Chen and Jie Yu

**Abstract** MOX (metal oxide) sensors for gas sensing, such as toxic as well as flammable, which is harmful to human health, show a variety of performances on diverse substrates. Among state of the art of various substrates, plastic combination with a hotplate indicates the lowest power consumption in gas monitoring. Meanwhile, SnO<sub>2</sub>-based sensors are good at sensing volatile organic compounds (VOCs) as well as reducing/oxidizing gases. As one of the key issues in sensing is the effect of humidity and temperature, some researchers find that the variation in the sensing property of SnO<sub>2</sub>-based CO gas sensors with respect to temperature and humidity is effectively suppressed by the surface modifications with platinum. In addition, compared with SnO<sub>2</sub> film introduction with oxygen, SnO<sub>2</sub> doped with Pd/In can exhibit a superior sensitivity to CO concentration as low as 1 ppm. Researches also indicate that the La<sub>2</sub>O<sub>3</sub> doped to SnO<sub>2</sub> shows higher response among most sensors but lower than PdO loaded SnO<sub>2</sub> accordingly. Moreover, the influence of time drift and replacement of sensors implemented after fabrication should be decreased by recalibration and compensation. Therefore, multi-function sensor with chemical element, oxide or combination doped in SnO<sub>2</sub> layer performing high sensitivity and thermal stability for long term stability is in expectation in near future.

---

Xi-ZhangChen (✉)

School of Mechanical and Electrical Engineering, Wenzhou University,  
325035 Wenzhou, China  
e-mail: chenxizhang@wzu.edu.cn

J. Yu

Shandong Nuclear Power Equipment Manufacturing Co. Ltd,  
Haiyang 265100, Shandong, China

## 1 Introduction

The increasing interest in environmental conservation which is closely related with to human health has heightened the need for the in-site monitoring some toxic or flammable gases in the environment. The representative gases include volatile organic compounds (VOCs), carbonic oxide, ethanol and hydrogen et al. Humans are easily exposed to these chemicals through the skin, by breathing, and eating, and even at low concentrations this exposure can present long-term health risks [1]. By nature, hydrogen is explosive [2], which in some way is hazardous. Therefore, a variety of sensors are implemented for environment monitoring. The metal oxide (MOX) gas sensors applications for safety have been extensively studied in recent years. The field experience of the research group has shown that the metal oxide-based gas sensors are the best chemical sensors for long term application, more than 1 year of continuous working. Besides, metal oxide layers are sensitive to many different gases or mixtures of gases. Design high-performance gas sensors that show low humidity dependence and rapid recovery kinetics [3, 4]. However, its yield is directly dependent on temperature, which is the limitation of application fields of MOX gas sensors. What's more, it has to automatically compensate the time drift [5]. Moreover, the temporal drift of operating characteristics, along with the low selectivity of sensor responses, are considered to be major disadvantages of these devices [6]. On the other hand, as for metal oxide gas sensors, selectivity has not been an easy task to assure an acceptable value for commercial applications. Low-dimensional carbon structures, silicon oxide and alumina are advantageous for achieving high sensitivity [7, 8]. In addition, some applications, which should be undertaken in high temperature, to some extent are restricted. Consequently, gas sensors with good thermal stability can full play to the advantages of some particular applications. Given that it is capable of thermo stability in high temperature, SiC appears to be the strongest candidate wide and gap semiconductor for harsh environment applications [9]. Simultaneously, the influence of temperature or humidity can have an impact on sensitivity, reliability, resolution etc. Then an advanced multi-function sensor which combines polymer-based capacitive sensors for humidity and VOCs, semi-conducting MOX based chemo resistive sensors for reducing/oxidizing gases and a Pt thermometer on a polyimide sheet [10] shows a good performance in environmental monitoring. This paper introduces some MOX gases sensors properties on diverse major substrates with various SnO<sub>2</sub> layers in terms of the CO concentration, sensitivity, resistance and so on detections, advantages as well as defects.

## 2 Principle and Experimental

### 2.1 MOX Gas Sensor Principle

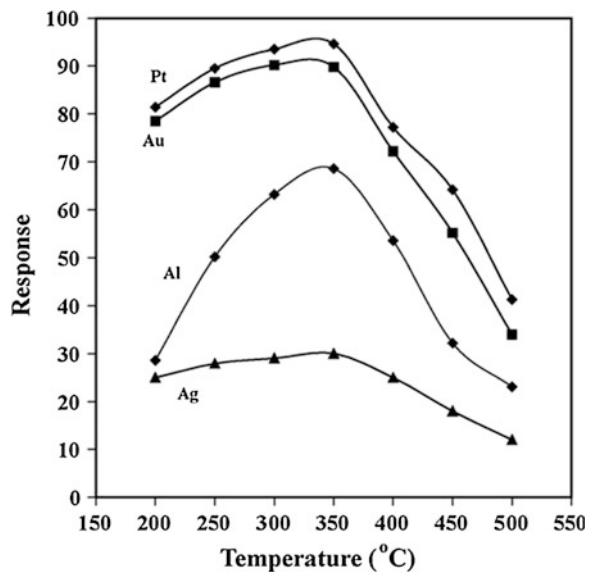
Over recent years, MOX sensors for gas sensing are implemented more and more widely, especially in monitoring oxidizing and reducing gases as well as flammable

gases on different substrates. Furthermore, the response of MOX sensors to gas is mainly induced by heterogeneous chemical reactions between the gas and the adsorbate on the surfaces [11].

Generally speaking, the MOX gas sensor consists of three portions, which from down to up accordingly are substrate, oxide layer and metal electrode. In fact, metal electrode is the function of catalytic to improve the sensitivity of the oxide layer for a monitoring variety of gases, such as CO, C<sub>2</sub>H<sub>5</sub>OH, CH<sub>4</sub> and H<sub>2</sub> and so on. On the whole, catalytic activity rate of metal electrode is in the order of Fig. 1: Ag < Al < Au < Pt. In the mass, compared to other catalytic materials, Pt is the better selection which is implemented as the metal electrode on various kinds of substrates. An oxide layer in certain thickness is required so that no air current will flow through. It is found that most of the oxide layers have been fabricated are reactive metal oxide since it can be used as catalytic layers on devices, where the material does not need to conduct large currents [12]. Therefore, an oxide layer is often fabricated on sensor as not only a dielectric layer, but also as an insulating layer in case that metal electrode can be in good performance. Metal oxides are chemically reactive materials [13]. Up to now, plastic, metal oxide and SiC are representative substrates materials extensively put into use in sensor fields.

Metal oxide substrate sensors are good at monitoring off-odours performed as e-nose. Meanwhile, TGS2620 is a representative one to be capable of monitoring odours as well as off-odours, which is widely used in experiments. Its configuration in order basically is: ZnO substrate, SnO<sub>2</sub>-based oxide layer and Pt metal electrode. Compared with metal oxide substrate sensors, plastic substrate ones are higher at thermal stability. Furthermore, to decrease the power consumption, smaller micro-hotplates are designed and fabricated on plastic foil [14]. By the way, Pt is

**Fig. 1** Effects of electrode metal on the response of a SnO<sub>2</sub> sensor with the temperature increasing [14]



used as conductor since it exhibits a very good stability as heating element [15]. Nevertheless, SiC-based MOX sensors are the promising ones to exhibit good performance in specific situation especially harsh environmental monitoring, such as hydrogen atmosphere. Moreover, its oxide layer is  $\text{SiO}_2$  in most situations, which is at higher growth rate on SiC substrate. The excellent electronic and mechanical properties of SiC coupled with high temperature stability of the material are the underlying rational for investments in SiC technology. Therefore, they are promising for more challenging applications than those possible with Si devices, especially in harsh environment applications [16].

## 2.2 Related Works

Metal oxide thin film sensors have been widely used for gas sensing applications thanks to their sensitivity toward a large variety of gases [17]. Besides, the factors influenced characteristics of MOX mainly include selectivity, sensitivity, response, life time, thermal, humidity stability and so on. Generally speaking, the representative properties, which are studied by researchers currently, are response, sensibility, stability, consumption and time drift. Nevertheless, there are closed relationship between each other. The brief introductions for the major performances are as follows.

### 2.2.1 Response and Sensibility for CO Monitoring

CO sensors have attracted special attention among other gas ones. Due to the substantive characteristics of CO are colorless and odorless, it is an essential potential risks poisonous gas to human health, which is majority from automobiles, incomplete combustion of fossil fuels, industrial productions, residential buildings, etc. [18]. For the majority of CO sensors,  $\text{SnO}_2$ -based are the most widely implemented in gas monitoring available nowadays. Therefore, here are the experiments of CO detection to show its advantages on this fabrication as follows.

Monitoring of CO (10–100 ppm) is on a drop-coated MOX gas sensor on polyimide foil, which the metal electrode is consisted by an active area, and four widths for the active area are investigated for this study: 100, 50, 25 and 15  $\mu\text{m}$  [19]. What's more, the MOX layer material is  $\text{SnO}_2: 3\% \text{Pd}$ , which exhibits a good gas sensing performances.

According to the experiment, in contrast to the constant mode, the use of a pulsed brings two advantages. It reduces the power consumption and improves the selectivity of the sensor. In addition, the total power consumption of the system on plastic substrate with a hotplate is of 1.9 mW when operating in pulsed temperature mode as well as in a duty cycle of 10 % [19], which is a promising advantage of wireless application.

However, humidity is also an important factor for long term application of gas sensors so that a combination of the surface modification with the platinum group metals is the method to further improve the temperature–humidity dependence and to markedly induce excellent long-term stability of the SnO<sub>2</sub>-based CO gas sensor [20].

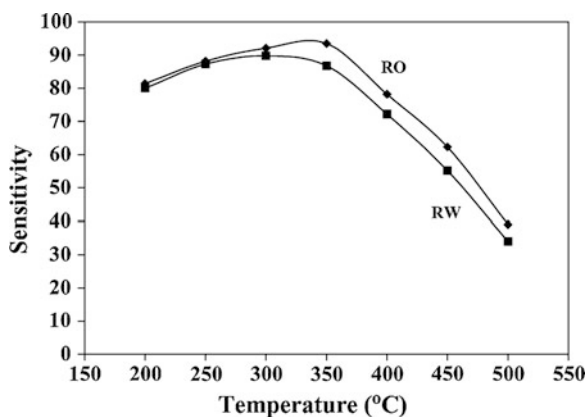
Nowadays, the air quality is worse than ever, in contrast to that, the hazard gas concentration is lower but variety complex, respectively. As a result, the higher sensitivity gas sensors should detect the CO concentration as low as possible in harsh environment.

Figure 2 shows the sensitivity variation against temperature curves for two different types of films of SnO<sub>2</sub>. Obviously, the sensitivity of RO-type of films is higher than the RW-type, due to lower refractive index of the RO-type of films as compared with the same for the RW-type. Similar observations are made for HfO<sub>2</sub> [21].

It can be easily to detect the CO concentration as small as 10 ppm [22]. In addition, the sensitivity improves gradually with the CO concentration increasing apparently. At the same time, the Fig. 3 also indicates that the sensor is highly selective to CO at temperatures lower than 450 °C. Therefore, higher sensitivity can be obtained where the CO concentration is dense accordingly.

By the way, the average crystallite size decreases with In/Pd doping [23], which generates excellent porosity of SnO<sub>2</sub> film to extend more area for absorbing CO. Hence, it can exhibit an excellent sensitivity performance in low CO concentration.

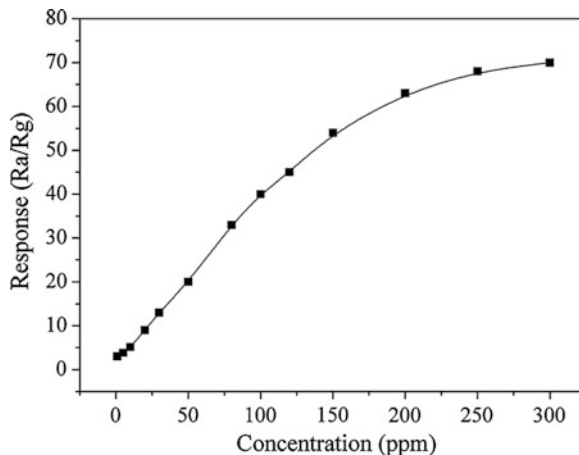
Compared to the values of ~110 for Au-nanoparticle-doped SnO<sub>2</sub> at 150 ppm CO [24], ~70 for In/Pd-doped SnO<sub>2</sub> at 300 ppm CO [23]. And ~10 for the SnO<sub>2</sub> doped with Au/V at 1000 ppm CO [25], the La<sub>2</sub>O<sub>3</sub> doped to SnO<sub>2</sub> is effective in improving the sensitivity to CO, which exhibits a remarkable sensitivity improvement from 5.2 to 213.7 (in Fig. 4) with the CO concentration increasing from 10 to 75 ppm.



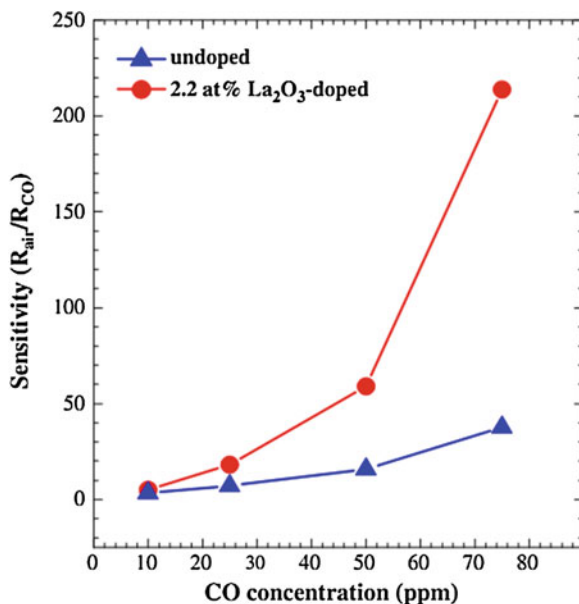
**Fig. 2** Effects of film preparation conditions on the sensitivity. Sensitivity as a function of temperature for SnO<sub>2</sub> films deposited under different conditions but having nearly same thickness (about 400 nm; RO films prepared on unheated substrates with introduction of oxygen; RW films prepared on unheated substrates without introduction of oxygen [22])



**Fig. 3** The In/Pd-doped SnO<sub>2</sub> sensor response to different CO concentrations [23]



**Fig. 4** The CO sensitivity of the undoped SnO<sub>2</sub> and the 2.2 at.% La<sub>2</sub>O<sub>3</sub>-doped SnO<sub>2</sub> versus CO concentration [26]



The remarkable difference between the undoped SnO<sub>2</sub> and the 2.2 at.% La<sub>2</sub>O<sub>3</sub>-doped SnO<sub>2</sub> can be distinguished by the trend of two color curves of the CO sensitivity [26].

However, the value of 320 for PdO-loaded SnO<sub>2</sub> at 200 ppm CO [27] is much higher than La<sub>2</sub>O<sub>3</sub> doped to SnO<sub>2</sub>. Besides, it is apparently to find that Pd loaded approximate 0.1 mol% is the optimum response of such sensor.

Furthermore, the method tungsten oxide nanostructures functionalized with gold or platinum NPs shows higher responses to low concentrations of CO at low

temperatures (100 ppm, 150 °C) with the advantage of fewer step processes, relatively low processing temperature and no requirement for substrate pre-treatment [28]. It's a prospective method for the development of MOX sensors as well as applications of CO detection.

### 2.2.2 Stability and Selectivity

Considering many works on response and sensitivity of MOX sensors, However, Some key points such as selectivity and stability at high temperatures and in a harsh environment still have to be fully addressed. The sensors using the  $\text{Nb}_2\text{O}_5:\text{Ta}_2\text{O}_5$  mixture electrode show the best performance in terms of compromising selectivity and stability with keeping large response and sensitivity values [29].

The changes of sensor parameters, such as compositions on the sensor substrate and base materials, are important ways to obtain excellent properties. However, Many applications of metal oxide gas sensors can benefit from reliable algorithms to detect significant changes in the sensor response. Detecting significant changes in the response of metal oxide (MOX) gas sensors is important for many applications such as gas leak detection in coal mines [30, 31], large scale pollution monitoring [32, 33] or the mapping of gas detection events [34].

The method introduced in [35] allows to interpret the response of MOX sensors in OSS (open sampling system) configuration and to detect change points. The TREFEX (TREnd Filtering with EXponential algorithm) is proposed to improve the stability and advantage of on-line version in uncontrolled outdoor environments.

The effects of bias current on sensitivity and selectivity of resistive Metal-Oxide (MOX) sensors toward gases have been investigated. Sensitivity toward gases, which is closely related to these phenomena that resistance of rectifying junctions of MOX films depends on the polarization [36, 37], also turns out to be polarization dependant [38]. It is realized to increase the sensitivity and selectivity of Metal Oxide Gas Sensors by adjusting the polarization of different sensitive layers [39]. This will be a breakthrough in the development of smart E-Nose for the environment monitoring.

### 2.2.3 Improvement of Lifetime

Different instruments exist to assess the concentration of pollutants presence in air, but the cost of the deployment and the skills necessary to use these tools make the monitoring not affordable to ordinary people. Therefore the devices to reduce the operation power and decrease consumption are the major trade in this application field. Wang et al. in [40] present a sensor network, which reduces the consumption, provides enough energy to sustain the monitoring requirements as well as running a long time for outdoor. The works [41, 42] are some examples, nevertheless no

improvements are proposed to address and significant reduction of the consumption of chemo-resistive sensors.

In the fields of WGSN (Wireless Gas Sensor Network, also known as wireless electronic-nose networks), it makes sense for gas sensors to be low-power consumption. Somov et al. [43] have focused their efforts on the development of the device to reach, theoretically, two years of lifetime to necessitate very little energy.

The work [44] proposes a new strategy to use commercial MOX gas sensors by processing the initial transient of output signal to reduce the power consumption of a single measurement. As a result, it attains to a long lifetime, low cross sensitivity and long term stability. Especially the cost is reduced by  $20\times$  the power, and make it possible to identify and measure from very-low (0; 1 %) to high (1 %) methane concentrations in air.

The future of the research is in the development of techniques to reduce energy consumption. Innovative hardware solutions must be designed to reduce the energy wasted and batteries alone are not able to guarantee long lasting performance [45].

The sensitivity, selectivity, and response time of semiconducting MOX gas sensors strongly depend on the sensing layer temperature, which is usually determined by a heating resistor integrated in the sensor structure. A system described in [46] and already used in [47] for the dynamic control and thermal characterization of ultra low power gas sensors is proposed by Rastrello et al. [48].

#### 2.2.4 Sensor Time Drift and Replacement

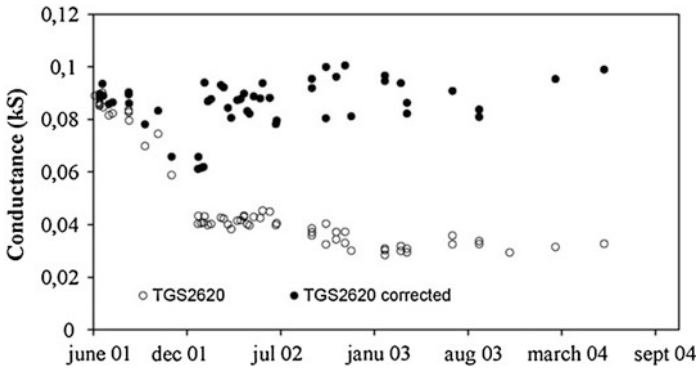
In a constant operating current or voltage conditions, the sensors would drift in time, while the range of calibration, which is much smaller than the large range of temperature variation, influences shifts in the dynamic features [49].

TGS2620 is a MOX gas sensor with  $\text{SnO}_2$ -based on the ZnO substrate, which is widely implemented in monitoring VOCs. Simultaneously, the representative gas is  $\text{C}_2\text{H}_5\text{OH}$ . Besides, it is not only the chemical, but also physical factors have dramatically impacted on sensitivity, resolution, and life time and so on. Therefore, time drift and replacement should be taken seriously in long term stability applications as well.

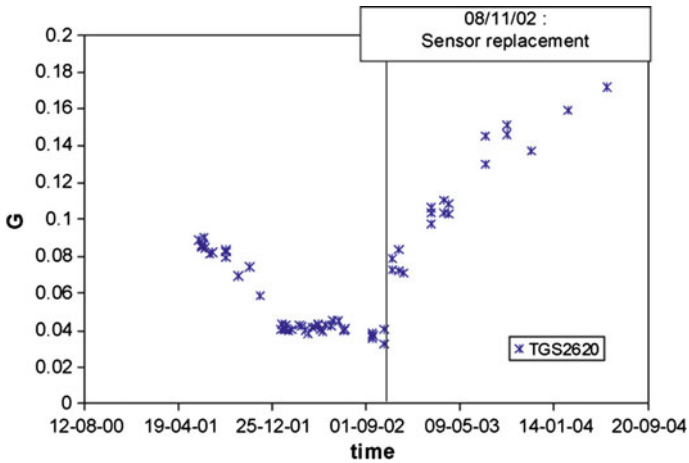
Figure 5 illustrates the drift compensation effect for the TGS2620 by a multiplicative factor,  $q(t')$ , estimated from calibration measurements. Apparently from Fig. 6, the remarkable change between the corrected one with uncorrected shows with time elapse.

Figure 6 shows the “jump” of replacement of the old one by a new one, which indicates its notable influence. Hence, it’s necessary to recalibrate and compensate the new ones to obtain the accurate sensitivity as well as resolution in monitoring.

Nevertheless, above experiments are advanced in the state of the art but not ultimate so that much further study on doped- $\text{SnO}_2$  MOX gas sensors should be carried on for CO concentration detection as well as long term stability in environmental monitoring.



**Fig. 5** Drift correction of the sensor TGS2620 by multiplicative factor estimated by calibration gas measurements [50]



**Fig. 6** “Jump” effect and new time evolution after the replacement of the old TGS2620 by a new one [50]

There are few studies in this area which investigated the sensor drift caused by environmental variables [51–54], while less emphasis is on the mechanism of temperature influence itself that causes the drift. In the paper [55], the initial drift upon the modest changes of ambient temperature is studied, which provide an understanding in sensor drift phenomenon for further drift compensation study. The phenomenon of drift caused by environmental temperature plays a substantial impact to the decreasing of sensor sensitivity and, hence, the instability of the sensor performance [56].

In future work, the focus will be pointed to the development of compensation model to compensate the drift effects that caused by temperature fluctuations. This compensation will eliminate the drift effects caused by the environmental variables and recalibrate the sensor drift, so that the sensor reliability could be enhanced.

### 3 Conclusion

The remarkable effects of the surface modification are SnO<sub>2</sub> doped with platinum on the CO sensing properties against temperature and humidity changes. Simultaneously, with introduction of oxygen in SnO<sub>2</sub> film can improve the sensitivity of CO in low concentration. In addition, compared with SnO<sub>2</sub> film introduction with oxygen, SnO<sub>2</sub> doped with Pd/In can exhibit a superior sensitivity to CO concentration as low as 1 ppm. Furthermore, the La<sub>2</sub>O<sub>3</sub> doped to SnO<sub>2</sub> shows higher response among most sensors but lower than PdO loaded SnO<sub>2</sub> accordingly. What's more, SiC substrate is the promising candidate where the fields of higher thermal stability while operating in high temperature. In addition, the method of multi-sensor on plastic substrate is also an improvement of sensing against the influences from environment, of which notable advantage is low power consumption, through adding a micro-hotplate on its substrate. The method tungsten oxide nanostructures functionalized with gold or platinum NPs shows higher responses to low concentrations of CO at low temperatures (100 ppm, 150 °C) with the advantage of fewer step processes, relatively low processing temperature and no requirement for substrate pre-treatment. So the optimization of configuration of MOX sensors is the major way to improve its properties, on the other hand, the development of reliable algorithms of sensor system will be a potential method for promoting performances of MOX sensors.

### 4 Prospective

Moreover, the compensation of time drift and replacement of sensors is also a significant improvement in long term stability of the sensors in gas monitoring. In future work, the focus will be pointed to the development of compensation model to compensate the drift effects that caused by temperature fluctuations. This compensation will eliminate the drift effects caused by the environmental variables and recalibrate the sensor drift, so that the sensor reliability could be enhanced. Nowadays, the selectivity of gas sensors is still a challenge for commercial applications. In future, chemical element, oxide or combination of both doped in SnO<sub>2</sub> layer is a promising selective for MOX gas sensors implemented in variety applications fields. Ultimately, we'll foresee a superiority sensor with high sensitivity, thermal stability, and sensing accuracy for long term stability in environmental monitoring.

## References

1. Boeglin ML, Wessels D, Henshel D (2006) An investigation of the relationship between air emissions of volatile organic compounds and the incidence of cancer in Indiana counties. *Environ Res* 100:242–254
2. Sawaguchi N, Shin W, Izu N, Matsubara I, Murayama N (2006) Enhanced hydrogen selectivity of thermoelectric gas sensor by modification of platinum catalyst surface. *Mater Lett* 60:313–316
3. Kim H-R, Haensch A, Kim I-D, Barsan N, Weimar U, Lee J-H (2011) Role of NiO doping in reducing the humidity impact on the performance of SnO<sub>2</sub>-based gas sensors: synthesis strategies, phenomenological and spectroscopic studies. *Adv Funct Mater* 21:4456–4463
4. Kim H-R, Choi K-I, Kim K-M, Kim I-D, Cao G, Lee J-H (2010) Ultra-fast responding and recovering C<sub>2</sub>H<sub>5</sub>OH sensors using SnO<sub>2</sub> hollow spheres prepared and activated by Ni templates. *Chem Commun* 46:5061–5063
5. Romain AC, André P, Nicolas J (2002) Three years experiment with the same tin oxide sensor arrays for the identification of malodorous sources in the environment. *Sens Actuators B* 84(2–3):271–277
6. Korotcenkov G, Cho BK (2011) Instability of metal oxide-based conductometric gas sensors and approaches to stability improvement (short survey). *Sens Actuators B* 156:527–538
7. Llobet E (2013) Gas sensors using carbon nanomaterials: a review. *Sens Actuators B* 179:32–45
8. Gardon M, Guilemany JM (2013) A review on fabrication, sensing mechanisms and performance of metal oxide gas sensors. *Sci: Mater Electron* 24:1410–1421
9. Hunter GW, Neudeck PG, Okojie RS, Beheim GM, Powell JA, Chen LY (2003) An overview of high-temperature electronics and sensor development at NASA Glenn Research Center. *J Turbo Mach* 125:658–664
10. Courbat J, Brianda D, Opreab A et al (2009) *Procedia Chem* 1:597–600
11. Galdikas A, Kancleris Ž, Senulienė D, Šetkus A (2003) Influence of heterogeneous reaction rate on response kinetics of metal oxide gas sensors: application to the recognition of an odour. *Sens Actuators B* 95:244–251
12. Spetz AL, Savage S (2004) Advances in SiC field effect gas sensors. In: Choyke WJ, Matsunami H, Pensl G (eds) *Silicon carbide recent major advances*. Springer, Berlin, pp 870–896
13. Hunter GW, Neudeck PG, Gray M, Androjna D, Chen LY, Hoffman RW Jr, Liu CC, Wu QH (2000) SiC-based gas sensor development. *Mater Sci Forum* 338–342:1439–1442
14. Durrani SMA (2006) The influence of electrode metals and its configuration on the response of tin oxide thin film CO sensor. *Talanta* 68:1732–1735
15. Courbat J, Canonica M, Teyssieux D, Briand D, de Rooij NF (2011) Design and fabrication of micro-hotplates made on polyimide foil: electrothermal simulation and characterization to achieve power consumptions in the low mw range. *J Micromech Microeng* 21:015014
16. Courbat J, Briand D, de Rooij NF (2008) Reliability improvement of suspended platinum-based micro-heating elements. *Sens Actuators A* 142:284–291
17. Wright NG, Horsfall AB, Vassilevski K (2008) Prospects for SiC electronics and sensors. *Mater Today* 11:16–21
18. Wang C, Yin L, Zhang L, Xiang D, Gao R (2010) Metal oxide gas sensors: sensitivity and influencing factors. *Sensors* 10:2088–2106
19. Phawachalotorn C, Sanguanruang O, Ishihara T (2012) Highly selective amperometric sensors for carbon monoxide detection in exhaust gas. *Sens Actuators B* 161:635–640
20. Courbat J, Briand D, Yue L, Raible S, de Rooij NF (2012) Drop-coated metal-oxide gas sensor on polyimide foil with reduced power consumption for wireless applications. *Sens Actuators B* 161:862–868
21. Morimitsu M, Ozaki Y, Suzuki S, Matsunaga M (2000) Effects of surface modification with platinum and ruthenium on temperature and humidity dependence of SnO<sub>2</sub>-based CO gas sensors. *Sens Actuators B* 67:184–188
22. Al-Kuhaili MF, Durrani SMA, Khawaja EE (2004) *J Phys D Appl Phys* 37:1254

23. Durrani SMA, Khawaja EE, Al-Kuhaili MF (2005) CO-sensing properties of undoped and doped tin oxide thin films prepared by electron beam evaporation. *Talanta* 65:1162–1167
24. Zhang T, Liu L, Qi Q, Li S, Lu G (2009) Development of microstructure In/Pd-doped SnO<sub>2</sub> sensor for low-level CO detection. *Sens Actuators B* 139:287–291
25. Bahrami B, Khodadadi A, Kazemini M, Mortazavi Y (2008) Enhanced CO sensitivity and selectivity of gold nanoparticles-doped SnO<sub>2</sub> sensor in presence of propane and methane. *Sens Actuators B* 133:352–356
26. Wang C-T, Chen H-Y, Chen Y-C (2013) Gold/vanadium–tin oxide nanocomposites prepared by co-precipitation method for carbon monoxide gas sensors. *Sens Actuators B* 176:945–951
27. Choi JY, Oh TS (2013) CO sensitivity of La<sub>2</sub>O<sub>3</sub>-doped SnO<sub>2</sub> thick film gas sensor, *Thin Solid Films* 547:230–234
28. Yuasa M, Masaki T, Kida T, Shimano K, Yamazoe N (2009) Nano-sized PdO loaded SnO<sub>2</sub> nanoparticles by reverse micelle method for highly sensitive CO gas sensor. *Sens Actuators B* 136:99–104
29. Vallejos S, Umek P, Stoycheva T et al (2013) Single-step deposition of Au- and Pt-nanoparticle functionalized tungsten oxide nanoneedles synthesized via aerosol-assisted CVD, and used for fabrication of selective gas microsensor arrays. *Adv Funct Mater* 23:1313–1322
30. Chevallier L, Traversa E, Di Bartolomeo E (2010) Propene detection at high temperatures using highly sensitive non-nernstian electrochemical sensors based on Nb and Ta oxides. *J Electrochem Soc* 157(11):J386–J391
31. Wang XR, Lizier JT, Obst O, Prokopenko M, Wang P (2008) Spatiotemporal anomaly detection in gas monitoring sensor networks. *Lect Note Comput Sci* 4913:90–105
32. Li M, Liu Y, Chen L (2007) Non-threshold based event detection for 3D environment monitoring in sensor networks. In: *Proceedings of the 27th international conference on distributed computing systems, ICDCS'07*. Toronto, 25–29 June 2007, p 9
33. CitiSense. Available online: <https://sosa.ucsd.edu/confluence/display/CitiSensePublic/CitiSense> (accessed on 3 June 2013)
34. Air quality egg. Available online: <http://www.Kickstarter.com/projects/edborden/air-quality-egg> (accessed on 3 June 2013)
35. Lilienthal A, Trincavelli M, Schaffernicht E (2013) It's always smelly around here! Modeling the spatial distribution of gas detection events with based grid maps. Accepted for publication in *Proceedings of international symposium on olfaction and electronic nose 2013, ISOEN'13*, Daegu, 2–5 July 2013
36. Pashami S, Lilienthal AJ, Schaffernicht E, Trincavelli M (2013) Trend estimation and change detection in the response of MOX gas sensors sensors 13(6):7323–7344
37. Min Y (2003) Properties and sensor performance of zinc oxide thin films. PhD in Electronic, Photonic and Magnetic Materials, Massachusetts Institute of Technology
38. Simakov VV, Yakusheva OV, Grebennikov AI, Kisin VV (2005) Current-voltage characteristics of thin-film gas sensor structures based on tin dioxide. *Tech Phys Lett* 31:339–340
39. Varpula A, Novikov S, Sinkkonen J, Utriainen M (2008) Bias dependent sensitivity in metal-oxide gas sensors. *Sens Actuators B* 131:134–142
40. Wang D, Agrawal DP, Toruksa W, Chaiwatpongsakorn C, Lu M, Keener TC (2010) Monitoring ambient air quality with carbon monoxide wireless network. *Commun ACM* 53(5):138–141
41. Jelacic V, Magno M, Brunelli D, Paci G, Benini L (2013) Contextadaptive multimodal wireless sensor network for energy-efficient gas monitoring. *IEEE Sens J* 13(1):328–338
42. Bhattacharyya P, Verma D, Banerjee D (2010) Microcontroller based power efficient signal conditioning unit for detection of a single gas using mems based sensor. *Int J Smart Sens Intell Syst* 3(4)
43. Somov A, Baranov A, Savkin A, Ivanov M, Calliari L, Passerone R, Karpov E, Suchkov A (2012) Energy-aware gas sensing using wireless sensor networks. In: *Wireless sensor networks, 9th European Conference, EWSN 2012*, ser. *Lecture Notes in Computer Science*, vol 7158. Springer, Heidelberg, pp 245–260

44. Rossi M, Brunelli D (2013) Analyzing the transient response of MOX gas sensors to improve the lifetime of distributed sensing systems. In: IEEE international workshop on advances in sensors and interfaces, pp 211–216
45. Caione C, Brunelli D, Benini L (2012) Distributed compressive sampling for lifetime optimization in dense wireless sensor networks. *IEEE Trans Industr Inf* 8(1):30–40
46. Bissi L, Cicioni M, Placidi P, Zampolli S, Elmi I, Scorzoni A (2011) A programmable interface circuit for an ultralow power gas sensor. *IEEE Trans Instrum Meas* (99):1–8. doi:[10.1109/TIM.2010.2049182](https://doi.org/10.1109/TIM.2010.2049182)
47. Rastrello F, Placidi P, Bissi L, Scorzoni A, Cozzani E, Elmi I, Zampolli S, Cardinali GC (2010) Characterization of the thermal transients of an ultra low power micromachined sensor. In: Proceedings of the IEEE Int. Instrum. Meas. Technol. Conf., Austin, TX, May 3–6, 2010, pp 1591–1595
48. Rastrello F, Placidi P, Scorzoni A (2011) A system for the dynamic control and thermal characterization of ultra low power gas sensors. *IEEE Trans Instrum Meas* 60(5):1876–1883
49. Marco S, Gutierrez-Galvez A (2012) Signal and data processing for machine olfaction and chemical sensing: a review. *IEEE Sens J* 12(11):3189–3214
50. Romain AC, Nicolas J (2010) Long term stability of metal oxide-based gas sensors for e-nose environmental applications: an overview. *Sens Actuators B* 146:502–506
51. Hajmirzaheydarali M, Ghafarinia V (2011) A smart gas sensor insensitive to humidity and temperature variations. *Mater Sci Eng* 17
52. Sohn JH, Atzeni M, Zeller L, Pioggia G (2008) Characterisation of humidity dependence of a metal oxide semiconductor sensor array using partial least squares. *Sens Actuators B* 131(1):230–235
53. Mumyalmaz B, Ozmen A, Ebeoglu MA, Tasaltin C, Gurol I (2010) A study on the development of a compensation method for humidity effect in QCM sensor responses. *Sens Actuators B* 147(1):277–282
54. Tian F, Pan L, Xiao B, Yang SX, Guo J, Feng J, Kadri C (2012) Study of the temperature and humidity dependence of a metal oxide semiconductor sensor array. *J Comput Inf Syst* 8(11):4495–4503
55. Abidin MZ, Asmat A, Hamidon MN (2013) Identification of initial drift in semiconductor gas sensors caused by temperature variation. In: IEEE 9th international colloquium on signal processing and its applications, pp 285–288
56. Koretchenkov G, Cho BK (2011) Instability of metal oxide based conductometric gas sensors and approaches to stability improvement (short survey). *Sens Actuators B* 156(2):527–538



# Temperature Field of Double-Sided Asymmetrical MAG Backing Welding for Thick Plates

Yu-Xi Chen, Yan-Ling Xu, Hua-Bin Chen, Hua-Jun Zhang, Shan-Ben Chen and Yu Han

**Abstract** A double elliptic distribution model of moving heat-source was used to double-side asymmetrical MAG backing welding of thick plate, and a 3-D non-linear FEM analysis model was established based on ABAQUS software. The transient temperature of different arc distance was calculated. To verify the numerical results, the temperature was measured and the calculated results agree approximately with experimental data. Farther, the effect of arc distance on temperature field and weld pool size was discussed. The results show that the arc distance will influence the distribution of temperature field and the weld shape. The arc distance is a very important factor to affect the quality of double-side asymmetrical MAG backing welding of thick plate.

## 1 Introduction

Welding structure of thick plate of low-alloy high-tensile steel is extensively used in the fabrication industry, including shipbuilding, offshore structures, high-pressure vessel and so on [1–3]. At present, these structures adopt conventional welding technology such as manual and semi-automatic arc welding, which are very complicated and of low productivity. The process of the production is as follows: preheating, gas metal arc welding (GMAW) in one side, then back chipping by carbon arc air gouging, polishing, magnetic particle examination, preheating again, GMAW on the other side again, finally post heating and so on [4]. In order to

---

Y.-X. Chen (✉) · Y.-L. Xu · H.-B. Chen · S.-B. Chen  
School of Materials Science and Engineering, Shanghai Jiao Tong University,  
200240 Shanghai, China  
e-mail: yxchen-sjtu@sjtu.edu.cn

H.-J. Zhang  
Shanghai Zhenhua Heavy Industries Co., Ltd, 200125 Shanghai, China

Y. Han  
Jiangsu Automation Research Institute, 222006 Jiangsu, China

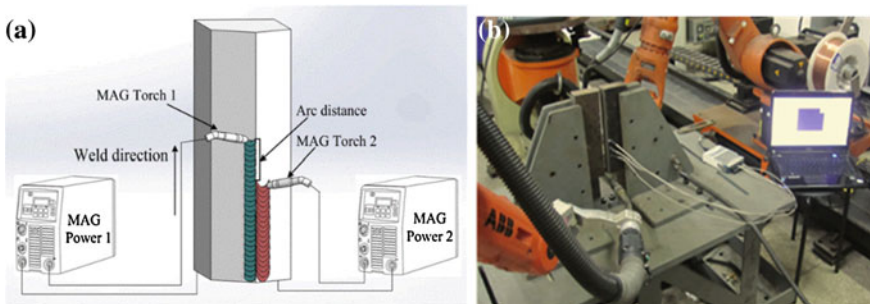
improve the welding production efficiency, some new methods come forth, among which is double-sided double arc welding (DSAW) [5–7]. The weldment welded by DSAW need not back chipping, so DSAW has been applied in the welding of thick plates. But few related theories have been reported. Therefore, it is very significant to have further theory research to this method so as to guide the production.

It is well known that thick plate welding generally adopts multi-layer and multi-pass welding, and backing welding is the most important pass. In the backing welding, the double MAG welding arcs on double sides keep a proper distance to realize temperature controlling because low-alloy high-tensile steel is strict with welding heat input. The thermal cycles have an important influence on the microstructure, shape, stress, distortion and mechanical property [8–10], but the effect of arc distance on the temperature field and weld shape is not clear. Therefore, numerical simulation based on ABAQUS is applied to research the relationship between arc distances and weld shape in DSAW. In addition, the welding experiments are also carried out to verify the numerical results.

## 2 DSAW Experiment

The basic principle of DSAW process and the real system established in this paper are shown in Fig. 1. Two weld guns are laid on the two sides of the plate and supplied by weld power 1 and power 2 individually. Double sided metal active gas (MAG) torches keep an arc distance to realize asymmetric DSAW.

To verify the numerical results, low-alloy high-tensile steel plates, 30 mm in thickness, 70 mm in width and 240 mm in length, double-V symmetry groove (angle =  $45^\circ$ ), root gap of 3 mm are welded at vertical position using the asymmetric DSAW process at an arc distance. The welding parameters used in the experiment are: welding speed 2 mm/s, welding voltage of fore arc 20 V and welding current 114 A, welding voltage of rear arc 19 V and welding current 108 A. The temperature measurement was implemented using K-type thermocouples. The locations of the thermocouples are also shown in Fig. 1.



**Fig. 1** The basic principle of DSAW process and the real system

### 3 Finite Element Model

#### 3.1 Three-Dimensional Model

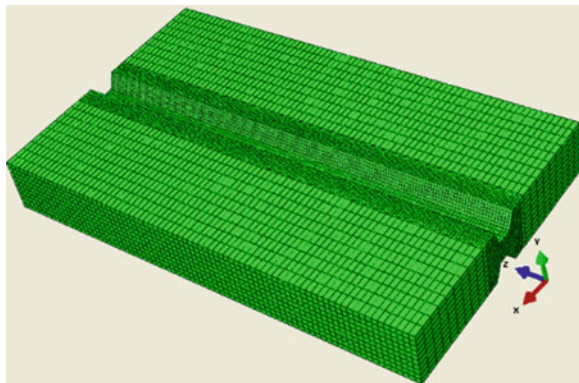
Figure 2 shows the symmetric finite element model used in the welded butt joint plate ( $240 \times 140 \times 30$  mm). The three-dimensional model was established using the simulation software ABAQUS. Considering that the temperature and stress gradient of weld zone are very high, fine mesh is used in weld and heat affected zone and the coarse mesh is used in regions away from the weld. The total numbers of elements and nodes used were 64,160 and 71,980 respectively. The X axis is the plate width direction, the Y axis is the plate thickness direction, and the Z axis is the welding direction.

#### 3.2 Heat Source and Thermal Analysis

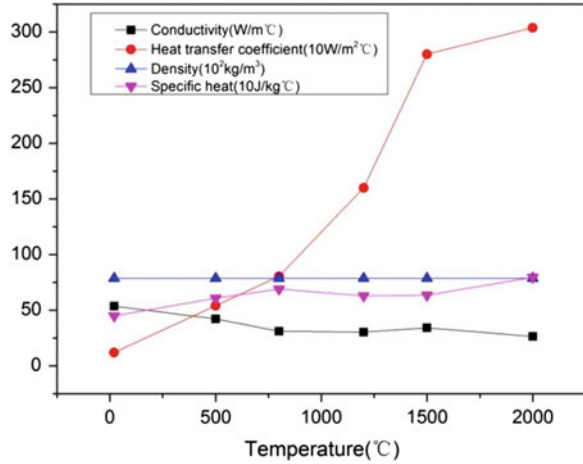
In this study, the isotropic behavior of the material is assumed. At the ambient temperature, the Poisson's ratio is 0.29, the density is  $7860 \text{ kg m}^{-3}$  and the melting point is  $1450 \text{ }^\circ\text{C}$ . Figure 3 shows the physical properties which are temperature dependent. The heat from the moving welding arc is applied as a volumetric heat source with a double ellipsoidal distribution proposed by Goldak [11]. The heat analysis near the weld molten pool zone mainly appears heat radiation. However the farther place mainly appears surface heat exchange. Considering the common effects of radiation and surface heat exchange, the formula of compound heat conduction coefficient as follows [12]:

$$h = \frac{\varepsilon_{em} \sigma_{bol} (T^4 - T_{amb}^4)}{T - T_{amb}} + h_{con}$$

**Fig. 2** 3D finite element model and meshing in welding simulation



**Fig. 3** Temperature dependent thermal physical properties



where  $h$  is the compound heat conduction,  $\epsilon_{em}$  is the radiation coefficient,  $h_{con}$  is the convection coefficient,  $\sigma_{bol}$  is the Stefan–Boltzmann constant,  $T$  is the absolute temperature,  $T_{amb}$  is the surrounding temperature.

### 3.3 Load Case Design

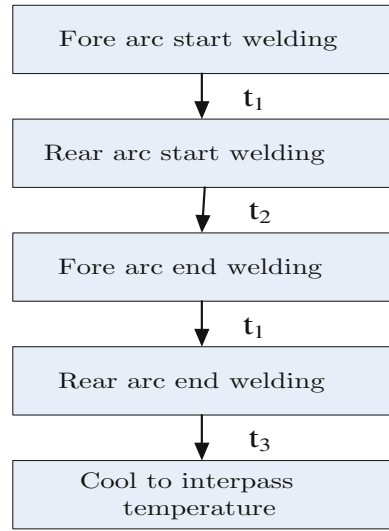
To investigate the effect of arc distance on the temperature field, five cases are developed according to different arc distances: 0, 20, 40, 60 and 80 mm respectively. The realisation of the DSAW process is shown in Fig. 4. Arc distance variant is set as  $d$ , and fore torch is ahead of the rear torch by an arc distance  $d$  during welding at the same speed: first, fore arc is loaded,  $t_1$  (s) later, the rear arc is loaded,  $t_2$  later, fore arc is unloaded,  $t_1$  later, the rear starts to be unloaded and workpiece starts to be naturally cooling in the air, and  $t_3$  later, the average temperature of workpiece falls close to ambient temperature. Fore torch is ahead of the rear torch by an arc distance  $d$ , i.e. according to the welding speed, the foregoing time  $t_1$  is expressed as follows.

$$t_1 = \frac{d}{v_1}$$

Then the fore and rear torches have been going simultaneously for a period of time  $t_2$  as follows.

$$t_2 = \frac{L - d}{v_1}$$

**Fig. 4** Load of welding job



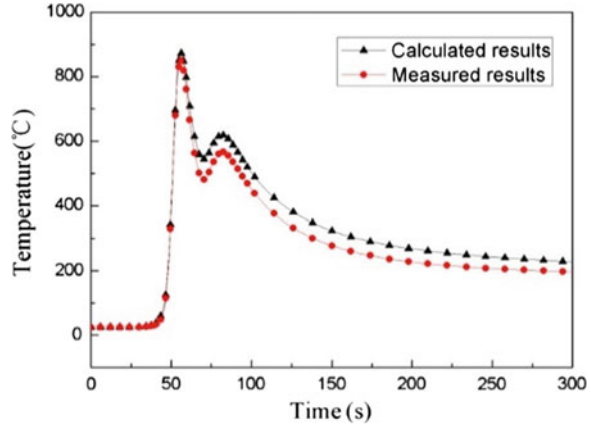
where  $L$  is the length of plate (mm),  $d$  is the arc distance (mm) and  $v_1$  is the welding speed (mm/s). The time of cooling to ambient temperature cannot be determined quantitatively because it will be different with different arc distance.

## 4 Results and Analysis

### 4.1 Comparison of Experimental and Calculated Results of Temperature

In order to verify the accuracy of numerical simulation, the transient temperature at arc distance 40 mm is measured by the thermocouples. The calculated and experimental results are shown in Fig. 5. The whole evolution trend of experimental temperature agrees approximately with that of calculated temperature, but the peak temperature of measured curve is slightly higher than that of numerical curve. Calculated and experimental results show that there are two peaks appear in the temperature curve. The fore pass induces preheat action to the rear pass, and the rear arc has the postheat action on the fore pass. The double peak characteristic of DSAW temperature will be helpful for the weld microstructure and alleviate the cold crack.

**Fig. 5** Comparison of temperature history between experiment and finite element simulation



## 4.2 Effect of Arc Distance on Temperature

In order to investigate the effect of arc distance on the temperature field, five cases are developed according to different arc distances: 0, 20, 40, 60 and 80 mm respectively. Figure 6 shows the history plots of the temperature at different arc distance. The figures illustrate that with the increase of the arc distance, the thermal cycle curves present different characteristics. At arc distance 0 mm, the molten pools of the fore and rear completely added together, which can be approximately regarded as one pool. The temperature distribution has a single peak, and the process can be regarded as single arc welding process. When the arc distance increase to 20 mm, the temperature curves is not strict unimodal or bimodal structure, but a kind of approximate unimodal structure. Compared the thermal cycle curves at different arc distance, the peak temperature of the fore pass is basically unchanged, but the peak temperature of the rear pass at 20 mm is higher than other arc temperature, even higher than the peak temperature of the fore pass. It indicates that the fore arc and rear arc have a great influence on each other, the fore arc has the preheat action on the rear pass, and the rear arc has the postheat action on the fore pass. However, the rear weld in high temperature for a long time, it will prone to overheating and affect the welding quality. Temperature curves have double peaks when arc distance is from 20 to 80 mm and the bimodal structure is more and more obvious with the increase of the arc distance. In summary, the peak temperature of the fore pass is decreasing with the increase of arc distance, which indicates that postheat effect of the rear arc on fore pass becomes small. The peak temperature of the rear pass is increasing firstly, and then decreasing along with the arc distance increasing because the preheat temperature is decreasing with the arc distance increasing.

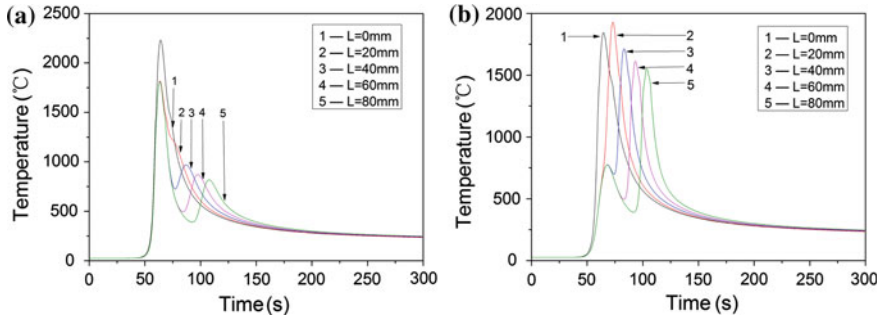


Fig. 6 Thermal cycle curves with different arc distances. a Fore pass. b Rear pass

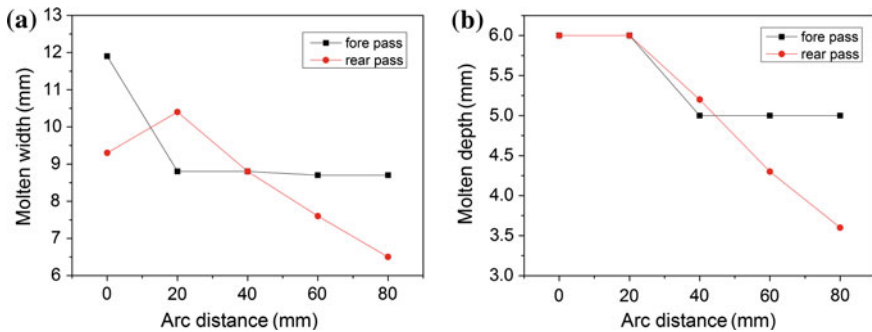


Fig. 7 Molten shape parameters with different arc distances. a Molten width. b Molten depth

### 4.3 Effect of Arc Distance on Weld Pool Size

Figure 7 shows the effect of arc distance on weld pool size. It can be seen that the penetrations of the fore weld and rear weld change slightly with the increase of arc distance 0–20 mm. With the increase of arc distance 0–20 mm, the width of fore weld pool decreases from 11.8 to 8.6 mm, but the width of rear weld pool increases from 9.3 to 10.4 mm, which agrees with the peak temperature on rear weld. The reason is that the molten pools of the fore and the rear can be approximately regarded as one pool when the arc distance is very small. The effect which the fore arc act on the rear arc is bigger than that the rear arc influence the fore arc. The energy of the arc concentrate and the peak temperature rise. When the arc distance becomes larger, the width and penetration of the rear weld decreases obviously, but the weld pool size of the fore weld have little changes.

## 5 Conclusion

1. A 3-D non-linear FEM analysis model was established for double-side asymmetrical MAG backing welding of thick plate. The transient temperature was measured and the calculated results agree approximately with experimental data. The results show that the fore arc has the preheating effect on the rear pass, and the rear arc has the post-heating effect on the fore pass.
2. The thermal cycle curves show unimodal or approximate single-peak structure when arc distance is from 0 to 20 mm. There is a greater influence on the interaction between the two arcs. The curves have double peaks when arc distance is from 20 to 80 mm. The effects of preheat and post heat weakened with the increase of the arc distance.
3. The molten pools of the fore and the rear can be approximately regarded as one pool when the arc distance is very small. With the increase of arc distance 0–20 mm, the width of fore weld pool decreases from 11.8 to 8.6 mm, but the width of rear weld pool increases from 9.3 to 10.4 mm. The penetrations of the fore weld and rear weld change slightly with the increase of arc distance 0–20 mm. When the arc distance becomes larger, the width and penetration of the rear weld decreases obviously, but the weld pool size of the fore weld have little changes.

**Acknowledgement** This work is supported by the National Natural Science Foundation of China under the Grant No. 61374071, 51405298 and 61305050, the NDRC of China, under the Grant No. HT[2012] 2144, and the National Natural Science Foundation of Jiangsu Province (BK2012236).

## References

1. Ohnishi T, Kawahito Y, Mizutani M et al (2013) Butt welding of thick, high strength steel plate with a high power laser and hot wire to improve tolerance to gap variance and control weld metal oxygen content. *Sci Technol Weld Joining* 18(4):314–322
2. Hashemi SH (2011) Strength–hardness statistical correlation in API X65 steel. *Mater Sci Eng A* 528(3):1648–1655
3. Gomez M, Valles P, Medina SF (2011) Evolution of microstructure and precipitation state during thermomechanical processing of a X80 microalloyed steel. *Mater Sci Eng A* 528(13):4761–4773
4. Zhang HJ, Zhang GJ, Cai CB et al (2009) Numerical simulation of three-dimension stress field in double-sided double arc multipass welding process. *Mater Sci Eng A* 499(1):309–314
5. Zhang HJ, Zhang GJ, Cai CB et al (2009) The realization of low stress and nonangular distortion by double-sided double arc welding. *J Manuf Sci Eng* 131(2):021004
6. Zhang H, Zhang G, Wang J et al (2007) Effect of thermal cycles of DSAW on microstructure in low alloy high strength steel. *Trans-China Weld Inst* 28(10):81
7. Yang CD, Huang HY, Zhang HJ et al (2012) Multi-pass route planning for thick plate of low alloy high strength steel by double-sided double arc welding. *Adv Mater Res* 590:28–34



8. Zhu XK, Chao YJ (2004) Numerical simulation of transient temperature and residual stresses in friction stir welding of 304L stainless steel. *J Mater Process Technol* 146(2):263–272
9. Reynolds AP, Tang W, Gnaupel-Herold T et al (2003) Structure, properties, and residual stress of 304L stainless steel friction stir welds. *Scripta Mater* 48(9):1289–1294
10. Deng D, Murakawa H (2008) Prediction of welding distortion and residual stress in a thin plate butt-welded joint. *Comput Mater Sci* 43(2):353–365
11. Goldak J, Chakravarti A, Bibby M (1984) A new finite element model for welding heat sources. *Metall Trans B* 15(2):299–305
12. Abid M, Siddique M (2005) Numerical simulation to study the effect of tack welds and root gap on welding deformations and residual stresses of a pipe-flange joint. *Int J Press Vessels Pip* 82(11):860–871

# Research on Visual Weld Trace Detection Method Based on Invariant Moment Features

Jin-Le Zeng, Yi-Rong Zou, Dong Du, Bao-Hua Chang  
and Ji-Luan Pan

**Abstract** A visual weld trace detection method based on invariant moment features is proposed in this paper for cosmetic welding inspection. The proposed method can not only overcome the absence of distortion in structural light detection, but also solve the problems of existing detection method based on grayscale weld image such as many priori parameters needed, time-consuming feature extraction process, instable features etc. This research shows that the proposed detection method has advantages in better adaptability, fewer priori parameters and higher efficiency. The detection error of the proposed method is not more than 0.3 mm. The seam and base metal region can be classified effectively. The proposed method is expected to be applied to real-time seam tracking in multi-layer welding.

## 1 Introduction

Visual weld detection is of great significance in fast off-line path planning [1], process control of welding [2, 3] and nondestructive testing of weldment [4], in order to obtain a combination of good forming and metallurgical quality [5–9]. Visual weld detection is in fact a process to distinguish the seam and base metal by characterizing them with some kinds of remarkable visual features.

Nowadays, structured light detection [3, 10, 11] based on geometric features of weld is the most widely used method in practical industrial use. The reliability of structured light detection method depends largely on the extent of laser distortion. However, in multi-layer and multi-pass weld tracking (e.g. cosmetic welding) or nondestructive testing of formed weld, laser distortion becomes unremarkable [12], because the region of existing beads becomes smooth as the welding process goes

---

J.-L. Zeng · Y.-R. Zou · B.-H. Chang · J.-L. Pan  
Key Laboratory for Advanced Materials Processing Technology, Ministry of Education,  
Tsinghua University, Beijing 100084, China

D. Du (✉)  
Department of Mechanical Engineering, Tsinghua University, Beijing 100084, China  
e-mail: dudong@tsinghua.edu.cn

on, which may consequently result in a detection failure. It is essential to develop a new visual detection method to distinguish the seam and base metal in these applications.

Researchers have proposed many methods based on other visual features. In these researches, grayscale or color images of weld are captured by cameras. Template matching [13] is one of these weld detection methods. During the detecting process, a chosen seam template travels across the image and correlation coefficients in each position are calculated. The positions where correlation coefficients reach high values indicate the real seam region. It is doubtful whether the chosen template is applicable and adaptive to variable welding conditions, however. Moreover, template matching is so difficult and may fail to give an accurate detecting result when the trend of weld changes unpredictably.

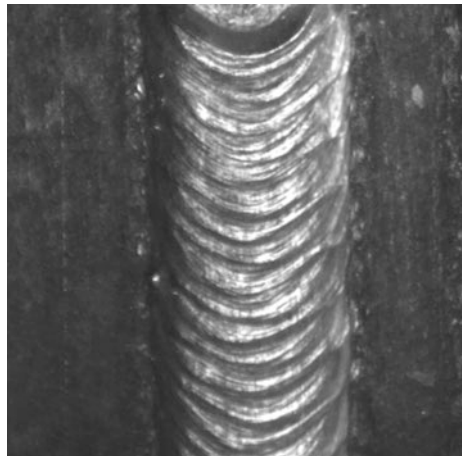
Differences in grayscale distribution, i.e., texture, between seam and base metal are used in weld detection as well. Haralick texture features extracted from gray level co-occurrence matrix (GLCM) are proposed to detect the weld in [14]. These features are sensitive to many priori parameters during the calculation of GLCM, such as gray-level, distance and angle parameters of pixel pairs. Besides, the process to compute Haralick texture features is time-consuming.

In this paper, a weld detection method based on invariant moments is proposed to distinguish two different regions (seam and base metal) in the weld image. The proposed method is expected to be adaptive to variable welding conditions for the stability of invariant moment features. Fewer priori parameters are required and the efficiency of detecting algorithm is improved.

## 2 Invariant Moments Extraction and Properties

Figure 1 shows a stainless steel cosmetic weld image captured by CCD camera using MIG weaving welding method. The welding current, voltage, speed and weaving frequency are 140 A, 19 V, 80 mm/min and 0.5 Hz respectively.

**Fig. 1** Stainless steel cosmetic weld image using MIG weaving welding



The width of the seam is about 15 mm. The image size is  $300 \times 300$  and field of view is about  $35 \text{ mm} \times 35 \text{ mm}$ . In order to distinguish the seam and base metal, suitable visual features should be chosen first to characterize both regions.

In this study, invariant moments are chosen to characterize seam and base metal. According to Hu's theory [15], 7 invariant moments of digital image  $I(x, y)$  are defined as:

$$\begin{aligned}
 \varphi_1 &= \eta_{20} + \eta_{02} \\
 \varphi_2 &= (\eta_{20} - \eta_{02})^2 + 4\eta_{11}^2 \\
 \varphi_3 &= (\eta_{30} - 3\eta_{12})^2 + (3\eta_{21} - \eta_{03})^2 \\
 \varphi_4 &= (\eta_{30} + \eta_{12})^2 + (\eta_{21} + \eta_{03})^2 \\
 \varphi_5 &= (\eta_{30} - 3\eta_{12})(\eta_{30} + \eta_{12}) \cdot [(\eta_{30} + \eta_{12})^2 - 3(\eta_{21} + \eta_{03})^2] \\
 &\quad + (3\eta_{21} - \eta_{03})(\eta_{21} + \eta_{03}) \cdot [3(\eta_{30} + \eta_{12})^2 - (\eta_{21} + \eta_{03})^2] \\
 \varphi_6 &= (\eta_{20} - \eta_{02})[(\eta_{30} + \eta_{12})^2 - (\eta_{21} + \eta_{03})^2] + 4\eta_{11}(\eta_{30} + \eta_{12})(\eta_{21} + \eta_{03}) \\
 \varphi_7 &= (3\eta_{21} - \eta_{03})(\eta_{30} + \eta_{12}) \cdot [(\eta_{30} + \eta_{12})^2 - 3(\eta_{21} + \eta_{03})^2] \\
 &\quad + (3\eta_{12} - \eta_{30})(\eta_{21} + \eta_{03}) \cdot [3(\eta_{30} + \eta_{12})^2 - (\eta_{21} + \eta_{03})^2]
 \end{aligned}$$

where  $\eta_{pq}$  is the  $pq$ -order normalized central moment:

$$\eta_{pq} = \frac{\left[ \sum_{x=1}^M \sum_{y=1}^N (x - \bar{x})^p (y - \bar{y})^q I(x, y) \right]}{\left[ \sum_{x=1}^M \sum_{y=1}^N I(x, y) \right]^{\frac{p+q}{2}+1}}$$

where the image size of  $I(x, y)$  is  $M \times N$ .

Take the 1st invariant moment  $\phi_1$  for example. For a stable and adaptive detection, the invariant moment  $\phi_1$  is expected to meet the following needs.

## 2.1 High Degree of Self-similarity and Separation

The feature should almost stay unchanged in different parts of the same seam (or the same base metal). Besides, it is important to keep high separation degree for a better classification of seam and base metal. In order to validate high degree of self-similarity and separation of  $\phi_1$ , the weld image in Fig. 1 is segmented into several  $\Delta M \times \Delta N$  sub-images and adjacent sub-images are overlapped half, as shown in Fig. 2a. Invariant moment  $\phi_1$  of each sub-image is calculated. The distribution of  $\phi_1$  is shown in Fig. 2b when  $\Delta M = 20$  and  $\Delta N = 20$ . Figure 2b shows that the invariant moment  $\phi_1$  of seam is distinguished from that of base metal and it is smaller.

With-class to among-class deviation ratio (WADR) is used to quantitatively describe the degree of self-similarity and separation of invariant moment feature proposed in this study and gray level co-occurrence feature proposed in [14]. The WADR of invariant moment feature is about 1.115, which is similar to that of gray level co-occurrence feature (about 1.110–1.117). It can be seen that the proposed feature is expected to effectively distinguish the seam and base metal region.

## 2.2 Affine Invariance

Affine invariance (including translational, rotational and scale invariance) is necessary for characterizing seam and base metal, in order to be adaptive to (1) the time-varying relative position and pose between the work piece and camera, (2) the time-varying trend of weld, and (3) dimension differences of diversities of seams.

It is proved by Hu that the invariant moments are translational, rotational and scale invariant when a full image is taken into account. However, affine invariance of a sub-image, especially rotational invariance, has not been discussed, which is important to judge whether the sub-image in Fig. 2a belongs to seam region or not.

A rotated ROI (sub-image) with rotation degree  $\theta$  is chosen in seam region as shown in Fig. 3a. The ratio of invariant moment  $\phi_1$  between rotated ROI and ROI without rotation is shown in Fig. 3b. The ratio is between 0.98 and 1.02. It can be concluded that the invariant moment  $\phi_1$  is sub-image rotational invariant.

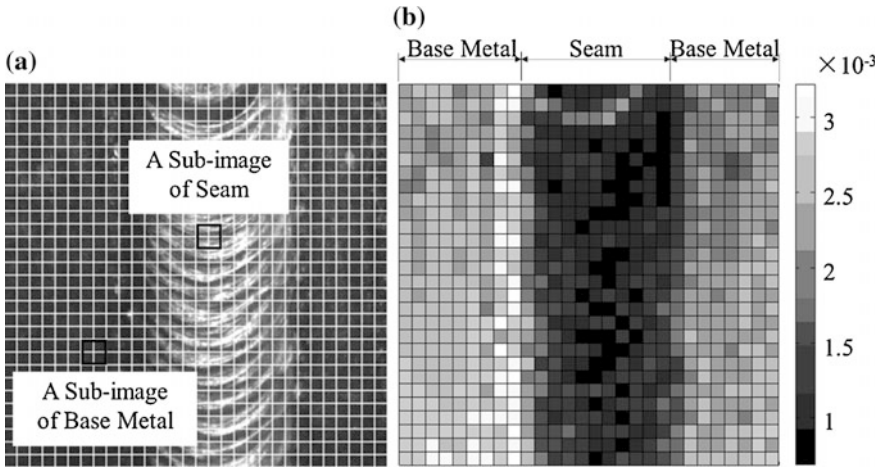


Fig. 2 Segmentation of weld image and distribution of invariant moment  $\phi_1$  of weld image

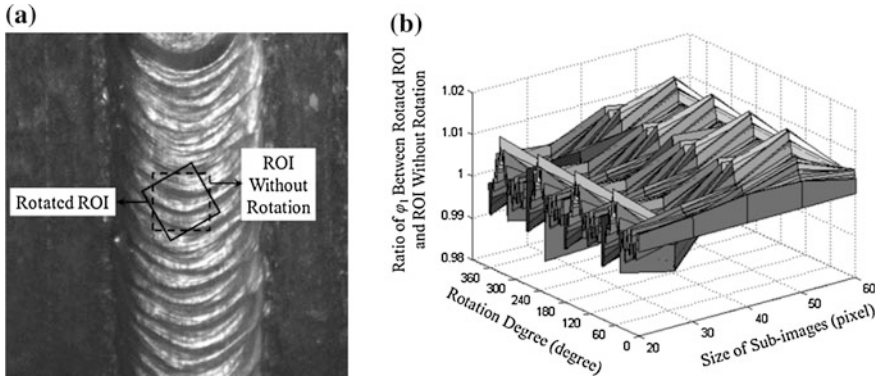


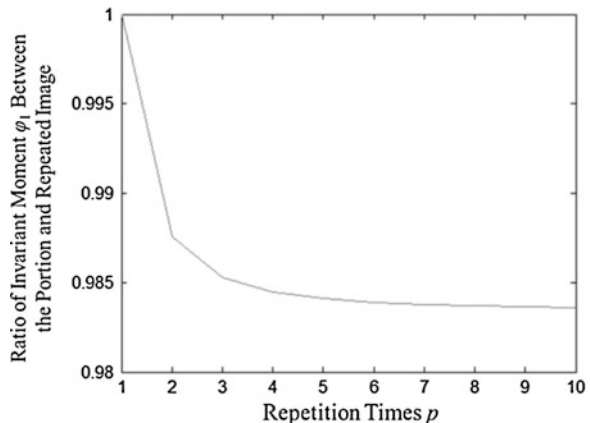
Fig. 3 Ratio of invariant moment  $\phi_1$  between rotated ROI and ROI without rotation

### 2.3 Repetition Invariance

If the detected target appears repeatedly and adjacently in one captured image, the repeated target should have the same properties as the single target. The whole seam can be regarded as a repeated pattern of its portion. For a stable and adaptive weld detection method, an equivalent feature should be shared by both of the whole seam and its portion.

To validate the repetition invariance of invariant moment, a portion of seam region is chosen first. Then a repeated image is created consisting of a  $p$ -by- $p$  tiling of copies of this portion. The ratio of invariant moment  $\phi_1$  between the portion and repeated image is shown in Fig. 4. The invariant moment  $\phi_1$  of repeated image is almost the same as that of the portion. In other words, the invariant moment  $\phi_1$  is repetition invariant.

Fig. 4 Ratio of invariant moment  $\phi_1$  between the portion and repeated image



### 3 Weld Inspection Method Based on Invariant Moments

Considering the high degree of self-similarity and separation, affine invariance and repetition invariance of invariant moment  $\phi_1$ , it is expected to develop a stable and adaptive weld detection method based on invariant moment and it is proposed in this study.

#### 3.1 Image Segmentation and Invariant Moment Feature Extraction

First of all, the weld image is segmented into several  $\Delta M \times \Delta N$  sub-images and adjacent sub-images are overlapped half, as shown in Fig. 2a. Suppose there are  $S_M \times S_N$  sub-images in Fig. 2a. The invariant moment  $\phi_1$  of each sub-image is calculated and a two-dimensional array  $\phi_1[i][j]$  is obtained, where  $1 \leq i \leq S_M$  and  $1 \leq j \leq S_N$ .

#### 3.2 K-Means Adaptive Thresholding

K-Means adaptive thresholding is applied to each row of  $\phi_1[i][j]$ . Considering the probable different lighting conditions of two-sided base metal, two different thresholds are used to different side of base metal. The algorithm flow of thresholding is as follows: for each row  $i$  of  $\phi_1[i][j]$ ,

Find the column index in which  $\phi_1[i][j]$  reaches its minimum:

$$s[i] = \arg \min_{1 \leq j \leq S_N} \phi_1[i][j]$$

Since the invariant moment  $\phi_1$  of seam region is smaller than that of base metal, the region neighbored to the sub-image where  $\phi_1$  reaches its minimum is expected to be the seam.

For  $\phi_1[i][j]$ ,  $1 \leq j \leq s[i]$  and  $\phi_1[i][j]$ ,  $s[i] \leq j \leq S_N$ , K-Means adaptive thresholding is applied respectively. Two thresholds, namely  $T_L[i]$  and  $T_R[i]$ , are obtained. A two-dimensional array  $F[i][j]$  is used to record the thresholding results:

$$F[i][j] = \begin{cases} 1, & 1 \leq j \leq s[i] \quad \text{and} \quad \phi_1[i][j] \leq T_L[i] \\ 1, & s[i] \leq j \leq S_N \quad \text{and} \quad \phi_1[i][j] \leq T_R[i] \\ 0, & \text{otherwise} \end{cases}$$

The thresholding result is shown in Fig. 5.

**Fig. 5** The thresholding results of invariant moment  $\phi_1[i][j]$



### 3.3 Maximum Connected Domain Detection

There may be many isolated noise regions after thresholding. A maximum connected domain detection method is proposed to eliminate those isolated noise regions. The maximum connected domain of the thresholded image is expected to be the candidate of seam region. Extract the two edges of the maximum connected domain, and denote the column indexes of edges as  $EN_L[i]$  and  $EN_R[i]$  respectively.

### 3.4 Edge Position Refinement

The edge pixel coordinates can be figured out according to the column indexes  $EN_L[i]$  and  $EN_R[i]$  by multiplying sub-image size. However, the detection accuracy of proposed method may depend largely on the size of sub-images if it is done. In this study, a linear interpolation method is introduced to refine the accurate sub-pixel coordinates of edges.

Supposing that invariant moment  $\phi_1$  is equal to threshold  $T_L[i]$  (or  $T_R[i]$ ) where the real edge point locates, the real edge positions  $E_L[j]$  and  $E_R[j]$  meet the following interpolated equations:

$$\frac{E_L[i] - (EN_L[i] - 1)}{(EN_L[i] + 1) - (EN_L[i] - 1)} = \frac{T_L[i] - \phi_1[i][EN_L[i] - 1]}{\phi_1[i][EN_L[i] + 1] - \phi_1[i][EN_L[i] - 1]}$$

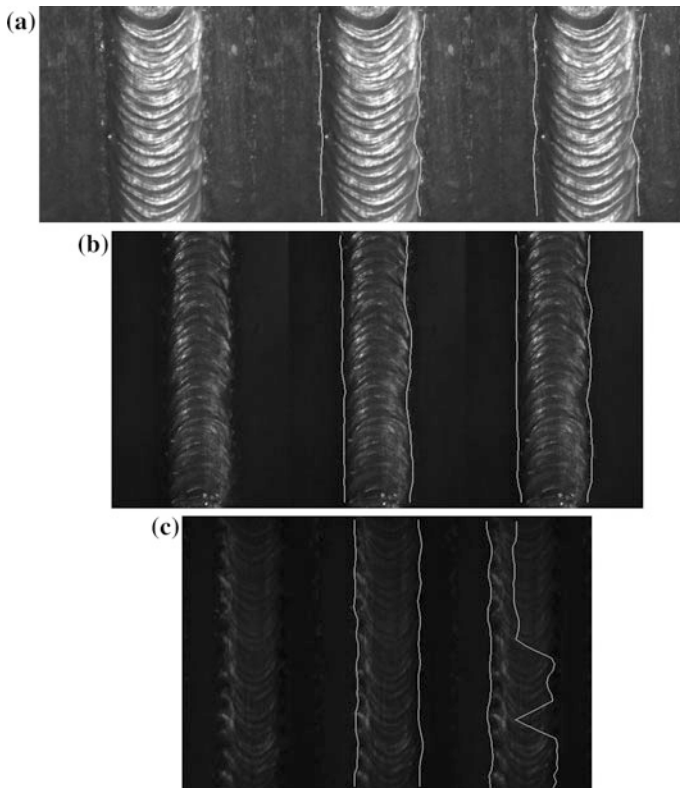
$$\frac{E_R[i] - (EN_R[i] - 1)}{(EN_R[i] + 1) - (EN_R[i] - 1)} = \frac{T_R[i] - \phi_1[i][EN_R[i] - 1]}{\phi_1[i][EN_R[i] + 1] - \phi_1[i][EN_R[i] - 1]}$$

Thus, the refined sub-pixel edge positions  $EL[i]$  and  $ER[i]$  can be obtained.



## 4 Processing Results and Discussions

Figure 6a shows the image processing result (Fig. 1) of proposed algorithm. The size of sub-images is  $20 \times 20$ . All tests are carried out on a PC (4-core, 8-thread 3.40 GHz CPU, 8 GB RAM). Other weld images in different conditions (exposure time and welding parameter) are also captured and the proposed method and gray level co-occurrence (GLCF) feature method in [14] are applied to figure out the edge between seam and base metal too in Fig. 6b and c. Images in the left column of Fig. 6 are the original images. Images in the middle and right column are the processed images using the proposed method and GLCF method respectively (the white curves in the images indicate edges of seam and base metal). The detection error of proposed method does not exceed 0.3 mm. The proposed method is more efficient than GLCF method. When the contrast between seam and base metal is



**Fig. 6** Image processing result of proposed method and *Gray* level co-occurrence feature method. **a** Full image  $300 \times 300$ , sub-image  $20 \times 20$ , process time cost 2.7 ms (*middle*) and 5 ms (*right*), **b** full image  $410 \times 260$ , sub-image  $20 \times 20$ , process time cost 3.4 ms (*middle*) and 5.6 ms (*right*), **c** full image  $450 \times 200$ , sub-image  $20 \times 20$ , process time cost 3.2 ms (*middle*) and 4.6 ms (*right*)

rather low as shown in Fig. 6c, the proposed method successfully detects accurate edges while GLCF method fails. Furthermore, there are only two priori parameters needed in proposed method (sub-image size), which are fewer than that needed in GLCF method.

## 5 Conclusion

A weld detection method based on invariant features is proposed in this paper. The first invariant moment chosen to characterize the seam and base metal has the properties of high degree of self-similarity and separation, affine invariance and repetition invariance, which contributes to a stable and adaptive weld detection process. A linear interpolation method is applied to refine the edge position between seam and base metal and the detection error is not more than 0.3 mm, overcoming shortages that detection accuracy is restricted to sub-image size when sub-image segmentation is applied. Compared to the existing weld detection method, the proposed method has advantages in better adaptability, fewer priori parameters and higher efficiency. It is expected to be applied to real-time seam tracking in multi-layer welding applications in the future.

**Acknowledgment** This work is supported by the National Natural Science Foundation of China under Grant Number 51375257.

## References

1. Zhang T, Wu M, Zhao Y et al (2014) Optimal motion planning of mobile welding robot based on multivariable broken line seams. *Int J Robot Autom* 29(2):215–223
2. Xu D, Yan Z, Fang Z et al (2011) Vision tracking system for narrow butt seams with CO<sub>2</sub> gas shielded arc welding. In: *Proceedings of the 5th international conference on automation, robotics and applications*, pp 480–485
3. Kim T, Lee S, Baek S et al (2010) A study on the welding seam tracking by using laser vision sensor. In: *Proceedings of international conference on control, automation and systems*, pp 779–782
4. Schreiber D, Cambrini L, Biber J (2009) Online visual quality inspection for weld seams. *Int J Adv Manuf Technol* 42(5):497–504
5. Wilson M (2002) The role of seam tracking in robotic welding and bonding. *Ind Robot Ind J* 29(2):132–137
6. Chen SB, Ye Z, Fang G (2014) Intelligentized technologies for welding manufacturing. In: *Proceedings of the 15th international conference on advances in materials and processing technologies*, pp 773–774
7. Tsai MJ, Lee H-W, Ann N-J (2011) Machine vision based path planning for a robotic golf club head welding system. *Robot Comput Integr Manuf* 27(4):843–849
8. Du D, Zou Y, Chang B (2010) Current status and development of welding visual sensor and automatic tracking technology. *Aeronaut Manuf Technol* 9:40–42

9. You DY, Gao XD, Katayama S (2014) Review of laser welding monitoring. *Sci Technol Weld Joining* 19(3):181–201
10. Meta vision. <http://www.meta-mvs.com/>
11. Sung K, Lee H, Choi YS et al (2009) Development of a multiline laser vision sensor for joint tracking in welding. *Weld J* 88(4):79–85
12. Zou Y, Du D, Zeng J et al (2013) Visual method for weld seam recognition based on multi-feature extraction and information fusion. *Trans China Weld Inst* 34(5):33–36
13. Zou Y, Wang S, Du D et al (2009) Method of weld recognition based on texture feature matching. *China Weld* 18(4):21–25
14. Wang S, Du D, Zeng K et al (2009) Weld recognition based on texture feature. *Trans China Weld Inst* 29(11):5–8
15. Hu MK (1962) Visual pattern recognition by moment invariants. *IRE Trans Inf Theor* 8 (2):179–187

# Mechanism Analysis and Feature Extraction of Arc Sound Channel for Pulse GTAW Welding Dynamic Process

Na Lv, Yan-ling Xu, Gu Fang, Hui Zhao and Shan-ben Chen

**Abstract** Arc sound signal has been proved to be an effective information for on-line monitoring and control for the quality of GTAW welding. Lots of studies focused on the sound source analysis. In this paper, an analysis of the generation and mechanism of sound channel during GTAW welding is completed, a method of establishing the equivalent model based on cepstral coefficient is proposed. The sound channel is expressed by complex cepstral coefficient through Z transform. The cepstral coefficient and spectral envelope of three different penetration states have been identified. Results show that the models of sound channel for full penetration, partial penetration and excessive penetration are clearly distinguishing the different fusion state of welding process. The sound channel for normal weld is more stable and balanceable than the abnormal weld. Thus, the cepstral coefficient for sound channel is proved to be an effective feature for the identification of dynamic welding process.

## 1 Introduction

The implementation for real-time monitoring of welding quality is actually a bionic process of imitating human behavior, especially how the welder achieve the sensory information acquisition during the operation process [1, 2]. After analysis by the human brain, the information is considered as a criterion of welding process stability. Then the judging results are determining the welding operation directly as the

---

N. Lv · Y. Xu (✉) · H. Zhao · S. Chen

Intelligentized Robotic Welding Technology Laboratory, School of Materials Science and Engineering, Shanghai Jiao Tong University (SJTU), Shanghai 200240, People's Republic of China  
e-mail: xuyanling991@sina.com

N. Lv · G. Fang

School of Computing, Engineering and Mathematics, University of Western Sydney (UWS), Locked Bag 1797, Penrith, NSW 2751, Australia

feedback from the dynamic welding process. Thus, collecting the most accurate and comprehensive fusion features from dynamic welding process becomes the primary and necessary step for real-time monitoring of welding quality. Taking the example by welder's judgment for welding quality using sensory information, the visual sensor and acoustic sensor is the most popular feature vector for achieving the welding penetration state monitoring and control. Due to its better intuitive and huge amount of information content, the visual sensor is concerned by a lot of scholars. The research covers the range from automated weld torch guidance before welding, weld seam tracking and weld quality monitoring during the welding process [3–5]. The arc sound signal is another sensor which is a type of non-contact vibration source of the signal. And the visual sensor has its disadvantage that the equipment is too large for the complex shape of the workpiece and unpredictable work environment. Therefore, many researchers pay attention to the research of the acoustic sensor. The sound information has been studied more and more because of its good indirectness and well adaptability. Nowadays, the research of arc sound signal is becoming a hot topic in the area of welding quality monitoring and control [6–11].

The acoustic signal is generated from the vibration of weld pool and the transformation of arc energy, so arc sound signal is a potential and valuable research direction for real-time online weld quality monitoring. Many researchers have focused on the study of acoustic signal during welding process. The research covers different subject areas like the generation source of acoustic signal, the feature extraction of arc sound signal and the modeling of dynamic welding process based on acoustic signal and welding parameters, and also the analysis of sound channel for the welding arc sound signal [6–11]. According to the study, arc sound signal is a signal which could be transmitted in a variety of medium, just like the speech signal. And the speech signal consists of the sound source signal and the modulation of vocal tract system. Identically, the arc sound signal has the same generating mechanism with the speech signal. The arc sound signal source comes from variation energy of the arc, the sound channel is generated from motivation of sound source. While the sound source is constant, the sound channel could be considered as a linear time-invariant system. Some researchers have focused on the sound channel during the welding process, however their studies mainly concentrated on MIG welding. There's less study about the sound channel for the GTAW dynamic welding process.

In this paper, the experiment was designed to create three different penetration states, such as full penetration, partial penetration and excessive penetration. Firstly, the generation mechanism of arc sound channel for GTAW welding was analyzed via the spectral analysis. Then, the sound channel model was set up through the cepstral coefficients of the arc sound signal.

## 2 Experiment System and Experiment Description

The schematic diagram of the experimental apparatus is shown in Fig. 1. The system is composed of four parts: the robotic system, the audio sensing system, the control system, and the welding system. The robotic system is a 6 degree of freedom industry robot made by Yaskawa Corporation. It contains a robot controller, a robot positioner and a teach box. The welding system includes: an INVERTER ELESON 500 P type AC/DC GTAW welding power source which is provided by Japan OTC company, a CM-271 type wire feeder, an HC-71 type wire feeding control box, an FR-IA gas flow controller, a water cooling fitting, a water box, protect cylinders and some other auxiliary equipment. The control system is composed of a control circuit board and a computer. The isolation unit is a self-made circuit to isolate the computer and the weld power supply from high-frequency interference at the beginning of welding. The computer, which is an industrial computer, runs the acoustic signal processing, welding control programs, and acts as the man-machine interface for this experimental system. The audio sensing system is composed of a microphone and a signal conditioner (Fig. 2).

The audio sensing system is responsible for the acquisition of acoustic signals during the welding process. The arc sound signal of welding is collected at 36 kHz sampling rate and 12 bits precision. The arc sound is picked by MP201 an omni-directional capacitance microphone, of which the frequency response range is from 20–20 kHz, the sensitivity is 50 mV/Pa, and the dynamic range is >146 dB. The microphone is settled at 75° horizontal angle to the work piece. The arc sound is filtered by the MC104 signal conditioner which has a steep dropping characteristics. The major parameters of the microphone are shown in Table 1. All the data collection and system software are programmed using Visual C++. The signal was processed by the Matrix laboratory platform.

Figure 3 shows three different penetration states beyond the equal arc length situation. In the figure the first row represents the image of welding surface, the second row shows the backside of the welding piece while the third row contains images captured during the welding process. As the welding is a process of gradual

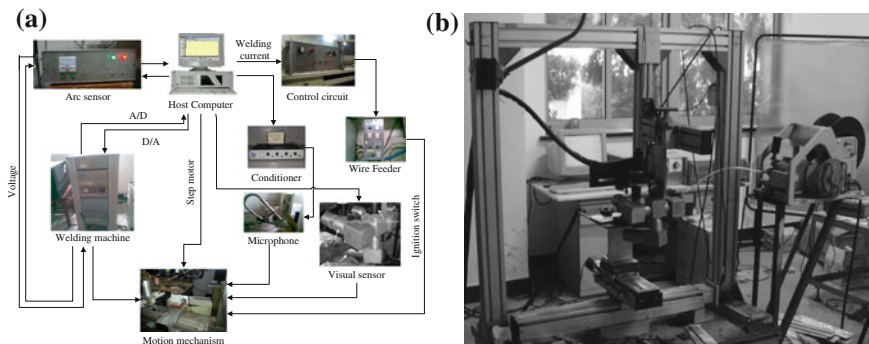
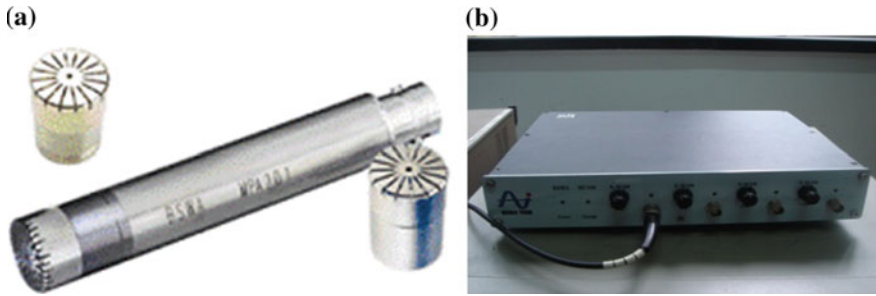


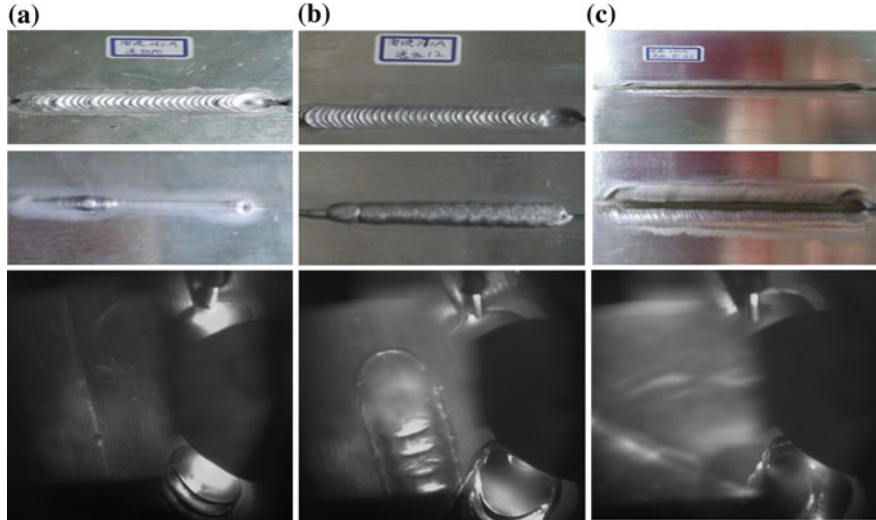
Fig. 1 a Components and communication of system, b real experiment system



**Fig. 2** Weld sound arc sensor: **a** microphone, **b** signal conditioner

**Table 1** Experiment conditions of arc height changed experiment

Parameter type	Value	Parameter type	Value
Impulse frequency (Hz)	2	Polar diameter $\phi$ (mm)	3.2
Peak current $I_p$ (A)	180	Duty ratio $\delta$ (%)	50
Base current $I_b$ (A)	45	Ar air flow L (l/min)	10
Wire feed speed $V_f$ (mm/s)	10	Arc height (mm)	3–6 mm
Welding speed V (mm/s)	4.5	Material type	Aluminum alloy LF6

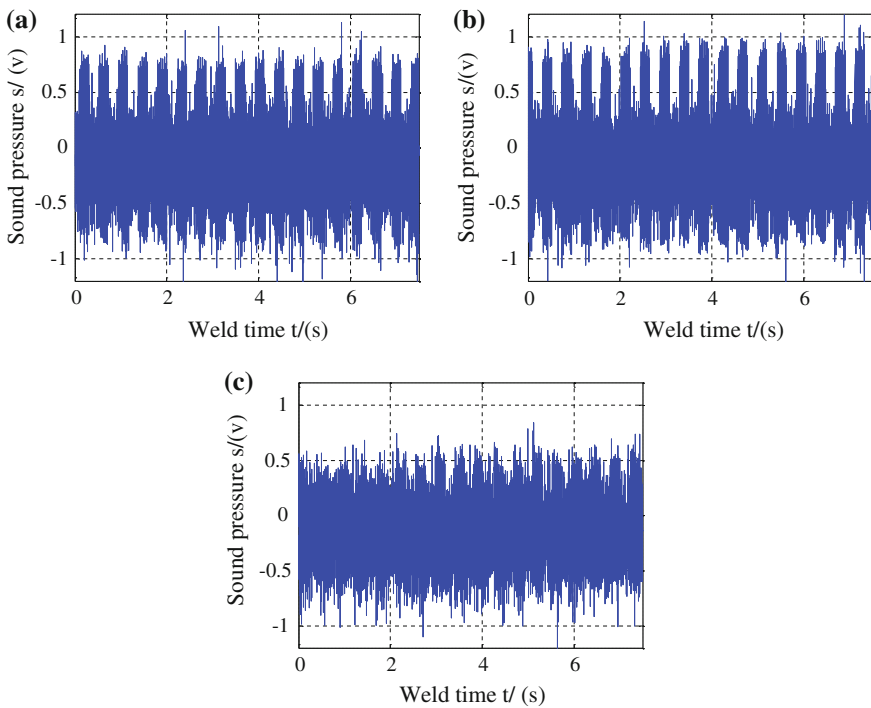


**Fig. 3** Three different penetration states: **a** partial penetration, **b** full penetration, **c** excessive penetration

penetration from base metal to fusion metal, so there are lots of intermediate states during the process. However, in order to study the properties of arc sound signal, it is necessary to simplify the definition of dynamic welding penetration state. So in this paper, three penetration states, i.e., partial penetration, full penetration and excessive penetration, are designed to be the research target. The arc sound signal is collected during the whole welding process and divided into three types of acoustic data. According to previous studies, the arc sound signal is composed of actual original sound signal and noise signal. In this paper, the generation mechanism of arc sound source is not considered for the study of arc sound channel of GTAW dynamic welding process.

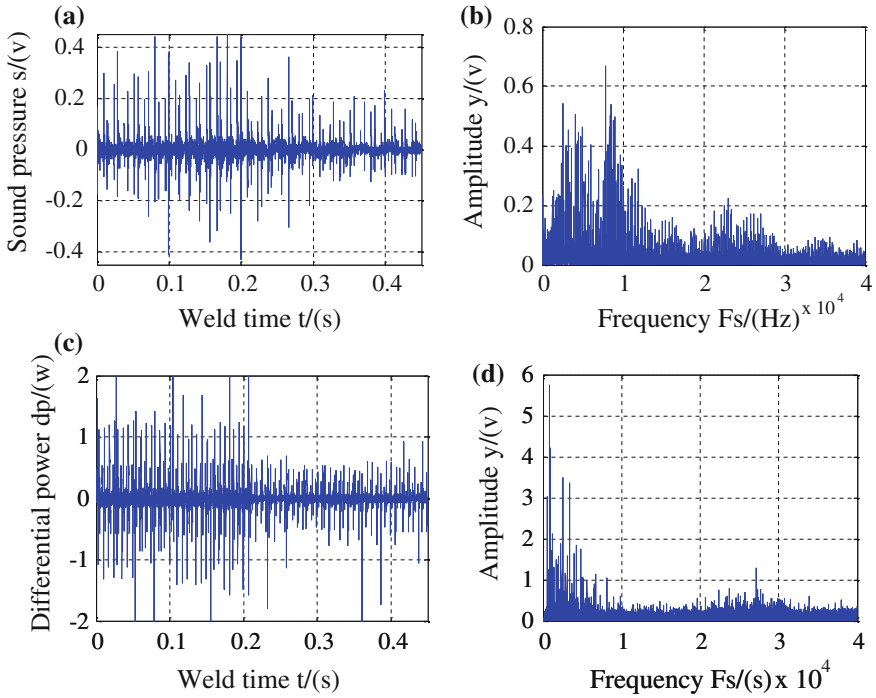
### 3 Analysis of Generation Mechanism for Sound Channel

According to the amplified figure shown in Fig. 4, the pulse characteristic of the pulse GTAW leads to pulse-like arc sound signals. From the figure, it can be seen that the positive arc sound pressure is larger and abundant than the negative arc sound pressure. The image shows that the time domain feature of arc sound signals



**Fig. 4** The time-domain waveform of different penetration state: **a** partial penetration, **b** full penetration, **c** excessive penetration





**Fig. 5** The contrast of frequency feature between arc sound and differential power: **a** arc sound signal, **b** the frequency feature of arc sound, **c** differential power, **d** the frequency feature of differential power

during different penetration are different from each other. The acoustic signal of partial penetration is similar to that of the full penetration. They both have the clear pulse characteristics. However, the excessive penetration gets a lot of noise during the collection process. The reason of why the signal of excessive penetration has more noise had been discussed in various papers [12–15]. It was found that when the weld joint has been excessively welded, the material stability in welding joint has been broken by the arc blow force. The sound source energy of arc sound signal is unstable to express the feature of pulse exchange and the deforming metal leads to the generation of welding noise. The sound pressure of excessive penetration is also less than those of the other two states, so the excessive penetration state is the most easily identified state of the three penetration states. The time-domain waveform shows the characteristic of the sound source for arc sound signal. This paper focuses on the analysis of sound channel of the arc sound. The analysis about the sound source of arc sound signal can be found in [14, 15].

As we know from previous studies, the arc energy is the key factor for the generation of arc sound signal, and the arc power determines the arc energy. This means that the arc power should be reflected by the features of arc sound signals. In Fig. 5, the sound signal and the differential power signal for one pulse cycle have

been presented. It can be seen that there are clear differences between the sound signals (Fig. 5a) and the arc differential power (Fig. 5c). The arc sound contains lots of noise (Fig. 5b) and the arc power (Fig. 5d) has a very clear pulse characteristic in the time-domain waveform. It can be concluded from the frequency-domain analysis that arc sound signal contains lots of formant and the formant distributes in every frequency band. However, the arc power doesn't have much formant in frequency-domain analysis.

Thus, it can be concluded that the arc sound signal is not only influenced by the changing of sound source, but also affected by other factors. It can be assumed that there is a modulating sound channel system existed in arc sound production process. The modulating sound channel is mainly determined by the formant of the arc sound channel. The arc sound channel can be considered as a conical cavity covered by shielding gas atmosphere between the tungsten electrode and the welding plate. Its geometrical morphology and properties are caused by the behavior of welding arc, protective gas velocity and density of medium. Changing of these factors could impact the resonant frequency of the arc sound channel. The resonant frequency could influence the frequency feature of arc sound signal, some parts of frequency information are reduced and some of them are amplified. Finally it turns out to be the actual arc sound which has been actually collected.

## **4 Establishing the Mathematical Model Based on Linear Prediction Cepstrum Coefficients**

In the process of feature extraction for speech recognition, a rectangular cepstrum window is usually used to extract the feature of a sound channel, like cepstrum coefficients. The low frequency part is considered as the system function of sound channel, and the high frequency part can be used to distinguish the voiceless sound and the dull sound. Cepstrum analysis is used for genetic testing and resonance peak detection in speech recognition. Based on the above analysis of arc sound channel generation, since there are lots of resonant frequencies generated in the sound channel through the arc energy modulation, the formant also happens during the process. Thus, the cepstrum analysis method is suitable for the estimation of the characteristic of the arc sound channel.

### ***4.1 A Mathematical Model Based on Cepstrum Analysis***

In the processing of speech recognition, the sound is divided into two kinds of voices according to different time-domain and frequency-domain features: they are voiceless sound and voiced sound. The voiceless sound is considered as a linear

time-invariant system stimulated by a random noise. And the voiced sound is considered as a linear time-invariant system stimulated by a periodical impact string. The arc sound signal of a pulse TIG welding is a kind of vibration signal generated by pulsed and periodical stimulation. Thus, it could be estimated, and the equivalent model can be obtained according to the known mathematic model of the voiced sound. So the arc sound signal can be described as:

$$s(n) = p(n) * g(n) * v(n) * r(n) = p(n) * h_v(n) \tag{4.1}$$

Among them,  $p(n)$  represents the periodical impact train, the period is  $N_p$ ,  $v(n)$  represents the impulse response of the sound channel,  $r(n)$  stands for the radiation impulse response during the sound spreading process,  $g(n)$  stands for the glottis wave,  $h_v(n)$  stands for the impulse response of the linear system during welding atmosphere, the  $*$  is the convolution calculation. And,

$$p(n) = \sum_{r=0}^{M-1} \delta(n - rN_p) \tag{4.2}$$

So,

$$s(n) = \sum_{r=0}^{M-1} a_r \delta(n - rN_p) \tag{4.3}$$

The  $h_v(n)$  could be considered as the convolution of the glottis wave  $g(n)$ , impulse response of sound channel  $v(n)$  and the radiation impulse response  $r(n)$ . The model of sound channel could be described as:

$$h_v(n) = g(n) * v(n) * r(n) \tag{4.4}$$

After the Z transform, it can be described as:

$$H_v(z) = G(z) \cdot V(z) \cdot R(z) \tag{4.5}$$

The Z transform is used to the sound signal  $s(n)$ , result show as the follow:

$$\begin{aligned} S(n) &= \sum_{n=-\infty}^{\infty} s(n)z^{-n} = \sum_{n=-\infty}^{\infty} a_r z^{-m} \\ &= a_0 \left[ 1 + \frac{a_1}{a_0} z^{-N_p} + \dots + \frac{a_M}{a_0} z^{-MN_p} \right] \\ &= a_0 \prod_{r=0}^M [1 - a_r (z^{N_p})^{-1}] \end{aligned} \tag{4.6}$$

If the pole zero model is used to describe the sound channel impulse train, as

$$X(z) = |A| \frac{\prod_{k=1}^{m_i} (1 - a_k z^{-1}) \prod_{k=1}^{m_o} (1 - b_k z^{-1})}{\prod_{k=1}^{p_i} (1 - c_k z^{-1}) \prod_{k=1}^{p_o} (1 - d_k z^{-1})} \tag{4.7}$$

Deconvolution is the key method for analysis of sound signal, and also it could get the impulse response  $h_v(n)$  reflecting the sound channel. According to the complex cepstrum analysis, the complex cepstrum of  $x(n)$  could be expressed as:

$$\hat{x}(n) = \frac{1}{2\pi} \int_{-\pi}^{\pi} \hat{X}(e^{j\omega}) e^{j\omega n} d\omega \tag{4.8}$$

Put the results of Z transform (4.5) into (4.6), and ignore the negative part. The complex cepstrum could also be expressed as:

$$\hat{x}(n) = \begin{cases} \ln[A], & n = 0 \\ \sum_{k=1}^{N_i} \frac{c_k^n}{n} - \sum_{k=1}^{M_i} \frac{a_k^n}{n}, & n > 0 \\ \sum_{k=1}^{M_o} \frac{b_k^{-n}}{n} - \sum_{k=1}^{N_o} \frac{d_k^{-n}}{n}, & n < 0 \end{cases} \tag{4.9}$$

Among them,  $|a_k|, |b_k|, |c_k|, |d_k|$  are all less than 1, so  $|\hat{h}_v(n)|$  is gradually decreasing as the  $n$  is getting bigger.

For the arc sound signal, the pulse excitation signal and the complex cepstrum are both periodic impulse string with interval  $N_p$ . It is difficult to clearly separate the sound channel  $h_v(n)$  from  $s(n)$  because they are convolutions between the periodic impulse signal and  $h_v(n)$  in time-domain analysis. They would have an aliasing effect between each cycle. However, it is easier to get the sound channel  $h_v(n)$  in the complex domain because the convolution becomes addition between  $h_v(n)$  and the impulse signal. The periodical motivation can be removed using the complex cepstrum window with a width less than  $N_p$ . After the valuation coefficient is calculated, the  $h_v(n)$  can be obtained by convolution of the characteristic system. The cepstrum window can be defined as:

$$l(n) = \begin{cases} 1, & |n| < n_0 \\ 0, & |n| \geq n_0 \end{cases} \tag{4.10}$$

The rectangular window will lead to the smooth information loss due to its special characteristic like using the same threshold value for different frequency band signal. So a half sine function is chosen for smoothing which is small at both ends and big in the middle. This weighted cepstrum window can be described as:

$$l(n) = \begin{cases} |\sin(\pi n/n_0)|, & |n| < n_0 \\ 0, & |n| \geq n_0 \end{cases} \quad (4.11)$$

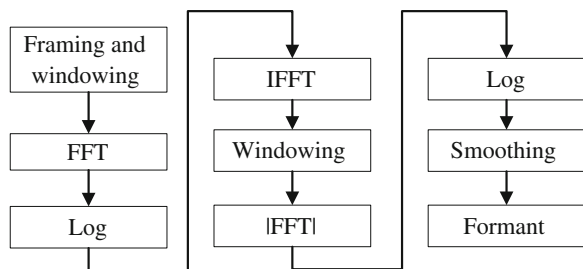
Finally, the weighted cepstrum coefficients can be got, the low parts of them can be considered as a function of the sound channel system.

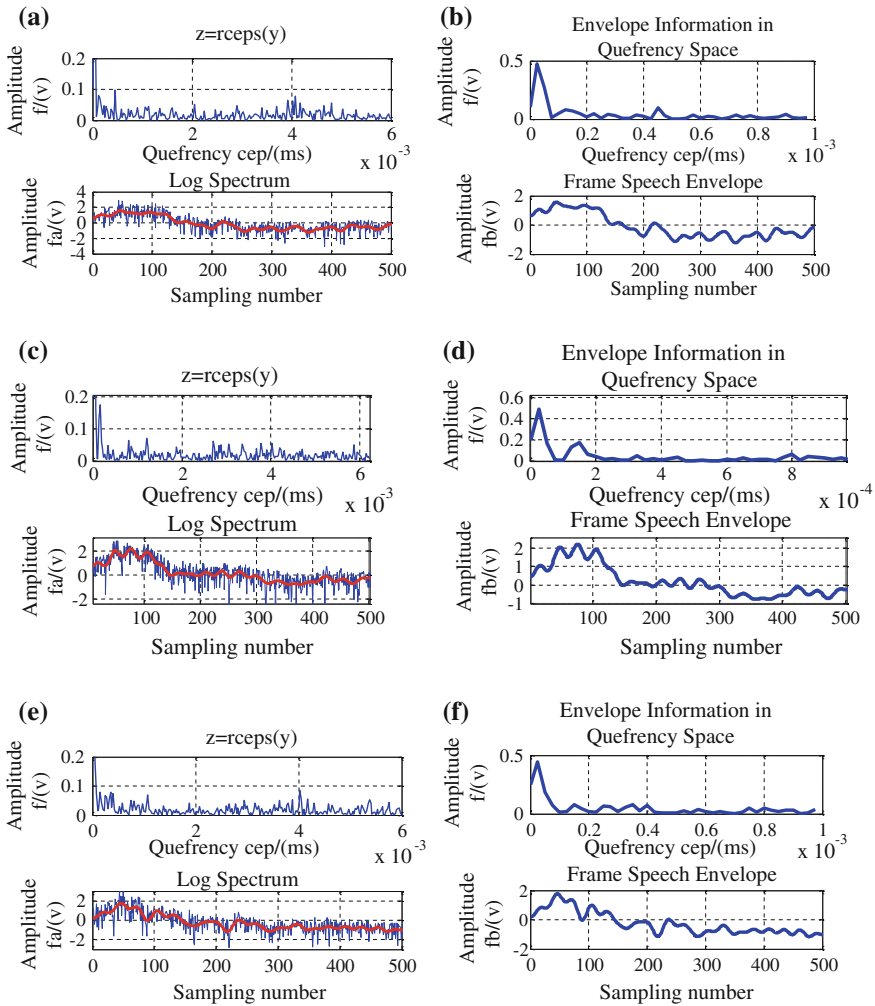
### 4.2 Cepstrum Coefficients Model of the Arc Sound Signal

The arc sound signal of the pulse GTAW welding is composed of sound source incentive and sound channel system. The model of sound channel could be expressed as formula 4.4. Sound channel is determined by the formant feature, and the formant is contained in the spectral envelope. Thus, the key point of sound channel coefficient is to estimate the natural speech spectral envelope. Generally speaking, the maximum in spectral envelope is to separate the formant frequency spectrum. The cepstral analysis is the most popular method to extract the formant feature coefficients. The low time part of cepstral contains the main feature. Thus, the selection of a low time window is achieved by cepstral analysis, then the smoothed output signal is processed using a logarithm function. This spectrum function is corresponding to the resonant structure of the arc sound, which means that the peak value is corresponding to the formant frequency. As long as the smoothed logarithmic spectrum peak of arc sound signal can be located, there will be the formant coefficient. The flow chart of ceptrum analysis is shown in Fig. 6.

The results of cepstrum analysis for three different penetration states are shown in Fig. 7. Firstly, the cepstrum coefficients of different arc sound from three penetration states were collected, as shown in Fig. 7a, c, e. The cepstrum analysis could separate the impulse sound signal from the spectral envelope of sound channel formant through the logarithmic and quadratic transformation. Based on the characteristic of the cepstrum, the window is used for extracting the feature signal and achieving the DFT (Discrete Fourier Transform?) transform of arc sound signal. Finally the discrete spectrum curve was obtained. It could reflect the dynamic features well of the resonance peak, due to the decreasing of the influence from the sound source excitation.

Fig. 6 The flow chart of cepstrum analysis





**Fig. 7** The cepstral coefficient and spectral envelope of arc sound signal for three penetration state: **a** the cepstrum and logarithmic spectrum for partial penetration, **b** the spectral envelope for partial penetration, **c** the cepstrum and logarithmic spectrum for full penetration, **d** the spectral envelope for full penetration **e** the cepstrum and logarithmic spectrum for excessive penetration, **f** the spectral envelope for excessive penetration

It can be concluded from the figure of cepstral coefficient and spectral envelope during different penetration state in Fig. 7 that different penetration has different formant distribution and special characteristic. The spectral envelope of the full penetration state has the best smoothness and uniformity, the distribution of the peak frequency is average, the stiffness of peak value is more stable. It is all because

that the full penetration state is a stable and balanced state?. In this state, the shape of the weld pool remains unchanged which means the sound channel system is a smooth and stable cavity. So the spectral envelope is the most stable and periodic. And the spectral envelope of the excessive penetration state has noisier sound signals. The noise distribution is random, the peak value is distributing without periodic. Because the welding leakage and over collapse happened during excessive penetration, so the sound channel system has been destroyed during the welding process and could not have the resonant frequency. The partial penetration state has the least formant in spectrum envelope. Although the curve is very smooth, however it can't form the resonance due to the partial fusion of weld pool. So the semisolid and semifluid weld pool dose not lead to the generation of resonant. Finally, it means the cepstrum coefficient analysis could reflect the difference between different penetration states. Therefore, the coefficient could be used to form the model of sound channel system.

## 5 Conclusion

In this paper, the sound channel of the arc sound signal was analyzed and established through cepstrum analysis. The results showed that:

- (1) The hypothesis of sound channel for arc sound signal has been proved through the comparison between the sound source signal and the original arc sound signal.
- (2) The generation and mechanism of sound channel during GTAW welding could be considered as a cave composed of the shielding gas between the tungsten electrode and the weld plates.
- (3) The equivalent model based on cepstral coefficient is proposed. The sound channel is expressed by complex cepstral coefficient through Z transform. The cepstral coefficient and spectral envelope of three different penetration states have been identified.
- (4) The results of cepstral coefficient and spectral envelope show that the models can clearly distinguishing the different penetration state of welding process. The sound channel for normal weld is more stable and well-regulated than the abnormal weld. Thus, the cepstral coefficient for sound channel is proved to be an effective feature for the quality identification of dynamic welding process.

**Acknowledgement** This work is supported by the National Natural Science Foundation of China under the Grant No. 61401275, 61374071 and the Australian Research Council under project ID LP0991108 and the Lincoln Electric Company Australia. This work is also partly supported by the National Natural Science Foundation of China under the Grant No. 51405298.

## References

1. Chen S (2007) On the key technologies of intelligentized welding robot. In: *Robotic welding, intelligence and automation*. Springer, Berlin, pp 105–115
2. Tarn TJ, Chen SB, Zhou CJ (2007) *Robotic welding, intelligence and automation*. Springer, Berlin
3. Dinham M, Fang G (2013) Autonomous weld seam detection and localisation using eye-in-hand stereo vision for robotic arc welding. *J Robot Comput Integr Manuf* 29(5):288–301
4. Dinham M, Fang G (2013) Detection of fillet weld joints using an adaptive line growing algorithm for robotic arc welding. *J Robot Comput Integr Manuf* 30:229–243
5. Chen SB, Wu L, Wang QL (1997) Self-learning fuzzy neural networks for control of uncertain systems with time delays. *IEEE Trans Syst Man Cybern-Part B Cybern* 27(1):142–148
6. Ma YZ, Jin H, Liang WD, Zhang PX (2003) Signal characteristics of short-circuit GMAW arc sound and its formation mechanism. *J Gansu Univ Technol* 29(1):11–14
7. Wang JF, Yu HD, Qian YZ et al (2011) Feature extraction in welding penetration monitoring with arc sound signals. *Proc Inst Mech Eng Part B J Eng Manuf* 225(9):1683–1691
8. Wang JF, Chen B, Chen HB, Chen SB (2009) Analysis of arc sound characteristics for gas tungsten argon welding. *Sens Rev* 29(3):240–249
9. Sánchez Roca A, Carvajal Fals H, Blanco Fernández J et al (2009) Stability analysis of the gas metal arc welding process based on acoustic emission technique. *Weld Int* 23(3):173–180
10. Liu LJ, Yu ZW, Lan H, Gao HM (2010) Separating technology of arc sound noise based on ICA in MIG welding. *Trans China Weld Inst* 31(4):53–58
11. Wang JF, Yu HD, Qian YZ et al (2011) Feature extraction in welding penetration monitoring with arc sound signals. *Proc Inst Mech Eng Part B J Eng Manuf* 225(9):1683–1691
12. Lv N, Zhong J, Wang J et al (2014) Automatic measuring and processing system of audio sensing for real-time arc height control of pulsed GTAW. *Sens Rev* 34(1):51–66
13. Lv N, Zhong J, Chen H, et al (2014) Real-time control of welding penetration during robotic GTAW dynamical process by audio sensing of arc length. *Int J Adv Manuf Technol* 1–15
14. Lv N, Xu Y, Zhang Z et al (2013) Audio sensing and modeling of arc dynamic characteristic during pulsed Al alloy GTAW process. *Sens Rev* 33(2):7–7
15. Lv N, Xu Y, Zhong J et al (2013) Research on detection of welding penetration state during robotic GTAW process based on audible arc sound. *Ind Robot Int J* 40(5):8–8



# Online Diagnosis of Joints Quality in Resistance Spot Welding for Sedan Body

Peng-Xian Zhang, Zhi-Fen Zhang and Jian-Hong Chen

**Abstract** The manufacture and assembly of sedan body are primarily accomplished by resistance spot welding (RSW). During the welding process, substandard solders are caused by some random failure factors. In this paper, in order to evaluate the quality of solders a secondary evaluation method was put forward based on electrode displacement signals. Firstly, characteristic parameters of singularity signals were extracted by analyzing the electrode displacement signal of normal state and fault state welding. Then, on-line diagnosis of fault state appearing in the welding process was achieved based on a first-class SVM (support vector machine) recognition model for singular solder joints. Secondly, characteristic parameters as the representation of singularity joints' quality were extracted from the electrode displacement signal of fault state welding. Then, a second-class SVM model of solder joints quality evaluation was established based on shear strength and indentation depth of solder joints. Further, the quality of singular solder joint was identified. Its verifying results shows that the accuracy rate of the evaluation model come up to 97.1429 %.

## 1 Introduction

Resistance spot welding (RSW) is extensively used for the assembly of car bodies, during which the formation of nugget is easily affected by random factors that can result in the unstable quality of welds. At present, to develop a quality evaluation method which is nondestructive, low-cost and online for every spot weld has

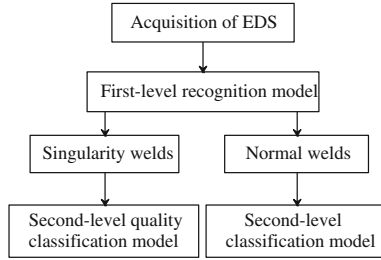
---

P.-X. Zhang (✉) · J.-H. Chen

Key Laboratory of Non-ferrous Metal Alloys, The Ministry of Education,  
Lanzhou University of Technology, Lanzhou 730050, China  
e-mail: 1816997668@qq.com

Z.-F. Zhang

Institute of Welding Engineering, Material Science and Engineering,  
Shanghai Jiao Tong University, Shanghai 200240, China  
e-mail: zzf919@sjtu.edu.cn



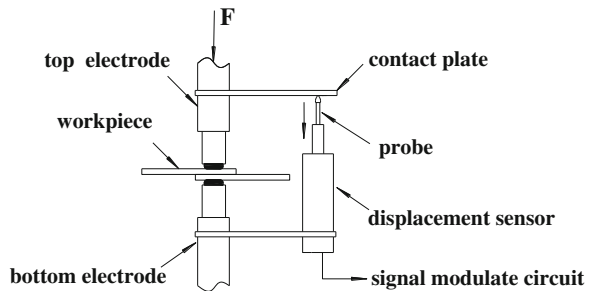
**Fig. 1** Diagram of the quality evaluation method based on signal separation

become a hot technical issue [1–7]. However, there are few reports about decoupling of quality information which is suitable for machine to learn by itself. This paper proposes a two-level evaluation method called Quality Evaluation based on Fault Diagnosis (QEFD) for the RSW production site of automobile body assemblies. Firstly the fault condition of weld process is diagnosed in-line based on the electrode displacement signal. Then the quality state of singularity weld is further evaluated. Figure 1 shows the diagram of the quality evaluation method based on signal separation.

## 2 Experimental Setup

In this paper, the pedestal spot welding machine is used to weld mild steel with the size of  $100 \times 30 \times 1$ (mm). The Electrode Displacement Signal (EDS) was acquired based on the direct-current linear variable differential transformer (DC-DC LVDT) displacement transducer which was installed as shown in Fig. 2. The output value of EDS was calibrated to zero before welding, and then sent into the signal modulate circuit for A/D conversion, signal amplification etc. At last, the curve of EDS was monitored in a pc through the transmission and communication of a data collecting card [8, 9].

**Fig. 2** Installation diagram of displacement sensor



During the process of RSW, the quality of the welds can be quite unstable due to some fault factors [10]. In this paper, normal welding process and fault welding process, such as electrode axial dislocation, work piece warping, poor conductivity, contaminants, voltage fluctuation were designed to monitor the quality of every weld on-line. Welding current is 4 kA, welding time is 30 cycles, electrode force is 0.4 MPa and the diameter of the working face of electrode tip is 6 mm.

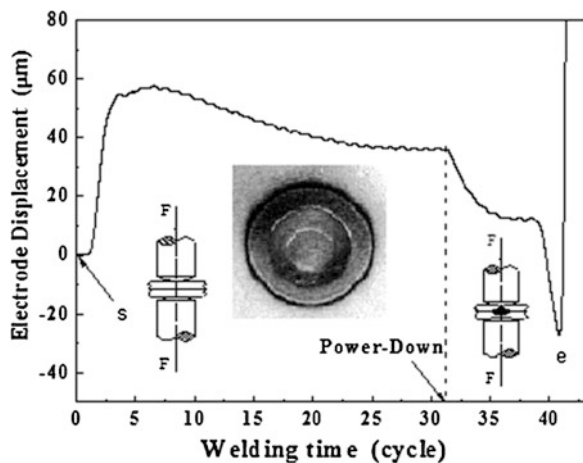
### 3 Results and Discussions

#### 3.1 Analysis of Real-Time Signals

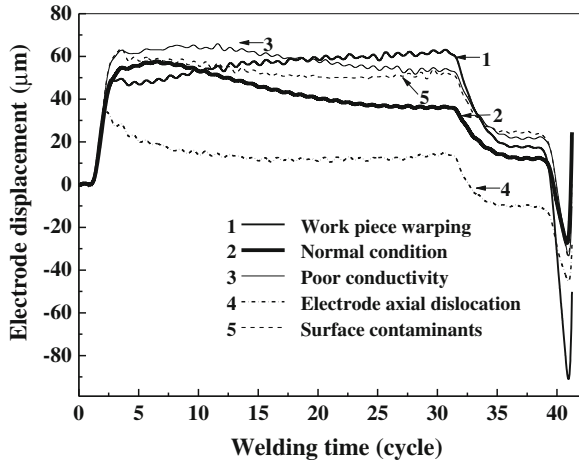
After the EDS were captured in real-time, these original signals were pretreated through low-pass filtering and wavelet denoising based on Matlab. The EDS curves showed different feature in different welding condition.

As shown in Fig. 3, the normal welding process can be divided into five stages, e.g., Pre-compression, Nugget Formation, Nugget, Plastic Ring Expansion, Steady and Cooling Stage. After the whole five stages, the weld with a certain depth indentation was obtained. As shown in Fig. 3, point “s” presents the condition of the work piece Pre-compression before the welding, while point “e” was the end for the welding. So the displacement value of point e,  $S_e$ , can reflect the size of indentation depth as shown in the picture of weld with indentation. Figure 4 shows some typical EDS curves on different fault welding conditions. Compared to the EDS curve of the normal weld, the EDS curves of these singularity welds display a great deal of singularity in certain stages. For instance, to warping work pieces the contact area was less than the normal condition, thus there was less metal molten. In

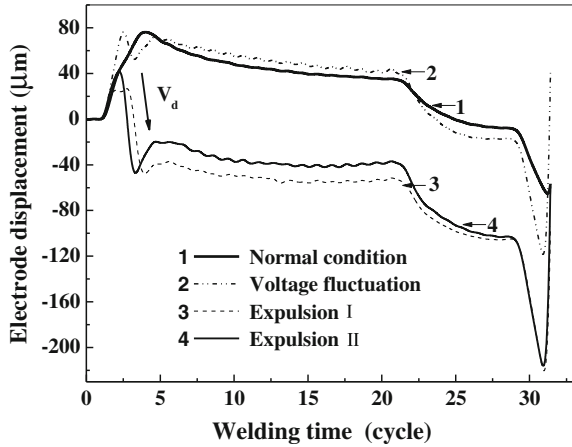
Fig. 3 The EDS curve of normal welding condition



**Fig. 4** EDS curves of singularity welds



**Fig. 5** EDS curves of expulsion welds



stage II, the peak value of EDS didn't occur. After that as the contact area enlarged, there was more and more metal heated to expand. Hence, the value of EDS kept increasing until the end of welding. When the work piece surface had poor conductivity or contaminants, the peak value of the EDS curves were above the normal value due to the greater metal expansion caused by the uneven heating. Besides, the drop value in the nugget expansion stage also decreased as a result of the formation of smaller nugget.

In Fig. 5, when the expulsion occurred, some liquid metal sprayed out of the abutted surface of work pieces, which caused the significant drop of EDS curve. After that the EDS curve rose again as the remaining metal experienced second heat process. The difference between the two expulsions was that the extent of metal expansion in the second heat process.

### 3.2 Identification of Singular Welds

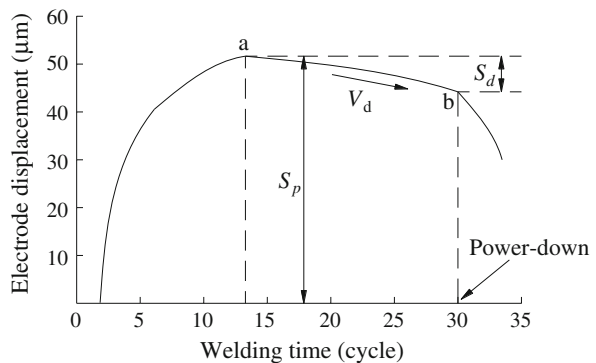
#### 3.2.1 Extraction of Characteristic Parameters

There is abundant information which can present the different welding process in the EDS curve.

Figure 6 shows the extraction of characteristic parameters in the EDS curve. It has two inflections designated a and b. Point a is the peak of EDS curve. It can provide an indication of the value of molten liquid metal and the expansion extent. Point b occurs when the power supply ends. The difference value,  $S_d$ , between the ED value of a,  $S_p$ , and ED value of b can indicate the drop value of EDS curve during the time of a–b. Then, the drop rate is  $V_d = S_d/(t_b - t_a)$ ; the parameter extraction of  $V_d$  for expulsion welds is showed in Fig. 6. Their drop rate,  $V_d$ , was extracted from the first heat process during which expulsion occurred. So did the welds of voltage fluctuation. The variation range of  $V_d$  extracted from normal welds and singularity welds is showed in Table 1.

Further the ED peak value of a,  $S_p$ , was extracted as the characteristic parameters in order to ensure the accuracy of identification. Figure 7 showed the Scatter distribution diagram of normal welds and singularity welds based on the two characteristic parameters  $V_d$  and  $S_p$ . It can be seen from the figure that normal welds and singularity welds distributed in different areas.

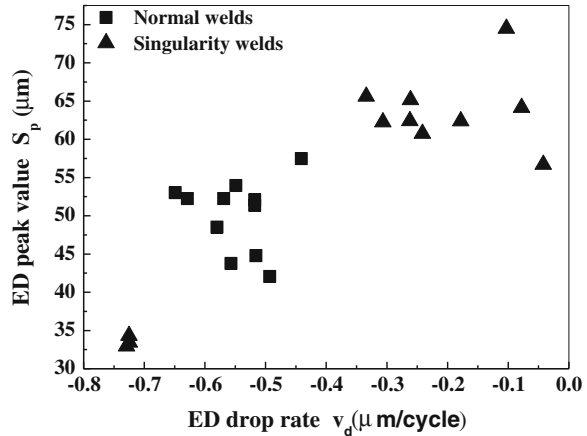
**Fig. 6** Feature extraction from EDS curve



**Table 1** Variation range of  $V_d$

Type	Drop rate $V_d$ ( $\mu\text{m}/\text{cycle}$ )
Normal condition	-0.44 to -0.65
Surface contaminants	-0.17 to -0.31
Electrode axial dislocation	-0.7246 to -0.729
Poor surface conductivity	-0.261 to -0.334
Work piece warping	-0.04 to -0.10
Voltage fluctuation	-1.85 to -2.69
Expulsion I and II	-27.13 to -63.77

**Fig. 7** Scatter distribution of different welds



### 3.2.2 SVM Identification First-Level Model of Singular Welds

Support Vector Machine (SVM) is a pattern recognition method based on statistical learning theory, and performs the unique advantage in solving some pattern recognition problems such as small sample, nonlinear and high dimensional [11, 12]. The Performance of SVM is mainly affected by the kernel parameters and the error penalty factor  $C$ , also can get good generalization ability only when the two match each other well [13, 14]. After repeated training and simulation experiments the parameters  $c = 5$  and  $\gamma = 2$  were obtained by cross footing tests. The Libsvm software package based on Matlab was used in this paper, and can easily and quickly achieve the SVM pattern recognition and regression, also can solve multi-class pattern recognition problems [15, 16]. The characteristic parameters  $S_p$  and  $V_d$  extracted from the EDS curve of every weld were chosen as input vectors, and the output values were 1,  $-1$  representing the normal welds and singularity welds respectively. Table 2 shows the typical training sample of SVM model. The total data set has 200 pairs and is randomly split into two subsets, with 170 pairs being used to provide the training data, and the others being used to provide the verification data that would provide an indication of how successful the SVM model was in separating the normal welds and singularity welds.

Table 3 shows the different verification results on the condition of different kernel function. As we can see, when the RBF kernel was chosen for the model, it can obtain the highest accuracy 96.7742 %, the smallest Mean squared error 0.129032, and the squared correlation coefficient is the most close to 1, in which a singularity weld on the condition of electrode axial dislocation was judged as a normal one mistakenly.

**Table 2** Training samples of first-level SVM model

Sp (μm)	Vd (μm/cycle)	Output	Sp (μm)	Vd (μm/cycle)	Output
57.476	-0.441	1 (Normal welds)	34.645	-0.729	-1 (Singularity welds)
52.074	-0.518		63.1537	-0.279	
53.942	-0.549		64.1526	-0.281	
48.5212	-0.58		56.1075	-0.0903	
51.3723	-0.518		61.1231	-0.083	
52.2324	-0.564		70.603	-2.293	
53.0297	-0.649		67.525	-2.382	
52.2463	-0.627		56.427	-30.125	
43.7595	-0.557		55.729	-55.131	
44.7816	-0.516		56.661	-64.142	

**Table 3** Verification results of first-level SVM model with different kernel function

Kernel function	Accuracy (%)	Mean squared error	Squared correlation coefficient
Linear	87.0968	0.516129	0.528008
Polynomial	87.0968	0.516129	0.528008
RBF	96.7742	0.129032	0.865801
Sigmoid	67.7419	1.29032	Invalid value

### 3.3 Classification of Singular Welds Quality

In the present work, the quality level of a RSW joint is estimated from its tensile shear strength and indentation depth. According to the quality requirements made by U.S. RWMA (Resistance welding machine Manufacturers Association) on the 1 mm thick mild steel plate, the shear strength of solder joint should be greater than 3.89 kN, while the indentation depth should be less than 20 % of the plate’s thickness [17, 18]. Table 4 shows the variation range of shear strength and indentation depth of welds in different fault welding condition, in which the shear strength of solder joints state can not meet the quality requirements when the work piece warpage occurred. Besides, the quality of the expulsion welds was both unqualified because its strength was extremely unstable, and its indentation depth value |Se| can not meet the quality requirements too. The quality state of other solder joints was qualified as shown in Table 4.

#### 3.3.1 Extraction of Characteristic Parameters

To further the quality of solder joints on the singular evaluation, selected from the electrode displacement curve parameters of the new features.

**Table 4** Shear strength, indentation depth of different welds

Type	Shear strength (kN)	Indentation depth  Se  (μm)	Outcome
Normal condition	4.75–5.02	29.5–44.277	Qualified
Surface contaminants	4.02–4.25	67.4–85.271	
Electrode axial dislocation	4.12–4.44	46.5–70.896	
Poor surface conductivity	4.58–4.80	76.4–82.667	
Voltage fluctuation	4.30–4.60	45.8–51.133	
Work piece warping	2.94–3.42	56.1–86.671	Dis-qualified
Expulsion	2.87–5.32	153–280.79	

**Fig. 8** Diagram of the EDS curve

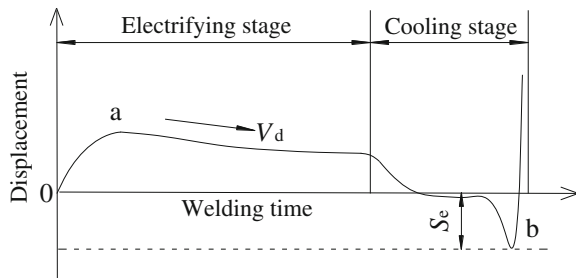


Figure 8 shows the extraction of characteristic parameters from the diagram of EDS curve. During the cooling stage, the surface indentation owning a certain depth was gained while the solder joint was formed under the die-casting power of electrode force. The depth value of indentation can be presented by the Se at the end of time. Combined with Figs. 2 and 3, the welds of different welding conditions had various values of Se. In addition, when the expulsion happened, the Se depth of surface indentation had a bigger value. Therefore, the value Vd and Se were extracted as the characteristic parameter.

### 3.3.2 SVM Classification Second-Level Model of Singular Welds

The characteristic parameters Vd and Se extracted from the EDS curve of every singularity weld were chosen as input vectors, and the output values were 1, -1 representing the qualified welds and unqualified welds respectively based on Table 2. Table 5 shows the typical training sample of SVM model. After repeated training and simulation experiments the parameters  $c = 5$  and  $\gamma = 2$  were obtained by cross footing tests. Table 5 shows the different verification results on the condition of different kernel function. As we can see, when the Polynomial kernel was chosen for the model, it can obtain the highest accuracy 97.1429 %, the smallest Mean squared error 0.114286, and the squared correlation coefficient is 0.888889, in which an unqualified weld of expulsion state II was judged as the qualified one mistakenly (Table 6).



**Table 5** Training samples of second-level SVM model

Vd (µm/cycle)	Se (µm)	Output	Vd (µm/cycle)	Se (µm)	Output
-0.729	-70.896	1 (Qualified)	-2.693	-48.125	-1 (Dis-qualified)
-0.725	-46.559		-1.83633	-44.281	
-0.7246	-68.798		-0.042	-61.113	
-0.262	-79		-0.078	-63.681	
-0.261	-76		-28.414	-153.032	
-0.334	-82		-27.137	-177.157	
-0.3065	-85		-40.346	-191.171	
-0.2414	-76		-42.772	-222.812	
-0.1782	-67		-63.769	-109.878	

**Table 6** Validation result of second-level SVM model

Kernel function	Accuracy (%)	Mean squared error	Squared correlation coefficient
Linear	85.7143	0.533333	0.571429
Polynomial	97.1429	0.114286	0.888889
RBF	94.2857	0.228571	0.794118
Sigmoid	57.1429	1.71429	Invalid value

## 4 Conclusion

From the present work the following conclusions can be drawn:

1. The EDS curve obtained showed a great deal of information about the growth and formation of weld nugget. Not only that, but it also captured some singularity changes when the fault weld condition occurred.
2. The singularity welds were separated from normal welds successfully by the SVM recognition first-level model established based on the characteristic parameters extracted from the EDS curve.
3. The quality of singularity welds was classified through the SVM evaluation second-level model based on the tensile shear strength and indentation depth of singularity welds.

## References

1. Gedeon SA, Sorensen CD, Ulrich KT et al (1987) Measurement of dynamic electrical and mechanical properties of resistance spot welding. *Weld J* 66(12):378–385
2. Dickinson DW, Franklin JE (1980) Characterization of spot welding behavior by dynamic electrical parameter monitoring. *Weld J* 59(6):170–176
3. Patange SR, Reddy GP (1985) Microprocessor-based resistance spot welding monitoring. *Weld J* 64(12):170–176

4. Dickson DW et al (1991) Analysis and development of a real-time control methodology in resistance spot welding. *Weld J* 70(12):339–351
5. Messler, RW Jr, Jou M (1995) Intelligent control system for resistance spot welding using a neural network and fuzzy logic. In: IEEE conference record-IAS annual meeting
6. Javed MA, Sanders SAC (1991) Neural networks based learning and adaptive control for manufacturing systems, IEEE, pp 242–246
7. Martín O, López M, Martín F (2007) Artificial neural networks for quality control by ultrasonic testing in resistance spot welding. *J Mater Process Technol* 183:226–233
8. Jou M (2003) Real time monitoring weld quality of resistance spot welding for the fabrication of sheet metal assemblies. *J Mater Process Technol* 132:102–113
9. Cullen JD\*, Athi N, Jader M.AI, Johnson P, Shamma'a A.I.AI, Shaw A, El-Rsheed MA (2008) Multisensor fusion for online monitoring of the quality of spot welding in automotive industry. *Measurement* 41:412–423
10. Hao M, Osman KA (1996) Development in characterization of resistance spot welding of aluminum. *Weld J* 75(1):1–8
11. Cristianini N, Shawe-Taylor J (2008) An introduction to support vector machines and other kernel—based learning methods. Publishing House of Electronics Industry, Beijing, vol 38 (12), pp 66–69, 82–128
12. Fan RE, Chen PH, Lin CJ (2005) Working set selection using second order information for training support vector machine. *J Mach Learn Res* 6:1889–1918
13. Chang CC, Hsu CW, Lin CJ (1999) The analysis of decomposition methods for support vector machines. In: proceeding of the workshop on support vector machines, sixteenth international joint conference on artificial intelligence (IJCAI 99)
14. Hsu CW, Lin CJ (2002) A simple decomposition method for support vector machines. *Mach Learn* 46:291–314
15. Chang CC, Lin CJ (2001) LIBSVM: a library for support vector machines. Software available at <http://www.csie.ntu.edu.tw/~cjlin/libsvm>
16. BurgesC JC (1998) A tutorial on support vector machines for pattern recognition. *Data M Know IDisc* 2(2):121–167
17. Cho HS, Rhee S (2003) Experimental study of nugget formation in resistance spot welding. *Weld J* 82(4):195–200
18. Özyürek D (2008) An effect of weld current and weld atmosphere on the resistance spot weld ability of 304 Austenitic stainless steel. *Mater Des* 29:597–603

# A Low-Cost Vision System for Open Arc Welding Based on Multi-exposure

Xiang Luo, Zong-Yi Wang and Chun-Bo Jia

**Abstract** In order to get real-time visual information about the extremely bright weld arc and the neighboring dark areas in the open arc welding process, a low-cost vision system is proposed. The vision system contains three main components: a single off-the-shelf CCD/CMOS digital camera, a welding glass and an IPC (Industrial Personal Computer). A software-based method of capturing multi-exposure images is investigated; it changes exposure gain and shutter time by sending exposure parameters through PC program. By using software trigger method, the system captures sets of two exposures, such as “dark”, “light”, repeatedly. To obtain an image with sufficient details of the weld process, a simple and little time-consuming algorithm which adds every two continuous multi-exposure images is discussed. The approach can render videos of 640 by 480 pixel resolution at up to 22 frames per second.

## 1 Introduction

Welding plays an important role in modern industry and the open arc welding has been the dominant process for many years. However, the majority of arc welding has still been made manually or semi-automatically. Most operators who control and adjust welding robot have to observe the welding process in the direct weld area which is typically too congested or too dangerous. This problem can be solved effectively by using a vision system that can capture all the features which are necessary for the operators.

---

X. Luo (✉) · Z.-Y. Wang  
College of Automation, Harbin Engineering University (HEU), Harbin 150001  
People's Republic of China  
e-mail: helloluoxiang@163.com

C.-B. Jia  
Harbin Xirobot Co. Ltd., Harbin 150070, People's Republic of China

Many researchers have been motivated to develop vision systems for remote control by using cameras. Nevertheless, the interference of the high intensity arc light often prevents the acquisition of satisfactory. The reason is that the weld environment contains a dynamic range that is far greater than can be captured with any common industrial camera sensor. To address this problem, researchers have developed monitoring systems in two ways: to decrease the dynamic range of the welding environment, and/or to increase dynamic range of the camera.

The use of auxiliary light source to illuminate the weld pool region and narrow band pass filter in front of the camera [1, 2], hence reduce the dynamic range of the weld area, has been investigated. However, it is preferable not to involve auxiliary light sources for safety reason in industrial environment. Using narrow band filter is not practical in some workshop because the center wavelength of the filter should be carefully-selected according to the different welding types and conditions.

There are also many ways to improve the dynamic range of the camera. A HDR Camera with image sensor of 120 dB dynamic range is utilized in online monitoring applications [3]. Another Camera can be set into the HDR mode in which it cycles between 4 user-defined shutter and gain settings, applying one gain and shutter value pair per frame [4]. This allows images representing a wide range of shutter and gain settings to be collected in a short time. However, these cameras are expensive and difficult to use widely.

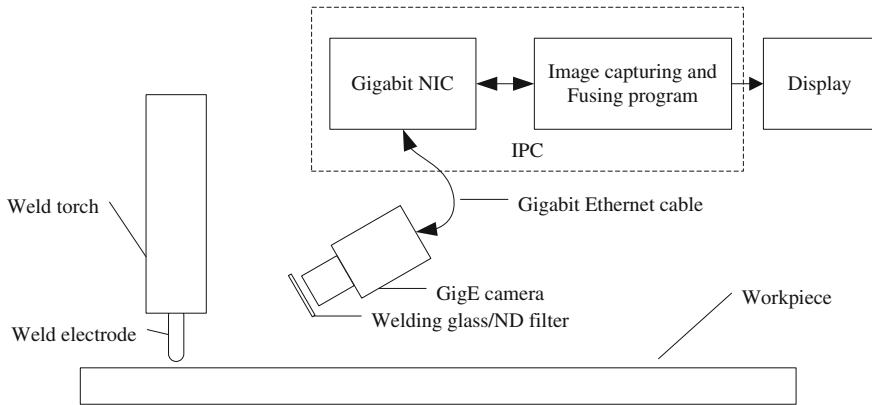
In this paper, the focus is to get the details of the welding arc and the area nearby using a low-cost solution. Our solution is based on the idea of the camera with the HDR mode mentioned above. Alternatively, we use off-the-shelf digital cameras instead of high-priced cameras with the HDR mode or special hardware designed cameras to get the multi-exposure images, and as we know the off-the-shelf digital camera is low-cost and widely used. On the software side, a real-time algorithm is proposed to get the resulting images with high quality.

## 2 Image Capture System and Method

Image capture system consists of hardware and software components. The structure of the vision system is given by Fig. 1. For the hardware side, a GigE (Gigabit Ethernet) camera or any other digital camera whose exposure parameters can be changed online, a standard IPC with Gigabit NIC (Network Interface Card) and a welding glass (or a ND (Neutral Density) filter) are used. For the software side, a software program to get multi-exposure images is installed in the IPC.

### 2.1 Image Capture System Structure

Off-the-shelf digital camera taking the place of the special HDR camera is selected to capture multi-exposure images. Why the digital camera is chosen? As is



**Fig. 1** The structure of the vision system

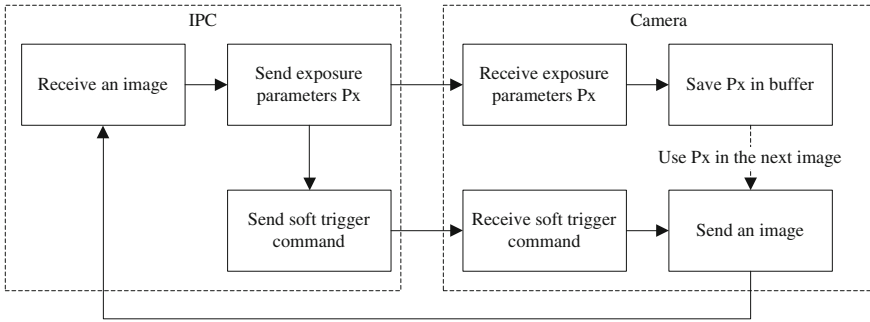
well-known, the digital cameras are more and more widely used in the industrial field and the prices continue to decline. Most importantly, the digital camera can be controlled on the fly to capture each frame with different shutter time and exposure gain value by PC program, the PC and camera interface can be GigE, USB, IEEE1394 and Camera Link. In this paper, the GigE camera is used.

ND filter is a filter that reduces or modifies the intensity of all the wavelengths or colors of light equally, giving no changes in hue of color rendition. The ND filter is necessary in our vision system to reduce the intensity of all the weld areas, but it cannot suppress the dynamic range of the light entering the camera like narrow band pass filter. A ND filter is easier to choose and cheaper than a narrow band pass filter which is not necessary when we increase the dynamic range of the camera. Instead of the ND filter, we can also use a welding glass which is normally mounted in the welding helmet to protect the welding operators' eyes. Welding glass is a filter that reduces the wavelengths of light unequally, and it is not monochromatic color, sometimes dark green, with the maximum transmittance wavelength between 500 and 620 nm. As the operators see the weld process through a welding glass, we can use our vision system to obtain sufficient weld details through the welding glass too. The advantage of using welding glass is that the welding glass can be gotten easily in the welding shop and its price is low.

IPC is programmed to control the camera's exposure and get the resulting video by fusing the multi-exposure images. A gigabit network card is necessary for connecting the computer and the camera.

## 2.2 Image Capture Method

In order to improve the dynamic range of general digital camera, we get multi-exposure images with different shutter time and exposure gain. In this paper,



**Fig. 2** The process of capturing multi-exposure images

a software-based method is developed to control the exposure time and gain on the fly. Long exposure time and large gain is used for weld bead and work pieces detection, short exposure time and small gain for weld pool and weld arc sensing.

Unlike the method using HDR camera, we use a software-based approach to get multi-exposure images. To achieve the goal, we use the function of software trigger which is a feature of most digital cameras. Rather than using hardware circuits to determine when to capture, software trigger is tempting to configure a software program and let it determine when to capture. With changing the exposure parameters, a sequence of two exposures, such as “dark”, “light”, repeatedly, is captured.

Following the steps of obtaining the multi-exposure images:

1. Send exposure parameters command to the camera for changing the exposure in the next frame.
2. Send software trigger command to the camera for capturing an image.
3. Change the value of the exposure parameters and then execute the previous steps 1–2.

Figure 2 shows how to get multi-exposure images more clearly.  $P_x$  is changed among  $P_1$ ,  $P_2$  in order repeatedly. The number of frames to achieve a final image is variable. More frames may get more details, but there will be motion blur in the fused image due to the longer period time of capturing images. Fewer frames may have fewer details, but there will be a faster video frame rate. In this paper, our objective is to monitor the weld process in real time, so we make two images a set to be fused.

### 3 Fusion of the Multi-exposure Images

In this section, the multiple exposure image sets are fused into detail-rich video frames which contain the features needed in the weld monitoring.

### 3.1 Methods of Image Fusion

There are two classic techniques to get the resulting based on multi-exposure. One has been proposed by Debevec and Malik [5]. Firstly, the radiometric response function is estimated from the aligned images. Secondly, the radiance map is estimates by selecting or blending pixels from different exposures. And finally, the resulting HDR image is toned map back into a displayable gamut. The other technique has been developed by Mertens [6], it, so it avoids camera response curve calibration. Both of them can obtain good results, but each of them has their own limitations. Because of their complexity and time-consuming, they cannot be used in the real-time system.

Before we choose a method to solve the problem, the goal of the vision system must be clear and definite. Most of the multi-exposure fused methods are designed to restore accurately the nature of the scene in the conventional display, the hue reproduction accuracy and brightness reproduction accuracy is very important assessment criteria. In contrast, how much welding information can be seen is about which we concerned mostly in the welding process.

After many experiments and data analyses, the method of weighting has been found that it reserves details well and gets good quality weld images in real-time. The model of the weighted method is expressed in Eq. (1).

$$I = k_1I_1 + k_2I_2 + \cdots + k_iI_i. \quad (1)$$

$I$  The resulting image

$i$  The index of the multi-exposure images to be fused

$I_i$  The  $i$ th image to be fused

$k_i$  The weight of the  $i$ th image to be fused, and  $k_1 + k_2 + \cdots + k_i = 1$

In this paper,  $I_1$  (with short exposure time and small gain) and  $I_2$  (with long exposure time and large gain) are used to get  $I$ .  $I_1$  with short exposure time must be captured before  $I_2$  for reducing the time interval between  $I_1$  and  $I_2$ . The longer time interval is, the more obvious motion blur in the resulting image  $I$  is.

$k_i$  is the weight of the image  $I_i$ , the larger the  $k_i$  is, the more details in  $I_i$  will appear in  $I$ . It means that if the weld pool information, which is captured in  $I_1$  is more significant,  $k_1$  should be set larger than  $k_2$ , and vice versa.

### 3.2 Entropy for Evaluating the Result

In order to describe the effectiveness of the weighted method better, image entropy is used for evaluation.

Image entropy is a form of feature statistics; it reflects expected value of the information in an image. In order to characterize the spatial characteristics, 2-D image entropy is introduced. 2-D (two-dimensional) gray image entropy is defined as:

$$H = - \sum_{i=0}^{255} p_{ij} \log_2 p_{ij} \quad (2)$$

$p_{ij}$  is the proportion of the two-tuples  $(i, j)$  in the image.  $(i, j)$  is a tuple composed by  $i$  and  $j$ ,  $i$  is the gray value of a pixel,  $j$  is the average value of the neighborhood of the pixel. The 2-D image entropy highlights the location of the gray pixels in the image information, and a comprehensive feature pixel intensity distribution of the neighborhood.

In the experiment, the 2-D entropy is used to measure the amount of information in the output image. By contrasting the entropy value obtained by different fusion method, the evaluation of the result can be made.

## 4 Experiments and Results

A GigE CMOS monochrome camera is utilized with 60FPS (Frames per Second) for 752 by 480 pixel resolution and 70FPS for 640 by 480 pixel resolution. An IPC with CPU of CORE i3 and a welding glass of #7 grade is applied. In this section, we will present the results of applying the vision system to two different weld types which are GTAW (Gas Tungsten Arc Welding) and GMAW (Gas Metal Arc Welding). The detailed description of the weld parameters used in the applications is given in Table 1.

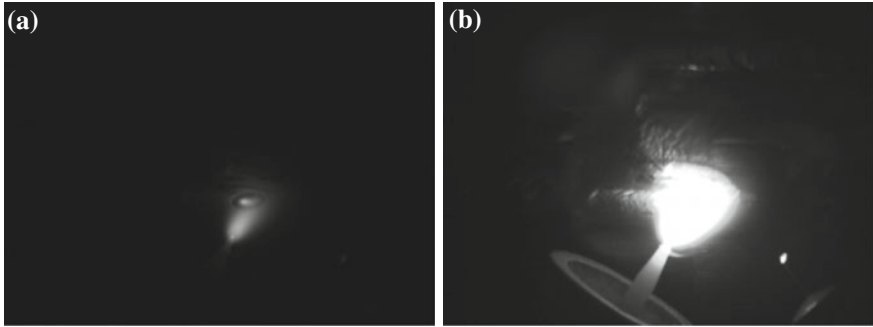
By using software trigger, an average frame rate of 44FPS is achieved for the 640 by 480 pixel resolution. Because every two images fuse into one final image, rate of 22 FPS is obtained.

Figure 3 gives the multi-exposure images captured in GTAW and Fig. 4 in GMAW. Figure 5 is the resulting images of GTAW and GMAW by using the weighted method ( $k_1 = k_2 = 0.5$ ). The method generates final images that weld pool, weld bead, weld arc, work piece around the arc, weld torch and weld electrode can be seen.

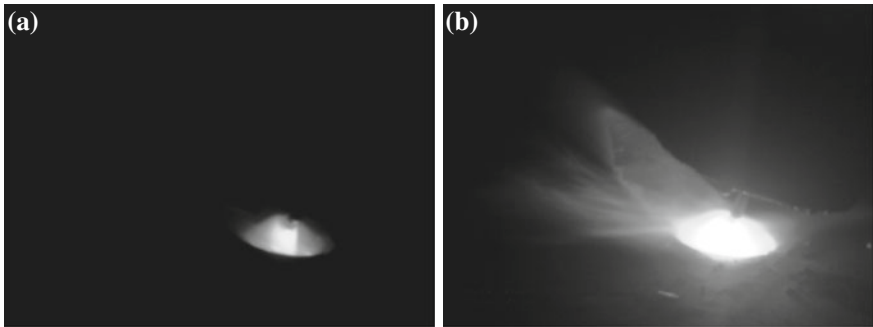
**Table 1** Experimental conditions of GTAW and GMAW

	GTAW	GMAW
Weld speed	400 mm/min	450 mm/min
Work piece	Carbon steel	Carbon steel
Wire diameter	0.8 mm	1.2 mm
Reference voltage	void	20.5 V
Measured current	120 A	180 A
Shielding gas	Argon	Argon and CO <sub>2</sub>
Gas flow rate	5 L/min	10 L/min

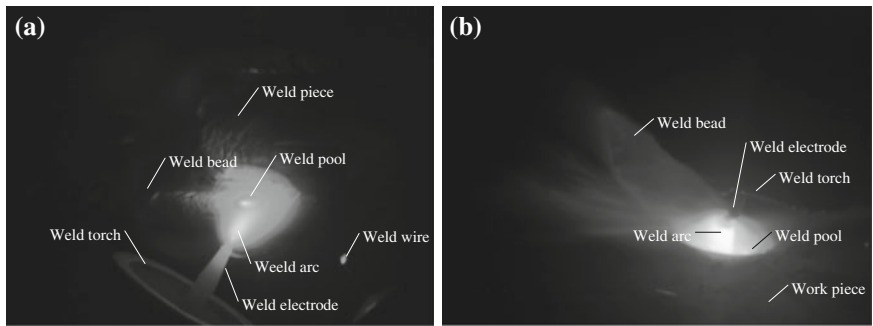




**Fig. 3** The multi-exposure images captured in GTAW. **a** “Dark” image shutter time = 94  $\mu$ s, exposure gain = 0 dB, **b** “light” image shutter time = 7990  $\mu$ s, exposure gain = 20 dB



**Fig. 4** The multi-exposure images captured in GMAW. **a** “Dark” image shutter time = 165  $\mu$ s, exposure gain = 0 dB, **b** “light” image shutter time = 3972  $\mu$ s, exposure gain = 20 dB



**Fig. 5** The resulting images achieved by the weighted method. **a** GTAW, **b** GMAW

**Table 2** Average 2-D entropy and computing time in MATLAB

	2-D entropy (GTAW)	2-D entropy (GMAW)	Time (ms)
Weighted method	2.78	3.49	3.313
T. Mertens's method	2.69	3.02	904.818

Average 2-D image entropy and algorithm computing time in MATLAB of 1000 resulting images are given in Table 2 by using weighted method and T. Mertens's fusion method.

From the results, we can find that the 2-D image entropy using weighted method larger than the entropy using T. Mertens's fusion method. In a sense, the information in the images got by weighted method is more. From human visual perception, the weighted method can reserve the elements in the "dark" image and the "light" image. At the same time, because of its little time consuming, the weighted method can be done in real-time systems.

## 5 Conclusion

In order to gets a low-cost visual monitoring system for open arc welding, a software-based method for obtaining multi-exposure images is proposed. In conclusion, the software trigger method can get a final 22 FPS frame rate video, the camera with a welding glass can get details for welder to control and adjust the weld robot, and the images weighted method reserves the sufficient information of the multi-exposure images. The software-only method can be extended to the digital cameras with USB, IEEE1394 and Camera Link interface.

**Acknowledgement** The author would like to express his appreciation for the help provided by Harbin Xirobot Co., Ltd. while doing research for this paper.

## References

1. Liu J, Fan Z, Olsen SI (2011) Weld pool visual sensing without external illumination. In: IEEE international conference on automation science and engineering, 24–27 Aug 2011, pp 145–150
2. Wang J-J, Lin T, Chen S-B, Wang W (2002) Method of image conducting in AC tungsten inert gases welding of aluminum alloy. *J Shanghai Jiaotong Univ* 36:5–8
3. Mistodie L, Constantin E, Iordachescu D (2005) Quality assessment of GMAW-P welding through real-time control system using HDRC camera. *Institut International de la Soudure*, p 414
4. Kang SB, Uyttendaele M, Winder S, Szeliski R (2003) High dynamic range video, ACM SIGGRAPH 2003 Papers, SIGGRAPH '03, 27–31 July 2003. Association for Computing Machinery, San Diego, pp 319–325

5. Debevec PE, Malik J (1997) Recovering high dynamic range radiance maps from photographs. In: Proceedings of the 1997 conference on computer graphics, SIGGRAPH, 3–8 Aug 1997. ACM, Los Angeles, pp 369–378
6. Mertens T, Kautz J, Van Reeth F (2009) Exposure fusion: a simple and practical alternative to high dynamic range photography. *Comput Graph Forum* 28:161–171

# Study on Vision-Based Dimensional Position Extraction of Plane Workpiece for Groove Automatic Cutting

Hui-Hui Chu, Yu Ji, Xing-Jian Wang and Zong-Yi Wang

**Abstract** At present, most groove cutting robot serving in practical production is still “teaching and playback” type, which cannot meet requirement of quality and diversification. In order to enhance the flexibility of the robotic groove cutting, it is necessary to generate the robot cutting path automatically no matter how workpiece is placed. This paper mainly states the implementation of the automatic measurement of the cutting robot for free-formed workpiece and the procedure of getting the 3D data of the workpiece edge by laser vision sensor. The geometric modeling of workpiece contour is performed from sequential 3D data. Once the geometric model of workpiece is determined, the path of the cutting robot is automatically generated. Previous experiments show that the proposed method performed successfully.

## 1 Introduction

Nowadays, the development of welding technology is booming in industry. As a pre-step of welding, groove cutting gradually attracts people’s attention. In the modern manufacturing industry, there are various kinds of workpieces that need to go through the cutting process, for instance, rectangular, round and irregular shapes and so on. Now there are three different ways to realize the plane workpiece groove cutting: manual groove cutting completely relies on workers, semi-automatic groove cutting relies on simple machine tools and CNC groove cutting that can realize automatic programming.

Manual and semi-automatic groove cutting belong to traditional cutting methods. First, some specific parts are cut off from the steel and processed two or three

---

H.-H. Chu · Y. Ji (✉) · Z.-Y. Wang  
College of Automation Harbin Engineering University, Harbin 150001  
People’s Republic of China  
e-mail: ji\_yu@hrbeu.edu.cn

X.-J. Wang  
University of Wisconsin, Madison 53706, USA

times by edge planing machine, groove-cutting robot and small cutting machine. After these processes, the welding groove process is completed. This method has many weaknesses, for example complicated working procedure, large labor intensity and severe steel waste. Therefore, the market has an urgent demand of a high efficient, simple-operative and high stable groove cutting robot.

Automatic CNC groove cutting refers to the cutting which is completed by the cutting robot with intelligent and high automation degree. Workers only need to complete the simple programming and input parameter in this way. Cutting robot can plan the cutting path automatically by using the advanced nesting software, which can achieves high precision and high efficiency automatic cutting [1]. Now most of the cutting robots serving in practical production still are “teaching and playback” type, and they cannot meet requirement of quality and diversification because these robots have no ability to adapt to circumstance changes and uncertain disturbances during cutting process [2, 3]. What’s more, groove cutting robot with nesting software often cuts workpieces and groove one-time in a whole plate. This cutting approach improves the efficiency of production; nevertheless, it leads to a waste of steel.

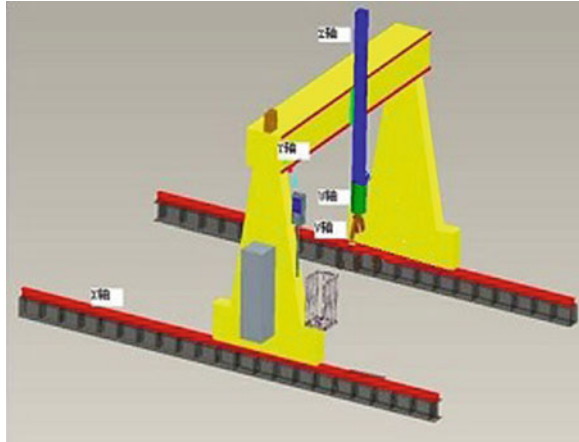
In order to overcome or restrain these shortcomings, it will be an effective approach to develop and improve intelligent technologies for cutting robot. After the analysis of the characteristics of various cutting ways, the machine vision system solves these problems and achieves automation. In this study, computer vision is applied in the closed loop system to control the robot movement in real-time.

## 2 System Configuration

The vision-based groove cutting robot system includes a five-axis gantry structure robot, a laser vision sensor and a control computer. Figure 1 shows the set-up of the five-axis gantry structure robot. It consists of three Cartesian axes ( $X, Y, Z$ ) and two rotary axes ( $U, V$ ) to control the torch orientation for groove cutting.

The laser vision sensor attaches to the  $Z$ -axis. The visual sensor is composed of a CCD camera, two laser generators and a white light-emitting diode (LED) light source as shown in Fig. 2 [4]. The structured light generated by the cylindrical lens is projected onto the workpiece. The camera captures the images of the workpiece edge and sends them to the Image acquisition card. Subsequently, the images are processed to detect the workpiece edge and the intersection between the workpiece edge and the structured light in the image coordinate system. The 3D data of the workpiece edge are produced by the intersection transformed using the triangulation principle. After accurate calibration procedure between the laser and the CCD, 3D data acquired from the sensor can be described in the robot coordinate frame. After running a lap around the workpiece edge, sequential 3D data are obtained, and the geometric modeling of workpiece contour is performed from sequential 3D data [5].

**Fig. 1** 3D schematic of groove cutting robot



**Fig. 2** The prototype of the laser sensor



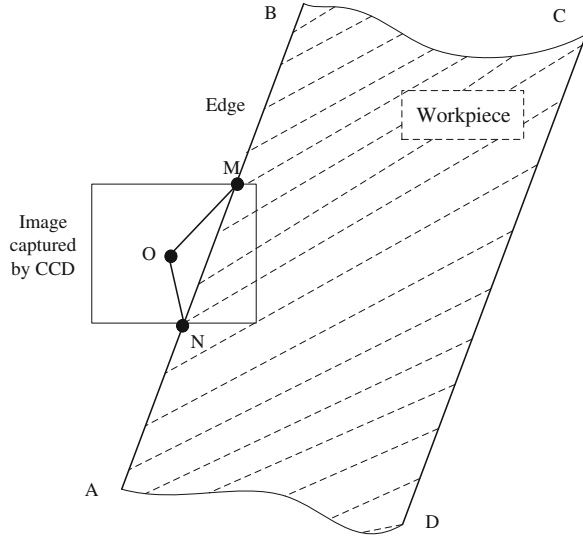
### 3 Tracking Strategy and Image Processing

#### 3.1 Tracking Strategy

The groove cutting process shows: the 3D contour information of workpiece should be acquired before cutting. Therefore, how to control the robot to achieve the workpiece edge tracking is the primary problem in the visual system.

Due to the uncertain of the shape of the workpiece and dimensional position, in order to achieve the 3D contour information collection, the camera must track the edge of workpiece automatically. Since the lens distortion, the point in the image

**Fig. 3** The schematic of edge tracking



coordinate provides the information with error, and the error is proportional to the distance between the point and the image center, the farther the distance and the greater the error. From the above analysis, the tracking process must complete the following two goals:

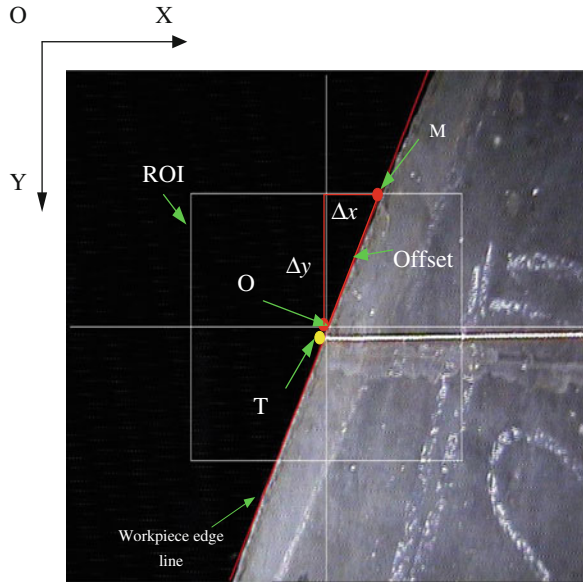
- (a) The robot is controlled to run along the workpiece edge, and the main goal is to collect the 3D information of workpiece contour.
- (b) The center of image is always on the workpiece edge to ensure accuracy.

The schematic of edge tracking is shown in Fig. 3. The camera motion is equivalent to the motion of the optical center, i.e. the center point O. In order to achieve the above goals, the point to be obtained in next step point is M or the point N. In this study, the robot is designed to run around the workpiece edge clockwise. In Fig. 3 the motion trajectory is:  $A \rightarrow B \rightarrow C \rightarrow D \rightarrow A$ . So the next point is M.

### 3.2 Image Processing

The next step of robot running is defined as getting the distance from the image center to the intersection between workpiece edge and one of image edge based on the running direction, as shown in Fig. 4, which is captured from an edge of a workpiece model by using the CCD under white LED light irradiation. For tracking, the next step is OM,  $\Delta x$  stands for distance on the X-axis and  $\Delta y$  stands for distance on the Y-axis respectively. For structured light, T is the target point to calculate the 3D information of workpiece edge. So, the goal of image processing is to obtain coordinate of the point M and the point T.

**Fig. 4** The definition of the target point



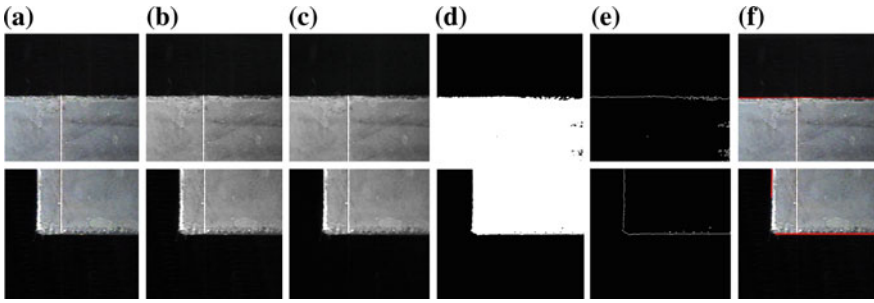
To avoid noises and improve the inspection results, inspections are restricted within a defined region of interest (ROI). The white rectangle is defined and labeled as ROI, as shown in Fig. 4. The center of the ROI is the same as the original image. The ROI contains not only workpiece edge information but also structured light information.

The image processing sequence for obtaining workpiece edge contains: color space conversion, median filter, threshold segmentation (using Otsu method), edge detection by canny operator, Hough Transform to detect line, line classification, target point determination. Compared with the sequence for obtaining edge of workpiece, the image processing of getting structured light is similar. Process is as follows: color space conversion, median filter, threshold segmentation (global threshold), Hough Transform to detect structure light, line classification, target point determination. The image processing result of workpiece edge and structure light are shown in Figs. 5 and 6.

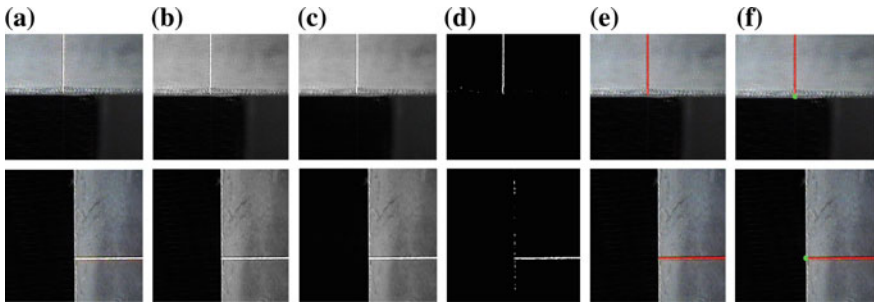
Hough Transform is used to detect the workpiece edge further in the form of line. By classifying line, there are two cases: one line and two lines. A line stands for the situation that robot is located in the workpiece edge and two lines stand for the situation that robot is on the corner of workpiece. Finally, the information of line and the direction of robot running are taken advantage of to obtain the target point.

In the study, dual-beam structured light is adopted. The image about two structured light have obvious characteristics. One of the structured lights is parallel to the x-axis of the image coordinate system; the other one is parallel to the y-axis of the image coordinate system. In addition, the intersection between two structures





**Fig. 5** Image processing for workpiece edge (two different situations, workpiece edge and workpiece corner): **a** original image, **b** grayscale image, **c** median filter, **d** threshold, **e** edge detection, **f** Hough line detect



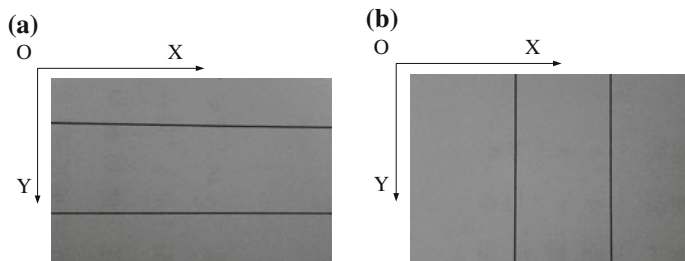
**Fig. 6** Image processing about structured light generated by two different lasers: **a** original image, **b** grayscale image, **c** median filter, **d** threshold, **e** Hough line detect, **f** target point determination

lights is the image center at best. According to the features, the line of structure light can be obtained easily by Hough Transform. Lastly, when the information of structured light is gotten, the intersection between structured light and workpiece edge can be gotten.

## 4 Calibrations

### 4.1 Standard Transformation Formula for Tracking

To convert a specific distance of the image coordinate system to that of the robot coordinate system, the transformation formula is needed in advance. A calibration board with two parallel lines, as shown in Fig. 7, is stated in this paper. In this visual system, the image frame is parallel to the camera frame, and meanwhile the camera frame is parallel to the robot frame.



**Fig. 7** **a** The line parallel to the X-axis, **b** the line parallel to the Y-axis

The two lines in Fig. 7a are parallel to the X-axis and the lines in Fig. 7b are parallel to the Y-axis of the image coordinate. The center of the two lines is in the small area near the image center, in order to get more accurate result. The transformation formula can be represented by Eq. (1) and holds when the height of the robot operation is a fixed value. In this paper the height is 120 mm.

$$\begin{cases} UX = \frac{\Delta RobotX}{\Delta ImageX} \\ UY = \frac{\Delta RobotY}{\Delta ImageY} \end{cases} \quad (1)$$

where  $\Delta RobotX$  and  $\Delta RobotY$  are the displacements along the x-axis direction and the y-axis direction in the robot coordinate system; similarly,  $\Delta ImageX$  and  $\Delta ImageY$  are the displacements in the image coordinate system. In this paper, the distance between the two parallel lines is 20 mm, namely,  $\Delta RobotX$  and  $\Delta RobotY$  is 20 mm.

According to Eq. (1), the distance that the robot runs in next step in the robot coordinate system ( $D_{real}(x), D_{real}(y)$ ) is given as follows:

$$\begin{cases} D_{real}(x) = D_{image}(x) \times UX \\ D_{real}(y) = D_{image}(y) \times UY \end{cases} \quad (2)$$

$$\begin{cases} D_{image}(x) = target(x) - CWidth/2 \\ D_{image}(y) = target(y) - CHeight/2 \end{cases} \quad (3)$$

Variables above, ( $D_{image}(x), D_{image}(y)$ ) is the distance that the robot runs in the image coordinate. ( $target(x), target(y)$ ) is the coordinate of the target, i.e. the point M in the Fig. 4,  $CWidth$  is the width of the image and  $CHeight$  is the height of the image. Equation (3) shows that the principle of tracking is that the image center is always on the edge of the workpiece.

## 4.2 Standard Transformation Formula for Structured Light

Vanishing point method, as a calibration method, is employed to calibrate the parameter of the structured light, including Projection angle  $\beta$ , Baseline length  $L$  and Focal length  $f$ . The sensor operates on the principle of active triangulation ranging. According to the Ref. [6], the three parameters are calculated. Then the relationship between image coordinate and camera coordinate can be presented in Eqs. (4) and (5) [6]:

$$\begin{cases} x_c = \frac{W_x(N_x - CWidth/2) \cdot L}{f \cdot ctg\beta - W_x(N_x - CWidth/2)} \\ y_c = \frac{W_y(N_y - CHeight/2) \cdot L}{f \cdot ctg\beta - W_x(N_x - CWidth/2)} \\ z_c = \frac{f \cdot L}{f \cdot ctg\beta - W_x(N_x - CWidth/2)} \end{cases} \quad (4)$$

$$\begin{cases} x_c = \frac{W_x(N_x - CWidth/2) \cdot L}{f \cdot ctg\beta - W_y(N_y - CHeight/2)} \\ y_c = \frac{W_y(N_y - CHeight/2) \cdot L}{f \cdot ctg\beta - W_y(N_y - CHeight/2)} \\ z_c = \frac{f \cdot L}{f \cdot ctg\beta - W_y(N_y - CHeight/2)} \end{cases} \quad (5)$$

Equation (4) represents the transformation formula which the projection surface is parallel to the y-axis, and Eq. (5) represents the transformation formula which the projection surface is parallel to the x-axis.  $(N_x, N_y)$  is the coordinate of target T in image coordinate, and  $(W_x, W_y)$  is the actual size of pixel.  $(x_c, y_c, z_c)$  is the coordinate in camera coordinate. So far, we can obtain the three-dimensional coordinate of workpiece edge.

In practical applications, 3D data derived from the two structured light is not identical. So, it is essential that the 3D coordinate obtained by different structure light needs to be converted to the same coordinate. To the same point, 3D coordinate obtained by the structured light parallel to the y-axis as the standard, the other one is converted; the modified transformation formula can be represented by Eq. (6).

$$\begin{cases} \Delta x_c = x_{c1} - x_{c2} \\ \Delta y_c = y_{c1} - y_{c2} \\ \Delta z_c = z_{c1} - z_{c2} \end{cases} \quad (6)$$

Some variables  $(x_{c1}, y_{c1}, z_{c1})$  is the 3D coordinate obtained by the structured light parallel to the y-axis,  $(x_{c2}, y_{c2}, z_{c2})$  is the 3D coordinate obtained by the other, and  $(\Delta x_c, \Delta y_c, \Delta z_c)$  is the difference. Through the calculations below, the precise value of  $(\Delta x_c, \Delta y_c, \Delta z_c)$  can be got.

$$\begin{cases} x'_{c1} = x_{c2} + \Delta x_c \\ y'_{c1} = y_{c2} + \Delta y_c \\ z'_{c1} = z_{c2} + \Delta z_c \end{cases} \quad (7)$$

where variable  $(x'_{c1}, y'_{c1}, z'_{c1})$  is the 3D coordinate converted according to  $(x_{c2}, y_{c2}, z_{c2})$ . So far, 3D information derived from the two structured light is identical.

## 5 Experimental Results and Discussion

To investigate the performance of the developed visual system, a test has been carried out. The proposed method is implemented in Visual C++6.0 and OpenCV in real environment. Guided by the vision sensor, edge tracking experiment is carried out on a gantry structure robot platform. The model, shown in Fig. 8 as an example is used to test.

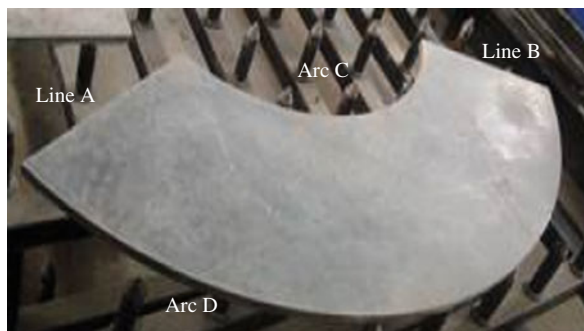
According to the 3D data, the geometric modeling of workpiece can be recovered. The ideal model and the recovered model can be shown in the same coordinate in order to be compared, as shown in Fig. 9 (the blue line represents recovered model, and the red line represents ideal model described by CAD). The detailed description is given in Table 1.

In the Table 1, the biggest error distance between ideal workpiece and recovered workpiece is 1 mm, and the smallest only 0.1 mm. So, this system can meet the required accuracy of the cutting fully.

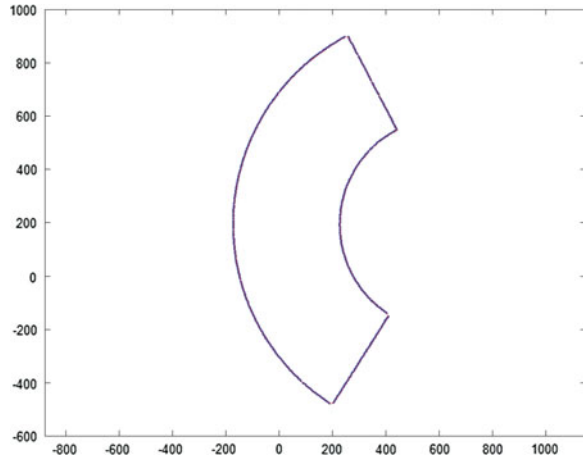
The developed visual measurement system is a multi-tasking data processing that consists of image processing, workpiece edge tracking, workpiece edge 3D calculation and communication between the robot and the computer. The precision of the system is affected by various kinds of factors, including the light scanning system, calibration, the image processing. The main error analysis is as follows:

1. Calibration error. In the study, calibration consists of two parts: calibration for the robot, camera and structured light calibration. Once the robot is assembled, no error is expected on the robot currently. The error raised by lens distortion is not considered in the process of camera calibration. The structured light calibration is carried out by the “vanishing point” method. In dual-structure light system, the three-dimensional coordinate obtained by different structure light

**Fig. 8** Workpiece model



**Fig. 9** The comparison between two models



**Table 1** Experimental result

	Line A	Line B	Arc C	Arc D
Tested length/ideal length (mm)	399.5/400	399.8/400		
Tested radius/ideal radius (mm)			399.0/400	800.2/800
Central angle (°)			119.7/120	120.2/120

need to convert to the same coordinate, which is one of the reasons that error exists in the transformation formula.

- Image processing error. The image processing error results from the procedure of seeking intersection between structured light and workpiece edge. If the difference between ideal target point and the detected point is a pixel in the image coordinate system, then, the real difference in the robot coordinate system is 0.05 mm.

## 6 Conclusion

In this study, a dimensional position extraction system for groove automatic cutting is proposed based on dual-beam structured light. The workpiece edge and structured light image can be acquired using the proposed visual sensor, while edge can be extracted using the proposed image processing method. When the track ends, the workpiece dimensional position is identified by the 3D information collected by the dual-beam structured light system. Finally, the experiment confirms the feasibility of the developed system.

**Acknowledgement** The author is particularly grateful to Harbin XiRobot Technology Co., Ltd. for its help during the study.

## References

1. Chen SB, Chen SZ, Qiu T (2005) Acquisition of weld seam dimensional position information for arc welding robot based on vision computing. *J Intell Robot Syst* 43:77–97
2. Chen H, Liu K, Xing G, Dong Y (2014) A robust visual servo control system for narrow seam double head welding robot. *Int J Adv Manuf Technol*
3. Luo Hong, Chen Xiaoqi (2005) Laser visual sensing for seam tracking in robotic arc welding of titanium alloys. *Int J Adv Manuf Technol* 26:1012–1017
4. Zhen Y, Fang G, Chen S, Zou J (2013) Passive vision based seam tracking system for pulse-MAG welding. *Int J Adv Manuf Technol* 67:1987–1996
5. Nele L, Sarno E, Keshari A (2013) An image acquisition system for real-time seam tracking. *Int J Adv Manuf Technol* 69:2099
6. Hai X, Ming L, Wang C, Ye S (1996) A line structured light 3D visual sensor calibration by vanishing point method. *Opto-Electron Eng* 23(3):53–58

# A Novel Center Line Extraction Algorithm on Structured Light Strip Based on Anisotropic Heat Diffusion

Xin-Tang Lin, Zong-Yi Wang and Yu Ji

**Abstract** There are problems needed to be solved when extracting centerline of structured light strip on multi-pass seam. The problems include complex shape, non-uniform intensity distribution, disconnected caused by welding beans or occlusion and environmental noise etc. To solve these problems, a novel centerline extraction algorithm is proposed based on anisotropic heat diffusion. Putting pixels gray values as the temperature, the algorithm could get centerline composed by highest energy pixels, through heat diffusion along same temperature curve normal directions. The higher accuracy and efficiency of our algorithm is proved by experiments.

## 1 Introduction

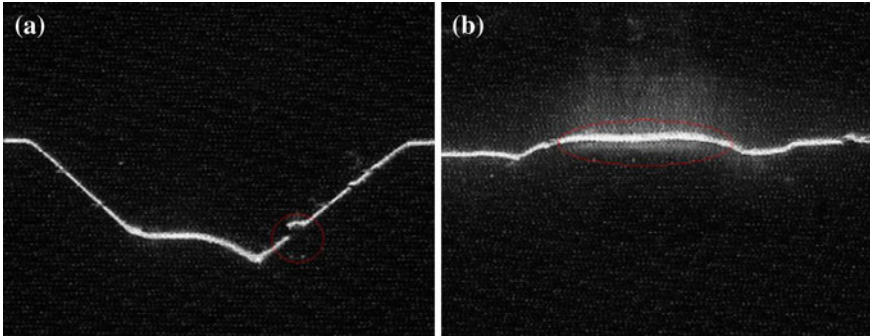
The current multi-pass welding automation mainly uses offline programming approach, and welding parameters can't be adjusted according to the actual situation of the current weld. Off-line welding affects the quality of welding and applicability to complex welding goals, since lots of welding factors is unpredictable. In order to achieve multi-pass welding process automation, three-dimensional information of multi-pass weld needed to be detected, providing a starting point, welding parameters and welding path information.

Currently, the most mature and reliable detection method is structured light detection. To provide accurate structure information of seam sectional, the extraction accuracy of the centerline played a decisive role. Complex shape, non-uniform intensity distribution, disconnected because of welding beans or

---

X.-T. Lin (✉) · Z.-Y. Wang · Y. Ji  
Pattern Recognition and Intelligent Systems Laboratory, College of Automation, Harbin Engineering University, Harbin 150001, China  
e-mail: linxintang@hrbeu.edu.cn

Z.-Y. Wang · Y. Ji  
Harbin XiRobot Co. Ltd., Harbin 150060, China



**Fig. 1** Structured light strip of multi-pass seam

occlusion etc. and environmental noise frequently appear which makes centerline extraction become more difficult, as shown in Fig. 1.

For these problems of multi-pass weld centerline extraction of structured light, a novel center line extraction algorithm is proposed based on anisotropic heat diffusion. The higher accuracy and efficiency of our algorithm is proved by experiments.

## 2 Prior Work

The typical image of a multi-pass weld structured light stripe. As shown in Fig. 1. The disconnection in red circle of Fig. 1a, cause by welding beans; non-uniform intensity distribution in red circle of Fig. 1b, cause by uneven reflection.

Aiming to get high-precision optical centerlines, domestic and foreign researchers from different research directions are involved in this problem. We divided centerline extract algorithms into: symmetry algorithm, asymmetric algorithm, skeleton refinement algorithm and gray gradient algorithm.

The basic idea of symmetry algorithm is to assume geometry and grayscale distributed symmetrical along both sides of the center line. This method is obviously not suitable for the problem.

To overcome the problem of asymmetric on section, center of gravity algorithm, extreme value algorithm, ridge line tracing algorithm and fitting algorithm are proposed. However, the normal of light strip must be known for center of gravity algorithm and extreme value algorithm. Being sensitive to noise is another weakness for those classes algorithm. Ridge line tracing algorithm can't handle the discontinuous light stripe. Fitting algorithm is not a reasonable method to handle light strip of complex structures.

The basic idea of skeleton refinement algorithm is processing original image binary arithmetic first, and then removing the boundary pixels to get centerline. It includes template refinement algorithm and the one based on geometric distance [1].



However, the result of this class algorithm is the geometric center of light stripe image, not that of the centerline.

Gray gradient method is to use gray value change on cross-section curve of light strip and looking for the smallest gradient on curve as pixels in the center line. This class algorithm includes Hessian matrix algorithm [2], Bazen matrix algorithm [3] and GVF algorithm [4] etc. The advantages of this algorithm is the sufficient use of information of each pixel within the light strip. On the top of that, it is also adaptability and highly precise. Nevertheless, using such extremes to find the vector changes requires multiple convolution to calculate the large and is especially susceptible to noise interference. Although many of the recent algorithms focuses on reducing computational complexity [5], the problems of finding extremes of vector changes is not resolved as the inherent shortcomings.

This paper draws on the advantages of gray gradient method that makes full use of the optical texture information. Anisotropic heat diffusion is introduced to each pixel on the light strip heat diffusion at the same time. The centerline will finally get composed by highest temperature pixel in structured light.

### 3 Proposed Centerline Extraction

$$\begin{cases} \frac{\partial u}{\partial t} = \alpha(x, y, z)\Delta u(x, y, z, t) \\ u|_{t=0} = u_0 \end{cases} \quad (1)$$

Heat diffusion equation is shown above.  $u(x, y, z, t)$  is the temperature in the space of time  $t$  and at position  $(x, y, z)$ . Parameter  $\alpha(x, y, z)$  indicates the heat diffusion parameters.  $\Delta$  satisfies the following formula

$$\Delta = \frac{\partial^2}{\partial x^2} + \frac{\partial^2}{\partial y^2} + \frac{\partial^2}{\partial z^2} \quad (2)$$

The Eq. (1) indicates temperature is varying based on the change of time parameter  $t$ . Unidirectional energy transfers from high temperature to low temperature. If diffusion equation changes with time in the degree of variation of energy up to the same extent which will be called isotropic thermal diffusion; if the extent is not same in different direction, it will be called anisotropic thermal diffusion. This technology was first introduced in image processing to remove noise or skeleton extraction [6].

As show in Fig. 2, the gradation value of each pixel shows the temperature.  $l_T$  is a temperature curve which is composed of pixels of same temperature. Each curve diffuses energy along direction, which is charted by normal vector  $\eta$  and tangent vector  $\tau$ . After diffusion, the low energy part is removed and the high-energy part is left. Then the centerline of light strip that is composed of highest-energy light pixels left over after heat diffusion could be extracted.

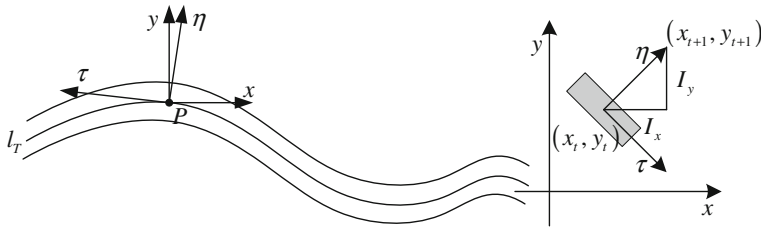


Fig. 2 Direction of light strip thermal diffusion

After coordinate transformation, we change formula (1) to:

$$\begin{cases} \frac{\partial I}{\partial t} = I_{\eta\eta} + pI_{\tau\tau} \\ I|_{t=0} = I_0 \end{cases} \tag{3}$$

Parameter  $p = 0.2$  is defined from the experiment. From Fig. 2, coordinate system relationship can be derived as follows:

$$\eta = \frac{(I_x, I_y)}{\sqrt{I_x^2 + I_y^2}}, \quad \tau = \frac{(-I_y, I_x)}{\sqrt{I_x^2 + I_y^2}} \tag{4}$$

where  $\eta$  is the normal unit vector at point  $(x, y)$ ;  $\tau$  is the tangent unit vector at point  $(x, y)$ . The coordinate transformation matrix is constant. From formula (4) and relation between unit vector  $\eta$  and unit vector  $\tau$ , variables of original coordinate system could be expressed as  $x = x(\eta)$  and  $y = y(\eta)$ . Then the first and the second normal derivative of temperature  $I(x, y)$  are:

$$\begin{aligned} I_\eta &= I_x x_\eta + I_y y_\eta \\ I_{\eta\eta} &= I_{xx} x_\eta^2 + 2 \times I_{xy} x_\eta y_\eta + I_{yy} y_\eta^2 + I_x x_{\eta\eta} + I_y y_{\eta\eta} \end{aligned} \tag{5}$$

From the right image of Fig. 2, the first normal derivative of original coordinate system variables is:

$$x_\eta = \frac{I_x}{\sqrt{I_x^2 + I_y^2}}, \quad y_\eta = \frac{I_y}{\sqrt{I_x^2 + I_y^2}} \tag{6}$$

Meanwhile, coordinate transformation matrix  $Q$  is a constant matrix, the second normal derivative is  $x_{\eta\eta} = 0$  and  $y_{\eta\eta} = 0$ . Taking  $x_{\eta\eta}$ ,  $y_{\eta\eta}$  and formula (6) into (5), we can get heat diffusion change in normal direction  $\eta$  as follow:

$$\frac{\partial I}{\partial t} = I_{\eta\eta} = \frac{I_{xx} I_x^2 + 2I_{xy} I_x I_y + I_{yy} I_y^2}{I_x^2 + I_y^2} \tag{7}$$

On the other hand, heat diffusion change in tangent direction  $\tau$  proved by literature [7] is as follow:

$$\frac{\partial I}{\partial t} = I_{\tau\tau} = \frac{I_{xx}I_y^2 - 2I_{xy}I_xI_y + I_{yy}I_x^2}{I_x^2 + I_y^2} \tag{8}$$

From formula (8) and (9), the heat diffusion equation is:

$$I_{After} = I_{Original} + \frac{I_{xx}I_x^2 + 2I_{xy}I_xI_y + I_{yy}I_y^2}{I_x^2 + I_y^2} + p \frac{I_{xx}I_y^2 - 2I_{xy}I_xI_y + I_{yy}I_x^2}{I_x^2 + I_y^2} \tag{9}$$

Each pixel of the light diffusion at a same time, the highest energy pixel finally obtained after iteration. In the actual calculation process, without iteration, the operation is performed only once to complete the diffusion of the detection light centerline. Calculation steps is shown below.

We create a standard map as target image. Sectional width varies because of the sin function, uneven distribution. A standard noise figure is formed intermittently, whose size is  $1200 \times 900$ , as shown in Fig. 3.

First, the development of a field value determines the pixel requires computing. Choose a peak of 60 % in this study. To increase the temperature level, Gaussian smoothing process is introduced:

$$k = \exp(-(x^2 + y^2)/\sigma) \tag{10}$$

We chose  $\sigma = 1.5$  as smooth range (Fig. 4).

After the process of smooth using Eq. (8), anisotropic thermal diffusion is used to each pixel which gray values bigger than zero. Result as in Fig. 5.



Fig. 3 Standard structured light strip



Fig. 4 Smoothed image

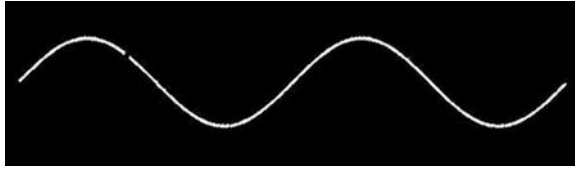


Fig. 5 Heat diffusion once

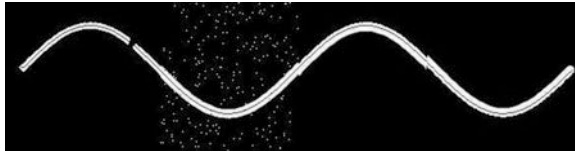


Fig. 6 Centerline extraction result

We get the picture after the diffusion of each pixel which is greater than zero were calculated gray gravity vector corresponding section of the law, and get as in Fig. 6.

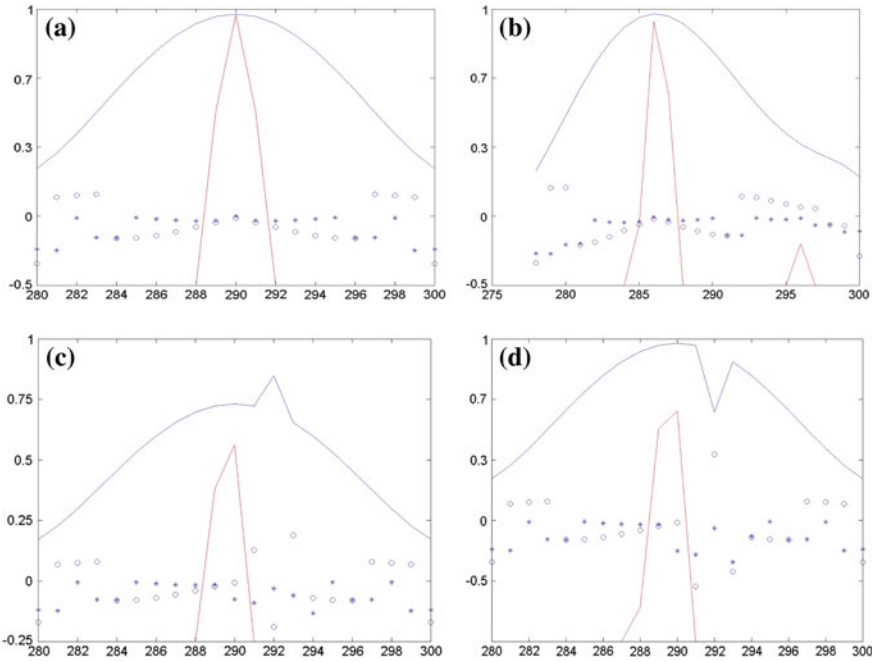
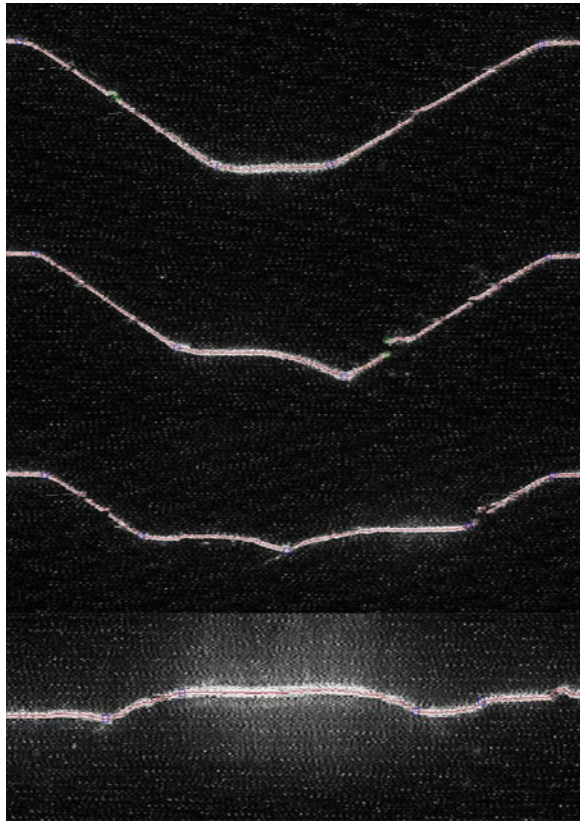


Fig. 7 Diffusion result of strip cross-section **a** normal result, **b** uneven result, **c** high value noise influence result, **d** low value noise influence result

### 4 Experiment

In order to prove the efficiency and accuracy of our algorithm, three experiments were carried out. (1) Change of cross-section before (blue line) and after (red line) heat diffusion in different situation, as shown in Fig. 7; (2) Centerline extraction in different actual seam cross-section structure, as shown in Fig. 8; The comparison of centerline extraction result of standard strip, between DS algorithm [1], IH algorithm [5] and our algorithm. Centerline extraction results is shown in Table 1.

**Fig. 8** Multi-passes light strip centerline extraction



**Table 1** Result table of comparative experiment

	Error	Standard map	Time (ms)
DS	$\epsilon$	2.05	551
	$\sigma$	34.19	
IH	$\epsilon$	0.58	1255
	$\sigma$	21.93	
Ours	$\epsilon$	0.92	324
	$\sigma$	23.17	

## 5 Conclusion

From the above proof and experiment results, we can get the following conclusions:

We have presented a novel and an effective centerline extraction algorithm based on anisotropic heat diffusion. Our algorithm can deal with complex shapes, uneven distribution of light intensity, intermittent and impact noise. Compared with existing algorithms, our algorithm has the advantage of high accuracy and speed.

**Acknowledgments** The author would like to express his appreciation for the help provided by Harbin XiRobot Technology Co. Ltd while doing research for this paper.

## References

1. Pei Y, Zhong L et al (2013) A method of line target detection in the 3D CT image. *Appl Res Comput* 30(9):2855–2858
2. Steger C (1998) An unbiased detector of curvilinear structures. *IEEE Trans Pattern Anal Mach Intell* 20(2):113–125
3. Bazen AM, Gerez SH (2002) Systematic methods for the computation of the directional fields and singular points of finger prints. *IEEE Trans Pattern Anal Mach Intell* 24(7):905–919
4. Chi-Ming L, Chia-Ming J, Jie-Hao C et al (2006) Extraction of edge and skeleton from curvilinear structure object. *J Comput Aided Des Comput Graph* 18(7):971–975
5. Wu Q, He T, Shi T (2012) High-precision gasket thickness measuring and classifying system based on line-structured light. In: *Proceedings of SPIE Eighth international symposium on precision engineering measurement and instrumentation*, vol 8759(8), pp 87593U1–87593U7
6. Kimia BB, Siddiqi K (1994) Geometric heat equation and nonlinear diffusion of shapes and images. In: *Proceedings IEEE Int'l. computer vision and pattern recognition*, pp 113–120
7. osher S, Sethia J (1988) Fronts propagating with curvature dependent speed: algorithms based on Hamilton-Jacobi formulations. *J Comput Phys* 79:12–49

# Image Feature Analysis of Weld Pool in Aluminium Alloy Twin Arc PMIG Welding Based on Snake Model

Jia-Jia Yang, Ke-Hong Wang, Tong-Li Wu and Ai-Min Wei

**Abstract** Continuous weld pool images of 6 mm aluminum alloy from rear and side directions in twin arc welding were successfully obtained with a near-infrared filter and a neutral density filter at an exposure time shorter than pulse period. A modified Snake active contour model for weld pool contour extraction was proposed and the contours of the two directional weld pool images were extracted accurately. Through analyzing the two directional continuous weld pool images it was found that the average geometric feature of continuous multi frame images of weld pools other than one single image can reflect the actual welding process.

## 1 Introduction

Twin arc welding is applicable for aluminum alloy because of its high efficiency and good welding quality. Comparing with electrical, acoustic and other sensing method, optical sensing is not in contact with welding circuit and does not affect the welding process, so it is more and more widely used in welding [1–3]. Research on visual sensing of aluminum alloy is gradually increased in recent years. In Ref. [4], clear weld pool of aluminum alloy in GTAW was obtained by secondary broad-band pass filtering system. In Ref. [5], clear aluminum alloy weld pool image in GMAW was acquired by using a broad-band pass filter with a central wavelength of 610 nm. In Ref. [6] a near-infrared compound filtering method was proposed and weld pool image of thick aluminum alloy was obtained. In this paper, the filtering method in Ref. [6] is utilized in visual sensing of 6 mm aluminum alloy, by controlling the shutter exposure time, continuous clear weld pool image of rear and side directions are obtained. Then the Snake active contour model is proposed to extract the weld pool edges accurately. At last the characteristic parameters of weld pool geometry of aluminum alloy are defined and analyzed.

---

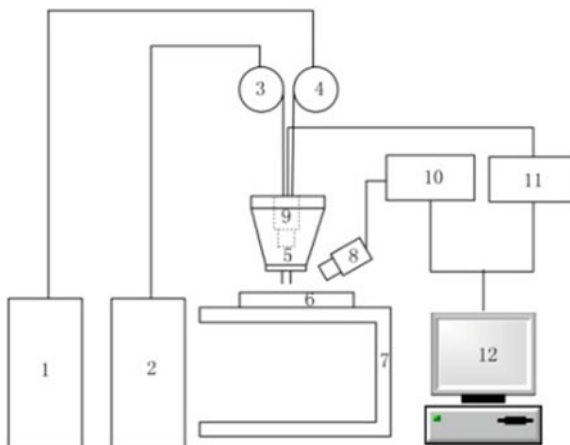
J.-J. Yang · K.-H. Wang (✉) · T.-L. Wu · A.-M. Wei  
School of Materials Science and Engineering, Nanjing University of Science  
and Technology (NUST), Nanjing 210094, People's Republic of China  
e-mail: wkh1602@126.com

## 2 Experiment System

The sketch of the experimental system is shown in Fig. 1 consisting of a pulsed MIG welding subsystem and a visual sensing subsystem. In the welding subsystem, the SAF TOPMAG450 twin arc automatic welding system is used, with two welding machines, two wire feeding system and one welding torch. And the sensing subsystem consists of a computer, two image capturing cards, two CCD (charge-coupled device) cameras, two optical lenses, two compound filters and a specific fixture. The CCD camera is black and white with the resolution of  $795 \times 596$  and the sampling rate of 25 frames per second. The focus length of lens is 12 mm. The composite filter system with a central wavelength of 980 nm and a bandwidth of 20 nm, a neutral density filter with a transparency of 0.5 %, as well as an ordinary optical glass equipped in front of the 12 mm focal length lens are adopted in the sensing system.

## 3 Two-Directional Weld Pool Visual Sensing

The base metal is 3A21 aluminum alloy with a dimension of  $300 \text{ mm} \times 150 \text{ mm} \times 6 \text{ mm}$ , and the welding filler is ER1100, with a diameter of 1.6 mm. The shielding gas is Ar with a flowing rate of 20 L/min. The sensing positions of the two CCD cameras from the rear and side direction have been obtained after many experiments: The angle between the CCD axis of the rear and side and the horizontal plane is  $30^\circ$  and  $35^\circ$ , the aperture is 4 and 6, the shutter time is 2 and 1 ms



**Fig. 1** The two-directional weld pool visual sensing system in Twin Arc Welding (1 Master power 2 Slave power 3 Slave wire feeder 4 Master wire feeder 5 weld torch 6 base metal 7 worktable 8, 9 CCD cameras 10, 11 image grabbing cards 12 computer)



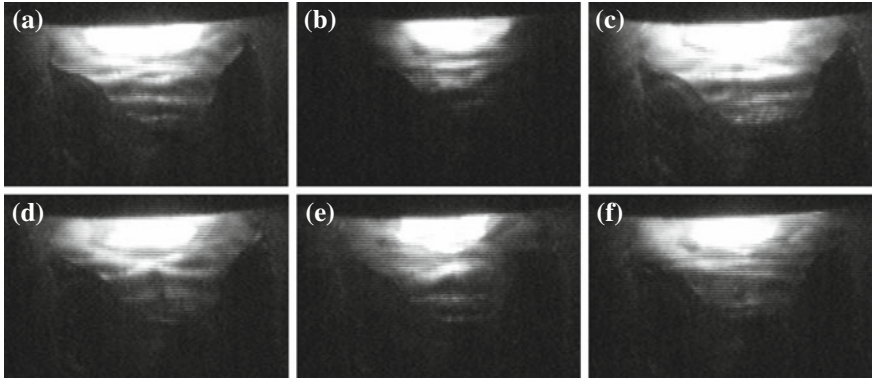


Fig. 2 The weld pool image sequence in rear direction

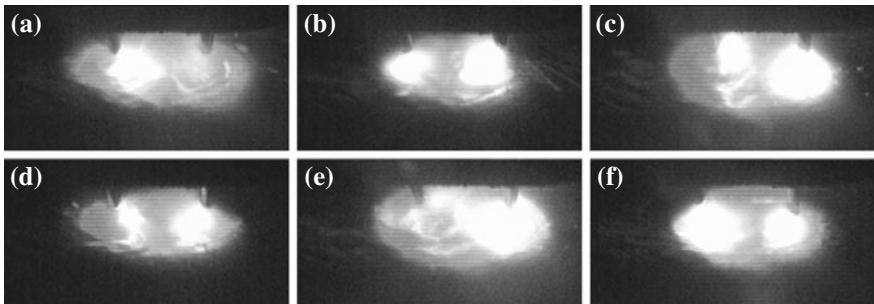


Fig. 3 The weld pool image sequence from side direction

respectively. The continuous two-directional weld pool images captured simultaneously are shown in Figs. 2 and 3.

It can be seen from Figs. 2 and 3, whether the two arc lights are both strong or one arc light is strong and the other is weak, clear images of the two directional weld pools with rich information can be obtained successfully. In each image of Fig. 2(a) to (f), the bright arc, molten pool and dark stripes caused by pool surface undulating can be seen from the rear weld pool image and the boundary of the arc, the molten pool and the base metal is clear. In Fig. 3 forward and backward wires, arc as well as solidifying weld can be seen clearly. And not only the change of forward and backward arc light, but also the attracting between the two arcs can be observed. The length of wire extension is basically consistent, which reflects the small change of arc length and stable welding process. When the intensities of the two arcs are strong, the reflection light of the bead and the surrounding base metal can be observed.

In Fig. 3, (a) the forward wire just finishes droplet transfer, at frame (b) the two arcs are in the medium intensity, at frame (c) the intensity of forward wire arc

continues to increase, the backward wire is ready to transfer droplet, at frame (d) both the two arc intensity are small, at frame (e) the forward arc is very strong, and the backward wire is droplet transferring, at frame (f) the forward arc light intensity is small, and the backward arc is very strong. In this sensing process, the shutter time is 1 ms and the welding pulse cycle is 10 ms, which can guarantee the clear weld pool images of low arc intensity during the base current period.

## 4 Image Processing Algorithm of Weld Pool

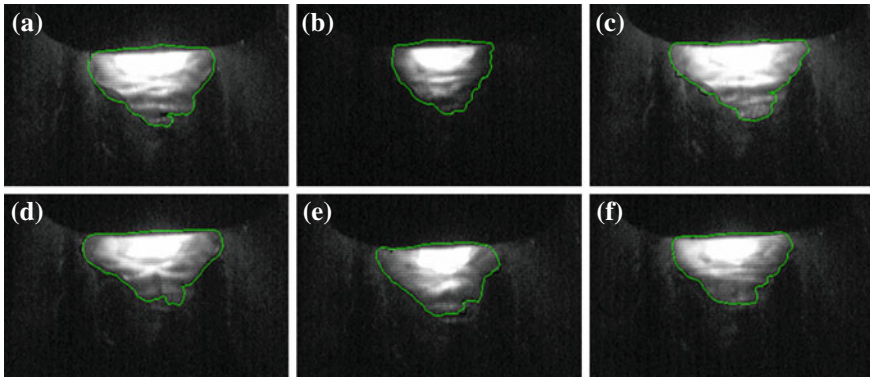
Since mechanical vibration and electromagnetic interference can cause interference in the weld pool images obtained, image processing methods are usually required to get the contour of weld pool image, the traditional edge extracting method usually consist of median filter, gray stretch, threshold segmentation, morphological processing, edge detection and so on. However this method is susceptible to noise at the edge detection and easy to generate a false or discontinuous edge and it is time-consuming because of its multi-step process.

Snake model adopts a new strategy for contour extraction and the final position of the contour curve is the result of a function of the model correlation energy minimization. Snake model can be seen as the moving deformation contour line under the interaction of the force which can represent the curve itself and the external force which can represent the image data. The force acting on Snake model decide how the contour changes in space based on the location and shape of the contour. Internal force roles in the smoothness constraint and external forces guide Snake model moving to image features. Parameterized Snake curve is defined as  $u(s) = ((x(s), y(s)))$ , Wherein  $x(s)$ ,  $y(s)$  is the coordinate value of the contour, arc length parameter  $s \in [0, 1]$ . The total energy function of snake model is as Eq. (1).

$$E(u) = \int_0^1 \left( \alpha \left\| \frac{du(s)}{ds} \right\|^2 + \beta \left\| \frac{d^2u(s)}{ds} \right\|^2 + \gamma E_{image}u(s) + E_{con}u(s) \right) ds \quad (1)$$

In Eq. (1) the first two data represent the internal energy, the first derivative and second derivative of  $u(s)$  represent the elastic energy and bending energy of curve respectively. Elastic energy ensures that the curve has a certain tension, so that the distance between each control node tends to the same. Bending energy ensures the curve smooth to avoid excessive curvature. The energy of the image is denoted by  $E_{image}(u(s))$ , the last  $E_{con}(u(s))ds$  represents the external constraint energy which is also the energy attracting contour curve to the target contour curve.

The contour extraction method of Snake model is based on active contour tracking which makes image processing speed improved; moreover accuracy and better detection result of moving target can be obtained. But the main drawback of Snake model is that it's difficult to find an initial outline, the final contour is also extremely sensitive to the initial position.



**Fig. 4** Contour extraction of continuous weld pool images from rear direction

Here a modified Snake model for weld pool contour extraction is proposed. At first the initial contour is acquired by gray segmentation and a certain number of arc length points combined with prior knowledge. Then after controlling the elastic energy weight  $\alpha$ , the bending energy weight  $\beta$  and the image energy weight  $\gamma$ , the contour with minimum Snake model energy is finally found. Using this algorithm, all the contours of weld pool images of frame (a) to (f) in Fig. 2 are extracted, which is shown in Fig. 4(a) to (f) correspondingly. Also, accurate contour extraction of weld pool images from side direction can be acquired.

## 5 Analysis of Weld Pool Feature

The maximum transverse distance of the rear of the contour is defined as the weld width  $W_r$ , the maximum length is defined as the half-length  $L_r$ , and the area and perimeter of the profile is defined as the area  $S_r$  and perimeter  $P_r$  of the weld pool respectively, and the opening angle between the maximum transverse distance and the lowest point of longitudinal direction is defined as the rear angle of the weld pool. After getting the contours of continuous pool images in Fig. 4(a) to (f), geometric parameters of each weld pool image are obtained, as is shown in Table 1.

**Table 1** The geometric parameters of the six continuous weld pool images from rear direction

	$S_r/\text{pixel}$	$P_r/\text{pixel}$	$W_r/\text{pixel}$	$L_r/\text{pixel}$	$\alpha/^\circ$
Fig. 4(a)	8931	456.451	156	66	99.5147
Fig. 4(b)	4143	272.024	93	47	87.737
Fig. 4(c)	8749	477.279	159	72	95.6635
Fig. 4(d)	7575	435.622	151	59	101.038
Fig. 4(e)	6765	410.652	139	62	96.7396
Fig. 4(f)	7410.5	441.38	147	68	93.8991

**Table 2** The average geometric parameters of the rear weld pool at different welding speeds

Weld rate/cm min <sup>-1</sup>	Sr/pixel	Pr/pixel	Wr/pixel	Lr/pixel	$\alpha/^\circ$
40	11996.1	563.9	170.2	88.8	87.0
50	9674.8	517.2	156.3	79.3	88.6
60	7262.3	415.6	140.8	62.3	95.8

As we can see from Table 1, the change of the weld pool area from Fig. 2 is significantly reducing, increasing, slightly reducing, continually reducing and finally increasing. The perimeter, pool width and half length reach highest in frame (c). The area, perimeter, pool width, half length and rear angle are the lowest in frame (b), compared with the image of the side pool, the intensity of the two arc lights are both small at this moment. The reason is that at this moment the arcs begin to burn soon after the droplet transfer.

Because the two arc instantaneous change quickly in welding process and the weld pool is also correspondingly changing fast, it is not accurate to analyze weld pool feature just using one single image. Thus continuous images are used to analyze the welding process. Welding experiments at three welding speeds of 40, 50 and 60 cm/min with the same weld voltage, current and other welding parameters have been implemented, and the average image features of six continuous weld pool images at each welding speed have been calculated by modified Snake image processing algorithm, which is shown in Table 2.

From Table 2 we can know that, with the increasing of the welding speed, the weld area Sr, weld perimeter Pr, weld width Wr as well as half length Lr of weld pool is obviously reducing, however the rear angle is increasing. The reason is that with the same input voltage and current, the heat input and the weld pool size decreased gradually with the welding speed increasing. This result corresponds well with the actual welding process.

## 6 Conclusion

Clear continuous weld pool images from the rear and side directions of aluminum alloy in twin arc welding process can be obtained by using near infrared narrow-band filter with a central wavelength of 980 nm and a neutral density filter with a transparency of 0.5 % which can remove most of the arc light at the shutter exposure time shorter than the pulse period. A modified Snake model for weld pool contour extraction is proposed and the contours of the weld pool images are extracted. By defining and analyzing the characteristic parameters of weld pool geometry it's concluded that the average geometric features of continuous multi frame weld pool images other than one single image can reflect the actual welding process.

**Acknowledgement** This work is supported by the National Natural Science Foundation of China (Grant No. 51075214).

## References

1. Chuansong W, Jinqiang G (2002) Extracting weld penetration information in tungsten-inert gas arc welding. *Proc Inst Mech Eng Part B Eng Manuf* 216(2):207–214
2. Kehong W, Xinchun T, Jian Y et al (2003) Method of visual detecting MAG weld pool information. *Trans Nonferrous Metals Soc China* 15(3):369–374
3. Saeed G, Yuming Z (2007) Weld pool surface depth measurement using a calibrated camera and structured light. *Meas Sci Technol* 18(8):2570–2578
4. Jianjun W, Tao L, Shanben C et al (2002) Method of image conducting in AC Tungsten inert gases welding of aluminum alloy. *J Shanghai Jiaotong Univ* 36(1):5–8 (In Chinese)
5. Yu S, Defeng Z, Ding F et al (2006) Robotic vision sensing system for welding pool image taking and processing in aluminum alloy MIG welding process. *Electri Weld Mach* 36(3):27–32 (In Chinese)
6. Kehong W, Yang J, Feng Q et al (2007) Molten pool image gathering and processing of aluminum alloy twin-wire MIG welding. *Trans China Weld Inst* 28(1):53–60 (In Chinese)

# A Detection Framework for Weld Seam Profiles Based on Visual Saliency

Yin-Shui He, Yu-Xi Chen, Di Wu, Yi-Ming Huang, Shan-Ben Chen and Yu Han

**Abstract** To guide the accurate shift of welding robots in welding processes in real time, a newly designed visual sensor based on structure light is positioned on the torch in the robotic welding system. Through the sensor, one weld seam image includes the information of weld pools, laser stripe as well as the strong arc glare simultaneously. In order to accomplish the guiding task, a novel framework based on visual saliency is presented to detect the weld seam profile. Considerable image-processing experiments demonstrate the proposed framework is effective even in the background of lots of disturbances of fume, spatter and arc glare.

## 1 Introduction

Autonomous-robot welding is a pursuing objective for the researchers in the welding field. The related intelligent techniques and robotic welding systems have been studied and proposed in the literature. Nevertheless, the really and completely automated robotic welding is still hard to implement due to its nonlinear features and lacking reliable image-processing algorithms. A variety of methodologies about weld seam identification for thick-plate welding and sheet metal welding have been suggested in many papers. For instance, band pass filter [1], median filter [2, 3] and mean filter [4, 5] are adopted to eliminate various noises. To extract weld seam edges, a great number of edge detection operators are used encompassing Canny

---

Y.-S. He · Y.-X. Chen · D. Wu · Y.-M. Huang · S.-B. Chen (✉)  
School of Materials Science and Engineering, Shanghai Jiao Tong University,  
Shanghai 200240, China  
e-mail: sbchen@sjtu.edu.cn

Y.-S. He  
School of Environment and Chemical Engineering, Nanchang University, Nanchang 330031,  
China

Y. Han  
Jiangsu Automation Research Institute, Jiangsu 222006, China

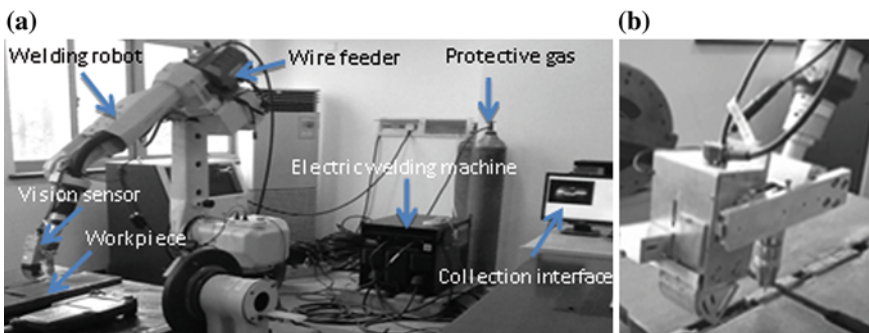
operator [6, 7], Roberts operator [2, 8] and Sobel operator [3]. In addition, wavelet transforms [9] are selected to remove noise and detect the edges of weld seam [10]. In the recent years, visual attention mechanism is a hot research area, which is commonly used for visual tracking, graph classification, and achieving the region of interest (ROI) and so on. At present, the classic models include Itti model [11–14], GBVS model [15] and Hou et al. [16]. There is little research of applying visual attention models to detect weld seam profiles on the internet or magazines. Weld seam profiles can instruct robots to start welding, while the information of molten pools can reflect welding quality [17]. In this paper, we will lay stress upon the recognition of weld seam profiles.

In the next section, we introduce our experimental setup in detail. We give a short summary of the employed framework for the detection of weld seam profiles in Sect. 3. Section 4 dwells on the implementation of the framework, and Sect. 5 presents an experimental verification. Finally, a brief discussion on image-processing experiments and some potential areas of improving the proposed framework are given, followed by conclusions in Sect. 6.

## 2 Experimental Setup

In this paper, the robotic welding system is shown in Fig. 1. It makes up of three parts: a robotic system, an image collection system, and a welding system including a wire feeder, and an electric welding machine. In fact, the image collection system comprises a laser vision sensor (including a CCD camera, a laser based on structure light, filters and dimmer glass), a set of hardware/software subsystem, as well as an industrial PC. The third part contains a wire feeder, a electric welding machine and a welding torch. Here, the laser acts as an auxiliary light source shining the workpiece perpendicularly [3].

In our experiments, the laser's wavelength is 664 nm, versus the power of 200 mw, which is based on the characteristic of MAG welding arc glare spectrum



**Fig. 1** a Components of the robotic welding system. b Visual sensor

of steel. Additionally, to eliminate the effect of arc glare, a narrow band optical filter was used here, whose center wavelength is 660 nm and transmittance is 80 %, along with a narrow band dimmer glass with the transmittance of 2 % approximately.

Meanwhile, the base metal was Q345b, whose thickness was 30 mm. The welding way was swing-welding plus pauses on two endpoints (0.5 s was set for each endpoint), and its swing amplitude was 12 mm, while the swing frequency was 0.8 Hz. Through consulting welding handbook, the welding voltage was set at 21 V, and current was 165 A.

### 3 The Proposed Framework

The proposed framework is mainly divided into two stages. First, in simulating the human eye observation processes, brightness and orientation is select as primary visual features, and brightness and orientation saliency maps could be generated through different metric functions. Second, how to acquire the weld seam profile via orientation and brightness saliency maps was studied and suggested here. A block diagram of the whole proposed framework is shown in Fig. 2. In the second step, specifically, the Threshold segmentation was carried out using OSTU algorithm. It should be note that in the second step, after clustering was executed, the largest cluster possessed the most data.

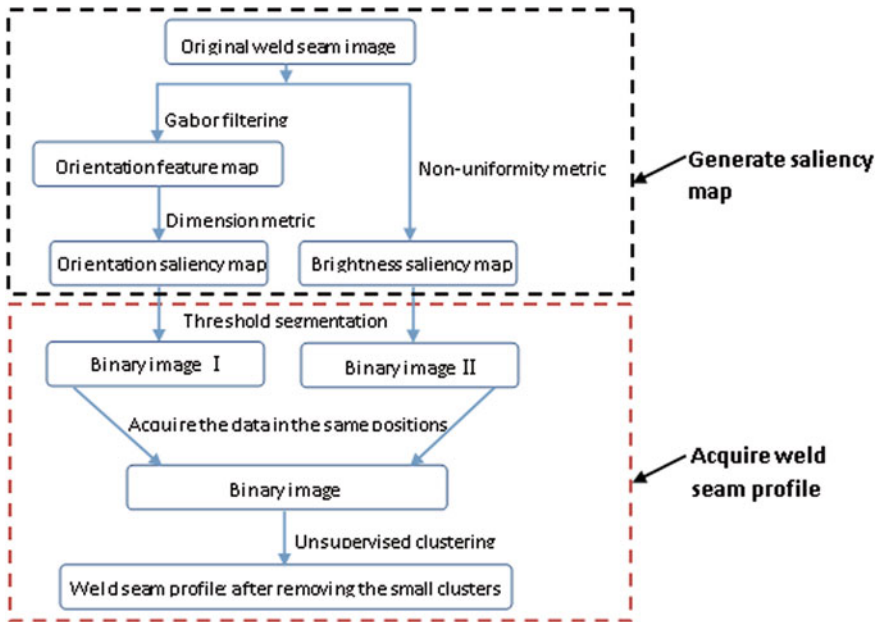


Fig. 2 Block diagram of the proposed framework



## 4 Implementation of the Proposed Framework

### 4.1 Gabor Filtering

$$G(x, y) = e^{-\left(\frac{x_0^2}{2\sigma_x} + \frac{y_0^2}{2\sigma_y}\right)} \cdot \cos(2\pi f x_0) \quad (1)$$

$x_0$  and  $y_0$  are given as follows:

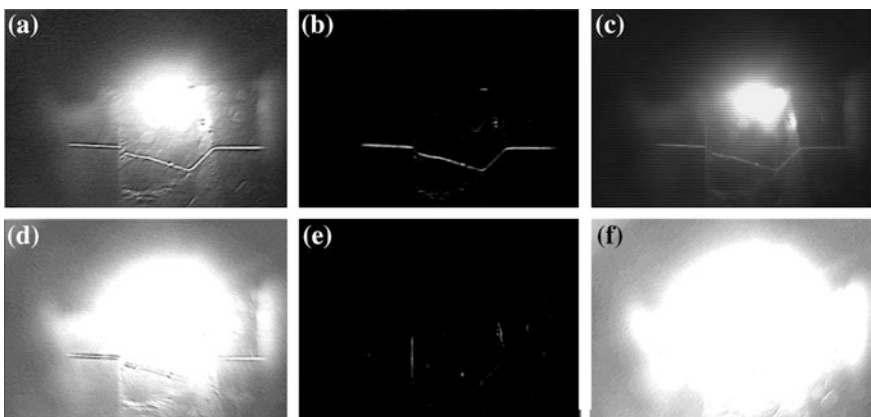
$$\begin{aligned} x_0 &= x \cos \theta + y \sin \theta \\ y_0 &= y \cos \theta - x \sin \theta \end{aligned} \quad (2)$$

where  $f$  is filtering frequency, which is set at  $1/7.82$ ,  $\theta$  is filtering orientation, and  $\sigma_x, \sigma_y$  are standard deviations given below:  $\sigma_x = \sigma_y = 4.12$ . The best values of  $f, \theta, \sigma_x$  and  $\sigma_y$  were all determined by various image-processing experiments offline. The Gabor filtering testing is as follows.

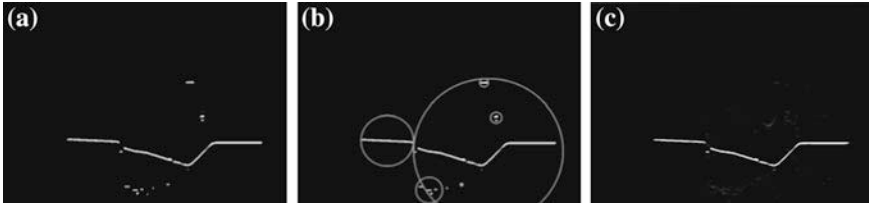
From Fig. 3b we can see that  $\theta = 60$  is the best angle with which Gabor filtering is able to detect weld seam profiles completely. Therefore Fig. 3b is deemed the orientation saliency map.

### 4.2 Dimension Metric

It is obvious that large-scale objects may be more easily noticed than the small-scale ones by our eyes. Hence, the large-scale objects should be higher saliency. The above phenomenon can be imitated with three-step processing. First, threshold



**Fig. 3** Gabor filtering results with different  $\theta$ . **a** Raw image. **b**  $\theta = 6^\circ$  orientation feature map. **c**  $\theta = 20^\circ$ . **d**  $\theta = 45^\circ$ . **e**  $\theta = 90^\circ$ . **f**  $\theta = 150^\circ$



**Fig. 4** **a** The binary image after threshold segmentation. **b** The clustering results; different circles represents different clusters. **c** The final metric result; orientation saliency map

segmentation was employed. Then, clustering was followed based on the Euclidean distance (here the Euclidean distance threshold was set to 20 in pixel) and the nearest neighbor rule. Finally, different clusters achieved their weights in terms of their space dimension which influences their saliency. The third step is formulated as Eq. 3.

$$F_{c_i}^{New}(x,y) = \begin{cases} F_{c_i}^{Old}(x,y) \frac{\max(d_{c_i})}{\frac{1}{NC} \sum_{i=1}^{NC} \max(d_{c_i})}, & 0 \leq F_{c_i}^{Old}(x,y) \frac{\max(d_{c_i})}{\frac{1}{NC} \sum_{i=1}^{NC} \max(d_{c_i})} < 255 \\ 255, & otherwise \end{cases} \quad (3)$$

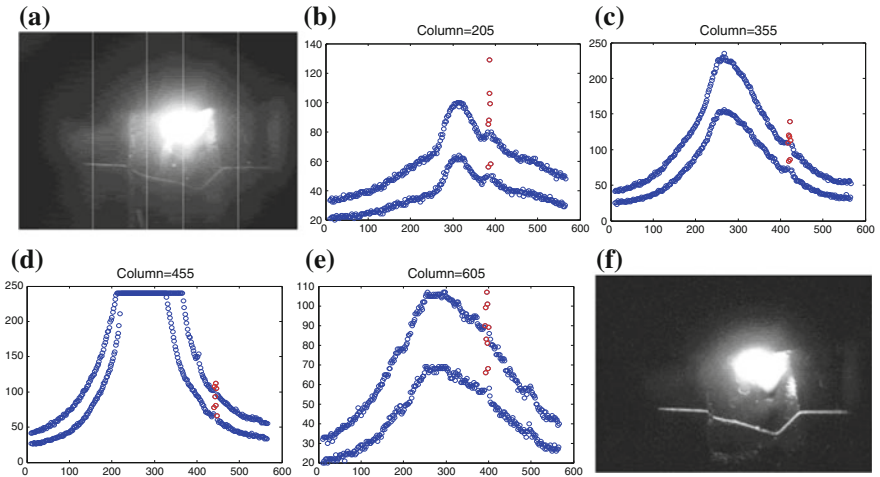
where  $d_{c_i}$  is the Euclidean distance between two different members of the  $i$ th cluster. While  $NC$  represents the number of clusters,  $F_{c_i}^{Old}(x, y)$  is the original orientation feature map, and  $\frac{\max(d_{c_i})}{\frac{1}{NC} \sum_{i=1}^{NC} \max(d_{c_i})}$  denotes the corresponding weights.

The entire process is so-called dimension metric. Figure 4 displays the whole processing, and the final metric result of Fig. 3b is shown in Fig. 4c.

As shown in Fig. 4c, in contrast to Fig. 3b, the large-scale objects get higher gray values, the small-scale objects are on the contrary. The ultimate effect is that the weld seam profile is emphasized.

### 4.3 Non-uniformity Metric

The weld seam image itself—BMP format—represents brightness information, and how to highlight the laser stripe from the original weld seam image is the key target here. From considerable analysis of the data of weld seam images, there is a notable feature that the data belong to the laser stripe are non-uniformity (these data are heavily different). Figure 5b–e show the data indicated by red. The non-uniformity metric result is displayed in Fig. 5f. Obviously, the laser stripe is successfully strengthened.

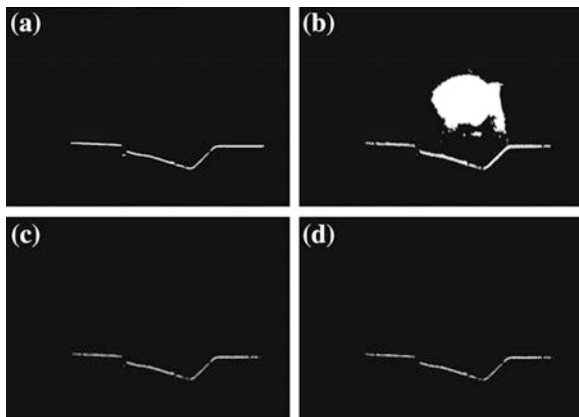


**Fig. 5** The characteristic of the data belong to the laser stripe. **a** Four *white lines* specify the positions of four columns of data. **b–e** Show the four columns of data, and the data belong to the regions of the laser stripe are marked by *red color*. **f** The non-uniformity metric result; it also shows that the laser stripe is obviously highlighted; brightness saliency map

### 4.4 Threshold Segmentation

Threshold segmentation is the first processing in the second stage of the framework. To date, a variety of algorithms of threshold segmentation have been presented in the literature. OSTU is the famous one, which was chosen in this paper here. The results of applying threshold segmentation to the orientation saliency map (Fig. 4c) and the brightness saliency map (Fig. 5f) are shown in Fig. 6a, b, respectively.

**Fig. 6** **a** Binary image I, **b** binary image II, **c** the data in the same positions in the binary image I and II; it is a binary image too and **d** the weld seam profile



### 4.5 Acquiring the Data in the Same Positions

In this processing, binary image I and II have some overlapping white dots in different regions, and the laser stripe must be belonged to these overlapping regions, which were pick out and shown in Fig. 6c.

### 4.6 Unsupervised Clustering

In the last processing, Fig. 6c contains not only the data belong to the weld seam profile but also some disturbance data, which ordinarily appear around the weld seam profile, and there is the need for removing them to determine the real weld seam profiles. Clustering is an effective way which is fit for this job. The clustering algorithm and its parameter setting adopted here is the same with the above, while the member number of every small cluster was set to 400, namely the clusters whose number of members is less than 400 will be removed. The weld seam profile was extract shown in Fig. 6d.

## 5 Experimental Verification

To verify the effectiveness of the proposed framework, a weld seam image with strong arc glare and spatter is given in Fig. 7a. For simplifications, some middle image-processing results are omitted here.

As shown in Fig. 7, it is not hard to see that the proposed framework can accurately detect the weld seam profile even though the weld seam image has arc glare, welding spatter and sparks, etc.



**Fig. 7** **a** The original image with lots of spatter. **b** The dots in the same positions in the according binary image I and II. **c** The extracted profile

## 6 Discussion and Conclusion

In summary, through numerous experiments of the detection for weld seam profiles, the presented framework can accurately extract the weld seam profile, but there are some limitations within the framework. For example, clustering algorithm is executed twice, and its parameter needs to be set by our experience. Furthermore, to achieve the real weld seam profile, we must remove disturbance data in terms of the size of clusters, which is determined still by depending on our experience. Thus, how to set these parameters automatically is a further research area, and better metric functions designed are another research priority in the future. Eventually, this study lays a good foundation for the following seam tracking.

**Acknowledgement** This work is supported by the National Natural Science Foundation of China under the Grant No. 61374071, 61305050, the NDRC of China, under the Grant No. HT[2012] 2144, and the National Natural Science Foundation of Jiangsu Province (BK2012236).

## References

1. Moon HS, Kim YB, Beattie RJ (2006) Multi sensor data fusion for improving performance and reliability of fully automatic welding system. *Int J Adv Manuf Technol* 28(3–4):286–293
2. Shen H, Lin T, Chen S, Li L (2010) Real-time seam tracking technology of welding robot with visual sensing. *J Intell Robot Syst* 59(3–4):283–298
3. Gu WP, Xiong ZY, Wan W (2013) Autonomous seam acquisition and tracking system for multi-pass welding based on vision sensor. *Int J Adv Manuf Technol* 69(1–4):451–460
4. Ye Z, Fang G, Chen Shanben, Zou JJ (2013) Passive vision based seam tracking system for pulse-MAG welding. *Int J Adv Manuf Technol* 67(9–12):1987–1996
5. Zhang H, Zhang G, Cai C, Gao H, Wu L (2009) Laser-based visual recognition of multi-pass seam in robot arc welding. *Trans China Weld Inst* 30(4):105–108
6. Chen JS, Su GD, Xiang SB (2012) Robust welding seam tracking using image seam extraction. *Sci Technol Weld Joining* 17(2):155–161
7. Wei S, Kong M, Lin T, Chen S (2011) Three-dimensional weld seam tracking for robotic welding by composite sensing technology. *Ind Robot Int J* 38(5):500–508
8. Liu X, Xie C (2007) Arc-light based real-time seam tracking system in welding robot In: *Proceedings of the IEEE control and automation conference, Guangzhou, May 30 to June 1, 2007*, pp 2642–2647
9. Liu X, Wang G, Shi Y (2006) Image processing of welding seam based on single-stripe laser vision system. In: *Intelligent systems design and applications, in proceedings of the 6th international conference ISDA, vol. 2, pp 463–470 Jinan, 16–18 Oct 2006*
10. Cai Z, Chen R, Yu F, Zhang H, Hu B (2008) Study on multipass welding seam recognition based on wavelet transform. *J Image Graph* 13(12):2344–2350
11. Itti L, Koch C, Niebur E (1998) A model of saliency-based visual attention for rapid scene analysis. *IEEE Trans Patt Anal Mach Intell* 20(11):1254–1259
12. Itti L, Koch C (2000) A saliency-based search mechanism for overt and covert shifts of visual attention. *Vision Res* 40(10–12):1489–1506
13. Itti L, Koch C (2001) Computational modeling of visual attention. *Nat Rev Neurosci* 2(3):194–230
14. Itti L (2005) Models of bottom-up attention and saliency. In: Itti, L., Rees, G., Tsotsos, J. (eds.) *Neurobiology of Attention*, Elsevier, Amsterdam, pp 576–582

15. Harel J, Koch C, Perona P (2006) Graph-based visual saliency. In: Proceedings of the conference advances in neural information processing systems 19, Vancouver, pp 545–552
16. Hou X, Harel J, Koch C (2012) Image signature: highlighting sparse salient regions. *IEEE Trans Pattern Anal Mach Intell* 34(1):194–201
17. Wang K, Shen YJ, Qian F, You QR (2006) MAG welding molten pool image character and useful information analysis. *Trans China Weld Inst* 27(11):53–56

# The Effects of Arc Length on Welding Arc Characteristics in Al–Mg Alloy Pulsed Gas Tungsten Arc Welding

Huanwei Yu, Jinqun Song, Guoan Zhang, Jianzhong Pu,  
Huabin Chen and Shanben Chen

**Abstract** In order to perform height tracing of the welding torch for sound welding quality in the Al–Mg alloy pulsed GTAW, an arc length sensing method based on arc light was introduced and the essential factors involved in the sensing process was studied by means of visual and spectroscopic technologies. The results showed that the arc light intensity and the arc length were in quadratic relationship rather than in linear relationship and that the relationship deviates from a linear relation was because of the arc heat loss. Based on the quadratic relationship between the spectral line intensity at Ar I 852.14 nm for peak current and the arc length, the arc spectroscopic technology can sense arc length precisely with an error not more than 0.2 mm. While the arc length reached to large values, cooling effects caused by the increment of arc volume and the metal vapor would decrease the arc heat transferred to weld pool and also caused arc center column constriction, and thus there was an optimum arc length for the best arc heat efficiency in the Al–Mg alloy pulsed GTAW.

## 1 Introduction

Gas tungsten arc welding (GTAW), characterized with high controllability and low equipment cost, is widely applied in occasions where quality and reliability are the primary concerns [1]. In order to promote development of the high-efficiency welding technology, many authors have targeted to the fundamental aspects, such as arc current density and heat intensity distributions at the anode surface [2, 3], and effect of anode heat transfer on the weld penetration [4, 5]. The results showed that

---

H. Yu (✉) · J. Song · G. Zhang · J. Pu  
Shaoxing Special Equipment Testing Institute, Shaoxing 312071, China  
e-mail: yuhuanwei@sjtu.edu.cn

H. Chen · S. Chen  
School of Materials Science and Engineering, Shanghai Jiao Tong University,  
Shanghai 200240, China

the arc properties and the arc heat varied depending on any variation in the welding parameters. Arc heat transferred from the arc to the weld pool is mainly determined by the current and arc length (arc voltage) [6, 7]. A longer arc length would produce shallower penetration and a too small arc length might also give rise to poor penetration [8]. It was also found that the arc central temperature decreased with the arc length while the convection heat loss increased in proportion to the gas flow-rate and the appearance arc length [9]. As the other weld parameters have been fixed, arc length plays the most important role on the weld quality. However, because of the assembly precision and the machining accuracy of workpiece and the burning loss of tungsten electrode, it is mostly more difficult to make precise control over arc length than over the other weld parameters.

The traditional arc voltage sensors have been widely used in sensing and control of arc length [10, 11], but the arc voltage depends not only on the arc length but also on the tungsten electrode and the weld joint [12]. Unavoidable variations in welding conditions and the high-frequency interference in arc striking moments limit the potential of arc voltage in precision sensing of arc length. Researchers have found that the arc light had a similar linear relation with the arc length and could offer a more accurate measurement of the arc length [13, 14]. However, researches rarely considered the effects of external conditions on welding arc. Actually, the surrounding environment and the metal vapor from weld pool have large cooling effects on arc plasma and the arc characteristics are thus changed [15, 16]. Especially in the Al–Mg alloy pulsed GTAW, where the alloy materials with the lower vaporization temperature and excitation temperature are more sensitive to the arc heat source, the cooling effects not only decrease the arc heat efficiency but also change the arc light emission performance used for arc length sensing.

In this work, in order to control the arc length at an optimal value in the Al–Mg alloy pulsed GTAW, both the arc characteristics and the welding formation under different arc lengths were studied. By means of vision sensor and image processing technique, the shape parameters of weld pool and arc center column were extracted to estimate the effects of arc length. By means of spectroscopy technology, the arc center temperature near the weld pool surface was estimated, and then the relationship between the arc light intensity and the arc length were discussed. The results have significance for optimizing the arc heat efficiency and for improving the accuracy of arc length sensing technique in the Al–Mg alloy pulsed GTAW.

## 2 Experimental

### 2.1 GTAW System

The experiments were performed on an automatic welding system, as shown in Fig. 1. A host computer was employed to control the system in welding process. The welding devices includes a welding test-bed, a welding power source (OTC



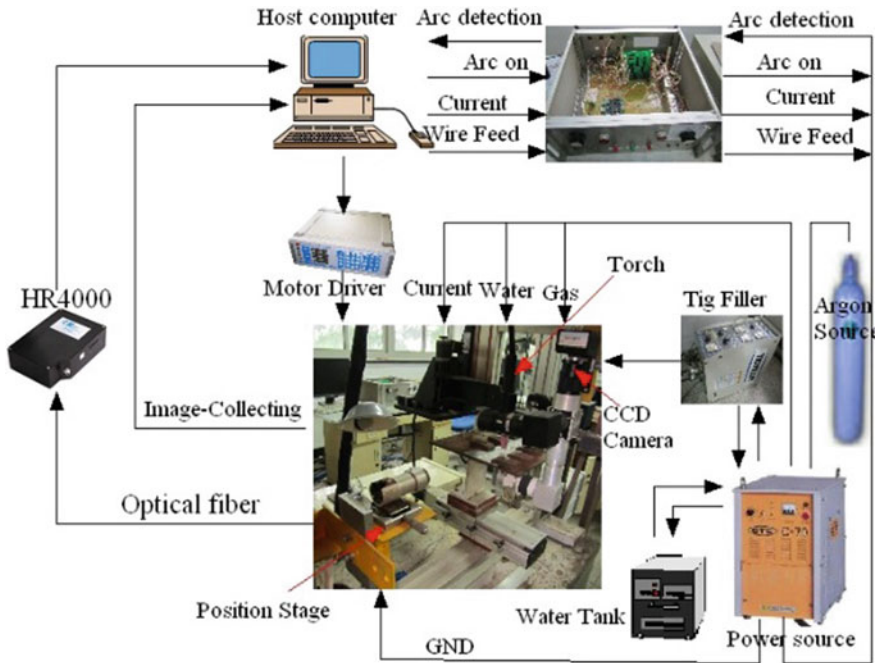
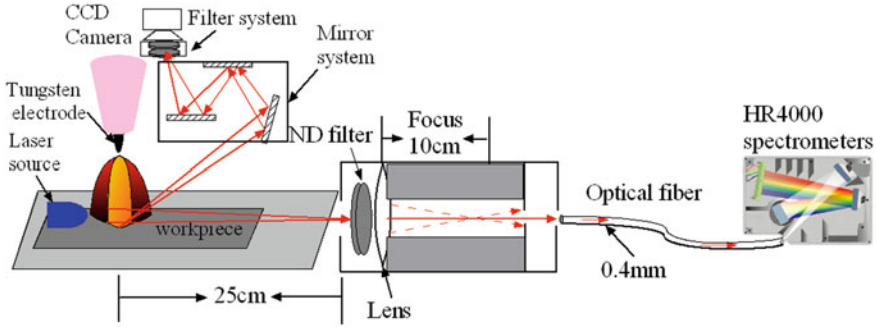


Fig. 1 Schematic diagram of the experiment system

Inverter Elecon 500P), a water-cooled GTA torch and an automatic wire feeder. The welding test-bed can move along a slideway in three dimensions with an accuracy of 0.002 mm. A 3.2 mm diameter tungsten electrode added 2 % ThO<sub>2</sub> with a cone angle of 110° was employed. The torch is connected with step motors and can move in vertical direction to change the arc length consecutively in the welding process.

## 2.2 Data Acquisition System

Figure 2 shows a schematic diagram of the arc spectra-collecting module including a low-cost 3648 pixels spectrometer (Ocean Optics HR4000) and an optical fiber. The spectrometer with a wavelength resolution of 0.2 nm ranges from 185 to 1100 nm. An optical probe orthogonal to the torch axis was fixed at a two-dimensional positioning stage. A laser light source was placed below the electrode for calibration. Before the start of welding, the probe was adjusted to make the incident laser beam into spectrometer reach the maximum intensity, and then it was fixed and remained unchanged throughout the entire experiments. The spectral sampling period was 75 ms, including a spectral integral period of 35 ms



**Fig. 2** Schematic illustration of the arc spectra and the images acquisition system

and a data storage period of 40 ms. A CCD camera (DH-SV1420FM) with a filter and mirror system shown in Fig. 2 is mounted on the upper direction to capture images of the weld pool and the arc column during base periods.

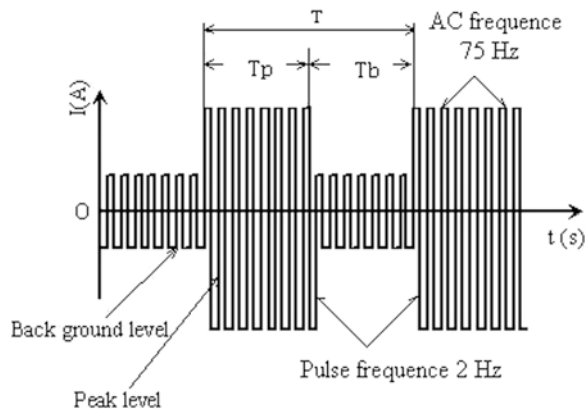
### 2.3 Experimental Materials and Methods

5A06 Al–Mg alloys sheets of 3 mm thickness were welded with no wire feed and no grooves. The alloy contains 5.8–6.8 wt% magnesium element and the specific welding parameters are shown in Table 1. As shown in Fig. 3, 2 Hz low-frequency pulsed AC current was employed and the base current was fixed at 50 A throughout

**Table 1** Welding parameters adopted in this work

Pulse frequency	Base current	Welding speed	Argon flow	Pulse duty ratio
2 Hz	50 A	3 mm/s	15 L/min	45 %

**Fig. 3** Wave form of the welding current:  $T_p$  and  $T_b$  are the peak and base period respectively



the welding experiments. The pulse period consists of a base period  $T_b$  and a peak period  $T_p$ , and the duty cycle  $\gamma = T_p/(T_b + T_p)$  is about 45 %. In order to study the effects of arc length on arc heat efficiency, welding experiments with the different arc lengths of 2, 2.5, 3, 3.5, 4 and 5.5 mm were performed under the same peak current 100 A. To study the relationship between the arc length and the arc light intensity, welding experiments were performed with the peak currents 100, 140, 180 and 220 A respectively, while the arc length decreased consecutively from 7 to 1.6 mm by moving the torch in vertical direction in each welding. In the normal welding process, the torch kept motionless in welding direction, while the work-piece fixed on the test-bed moved in the opposite welding direction. Suitable welding fixtures were adopted to prevent the thermal deformation of weld seam and the arc length was recalibrated after every welding.

### 3 Results and Discussion

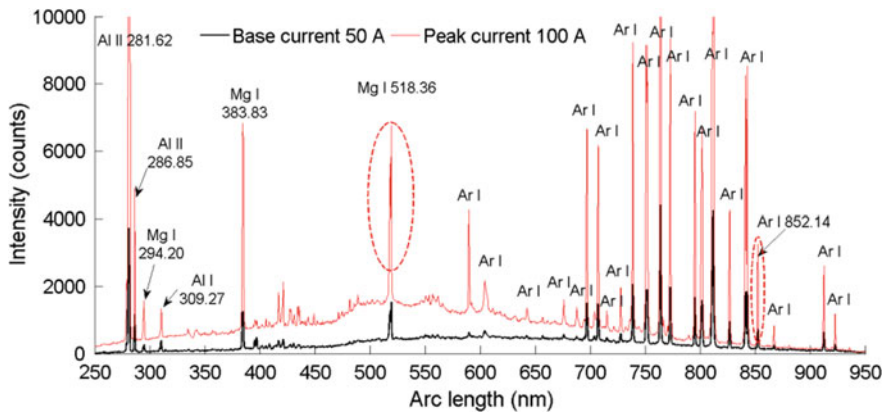
#### 3.1 Arc Length Precision Sensing Based on Arc Light Intensity

Based on the linear relationship between the arc length and the arc light intensity, Li and Zhang [14] have controlled the arc length with an accuracy of 0.2 mm in stainless steel GTAW. However, Al–Mg alloy is much more sensitive to the arc heat source than the steel and the welding current used in this work is pulsed, cooling effects on welding arc not only change the arc characteristics for arc heat efficiency but also may deflect the linear relationship between the arc length and the arc light intensity.

Figure 4 shows spectra of arc plasma in base and peak periods. The spectral lines are identified mainly as Ar I lines concentrating in 650–950 nm and as metal lines concentrating in 280–550 nm by means of the Atomic Spectra Database element standard spectrum data in NIST [17]. Generally, each of Ar I lines from the arc plasma would produce the same effects on arc length sensing, however, due to influences of spectral line self-absorption and continuous spectrum, Ar I lines have different effects on the arc length sensing. As shown in Fig. 4, spectral line at Ar I 852.14 nm which is within ground multiplets, is in low intensity and less affected by self-absorption [21], and is also overlapped with the lower continuous spectrum. Figure 5a shows the line intensity at Ar I 852.14 nm in a welding with peak current 140 A, where the arc length decreased consecutively from 7 to 1.6 mm. The spectral intensity is normalized by the following formula (1):

$$I_{normal} = I/I_{base} \quad (1)$$

where  $I_{normal}$  is the normalized intensity,  $I$  is the raw intensity,  $I_{base}$  is the mean intensity at base period under the 3 mm arc length. Figure 5b shows the normalized intensity versus the arc length for peak current; linear and quadratic fitting methods

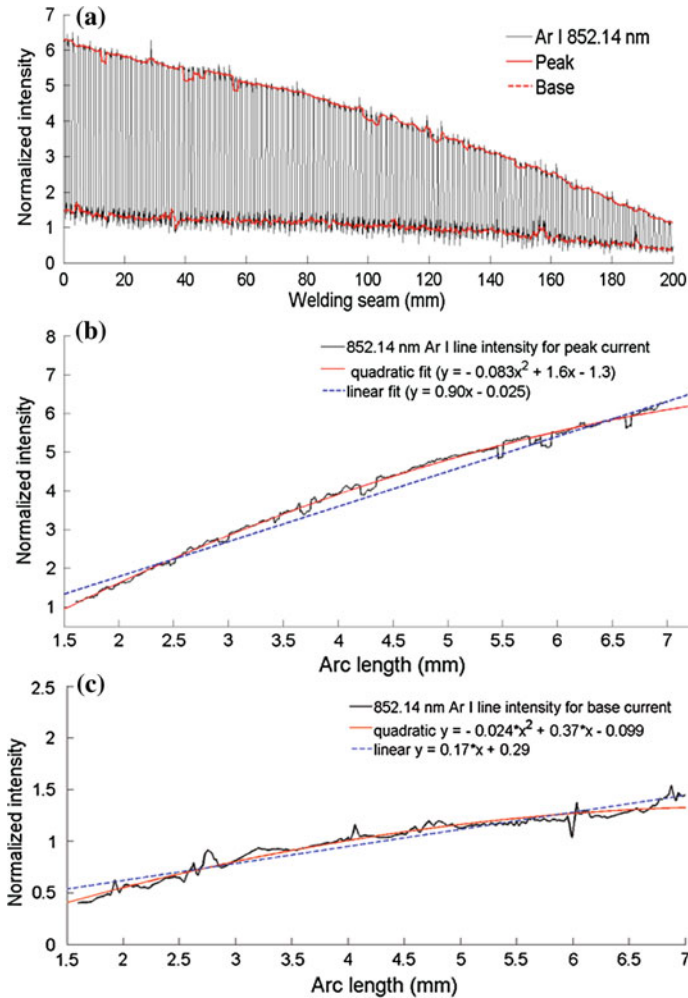


**Fig. 4** Spectra of arc plasma in base and peak periods

are applied to extract the relationship between the line intensity and the arc length. The fitting results show that the relationship is in quadratic relationship rather than in linear relationship with the norm of fitting residuals 2.5 and 5.7, respectively. Figure 5c shows the normalized intensity versus the arc length for base current and it can be observed that the line intensity during peak period increases more significantly than the one during base period dose as arc length increasing, which indicates that the arc length plays a more important role in arc plasma under the larger current.

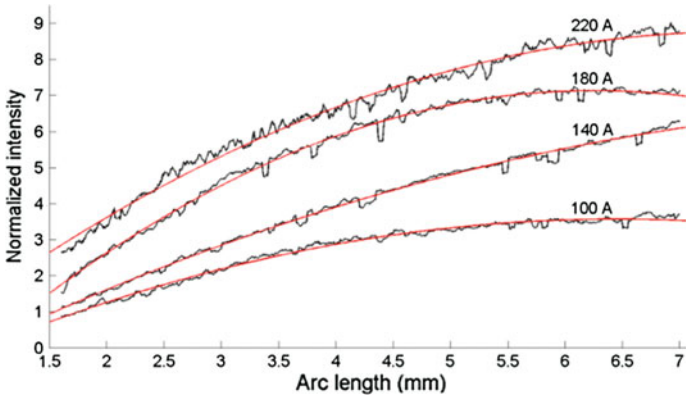
Figure 6 shows the normalized intensities at Ar I 852.14 nm for different peak currents and they also display clear quadratic relations to the arc length. The slopes of Ar I line intensity curves decrease as arc length increasing, specially, when the arc length is less than 4 mm the slopes decrease little but decrease more when the arc length is more than 4 mm. This phenomenon shows that the amplification of the unit arc length (arc voltage) for argon radiation intensity is reducing with the increasing arc length.

In order to verify the validity of the extracted quadratic relationships for arc length precision sensing, a welding experiment with a changing arc length and a fixed peak current of 140 A has been performed. As shown in Fig. 7a, when the arc length is raised from 2.5 to 4.5 mm by a step motor in the welding, the line intensity increases accordingly. Figure 7b shows the predicted values of arc length based on the two fitted mathematical relationships depicted in Fig. 5b. Under the arc length of 2.5 mm, both the quadratic and the linear relationships sense the arc length precisely with an error of 0.11 mm; under the arc length of 4.5 mm, the quadratic relationship senses the arc length with an average error of 0.15 mm, however, the average error of the linear relationship is aggravated as much as 0.32 mm. The results show that the arc light intensity can make a precision sensing of arc length and that the quadratic relation is much more accurate to depict the relationship between them.

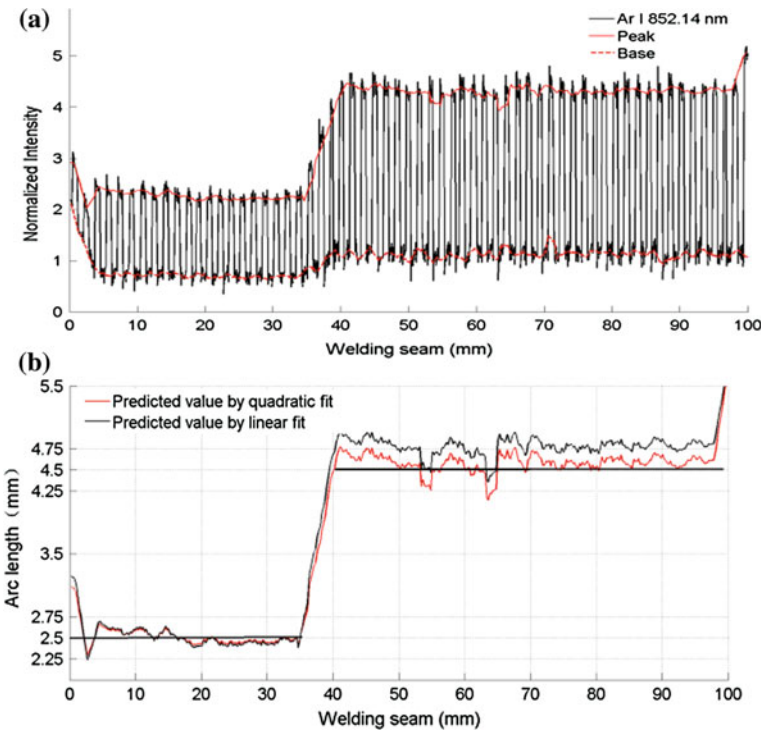


**Fig. 5** a Normalized intensity of Ar I 852.14 nm acquired in the welding with a decreasing arc length from 7 to 1.6 mm and a peak current of 140 A; b the normalized intensity versus the arc length for peak current; c the normalized intensity versus the arc length for base current

In order to clarify the reason why the relationship between the Ar I line intensity and the arc length deviates from a linear relation, changes of arc heat and arc appearance with the increasing arc length are studied. Actually, it is difficult to determine the arc heat under different arc lengths, but it can be relatively measured by their welding results. In general, the larger size of welding pool corresponds to the greater arc heat output under the same welding conditions.



**Fig. 6** The quadratic relationships between the line intensity of Ar I 852.14 nm for different peak currents and the arc length



**Fig. 7** **a** Line intensity of Ar I 852.14 nm with the arc length jump from 2.5 to 4.5 mm; **b** Sensing of arc length based on the linear and the quadratic relationships

### 3.2 Weld Formation and Arc Appearance

The welding arc is bell shaped and shows a high temperature in arc center regions but a relatively low temperature in the winging regions, as shown in Fig. 8a acquired by high-speed photography. By means of the vision sensor depicted in Fig. 2, images of weld pools and arc center columns were acquired clearly in the welding processes, as shown in Fig. 8b. It can be observed that the weld pool and the arc center column show different appearances with the same peak current 100 A but the different arc lengths. In order to estimate these changes caused by the arc length, the maximum width WP of weld pool and the maximum width WA of arc center column are extracted by the image processing techniques shown in Fig. 9.

Figure 10 shows the average values of WP and WA for different arc lengths. It can be observed that WP is almost constant as the arc length is not more than 3 mm, but decreases by 30.36 % as the arc length increasing from 3 to 5.5 mm. WA first increases by 11.1 % as the arc length increasing from 2 to 2.5 mm, and then shrinks by 23.61 % as the arc length increasing to 5.5 mm. The decrease in pool width indicates a reduction of arc heat transferred to the weld pool, while the decrease in arc center width indicates an augment of cooling effect on arc plasma.

### 3.3 Electron Temperature for Arc Center Column

Al–Mg alloy has a low vaporization temperature and is vaporized strongly near the weld pool surface because of the high arc temperature. Because the metal atoms are more easily ionized than argon atoms, arc properties vary in many respects with the presence of metal vapor [16, 19]. In order to measure the variations in both the excited metal and argon atoms near the weld pool surface, two indexes defined in Eqs. (2) and (3) are introduced.

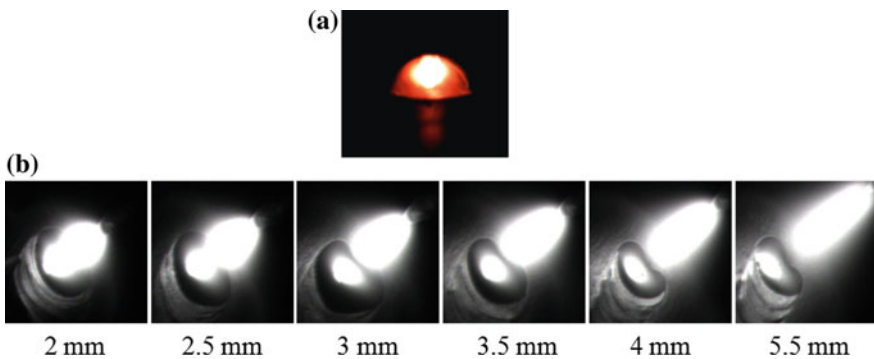
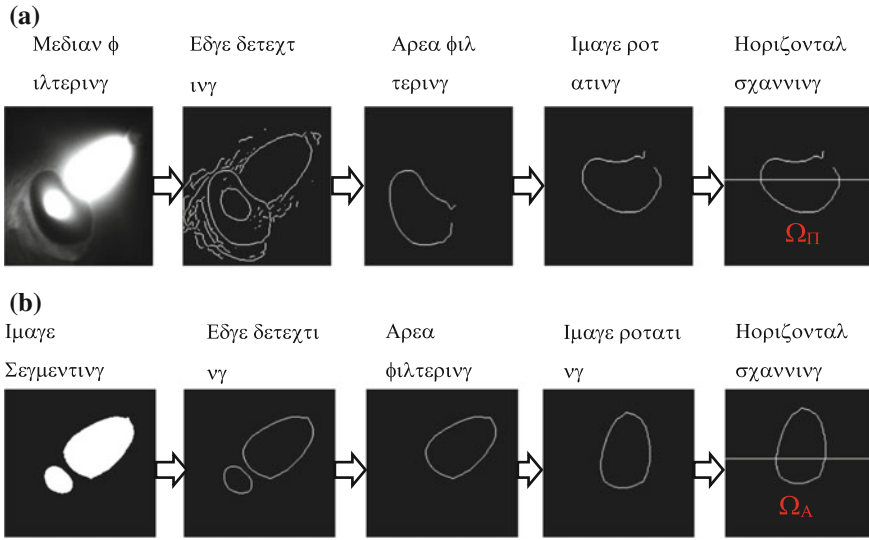
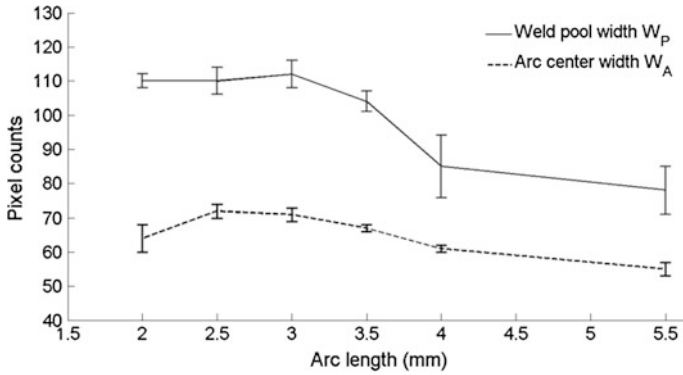


Fig. 8 Images of both the weld pools and the arc center columns with different arc lengths



**Fig. 9** Image processing techniques for WP and WA. **a** Processes of weld pool image processing; **b** processes of arc column image processing



**Fig. 10** Variations in WP and WA with an increasing arc length

$$Mg_r = \frac{1}{m} \sum_{i=1}^m \left( \frac{I_{518.59}}{Arc_{mean}} \right)_i \tag{2}$$

$$Ar_r = \frac{1}{m} \sum_{i=1}^m \left( \frac{Ar_{mean}}{Arc_{mean}} \right)_i \tag{3}$$



where  $m$  is the total number of the data points in a pulse period,  $Arc_{mean}$  is the mean intensity of the total arc spectrum,  $I_{518.59}$  is the intensity of Mg I line at 518.59 nm,  $Ar_{mean}$  is the mean intensity of the 23 Ar I lines.

The two indexes  $Mg_r$  and  $Ar_r$ , corresponding to a certain weld pool, represent the proportions of the excited magnesium and argon atoms in the arc column near the weld pool surface, and will keep the constant values approximately when the welding parameters are fixed. Figure 11 shows the values of  $Mg_r$  and  $Ar_r$  at different arc lengths and it can be observed that as arc length increases from 2 to 5.5 mm,  $Mg_r$  increases by 30.9 % and  $Ar_r$  increases by 66.3 %, which indicate the increases of the excited magnesium and argon atoms near the weld pool surface. However, when arc length increasing from 4 to 5.5 mm,  $Ar_r$  decrease a little implying that the proportion of excited argon atoms is decreasing.  $Mg_r$  increases more fast as arc length increasing from 3.5 to 5.5 mm, which indicates an aggravation of metal vaporization near the weld pool surface.

Marotta [20] has proposed an approximate formula without Abel inversion for the determination of axial temperatures which is based on recording the spatially integrated radiances of spectral lines in plasmas, as shown in Eq. (1)

$$\ln\left(\frac{E_m I_{mn} \lambda_{mn}}{A_{mn} g_{mn}}\right) = \ln\left(\frac{khcT_e n(T_e)}{4\zeta U(T_e)}\right) - \frac{E_m}{kT_e} \tag{4}$$

where  $I_{mn}$  is the spectral line intensity from the level  $m$  to the level  $n$ ,  $A_{mn}$  is the transition probability,  $g_{mn}$  is the statistical weight,  $E_m$  is the excited energy,  $\lambda_{mn}$  is the wavelength,  $T_e$  is the electron temperature at the centre of the plasma column,  $n(T_e)$  is the species density,  $U(T_e)$  is the partition function,  $\zeta$  is an empirical constant,  $k$  is the Boltzmann constant,  $h$  is the Planck constant and  $c$  is the light velocity in vacuum. If taking Eq. (4) as a liner function and plotting it with  $E_m$  in the horizontal axis and with  $\ln(E_m I_{mn} \lambda_{mn} / A_{mn} g_{mn})$  in the vertical axis will result in a straight line, then  $T_e$  can be determined by the slope  $-1/kT_e$ . This method for  $T_e$  is so called Boltzmann plot method [21]. In this paper, considering that self-absorption would lower emission line intensities but sufficient spectral lines contribute to the

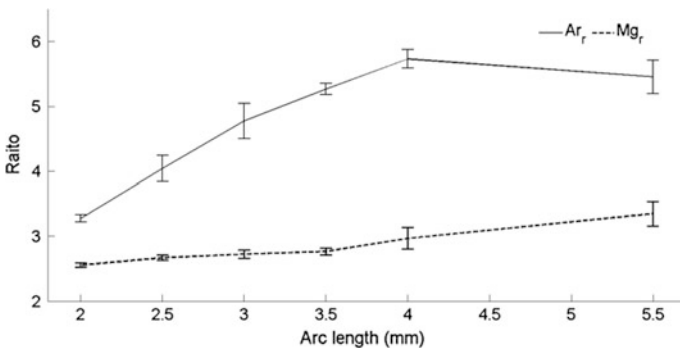


Fig. 11 Variations of  $Mg_r$  and  $Ar_r$  with an increasing arc length

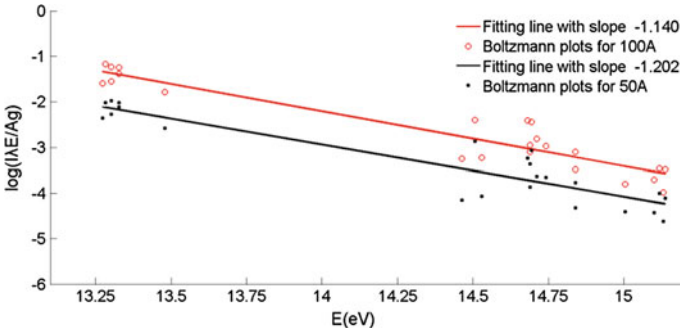


Fig. 12 Boltzmann plots method for electron temperature

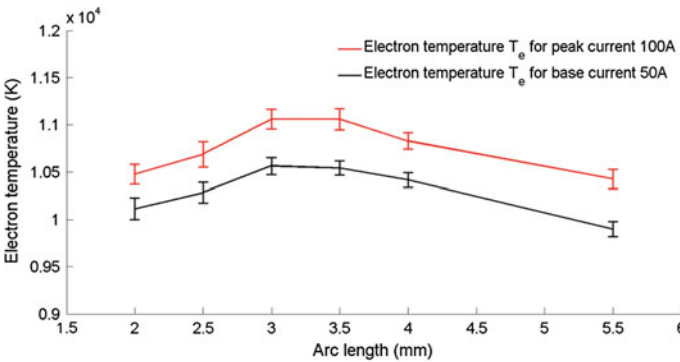


Fig. 13 The arc center temperature  $T_e$  with an increasing arc length

temperature accuracy, 23 Ar I spectral lines with a wide energy level spread are selected to determine  $T_e$  by the Boltzmann plot method, as shown in Fig. 12.

The arc center temperature near the weld pool surface are estimated by the above mentioned method and these estimated values are averaged in base and peak periods respectively, as shown in Fig. 13. For both base and peak periods,  $T_e$  achieve the maximum of 10,560 and 11,060 K at the arc length of 3 mm, and then decrease as arc length increasing to 5.5 mm.

### 3.4 Discussion for the Cooling Effects on Welding Arc

In the Al–Mg alloy pulsed GTAW, arc length plays an important role on the weld quality as the other weld parameters have been fixed. As arc length increasing, the total arc energy is enlarged because of the volt-ampere characteristics, and that the

volume of arc column increases as well. However, as shown in Figs. 8 and 10, the weld pool size is first increasing as arc length increasing from 2 to 3 mm and then decreasing as arc length increasing from 3 to 5.5 mm. The arc center temperature near the weld pool surface, as shown in Fig. 13, has the similar trend as the weld pool size. These phenomena indicate that when the arc is about 3 mm length it has the maximum heat efficiency for welding, while a too long arc length would pull down the arc heat efficiency.

A. Berthier has found that that the magnesium fluoride would elevate arc temperature and make arc constriction in A-TIG (with  $MgF_2$ ) welding of 304 L at 80 A; both the average arc temperatures of A-TIG and TIG welding near the welded material increased as the arc length increasing from 3 to 5 mm, however, the average arc temperature of A-TIG is lower than that of TIG at the large arc length 5 mm. In this work, the arc center temperature near the weld pool surface firstly increases and then decreases as arc length increasing from 2 to 5.5 mm. The reason can be explained in two aspects. Firstly, as arc length increasing both the total arc energy and the arc volume would increase, but cooling effect of the arc surrounding environment is also enlarged by the increasing arc volume. The cooling effect on welding arc would decrease the arc heat transferred to weld pool and also cause arc center column constriction. Figure 10 shows that as arc length increases from 2.5 to 5.5 mm the arc center width shrinks by 23.61 % to lower the arc heat loss and the phenomenon of arc constriction demonstrates the cooling effect on welding arc as the arc length is more than 3.5 mm, however it only slows down but cannot prevent the heat loss. Secondly, metal vapor concentrated around the weld pool surface not only absorb some of arc heat during its production and ionization, but also decrease the arc voltage gradient. Aluminum and magnesium elements having the lower vaporization temperature and excitation temperature are more easily vaporized and excited with the higher arc voltage as arc length increasing. As shown in Fig. 11, when arc length increasing from 4 to 5.5 mm, the decreasing index  $Ar_r$  indicates that the arc heat has been not sufficient enough to excite the argon atoms, and the increasing  $Mg_r$  indicates that the metal vaporization and excitation are aggravating all the time as arc length increasing from 2 to 5.5 mm.

According to the above analysis, it is clear that arc light can sense the arc length precisely in the Al-Mg alloy pulsed GTAW, and that relationship between the Ar I line intensity and the arc length often deviates from a linear relation but appears to be a quadratic relation because of the arc heat loss. Furthermore, because of the cooling effect of the arc external environment volume and the metal vapor, there is an optimal arc length for the highest heat efficiency and it is within 3 to 3.5 mm under the current welding conditions.

## 4 Conclusion

From the results and discussion, we could draw the following conclusions:

1. In the Al–Mg alloy pulsed GTAW, the arc light intensity and the arc length are in quadratic relationship rather than in linear relationship and this is caused by the aggravating cooling effects on welding arc when the arc length involves in too large values. Based on the quadratic relationship between the line intensity at Ar I 852.14 nm for peak current and the arc length, the arc spectroscopic technology can sense arc length precisely with an error not more than 0.2 mm.
2. As arc length increasing to too large values, cooling effects on welding arc are mainly caused by the increment of arc volume and the metal vapor near weld pool surface, which would decrease the arc heat transferred to weld pool and also cause arc constriction.
3. There is an optimum arc length for the best arc heat efficiency in the Al–Mg alloy pulsed GTAW, while a too long arc length would pull down both the arc center temperature and the arc heat efficiency. With the peak current 100 A, the optimal arc length is determined as about 3 mm under the current welding conditions.

## References

1. Norberto Pires J, Loureiro A, Böllmsjö G (2006) *Welding robots*, 1st edn. Springer, London
2. Nestor OH (1962) Heat intensity and current density distributions at the anode of high-current, inert gas arcs. *J Appl Phys* 33:1638–1648
3. Bergner A, Westermeier M, Ruhrmann C, Awakowicz P, Mentel J (2011) Temperature measurements at thoriated tungsten electrodes in a model lamp and their interpretation by numerical simulation. *J Phys D Appl Phys* 44:505203
4. Tanaka M, Terasaki H, Fujii H, Ushio M, Narita R, Kobayashi K (2006) Anode heat transfer in TIG welding and its effect on the cross-sectional area of weld penetration. *Weld Int* 20:268–274
5. Tanaka M, Tashiro S, Lowke JJ (2007) Predictions of weld formation using gas tungsten arcs for various arc lengths from unified arc-electrode model. *Sci Technol Weld J* 12:2–9
6. Sforza P, de Blasiis D (2002) On-line optical monitoring system for arc welding. *NDT & E Int* 35:37–43
7. Lu W, Zhang Y (2006) Robust sensing and control of the weld pool surface. *Meas Sci Technol* 17:2437–2446
8. Nagesh DS, Datta GL (2002) Prediction of weld bead geometry and penetration in shielded metal-arc welding using artificial neural networks. *J Mater Process Technol* 123:303–312
9. Iwao T, Inaba T (2002) Plasma length on characteristics of DC argon plasma torch arc. *Vacuum* 65:299–304
10. Ushio M, Mao W (1994) Sensors for arc welding: advantages and limitations. *Trans JWRI* 23:135–141
11. Ge WQ, Huang SS (2010) Study on fuzzy controller of welding arc length. *Adv Mater Res* 97–101:3952–3956
12. Skolnik M, Jones TB (1952) Characteristics of the high current tungsten arc in argon, helium, and their mixtures. *J Appl Phys* 23:1702272

13. Lee JH, Na SJ (2001) An analysis of volumetric radiation heat flux and experimental comparison with arc light sensing in GTA welding process. *J Mater Process Technol* 110:104–110
14. Li PJ, Zhang YM (2001) Robust sensing of arc length. *IEEE Trans Instrum Meas* 50:697–704
15. Razafinimanana M, El Hamidi L, Gleizes A, Vacquie S (1995) Experimental study of the influence of anode ablation on the characteristics of an argon transferred arc. *Plasma Sources Sci Technol* 4:501–510
16. Menart J, Lin L (1999) Numerical study of a free-burning argon arc with copper contamination from the anode. *Plasma Chem Plasma P* 19:153–170
17. Physical Measurement Labor, NIST, Physical Reference Data: atomic Spectra Database, 2011. <http://www.nist.gov/pml/data/asd.cfm/>. Accessed 15 Nov 2011
18. Gudimenko E, Milosavljević V, Daniels S (2012) Influence of self-absorption on plasma diagnostics by emission spectral lines. *Opt Express* 20:12699–12709
19. Yli-Harja O, Astola J, Neuvo Y (1991) Analysis of the properties of median and weighted median filters using threshold logic and stack filter representation. *IEEE Trans Signal Process* 39:395–410
20. Marotta A (1993) Determination of axial thermal plasma temperatures without Abel inversion. *J Phys D Appl Phys* 27:268–272
21. Konjevic N (1999) Plasma broadening and shifting of non-hydrogenic spectral lines: present status and applications. *Phys Rep* 316:339–401

# Review of Sensors and Its Applications in the Welding Robot

Xue-Qin Lu, Wen-Ming Liu and Yi-Xiong Wu

**Abstract** The use of sensors is of paramount importance for closing the feedback control loops that secure efficient and automated/autonomous operation of mobile robots in real-life applications. This paper reviews the development of sensing in welding robot and vision sensing for the weld line inspection. The robot requires several types of sensors for balancing and path planning. High accuracy and resolution of these sensors is of paramount importance for successful control of the robot. In this paper we review some of these sensors and evaluate their suitability for use in the robot. Various vision sensors and position sensors are reviewed and their advantages and disadvantages are discussed. These sensors have been incorporated and evaluated.

## 1 Introduction

The robot requires several types of sensors for balancing and path planning. High accuracy and resolution of these sensors is of paramount importance for successful control of the robot.

In a realistic setting, path planning of a robot cannot be based on complete a priori knowledge of the environment. Therefore, much attention has been paid to sensor-based path planning of mobile robots in unknown, complex and dynamic environments, and this paper focuses also on this topic. The path planning is to find a path between an initial and a final point on the roadmap. Global sensor-based path planning methods can guarantee the global convergence and generate a shorter

---

X.-Q. Lu (✉) · W.-M. Liu  
School of Automation Engineering, Shanghai University of Electric Power,  
200090 Shanghai, China  
e-mail: lvxueqin@shiep.edu.cn

Y.-X. Wu  
School of Material Science and Engineering, Shanghai Jiao Tong University,  
200030 Shanghai, China

path. The shortcoming is the heavy computational burden because the tracking path needs to be frequently recomputed as new information is discovered continuously in the local path planning. In local sensor-based path-planners, the artificial potential field method (APF) is influential, which uses local sensory information in a purely reactive fashion.

The paper is organized as follows: In Sect. 1 we review position sensors. Section 2 details three types of vision sensors. Section 3: The inertial onboard sensors are reviewed. The other sensors in welding such as ARC sensors and multi-sensor spot welding monitor using wireless sensor network are presented in Sect. 4. Some conclusions drawn from this review are presented in Sect. 5.

## 2 Position Sensors

In the last years, optical system have been becoming more and more strategic in many applications, in particular in endoscope systems by means of nano-composite materials [1, 2].

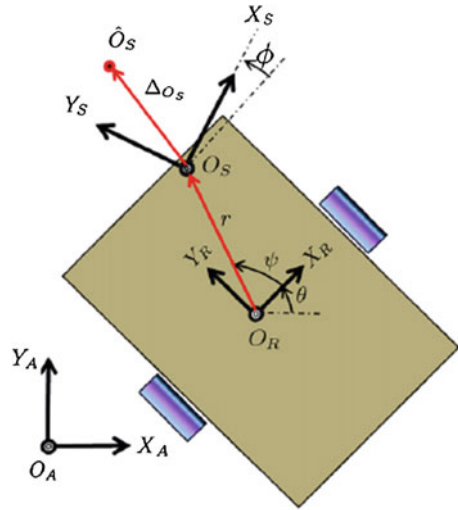
The problem of using optical sensors to detect the position of a mobile robot has been recently considered in the literatures [3–6]. The use of optical sensors as dead-reckoning sensors has the advantage that the position measurements are not dependent on the kinematics of the robot or on the rotation of the robot wheels. Therefore, the position measurements are not affected by two of the most common sources of measurement errors: (1) slipping, which occurs when a rotation of the traction wheels does not generate a corresponding motion of the robot and (2) crawling, which corresponds to a motion of the robot not measurable by incremental encoders. Two of the main advantages of optical sensors over GPS and camera-based sensors are their low cost and high resolution sensing capability. However, like every dead-reckoning method, the position measurement based on optical mice can be affected by systematic errors [7, 8].

Optical mouse sensors have been utilized recently to measure the position and orientation of a mobile robot. A systematic procedure was developed to determine the optical location of mouse sensors on mobile robot platforms with the aim of increasing the sensibility of the sensors to robot displacements. Additional constraints are utilized to force the solution to stay inside the perimeter of the robot platform.

Consider the mobile robot shown in Fig. 1, where three coordinate frames are considered to describe the robot motion. In Fig. 1, the superscripts A, R and S will be utilized for each vector to denote the frame with respect to which the vector itself is expressed [9].

Future work will consider the optimization of the sensor localization in a dynamical framework where the estimation of the robot position is affected by nonsystematic errors.

**Fig. 1** Sensor kinematics:  
coordinate axis



### 3 Vision Sensors

#### 3.1 Vision Sensor System Design

Vision sensor system is an important part of the robot welding detection system; it will directly affect the precision and forming quality in follow-up welding process. If the image acquired by vision sensor is not perfect, it will make the weld seam tracking very difficult, and even directly lead to poor quality of welding joint forming. In this paper, the design of passive vision sensor is shown in Fig. 2, which is mainly composed of CCD camera, image acquisition card, automatic transmission mechanism, dimmer-filter system, secondary reflector frame, wire feed machine, stents, etc. It has many functions, such as welding environment identifying, initial welding seam guiding, seam tracking, penetration controlling, and remote controlling. In comparison with traditional visual sensor, especially the laser sensor, the cost of production of this visual sensor is much lower.

#### 3.2 Nanocomposite Optical Sensor

In the last years, optical systems have been becoming more and more strategic in many applications, in particular in endoscope systems by means of nano-composite materials. The innovative sensor is based on the detection of the radiated optical field enhanced by gold micro/nanoparticles embedded in PDMS polymer film. The PDMS elastomer is obtained by mixing a curing agent of 1:10 weight ratio to base monomer. The aperiodicity is due to the poly dispersity of the gold nano



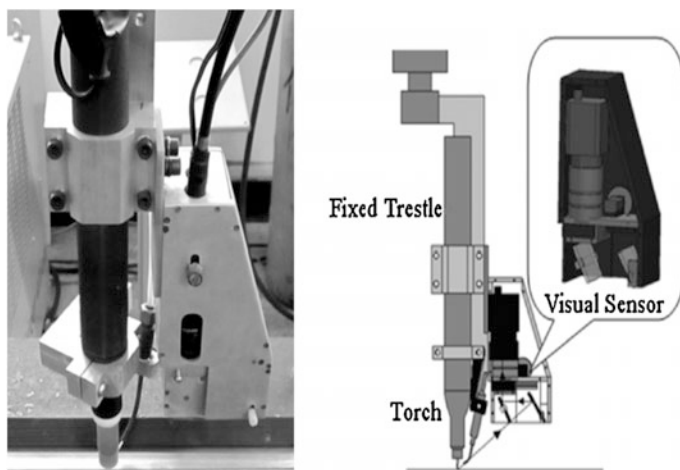


Fig. 2 The design of passive vision sensor

particles and to the not-completely homogeneous gold particle concentration. The proposed sensor is illustrated in Fig. 3a, b. In particular, in Fig. 3b the basic principle of the optical system is schematically explained [10–13]: (I) a central

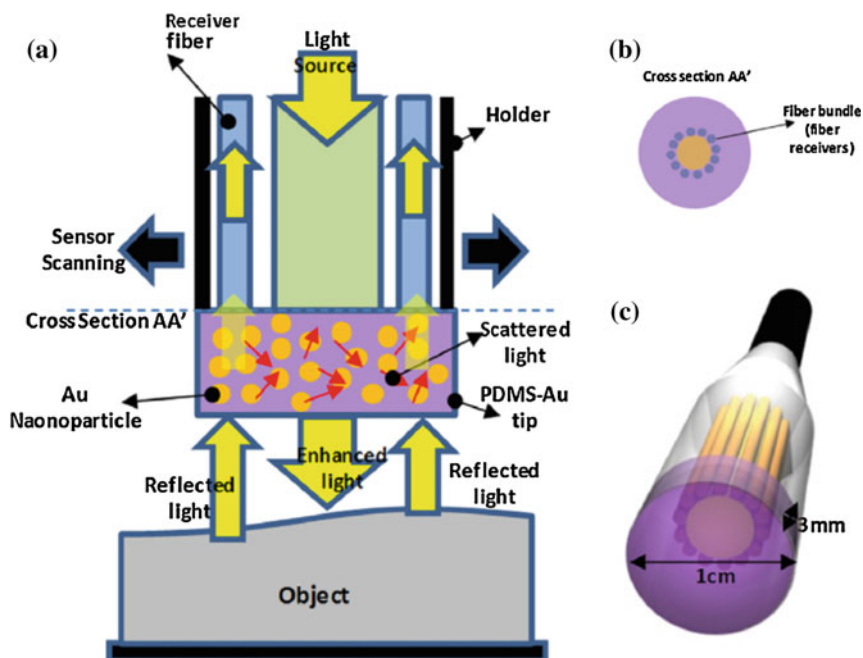
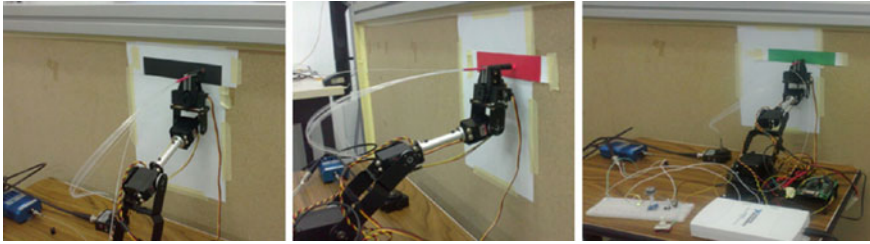


Fig. 3 a Scheme of the basic principle of optical object recognition, b cross section of the nano-composite tip and c 3D perspective of the robotic optical system



**Fig. 4** The *Black*, the *Red* and the *Green* Strip of paper for automatic color differentiation. (For interpretation of the references to color in this figure legend, the reader is referred to the web version of this article.)

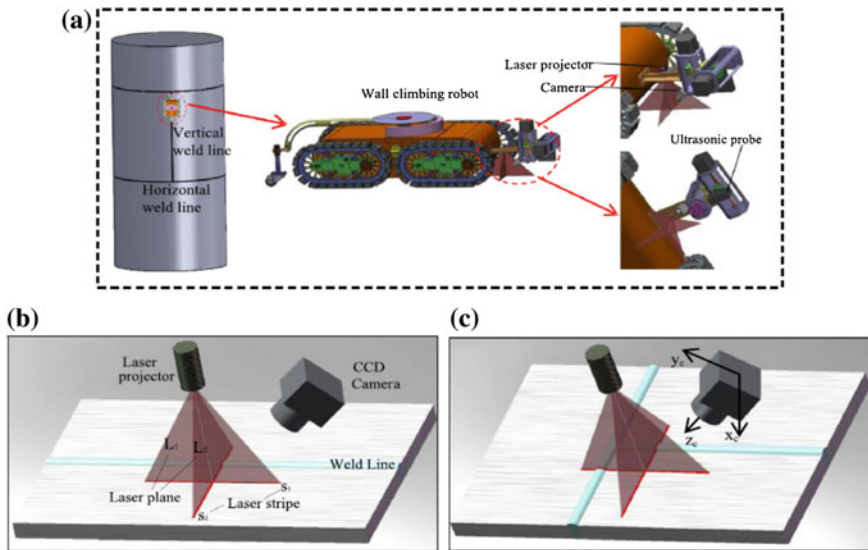
multimode input fiber is coupled to a light source; (II) the light is enhanced by a PDMS-Au nano-composite tip; (III) the enhanced light is backscattered by the target object; (IV) the backscattered light is enhanced again by PDMS-Au tip and coupled by a receiver optical fiber bundle arranged around the central fiber (as shown in Fig. 3b). As in active (doped materials) nonlinear materials, and in doped fiber amplifier [14], the input energy of light may change its intensity depending on the excitation band and on the effective complex refractive index which is function of the metal concentration as volume filling factor [15].

In order to recognize 3D features of objects, the proposed sensor is mounted on the end-effector of a robotic arm, as illustrated in Fig. 4. The optical sensor is also able to provide useful information on the color of the reflecting surface. Many experimental tests were carried out by hanging some colored stripes of paper on the wooden panel. Three different colored stripes were used in two different scanning processes: a black, a red and a green strip (the stripes are pictured in Fig. 4).

The sensor is moved in such a way as to scan a surface without coming into contact with such surface. The proposed work describes and characterizes the nano-composite sensor, providing all the technological details. Moreover, the experimental setup was accurately studied permitting to detect some 3D target objects adding information about their colors. All the testing process is performed by a multilevel robotic arm scanning.

### ***3.3 Laser Vision Sensor for Weld Line Detection on Wall-Climbing Robot***

To perform non-destructive testing very important to guarantee the safety operation of lots of industry facilities, such as towers of the wind turbines and oil storage tanks. In automatic non destructive testing (NDT) systems, automatic weld line detection and tracking can navigate moving plat form sand improve the testing performance and efficiency significantly. In literatures [16–18], distance measurement, monocular vision and structured light some approach shave been applied to detect the weld lines.

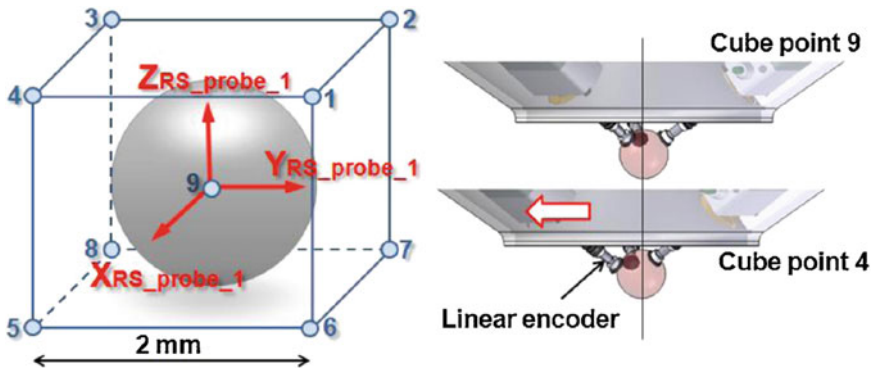


**Fig. 5** Weld line detection and tracking system. **a** The platform, **b** the CSL projector and imaging CCD on straight weld line and **c** on cross weld lines

The weld line detection and tracking system platform is shown in Fig. 5a [19]. It is composed of a wall-climbing robot, an ultrasonic device of NDT and a CSL sensor. Figure 5b, c illustrate the CSL projector and image capturing CCD on straight weld line and cross weld lines, respectively. The laser projector is fixed on the robot and perpendicular to the weldment. Two stripes  $s_1$  and  $s_2$  are formed by intersection lines between weldment and two orthogonal laser planes  $L_1$  and  $L_2$ . The laser projector projects across laser beam on the weld line, forming convex light stripe around weld line. According to the laser triangulation measurement method, the 3D information of the weldment surface can be obtained by calculating the camera coordinates of the points on the lights tripe transformed from the image coordinates. In general, when the robot moves along the straight weld line, only a convex arc exists on the stripe  $s_2$ , as shown in Fig. 5b. When the robot is close to a T-intersection of vertical and horizontal weld lines, two convex arcs will appear at the strips, as showed in Fig. 5c. The sensor can simultaneously detect the locations of the horizontal and the vertical weld lines, which are used to plan the motion path of the robot.

## 4 The Inertial Onboard Sensor

Santolaria et al. [20] presents a technique for auto-calibration of contact measurement systems mounted on a robot for use in data acquisition for parameter identification and calibration of robots through measurements made in geometrical gauges.



**Fig. 6** Trajectories describing the cube and points captured to determine the orientation of the probe frame in the robot global frame. Detail of the linear encoders position probing two points of the trajectories

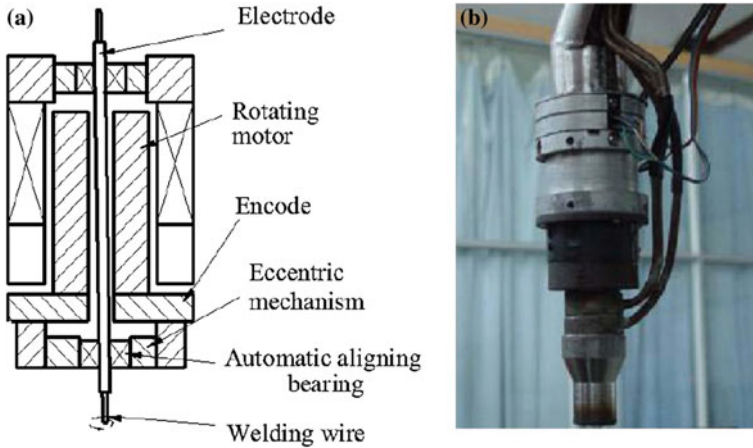
The first step in locating the sensor frame is obtaining the rotational matrix between the sensor and the global frame of the robot. To do this, the robot TCP is manually positioned so that the three linear encoders of the self-centering probe are touching the calibration sphere and at the same time are approximately in the middle of their workspace range. This is the starting pose for the linear trajectories in which the robot TCP will trace the lines between the edges of a cube centered in this initial position without modifying the frame orientation (Fig. 6). A total of nine target points are captured along these trajectories, corresponding to the eight edges of the cube and its center. The self-centering probe data and the angle of each articulation of the robot are captured in each target point. The X, Y, Z coordinates are obtained from the self-centering probe data expressed in the self-centering probe frame, while the pose of the last frame of the robot kinematic chain is obtained from the angles of each articulation through the kinematic model.

Although the technique is presented for a self-centering probe used to measure a gauge ball bar, it is also applicable to other on-board contact or non-contact measurement sensors, as well as in data acquisition through external measuring equipment that materializes points measured using reflectors mounted on the hand or body of a robot.

## 5 The Other Sensors in Welding

### 5.1 ARC Sensors

Arc welding is one of the most important areas of application for industrial robots. In most manufacturing situations, uncertainties in dimensions of the part, geometry of the joint, and the welding process itself make the use of sensors essential to



**Fig. 7** High speed rotating arc sensor: **a** sensor configuration and **b** high speed rotating arc sensor installed on robot

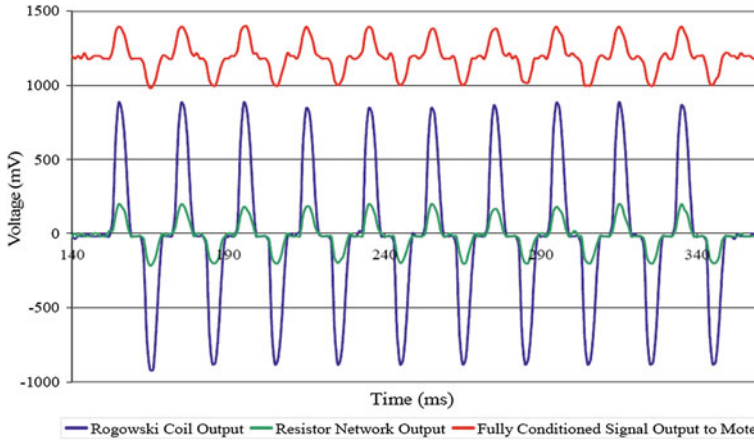
maintaining weld quality. In literature [22], three types of control systems for arc welding robots are described: (1) tracking systems for centering the weld puddle over the joint, (2) weld process controls for maintaining proper seam width and penetration, and (3) supervisory controls for sequencing welding operations. These control functions have been implemented successfully in production using a computer vision sensor integrated into the welding torch. Experimental results are presented demonstrating the capabilities of the system.

The seam tracking accuracy is not enough relying solely on the mobile body because of high precision request of seam tracking and mobile welding robot inertia of a larger whole. Therefore, the robot system uses two stage tracking strategy by moving the body for coarse tracking and moving the cross slide for accurate tracking [23].

Schematic diagram of devised rotation mechanism, which replaces the original torch of the robot, is showed in Fig. 7 [24]. The rotating welding wire is driven by hollow shaft electromotor. The value of welding current is taken in form of a sensor voltage and serves the seam tracking process control as real value.

## ***5.2 Multi-sensor Spot Welding Monitor Using Wireless Sensor Network***

Spot welding is an important welding technique that has been long established and extensively used in industry, especially the automotive industry. The main quality control tests are the destructive chisel test and peel test, which are carried out on



**Fig. 8** Measured signal levels from sensor conditioning circuit

welds obtained from the production line of the product. The failure rates are then detected, examined, and evaluated.

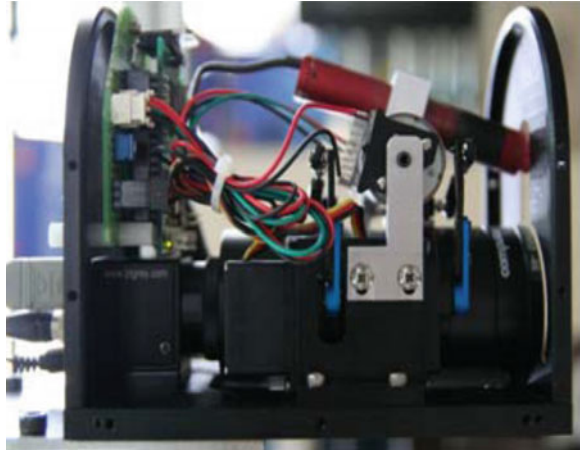
To counter the need to destructively test so many spot welds the use of a sensor cluster comprising a series of sensors was investigated to meet industrial requirements. The multiple outputs of the sensor cluster would give a prediction of the nugget size, upon which a decision of weld quality was made [25]. An additional sensor input to the cluster is the condition of the electrode, since a poor electrode changes the current density through the metal, resulting in either excessive or insufficient heating. A conditioning circuit was designed to take the output of the current sensor and reduce the signal amplitude as well as shifting it such that it varied over the range of approximately 0.1–2.1 V. Figure 8 shows the measured results from the circuit once it was built. Measurements were taken with a GDS-810S oscilloscope.

### 5.3 Laser Sensors

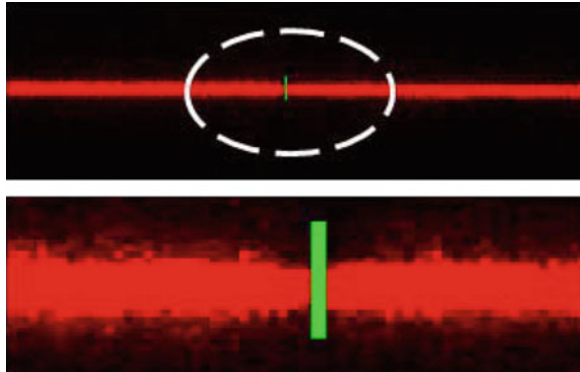
There is an increasing demand for the laser welding in automotive industry. Compared with the spot welding, the laser welding technology enables the car body to have a strong weld and light weight. Recently, the robot systems have been used in the laser welding manufacturing and they are equipped with a laser source and an optical fiber, which was shown in Fig. 9. In addition, a real-time tracking is demanded in industries [26].

In Fig. 10, a sample image of the butt joint is given. Minute differences can be found at the seam location and the thickness of the laser line is smaller than other

**Fig. 9** Developed welding profile sensor



**Fig. 10** Seam detection of a butt joint

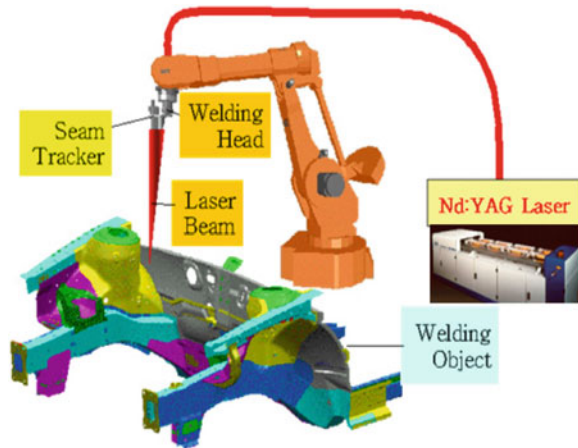


regions. Therefore, the recognition of the narrow laser line as well as the edge detection is used for the seam detection of a butt joint. The detected seam location is also indicated.

The developed welding profile sensor is applied to the laser welding robot system. The robot, the seam tracking system and CW Nd: YAG laser are used for three dimensional robot laser welding as shown in Fig. 11. A 4 kW Nd:YAG laser and the 6 axes industrial robot are used in this study. The precise positioning ( $<200 \mu\text{m}$ ) of the laser beam on the joint to be assembled is achieved by the seam tracker. In this system, the developed welding profile sensor is substituted for the previous seam tracker. Butt and lap joints are considered as the welding joints of car body.



**Fig. 11** Three dimensional laser welding



## 6 Conclusion

The developed welding profile sensor is applied to the laser welding robot system and the sensor is substituted for the commercial seam tracker. With the guide of the sensor, the robot can follow the seam of the welding part.

This article aims to review the recent research into sensing technologies its application on welding robot. Following an introduction, this article discusses position sensing research and vision sensor, and other welding sensors.

The robot requires several types of sensors for balancing and path planning. High accuracy and resolution of these sensors is of paramount importance for successful control of the robot. In this paper we review some of these sensors and evaluate their suitability for use in the robot. Various vision sensors and position sensors are reviewed and their advantages and disadvantages are discussed. These sensors have been incorporated and evaluated.

For the future works, the robust technique to fill the occluded region will be implemented. Also, to make the image processing procedures more efficient and more robust is important to enhance the tracking performance.

**Acknowledgment** This project supported by National Natural Science Foundation of China (Grant No. 51405286), and Shanghai Key Laboratory of Power Station Automation Technology (No. 13 DZ2273800).

## References

1. Bishop AN, Fidan B, Anderson BDO et al (2010) Optimality analysis of sensor-target localization geometries. *Automatica* 46(3):479–492
2. Bonarini A, Matteucci M, Restelli M (2005) Automatic error detection and reduction for anodometric sensor based on two optical mice. In: Proceedings of the 2005 IEEE international conference on robotics and automation, pp 1675–1680



3. Cimino M, Pagilla PR (2010) Location of optical mouse sensors on mobile robots for odometry. In: Proceedings of the 2010 IEEE international conference on robotics and automation
4. Hyun D, Yang HS, Park HR et al (2009) Differential optical navigation sensor for mobile robots. *Sens Actuators A* 156(2):296–301
5. Kim S, Lee S (2008) Robustness analysis of mobile robot velocity estimation using a regular polygonal array of optical mice. In: Proceedings of the 17th IFAC world congress vol 17(1)
6. Lee S, Song J-B (2004) Mobile robot localization using optical flow sensors. *Int J Control Autom Syst* 2(4):485–493
7. Martínez S, Bullo F (2006) Optimal sensor placement and motion coordination for target tracking. *Automatica* 42(4):661–668
8. Sekimori D, Miyazaki F (2005) Self-localization for indoor mobile robots based on optical mouse sensor values and simple global camera information. In: 2005 IEEE international conference on robotics and biomimetics, pp 605–610
9. Cimino M, Pagilla PR (2011) Optimal location of mouse sensors on mobile robots for position sensing. *Automatica* 47:2267–2272
10. Ata AA, Rafeek A, Yusof H (2005) Sensory based colour sorting automated robotic cell. *J Intell Rob Syst* 43:99–110
11. Giannoccaro NI, Spedicato L, di Castri C (2012) A new strategy for spatial reconstruction of orthogonal planes using a rotating array of ultrasonic sensors. *IEEE Sens J* 12:1307–1316
12. Giannoccaro NI, Spedicato L (2013) Exploratory data analysis for robot perception of room environments by means of an in-air sonar scanner. *Ultrason Elsevier* 53(6):1163–1173
13. Spedicato L, Giannoccaro NI, Reina G, Bellone M (2013) Clustering and PCA for reconstructing two perpendicular planes using ultrasonic sensors. *Int J Adv Rob Syst* 210(10):1–9
14. Beecroft LL, Ober CK (1997) Nanocomposite materials for optical applications. *Chem Mater* 9:1302–1317
15. Massaro A, Spano F, Cingolani R, Athanassiou A (2011) Pillar type PDMS nanocomposite optical sensors for liquid detection systems. *J Mater Sci Eng B* 1:819–827
16. Molina L, Freire R, Carvalho E et al (2010) A model-based fault-tolerant weld line detection for automatic In section of storage tanks using visual information and  $\alpha$ - $\beta$  filter. In: Proceedings of Latin American robotics symposium and intelligent robotic meeting, pp 25–29
17. Wang X, Liang D, Zhang T (2007) A robust vision based weld center finding method in automatic ultrasonic nondestructive test. In: Proceedings of IEEE international control and automation conference, pp 162–165
18. Zhang L, Jiao J, Ye Q, et al (2012) Robust weldline detection with cross structured light and Hidden Markov Model. In: Proceedings of IEEE international mechatronics and automation conference, pp 1411–1416
19. Zhang L, Ke W, Ye Q et al (2014) A novel laser vision sensor for weld line detection on wall-climbing robot. *Optics Laser Technol* 60:69–79
20. Santolaria J, Brosed F-J, Velázquez J et al (2013) Self-alignment of on-board measurement sensors for robot kinematic calibration. *Precis Eng* 37: 699–710
21. Santolaria J, Brau A, Velázquez J, Aguilar JJ (2010) A self-centering active probing technique for kinematic parameter identification and verification of articulated arm coordinate measuring machines. *Measur Sci Technol* 2:055101
22. Xu Y, Yu H, Zhong J et al (2012) Real-time seam tracking control technology during welding robot GTAW process based on passive vision sensor. *J Mater Process Technol* 212:1654–1662
23. Mao Z-W, Pan J-L, Zhang H (2010) Mobile welding robot system based on rotating arc sensor applied for large fillet welding seam tracking. In: 2010 6th international conference on natural computation (ICNC 2010), pp 394–397
24. Jia J, Zhang H, Xiong Z (2006) A fuzzy tracking control system for ARC welding robot based on rotating ARC sensor. In: Proceedings of the 2006 IEEE international conference on information acquisition 20–23 Aug 2006, Weihai, Shandong, China, pp 967–971

25. Cullen JD, Mason A, Al-Jader M et al (2011) Multi-sensor spot welding monitor using wireless sensor network technology. In: 2011 IEEE symposium on computers and informatics, pp 806–810
26. Kim C-H, Choi T-Y, Lee J-J et al (2008) Intelligent vision sensor for the robotic laser welding. In: The IEEE international conference on industrial informatics (INDIN 2008) DCC, Daejeon, Korea July 13–16, 2008

# A Review and Preliminary Experiment on Application of Infrared Thermography in Welding

Chao Hu and Xi-Zhang Chen

**Abstract** Infrared thermography, as a convenient, non-contact, non-destructive and real-time detection method, has especially advantages for the welding technology because fusion welding always company with high temperature history. The aim of this publication is to review the state-of-the-art of instrumentation and methodology in the application of infrared thermography for welding, especially focusing on the welding quality control. Researches show that infrared thermography can be used to inspect weld joints and monitor the welding process, seam tracking, control the penetration depth and improve the quality of welds. The author also did some research and obtained some valuable results. Preliminary experiments are also carried out to acquire real time IR image and temperature profile in order to analyze the weld geometry and detect the welding defects.

## 1 Introduction

In conjunction with the rapid development of high quality welding today, industrial manufacturing has a growing demand for process monitoring and diagnosis. One of the most effective methods is infrared thermography. It has been widely used in automatic welding in order to monitor and improve the stability of welding process [1].

Electromagnetic wave with the wavelength of 0.75–1000  $\mu\text{m}$  is called infrared ray or infrared radiation. Objects with temperature above 0 K continuously emits infrared radiation. Infrared radiation (IR) include near infrared (0.75–3  $\mu\text{m}$ ), medium infrared (3–6  $\mu\text{m}$ ) and far infrared (6–1000  $\mu\text{m}$ ) [2]. It took almost two centuries to adopt infrared thermography in civil domain due to lack of mature technology and reliable

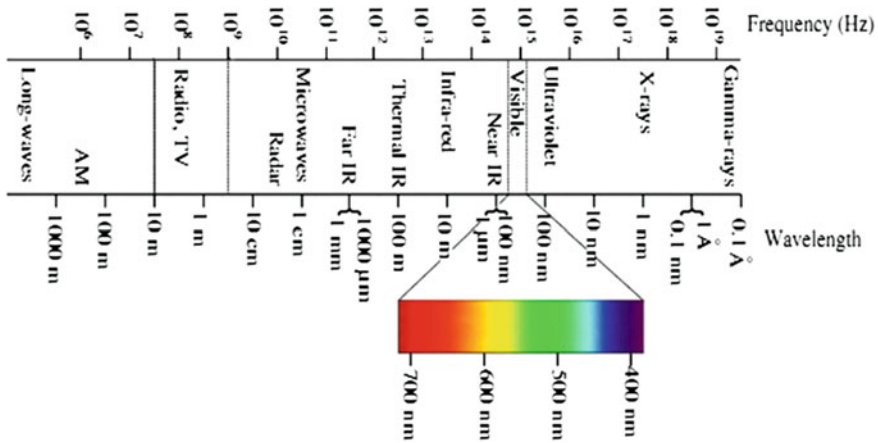
---

C. Hu

School of Material Science and Engineering, Jiangsu University,  
Zhenjiang 212013, China

X.-Z. Chen (✉)

School of Mechanical and Electrical Engineering, Wen Zhou University,  
Wenzhou 325035, China  
e-mail: kernel.chen@gmail.com



**Fig. 1** The complete electromagnetic spectrum [6]

performance of equipments. IR with wavelength between 2–13  $\mu\text{m}$  is perceived and used by infrared thermal imager, only the wavelength between 1–2.5  $\mu\text{m}$ , 3–5  $\mu\text{m}$  and 8–13  $\mu\text{m}$  can be transmitted through the air into the distance [3], thermal infrared detector is designed according to the characteristics of these three bands.

Infrared thermography has several advantages as wide measuring temperature range, strong real-time performance and fast measurement speed, and no illumination needed. Object emit infrared radiation, and the hotter it is, the greater the intensity of the radiation. IR cameras focus on the incoming radiation at each point into an electronic signal and displays in a thermal image. The brightest point in the image is the hottest [4]. Infrared thermography transforms thermal energy into a visible image and each energy level is represented by a color [5]. Thermal infrared energy is invisible to human eyes, but operates at a different region of the electromagnetic spectrum as shown in Fig. 1 [6]. It shows the wavelength of different thermal infrared energy.

## 2 Infrared Detector and Its Development

Infrared thermal imager is basically a camera that has an infrared detector. It can be used in imaging in the environment without sufficient light. Infrared camera detects the intensity of radiation and displays it as a digital image. Different pixel values in the image represent different infrared intensity. Many thermal infrared cameras are sensitive to electromagnetic energy with wavelengths in the range of 1–15  $\mu\text{m}$  [7].

Infrared detectors are the key of infrared thermal systems and can be generally classified into two categories as thermal and semiconductors. They are consisting of the optical arrangements (lens, mirrors, etc.), detect elements, cooling system and associated electronics. Infrared cameras have experienced many times of modification [3]. The first generation cameras consisted of a detector and two scanning

mirrors. The second generation used two similar scanning mirrors along with array detectors. The third generation had two dimensional array detectors without mirrors [8, 9]. The size of the IR cameras are smaller and smaller according to different application requirement, which leave more space for other devices and make it more applicable to industrial application. Light weight and portable handheld cameras with built-in display are also available nowadays. It takes several performance parameters into consideration before choosing an infrared camera in order to acquire a sharp and accurate thermal image. Venkataraman and Raj [10] reported a detailed study of these performance parameters. These parameters include spectral range, spatial resolution, temperature resolution, temperature range and frame rate.

### **3 The Characteristics of Infrared Thermography in Welding**

Welding is one of the most widely used methods in joining metal or nonmetal. The welded joints are often the weakest location to fail in structures. Hence it is necessary to inspect the quality of weld joints in order to ensure the safety of structures. Compared to the conventional methods, infrared thermography can not only be used for detecting welding defects, but also for real-time monitoring of the welding process, helping to analyze the causes of welding defects and enhance welding quality and the stability of welding process. In addition, infrared thermography is widely used in seam tracking, welding penetration testing, welding temperature field monitoring and welds mechanical properties evaluation.

### **4 The Applications of Infrared Thermography in Welding**

Real-time temperature distribution gradient images can be obtained by infrared thermography, which is necessary to monitor the welding temperature field, welding process and detect the welding defects.

#### ***4.1 Temperature Field Monitoring and Welding Quality Control***

Pulse thermography is widely used in quality inspection of metal and composite materials, using short-term heat pulse as an excitation source in order to acquire the transient temperature evolution of the measuring area. Chen et al. [11] integrated the ultrasonic energy into infrared thermal imaging. When the ultrasonic pulse is motivated, carried energy is rapidly spread in the specimen and almost instantaneous in solid specimen. When ultrasonic transmits to heterogeneous area, the heat

generated by the acoustic attenuation is more than homogeneous area, leading to the thermo-elastic effect and hysteresis effect [12]. Ultrasonic energy was converted into heat energy and transmitted to the specimen surface in the form of thermal wave. The infrared imager adopted the JADE III produced by CEDIP. The specimens were six pieces of 1 mm thick stainless steel plate respectively welding with 2 mm stainless plate after rolling. The laser power and welding speed of these six specimens were different. As shown in Fig. 2, the brightness degree of the infrared images represents that the welding quality of the dark line is better and the ambient temperature is higher. The dark line is the transition zone of weld and non-welding area. The two pieces of steel plates are not fully welded together, and it is characterized in bright area because the ultrasonic energy is converted into heat. As shown in Fig. 3, weld combined situation is analyzed by the infrared images to acquire better welding speed. Using infrared thermography to inspect the adhesion integrity of plastic welded joints [13] and ultrasound infrared thermography to detect micro-cracks in the dissimilar metal weld [14] are also reported.

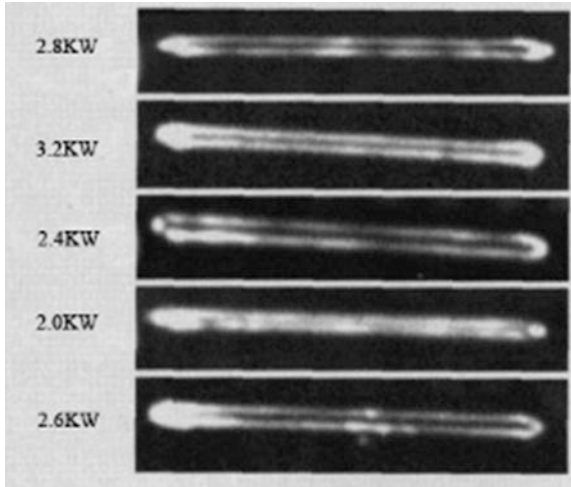


Fig. 2 Heat images of welding specimens with different welding power [26]

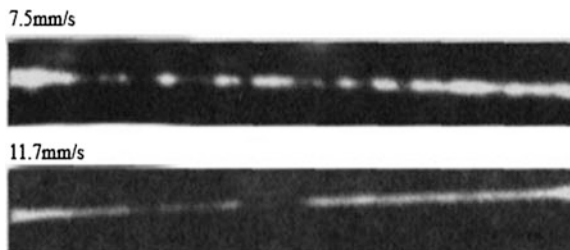


Fig. 3 Heat images of welding specimens with different welding rate [26]

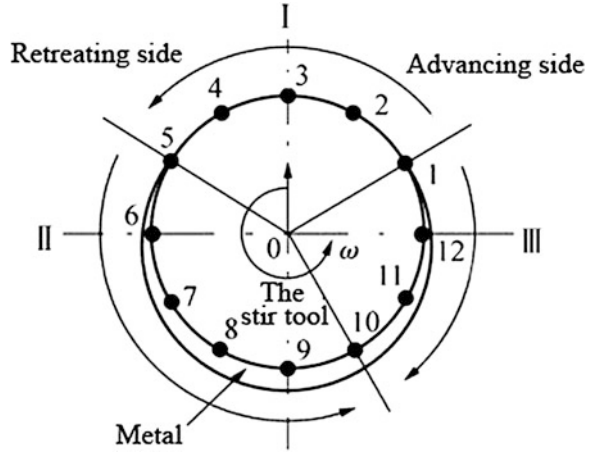
Zhao and Li [15] conducted infrared NDT by using a finite element analysis software ANSYS, the research mainly analyzed the porosity with a certain size. The temperature field of the porous parts and complete parts are different and the surface temperature of defective parts is higher than that of complete parts. The nature of the defects is quantitative judged according to the infrared thermal image features and the surface temperature rising, improving the stability of the infrared NDT. Applying infrared thermography for polyethylene pipe welding in the oil and natural gas transmission projects are also reported. Kafieh et al. [16] took advantages of infrared thermography to inspect welding defects of polyethylene pipes, they selected the thermal image in the fifth seconds of welding cooling process as the best image, preprocess the image through Gaussian filter and Gamma correction, obtained the final image through clustering algorithms and then analyzed the image with the MATLAB software. The method has a high accuracy in determining the location and category of defects and embodies a high maneuverability. Suriani et al. [4] applied infrared thermography for defects detection. The experiment made three groups of Kenaf/Epoxy specimens which were heated 60 min under 100 °C, and then analyzed the defects in the Kenaf/Epoxy specimens using thermal images. The optical microscope and SEM verified the defects detection accuracy is as high as 95 %. Using infrared thermography for nondestructive evaluation of welded joints and controlling the laser welding of amorphous polymers are also reported [17].

Infrared thermography was also applied for the fatigue life prediction of AZ31B and its welding joint. The infrared camera was VarioCAM hr, the detection was conducted by establishing the relationship between temperature evolution and fatigue life. Relation curves between the fatigue load and temperature evolution were drawn according to infrared thermal images of specimens under different fatigue load, and then obtained the temperature gradient and fatigue life curves through several calculation formulas. It has been proved that the maximum error in the fatigue life prediction of pristine specimens and the welded joints is 2.37 and 7.01 %, respectively [18].

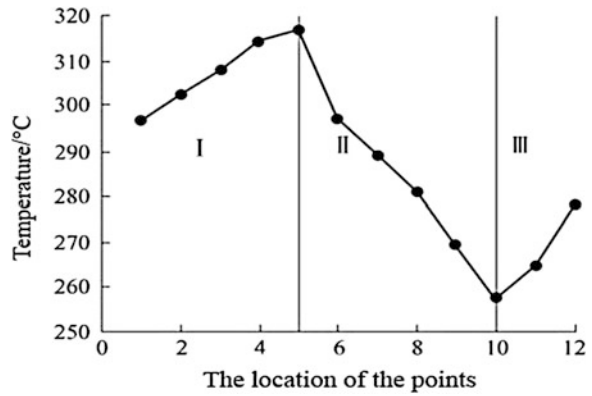
Friction stir welding is a kind of solid joining technology with low temperature, high efficiency and excellent performance. It has an obvious advantage in the welding of aluminum alloy, magnesium alloy and titanium alloy. But the method is easy to produce holes, grooves, lack of penetration and other defects. Gan et al. [19] used infrared thermography to analyze the formation mechanism of tunnel shaped holes in friction stir welding and found the causes of defects. Figure 4 shows the temperature measuring points and transfer diagram of the stir tool, Fig. 5 is the average temperature curves of the measuring points which are drawn according to infrared images, using these curves to analyze the heat transfer process of the welding process and acquiring the formation mechanism of holes.

Infrared thermography was used in measuring the laser-GTA welding temperature field of magnesium alloy. The experimental camera was uncooled focal plane camera SAT-HY6000A. The real-temperature correction and surface correction was done to infrared images, combine with numerical simulation of welding temperature field, getting the whole composite heat source distribution of laser-GTA welding temperature field of the magnesium alloy AZ31B [20].

**Fig. 4** The temperature measuring points and transfer diagram of the stir tool [19]



**Fig. 5** The average temperature curves of the measuring points [19]



Infrared thermography faces lots of interference such as: arc light, hot tungsten electrode and so on, the interference for high reflectivity materials is more serious [21]. Huang et al. [22] researched the interference of arc light, ceramic nozzle and laser nozzle in hybrid laser-GTA welding of magnesium alloy, they found the interferences can be transferred out of welding seam by placing the infrared thermography system perpendicularly to weld seam.

### 4.2 Seam Tracking

Vasudevan et al. [23] acquired GTA welding thermal images of 316LN stainless steel by taking advantage of infrared thermography. By comparison, the temperature mutations of melt pool in the coordinate system were corresponding to the macroscopic defects in the specimen. Base on the investigation, a close-loop



feed-back system was established to control the depth of penetration from infrared thermal images in real-time. Using a feedback system to measure visible and near-infrared light to control joint penetration is also reported [24].

Doubenskaia et al. [25] used infrared thermography to research the laser cladding temperature conditions of TiAlV4 alloy which was used for repairing the damage parts of base metal. Actual temperature evolution of the melt pool and cooling rates of the liquid and solid phases was found according to the IR images. Gao et al. [26] used IR to research seam tracking during fiber laser welding of austenitic stainless steel. The deviations between the laser-beam focus and the weld-seam center was extracted by thermal gradient parameter. The laser-beam focus position was adjusted in real time using calibration equations.

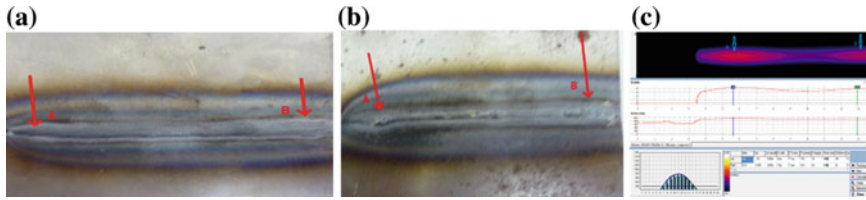
Sreedhar et al. [27] conducted the research of automatic defect identification by using thermal image analysis for online welding quality monitoring. The GTA welding temperature field of aluminum alloy AA2219 was monitored by IR camera. Compared with the infrared images and radiographic images, it has been proved that infrared thermography is reliable for real-time monitoring of welding defects. Alfaro and Franco [28] used infrared camera for real-time monitoring of GTA welding process and acquires the relationship between infrared signal and penetration depth.

### ***4.3 Welding Penetration Depth Control***

Wikle III et al. [29] used infrared sensor for penetration depth control of the submerged arc welding process. Heat transfer model was established first. When the temperature distribution on the surface of the plates changes, adjusting the welding voltage and wire feed speed according to feedback information and the welding heat input in order to compensate the changes of the plate geometric dimension, achieving the purpose of the penetration depth control.

### ***4.4 Preliminary Experiments***

The author also did some preliminary research on welding process monitoring, welding geometry calculation and welding defects detecting by IR. A special IR sensor was designed to real time scan welding temperature profile on work-pieces surface. Q235 steel was butt welded using GTA welding. Part of the experiments is shown in Fig. 6, the whole temperature profile and history are record and analyzed. AS shown in Fig. 6, Point A and B in Fig. 6a, b are the arc starting and end point, respectively. It is shown that the welding penetration depth near point A and B is deeper than other parts due to the arc retention in A and the limitation of heat dissipation in B. The temperature difference in the thermal image can help to illustrate the causes of the different welding penetration depth. The width of



**Fig. 6** Experiments on welding geometry detecting. **a** Front side, **b** Backside, **c** The infrared image and analysis

temperature profile in Fig. 6c also reveals both the front and backside weld width by some functions. Further researches are ongoing.

## 5 Summary and Outlook

A series of activities on the application of infrared thermography are being carried out under worldwide collaboration with many institutes, universities and companies. This paper briefly reviewed the application of IR in welding process monitoring, quality control and welding penetration depth control, such as laser welding, friction stir welding, laser cladding, polyethylene pipe welding, judging the welding defects, eliminating the radiated interference in the welding process. Some analytical methods and algorithms are also reviewed in this paper. Due to the special characteristics of IR in temperature and thermal related characters of welding process, infrared thermography is a promising technology for welding process monitoring, quality control and defects detecting. Our preliminary experiments also reveal it is possible to detect welding geometry, process monitoring and defects detecting.

## References

1. Kim JS, Son YT, Cho HS et al (1996) A robust visual seam tracking system for robotic arc welding. *Mechatronics* 6(2):141–163
2. Zhao L (2010) Research of infrared thermal wave non-destructive testing of aircraft engine turbine blades crack. Changchun University of Science and Technology
3. Bagavathiappan S, Lahiri BB, Saravanan T et al (2013) Infrared thermography for condition monitoring—a review. *Infrared Phys Technol* 60:35–55
4. Suriani MJ, Ali A, Khalina A et al (2012) Detection of defects in kenaf/epoxy using infrared thermal imaging technique. *Procedia Chemistry* 4:172–178
5. Meola C, Di Maio R, Roberti N et al (2005) Application of infrared thermography and geophysical methods for defect detection in architectural structures. *Eng Fail Anal* 12(6):875–892
6. Ralston JC, Strange AD (2013) Developing selective mining capability for longwall shearers using thermal infrared-based seam tracking. *Int J Min Sci Technol* 23(1):47–53

7. Brooker G (2009) Introduction to sensors for ranging and imaging. Scitech Publishing Inc., Raleigh
8. Zhang ZM, Tsai BK, Machin G (2010) Radiometric temperature measurements. Academic Press, Oxford
9. Jones DP (2010) Biomedical sensors. Momentum Press, New York
10. Venkataraman B, Raj B (2003) Performance parameters for thermal imaging systems. *Insight* 45:531–535
11. Chen DP, Li XL, Li YH et al (2008) Ultrasonic infrared thermography testing for the quality of laser welded seams. *Nondestr Test* 30(10):747–749
12. Hong Y, Miao PC, Zhang ZN et al (2003) The ultrasonic infrared thermography and its application in NDE. *J Nanjing Univ* 39(4):547–552
13. Omar M, Hassan M, Donohue K et al (2006) Infrared thermography for inspecting the adhesion integrity of plastic welded joints. *NDT E Int* 39(1):1–7
14. Park H, Choi M, Park J et al (2014) A study on detection of micro-cracks in the dissimilar metal weld through ultrasound infrared thermography. *Infrared Phys Technol* 62:124–131
15. Zhao YS, Li DP (2006) The infrared non-destructive testing for the detect in weld based on finite element method. *J Mech Electr Eng* 22(12):39–42
16. Kafieh R, Lotfi T, Amirfattahi R (2011) Automatic detection of defects on polyethylene pipe welding using thermal infrared imaging. *Infrared Phys Technol* 54(4):317–325
17. Meola C, Carlomagno GM, Squillace A et al (2004) The use of infrared thermography for nondestructive evaluation of joints. *Infrared Phys Technol* 46(1):93–99
18. Liu XQ, Zhang HX, Yan ZF et al (2013) Fatigue life prediction of AZ31B magnesium alloy and its welding joint through infrared thermography. *Theoret Appl Fract Mech* 67:46–52
19. Gan YF, Li JL, Xiong JT et al (2012) Analysis of tunnel defect formation produce by using infrared thermography. *Electric Weld Mach* 42(1):22–25
20. Huang RS, Liu LM, Chi MS (2006) Infrared measurement and numerical simulation of temperature field in hybrid laser-TIG welding process of magnesium alloys. *Trans China Weld Inst* 27(10):89–93
21. Wang JF, Yu HD, Qian YZ et al (2011) Interference analysis of infrared temperature measurement in hybrid welding. In: *Robotic welding, intelligence and automation*. Springer, Berlin, pp 369–374
22. Huang RS, Liu LM, Song G (2007) Infrared temperature measurement and interference analysis of magnesium alloys in hybrid laser-TIG welding process. *Mater Sci Eng A* 447(1):239–243
23. Vasudevan M, Chandrasekhar MN, Maduraimuthu MV et al (2011) Real-time monitoring of weld pool during GTAW using infra-red thermography and analysis of infra-red thermal images. *Weld World* 55(7–8):83–89
24. Bentley AE, Marburger SJ (1992) Arc welding penetration control using quantitative feedback theory. *Welding J New York* 71:397-s
25. Doubenskaia M, Pavlov M, Grigoriev S et al (2013) Definition of brightness temperature and restoration of true temperature in laser cladding using infrared camera. *Surf Coat Technol* 220:244–247
26. Gao XD, You DY, Katayama SJ (2012) Infrared image recognition for seam tracking monitoring during fiber laser welding. *Mechatronics* 22(4):370–380
27. Sreedhar U, Krishnamurthy CV, Balasubramaniam K et al (2012) Automatic defect identification using thermal image analysis for online weld quality monitoring. *J Mater Process Technol* 212(7):1557–1566
28. Alfaro SCA, Franco FD (2010) Exploring infrared sensing for real time welding defects monitoring in GTAW. *Sensors* 10(6):5962–5974
29. Wikle HC III, Kottilingam S, Zee RH et al (2001) Infrared sensing techniques for penetration depth control of the submerged arc welding process. *J Mater Process Technol* 113(1):228–233

# Active Shape Model for Visual Detection and Localization of Variable Polarity PAW Weld Pool

Di Wu, Ming-Hua Hu, Lu-Lu Chen, Hau-Bin Chen, Tao Lin  
and Shan-Ben Chen

**Abstract** In order to control the quality process of variable polarity PAW weld of aluminum alloys, extracting its characteristic parameters of weld pool is an important issue for automated and robotic welding, wherein the visual detection and localization of weld pool are critical steps. Previous methods of visual measurement of weld pool usually depend on artificial experience to detect weld pool and assume that the weld pool exists in a special shape and size. Considering these methods are based on idealized model and lack of enough accuracy, in this paper, we propose a robust visual detection and localization method for the pool of variable polarity PAW weld pool based on active shape model. It provides an elegant framework for representing the outline of a weld pool and is especially efficient for weld pool detection and localization in cluttered scenes. The result shows, it can detect and localize weld pool faster and more efficiently which lay a solid foundation for extraction of characteristic parameters.

## 1 Introduction

The variable polarity plasma arc welding (VPPAW) has some advantages such as small deformation, high productivity and “zero-defect” which can be widely used in welding of aerospace products. Visual image sensing is an effective way to ensure the quality of the welding process. In recent years, welding researchers have paid more and more attention to image sensing of welding pool to acquiring the characteristic signals reflecting full penetration and formation of the weld bead in gas tungsten arc weld (GTAW) and VPPAW. Wang et al. [1] assumed that the location and the size of the pulsed GTAW pool are nearly constant. They adopted the back propagation neural network to remove the noise edge pixel and took the remnant

---

D. Wu · M.-H. Hu · L.-L. Chen · H.-B. Chen (✉) · T. Lin · S.-B. Chen  
Intelligentized Robotic Welding Technology Laboratory, School of Materials Science  
and Engineering, Shanghai Jiao Tong University, Shanghai, People’s Republic of China  
e-mail: hbchen@sjtu.edu.cn

edge pixels as the pool edge. Shen et al. [2, 3] obtained the parameters of the weld pool indirectly by measuring the arc column area and assuming that there is only one major curve edge in the predefined fixed-size image window.

A clear image of the keyhole puddle of aluminum alloys from the workpiece front-side was acquired with a narrow-band filter system and a charge-coupled device (CCD) camera in VPPAW [4]. B. Zheng et al. proposed an algorithm for the image processing of the visible keyhole puddle to determine the geometrical sizes of the visible keyhole under the condition of an off-line welding process. Zhonghua et al. [5] put forward a wavelet transform which provides a multiscale analysis of the information of the histogram, the result shows that it is effective for the keyhole image to get the geometry parameters of the keyhole.

Based on the research above we found that existing methods often assume that the weld pool exists in a predefined area and its contour to be a specific geometric shape and size. Furthermore, existing methods mainly rely on artificial experience, hence they are lack of adequate accuracy and higher recognition efficiency. Therefore, it is necessary to develop more robust and intelligent methods to detect and localize the weld pool. This paper aims to put forward a method based on active shape model to recognize and localize weld pool edges. The remainder of this paper is organized as follows. Section 2 will introduce the principle of active shape models for object detection and localization. Section 3 describes the robust detection and localization of VPPAW weld pool by active shape model. In Sect. 4, we will take some experiments to demonstrate the performance of the proposed method.

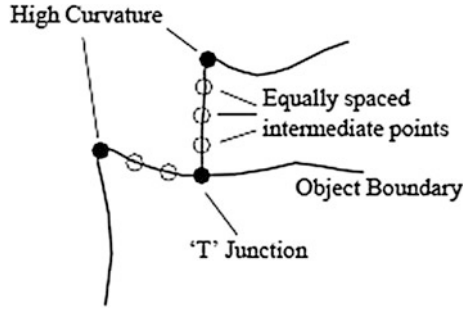
## **2 Active Shape Model for Object Detection and Localization**

Active shape model (ASM) was originally introduced by Cootes and Talon [6, 7] in 1992, which is a method of image searching based on statistic model. The idea defines a energy function by adjusting the model parameters to make the energy function minimization.

### ***2.1 Point Distribution Model***

The method of point distribution model assumes that we can get shape of the statistical description and its change from a training set of  $M$  samples. In two dimensions points could be placed at clear corners of object boundaries, 'T' junctions between boundaries or easily located biological landmarks. However, there are rarely enough of such points to give more than a sparse description of the shape of the target object. This list would be augmented with points along boundaries which are arranged to be equally spaced between well defined landmark points (Fig. 1).

**Fig. 1** Good landmarks points



If a shape is described  $n$  points in  $d$  dimensions, we represent the shape by an element vector formed by concatenating the elements of the individual point position vectors. For instance, in a 2-D image we can represent the  $n$  landmark points,  $\{(x_i, y_i)\}$ , for a single example as the  $2n$  element vector  $x$ , where

$$x = (x_1, \dots, x_n, y_1, \dots, y_n)^T \tag{1}$$

Given  $s$  training examples, we generate  $s$  such vectors  $x_j$ . Before we can perform statistical analysis on these vectors it is important that the shapes represented are in the same co-ordinate frame. We wish to remove variation which could be attributable to the allowed global transformation,  $T$ .

### 2.2 Aligning the Training Set

There is considerable literature on methods of aligning shapes into a common co-ordinate frame, the most popular approach being Procrustes Analysis [8]. This aligns each shape so that the sum of distances of each shape to the mean ( $D = \sum |x_i - \bar{x}|^2$ ) is minimised. It is poorly defined unless constraints are placed on the alignment of the mean (for instance, ensuring it is centred on the origin, has unit scale and some fixed but arbitrary orientation).

### 2.3 Global Shape Model

Consider our vector representation of a shape  $x_i = \{x_1, y_1, x_2, y_2, \dots, x_n, y_n\}$ . We can therefore consider a  $2n$  dimensional space and plot this shape as a point within that space. If we calculate the covariance matrix of this distribution, we obtain a concise description of how each point in the training set varies with all other points. Moreover, we can obtain eigenvectors and eigenvalues which give us the major and minor axis of this distribution. By sorting the eigenvalues by size, we have a list of the most significant variations across the training set.

In order to describe the whole training set, we require  $2n$  eigenvectors, however we can describe a large proportion of the training set with the first  $t$  eigenvectors. We choose  $t$  such that the sum of the first  $t$  eigenvalues is greater than a significant proportion of the sum of eigenvalues over the whole training set. Using these vectors, we can generate a new shape  $x$

$$x = \bar{x} + Pb \quad (2)$$

where  $P$  are the eigenvectors of the ASM, and  $b$  is a vector specifying the magnitude with which we move along each eigenvector from the mean. Cootes suggests that we only move along these eigenvectors of the order [9]:

$$-3\sqrt{\lambda_k} \leq b_k \leq 3\sqrt{\lambda_k} \quad (3)$$

where  $b_k$  is the eigenvalue of the  $k$ th eigenvector in order to maintain the integrity of the ASM.

## 2.4 Local Appearance Model

Suppose for a given point we sample along a profile  $k$  pixels either side of the model point in the  $i$ th training image. We have  $2k + 1$  samples which can be put in a vector  $g_i$ . To reduce the effects of global intensity changes we sample the derivative along the profile, rather than the absolute grey-level values. We then normalise the sample by dividing through by the sum of absolute element values,

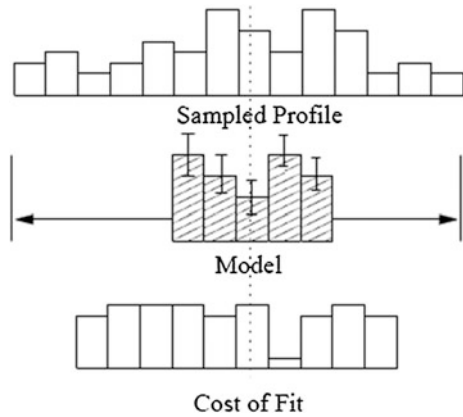
$$g_i \rightarrow \frac{1}{\sum_j |g_{ij}|} g_i \quad (4)$$

We repeat this for each training image, to get a set of normalised samples  $\{g_i\}$  for the given model point. We assume that these are distributed as a multivariate gaussian, and estimate their mean  $\bar{g}$  and covariance  $S_g$ . This gives a statistical model for the grey-level profile about the point. This is repeated for every model point, giving one grey-level model for each point. The quality of fit of a new sample,  $g_s$ , to the model is given by

$$f(g_s) = (g_s - \bar{g})^T S_g^{-1} (g_s - \bar{g}) \quad (5)$$

This is the Mahalanobis distance of the sample from the model mean, and is linearly related to the log of the probability that  $g_s$  is drawn from the distribution. Minimising  $f(g_s)$  is equivalent to maximising the probability that  $g_s$  comes from the distribution. During search we sample a profile  $m$  pixels either side of the current point ( $m > k$ ). We then test the quality of fit of the corresponding grey-level model

**Fig. 2** Search along sampled profile to find best fit of Grey-level model

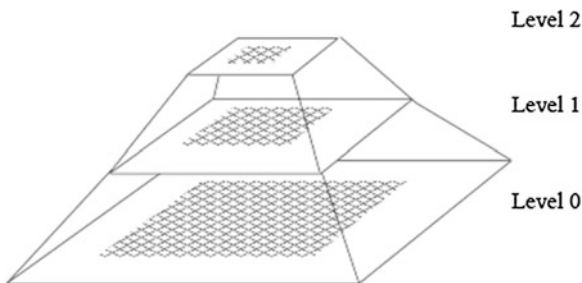


at each of the  $2(m - k) + 1$  possible positions along the sample (Fig. 2) and choose the one which gives the best match (lowest value of  $f(g_s)$ ).

This is repeated for every model point, giving a suggested new position for each point. We then apply one iteration of the algorithm given in (5) to update the current pose and shape parameters to best match the model to the new points.

### 2.5 Image Search Matching

To improve the efficiency and robustness of the algorithm, it is implemented in a multi-resolution framework. This involves first searching for the object in a coarse image, then refining the location in a series of finer resolution images. This leads to a faster algorithm, and one which is less likely to get stuck on the wrong image structure. For each training and test image, a gaussian image pyramid is built [10]. The base image (level 0) is the original image. The next image (level 1) is formed by smoothing the original then sub-sampling to obtain an image with half the number of pixels in each dimension. Subsequent levels are formed by further smoothing and sub-sampling (Fig. 3).



**Fig. 3** A Gaussian image pyramid is formed by repeated smoothing and sub-sampling



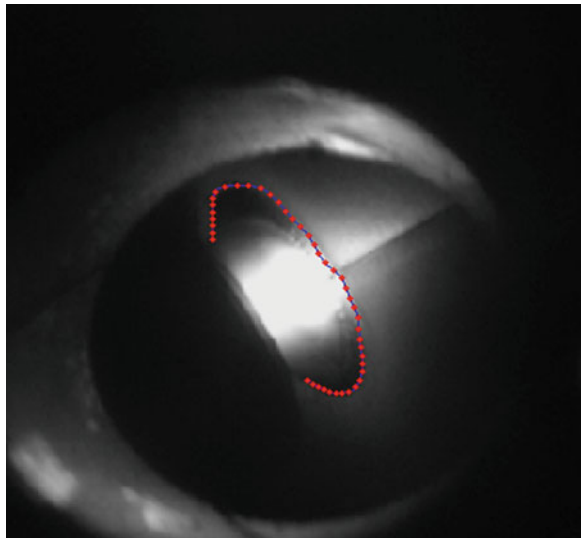
During training we build statistical models of the grey-levels along normal profiles through each point, at each level of the gaussian pyramid. We usually use the same number of pixels in each profile model, regardless of level. Since the pixels at level  $L$  are  $2L$  times the size of those of the original image, the models at the coarser levels represent more of the image. Similarly, during search we need only search a few pixels, ( $ns$ ), either side of the current point position at each level. At coarse levels this will allow quite large movements, and the model should converge to a good solution. At the finer resolution we need only modify this solution by small amounts.

### 3 Detection and Localization of Weld Pool by Active Shape Model

#### 3.1 *The Establishment of Point Distribution Model*

In this paper, we developed an active shape model for visual detection and localization of VPPAW pool. More specifically, we take some typical images for training and select twenty five landmark points manually in turn in each image, then we interpolate five points evenly spaced between landmark points and have a total of forty three points. Figure 4 is the distribution diagram of landmark points model, wherein red dots represent landmark points, which are saved as corresponding coordinates in the form of array.

**Fig. 4** The distribution diagram of landmark points



### 3.2 The Establishment of Shape Model

In order to remove the factors of rotation and scale from different images, we first align the training set using procrustes analysis, then we use PCA (Principal Component Analysis) to acquire accurate active shape model. The PCA use single value decomposition to obtaining mean vector, eigenvectors and eigenvalues and keep only 98 % of all eigenvectors (remove contour noise). Finally by making a PCA model, we make the Shape model, which finds the variations between contours in the training data sets. Figure 5 show the original image and reconstructed image using principal component analysis, wherein two images represent two main shafts respectively and the blue line stands for the original image, while the red line is reconstructed image. From Fig. 5, we can find the red line is close to the blue line which it demonstrate the accuracy of shape model.

### 3.3 The Establishment of Appearance Model

In this step, we make the appearance model, which samples a intensity pixel profile perpendicular to each contour point in each training dataset. It is used to build correlation matrices for each landmark point which are used in the optimization step to find the best fit.

In order to find the new position for every landmark point in the process of each iteration, we should establish each local characteristics respectively. For the  $i$ th point, the creation process is as follows: on both sides of  $i$ th point in the  $j$ th training image, we choose  $m$  pixels to form a vector of length of  $(2m + 1)$  along the direction which perpendicular to contour line, then we get a local texture from the

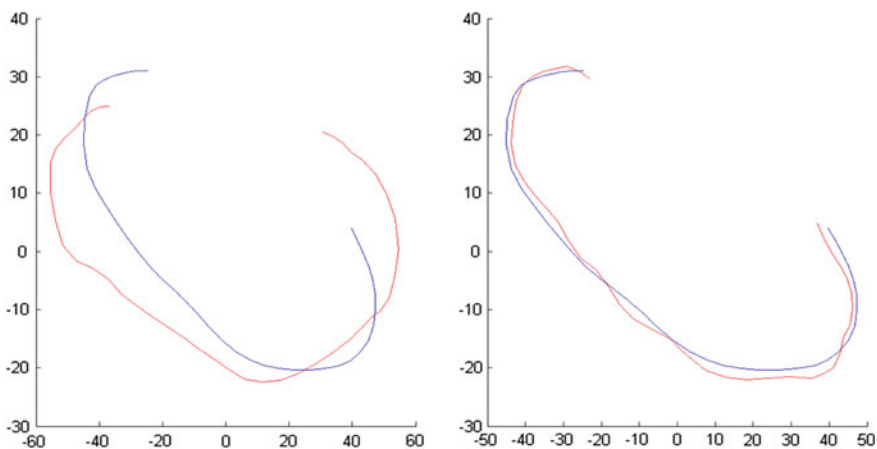


Fig. 5 The analysis result of PCA

derivation of pixel gray value. For the appearance model in this paper, we take  $m$  equal to eight. Then we adopt multi-resolution method to acquire local information of every landmark point (we take multi-resolution layers equal to four) and calculate a covariance matrix for all landmarks, finally we record all samples grayscale local information corresponding to landmark points from every layer.

### 4 Experiment and Discussion

In this section, we will conduct some experiments with real images to verify the proposed approach for detection and localization of VPPAW pool. The experiment system includes welding equipment, wire feeding machine, visual sensor, the robot operation and other equipment. Sensor system is mainly composed of CMOSIS camera, dimmer-filter glass and reflective device, wherein the center wavelength of filter glass is 660 nm and bandwidth is 35 nm. As shown in Fig. 6, we can acquire double-side images from the welding system platform.

Considering researching positive weld pool images mainly, Fig. 7 shows some weld pool images captured during a welding process, where each image is captured

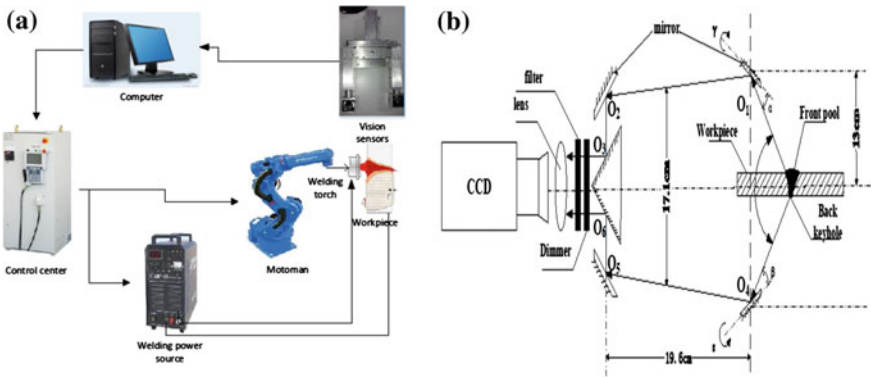


Fig. 6 Welding system platform. a Experiment system. b The light path diagram of visual sensor

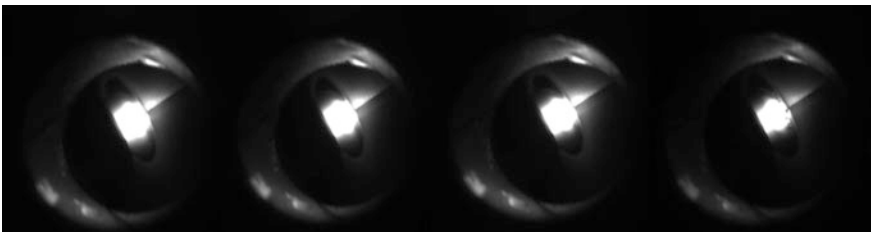
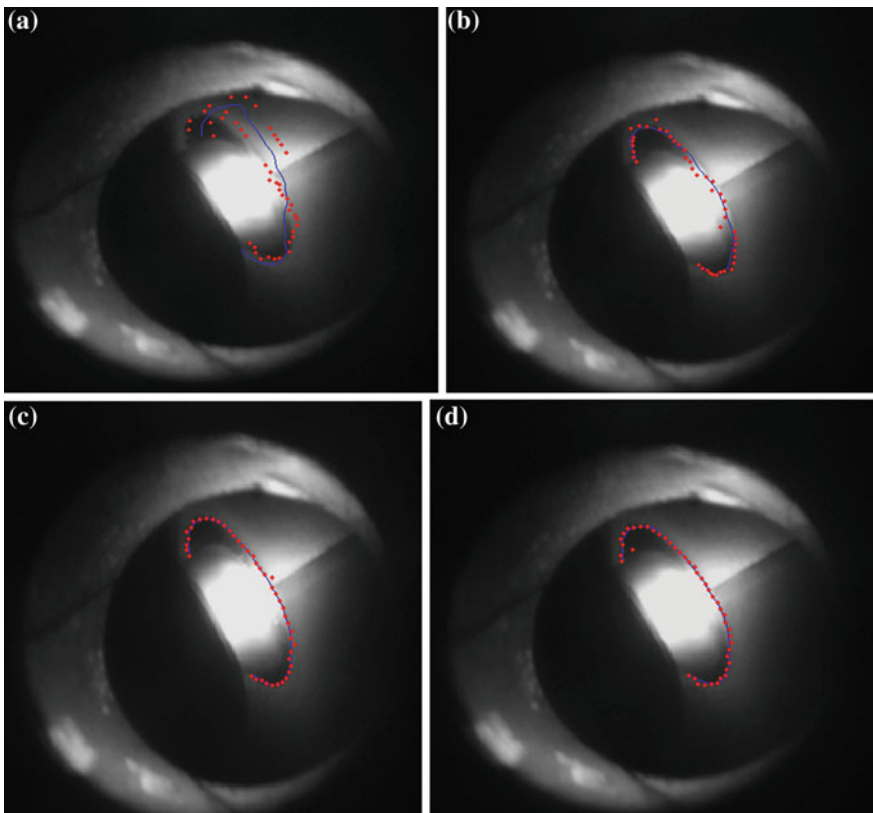


Fig. 7 Some weld pool images captured in a welding process

from the topside of the weld pool, and it is the region of interest in this paper. As we adopt aluminum alloy as workpiece in the test, the reflection of weld pool is less serious. In order to compare with identification effects which different number of training images lead to, we collected four groups of images, each group contain 3, 5, 7 and 9 training images respectively which each image size is  $230 \times 230$ . For these collected images, we will conduct a model training and a detection/localization test.

Firstly we select some landmark points manual and align the training set, then we establish their shape and appearance model respectively, finally we test some other weld pool images using ASM model. Figure 8 shows some detection and localization results of weld pool images, where red dots represent the final identifiable location. Figure a, b, c, d represent the recognition results of different groups of training images. From the results, we can see that the proposed method is very robust and keep high precision, it works even on weld pool image with strong reflection on its boundary.



**Fig. 8** Some results of visual detection and localization of weld pool. **a** Three training images. **b** Five training images. **c** Seven training images. **d** Nine training images

**Table 1** Comparative test of success rate under different amounts of training sample

Training images	3	5	7	9
Mean success rate (%)	53.49	78.37	88.89	91.16

In order to judge identification effect of weld pool quantitatively, we choose the distance (namely pixel) between red dot and its actual edge point as a threshold value, then we assume if the threshold value of red dot is not more than three, we consider it as an identification success point whereas it is a false point. Table 1 shows the result of the comparative tests under different training sample sizes (from 10 to 30 % of the total samples), where the total samples number is 30. From Table 1, we can see that with the increasing of training images, the success rate of image recognition improve. After that, adding more training samples can actually give less improvement.

## 5 Conclusion

In this paper, we proposed a robust visual detection and localization approach for VPPAW weld pool based on active shape modeling. This approach provides an elegant framework for representing the outline of a weld pool, especially efficient for weld pool detection and localization in cluttered scenes. This approach can provide an initial estimation of the geometric parameter measurement of weld pool. Experiments on real images verified the proposed method.

**Acknowledgment** This work is supported by the National Natural Science Foundation of China under the Grant 51275301 and the NDRC of China, under the Grant No. HT[2012]2144.

## References

1. Wang JJ, Lin T, Chen SB (2005) Obtaining weld pool vision information during aluminum alloy TIG welding. *Int J Adv Manuf Technol* 26(3):219–227
2. Shen HY, Ma HB, Lin T, Chen SB (2005) Research on weld pool control of welding robot with computer vision. *Ind Rob* 34(6):467–475
3. Shen HY, Wu J, Lin T, Chen SB (2008) Arc welding robot system with seam tracking and weld pool control based on passive vision. *Int J Adv Manuf Technol* 39(7–8):669–678
4. Zheng B, Wang H, Wang Q (1998) Front side image sensing of the keyhole puddle of aluminium alloys with narrow band filter system. *Trans China Weld Soc* 18(12):132–137
5. Zhonghua L, Oilong W, Jiagi Z (2001) Keyhole image precessing of variable polarity plasma arc welding based on wavelet transform. *Chin J Mech Eng* 14(1):62–66
6. Cootes TF, Talon CJ (1993) Active shape model research using local grey-level models: a quantitative evaluation. In: *British machine vision conference*
7. Cootes TF, Taylor CJ (2004) Technical report: statistical models of appearance for computer vision. The University of Manchester School of Medicine

8. Goodall C (1991) Procrustes methods in the statistical analysis of shape. *J Roy Stat Soc B* 53 (2):285–339
9. Cootes TF, Taylor CJ, Cooper DH, Graham J (1995) Active shape models—their training and application. *Comput Vis Image Underst* 61:38–59
10. Burt PJ (1984) The pyramid as a structure for efficient computation. *Multi Resolut Image Process Anal* 6:37–46

# Information Fusion in Pulsed GTAW Using ANFIS and Fuzzy Integral

Bo Chen and Shan-Ben Chen

**Abstract** Welding process is a complex process accompanied by various disturbances, so it is difficult to obtain the welding status by a single sensor. This paper used different sensors to obtain information of the pulsed GTAW (Gas Tungsten Arc Welding) process, and ANFIS (Adaptive Neuro-Fuzzy Inference System) was used to process the information obtained by each sensor, then fuzzy integral method was used to fuse the signal characteristics of each sensor and obtain the prediction results. Experiment results showed that the method could sufficiently use the information obtained by different sensors and obtain more precise prediction results than by using a single sensor alone. This laid the foundation for further controlling the welding quality automatically.

## 1 Introduction

Sensor technology is one of the key technologies in welding automation. In order to control the welding penetration status automatically, various welding sensors have been developed, such as arc sensor [1], visual sensor [2–4], acoustic emission sensor [5], spectrum sensor [6] and so on. However, it is well known that welding process is accompanied by many uncertain factors such as intense arc, noise, electromagnetic interference etc. Each sensor can only obtain partial information of welding process, so it's very difficult to predict the penetration status precisely by using a single sensor alone.

---

B. Chen

Shandong Provincial Key Laboratory of Special Welding Technology, Harbin Institute of Technology at Weihai, Harbin 264209, People's Republic of China

B. Chen · S.-B. Chen (✉)

School of Material Science and Engineering, Shanghai Jiao Tong University, Shanghai 200240, People's Republic of China  
e-mail: sbchen@sjtu.edu.cn

Multi-sensor information fusion techniques is an emerged area which combine information from multiple sensors to achieve improved accuracies and more specific inferences than could be achieved by the use of a single sensor alone [7, 8]. Some researchers have realized the advantages of multi-sensor information and applied them in welding process [9, 10], and showed the advantage of multi-sensor information fusion compared to single sensor. Commonly used multi-sensor information fusion technologies include Kalman filter [11], D-S evidence theory [12], neural networks [13] and fuzzy sets [14, 15]. Fuzzy set and fuzzy measure theory are two more general mathematical methods which can be applied to multi-sensor information fusion. Because welding process is generally regarded as a technology which determined more by welders' experience, this can be more described by fuzzy methods more easily. So this paper tried to use fuzzy theory as the main methods to process and fuse the information obtained during welding process.

In this paper, arc, visual and sound sensor were used simultaneously to obtain electronic, visual and sound information during the pulsed GTAW (Gas Tungsten Arc Welding) process. Then the signal features were fused by fuzzy integral to obtain the final prediction results of the penetration status about the welding process, and ANFIS (Adaptive Neuro-fuzzy Inference System) was used to obtain the parameters needed by fuzzy integral. Experiment results showed that multi-sensor information fusion could obtain more accurate prediction results than single sensor.

## 2 Theoretical Development

This paper used fuzzy integral as the fusion tool to fuse the information obtained by different sensors, first we will give a brief introduction about fuzzy measure and fuzzy integral.

### (A) Fuzzy measure and $g_\lambda$ -Fuzzy Measures

Fuzzy measure is the generalization of classical measure. The classical measure is additive. However, in some cases, the additivity can not be satisfied, for example the work efficiency of two workers is not the summation of two workers' work efficiencies. In 1974, Sugeno first brought forward the set functions using monotonicity to replace additivity which was called fuzzy measures [16].

If  $X$  is a finite set of sources i.e.  $X = \{x_1, x_2, \dots, x_k\}$ , then the  $\sigma$ -algebra set generated by  $X$  is  $\{\Phi, \{x_1\}, \{x_2\}, \{x_1, x_2\}, \dots, X\} = \Omega$ . A fuzzy measure, in the case of finite sets, is defined as a function  $\mu: \Omega \rightarrow [0, 1]$ , which satisfies the following [17]:

- (1)  $\mu(\Phi) = 0, \mu(X) = 1$
- (2)  $\mu(A) \leq \mu(B)$  if  $A \subseteq B \subseteq X$
- (3)  $f\{A_i\}_{i=1}^\infty$  is an increasing sequence of measurable set then



$$\lim_{i \rightarrow \infty} \mu(A_i) = \mu(\lim_{i \rightarrow \infty} A_i)$$

It should be noted that  $\mu$  is not necessarily additive, so by the nature of the definition of a fuzzy measure, the measure of the union of two disjoint subsets cannot be directly computed from the component measures. In light of this, Sugeno introduced the so-called  $g_\lambda$ -Fuzzy Measures satisfying the following additional property: for all  $A, B \subseteq X$  and  $A \cap B = \Phi$ ,

$$g(A \cup B) = g(A) + g(B) + \lambda g(A)g(B), \quad \text{for some } \lambda > -1 \quad (1)$$

**B. Properties of  $g_\lambda$ -Fuzzy Measures**

Let  $X = \{x_1, x_2, \dots, x_k\}$  be a finite set and let  $g^i = g(\{x_i\})$ . The mapping  $x_i \rightarrow g^i$  is called a fuzzy density function. Suppose

$$A = \{x_{i1}, \dots, x_{im}\} \subseteq X \quad (2)$$

Then we can write

$$\begin{aligned} g(A) &= \sum_{j=1}^m g^{i_j} + \lambda \sum_{j=1}^{m-1} \sum_{k=j+1}^m g^{i_j} g^{i_k} + \dots + \lambda^{m-1} g^{i_1} \dots g^{i_m} \\ &= \left[ \prod_{x_i \in A} (1 + \lambda g^i) - 1 \right] / \lambda, \quad \lambda \neq 0 \end{aligned} \quad (3)$$

Thus the value of  $\lambda$  can be obtained from the equation

$$g(X) = 1 \quad (4)$$

This is equivalent to solve the equation

$$\lambda + 1 = \prod_{i=1}^n (1 + \lambda g^i) \quad (5)$$

Hence if we know the fuzzy densities  $g^i, i = 1, \dots, n$ , the  $g_\lambda$ -Fuzzy Measures can be constructed. For the information fusion problem, the fuzzy density value  $g^i$  can be regarded as the degree of importance of some source  $x_i$  towards the final evaluation. The measure of an arbitrary set A represents the importance degree of the set of sources denoted by A towards a final decision.

**Sugeno fuzzy integrals**

Using the notation of fuzzy measures, Sugeno defined the concept of the fuzzy integral [17]:

Given a finite set  $X = \{x_1, x_2, \dots, x_k\}$  and a function  $f: X \rightarrow [0,1]$ , rearrange X such that  $0 \leq f(x_1) \leq f(x_2) \leq \dots \leq f(x_n) \leq 1$ , the fuzzy integral over  $A \subseteq X$  of the function f with respect to a fuzzy measure  $\mu$  is defined by

$$\int f(x) \circ \mu(x) = \bigvee_{i=1}^n [f(x_i) \wedge \mu(A_i)] \tag{6}$$

where  $A_i = \{x_i, \dots, x_n\}$ .

When  $\mu$  is a  $g_\lambda$ -Fuzzy Measures,  $g(A_i)$  can be calculated recursively ( $i = 1, \dots, n$ ) as

$$\begin{aligned} g(A_1) &= g(\{x_1\}) = g^1 \\ g(A_i) &= g^i + g(A_{i-1}) + \lambda g^i g(A_{i-1}) \end{aligned} \tag{7}$$

### 3 Adaptive Neuro-Fuzzy Inference System (ANFIS)

From the specialty of fuzzy integral it could be seen that to fuse the information by fuzzy integral, the set function value and the fuzzy measure value should be first obtained. The first step of the fusion process is to obtain a degree of partial matching which is needed by the fuzzy integrals as f-function. To date, there is not any unique tool to obtain the f-function, in this paper, ANFIS is used as the tool to obtain the needed f-function value.

The integration of neural network architectures with fuzzy inference system (FIS) has resulted in a very powerful strategy known as ANFIS. The ANFIS architecture consists of a fuzzy layer, product layer, normalized layer, defuzzy layer, and summation layer. A typical architecture of ANFIS with two rules is shown in Fig. 1, in which a circle indicates a fixed node, whereas a square indicates an adaptive node. For simplicity, it is assumed that the FIS has two inputs  $x$  and  $y$  and one output  $f$ . The ANFIS used in this paper implements a 1st order Sugeno fuzzy model [18]. Among many FIS models, the Sugeno fuzzy model is the most

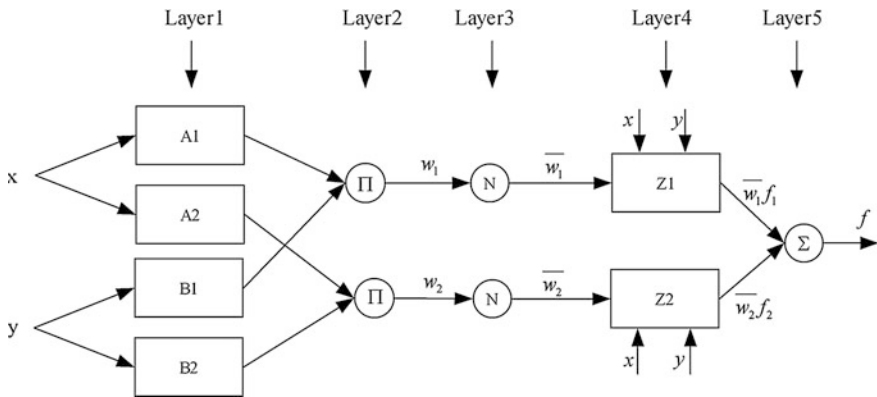


Fig. 1 ANFIS architecture

widely applied one for its high interpretability and computational efficiency, and built-in optimal and adaptive techniques. For a 1st order Sugeno fuzzy model, a typical rule set with two fuzzy if-then rules can be expressed as:

Rule 1: if  $x$  is  $A_1$  and  $y$  is  $B_1$ , then  $f_1 = p_1x + q_1y + r_1$

Rule 2: if  $x$  is  $A_2$  and  $y$  is  $B_2$ , then  $f_2 = p_2x + q_2y + r_2$

where  $A_i$  and  $B_i$  are the fuzzy sets in the antecedent and  $p_i$ ,  $q_i$  and  $r_i$  are the design parameters that are determined during the training process.

As shown in Fig. 1, the ANFIS consists of five layers:

In the first layer, all the nodes are adaptive nodes. The outputs of layer 1 are the fuzzy membership grade of the inputs, which are given by:

$$\begin{aligned} O_{1,i} &= \mu_{A_i}(x), \quad i = 1, 2 \\ O_{1,i} &= \mu_{B_{i-2}}(y), \quad i = 3, 4 \end{aligned} \tag{8}$$

where  $\mu_{A_i}(x)$  and  $\mu_{B_{i-2}}(y)$  can adopt any fuzzy membership functions. For example, if generalized bell shaped function is employed,  $\mu_{A_i}(x)$  is given by

$$\mu_A(x) = \frac{1}{1 + \left| \frac{x-c_i}{a_i} \right|^{2b_i}} \tag{9}$$

where  $\{a_i, b_i, c_i\}$  is the parameter set of the membership function, governing generalized bell shaped function accordingly.

In the second layer, the nodes are fixed nodes. They are labeled with  $\Pi$ , indicating that they perform as a simple multiplier. The outputs of this layer can be represented as:

$$O_{2,i} = \mu_{A_i}(x)\mu_{B_i}(y), \quad i = 1, 2 \tag{10}$$

which are the so-called firing strengths of the rules.

In the third layer, the nodes are also fixed nodes. They are labeled with  $N$ , indicating that they play a normalization role to the firing strengths from the previous layer. The outputs of this layer can be represented as:

$$O_{3,i} = \overline{w}_i = \frac{w_i}{w_1 + w_2}, \quad i = 1, 2 \tag{11}$$

which are the so-called normalized firing strengths.

In the fourth layer, the nodes are adaptive nodes. The output of each node in this layer is simply the product of the normalized firing strength and a 1st order polynomial (for a 1st order Sugeno model). Thus, the outputs of this layer are given by:

$$O_{4,i} = \overline{w}_i f_i = \overline{w}_i(p_i x + q_i y + r_i), \quad i = 1, 2 \tag{12}$$

In the fifth layer, there is only one single fixed node labeled with  $\Sigma$ . This node performs the summation of all incoming signals. Hence, the overall output of the model is given by:

$$O_{5,i} = \sum w_{fi} = \frac{\sum_i w_{fi}}{\sum_i w_i} \quad (13)$$

It can be observed that there are two adaptive layers in this ANFIS architecture, namely the first layer and the fourth layer. In the first layer, there are three modifiable parameters  $\{a_i, b_i, c_i\}$ , which are related to the input membership functions. These parameters are the so-called premise parameters. In the fourth layer, there are also three modifiable parameters  $\{p_i, q_i, r_i\}$ , pertaining to the 1st order polynomial. These parameters are the so-called consequent parameters [18].

After the ANFIS was built, it could be used to train the data and obtain a network which could be used as the fuzzy set function in fuzzy integral method. And the prediction accuracy of ANFIS could be used as the fuzzy density value  $g_i$ , then the fuzzy integral method could be used to fuse the information obtained by different sensors.

## 4 Experiment Apparatus and Experimental Procedures

### 4.1 Experiment Apparatus

Fuzzy integral was used in this paper to fuse the information obtained by different sensors in pulsed GTAW process to predict the penetration status, and the experiment system to obtain the information is shown in Fig. 2. The system was consisted of an electronic signal collecting module, a sound signal collecting model and a weld pool image collecting module. By simultaneously using of the three collecting modules, weld pool image, weld current, weld voltage and welding sound could be collected at the same time. Figure 3 shows the captured figure and the corresponding current, voltage and sound information during a welding process.

After the information was obtained, the signal features could be obtained by some signal processing algorithms [19]. Figure 4 shows the topside and backside image of the weld pool, from the image the geometric feature parameters of weld pool could be obtained. In this paper, the topside weld pool length LT and width WT were used, and the backside width WB was used to judge the current penetration status. Because the weld current during the base period is kept const, and relatively small compared with the peak period, the current and voltage values during the base period were not taken into account. For the current of peak period, virtual value during a pulse period was calculated, for the voltage of peak period, to

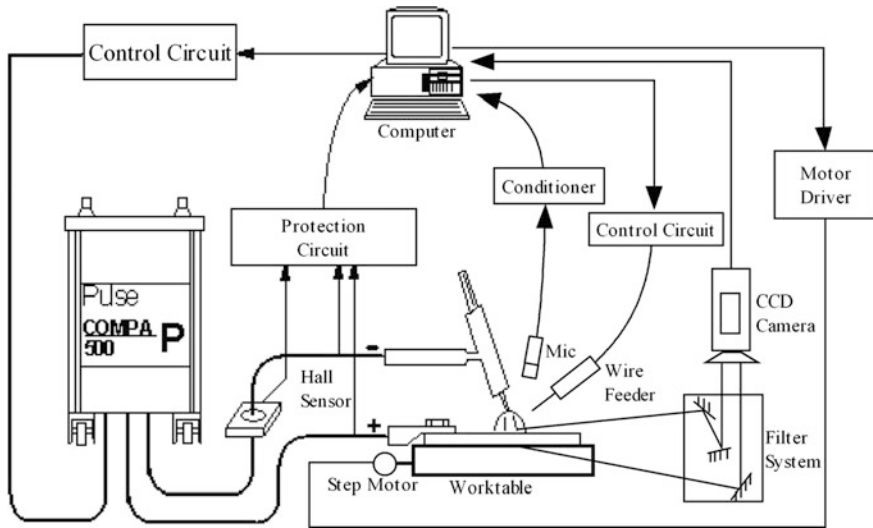
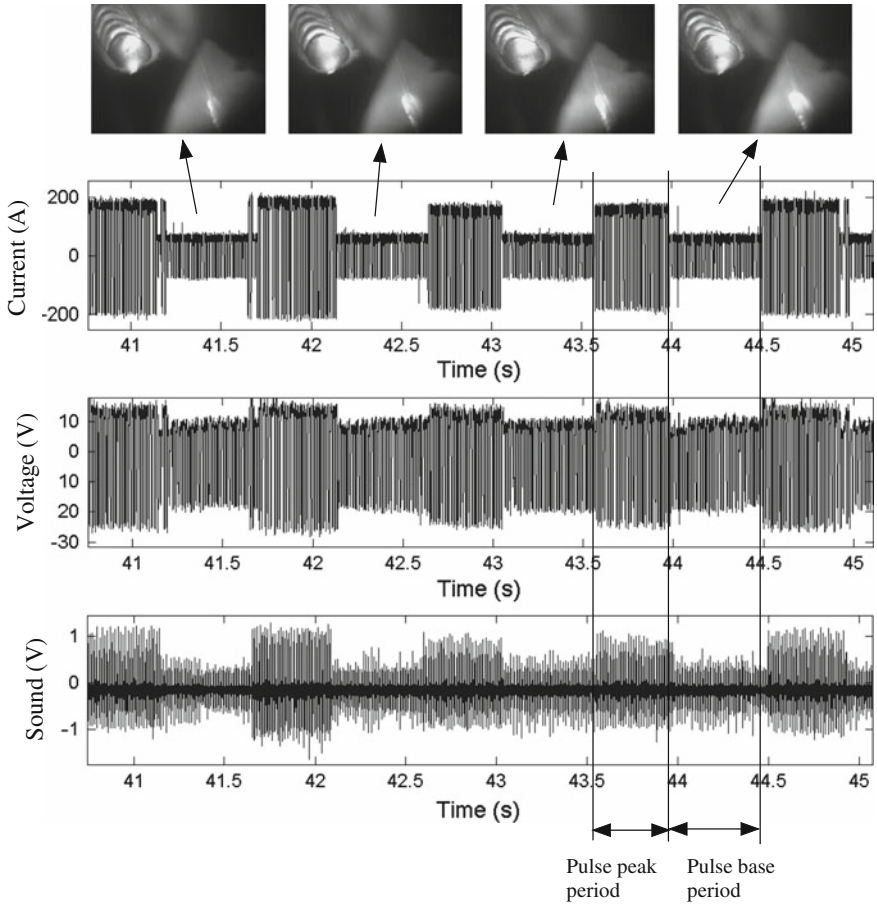


Fig. 2 Schematic diagram of the experiment system

avoid the influence of cathode spot, positive value of the voltage during a pulse period was used, and the mean value of the positive data of the voltage during a pulse period was calculated. For the sound information, sound intensity and sound spectrum intensity were taken as the signal features [19].

## 4.2 Experimental Procedures

To use the ANFIS to obtain the  $f$ -functions and the  $g_{\lambda}$  fuzzy measures, the ANFIS should first be trained so it could be used as the  $f$ -function and obtain the fuzzy density value. In order to obtain the training data, all kinds of welding conditions should be considered during the experiment design. In this study, welding current ( $I$ ) and wire feeding speed ( $R$ ) were taken as the control variables to influence the forming process of weld beam. Butt welding experiments were conducted on a 4-mm-thick aluminum alloy LF6 with V groove. A satisfactory weld shape was obtained with the following parameters:  $I = 170$  A,  $R = 11$  mm/s. To excite all the characteristics of the dynamic welding process, the welding peak current and wire feeding speed were designed with white noise signals, because of their characteristic of widespread spectrum and non-correlation on time. The pulse peak current and wire feeding speed were changed every pulse according to the generated white noise signal value. To receive a complete welding data, the variations of pulse peak current and wire feeding speed were set as follows:  $\Delta I = \pm 15$  A,  $\Delta R = \pm 4$  mm/s.



**Fig. 3** Visual, current, voltage and sound waveforms of four pulses

The obtained information's features were obtained by the above signal processing algorithms, and the signal features of every pulse were obtained. Totally 982 sampling data were obtained as shown in Fig. 5. In the figure, when the welding is penetration, the penetration status is 1, and when the welding is incomplete penetration, the penetration status is 0. From the figure it could be seen that all the variables varied by a wide range under the designed welding parameters, different welding parameters reflected different penetration status. Therefore, multiple welding states were activated and the experimental data could be thought as covering all the penetration situations.

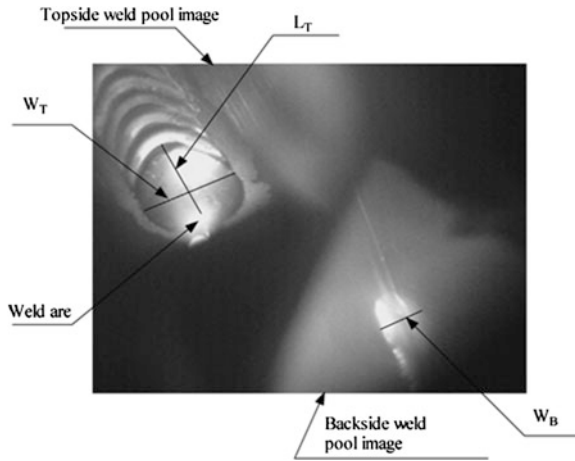


Fig. 4 A frame of a complete weld pool image of pulsed GTAW

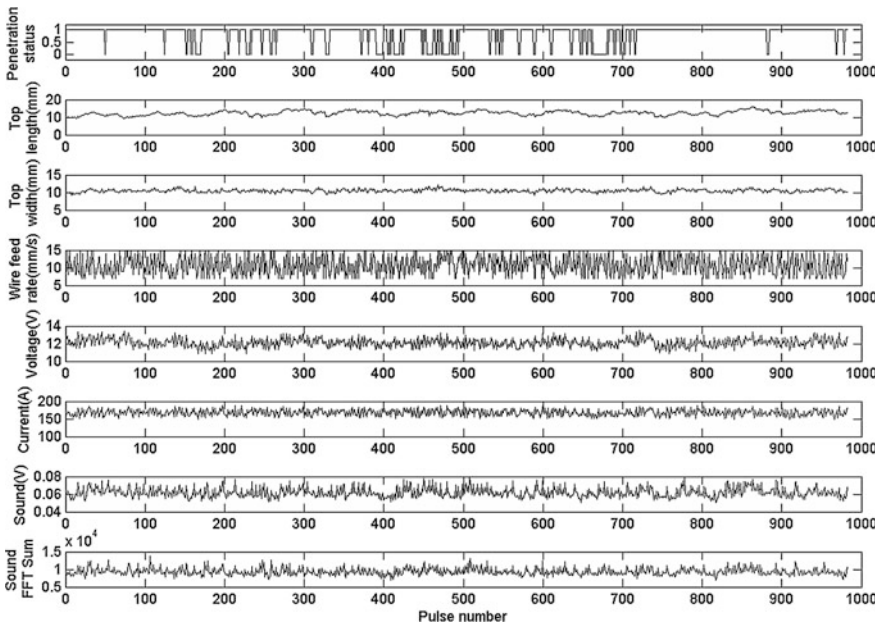


Fig. 5 Experiment results

**Table 1** Comparison of prediction rates between single sensor and multi-sensor

Times	Single sensor network			Sugeno integral fusion			
	Arc sensor	Sound sensor	Visual sensor	Arc and sound	Sound and visual	Arc and visual	Arc and sound and visual
1	0.7371	0.7689	0.7968	0.7888	0.7888	0.7928	0.7888
2	0.8848	0.7531	0.893	0.9588	0.9465	0.9753	0.9753
3	0.6908	0.6707	0.739	0.739	0.743	0.739	0.739
4	0.7787	0.75	0.8402	0.918	0.9221	0.9385	0.9549
5	0.7037	0.7243	0.7449	0.7654	0.7572	0.7531	0.7613
6	0.8601	0.7654	0.8848	0.9095	0.9218	0.9259	0.9259
7	0.7254	0.75	0.75	0.791	0.791	0.791	0.791
8	0.776	0.78	0.8	0.816	0.812	0.82	0.82
9	0.7711	0.7871	0.8394	0.8273	0.8353	0.8353	0.8353
10	0.9053	0.7984	0.9095	0.9383	0.9424	0.9383	0.9424
Average	0.7833	0.75479	0.81976	0.84521	0.84601	0.85092	0.85339

### 4.3 Multi-sensor Fusion Results

In order to sufficiently reveal the effectiveness of proposed method in multi-sensor information fusion, the method was also used to fuse the information obtained by two sensors as a comparison.

To validate the models, the data set is randomly split into 730 training samples and 252 test samples. The 730 training samples were used to train ANFIS, after ANFIS was trained, the recognition rates of ANFIS were used as the fuzzy densities, and the 252 test samples were used to test the capabilities of the fuzzy integral. The partitioning is repeated 10 times independently. The recognition rates between single sensor network and Sugeno integral fusion are listed in Table 1. In the table, the recognition rate of single sensor network presented the prediction result by a single sensor, the f-function obtained by ANFIS was used to judge the penetration status, and a f-function that is greater than “0.5” indicted that current welding status was penetrated, and a f-function that is less than “0.5” indicted that current welding is incomplete penetrated; in Table 1 the recognition rate of Sugeno integral fusion result represented the prediction rates after the f-functions were fused by Sugeno integral, and in the table both the prediction rates of fusing two sensors and fusing three sensors were tabulated.

From the table it can be seen that the prediction results of multi-sensor fusion are much better than the prediction results of single sensor. And the prediction results of ANFIS are better than the prediction results of BP neural network [19]. This shows the effectiveness of ANFIS. It could also be seen from the table that the



fusion results of three sensors were better than the fusion results of two sensors, this means multi-sensor information fusion can sufficiently use different sensors' information and obtain better results, which will be helpful to control the welding quality automatically.

## 5 Conclusions

Multi-sensor information fusion technology was used in this paper to predict the penetration status of pulsed GTAW process. Arc, visual and sound sensors were used simultaneously to obtain information about the process from different view of aspects, then the corresponding signal features reflecting the welding process were obtained, and ANFIS was used to process the features and obtain the f-function value for the fuzzy integral method. Fuzzy integral technology was used to fuse the processed features to predict the penetration status. Experiments were done to compare the prediction result between single sensor information and multi-sensor information fusion, and the results showed that the method could effectively use the information obtained by different sensors and give better prediction results.

**Acknowledgment** This work was supported by the National Natural Science Foundation of China under grant no. 51105103, China Postdoctoral Science Foundation under grant nos. 2012M510945 and 2013T60362, and Project (HIT.NSRIF.2015115) supported by Natural Scientific Research Innovation Foundation in Harbin Institute of Technology.

## References

1. Christner B, Lovell R, Campbell M (1998) Developing a GTAW penetration control system for the titan IV program. *Weld Metal Fabrication* 66(3):29–38
2. Wang JJ, Lin T, Chen SB (2005) Obtaining weld pool vision information during aluminium alloy TIG welding. *Int J Adv Manuf Technol* 26(3):219–227
3. Chen SB et al (2000) Intelligent methodology for sensing, modeling and control of pulsed GTAW: part 2: butt joint welding. *Weld J* 79(6):164–174
4. Chen SB et al (2000) Intelligent methodology for sensing, modeling and control of pulsed GTAW: part I—bead-on—plate welding. *Weld J* 79(6):151–163
5. Duley WW, Mao YL (1994) Effect of surface condition on acoustic emission during welding of aluminium with CO<sub>2</sub> laser radiation. *J Phys D Appl Phys* 27(7):1379–1383
6. Ancona A et al (2004) A sensing torch for on-line monitoring of the gas tungsten arc welding process of steel pipes. *Meas Sci Technol* 15(12):2412–2418
7. Hall DL, McMullen SAH (2004) *Mathematical techniques in multisensor data fusion*. Artech House, Massachusetts
8. Klein LA (1999) *Sensor and data fusion concepts and applications*. Society of photo-optical instrumentation engineers (SPIE). Bellingham
9. Chang Y et al (2007) Spot welding quality fuzzy control system based on multisensor information fusion. *Chin J Mech Eng* 20(4):36–39 (English Edition)
10. Cullen JD et al (2008) Multisensor fusion for on line monitoring of the quality of spot welding in automotive industry. *Meas J Int Meas Confederation* 41(4):412–423

11. Li Y et al (2004) Study on multi-sensor data fusion for the wheeled mobile robot. In: Proceedings of the world congress on intelligent control and automation (WCICA), Hangzhou
12. Xu LJ, Chen YZ, Cui PY (2004) Improvement of D-S evidential theory in multisensor data fusion system. In: Proceeding of the 5th world congress on intelligent control and automation, Hangzhou
13. Wan W, Fraser D (1999) Multisource data fusion with multiple self-organizing maps. *IEEE Trans Geosci Remote Sens* 37(31):1344–1349
14. Chanussot J, Mauris G, Lambert P (1999) Fuzzy fusion techniques for linear features detection in multitemporal SAR images. *IEEE Trans Geosci Remote Sens* 37(31):1292–1305
15. Russo F, Ramponi G (1994) Fuzzy methods for multisensor data fusion. *IEEE Trans Instrum Meas* 43(2):288–294
16. Sugeno M (1974) Theory of fuzzy integrals and its applications. Tokyo Institute of Technology, Tokyo
17. Sugeno M (1977) Fuzzy measures and fuzzy integrals: a survey. *Fuzzy automata and decision processes*, pp 89–102
18. Jang J-SR (1993) ANFIS: adaptive-network-based fuzzy inference system. *IEEE Trans Syst Ma Cybern* 23(3):665–685
19. Chen B, Wang J, Chen S (2010) Prediction of pulsed GTAW penetration status based on BP neural network and D-S evidence theory information fusion. *Int J Adv Manuf Technol* 48 (Compendex):83–94

# Study on the Relationship Between the Energy in Most Effective Frequency Range of Arc Sound Signal and the Change of Arc Height in Pulsed Al Alloy GTAW Process

Huan-Huan Zhang, Na Lv and Shan-Ben Chen

**Abstract** Welding sound signal is mainly produced by the arc heat and the vibration of weld pool. In order to seek the relationship between characteristics in sound signal frequency and arc length variation, energy in every frequency band had been analysed, we found that arc sound signal distributed in every frequency band of 0–20 kHz, while arc length increasing, the energy of every frequency band increases, and the energy of 0–5000 Hz frequency band can generally reflect the increase and mutation of arc length, the differences when arc increase same value are similar. So linear fitting has been done to the original signal and the signal after 2 layer db3 wavelet denoising, conclusions can be made as that the average total energy of sound peak signal and the arc length have linear relationship, and 2 layer db3 wavelet denoising can make the error of linear relation smaller.

## 1 Introduction

With the development of the automatic and intelligent technology, material connection technology is widely used in high-tech fields such as aerospace, underwater operation, nuclear power development. On one hand, the equipments in such special working environment require the equipments has excellent quality and high precision of welding, on the other hand, sometimes welders cannot complete welding work because of the complexity of the welding environment, therefore, in the area of welding research, the development of intelligent and automatic control

---

H.-H. Zhang (✉) · N. Lv · S.-B. Chen  
Intelligentized Robotic Welding Technology Laboratory, School of Materials Science and Engineering, Shanghai Jiao Tong University (SJTU), Shanghai 200240, People's Republic of China  
e-mail: huanhuan1223@sjtu.edu.cn

technology, and the realization of the state of welding pool dynamic process real-time monitoring become the most concerned problems [1].

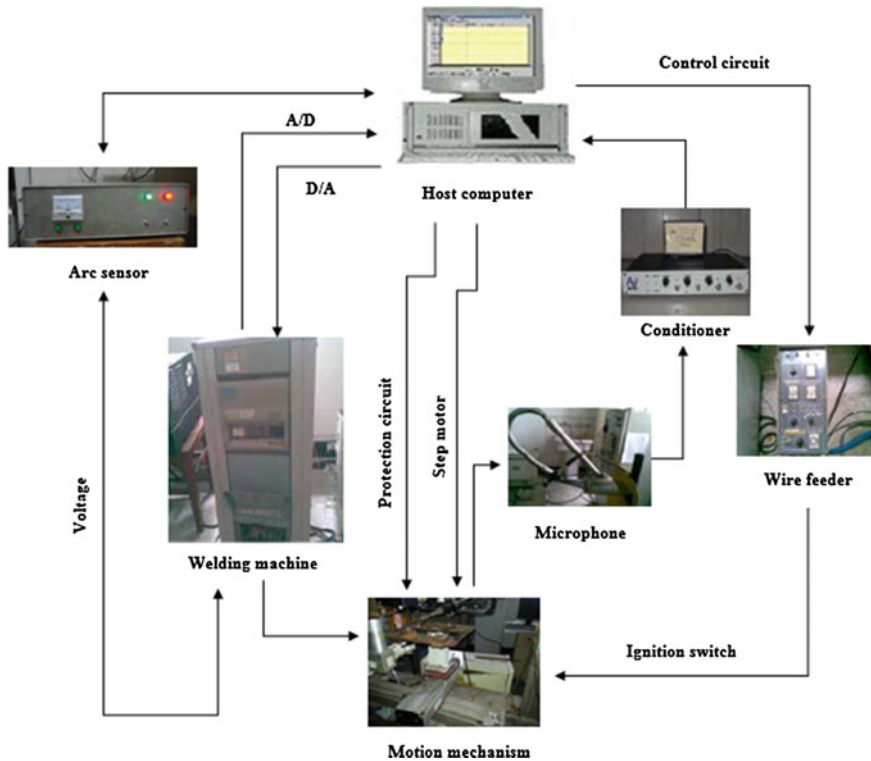
As the most a valuable signals in the online quality monitoring of welding, arc sound signal have been concerned and studied for a long time [2–5]. At present, the study of the state of the weld pool monitoring mainly concentrated in the aspect of visual information, but for the restriction of the complicated shape of weldment, the visual information is not easy to get. Arc sound, as non-contact vibration source signals, which generates from arc and molten pool heat vibration, contains a large amount of information of penetration states, and is not susceptible to the changes of weldment. Arc sound signals can effectively reflect pool height information and welding quality [6–8]. At present, the acquisition processing and analysis arc sound signal have achieved certain results in laser welding, CO<sub>2</sub> welding, MIG welding, spot welding, and other fields. However, the study of monitoring welding quality by acoustic signals in the field of aluminum alloy GTAW welding is still at fundamental stage. In Refs. [9, 10], scholars research the corresponding relationship between arc sound signals and welding current, and different transfer modes of short circuit, thus a transfer function about arc sound pressure and welding current was established. The Refs. [11] set a multiple regression model by studying various welding process parameters, implements the accurately forecast of weld width and the depth of molten, also provides the foundation of realizing of GMAW welding quality online prediction. In Refs. [12–14] Dr. Wang and Na made a conclusion of the effects of welding parameters to welding sound, including gas flow, welding speed and collection angle during GMAW welding. In addition, nowadays, researches about arc sound mainly focus on the time domain, research on time domain and time-frequency domain of sound signal is not mature, especially the relationship between frequency and the welding arc and the welding quality is not clear.

In this paper, it is tried to make a foundation work of finding a effective frequency range and building a relationship between arc height and arc sound energy of the frequency range. Because the arc height directly affects the arc energy, and the arc sound is generated from arc heat and vibration of weld pool, there must be a corresponding relationship between the energy characteristics of arc sound signal and arc height, however, due to the characteristics of the arc and workpiece their own, the sound signal produced by arc heat or vibration of weld pool should mainly distribute in specific frequency range. Thus the research is meaningful for real-time monitoring welding quality by utilizing arc sound signals.

## 2 Experimental System and Experimental Scheme

### 2.1 Experimental System

The schematic diagram of the experimental system shown in Fig. 1. The system is composed of two parts: welding system and audio sensing system. The welding system is basically including that, a INVERTER ELESON 500 P type ac/dc



**Fig. 1** The schematic diagram of the experimental system

GTAW welding power source which is provided by Japan OTC company, CM-271 type wire feeder, HC-71 type wire feeding control box, FR-IA gas flow controller, water cooling fitting, water box, protect cylinders and some other auxiliary equipment.

The audio sensing system mainly includes MP201 an omnidirectional capacitance microphone, MC104 signal conditioner. The frequency response range of the microphone is from 20 Hz to 20 kHz, its sensitivity is 50 mV/Pa, and the dynamic range is >146 dB. The arc sound signal of welding was collected at 40 kHz sampling rate and 12 bits precision. The microphone was settled at 75° horizontal angle to the work piece. The arc sound was picked by the omnidirectional capacitance microphone, then filtered by MC104 signal conditioner which is steep dropping characteristics. So the acoustic signal was decay signal. All the system software was programmed with Visual C++. The signal analysis was performed on the Matrix Laboratory platform. The parameters of the audio sensor are shown in Tables 1 and 2.

**Table 1** Major parameters of sound sensor

Type	MP201
Diaphragm and canning material	Nikle, nikle alloy
Open circuit sensitivity	$-26 \pm 2$ dB (50 mV/Pa)
Frequency response	20 Hz–2 kHz
Polarization voltage	0 V
Dynamic range	>146 dB
Background noise	<16 dBA

**Table 2** The major parameters of signal processor

Type	MC104
Channels	4
Input mode	BNC
Output mode	BNC
Gain	$\times 1, \times 10, \times 100$
Filtering	15 kHz low-pass
Polarization voltage	0 V

## 2.2 Experimental Scheme

In order to study the relationship between arc sound signal and arc height, a 2 mm step was placed in the middle of the work piece to produce different arc height in the process of welding. The step height was chosen at a suitable range that the corresponding tungsten height could not lead to arc extinction. In this experiment argon tungsten-arc welding was used and the tungsten electrode position remained unchanged to get stable arc length. Welding methods and conditions are described in Table 3. The experiments consist of three welding work piece, they are 2-4-6, 6-4-2, and 4-5-6 mm. The sketch map of work piece corresponding to arc height 2-4-6 mm is shown in Fig. 2. The other two situations are in the same way.

**Table 3** Welding methods and conditions

Parameter type	Value
Impulse frequency (Hz)	1
Peak current $I_p$ (A)	125
Base current $I_b$ (A)	50
Wire feed speed $V_f$ (mm/s)	10
Welding speed $V$ (mm/s)	3
Polar diameter $\Phi$ (mm)	3.2
Duty ratio $\delta$ (%)	50
Arc air flow $L$ (l/min)	10
Arc height (mm)	2-4-6
Material type	LF6 stainless aluminum alloy

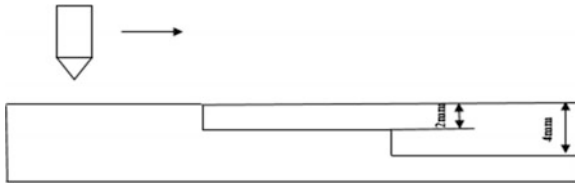


Fig. 2 Sketch map of arc height changed from 2 to 4 to 6 mm

### 3 Processing and Analysis of Arc Sound Signal

#### 3.1 Wiping off of DC Bias

The average value of arc sound signal drift from zero is DC bias, which is due to the direct-current coupling collection pattern and zero drift of signal conditioner. So, firstly we use the equation as follows to wipe off DC bias of sound signal  $s'$ :

$$s = s' - \text{mean}(s') \tag{1}$$

the comparison of sound signal before and after wiping off DC drift is shown in Fig. 3.

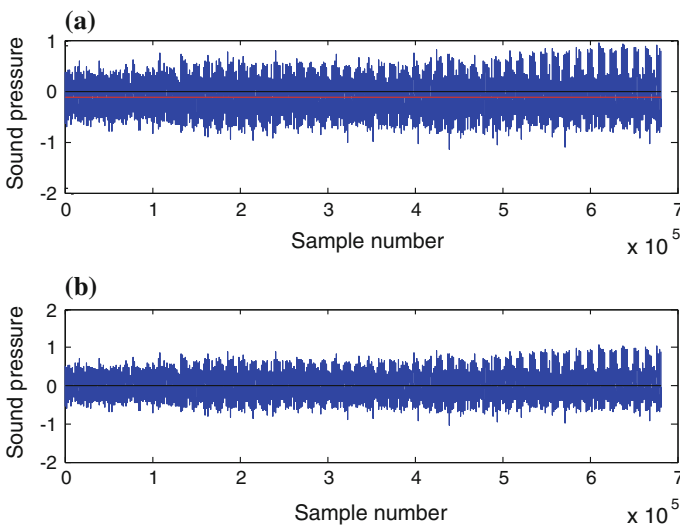


Fig. 3 The comparison of sound signal before and after wiping off DC drift. **a** Original signal. **b** Processed signal

### 3.2 Extraction of Peak Signal

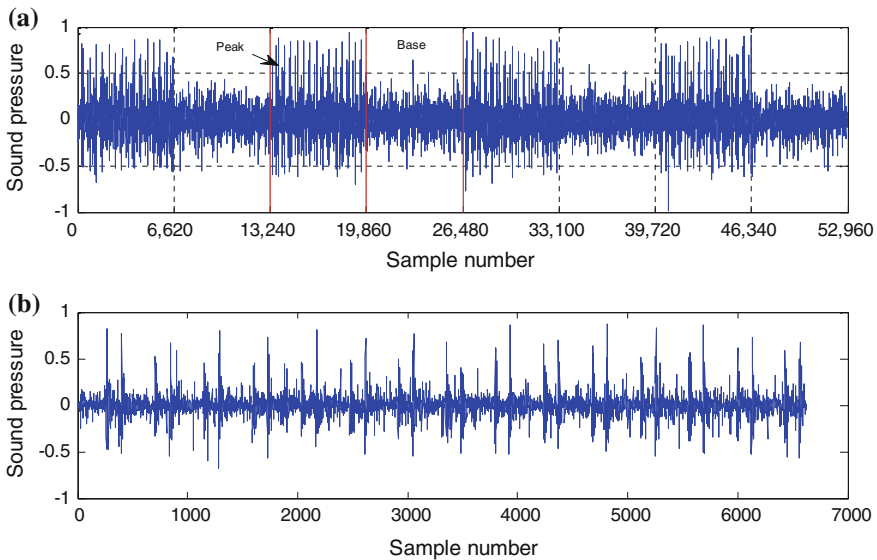
Arc sound signal is mainly produced by arc heat and vibration of weld pool, but the sound signal received unavoidably dop some noise of equipments and environmental noise, so it is very necessary for extraction of arc sound characteristics to do effective signal processing and analysis. The original waveform of arc sound signal is shown in Fig. 3. As we can see, the signal is composed of peak and base, the effective part of signal for welding is sound peak, so the first thing is to extract sound peak.

For the duty ratio of sound signal is 50 %. If the sample number of arc sound signal is  $N$ , which contains  $n_p$  peak and  $n_b$  base, then one sample number  $n$  in a peak expressed as:

$$n = \frac{N}{n_p + n_b} \quad (2)$$

We get the sample number in a sound peak is 6620 of the experiment in which arc height is 2-4-6 mm.

Figure 4 shows part of arc sound signal, the feasibility of the method above can be seen in Fig. 4, peak and base respectively contains 6620 sample points, then we can cut out peak signal easily from the whole sound signal, Fig. 4b shows one peak of arc sound signal. In this paper, we chose 5620 sample points in the middle of every peak to decrease errors.



**Fig. 4** Amplification of part sound signal. **a** Amplification of several peak. **b** Amplification of one peak



### 3.3 Analysis of Sound Energy in Every Frequency Range

In order to exactly extract the characteristics of arc sound signal and establish a effective relationship between arc sound signal and arc height, we should analyse the characteristics of every frequency range of arc sound and choose a suitable method of denoising.

Wavelet packet transform can decompose original sound signal into high and low frequency parts and can further decompose the parts of both high frequency signal and low frequency signal in arbitrary frequency range. The algorithms of wavelet packet was:

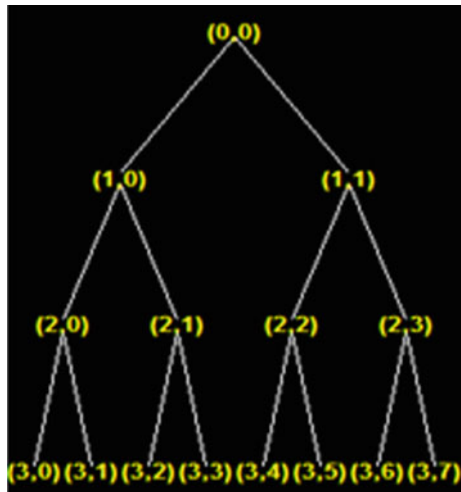
$$\begin{cases} d_j^{2^n}[k] = \sum_{l \in Z} h_{l-2k} d_{j+1}^n[l] \\ d_j^{2^{n+1}}[k] = \sum_{l \in Z} g_{l-2k} d_{j+1}^n[l] \end{cases} \tag{3}$$

In this paper, db3 wavelet basis function was used to analysis every peak of original arc sound signal in three layer wavelet packet. The energy of every frequency range of sound peak signal is calculated by summing the square of every node coefficients. The coefficient  $Wf(j, k)$  can be expressed as:

$$Wf(j, k) = 2^{-\frac{j}{2}} \sum_{n=0}^{N-1} f(n) \psi(2^{-j}n - K) \tag{4}$$

The structure of wavelet packet decomposition is shown in Fig. 5. The frequency range of arc sound signal is from 0 to 20 kHz. After wavelet packet transform, the

**Fig. 5** The structure of wavelet packet decomposition



**Table 4** The frequency range of each part of arc sound signal after decomposing

Signal	Energy	Frequency range/Hz
s	E-total	0–20,000
s1	E1	0–2500
s2	E2	2500–5000
s3	E3	5000–7500
s4	E4	7500–10,000
s5	E5	10,000–12,500
s6	E6	12,500–15,000
s7	E7	15,000–17,500
s8	E8	17,500–20,000

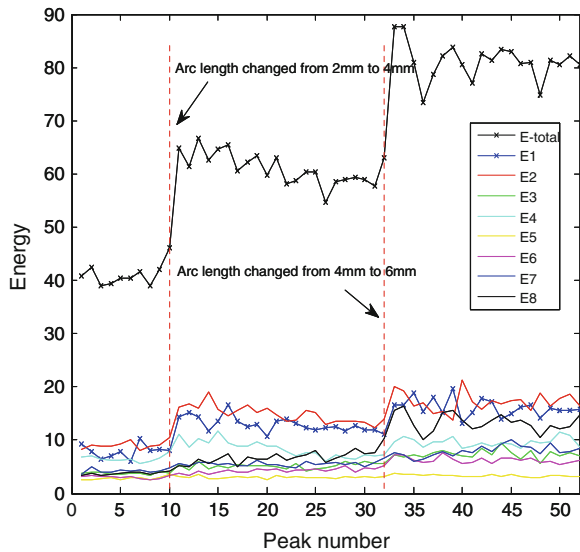
arc sound signal *s* is divided into eight different frequency bands, which can be denoted as:

$$s = s1 + s2 + s3 + s4 + s5 + s6 + s7 + s8 \tag{5}$$

where *s*1, *s*2, *s*3, *s*4, *s*5, *s*6, *s*7, *s*8 represent signals in different nodes (3, 0), (3, 1), (3, 2), (3, 3), (3, 4), (3, 5), (3, 6), (3, 7), (3, 8). *E*<sub>*i*</sub> represents corresponding energy of *s*<sub>*i*</sub>, *i* is integer from 1 to 8. Table 4 shows the frequency range of each part of arc sound signal after decomposing.

Figure 6 is the energy variation trend of arc height 2-4-6 mm. With the increasing of arc height, the total sound energy *E*-total increases, the *E*-total in 4 mm arc height is greater than that when arc height is 2 mm and less than that when arc height is 6 mm in the meantime. In addition, it is obvious that when the

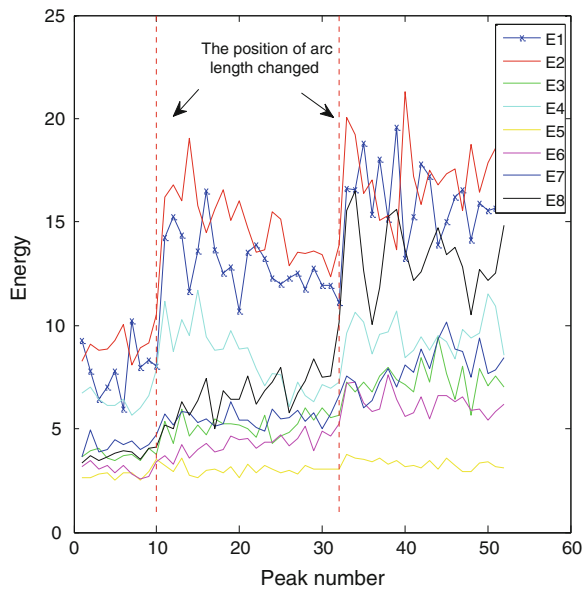
**Fig. 6** The energy variation trend of arc of height 2-4-6 mm

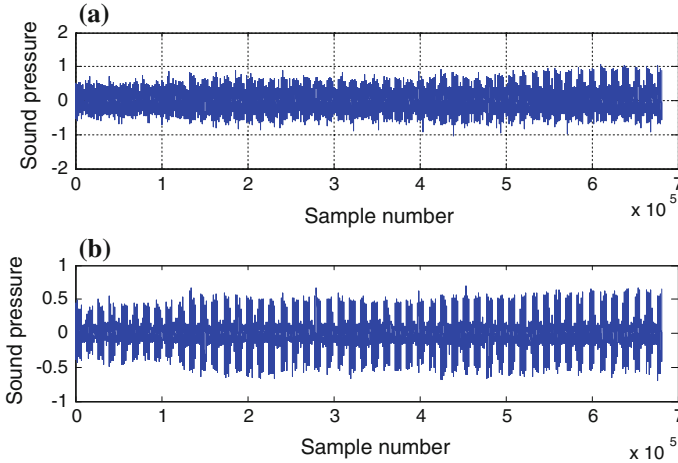


arc height mutates, the energy also appears ladder shape, and the value of E-total increase tends to be similar when the arc height increase from 4 to 6 mm and increases from 2 mm to 4 mm. Welding arc length increases, the plasma volume increases, arc energy increases, while the total energy of sound signal at this time will also increase. The variation shows that the sound signal is mainly produced by the arc energy and changes of weldment caused by the change of the welding arc energy, the sound of welding equipment and the random noise outside has little effect on the entire sound signal.

Figure 7 is the energy variation trend of every frequency range. As shown in Fig. 8, with the arc height increasing from 2 to 6 mm, energy in every frequency range increases. This indicates the arc sound signal directly or indirectly caused by arc height distributes in the whole range of 0–20,000 Hz. The increasing of E1 and E2 is the greatest and the ladder shape is the most obvious, E1 and E2 separately corresponds to the frequency range is 0–2500 and 2500–5000 Hz. This suggests that the motion of plasma causes periodic harmonic vibration of the surrounding particles, generates sound signal, transforming a part of arc energy into sound energy, the corresponding sound signal distributes in 0–5000 Hz. Moreover, the trend of this part energy is always synchronous with E-total, and E1 and E2 is much larger relative to energy in other frequency range, so sound signal in 0–5000 Hz can be generally respond to the changes of entire sound signal and the variation of arc height. In some researches, high frequency sound signal is forced to be removed in denoising process, and they get a good result in controlling welding quality by utilizing the variation trend of low frequency sound signal. The trends of E3, E6, E7 is close to a straight line, though the energy in these frequency bands go up as the

**Fig. 7** The energy variation trend every frequency range





**Fig. 8** Comparison of signal before and after denoising. **a** Signal before denoising. **b** Signal after denoising

arc height increasing, there is no obvious ladder shape when arc height mutates, so this part of energy should be relative to the changes of weldment state. For one thing, when arc length increases, the plasma volume between the cathode and the anode increases, arc energy increases, the heat weldment received increases per unit time. For the other thing, with the welding time increasing, the heat weldment received is also gradually accumulating. So the liquid part of weldment increases, that is the volume of weld pool increases, vibration of weld pool in welding process leads to the vibration of the surrounding particles, that leads to the formation of sound signal in these frequency bands. The changes of E5 is not obvious with the variation of arc height, but there is a little ladder shape at the position of arc height mutating, which presume that the sound signal in 10,000–12,500 Hz frequency band is produced by the vibration of solid part of weldment and the transmission of heat from solid part of weldment to surrounding particles. This situation is different from that of the liquid part of weldment, because the changed solid volume is relatively smaller for the entire solid part and the vibration of particles in solid is much slower than that in liquid, the energy transferred from solid part is less and slower, the variation trend in this frequency band is not sensitive to the change of arc height. The linear features and the ladder shape E4 and E8 are not obvious, E4 have sudden increase at the position when height has mutation, but there is no distinct difference in average energy for arc height is 4 and 6 mm. However, E8 have distinct increase in average energy of three phase, but only a sudden increase when arc length changed from 4 to 6 mm. So the sound signal in 7500–10,000 and 17,500–20,000 Hz is not only relative to the changes of arc length and changes of weldment state, but also has relationship with noise outside. To sum up, the sound signal in 0–5000 Hz can be used to forecast and even control the variation of arc length. E3, E6 and E7 corresponding to the sound signal in 5000–7500,

12,500–15,000 and 15,000–17,500 Hz frequency band can be used reflect the welding state and the welding quality.

## 4 Research on the Relationship Between Sound Signal and Arc Height

### 4.1 Denoising

According to the result above, the sound signal in 0–5000 Hz frequency band can be generally respond to the variation of arc height, that is sound signal in high frequency from 5000 to 20,000 Hz can be removed in order to decrease the influence of background noise, which maybe good for seeking effectively the relationship of sound signal and arc height, in this paper db3 wavelet packet function was used to do 2 layer wavelet denoising for every sound peak, the procedure of wavelet de-noising is:

- (1) Decompose the sound signal by utilizing wavelet transform.
- (2) Force the high frequency coefficients to be zero to remove the sound signal in high frequency.
- (3) Reconstruct the sound signal.

Wavelet decomposition algorithm is:

$$\begin{cases} c_{j+1}(n) = \sum_{m \in \mathbb{Z}} c_j(m)h(m-2n) \\ d_{j+1}(n) = \sum_{m \in \mathbb{Z}} c_j(m)g(m-2n) \end{cases} \quad (6)$$

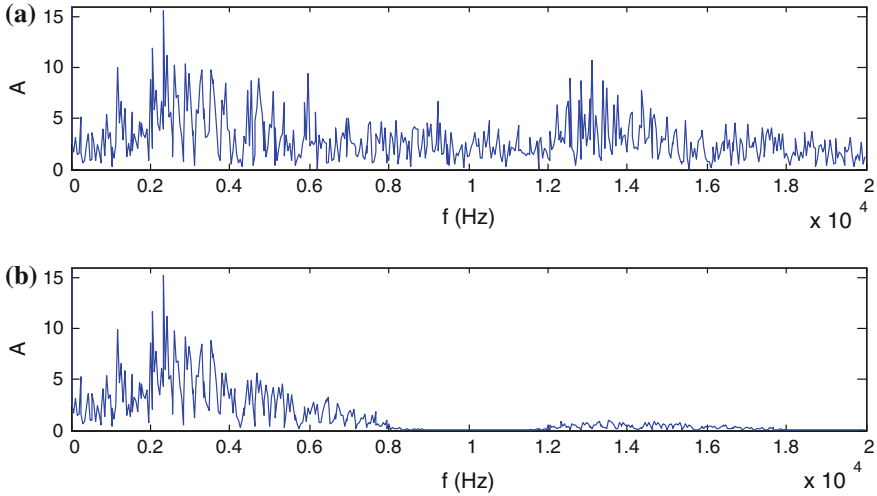
Wavelet reconstruction algorithm is:

$$c_j(n) = \sum_{m \in \mathbb{Z}} [c_{j+1}(m)h(n-2m) + d_{j+1}(m)g(n-2m)] \quad (7)$$

The result of wavelet decomposition can be see in Figs. 8 and 9 is the comparison of frequency distribution of sound signal before and after denoising. From Figs. 8 and 9, we can see that most of high frequency sound signal had be removed, the peak and the base is more clear after denoising.

### 4.2 Establishment of Linear Relationship Between Arc Sound Energy and Arc Length

As shown above, the value of E-total increasing tends to be similar when the arc height increase from 2 to 4 mm and increases from 4 to 6 mm, the relationship



**Fig. 9** The comparison of frequency distribution before and after denoising. **a** Amplitude-frequency before denoising. **b** Amplitude-frequency after denoising

between total energy and arc length should be linear. So we firstly calculated the average of every peak total energy in different arc length, then made a linear fitting for the arc length and average total energy. The fitting done to both the signal before denoising and after denoising for three experiments in arc length is respectively 2-4-6 mm, 6-4-2 and 4-5-6 mm. The result is shown in Table 5. The symbol and algorithm used can be seen below:

The average of total energy  $E_a$  in different arc length:

$$E_a = \frac{1}{n} \sum_{i=1}^n E_i \tag{8}$$

In which  $n$  is the number of peak in the same arc length,  $E_i$  is the  $i$ th total energy. The linear equation is

$$L = kE_a + b \tag{9}$$

where  $L$  is the arc length,  $k$  and  $b$  are both constants.

The standard deviation  $r$  is:

$$r = \sqrt{\frac{1}{m} \sum_{i=1}^m L(i) - L'(i)^2} \tag{10}$$

where  $m$  is the number of points used for fitting,  $L$  is the ideal arc length.

**Table 5** The result of fitting

Arc length variation	Signal state	Equation	r (mm)	$\varepsilon_1$ (mm)	$\varepsilon_4$	$\varepsilon_6$
2-4-6	Before denoising	$L = 0.0999E-2.1051$	0.0024	$\varepsilon_2 = 0.0029$	$\varepsilon_4 = 0.0059$	$\varepsilon_6 = 0.0029$
	After denoising	$L = 0.2356E-2.1475$	0.1757	$\varepsilon_2 = 0.1420$	$\varepsilon_4 = 0.4228$	$\varepsilon_6 = 0.2809$
6-4-2	Before denoising	$L = 0.0879E-1.7649$	0.0680	$\varepsilon_2 = 0.0935$	$\varepsilon_4 = 0.1661$	$\varepsilon_6 = 0.0727$
	After denoising	$L = 0.2098E-0.9524$	0.0575	$\varepsilon_2 = 0.0777$	$\varepsilon_4 = 0.1406$	$\varepsilon_6 = 0.0629$
4-5-6	Before denoising	$L = 0.1414E-5.7203$	0.2724	$\varepsilon_4 = 0.0616$	$\varepsilon_5 = 0.5445$	$\varepsilon_6 = 0.6061$
	After denoising	$L = 0.3642E-5.2078$	0.2321	$\varepsilon_4 = 0.4898$	$\varepsilon_5 = 0.4948$	$\varepsilon_6 = 0.0050$

The  $\varepsilon_i$  is the absolute error when arc length is  $i$  mm:

$$\varepsilon_i = |L(i) - L'(i)| \quad (11)$$

The result shows that, no matter whether the signal has been denoised, the relationship between the total energy and arc length could be expressed as linear, though the standard deviation and absolute errors before denoising is smaller than the signal after denoising in the first set of datas, in the other two set of datas, they are much larger, especially in the third experiment in which the arc length is 4-5-6 mm, the absolute errors reached 0.6061, which is too big for the largest arc length mutation is 1 mm. So overall, the signal after denoising is better for the establishment of the linear relationship between average total energy and arc length. Moreover, the difference in the slope of the equation maybe caused by the difference in the weldment, and the intercept can reflect the noise in the signal, there is always noise in the signal for the intercept are minuses.

## 5 Conclusion

Conclusions can be made as following though the processing and analysis above.

- (1) Most of sound signal is relative to the arc length and the weldment state, noise outside has little influence on sound signal received.
- (2) The sound signal relative to the arc length mainly distributes in 0–5000 Hz frequency band.
- (3) The average total energy and arc length have linear relationship, the minus intercept reflect the fact that the signal contains noise.
- (4) Using db3 in 2 layer Wavelet packet denoising is good for the establishment of linear relationship between average total energy and arc length.

**Acknowledgment** This work is supported by the National Natural Science Foundation of China under the Grant No. 61374071 and No. 61401275.

## References

1. Tarn TJ, Chen SB, Zhou CJ (2007) Robotic welding, intelligence and automation. Springer, Berlin
2. Cayo EH, Alfaro SCA (2009) A non-intrusive GMA welding process quality monitoring system using acoustic sensing. *Sensors* 9(9):7150–7166
3. Luksa K (2003) Correspondence between sound emissions generated in the GMA welding process and signals registered in the arc circuit. *Weld Int* 17(6):438–441
4. Pal K, Bhattacharya S, Pal SK (2010) Investigation on arc sound and metal transfer modes for on-line monitoring in pulsed gas metal arc welding. *J Mater Process Technol* 210(10):1397–1410



5. Chen CM, Kovaevie R, Jandgrie D (2003) Wavelet transform analysis of acoustic emission in monitoring friction stir welding of 6061 aluminum. *Int J Mach Tools Manuf* 43:1383–1390
6. Tam J, Huissoon J (2005) In Developing psycho-acoustic experiments in gas metal arc welding. In: *Proceedings of the IEEE international conference on mechatronics and automation, Niagara, Falls*, pp 1112–1117
7. Chen B, Wang JF, Chen SB (2010) A study on application of multi-sensor information fusion in pulsed GTAW. *Ind Robot Int J* 37(2):168–176
8. Ladislav G, Janez G, Ivan P, Janez MS (2004) Feasibility study of acoustic signal for on-line monitoring in short circuit gas metal arc welding. *Int J Mach Tools Manuf* 44(5):555–561
9. Schiebeck E, Mueller G (1991) Audible range acoustic diagnosis of the MAG welding arc. *Weld Int* 5(7):572–576
10. Sánchez Roca A, Carvajal Fals H, Blanco Fernández J et al (2009) Stability analysis of the gas metal arc welding process based on acoustic emission technique. *Weld Int* 23(3)
11. Kang MJ, Rhee S (1991) A study on the development of the arc stability index using multiple regression analysis in short-circuit transfer region of gas metal arc welding. *Proc Inst Mech Eng* 215(2):195–205
12. Wang JF, Chen B, Chen HB, Chen SB (2009) Analysis of arc sound characteristics for gas tungsten argon welding. *Sens Rev* 29(3):240–249
13. Lv N, Zhong J, Chen H et al (2014) Real-time control of welding penetration during robotic GTAW dynamical process by audio sensing of arc length. *Int J Adv Manufact Technol* 1–15
14. Lv N, Xu Y, Zhang Z et al (2013) Audio sensing and modeling of arc dynamic characteristic during pulsed Al alloy GTAW process. *Sens Rev* 33(2):7–7

# Data-Driven Feature Selection for Multisensory Quality Monitoring in Arc Welding

Zhifen Zhang and Shanben Chen

**Abstract** Feature selection is the key issue for multisensory data fusion-based online welding quality monitoring in the area of intelligent welding process. This paper mainly focus on the automatic detection of typical welding defect for Al alloy in gas tungsten arc welding (GTAW) by means of a series of analysis of synchronous online arc spectrum, arc sound pressure and arc voltage signal. Based on the developed feature selection algorithms, hybrid fisher-based filter and wrapper was successfully utilized to evaluate the sensitivity of each feature and reduce the feature dimensions. Finally, the optimal feature subset with 19 features was selected to obtain the highest accuracy, i.e., 94.72 % of the established classification model support vector machine-cross validation (SVM-CV).

## 1 Introduction

Sensor-based real-time monitoring of welding quality for aluminum alloy pulsed gas tungsten arc welding (GTAW) has been a hot issue for intelligent manufacturing process [1]. Several on-line sensing technique have been proposed, such as vision sensor [2], arc sensor [3], acoustic emission sensor [4], temperature sensor [5] and arc light spectrum sensor [6]. Recently, multi-sensor information fusion technology has been widely applied in different areas, such as robotics [7] and as well as welding penetration condition estimation in CO<sub>2</sub> laser welding [8]. However, as the number of sensors increases, feature reduction has become the key difficulty to be resolved. For the time being, only a few general methods, like PCA [9], SFS [10] were mainly applied in plasma spectrum signal-based welding

---

Z. Zhang (✉) · S. Chen

Institute of Welding Engineering, Material Science and Engineering,  
Shanghai Jiao Tong University, Shanghai 200240, China  
e-mail: zzf919@sjtu.edu.cn

in-process quality monitoring to select more relevant information. But, researches about feature selection for multisensory data have been rarely reported in terms of welding quality monitoring in pulsed gas tungsten arc welding (GTAW). In this paper, a novel methodology for feature selection, i.e., hybrid fisher-based filter and wrapper is presented based on data-driven technology and the fusion of arc light spectrum, arc sound pressure and voltage signals.

In order to simulating the welding disturbance and defects, the repeatable and controllable condition, like porosity caused by hydrogen, different seam penetration, local caving and so on were artificially produced for plates butt welding experiment. The feature-level-based data fusion frame was firmly constructed during the process of feature selection in Sect. 3.2.2, wherein the illustrating methodology, was proposed and utilized to select the optimal feature subset based on which the constructed classification architecture, namely, SVM-CV, can obtain the highest estimation accuracy of welding quality. The method presented is generic in nature, hence applicable to a wide range of problems typically seen in welding quality monitoring and other manufacturing process condition monitoring.

## 2 Experimental Setup

The experiments were performed on an automatic experimental system which was shown in Fig. 1. It consists of three parts: the welding system, the control and motion system and multisensory signal acquisition system, which includes spectral

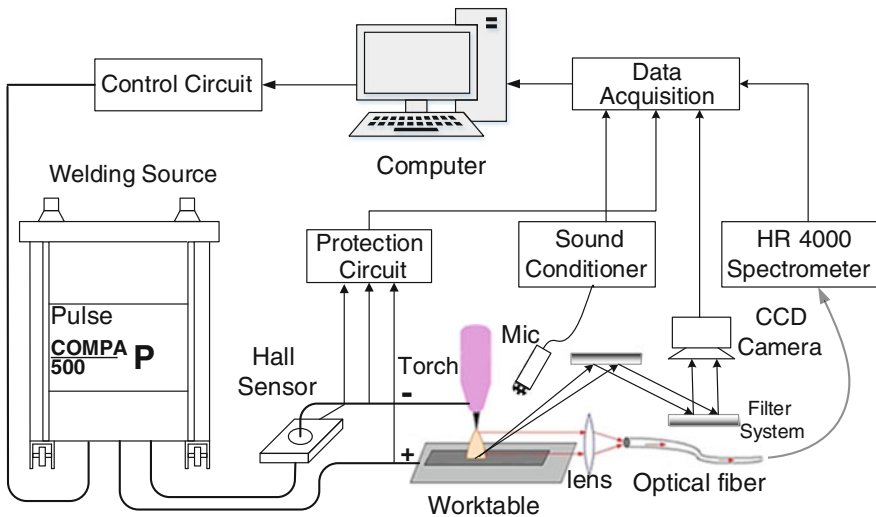
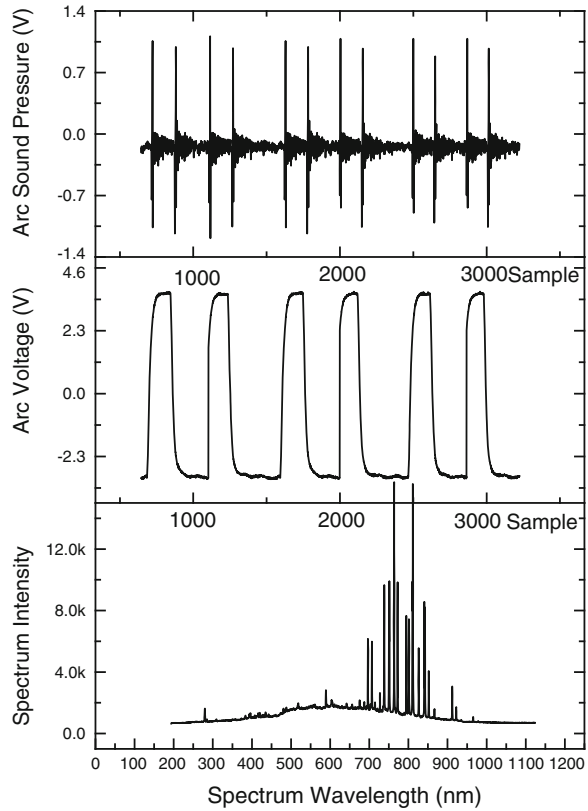


Fig. 1 Diagram of the experimental system

**Fig. 2** Multiple signals in one data block



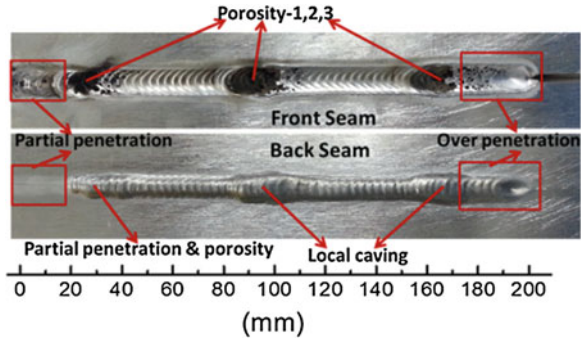
collecting system, arc sound pressure and arc voltage sensing system. A series of normal and defect GTAW welding experiment have been carried out as shown in Fig. 2.

At the end, different sensory data will be carefully analyzed in order to correlate the feature parameters and the designed disturbance, and then evaluate the welding quality based on proposed modeling method.

### 3 Methods and Results

Since these three signals are heterogeneous type of signal, in this paper, different approaches were utilized to extract feature parameters from different signals. Figure 2 has shown the three preprocessed signals in one data block from which the multiple feature parameters would be extracted respectively.

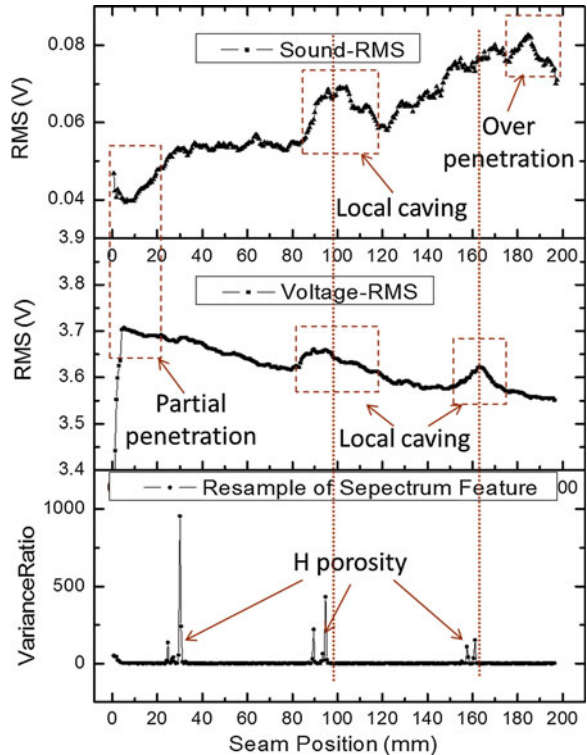
**Fig. 3** Welding seam with multiple defects



### 3.1 Feature Extraction

In this paper, the heterogeneous feature will be synchronized by means of down sampling the arc light spectrum feature before the feature selection. Figure 4 has showed the feature curves calculated in time domain after down sampling, from top to bottom is the RMS of arc sound pressure signal (>0.2 V), the RMS of voltage

**Fig. 4** Multi-sensor feature curves



signal ( $>3.5$  V) and the arc light spectrum feature. The corresponding seam with different welding defects designed was shown in Fig. 3.

It could be concluded that multisensory data has shown their complementary as well as the redundancy. Hence, it is quite necessary to remove the redundant signal feature with the feature selection method.

### 3.2 Feature Selection

Feature selection is a process of choosing a subset of preliminary features by removing irrelevant and redundant features based on certain rules. It has attracted intensive research for data mining, machine learning and so on [11]. Generally speaking, feature selection methods can be categorized into two families: filter-based and wrapper-based methods [12, 13]. In this section, the improved fisher distance criteria was proposed as a filter tool to pre-process and rank the 41 feature parameters extracted from Sect. 3.1, and then the wrapper method was applied in order to search the optimal feature subset from the ranking list during which the accuracy is estimated using the support vector machine (SVM) predictor architecture.

#### 3.2.1 Weighted Fisher Criteria for Filter Selection

Filter-based methods rank the features as a pre-processing step prior to the learning algorithm, and select those features with high-ranking scores. Wrapper-based methods score the features, usually the accuracy, by using the learning algorithm that will ultimately be employed.

Fisher score is one of the most widely used criteria for supervised feature selection due to its general good performance. The key idea of Fisher Distance criterion is to find a subset of features, such that in the data space spanned by the selected features, the distances between data points in different classes are as large as possible, while the distances between data points in the same class are as small as possible. The within-class scatter matrix and between-class scatter matrix are estimated by

$$S_w = \sum_{i=1}^C P_i \hat{S}_i \quad (1)$$

and

$$S_b = \sum_{i=1}^C P_i (\hat{\mu}_i - \hat{\mu})(\hat{\mu}_i - \hat{\mu})^T \quad (2)$$

respectively. For  $k$ th feature, it is calculated by

$$Fisher(k) = \frac{S_b^{(k)}}{S_w^{(k)}} \tag{3}$$

However, it is difficult to choose the better feature subset by only judging from their fisher distance. The developed fisher criteria has been presented in Fig. 5 and its result has been displayed in Table 1.

The voting for each feature parameter could be counted from the top 10 matrix while the total fisher distance for each feature could be also calculated. In the proposed selection algorithm, both aspects were considered by multiplying in carefully determined value of weighted factor, i.e. 0.3 and 0.7 respectively. It can be seen from Table 1 that the first feature might be deleted with its lower voting if only the voting was considered, although this feature has the highest value of fisher distance. Based on the algorithm proposed in this paper, the final value of fisher judge with weighting factor for this feature was up to 7.1, ranking first among all 41-feature parameters.

Furthermore, the 3D scatter distribution of the three selected feature parameters, whose number are 1, 6 and 16 respectively, has been plotted in Fig. 6, from which it can be seen that seven class of welding quality can be separated with the combination of those three feature parameters. However, the different combination of feature selected from Table 1, in other words, the feature subset can be of great variety in terms of the classification performance in the future classification algorithm modelling. In this paper, the wrapper method for further feature subset

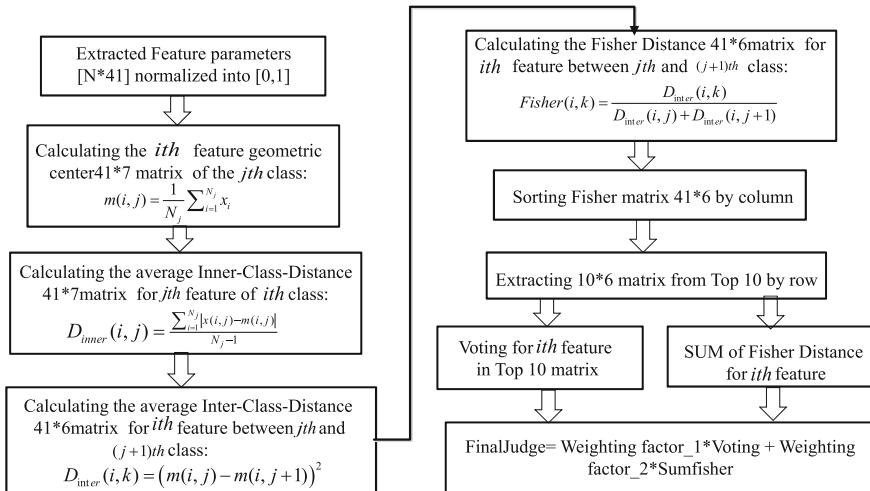
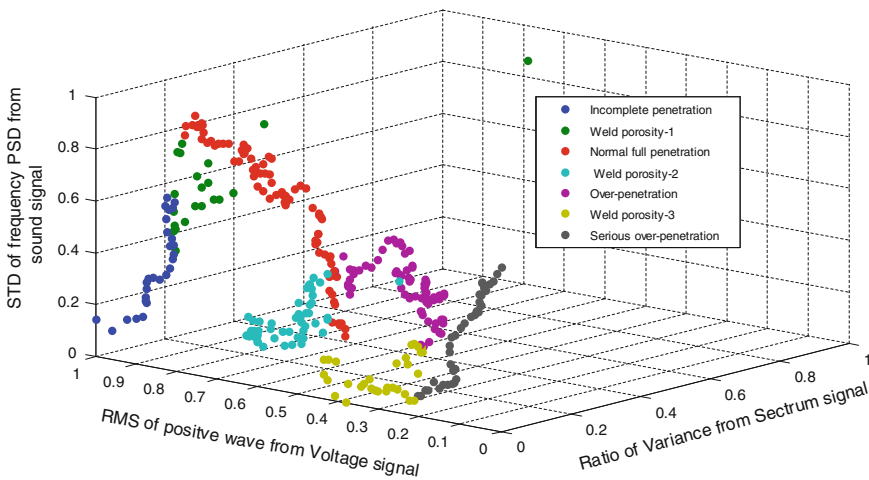


Fig. 5 Flow chart of developed fisher distance criteria

**Table 1** Pre-selection result based on proposed fisher distance criteria

Number and meaning of selected feature	Voting	Percent (%)	Sum of fisher distance	Final judge with weighting factor
1-arc light spectrum—variance ratio of H/Ar	2	2.77778	17.1109	7.07771
16-Sound-PSD-2-std	4	5.55556	5.90537	5.6605
28-Vol-PSD-1-std	2	2.77778	11.46077	5.38268
22-Sound-PSD-4-std	3	4.16667	8.12027	5.35275
19-Sound-PSD-3-std	2	2.77778	10.59348	5.12249
9-Vol-Nrms	2	2.77778	9.58678	4.82048
35-Vol-PSD-3-kur	2	2.77778	8.86933	4.60524
15-Sound-PSD-2-rms	3	4.16667	5.6102	4.59973
20-Sound-PSD-3-kur	3	4.16667	5.54744	4.5809



**Fig. 6** Scatter distribution for the seven status of welding quality (1-6-16)

selection was applied right after the fisher filter method which forms the hybrid fisher filter and wrapper.

### 3.2.2 Wrapper Selection of Feature Subset Based on SVM-CV Predictor

This section will introduce the second step of the proposed hybrid method of feature subset selection, namely, wrapper approach based on SVM-CV predictor. Figure 7 has plotted the flow chart of the proposed hybrid feature subset selection method, in



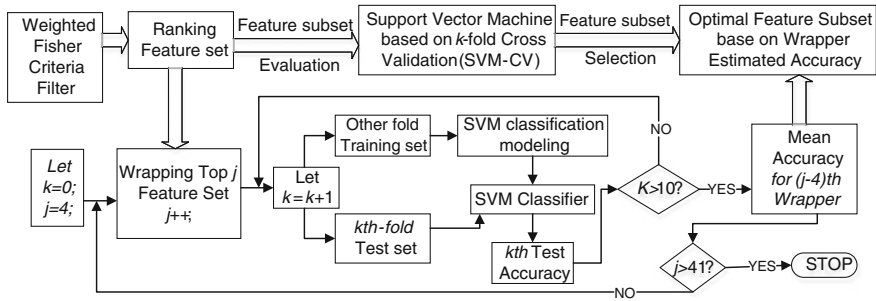


Fig. 7 Hybrid feature subset selection based on fisher filter and SVM-CV wrapper

which the ranking feature set was determined after the pre-evaluating of the entire feature set with the developed filter criteria. Then, the wrapper packing the top  $j$ , from 5th, feature parameters from the ranking list was orderly evaluated based on the SVM-CV data fusion model by their classification mean accuracy and eventually, the feature subset with the highest mean accuracy of proposed predictor was determined. It is also worth to mention that the feature-based multi-sensor fusion was also achieved by establishing and testing the SVM-CV model during the process of wrapping selection.

Recent research has indicated the considerable potential of SVM-based approaches for various intelligent classification issues since it is based on the notion that only the training samples that lie on the class boundaries are necessary for discrimination. In this paper, radial basis function (RBF) is chosen as the kernel in this paper,

$$k(x, x_i) = e^{-\gamma \|x - x_i\|^2} \tag{4}$$

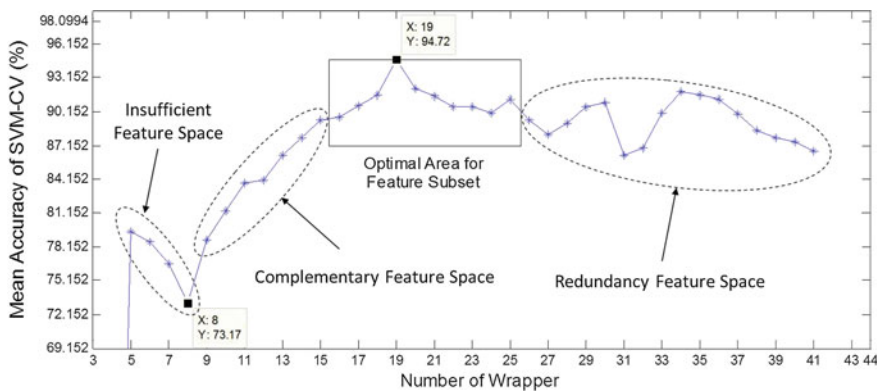


Fig. 8 Mean accuracy for each wrapper with increasing top feature parameters based on SVM-CV classifier

where  $\gamma$  and  $c$  is the parameter controlling the width of the Gaussian kernel. The accuracy with which a SVM may classify a data set is dependent on the magnitude of the parameters  $C$  and  $\gamma$  [14]. In this paper, cross-validation approach was applied to search the optimal value for these two parameters for the SVM model. Then, the classifier, i.e., SVM-CV was established based on cross-validation.

The k-fold cross-validation is widely used in the machine learning field in order to obtain a prediction error with more robustness and accuracy. The advantage of this method is that all observations are used for both training and validation, and each observation is used for validation exactly once. In this paper, 10-fold cross-validation is used and the mean accuracy for the established prediction model is achieved by calculating the mean value of each fold prediction. In addition, the training and predicting of the SVM-CV was achieved through the combination of LibSVM and Matlab. Figure 8 has shown the curve of the mean accuracy for every wrapper where the feature parameters were increasingly selected from the ranking list. For instance, the number 17 means that the top 17 feature parameters in the ranking list were wrapped as the input feature subset of the SVM-CV model and it begins from the 5th and ends in the 41th.

From Fig. 8, it can be seen that the mean accuracy basically increased as the wrapping number of feature parameters increased and peaks at the number of 19 with the highest accuracy of 94.725 while the smallest mean accuracy, which is 73.17 %, occurred when the top 8 parameters, were wrapped as the feature subset. The reason for this occurrence in Fig. 16 is that the smaller the number of the wrapping feature is, the more important role for each feature was playing, so a single wrong-selecting feature, like number 8 is insufficient for feature space, can cause the severe fall in the mean accuracy. Then, as the number rose, the feature space of the SVM-CV model was gradually complementary until it is around 25. After that, the curve drastically fluctuated and began to decrease from the number of 36 due to the redundancy of the feature space. Hence, the optimal area for feature subset was from the number of 15 to 25, which has been marked in Fig. 16, during which the mean accuracy was obtained around 90 % with little fluctuation.

## 4 Conclusions

A comprehensive multi-sensor-based method for real-time welding quality monitoring and defect detection of Al alloy GTAW was developed from signals acquisition, feature extraction and selection to multi-sensory data fusion.

The main conclusions are as follows:

- The proposed approach of feature selection, i.e., hybrid fisher-based filter and wrapper can automatically determine the optimal feature subset with the highest classification accuracy, therefore has successfully reduced the feature dimension.
- Multiple welding defects, like porosity, incomplete penetration and so on, have been successfully recognized by means of the established classification

architecture, SVM-CV, with the highest accuracy of 94.72 %. In addition, great robustness has been found within the optimal area of feature subset for the classifier, wherein the accuracy ranged from 89.41 to 94.72 % while the feature dimension varied from 15 to 25.

**Acknowledgment** This work is supported by the National Natural Science Foundation of China under the Grant No. 61374071 and the NDRC of China, under the Grant No. HT[2012]2144.

## References

1. Chen S-B, Wu J (2009) *Intelligentized methodology for arc welding dynamical processes*. Springer, Berlin
2. Zhang W, Zhang Y (2012) Modeling of human welder response to 3D weld pool surface: part II—results and analysis. *Weld J* 91:329s–353s
3. Christner B (1998) Developing a GTAW penetration control system for the Titan IV program. *Weld Metal fabrication* 66:29–38
4. Kannatey-Asibu E Jr (2009) *Principles of laser materials processing*. Wiley, Hoboken
5. Chen W, Chin B (1990) Monitoring joint penetration using infrared sensing techniques. *Weld J* 69:181s–185s
6. Zhang Z, Yu H, Lv N, Chen S (2013) Real-time defect detection in pulsed GTAW of Al alloys through on-line spectroscopy. *J Mater Process Technol* 213:1146–1156
7. Chilian A, Hirschmuller H, Gornier M (2011) Multisensor data fusion for robust pose estimation of a six-legged walking robot. In: 2011 IEEE/RSJ international conference on intelligent robots and systems (IROS), IEEE, pp 2497–2504
8. Sun A, Kannatey-Asibu E Jr, Gartner M (2002) Monitoring of laser weld penetration using sensor fusion. *J Laser Appl* 14:114–121
9. Lee S (2013) *Process and quality characterization for ultrasonic welding of lithium-ion batteries*. University of Michigan, Ann Arbor
10. Garcia-Allende P, Mirapeix J, Conde O, Cobo A, López-Higuera J (2009) Spectral processing technique based on feature selection and artificial neural networks for arc-welding quality monitoring. *NDT E Int* 42:56–63
11. Shea JE, Gardner C (1983) Spectroscopic measurement of hydrogen contamination in weld arc plasmas. *J Appl Phys* 54:4928–4938
12. Li J, Song Y (1994) Spectral information of arc and welding automation. *Weld World Lond* 34:317–317
13. Guyon I, Elisseeff A (2003) An introduction to variable and feature selection. *J Mach Learn Res* 3:1157–1182
14. Jain A, Zongker D (1997) Feature selection: evaluation, application, and small sample performance. *Pattern Anal Mach Intell IEEE Trans* 19:153–158

# Sensing Technology for Intelligentized Robotic Welding in Arc Welding Processes

Yanling Xu, Na Lv, Gu Fang, Tao Lin, Huabin Chen, Shanben Chen and Yu Han

**Abstract** As more and more extensive application of welding robot, intelligentized robotic welding technology will become the main development trend. This paper introduces some sensing technique of research works about welding robot, such as computer vision sensing technology, arc sensing technology, arc sound sensing technology and welding arc spectral technology. All of which will attempted to address some key problem and provide the scientific basis and the technology realistic way for welding quality controlling in robotic welding intellectualization.

## 1 Introduction

At present, the use of robot welding is becoming increasingly wider and deeper; a large number of welding robots have been applied in the modern industrial automation production; however, most of them are teach-and-playback robots. They all have some weakness, namely, they have not the function of self-rectify deviations and adjusting welding parameters in real time during the robotic welding process, especially which have no seam tracking and penetration control function. In the robotic welding intelligence, the seam tracking and penetration control should be solved as two critical technical difficulties, and they are also the most challenging difficult and hot spot in the robotic welding field.

Robotic arc welding is one of the most common welding methods, which mainly includes robotic Gas Tungsten Arc Welding (GTAW) and Gas Metal Arc Welding

---

Y. Xu · N. Lv (✉) · T. Lin · H. Chen · S. Chen  
School of Materials Science and Engineering, Shanghai Jiao Tong University,  
Shanghai, China  
e-mail: nana414526@163.com

G. Fang  
School of Engineering, University of Western Sydney, Sydney, Australia

Y. Han  
Jiangsu Automation Research Institute, 222006 Jiangsu, China

(GMAW). For now, the real-time seam tracking and penetration control is realized mainly by using the various sensors in the robotic arc welding process, such as arc sensors [1–7], acoustic sensors [8, 9], spectral sensors [10–12], electromagnetic sensors [13], ultrasonic sensors [14, 15] and vision sensors [16–21].

In order to promote the development of intelligent robot welding, this paper introduces some sensing technique of research works about welding robot, especially computer vision sensing technology, arc sensing technology, arc sound sensing technology and welding arc spectral technology. All of which will attempted to address some key problem and provide the scientific basis and the technology realistic way for quality controlling in robotic welding intellectualization.

## 2 Intelligent Welding Robot System

The intelligent welding robot system is shown in Fig. 1. It includes nine parts: the robot arm, the robot controller, computer vision sensing, arc sensing, arc sound sensing, welding arc spectral system, interface box, the weld power supply and the host computer. The welding system have many features, such as welding

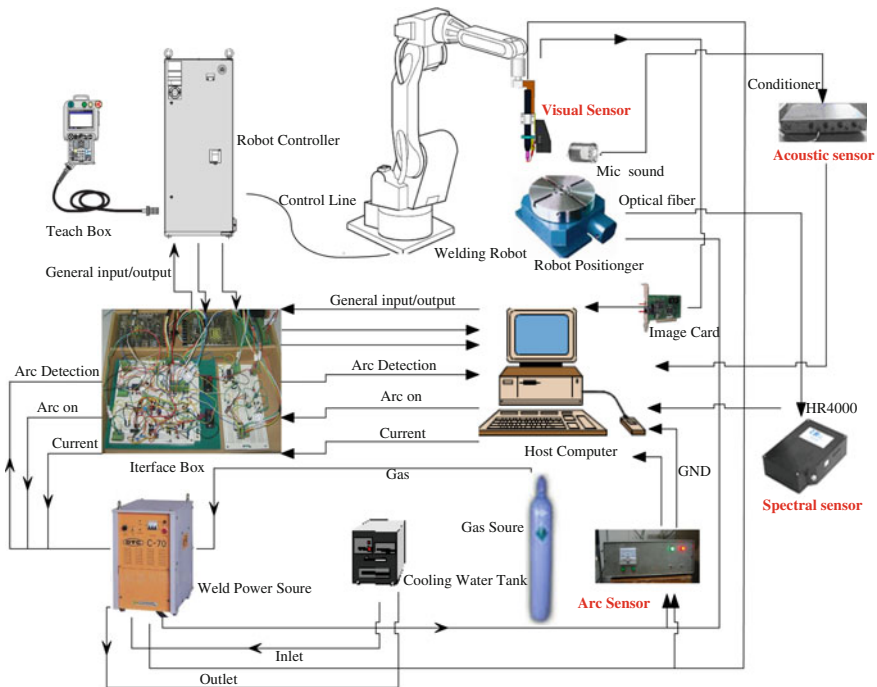
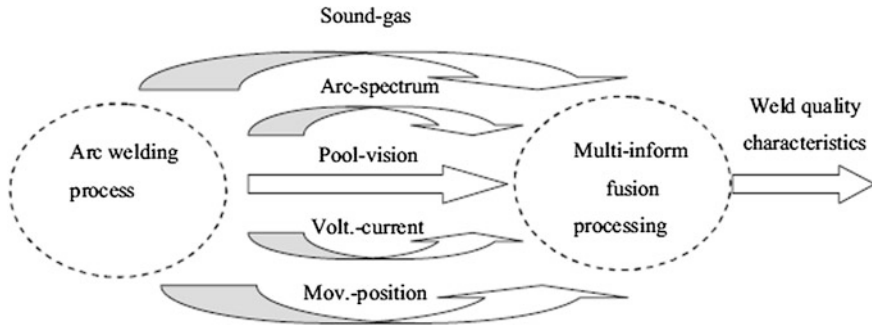


Fig. 1 The intelligent welding robot system schematic diagram



**Fig. 2** The schematic diagram of multi-information for arc welding process

environment identifying, initial welding seam guiding, seam tracking and penetration control.

In the intelligent welding robot system, computer vision sensor, arc sensor, arc sound sensor and welding arc spectral sensor are critical components. These sensors play an important role in robotic intelligent welding.

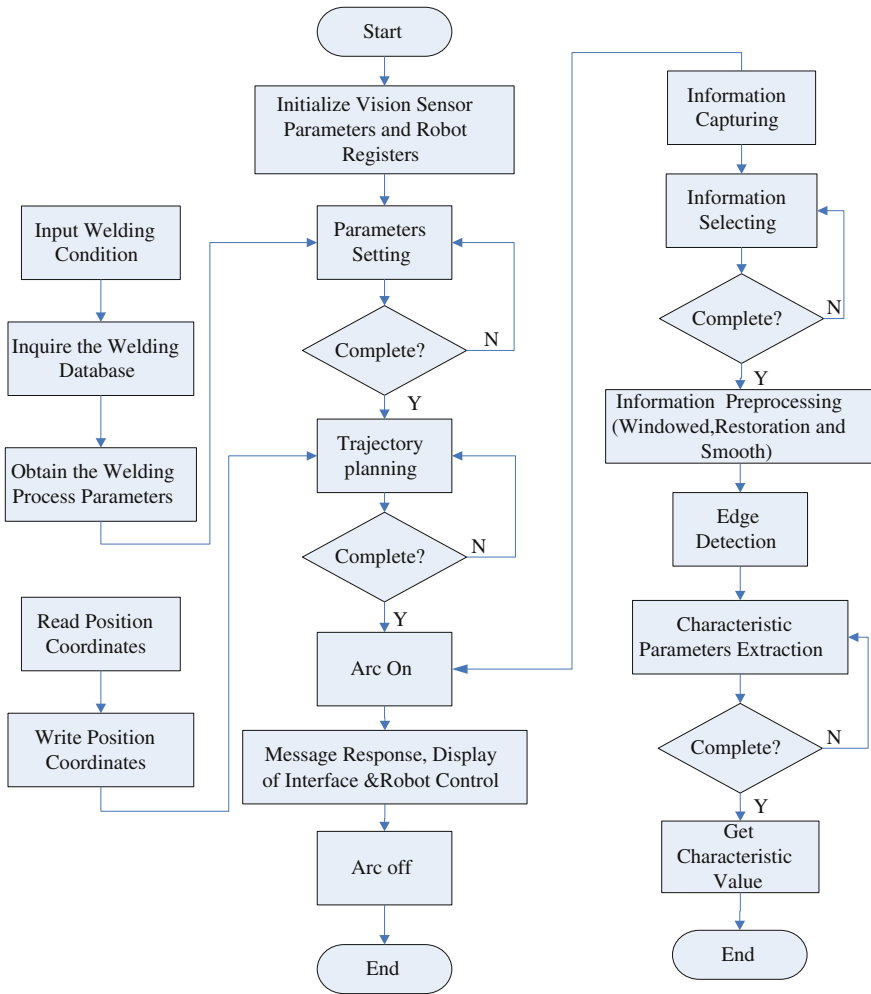
It is generally known that the robot arc welding process is a very complex and variable process, which often affect the welding quality. In order to control the weld quality, the effectual features of arc welding process must be obtained in real time, various signal processing methods have been applied for information of welding process, such as processing algorithms for arc voltage, current, pool, acoustic, visual, arc-spectrum, optical information. Figure 2 is the schematic diagram of multi-information for arc welding process.

Figure 3 is the flow chart of welding quality control program of robotic intelligent welding. In the system, the welding information processing processes mainly include information capturing, selecting and processing, especially vision sensing information, arc sensing information, arc sound sensing information and welding arc spectral information.

### 3 Computer Vision Technology

At present, there are various way sensor by using on the welding robot. The vision sensor is applied by many welding researchers, because the vision sensor has more advantage than other sensor, such as huge information content and non-contact, etc. For the seam tracking and penetration control of teach-and-playback welding robot, vision system plays a key role.

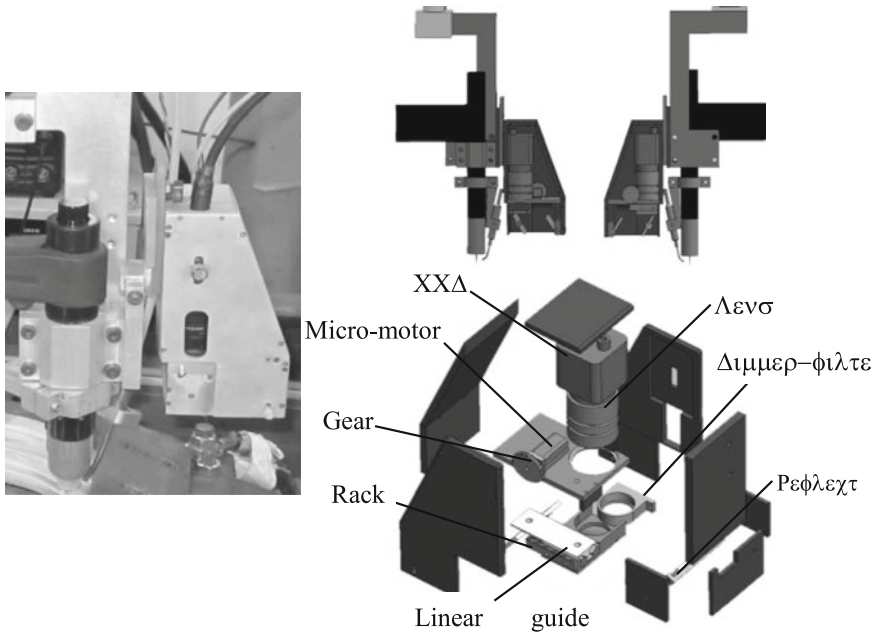
In accordance with the different light source, the vision system can be divided into two categories: the active vision system and the passive vision system. Because passive vision system is cheaper and can get enough seam information in robotic welding, this paper mainly introduces the passive vision sensor system for the



**Fig. 3** The flow chart of welding quality control program of robotic intelligent welding

welding robot. A passive vision system was purposely designed for seam tracking and penetration control. Figure 4 shows the structure design (right) and the picture of the passive vision system (left). (Patent number: 2012101210118579).

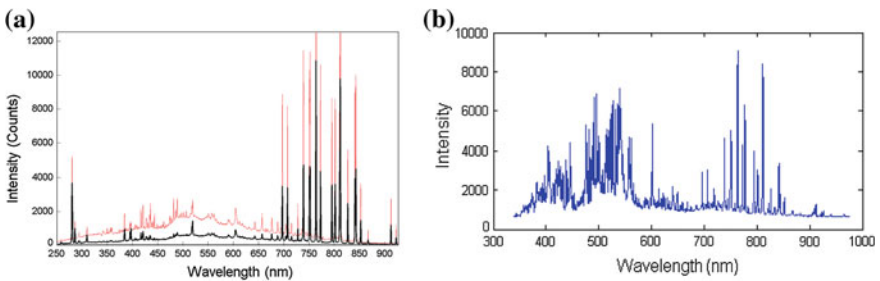
Using vision sensor in the robotic welding, a dimmer-filter system is the key component. It often needs to be removed from the CCD camera during welding environment identification and initial seam position guiding, while it must be put under the CCD camera during welding. In the passive vision system, the motorized mechanism can remove the dimmer-filter system automatically over long distances before welding and place them back during welding for seam tracking and penetration control. This automated mechanism allows the system to work in adverse



**Fig. 4** Design of a passive vision system

and dangerous conditions, such as in poisonous or nuclear radiation environments. The designed automatic transmission system includes a DC micro-motor, a pair of gear rack and a pair of linear guide rail.

To eliminate the disturbance of arc light during robotic seam tracking and penetration control, a dimmer-filter system is used. To perform a proper filtering of light, light spectrum of welding arc is analyzed. Taking the pulsed GTAW of Al alloy and Pulsed GMAW for Q235 steel as an example, Fig. 5 is the distribution map of the arc spectrum character. From the figure, it can be seen that the electric arc light range of 620–700 nm is the weakest and most stable, which can be used to



**Fig. 5** Distribution map of arc spectrum character of GTAW/GMAW. **a** Pulsed GTAW for Al alloy. **b** Pulsed GMAW for Q235 steel



capture welding images. Further experiment shows that an optical filter with the central wavelength of 660 nm is suitable for our welding system.

Through a large number of welding experiments, the clear and high quality images can be captured in robotic GTAW and GMAW by using the passive vision sensor. For example, for dimmer-filter system, the wavelength is about 660 nm, and the two dimmer glasses are 89 and 96 %, respectively. The image is captured when the current is at base current, and the value is 30 A. The best time of capturing images is 50 ms after the fall edge from the peak level to the background level. For detailed image capturing method, refer to the papers by Xu et al. [22]. Figure 6 shows the welding image of Al alloy during robotic GTAW by using the passive vision system. Figure 7 is the welding image of low carbon steel for GMAW. The complete processing flow of seam and pool image for robotic GMAW is shown in Fig. 8.

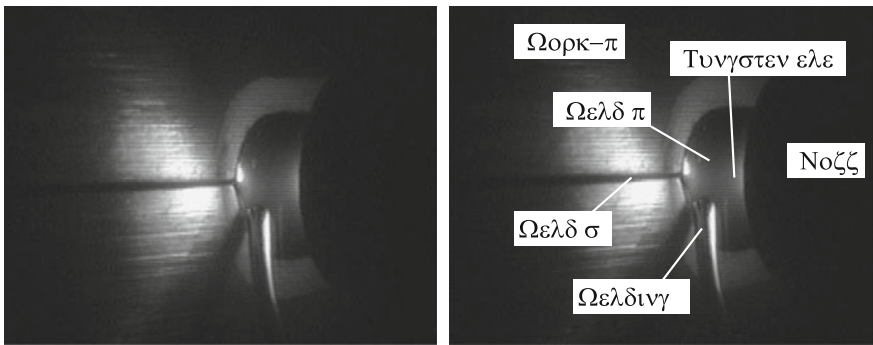


Fig. 6 The welding image during the GTAW process

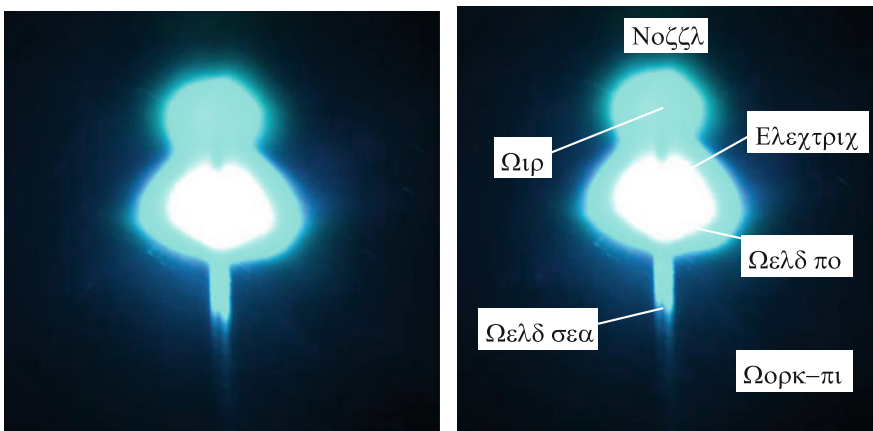


Fig. 7 The welding image of low carbon steel for GMAW

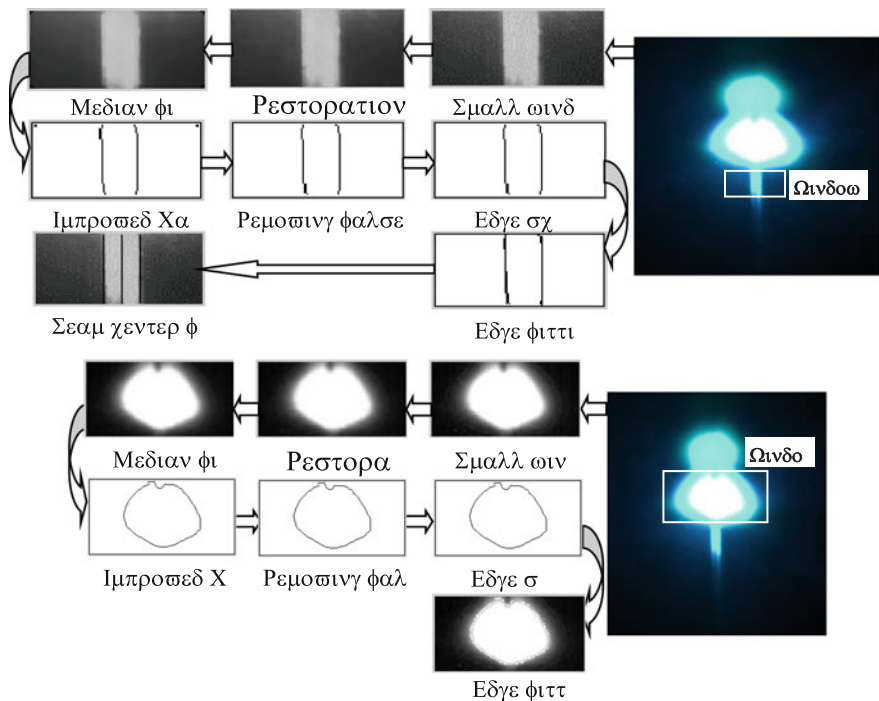


Fig. 8 The flow diagram of image processing during robot GMAW process

Through the process of welding image, the weld seam centerline and dynamic characteristic information of molten pool were extracted. These weld image information is needed for the seam tracking and penetration control of robotic intelligent welding.

#### 4 Arc Sensing Technology

In the practical welding process, most of the welding seams are three-dimensional, which are difficult for the only vision technology to real-time track and control. Among what have studied in weld seam tracking, the passive vision technology can accurately get the 2D seam-tracking information, but the height information should be acquired only through 3D reconstruction method. A pity then that most of the algorithms is too complex to be used in real-time control, which causes that the vision technology can hardly meet the requirements of real-time height track and control during actual robotic welding process. Thus, another technology must be used in height tracking while the visual sensor technology is used in real-time 3D seam tracking. The indirect method of height tracking of seam mainly uses the arc

sensor for it has many advantages, such as no additional device, using electric arc as monitoring section, no additional error and good real-time tracking. Therefore, it has received great attention from many researchers. The composite sensors based on visual sensor and arc sensor can be used in the weld of 3D seam, which provided a possibility to realize the function of real-time tracking of 3D welding seam.

In order to study the relation between the arc voltage and arc length, this paper take robotic GTAW process, for example. The work-piece is a ladder-type Al alloy sheet with 1.5 mm height differences, the height of initial welding is 3.5 mm. The robot was strictly taught along the contour line in the experiment, which the real arc length should be 3.5 and 2 mm, respectively. The arc voltage signal is shown in Fig. 9 [7].

In the actual robot welding, the arc voltage signals acquired by the arc sensor contain not only useful signals but also noise signals. If the arc voltage signals aren't de-noised, they cannot be used for the height tracking not to mention the precision of tracking. Therefore, in order to obtain the relational model between arc voltage and arc length, some signals processing methods must be studied to extract characteristic parameters from the arc voltage signals with a lot of pulse disturbance and non-stationary random disturbance signals. Figure 10 shows the whole procedures of signal processing.

Figure 10 shows the processes procedure of gathering and processing arc voltage. In the reference [4], according to the analysis of voltage signals processing, the relational model between arc voltage and arc length is  $u = 3.108h + 21.472$ . Then based on it, the arc length can be calculated by the detected arc voltage signals. The result is as shown in Table 1.

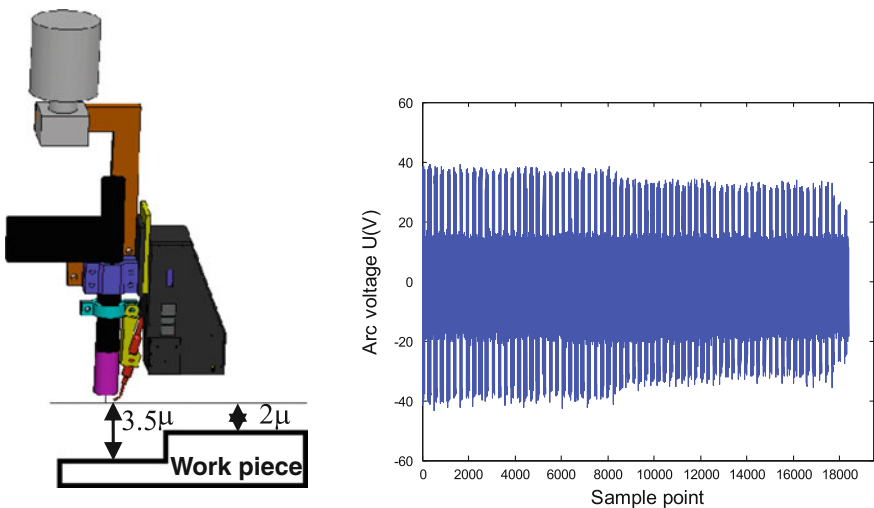
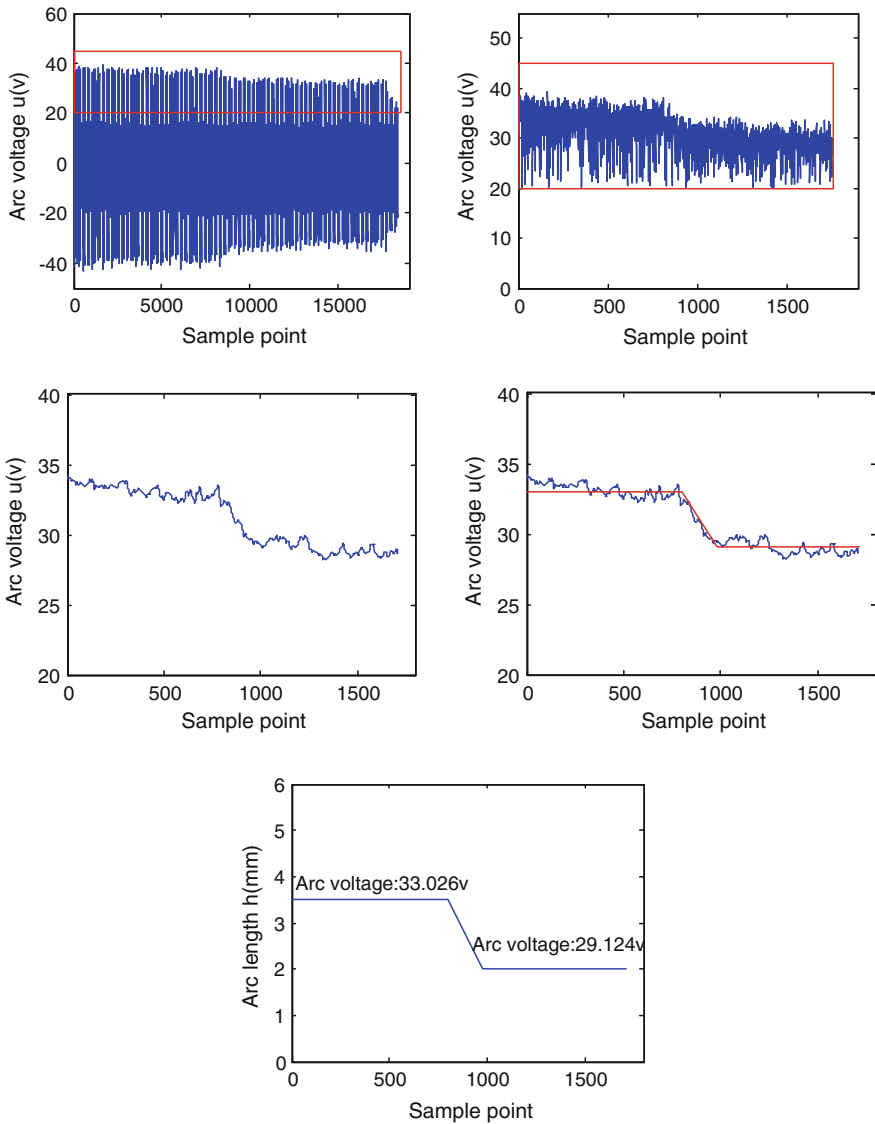


Fig. 9 Arc voltage signal of the welding height from 3.5 to 2 mm



**Fig. 10** The processing procedure of signal of the welding height from 3.5 to 2 mm

Table 1 shows the contrastive relation between the real arc length and the arc length calculated by the relational model. We can see clearly in Table 1 that while the arc lengths are 3.5 and 2 mm respectively, the absolute errors of arc length are 0.218 and 0.462 mm. Consequently, the arc voltage length calculated by the relational model is nearly the same as the real arc length, which is accurate enough to meet the requirements of tracking and control in height while robot welding.

**Table 1** The contrastive relation between the real arc length and the arc length calculated by the relational model

The relational model of the arc length and the arc voltage	Real arc voltage (V)	Real arc length (mm)	Calculated arc length (mm)	The absolute error of model (mm)
$u = 3.108h + 21.472$	33.026	3.5	3.718	0.218
$u = 3.108h + 21.472$	29.124	2	2.462	0.462

## 5 Arc Sound Sensing Technology

Research shows that the arc sound signal is the important information for monitoring of welding dynamic and quality characteristic. Figure 11 shows that the weld sound intensity is used as the variable reflecting changes of welding status. The time domain, frequency domain and wavelet packet features were extracted at different frequency band under different penetration states like partial penetration, full penetration and excessive penetration. Figure 12 shows different features of

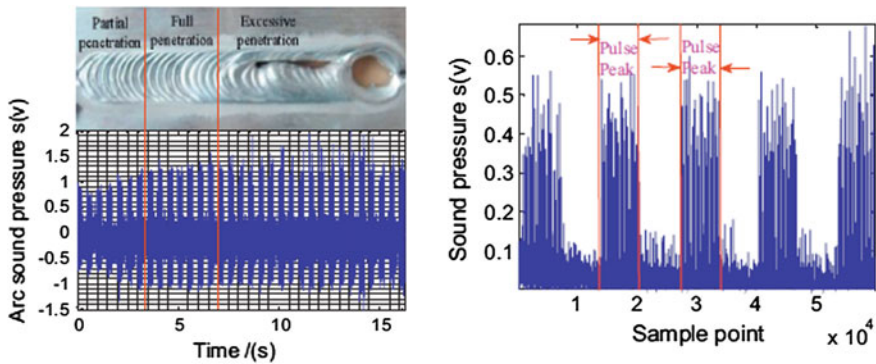


Fig. 11 The original arc sound signal

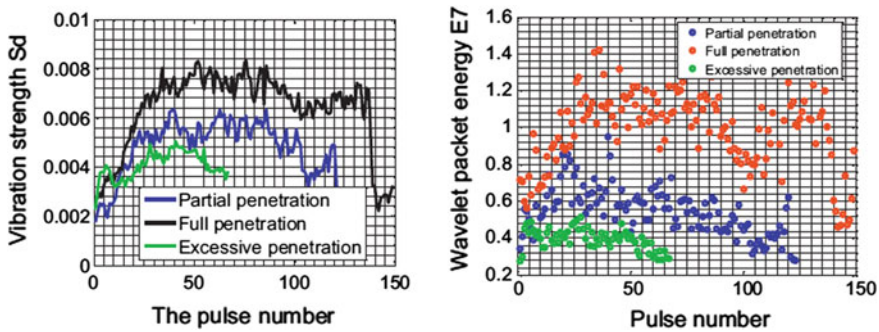


Fig. 12 The characteristic extraction of arc sound signal

three penetration states. Also some other algorithms were developed for extraction of welding status, e.g. penetration characteristics. The features of arc sound signal in time domain and frequency domain are essential factors for setting up a prediction model of welding quality control [23].

## 6 Welding Arc Spectral Technology

Arc plasma transfers energy from power source to the work-piece and emits large amount of spectra to the surrounding space. The arc spectra contain abundant information related to welding dynamic characteristics and quality status. The research background was welding quality control in 5A06 (LF6) aluminum alloy pulsed GTAW process. By means of welding arc the headstream of defects birth and formation, this paper adopted the modern spectral sensing and analysis techniques to study the welding dynamic process and defect characteristics. Firstly, a set of multi-information acquisition platform was designed, and a spectral information acquisition system was set up. By this experimental platform, we could control the welding automatic process in real time and achieved the multi-information of welding process acquisition and storage. In order to clarify the intrinsic relations

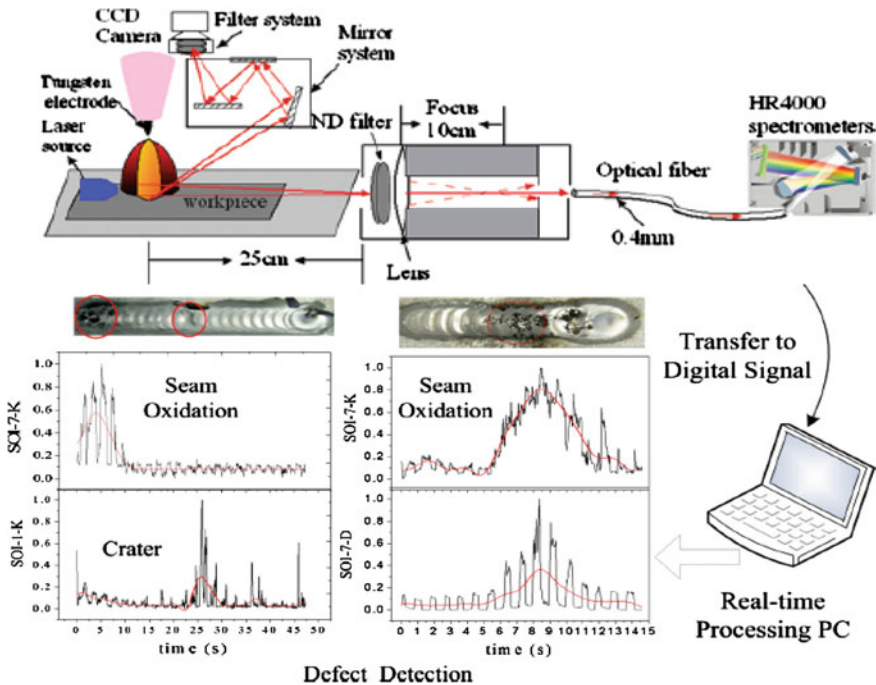


Fig. 13 The characteristic extraction of spectrum signal

between the arc spectral information and welding dynamic process, a L-M-K algorithm for plasma diagnostic based on spectral line broadening theory was proposed and then was applied to study 5A06 aluminum alloy pulsed GTAW arc by means of arc spectral information near welding pool surface. The plasma diagnostics have demonstrated that the arc plasma was in LTE state and have been used to study the arc plasma characteristics and the thermal transfer characteristics under different arc lengths. The relationships among these extracted signals and the defects caused by wire feed have been studied. Figure 13 shows the processing schematic of spectrum signal of welding defect. The defects of seam oxidation are produced by different disturbances, i.e., the oil painted on the surface of the plate and the non-removed insoluble oxide film of aluminum alloy [10–12, 23].

## 7 Conclusions

In order to further study and promote the robotic intelligent welding technology, this paper mainly introduces some sensing technique in robotic welding, especially the sensors technology, such as computer vision sensing technology, arc sensing technology, arc sound sensing technology and welding arc spectral technology. All of which will attempted to address some key problem and provide the scientific basis and the technology realistic way for welding quality controlling in robotic welding intellectualization. However, these technologies are just a start for robotic intelligent welding, some other aspects need improved and further researches should be done.

**Acknowledgements** This work is partly supported by the National Natural Science Foundation of China under the Grant No. 51405298, 61401275, 61374071, 51275301 and 61305050, the Australian Research Council under project ID LP0991108, and the Lincoln Electric Company (Australia), and the National Natural Science Foundation of Jiangsu Province (BK2012236). Under the Grant No. HT[2012]2144.

## References

1. Kim JW, Na SJ (1993) A self-organizing fuzzy control approach to arc sensor for weld joint tracking in gas metal arc welding of butt joints. *Weld Res Suppl* 2:60–66
2. Jeong SK, Lee GY, Lee WK, Kim SB (2001) Development of high speed rotating arc sensor and seam tracking controller for welding robots. *Ind Electron* 2:845–850
3. Shi YH, Yoo WS, Na SJ (2006) Mathematical modeling of rotational arc sensor in GMAW and its applications to seam tracking and endpoint detection. *Sci Technol Weld Joining* 11:723–730
4. Xu YL, Zhong JY, Ding MY, Chen HB, Chen SB (2013) The acquisition and processing of real-time information for height tracking of robotic GTAW process by arc sensor. *Int J Adv Manuf Technol* 65:1031–1043

5. Cook GE (1983) Robotic arc welding: research in sensory feedback control. *IEEE Trans Ind Electron* IE-30(3):252–268
6. Kong M, Wei S, Lin T, Chen S (2011) Three-dimensional space type welding seam tracking method with the composite sensors technology. *Ind Robot* 5:500–508
7. Xu Y, Lv N, Zhong J, Chen H, Chen S (2012) Research on the real-time tracking information of three-dimension welding seam in robotic GTAW process based on composite sensor technology. *J Intell Rob Syst* 68(2):89–103
8. Estoche EL, Neuman CP (1984) Application of acoustic sensors to robotic seam tracking. *Ind Electron* 3:219–224
9. Lv N, Xu YL, Zhang ZF, Wang JF, Chen B, Chen SB (2013) Audio sensing and modeling of arc dynamic characteristic during pulsed Al alloy GTAW process. *Sensor Rev* 33:141–156
10. Yu H, Xu Y, Lv N, Chen H, Chen S (2013) Arc spectral processing technique with its application to wire feed monitoring in Al-Mg alloy pulsed gas tungsten arc welding. *J Mater Process Technol* 213(5):707–716
11. Yu H, Chen H, Xu Y, Zhang Z, Chen S (2013) Spectroscopic diagnostics of pulsed gas tungsten arc welding plasma and its effect on weld formation of Al-Mg alloy. *Spectrosc Lett* 46(5):350–363
12. Yu H, Ye Z, Chen S (2013) Application of arc plasma spectral information in the monitor of Al-Mg alloy pulsed GTAW penetration status based on fuzzy logic system. *Int J Adv Manuf Technol* 68:2713–2727
13. Kim JW, Shin JH (2003) A study of a dual-electromagnetic sensor system for weld seam tracking of I-butt joints. *J Eng Manuf* 217:1305–1313
14. Maqueira B, Umeagukwu CI, Jarzynski J (1989) Application of ultrasonic sensors to robotic seam tracking. *IEEE Trans Robot Autom* 5:337–344
15. Mahajan A, Figueroa F (1997) Intelligent seam tracking using ultrasonic sensors for robotic welding. *Robotica* 15:275–281
16. Kawahara M (1983) Tracking control system using image sensor for arc welding. *Automatica* 19:357–363
17. Chen SB, Zhang Y, Qiu T, Lin T (2003) Robotic welding systems with vision sensing and self-learning neuron control of arc weld dynamic process. *J Intell Robot Syst* 36:191–208
18. Shen HY, Ma HB, Lin T, Chen SB (2007) Research on weld pool control of welding robot with computer vision. *Ind Robot* 34:467–475
19. Kong M, Chen SB (2009) Al alloy weld pool control of welding robot with passive vision. *Sensor Rev* 29:28–37
20. Xu YL, Yu HW, Zhong JY, Lin T, Chen SB (2012) Real-time seam tracking control technology during welding robot GTAW process based on passive vision sensor. *J Mater Process Technol* 212:1654–1662
21. Ye Z, Fang G, Chen SB, Dinham M (2013) A robust algorithm for weld seam extraction based on prior knowledge of weld seam. *Sensor Rev* 33:125–133
22. Xu YL, Yu HW, Zhong JY, Lin T, Chen SB (2012) Real-time image capturing and processing of seam and pool during robotic welding process. *Int J Ind Robot* 39:513–523
23. Chen SB, Lv N (2014) Research evolution on intelligentized technologies for arc welding process. *J Manuf Processes* 16:109–122



**Part III**  
**Modeling and Intelligent Control**  
**of Welding Processing**

# Fault Diagnosis of Inverter Power Supply Device Based on SVM

Fei Wang, Yue Wang, Xi-Xia Huang and Yong-Kui Zhang

**Abstract** In this paper, a kind of variable frequency power supply device simulating various fault states of inverter power supply was designed. The voltage waveform of inverter power supply in the normal state and in various fault states was measured and analyzed. The simulation experiment in Simulink of MATLAB was set up to testify the actual experiment. On the foundation of the analyzing of the output waveform and quality of the power, a method about fault diagnosing is put forward, that is the fault states of inverter are classified using a method of fault diagnosing based on SVM. At last, the SVM method is validated accurate through experimenting.

## 1 Introduction

In recent years, power quality problems have already caused extensive concern for the electric power department and users in many countries [1]. Due to its capacity to simulate the output grid index in different countries, the variable frequency power supply is more widely used. In order to ensure the output power quality, the rectifier and the inverter—the principal component of variable frequency power supply device—should operate regularly. Once the system fails, the fault or faults should be quickly found and fixed. Otherwise the stability of the supply would be destroyed which may cause economic losses and even endanger personal safety.

Therefore, the inverter fault diagnosis is of crucial importance. By using MATLAB simulation circuit and our handmade actual variable frequency power supply device circuit, all types of fault states are be emulated by the using both

---

F. Wang (✉) · X.-X. Huang · Y.-K. Zhang  
Scientific Research Academy, Shanghai Maritime University, Shanghai 201306,  
People's Republic of China  
e-mail: keypeople@163.com

Y. Wang  
Shanghai Zhenhua Heavy Industry Co., Ltd, Shanghai 200125, People's Republic of China

simulation and the actual device. The faults of the inverter are then diagnosed though the methods based on SVM (Support Vector Machine). One of the biggest advantages of SVM is its capacity for mode recognition with the limited sample information, which is very important, because the quantity of observed samples is often finite.

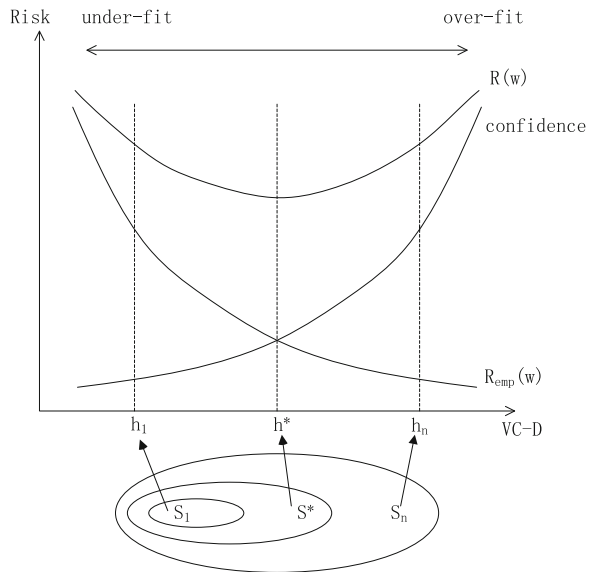
## 2 Theoretical Foundation

The purposes of statistical learning are to seek the minimum of empirical risk and confidence risk, instead of seeking the empirical risk minimization. This is the referred to as SRM (Structure Risk Minimization) and SVM is an algorithm that attempts to minimize the structural risk [3].

SRM considers both empirical risk and confidence risk though choosing an appropriate subset to get the best bounds of the empirical risk minimization. Figure 1 shows a graphical representation of the structural risk minimization. The model will have best generalization ability if the precision of data approximation and the complexity of approximation function get the optimal value.

The method of SVM is based on the VC dimension (Vapnik-Chervonenkis dimension) of statistical learning theory and the structural risk minimization principle. Our ultimate objective is to obtain the best generalization ability (Generalization Capability) of the model by finding the best compromise between model complexities (the learning accuracy of specific training samples) and

**Fig. 1** Illustration of structural risk minimization



learning ability (the capacity to identify any samples faultlessly) according to the limited sample information.

Given a training set of instance-label pairs  $(x_i, y_i), i = 1 \dots, l$ , where  $x_i \in R_n$  and  $y \in \{1, -1\}$ , the support vector machines (SVM) require the solution of the following optimization problem:

$$\min_{\omega, b, \xi} \frac{1}{2} \omega^T \omega + C \sum_{i=1}^l \xi_i$$

Subject to

$$\begin{aligned} y_i(\omega^T \phi(x_i) + b) &\geq 1 - \xi_i, \\ \xi_i &\geq 0. \end{aligned} \tag{1}$$

Here training vectors  $x_i$  are mapped into a higher (maybe infinite) dimensional space by the function  $\phi$ . SVM finds a linear separating hyperplane with the maximal margin in this higher dimensional space.  $C > 0$  is the penalty parameter of the error term. Furthermore,  $K(x_i, x_j) \equiv \phi(x_i)^T \phi(x_j)$  is called the kernel function.

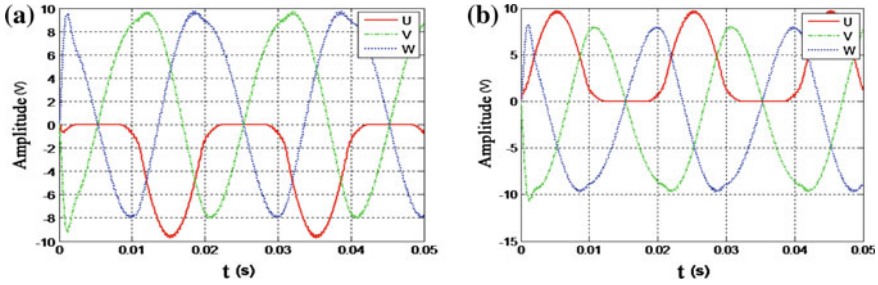
### 3 Waveform Analysis of Faults

#### 3.1 Simulation Waveform Analysis

To observe all kinds of fault states, a simulation circuit is set up in Simulink and different types of fault states will be simulated. Thus we can compare the results of the simulation circuit and the actual circuit. The frequency of three-phase rectifier input is set to an alternating current phase voltage at 50 Hz, and the rectifier module uses the three-phase bridge rectifier circuit. The output is three-phase alternating current with a frequency of 60 Hz.

In order to construct the fault, the bridge arm is set to non-conductive by not providing the corresponding bridge arm a trigger pulse. The probability of three or more MOS tubes out of commission simultaneously is very small; only one or two MOS tubes' faults are analyzed. There are six fault states when a single MOS tube is in the wrong operating condition. There is no space to cover them in depth here and the three phases (UVW) have symmetry, so only the two cases of them (top bridge arm and bottom bridge arm in U having fault) will be listed below.

Figure 2a shows the simulation of the top bridge in U phase having fault; Fig. 2b, the bottom bridge in U. As shown in Fig. 2a, there is no positive voltage but negative voltage when a top bridge arm in a certain phase possesses a fault and the negative voltage amplitude of the other two phases decreases slightly. Similarly, as shown in Fig. 2b, there is no negative voltage but positive voltage when a bottom



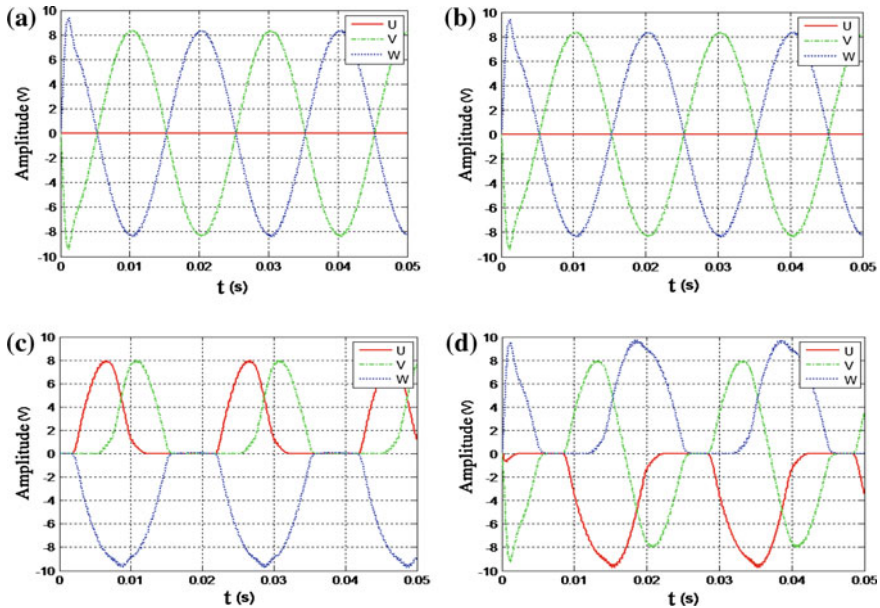
**Fig. 2** **a** Simulation of top bridge in U phase having fault; **b** Simulation of bottom bridge in U phase having fault

bridge arm in a certain phase possesses a fault and the positive voltage amplitude of the other two phases decreases slightly.

The voltage amplitude of the phase with a fault changes drastically while the voltage amplitude of the other two phases changes very minutely. So the former but not the latter is considered in the following analysis. In conclusion, the fault can be easily ascertained according to the phase output voltage having fault, when a bridge arm in any phase breaks down.

In total, there are as many as fifteen fault states when two MOS tubes among six are in wrong operating condition, which can be classified into four groups: (1) Both two bridge arms in the same phase having faults; (2) Any two top bridge arms having faults; (3) Any two bottom bridge arms having faults; (4) The top bridge arm in one phase and the bottom bridge arm in any of the other two phase having faults. An example of each case will be listed below.

(1) Figure 3a shows both two bridge arms in the same phase having faults. The output voltage amplitude of the phase having faults decreases to 0 when the output of the other two phases changes slightly. (2) Figure 3b shows any two top bridge arms having faults resulting in output waveform of three phases all changing. Take the top bridge arms both in U phase and in V phase as an example. In this case, there is only negative voltage output in U-phase and V-phase and only positive voltage output in W-phase. The output in U-phase and V-phase decrease to zero simultaneously when the output in W-phase is zero. (3) Figure 3c shows any two bottom bridge arms having faults resulting in output waveform of three phases all changing as well. Take the bottom bridge arms both in U phase and in V phase as an example. There are only positive voltage output in U-phase and V-phase and only negative voltage output in W-phase. According to Fig. 3b and c, the waveforms of two top bridge arms and two bottom arms having faults are symmetry. So classified these two cases into the same group. (4) Figure 3d shows the top bridge arm in one phase and the bottom bridge arm in any of the other two phase having faults. As a result, output waveform of three phases all change significantly. Take the top bridge arm in U-phase and the bottom bridge arm in V-phase as an example; the voltage output in V-phase are double polarity, while there are only negative



**Fig. 3** **a** Simulation of two bridge arm in U phase having fault; **b** Top two bridge arms in U phase and V phase having fault; **c** Bottom bridge arm in U phase and V phase having fault; **d** Top bridge arm in U and bottom bridge arm in W having fault

voltage output in U-phase and only positive voltage output in W-phase. The three-phase output decrease to zero simultaneously when the output in V-phase is zero in a certain period of time.

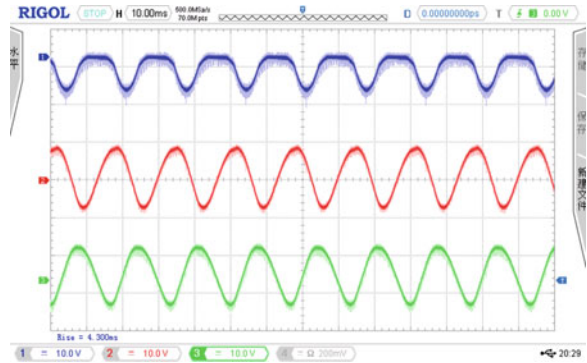
### 3.2 Actual Circuit Waveform Analysis

A physical experiment platform is set up, where the parameters of the actual circuit and simulation circuit remain identical. There are twenty-one different waveforms. The three-phase waveforms are symmetrical. So an example of each case will be listed below. As shown below, the first line (blue) is the output voltage waveform in U-phase, the second (red) V-phase, and the third (green) W-phase.

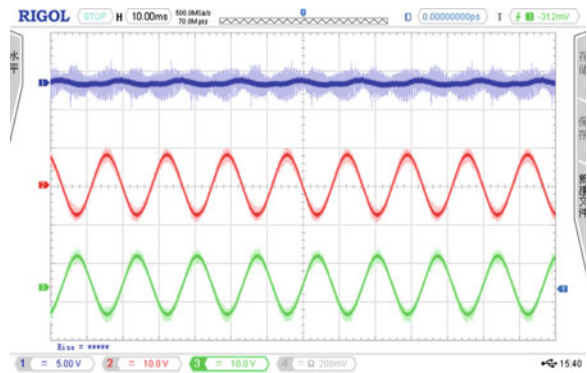
Compare Fig. 4 with Fig. 2a and b, we can draw a conclusion that there is only negative (positive) voltage output but not positive (negative) voltage in three-phase output when a top (bottom) bridge arm having fault. Slight decreases in the negative voltage amplitude are observed in the other two phases. In this instance, the operating results of actual circuit are consistent with simulation circuit results.

Additionally, by comparing Fig. 5 with Fig. 3a, Fig. 6 with Fig. 3b and c, and Fig. 7 with Fig. 3d, a similar conclusion can also be surmised—the operating results of actual circuit are consistent with simulation circuit results.

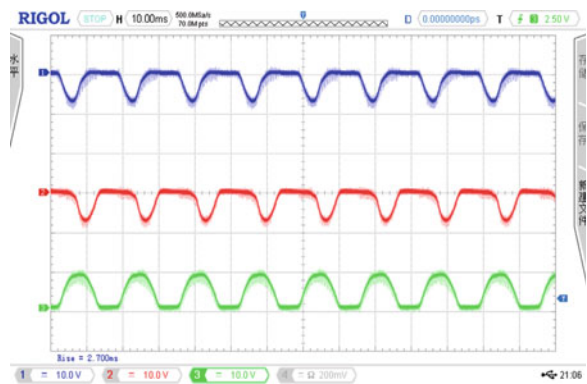
**Fig. 4** Fault of top bridge arm in U phase



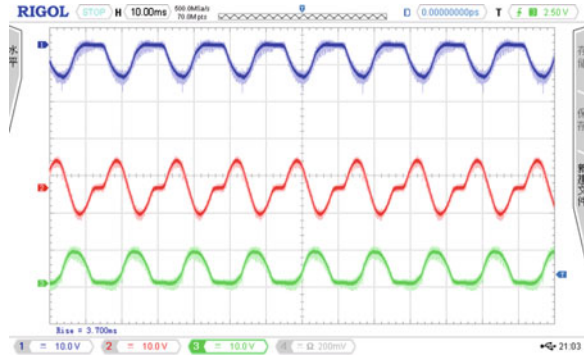
**Fig. 5** Fault of both bridge arms in U phase



**Fig. 6** Fault of two top/bottom bridge arms



**Fig. 7** Fault of two top and bottom bridge arms



### 4 Waveform Classification

To summarize the operating results of actual circuit and simulation circuit, according to the symmetry of the waveforms, the following summary can be presented: there are twenty-two different states of the circuit when no more than two MOS tubes operate in wrong condition, which can be divided into major five groups: (1) No bridge arm having faults; (2) Only a single bridge arm having faults; (3) Both two bridge arms in the same phase having faults; (4) Any two top bridge arms or any two bottom bridge arms having faults; (5) The top bridge arm in one phase and the bottom bridge arm in any of the other two phase having faults. These twenty-two waveforms are different from each other, so it is simple to identify whether Inverter Power Supply Device operates wrong and easily deduced which MOS tubes operated in a faulty condition according to the output waveform directly.

### 5 Harmonic Analysis

Performing FFT on the above four fault state, [4] we can get THD of variable frequency power supply as Table 1.

**Table 1** THD of inverter power supply device faults

Parameter	THD		
	U phase	V phase	W phase
Fault on the top bridge arm of U phase	34.6	1.16	0.96
Fault on two bridge arms of U phase	2.44	44.4	56.4
Fault on the top bridge arm of U & V phase	54.2	2.33	49.1
Fault on the top bridge arm of U phase & on the bottom bridge arm of V phase	22.4	34.9	26.7



According to Table 1, once having faults, the THD of Inverter Power Supply Device is very high.

## 6 Fault Diagnosis

### 6.1 Design of SVM

As observed, the output voltage characteristics of the fault states change significantly in both the simulation circuit and the actual circuit. However, we can only apply SVM to data samples, not the waveform characteristics. Considering that harmonic content contains waveform characteristics and easier to calculate, the harmonic content is selected as one of the input parameters. With the value ranging from +1, 0 to -1, the polarity of average voltage is another input parameter. This is important as the value +1 means that the average of output voltage in a signal cycle is greater than 0 and the value -1 less than 0 and the value 0 equal to zero. Considering the ideal value of 0 is difficult to achieve in practice, the value 0 indicates that the proportion of the average value in a signal cycle to Root Mean Square is less than 5 %.

Considering the output voltage is susceptible to load and input voltage, the two parameters, harmonic content and the polarity of average voltage, can give a good representation of the state changing of the inverter electronic components, so the harmonic content and the polarity of average voltage are chosen as the input parameters, rather than choose the voltage value directly.

SVM is a learning method based on kernel, and the performance of SVM depends on the kernel function and its associated parameters. Since research shows that it is better to select the radial basis function rather than any other kernel functions when there is no prior knowledge of the process [2], the radial basis function is applied in this paper. Two parameters,  $C$  and  $\gamma$ , should be set correctly to meet a certain accuracy required when using RBF.  $\gamma$  is a parameter of the radial basis function.  $C$ , the penalty coefficient, is greater than zero. The greater  $C$  is, the more cost for the data points beyond the classification plane is. The harmonic content, between zero and one and the polarity values of average voltage, ranging from +1, 0 to -1, all satisfy the normalization condition. The parameter  $\gamma$  takes the value of 0.001 and  $C$ , 1 in this paper.

## 7 Result and Analysis

As mentioned before, there are twenty-two different states of the circuit when no more than two MOS tubes operate in wrong condition. The twenty groups of the samples from an oscilloscope were randomly divided into two parts: training

**Table 2** Part of sample data and the results

Sample ID	U phase		V phase		W phase		Operating state inverter power supply
	Harmonic content (%)	Average voltage Polarity	Harmonic content (%)	Average voltage polarity	Harmonic content (%)	Average voltage polarity	
1	0.97	0	1.12	0	1.01	0	Normal state
2	34.6	-1	1.16	0	0.96	0	Fault on the top bridge arm of U phase
3	2.01	0	40.4	-1	1.35	0	Fault on the top bridge arm of V phase
4	2.4	0	1.88	0	43.1	1	Fault on the bottom bridge arm of W phase
5	2.44	0	44.4	0	56.4	0	Fault on two bridge arms of U phase
6	54.2	-1	2.33	1	49.1	-1	Fault on the top bridge arm of U and V phase
7	51.8	-1	56.6	-1	1.64	1	Fault on the top bridge arm of U and W phase
8	22.4	-1	34.9	0	26.7	1	Fault on the top bridge arm of U phase & the bottom bridge arm in W phase

samples and testing samples, the former (75 %) are used to set up a model based on SVM, and the later (25 %) for validating accuracy of the model based on SVM. As 110 samples are used to validate the model, from which 103 samples were classified successfully using the method of fault finding via SVM, the accuracy of classification is higher than 94 %. Table 2 show a part of sample data and the experiment results, from which we can see that the fault states of Inverter can be classified efficiently and effectively using this method of fault diagnosing based on SVM.

## 8 Conclusion

The voltage waveform of inverter power supply in the normal state and in various fault states were measured and analyzed. On the foundation of output voltage signal analysis and harmonic analysis, SVM, a method regarding fault diagnosis is put forward. It proves that the fault states of the inverter can be classified efficiently and effectively using this method of fault finding via SVM. It is very promising to observe that the classification accuracy rate is higher than 94 %. Meanwhile, the method of fault diagnosis of inverter power supply device based on SVM is validated accurately through both simulation experiments and actual circuit experiments.

**Acknowledgement** This work is supported by the National Natural Science Foundation of China under Grand No. 51209134, Shanghai Sciences & Technology Committee under Grand No. 12dz1200700 and No. 13dz1202800, People's Republic of China.

## References

1. Vannoy DB, McGranaghan MF, Halpin SM et al (2007) Roadmap for power quality standards development *Trans Ind Appl* 3(2):412–421
2. Lin C-J (2003) A practical guide to support vector classification. Technical report, Department of Computer Science and Information Engineering, National Taiwan University.
3. Xi'an-Wei L, Qi JJ, Zhang WX (2003) Knowledge discovery of decision table based on support vector machine. In: *Proceedings of the second international conference on machine learning and cybernetics*, pp 2–5
4. Lakshmikanth A, Morcos MM (2001) A power quality monitoring system. A case study in DSP-based solutions for power electronics. *IEEE Trans Instrum Meas* 50(3):724–731

# Process Planning Strategy for Wire and Arc Additive Manufacturing

Dong-Hong Ding, Zeng-Xi Pan, Cuiuri Dominic and Hui-Jun Li

**Abstract** Additive manufacturing has gained worldwide popularity in the last 20 years as many different methods and technologies for adding materials have been developed. Among them, wire and arc additive manufacturing (WAAM) is a promising alternative for fabricating high quality aerospace metal components economically. This study introduces a process planning strategy for WAAM that produces the path and parameters for the deposition process from CAD and process models. After introducing the framework for process planning, two important steps, tool-path generation and optimization of welding parameters, will be presented in detail. Based on the general requirements for a good quality AM tool-path, including high geometrical accuracy and a minimal number of tool-path passes and elements, two novel tool-path patterns suitable for various geometries are introduced. Using the proposed weld bead model and the overlapping model, appropriate welding parameters, such as the travel speed, wire-feed rate, and layer thickness, can be determined. The performance of the proposed process planning strategy is verified through building a sample impeller.

## 1 Introduction

In additive manufacturing (AM), a component is fabricated through layer-by-layer deposition of material, instead of starting from an over dimensioned raw block and removing unwanted material, as practiced in conventional subtractive manufacturing. AM has several advantages over conventional manufacturing. Firstly, it is a

---

D.-H. Ding (✉) · Z.-X. Pan · C. Dominic · H.-J. Li  
School of Mechanical, Materials, and Mechatronics Engineering, Faculty of Engineering and Information Science, University of Wollongong, Northfield Avenue, Wollongong, NSE 2500, Australia  
e-mail: dd443@uowmail.edu.au

Z.-X. Pan  
e-mail: zengxi@uow.edu.au

promising alternative for fabricating components made of expensive materials such as titanium and nickel alloys in the aerospace industry, where such components currently suffer an extremely low fly-to-buy ratio. In addition, since the AM process generalizes the component building process to successive deposition of thin two-dimensional (2D) layers, it is possible to automate the complete manufacturing process, which reduces both the production time and the amount of human intervention needed for each new part. Using AM technology also makes it possible to fabricate single-component structures with very complex geometry that would be impractical or impossible to make using traditional approaches.

Within additive manufacturing, many different methods and techniques have been developed to fabricate metal structures, such as Selective Laser Sintering [1], Direct Metal Deposition [2], Electron Beam Freeform Fabrication [3], Shape Deposition Manufacturing [4], and Wire and Arc Additive Manufacturing (WAAM) [5–7]. In terms of the power sources used, AM can be categorized into three groups, namely, laser, electron, and arc. WAAM is by definition an arc-based process which uses either the Gas Tungsten Arc Welding (GTAW) or the Gas Metal Arc Welding (GMAW) process as the power source. WAAM is considered to be a promising technology for manufacturing aerospace components of median to large size due to its higher deposition rate, lower costs, and safer operation. Generally, the deposition rate of WAAM is 50–130 g/min, compared to 2–10 g/min for laser or electron beam deposition [8].

However, a mature WAAM system is not commercially available at present due to a number of inherent technical challenges, such as residual stresses and distortions from excessive heat input, uneven weld bead geometry distribution at the start and end portions of a weld path, poor resolution and surface finish. Much research effort has been focused on mitigating the effects of residual stresses and distortion by optimizing the deposition patterns and sequences, and also preheating the substrate [9–11]. These technologies have been successfully applied to minimize residual stresses and distortion, but are beyond the scope of this study. Another technical challenge is the uneven weld bead geometry that is produced within individual weld passes by the GMAW process, particularly at the start and end portions. Because of the heat sinking effect of the large substrate, the penetration is lower when the arc starts. Thus the reinforcement height is higher at the start of the weld pass than in the subsequent portions of the weld. At the end of the weld pass, due to the flowing of the molten metal, a sloping shape is created gradually when arc stops [12]. These uneven weld bead geometries may not only lead to the accumulation of errors in the vertical direction after the deposition of several layers but also result in high porosity. In this study, an alternative tool-path generation method is presented which has the minimum number of tool-path passes to eliminate or reduce the effects of arc starting and arc stopping. Other limitations of WAAM processes are poor resolution and surface finish [13]. A laser deposition system can achieve a single deposition pass width of 0.7 mm, while the width of a stable welding pass is typically greater than 4 mm for the GMAW process. In order to produce geometrically accurate parts, geometry-related process parameters (such as weld bead width, layer thickness, wire diameter, wire feed rate, and welding speed) must be carefully controlled to achieve

a proper deposit size and shape. For certain geometries, this study presents a method to properly determine the geometry-related process parameters to achieve both high accuracy and low porosity.

This paper introduces a process planning strategy for WAAM system to generate robot program and welding parameters from standard STL CAD files and a specifically-developed GMAW process model. An integrated software environment was developed to provide options for part slicing, 2D tool-path pattern selection, and selection of deposition parameters. In this system, the appropriate tool-path and the optimum welding parameters are generated for the robot and welding equipment to automatically fabricate the designed components. A sample work piece was made to demonstrate the validity of the proposed process planning strategy.

The remainder of the paper proceeds as follows. Section 2 introduces the overall structure of process planning for a WAAM. Section 3 discusses the optimal tool-path strategy for various 2D geometries. Section 4 details the method for determining the welding parameters. Section 5 presents the experimental results through a case study and analyses the performance of the proposed process planning strategy, followed by a conclusion in Sect. 6.

## 2 Process Planning Framework

Generally, process planning in AM involves generating 3D CAD models (direct 3D CAD design, or digitalization such as 3D scanning in the sense of Reverse Engineering), representing the 3D CAD models in a suitable format, slicing 3D CAD models into a set of 2D geometries, generating the tool-path for each of these 2D geometries, setting the deposition parameters for each layer, generating the operational code for the equipment, and finally automatic fabrication. A flowchart of generic WAAM process, from initial 3D CAD model to final manufacturing process, is shown in Fig. 1.

STL, known as Standard Tessellation Language, is commonly used to represent 3D CAD models in AM process planning [14]. A section of a STL file and its 3D model are shown in Fig. 2. In an ASCII STL file, the 3D CAD model is represented by triangular facets, which are described by a set of X-, Y-, and Z-coordinates for each of three vertices and a unit normal vector to indicate the side of the facet which is outside the object.

Figure 3 shows the user interface of this process planning program. After loading and displaying the 3D STL CAD model, the tolerant slicing algorithm is used to slice the models based on specified layer heights. The generated 2D geometries for various models using this approach are shown in the second column of Fig. 4.

The next step is to plan the tool path for each sliced 2D contour. Many types of tool-path patterns have been developed for the AM process, such as raster, zigzag, contours, space filling curves, and hybrid tool-path planning approaches. Depending on the characteristics of the 2D geometries, such as solid or thin wall layers, different tool-path patterns are most suitable to a specified geometry.

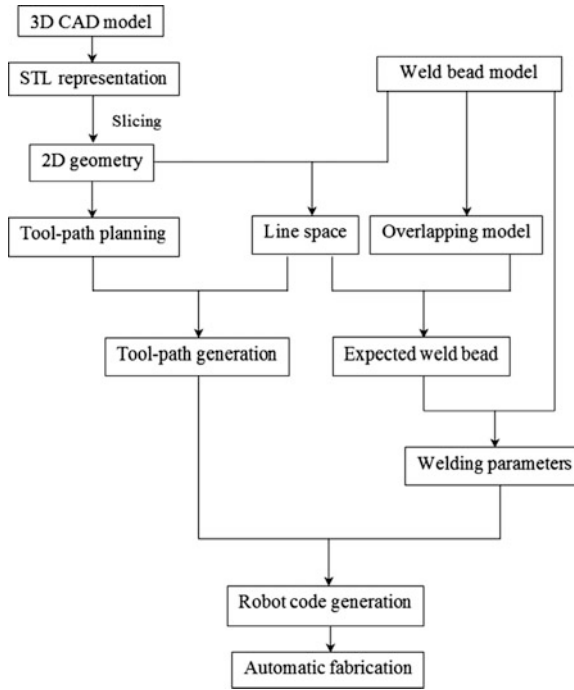


Fig. 1 Generic WAAM process planning framework

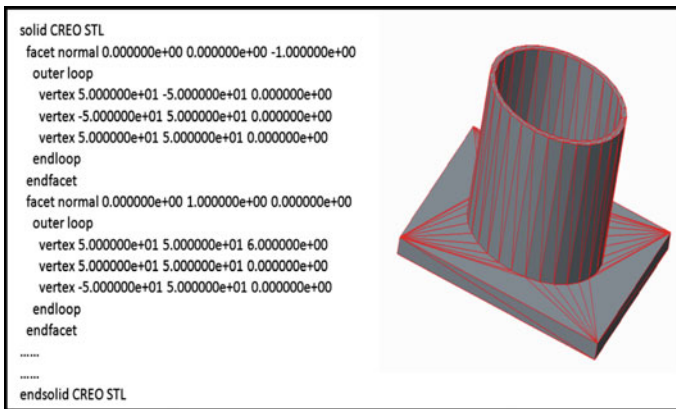


Fig. 2 A typical STL format and model

Tool-path planning is especially crucial in WAAM and will be detailed in the next section.

Much research effort has been directed towards developing a correlation between welding parameters and weld bead geometry by using regression analysis [5],

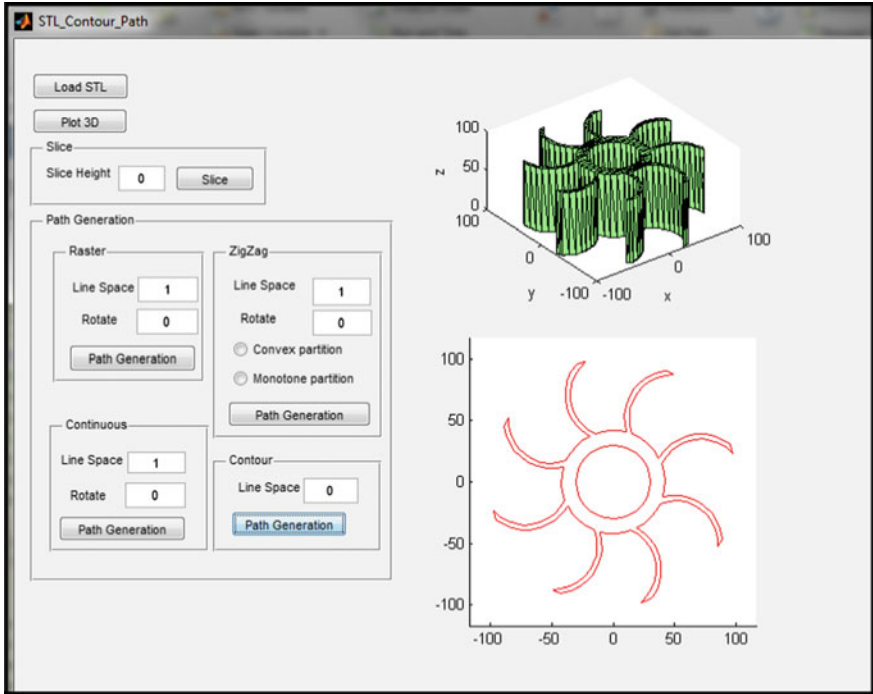


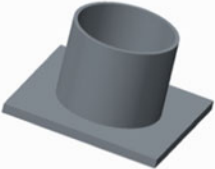



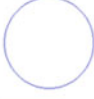

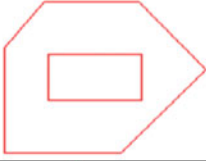
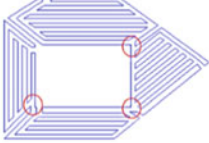

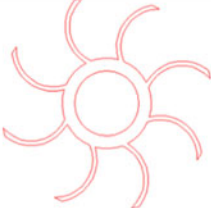
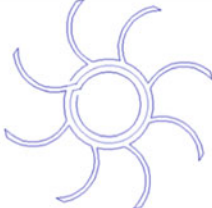
Fig. 3 Developed interface and a slice of an impeller

artificial neural networks, or combinations of these two techniques [15]. A symmetric parabola profile of the weld bead has been described by Suryakumar et al. [8], Cao et al. [16] fitted the weld bead boundary with Gaussian, logistic, parabola and sine functions, and found that the sine function can fit the measured data with highest accuracy. Xiong et al. [17] compared the measured weld beads under different welding parameters to three frequently-used profile models, namely circular arc, parabola, and cosine function. It was shown that the optimal model for the bead profile is largely dependent on the ratio of wire feed rate to welding speed. A model correlating weld bead geometry to the welding parameters is developed in this study and will be introduced in Sect. 4.

Line space is a user-defined parameter, but the range of the line space parameter is restricted by the weld bead model. Generally, the width of weld bead is within the range of 4–10 mm for the range of GMAW parameters used in AM. In addition, an appropriate line space should match the 2D geometry properly to achieve high geometrical accuracy.

Some preliminary investigations on multi-bead overlapping models have been made in recent years [8, 16–18]. A simple Flat-top Overlapping Model (FOM) has been developed in the literature. However, it has been observed through



Models	2D geometries	Tool-path
		
		
		
		

**Fig. 4** The proposed tool-path generation for various geometries

experimentation that it is impossible to achieve the ideally flat overlapped surface [8, 18]. This study establishes a tangent overlapping model, which is presented in Sect. 4.






The user-defined line space and the tangent overlapping model are used to determine the geometry of the expected weld bead. Then, the weld bead model is used again to predict the optimal welding parameters that will produce the desired bead geometry.

Once the tool-path pattern and the line space are determined, the tool-path is generated automatically. Associating with the predicted welding parameters, robot code is generated which includes the robot motions and the weld deposition process. Finally, the components are built automatically.

### 3 Tool-Path Planning

Many types of tool-path patterns have been developed for AM process, as summarized in Table 1. Examples are raster, zigzag, contours, continuous, and hybrid tool-path planning approaches.

**Table 1** A brief summary of AM tool-path generation methods

References	Tool-path pattern	Examples
[19]	Raster	
[20, 21]	Zigzag	
[22, 23]	Contour	
[12, 24]	Hybrid	
[25, 26]	Continuous	

The raster scanning path technique is based on planar ray casting along one direction [19]. Derived from the raster strategy, zigzag tool-path generation is the most popular method used in commercial AM systems. While it fills geometries line-by-line along one direction like the raster approach, the zigzag approach combines the separate parallel lines into a single continuous pass which significantly reduces the number of tool-path passes [20, 21]. However, the outline accuracy of the part for both raster and zigzag approaches is poor due to the discretization errors on any edge that is not parallel to the tool motion direction. Contour path generation, which is another typical method, can address this geometrical quality issue effectively by following the geometrical trend of the boundary contours [22, 23]. However, by offsetting the contours, the scheme generates numerous closed curves which are disconnected and therefore not suitable for WAAM. The hybrid path planning strategy is also promising as it shares some merits of various approaches. Generally, a combination of contour and zigzag pattern is commonly developed to meet both the geometrical accuracy and build efficiency requirements [12, 24]. Continuous path planning can be considered as another tool-path generation method [25, 26]. This method is able to generate filling patterns that allow continuous deposition in a single path to fill any arbitrarily shaped area. The number of welding passes is reduced significantly, thereby minimizing starting-stopping sequences, which is advantageous for the WAAM process.

Each tool-path generation method is suited to certain types of 2D geometries. The main requirements for tool-path planning in WAAM are a minimum number of tool-path passes, less tool-path elements, and good geometrical accuracy. Depending on the characteristics of the 2D geometries, however, different tool-path patterns are needed. In this study, two novel tool-path patterns are proposed. For geometries with solid structures, the outline path is generated using the contour path

planning method to improve the geometrical accuracy of the work piece. The interior area of each polygon is then filled using a zigzag path with an optimal direction that allows a minimum number of tool-path elements. Finally, these sub tool-paths are combined together to form a continuous path without any starting-stopping sequences to reduce the number of tool-path passes. The path generation algorithms could be found in our previous paper [26]. For geometries with thin walls, the contour path is generated first, then these closed curves are connected together to reduce the final tool-path passes, as shown in column 3 of Fig. 4. For a simple geometry such as in row 2, a continuous tool-path pattern is suitable, as it is able to meet the requirements of minimum tool-path passes and elements. For the circular ring in row 3, as the ring is thin, a contour path pattern is used. For the geometry in row 4, the proposed tool-path strategy is able to generate a continuous tool-path without start-stop consequences. In the proposed path planning algorithm, the geometry is firstly decomposed into a set of convex polygon. Then, various continuous sub-paths for each polygon are generated. Finally sub-paths are connected to form a continuous tool-path. For the geometry in the last row, a continuous contour tool-path is possible. It meets the requirement of good geometrical accuracy, and less tool-path passes. Only one tool-path pass is formed for producing the entire layer.

Both proposed tool-path strategies meet the requirement of good geometrical accuracy, while they are suitable for different geometries. In this study, both proposed tool-path patterns are applied to a certain given geometry, the optimal one is selected using the criterion of less tool-path passes and elements. So far, an algorithm to automatically determine which tool-path pattern should be used on a particular 2D geometry has not been devised. The challenge is to understand various geometries and use the geometrical information to automatically apply the different tool-path strategies.

In tool-path generation (column 3 of Fig. 4), the line space between each pass is a user-defined parameter according to the size of 2D geometries and the weld bead model. The line space,  $d$ , is equal to the overlapping center distance which will be detailed in the next section.

## 4 Optimization of Welding Parameters

While the requirements for the control of arc welding processes, including parameters such as metal transfer mode, welding current and arc voltage, have been discussed [12], the literatures concerning the method for determining the welding parameters that directly affect deposition shape, such as welding speed, wire feed-rate, and overlapping distance in WAAM, are relatively few. The geometry of a single weld bead as well as the multi-bead overlapping process is important for achieving high surface quality and dimensional accuracy on the fabricated parts.

In order to accurately predict the shape of weld beads that are deposited adjacently, the cross sections of two neighboring beads are modeled using a Tangent

Overlapping Model (TOM), shown in Fig. 5. The detailed TOM is introduced in our recent publication [27]. The overlapping center distance  $d$  is equal to the line space of the tool path. In addition, for a given weld bead, the overlapping center distance is correlated to the overlapping model.

Let a single bead have a height  $h$  and width  $w$ ; and the adjacent beads have a center distance  $d$ . The shape of the bead is modeled as an inverted parabola. The area of valley and overlapping area in adjacent beads are depicted in Fig. 5. The top of the valley is modeled as a straight line that is tangential to bead 2. The center distance  $d$  between adjacent beads will determine the surface quality and smoothness. When the center distance  $d$  is greater than the single bead width  $w$ , there is no overlap between the two adjacent beads. So the valley, overlapping area and tangent do not exist. As the center distance is decreased, the overlapping area in Fig. 5 increases, and the area of the valley decreases. As the center distance  $d$  decreases to a certain value  $d^*$ , the overlapping area becomes equal to the area of the valley and the overlapped surface will become a tangent line. This condition produces maximum surface smoothness because there is no valley between adjacent beads. The bead height  $h$  is effectively the WAAM layer thickness. With a further decreasing of  $d$ , excessive overlapping area leads to an increased thickness of the deposited layer and decreased surface smoothness. In the proposed overlapping model, the condition for a stable overlapping process can be determined solely through geometrical considerations, and is expressed as  $d \geq d^* = 0.738w$ . Experimental verification tests conducted in this study produced the results shown in Fig. 6. One can obtain:

$$w \leq \frac{d}{0.738} \quad (1)$$

The experimental conclusion is in very good agreement with the model predictions. If  $d$  in the Eq. (1) is the user defined line space from Sect. 3, then the proposed tangent overlapping model can be used to determine the weld bead width that needs to be produced by the welding equipment to produce a 2D geometrical deposit with optimum surface smoothness. The welding parameters that will produce the desired weld bead width are determined again by an appropriate weld bead model for the gas metal arc welding process. Much research has focused on the correlation between welding parameters and weld bead geometry [8, 15]. In model development experiments conducted as part of this study, combinations of 5 m/min wire feeding rate and 8 different travel speeds were conducted. Based on the experimental data shown in Fig. 7, when the wire-feed rate is fixed at 5 m/min, a second order polynomial model was generated for bead width  $w$  as a function of welding speed  $V_w$  as,

$$W = 10.15V_w^2 - 21.863V_w + 16.162 \quad (0.2 \leq V_w \leq 1) \quad (2)$$

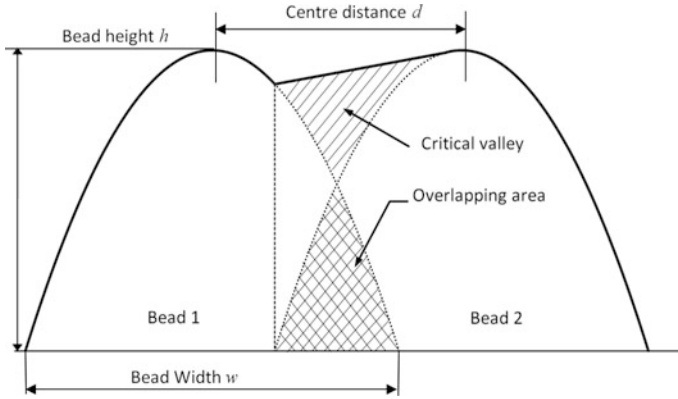


Fig. 5 Sketch of the proposed tangent overlapping model (TOM)

For certain wire-feed rate  $V_f$  and overlapping distance  $d$ ,  $V_w$  could be solved by combining Eqs. (1) and (2). Layer thickness  $h$ , or bead height in Fig. 5, is expressed as

$$h = \frac{A_{bead}}{d} = \frac{\pi V_f D_w^2}{4V_w d}. \quad (3)$$

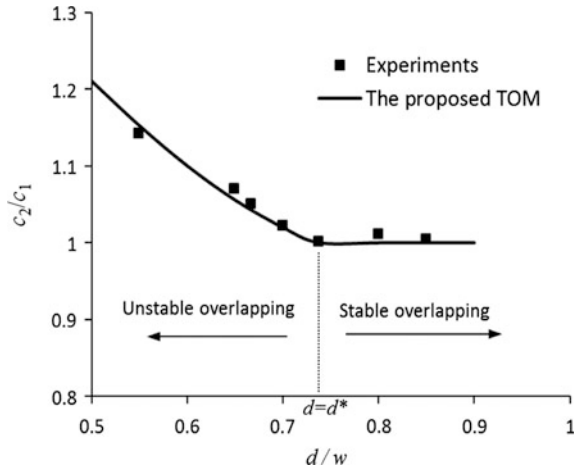
where,  $D_w$  is the diameter of the wire electrode, and  $A$  is the cross-sectional area of a single weld bead.

Through using the procedures described in this section, the welding parameters that are required for each layer of the WAAM component can be readily determined. From specifying the wire-feed rate and welding speed that are needed to meet the user-specified line space and simultaneously optimize the surface smoothness of each layer, the layer thickness can be determined.

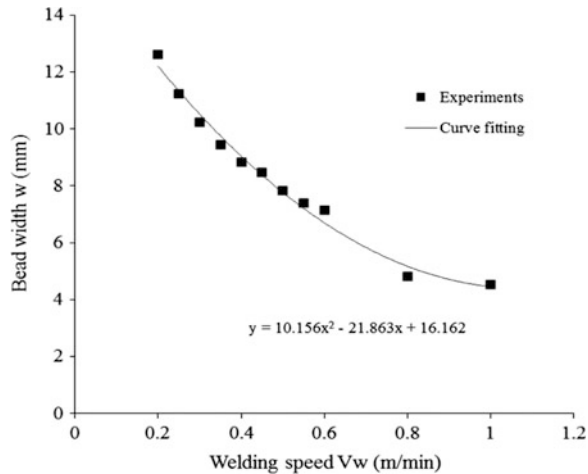
## 5 Results and Discussions

Using the tool-path trajectory and welding parameters generated from the proposed process planning framework, a sample impeller as shown in row 4 of Fig. 4 was fabricated using the robotic lean automation facility at the University of Wollongong. The generated tool-path is shown at column 3 row 4 in Fig. 4. The line space is user-set to 4 mm as the thickness of all 8 blades is 4 mm. The overlapping center distance is set to be 4 mm consequently. The wire-feed rate is 5 m/min, as it has been accurately modeled. According to the calculation presented in Sect. 4, the welding speed must be higher than 0.76 m/min. In this test, the welding speed of 0.8 m/min was chosen. Accordingly, the layer thickness  $h$  is predicted to be 1.77 mm, so this value was used in programming of the robot path.

**Fig. 6** Ratio of the height of the second bead to the first bead ( $c_2/c_1$ ) at various center distances

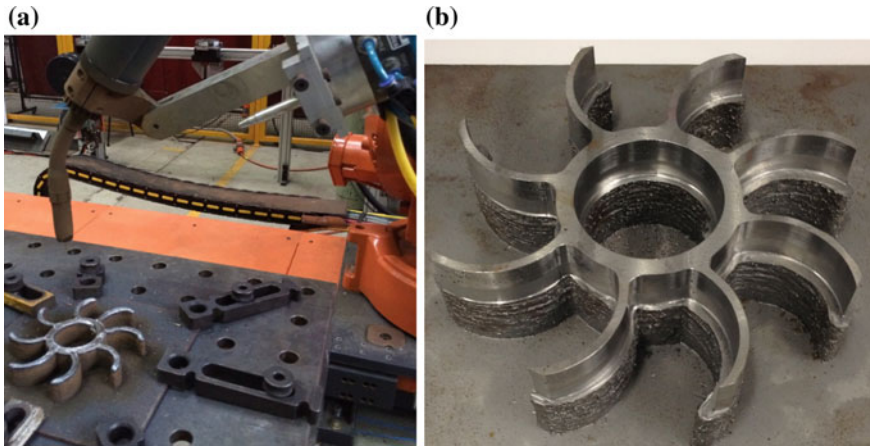


**Fig. 7** Bead width  $w$  as a function of welding speed  $V_w$  at the wire-feed rate of 5 m/min



During the deposition process, in order to obtain the proper substrate temperature, idle time is used between layers. Figure 8 shows a photograph of the experimental set-up and partially produced component. With the deposition of 40 layers, the impeller has a height of 70 mm. After cleaning and milling the top surface and part of the side walls, the partially machined component is illustrated in Fig. 8b.

In conducting this experiment, a few observations are worth mentioning. For example, the condition of the substrate, including temperature and geometrical shape, has a remarkable influence on the deposition accuracy and surface quality of the following layers. If the finished surface of a previous layer is not flat, bad surface quality of the next layer will occur due to the variation of stick out length for the GMAW wire electrode. Therefore, an intermediate milling operation is recommended from time to time. It was also found that it is difficult to accurately



**Fig. 8** a Experimental set-up; b Sample component after partially surface milling

re-fixture the component when the surface milling operation is carried out using a different machine. Therefore, to produce components with high accuracy, an integrated milling system with the deposition system is required to eliminate the re-fixture operations.

## 6 Conclusion

In this study, a process planning strategy has been introduced for the WAAM process in an attempt to provide an automated method for tool path planning and weld parameter selection. A process planning framework is firstly presented to cover the steps from component CAD model and welding process model to final tool path and welding setup. Two important steps of the process planning have been detailed, namely 2D tool-path generation and optimization of welding parameters. The WAAM process generally requires high geometrical accuracy and a minimized number of tool-path passes and elements. Consequently, two novel tool-path patterns suitable for different geometries have been described. Using a new weld bead model and the tangent overlapping model, more appropriate welding parameters, including the travel speed, wire feeding rate, and layer thickness, can be selected for better geometrical accuracy.

Using the tool path and welding parameters generated from the proposed process planning strategy, a sample impeller was built up using a robotic welding facility, and then milled to final size. The result was a component with a high overall quality of finish. The future work will integrate a machining capability within the robotic system to be able to generate a final part using a single machine.

**Acknowledgement** The authors would like to thank Professor J. Norrish for his expertise in the welding field. N. Larkin is especially thanked for his assistance with the experiments. The authors would also like to thank the Defence Materials Technology Centre (DMTC) and the University of Wollongong for providing the research facility. This work is supported in part by the State Scholarship Fund of the China Scholarship Council (No. 2011684067).

## References

1. Agarwala M et al (1995) Direct selective laser sintering of metals. *Rapid Prototyping J* 1 (1):26–36
2. Lewis GK, Schlienger E (2000) Practical considerations and capabilities for laser assisted direct metal deposition. *Mater Des* 21(4):417–423
3. Taminger KM, Hafley RA (2003) Electron beam freeform fabrication: a rapid metal deposition process. Proceedings of the 3rd annual automotive composites conference, pp 9–10
4. Merz R et al (1994) Shape deposition manufacturing: Engineering Design Research Center, 1994. Carnegie Mellon University
5. Almeida PS, Williams S (2010) Innovative process model of Ti–6Al–4V additive layer manufacturing using cold metal transfer (CMT). In: Proceedings of the twenty-first annual international solid freeform fabrication symposium, 2010. University of Texas at Austin, Austin
6. Ding J et al (2011) Thermo-mechanical analysis of wire and arc additive layer Manufacturing process on large multi-layer parts. *Comput Mater Sci* 50(12):3315–3322
7. Wang F et al (2011) Morphology investigation on direct current pulsed gas tungsten arc welded additive layer manufactured Ti6Al4V alloy. *Int J Adv Manuf Technol* 57(5–8):597–603
8. Suryakumar S et al (2011) Weld bead modeling and process optimization in hybrid layered manufacturing. *Comput Aided Des* 43(4):331–344
9. Nickel A et al (2001) Thermal stresses and deposition patterns in layered manufacturing. *Mater Sci Eng A* 317(1–2):59–64
10. Mughal M et al (2006) Finite element prediction of thermal stresses and deformations in layered manufacturing of metallic parts. *Acta Mech* 183(1–2):61–79
11. Chin R et al (1996) Thermomechanical modeling of molten metal droplet solidification applied to layered manufacturing. *Mech Mater* 24(4):257–271
12. Zhang Y et al (2003) Weld deposition-based rapid prototyping: a preliminary study. *J Mater Process Technol* 135(2–3):347–357
13. Lewis G et al (1998) Free form fabrication of metallic components using the Directed Light Fabrication process, Los Alamos National Laboratory, NM (United States)
14. Gibson I et al (2010) Additive manufacturing technologies: rapid prototyping to direct digital manufacturing. Springer, Berlin
15. Xiong J et al (2012) Bead geometry prediction for robotic GMAW-based rapid manufacturing through a neural network and a second-order regression analysis. *J Intell Manuf* 25(1):1–7
16. Cao Y et al (2011) Overlapping model of beads and curve fitting of bead section for rapid manufacturing by robotic MAG welding process. *Robotics Comput Int Manuf* 27(3):641–645
17. Xiong J et al (2012) Modeling of bead section profile and overlapping beads with experimental validation for robotic GMAW-based rapid manufacturing. *Robotics Comput Int Manuf* 29 (2):417–423
18. Aiyiti W et al (2006) Investigation of the overlapping parameters of MPAW-based rapid prototyping. *Rapid Prototyping J* 12(3):165–172
19. Dunlavey MR (1983) Efficient polygon-filling algorithms for raster displays. *ACM Trans Graph (TOG)* 2(4):264–273



20. Park SC, Choi BK (2000) Tool-path planning for direction-parallel area milling. *Comput Aided Des* 32(1):17–25
21. Rajan V et al (2001) The optimal zigzag direction for filling a two-dimensional region. *Rapid Prototyping J* 7(5):231–241
22. Farouki R et al (1995) Path planning with offset curves for layered fabrication processes. *J Manuf Syst* 14(5):355–368
23. Yang Y et al (2002) Equidistant path generation for improving scanning efficiency in layered manufacturing. *Rapid Prototyping J* 8(1):30–37
24. Jin G et al (2013) An adaptive process planning approach of rapid prototyping and manufacturing. *Robotics Computer Integr Manuf* 29(1):23–38
25. Dwivedi R, Kovacevic R (2004) Automated torch path planning using polygon subdivision for solid freeform fabrication based on welding. *J Manuf Syst* 23(4):278–291
26. Ding D et al (2014) A tool-path generation strategy for wire and arc additive manufacturing. *Int J Adv Manuf Technol* 73(1–4):173–183
27. Ding D et al (2015) A multi-bead overlapping model for robotic wire and arc additive manufacturing (WAAM). *Robotics Comput Integr Manuf* 31(1):101–110

# Modeling of Human Welder Response Against 3D Weld Pool Surface Using Machine-Human Cooperative Virtualized Welding Platform

Yu-Kang Liu, Ning Huang and Yu-Ming Zhang

**Abstract** This paper aims to present the modeling of human welder intelligence in pipe Gas Tungsten Arc Welding (GTAW) process. An innovative machine-human cooperative virtualized welding platform is teleoperated to conduct training experiments: the welding current is randomly changed to generate fluctuating weld pool surface and the human welder tries to adjust his arm movement (welding speed) based on his observation on the real-time weld pool feedback/image superimposed with an auxiliary visual signal which instructs the welder to increase/reduce the speed. Linear model and global Adaptive Neuro-Fuzzy Inference System (ANFIS) model are identified from the experimental data to correlate welder's adjustment on the welding speed to the 3D weld pool surface. To better distill the detailed behavior of the human welder, K-means clustering is performed on the input space such that a local ANFIS model is identified. To further improve the accuracy, an iterative procedure has been performed. Compared to the linear, global and local ANFIS model, the iterative local ANFIS model provides better modeling performance and reveals more detailed intelligence human welders possess.

## 1 Introduction

Automated welding systems produce repeatable results by accurately controlling the joint fit-up/welding conditions to reduce possible process variations. Comparably, in manual Gas Tungsten Arc Welding (GTAW) process [1] human welders can appraise the welding results on their real-time observation on the welding process and adaptively adjust welding parameters. In certain applications, human welders may be preferred over mechanized or automated machines.

---

Y.-K. Liu · N. Huang · Y.-M. Zhang (✉)

Department of Electrical Engineering, Institute for Sustainable Manufacturing,  
University of Kentucky, Lexington, KY 40506, USA  
e-mail: yuming.zhang@uky.edu

Unfortunately, skills needed for critical welding operations typically require a long time to develop [2]. Developing intelligent welding machines that can emulate skilled welders appears to be an effective solution.

Welding process monitoring and control for automated welding machines have been extensively studied in the past few decades [3–12]. In particular, the weld pool geometry is believed to provide valuable insights into the state of the welding process. Recently an innovative vision-based 3D weld pool sensing system for GTAW process was developed [10]. The weld penetration and weld pool surface have thus been controlled [11, 12]. However, to ensure such an ideal performance, the control algorithm (structure) needs to be carefully designed per the process dynamics [13]. Using a machine to cooperate a welder controlled process and utilizing welder's valuable knowledge to form a data-driven approach represents another type of control methodology, which is referred to as machine-human cooperative control scheme [14]. In this scheme, a machine algorithm assists human welder controlled process. With the proposed cooperative control, quality welds may be better produced by less experienced welders with less intensive concentration during a longer lasting period. It may also be beneficial to developing a welder training system that can help train unskilled welder faster. This paper proposed an iterative local ANFIS based data-driven approach to model the human welder's adjustment on the welding speed in pipe GTAW process.

## 2 Experimental System Setup

Figure 1 illustrates the schematic of the proposed control system [14]. The proposed cooperative controller performs three functions: (1) Welder reaction prediction: Use the identified welder reaction model to predict welder reactions/actions; (2) Welding process response prediction: Use the predicted welder actions (future control variables) and identified welding process model to predict the response of

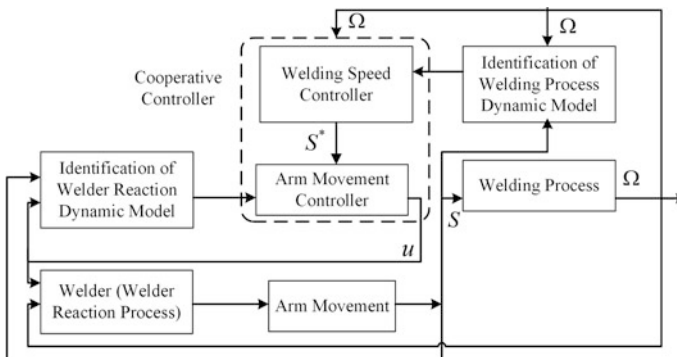
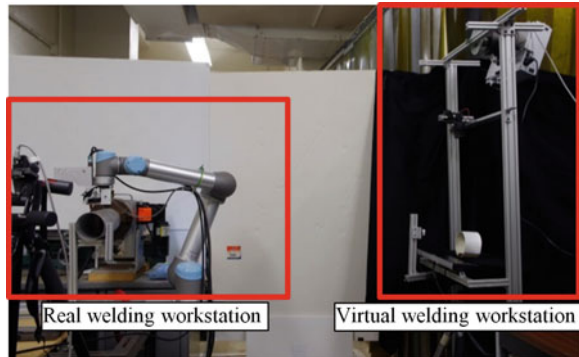


Fig. 1 Schematic of machine-human cooperative control [14]

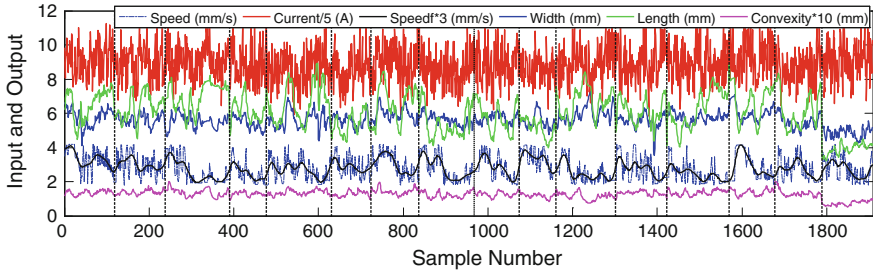
**Fig. 2** General view of the virtualized welding system [14]



the dynamic welding process; (3) Cooperative adjustment: The predicted weld pool will be related to the adjustment to be made by the human and optimization will be done to minimize deviation from a desired weld pool with respect to the machine adjustment. An optimized welding speed is calculated and will serve as the desired trajectory for the human welder to follow. The arm movement controller then calculates the needed visual signal input which will be provided to the human welder. The human welder sees the visual signal outputted by the arm movement controller, and moves his/her arm accordingly.

The experimental system is illustrated in Fig. 2 [14]. It consists of two workstations: welding station and virtual station. In the virtual station a human welder can view the mock up where the work-piece geometry (from direct viewing or eye view camera) is rendered and displayed, and moves the virtual welding gun accordingly as if he/she is right in front of the work-piece. The human welder movement is accurately captured by a Leap motion sensor [15], and the obtained virtual welding gun tip 3D coordinates will be sent to the PC. Welding station consists of an industrial welding robot, eye view camera, and a compact 3D weld pool sensing system. The robot utilized in this study is Universal Robot UR-5 with six Degree of Freedom (DOF). The robot is connected to a controller which is used to control the motions of the robot. The robot (client) and PC (server) is communicated via Ethernet using TCP/IP protocol and socket programming.

Stainless steel pipe is welded using the direct current electrode negative GTAW process. The material of the pipe is stainless steel 304. The outer diameter and wall thickness of the pipe are 113.5 and 2.03 mm, respectively. Sixteen dynamic experiments have been conducted to model the correlation between the human arm movements and weld pool characteristic parameters. In these experiments the welding current is randomly changed from 40 to 48 A resulting in a fluctuating weld pool surface. The welder sees the weld pool image overlaid with an assistant visual signal, and move the virtual welding torch accordingly. The robot follows the welder's movement and completes the welding task. Welder's fluctuating arm movement speed (i.e., welding speed) is filtered [16] to suppress the unwanted shaking during the experiments. The sampling period in this study is 0.5 s because



**Fig. 3** Measured system inputs and output in sixteen dynamic training experiments

the welder controls arm movement by observing the weld pool and is a relatively slow process. Figure 3 plots the inputs and welder's arm movement speed.

### 3 Linear and Global ANFIS Modeling

Based on the definition of system inputs and output detailed in previous section, a general model structured is described as:

$$\hat{y}(k) = f(W(k-1), L(k-1), C(k-1)) \quad (1)$$

where  $\hat{y}(k)$  is the model estimated speed at instant  $k$ ,  $W(k-1)$ ,  $L(k-1)$ ,  $C(k-1)$  are the width, length, and convexity at instant  $k-1$ , respectively.

The identified linear model parameters using standard least squares algorithm are:

$$\hat{y}(k) = 0.188W(k-1) - 0.071L(k-1) + 0.232C(k-1) \quad (2)$$

The static gains for the width, length, and convexity are 0.188,  $-0.071$ , and 0.232, respectively. It is found that the welding speed can be estimated by the linear model with acceptable accuracy. However, substantial static fitting errors are frequently observed.

In order to further improve the model accuracy, nonlinear ANFIS modeling method is utilized [17, 18]. Modeling trails suggest that when input parameters are partitioned by 2, a good trade-off is obtained between model performance and number of model parameters. The modeling result is shown in Fig. 4. It is seen that the model errors are improved by incorporating the nonlinear correlation between the inputs and model output.

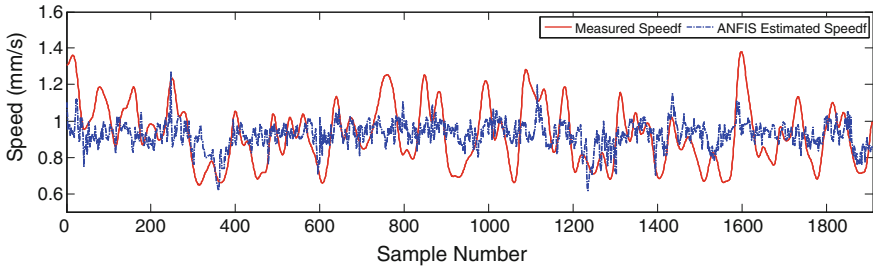


Fig. 4 Global ANFIS modeling result

### 4 Local ANFIS Modeling Using K-Means Clustering

To further improve the model accuracy, local ANFIS models based on clustering of the input space are constructed in this section.

K-means clustering [19] is one of the most commonly used unsupervised clustering algorithms and has found numerous applications. Based on the clustering result, local ANFIS is constructed and the overall fitting result is shown in Fig. 5. As can be seen, model performance is further enhanced by clustering the input space and constructing local ANFIS model. It is noted the clustering has outliers that may deteriorate the clustering and modeling performance. An iterative procedure is performed. During each iteration step 1 % of the data points that have the largest distance to the cluster centers (i.e., outliers) are thrown, and the iteration procedure stops when the maximum iteration number is reached (10 in this study).

It is apparent that the above observations provide us detailed knowledge about the correlation between the welder’s responses and weld pool geometry. If a linear model is used, the correlation acquired between the welder’s response and the weld pool geometrical parameters will only be an average over the entire range. Hence, the developed ANFIS modeling plays an important role in deriving the detailed correlation between the welder’s response and the weld pool geometry.

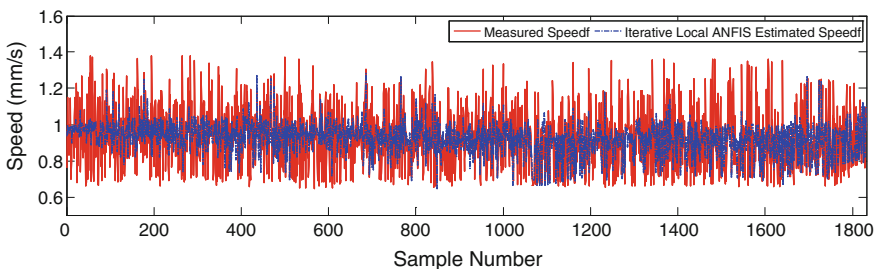


Fig. 5 Iterative local ANFIS modeling results

## 5 Conclusion

In this paper an innovative iterative local ANFIS model based data-driven approach to model human welder response is proposed. A machine-human cooperative control scheme in virtualized welding platform is utilized. Teleoperated training experiments are conducted by a human welder. Linear model is firstly identified and a global ANFIS model is proposed to improve the model accuracy. K-means clustering is performed on the input space and a local ANFIS model is proposed. Compared to the linear, global and local ANFIS models, the proposed iterative local ANFIS model provides better modeling performance and distills detailed intelligence human welder possess.

## References

- O'Brien R (ed) (1998) *Welding handbook*, 8th edn, vol 2-Welding Processes. AWS
- Utrachi GD (2007) Welder shortage requires new thinking. *Weld J* 86(1):6
- Renwick R, Richardson R (1983) Experimental investigation of GTA weld pool oscillations. *Weld J* 62(2):29s–35s
- Hardt D, Katz J (1984) Ultrasonic measurement of weld penetration. *Weld J* 63(9):273s–281s
- Guu AC, Rokhlin SI (1992) Arc weld process control using radiographic sensing. *Mater Eval* 50(11):1344
- Song JB, Hardt DE (1993) Closed-loop control of weld pool depth using a thermally based depth estimator. *Weld J* 72(10):471s–478s
- Ghanty P, Vasudevan M, Mukherjee DP et al (2008) Artificial neural network approach for estimating weld bead width and depth of penetration from infrared thermal image of weld pool. *Sci Technol Weld Join* 13(4):395–401
- Zhang YM, Kovacevic R (1998) Neuro-fuzzy model based predictive control of weld fusion zone geometry. *IEEE Trans Fuzzy Syst* 6(3):389–401
- Chen H, Lv F, Lin T et al (2009) Closed-loop control of robotic arc welding system with full-penetration monitoring. *J Intell Rob Syst* 56(5):565–578
- Zhang WJ, Liu YK, Wang X, Zhang YM (2012) Characterization of three dimensional weld pool surface in GTAW. *Weld J* 91(7):195s–203s
- Liu YK, Zhang YM (2013) Model-based predictive control of weld penetration in gas tungsten arc welding. *IEEE Trans Control Syst Technol* 1–12
- Liu YK, Zhang YM (2013) Control of 3D weld pool surface. *Control Eng Pract* 21(11):1469–1480
- Liu YK, Zhang W, Zhang YM (2013) Dynamic neuro-fuzzy based human intelligence modeling and control in GTAW. *IEEE Trans Autom Sci Eng* 1–12
- Liu YK, Zhang YM (2014) Control of human arm movement based on adaptive predictive ANFIS in machine-human cooperative welding process. *Control Eng Pract*
- Daniel T (2012) Leap motion: 3D hands-free motion control, unbound. Available [http://news.cnet.com/8301-11386\\_3-57437404-76/leap-motion-3d-hands-free-motion-control-unbound/](http://news.cnet.com/8301-11386_3-57437404-76/leap-motion-3d-hands-free-motion-control-unbound/). 20 May 2012
- Garcia D (2010) Robust smoothing of gridded data in one and higher dimensions with missing values. *Comput Stat Data Anal* 54:1167–1178
- Liu YK, Zhang YM, Kvidahl L (2014) Skilled human welder intelligence modeling and control: part I—modeling. *Weld J* 93:46s–52s

18. Liu YK, Zhang YM, Kvidahl L (2014) Skilled human welder intelligence modeling and control: part II—analysis and control applications. *Weld J* (accepted for publication)
19. Seber GAF (1984) *Multivariate observations*. Wiley, Hoboken, NJ



# Modeling Welding Deviation of Rotating Arc NGW Based on Support Vector Machine

Wen-Hang Li, Kai Gao, Jing Wu and Jia-You Wang

**Abstract** Support Vector Machine (SVM) was employed to describe welding deviation of welding seam tracking in multi-layer single pass, narrow gap rotating arc gas metal arc welding (GMAW). First, work piece was designed and processed to mimic multi-layer single pass welding groove to obtain experimental data under different deviations. Second, for data preprocessing, welding current signal in each rotating circle was divided into 12 parts, and the average value of each part and the difference of the according left-right part were selected and normalization to build an input-output table for predicting the weld deviation. Then, kernel function was selected and its parameters were determined by a grid search method using cross validation approach. The SVM model was built with the train set and was validated with the test set. It showed that the model can meet the criteria of welding seam tracking. In addition, comparison between SVM model and BP neural network model was made and it showed the former has better performance because it adapt to the little sample problem and can avoid the local extreme.

## 1 Introduction

As a high-efficiency welding method, rotating arc narrow gap welding (NGW) is accurate with its seam tracking to avoid welding defect [1]. The key is to find the welding deviation in real time. Because the welding process is inherently nonlinear, time-delayed, strongly coupling in its input/output and involves many uncertain

---

W.-H. Li (✉) · K. Gao · J.-Y. Wang

School of Material Science and Engineering, Jiangsu University of Science and Technology, Zhenjiang 212003, China  
e-mail: lwh\_abc@qq.com

J. Wu

Department of Mechanical Engineering, Aerospace and Biomedical Engineering, The University of Tennessee, Knoxville, TN 37996-2210, USA

factors (such as metallurgy, heat transfer, chemical reaction, arc physics, and magnetization), it is hard to build a precision mathematical model.

A new kind of statistical learning method—Support Vector Machine (SVM), introduced by Vapnik in 1995, is based on structural risk minimization principle and has very good generalization with few data samples [2]. SVM is a new generation learning system based on advances in statistical learning theory, enabling non-linear mapping of an  $n$ -dimensional input space into a higher-dimensional feature space where, for example, a linear classifier can be used. The SVM can train non-linear models based on the structural risk minimization principle that seeks to minimize an upper bound of the generalization error rather than minimize the empirical error as implemented in neural networks. This induction principle is based on the fact that the generalization error and a confidence interval term depending on the Vapnik-Chervonenkis (VC) dimension. Based on this principle, SVM can achieve an optimal model structure by balancing between the empirical error and the VC-confidence interval, leading eventually to a better generalization performance than other neural network models. An additional merit of SVM is that training SVM is a uniquely solvable quadratic optimization problem, and the complexity of the solution in SVM depends only on the complexity of the desired solution, rather than on the dimensionality of the input space. Thus, SVM use a non-linear mapping, based on a kernel function, to transform an input space to a high dimension space and then look for a non-linear relation between inputs and outputs in the higher dimension space. SVM not only has a rigorous theoretical background but also can find global optimal solutions for problems with small training samples, high dimension, non-linearity and local optima. Originally, SVM was developed for pattern recognition problems. Recently, SVM has been shown to give good performance for a wide variety of problems, such as non-linear regression.

As to the application in welding, SVM is applied to model identification in laser beam welding, which accurately identifying the model and controlling the weld width effectively [3]. Min Qu and Yuezhou Ma research on CO<sub>2</sub> welding shield gas flux classifier based on SVM, the welding shield gas flux is identified and classified effectively [4]. According to the problem of defect recognition within X-ray inspection weld, the method using SVM to recognize weld defects is put forward [5]. In order to determine friction welding technological parameters correctly and quickly, an optimization model for friction welding technological parameters based on least square support vector machine (LSSVM) and artificial fish-swarm algorithm (AFSA) was presented [6]. With the continuous development and advancement of the SVM theory and practice research, the applications in welding process based on SVM will be day by day prominent [7].

This paper applies the SVM theory into the welding deviation attraction for the rotating arc narrow gap welding. Its contents are organized as shown below: In Sect. 2, the procedure of the SVM modeling method is introduced. In Sects. 3–5, the SVM method is applied into rotating arc NGW. In Sect. 6, the SVM model is validated and compared with BP NN model. Conclusions are drawn accordingly in the end of this paper.

## 2 Procedure of SVM Modeling Method

Considering the character of narrow gap rotating arc MAG welding and SVM, the procedure of the SVM modeling method was put forward, as shown in Fig. 1. At first, experiment should be designed and done to obtain enough data. Second, the obtained data should be preprocessed. For example, the de-noising method is used to improve the data quality and the normalization is used to decrease the influence of large value data. Third, the experimental data are divided into train set and test set, where the former is used to build the model and the latter is used to validate the obtained model. For the train set, it need to select the kernel function and its parameters, then the model was build based on these parameters. When the SVM model meet the criteria of the welding application, it can be used to predict the sampling data online, otherwise the kernel function and its parameters should be modified.

## 3 Feature Generation

Here SVM is used to describe the welding deviation of rotating arc NGW. The high-speed rotating arc system was shown in Fig. 2a, where an electrode wire passes through the hollow axis of motor and then stretches out from an eccentric nozzle. The hollow-axis motor drives the offset nozzle and rotates the arc on the tip of wire at high speed, so as to make the welding torch smaller and lighter, as well as small noises and high precision of motion control. The detail of the welding torch can be found in [8].

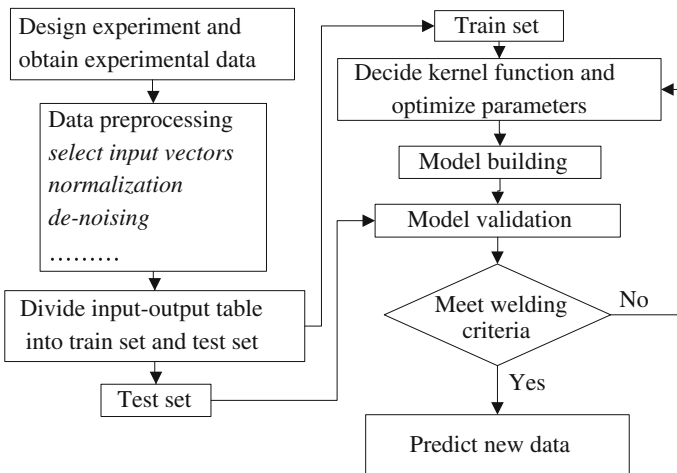
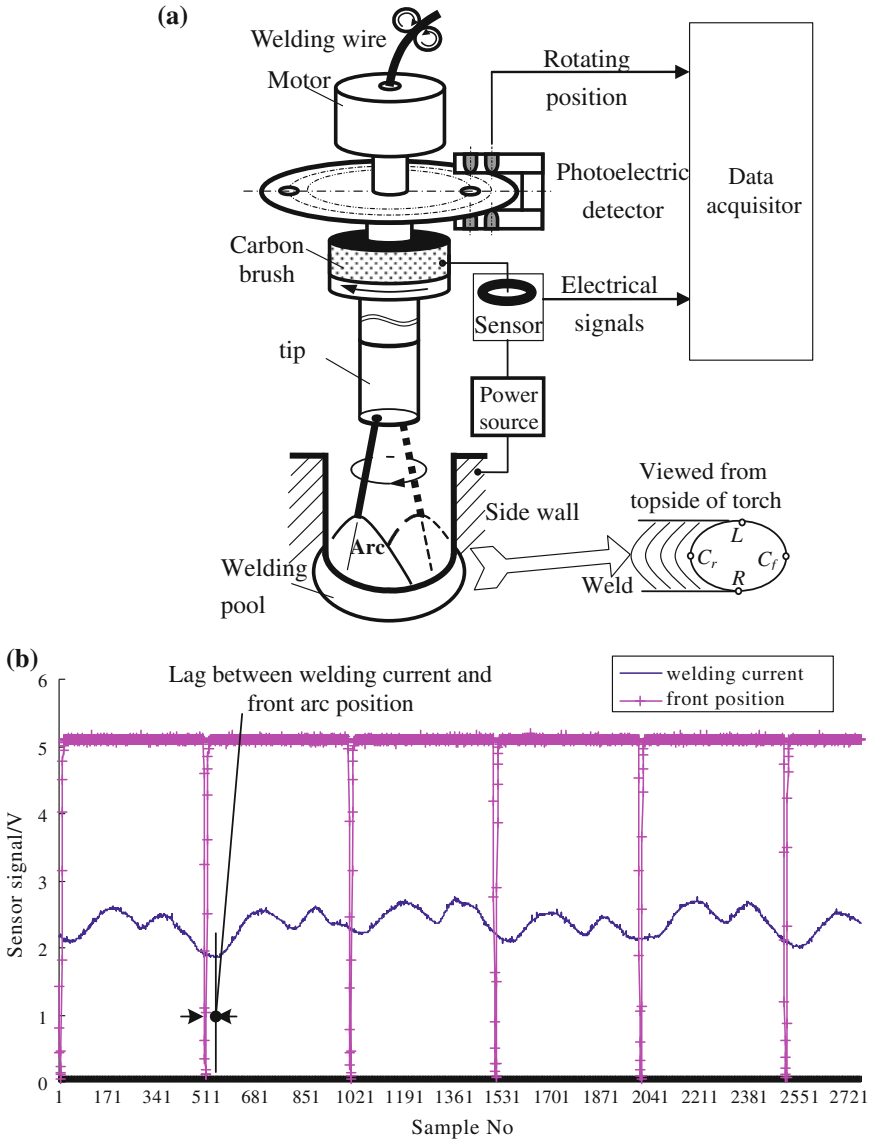


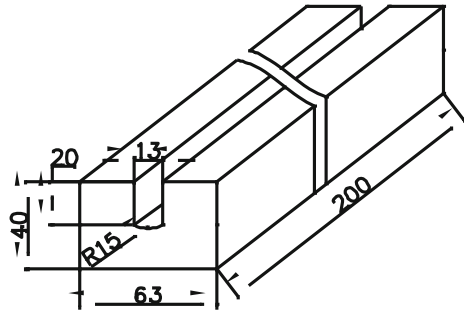
Fig. 1 Flow chart of SVM modeling method



**Fig. 2** The rotating torch and data acquisition equipment. **a** Welding and sensor equipment. **b** Obtained experiment data

To obtain the experiment data, the work piece is machined as showed in Fig. 3, which imitate the weld of multi-layer and single pass welding. The torch deviation of the welding torch is set to  $\pm 1$ ,  $\pm 0.5$  and 0 mm by the CNC operated equipment, where the positive value denotes the torch is on the left side of the welding direction. The welding parameters are showed in Table 1. When welding, the arc's

**Fig. 3** Dimension of U groove work piece



**Table 1** Welding parameters of narrow gap MAG welding

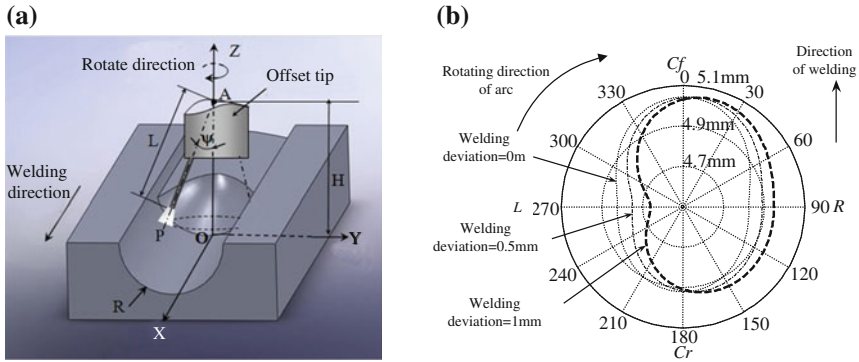
Parameter	Value
Torch height H, mm	20
Power source external characteristic	Constant-voltage
Welding current I, A	300 (setting value)
Welding voltage U, V	31
Welding speed v, mm min <sup>-1</sup>	230
Shield gas flow meter q, L min <sup>-1</sup>	30
Rotating frequency f, Hz	50

rotating position and the arc’s electrical signals are recorded by the data acquisition, as showed in Fig. 2b. Specially, the plus in rotating arc position denotes that the arc is in the welding direction, i.e. the front of the welding pool.

### 4 Data Preprocessing

As to the obtained data, they need to be preprocessed before be handled by SVM. First, we use the median filter method for the arc rotating position signal to reduce the noise influence. Then the welding current signal in each rotating cycle can be extracted by using the arc rotating position. Third, the input feature vectors should be selected. At last, normalization is usually necessary.

In this paper, the output feature vector is the welding deviation, and we need to select the input feature vectors. For arc sensor, the welding current varies according to the arc length, so it is necessary to know the arc length’s variation each circle at different welding deviation. Because the arc’s rotating speed is high, we assume that the wire extension doesn’t vary, and the front side welding pool is similar to half cylinder and the backside welding pool is similar to 1/4 ellipsoid, as showed in Fig. 4a. When L = 40 mm, AO = 50 mm,  $\psi = 2.5^\circ$ , the radius of the half cylinder is 5 mm, the radius of the 1/4 ellipsoid is “8 mm (x axis), 5 mm (y axis), 5 mm (z axis)”, and the arc length’s variation is showed in Fig. 4b, where the circle denotes the rotating arc/wire position and the pole axis denotes the length of arc. The detail calculation process can be found in Ref. [9].



**Fig. 4** The variation of arc length in a rotating circle. **a** Model for calculating arc length. **b** Arc length variation

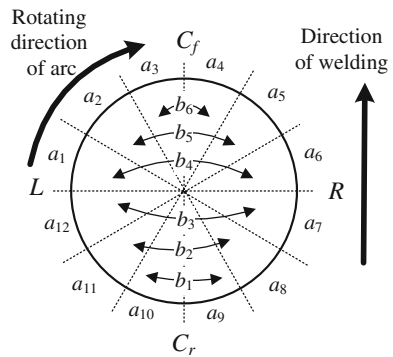
Figure 4b shows that if a rotating circle is divided into twelve intervals, the variation of arc length or welding current is obvious. So the mean value of each interval is calculated and used as an input feature vector. In addition, the difference between corresponding left and right groups is usually used in the arc sensor based welding tracking. So they are also used as input feature vectors (i.e.  $b_1 = a_{10} - a_9$ ;  $b_2 = a_{11} - a_8$ ;  $b_3 = a_{12} - a_7$ ;  $b_4 = a_1 - a_6$ ;  $b_5 = a_2 - a_5$ ;  $b_6 = a_3 - a_4$ ). All the input feature vectors are showed in Fig. 5, which was view from topside.

To make the model more adaptive, the welding current ( $a_1 - a_{12}$ ) was normalized used the following formula:

$$a_i = (I_{ai} - I_{min}) / (I_{max} - I_{min})$$

Then the interval difference ( $b_1 - b_6$ ) was calculated by the normalized welding current mean value. Data samples from the SVM dataset is showed in Table 2.

**Fig. 5** Division of welding current and selection of input feature vectors



**Table 2** Part data of the SVM data set after normalization

Sample no	Input									Output
	$a_1$	$a_2$	$a_{12}$	$b_1$	$b_2$	$b_3$	$b_4$	$b_5$	$b_6$	$d$
50	0.77	0.63	0.75	0.00	0.05	0.30	0.36	0.26	0.12	0.5
51	0.88	0.67	0.68	0.02	0.12	0.30	0.56	0.39	0.11	0.5
52	0.65	0.54	0.56	-0.02	-0.03	0.11	0.22	0.17	0.07	0.5
53	0.64	0.61	0.80	0.10	0.22	0.34	0.22	0.20	0.06	0.5
54	0.81	0.66	0.68	-0.07	0.02	0.15	0.30	0.18	0.05	0.5
55	0.67	0.48	0.42	0.02	-0.00	-0.08	0.21	0.11	0.01	0.5

### 5 SVM Modeling

A multi-class classification problem can be stated in following way: N training samples can be represented as a set of pairs  $(x_i, y_i)$ ,  $i = 1, 2, \dots, n$ , with  $y_i$  the label of the class which can be set to values of 1, 2, 3, ..., M and  $x \in R_n$  stands for feature vectors. In this paper, we will solve the welding deviation extraction problem; the welding deviation can be classified into 5 categories:  $\pm 1, \pm 0.5$  and 0 mm. We convert  $-1, -0.5, 0, +0.5, +1$  mm to 1, 2, 3, 4 and 5 labels for requirement of the multi-class classification.

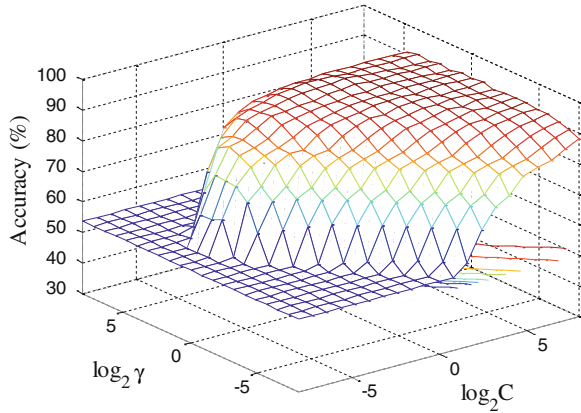
There are four types of frequently-used kernel functions for mapping data into high dimensional space, namely, linear, polynomial, radial basis function (RBF) and sigmoid kernels, as shown in Table 3.

As the most frequently-used kernel function, RBF kernel was employed in this paper for classification of welding deviation. For RBF (Radial Basis Function) kernel, width Gamma ( $\gamma$ ) and penalty parameters (C) are two most important parameters. C, a regularization parameter, controls the tradeoff between maximizing the margin and minimizing the training error. Too small C leads to insufficient stress on the training data, while too large C leads to over fitting. Usually, C should be set large enough to have a stable training process. The parameter of  $\gamma$  greatly affects the number of support vector (SV), which has a close relation with training time. Too many support vectors can produce overfitting and extend training time. Parameter  $\gamma$  also controls the amplitude of the Gaussian function and, therefore, affects the generalization ability of SVM [10]. In this study, the parameters of RBF were determined by a grid search method by cross validation using LIBSVM-mat-2.89 [11]. The main idea behind the grid search method is that

**Table 3** Four types of kernel functions

Kenal functions name	Kernel function
Linear kernels	$k(x_i \cdot x_j) = x_i^T x_j$
Polynomial kernels	$k(x_i \cdot x_j) = (\gamma x_i^T x_j + r)^d$
RBF kernels	$k(x_i \cdot x_j) = \exp(-\gamma \ x_i - x_j\ ^2)$
Sigmoid kernel	$k(x_i \cdot x_j) = \tanh(\gamma x_i^T x_j + r)$

**Fig. 6** Parameter selection result



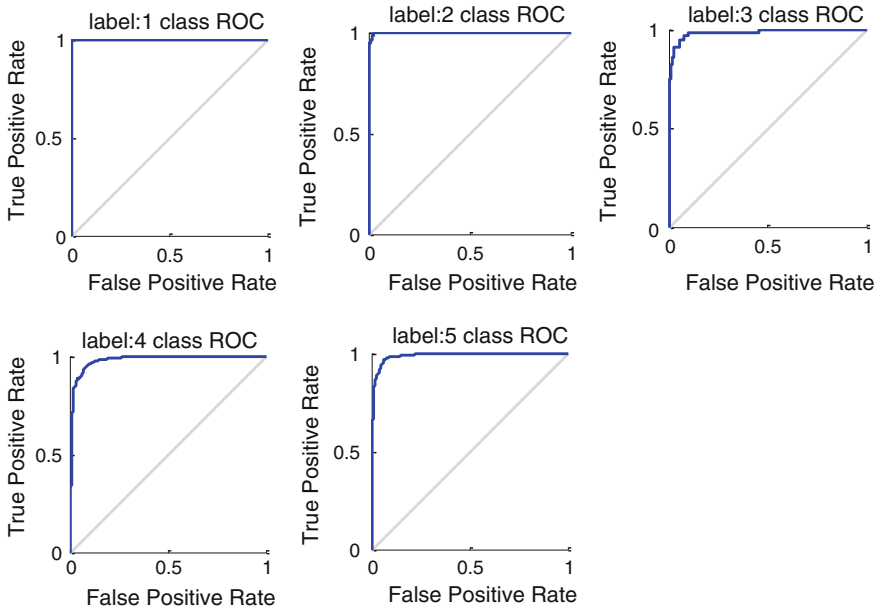
different parameter is tested and the one with the highest cross validation accuracy is selected. The method is conducted in two steps. In the first step, a coarser grid is applied with an exponentially growing sequence of  $(C, \gamma)$  with  $C = 2^{-8}, \dots, 2^8$  and  $\gamma = 2^{-8}, \dots, 2^8$ . In the second step, after identifying the optimal region on the grid, the finer grid search is executed. The results are used to perform the final training process [12]. The 3D image of  $C$ ,  $\gamma$  and accuracy is showed in Fig. 6, where the optimal parameters is  $C = 16$ ,  $\gamma = 3.0314$  and prediction accuracy = 92.6031 %. Then the SVM model is build by using the optimal parameters.

## 6 Model Validation

To evaluate the predict precision to unknown data, ten fold cross validation method is used. The prediction accuracy = 92.0779 % and the Receiver Operating Characteristic (ROC) curve is showed in Fig. 7. Changing the label to real value and it showed that the mean error is 0.0409 mm and the mean square error is  $0.0218 \text{ mm}^2$ . The result is satisfying and the SVM model can meet the criteria in welding tracking.

Furthermore, the SVM method is also compared with the BP neural network method. A standard three-layer BP neural network is used as a benchmark. There are 18 nodes in the input layer ( $a_1$ – $a_{12}$ ,  $b_1$ – $b_6$ ), 40 nodes in the hidden layer and one node ( $d$ ) in the output layer. The hidden nodes use the ‘tansig’ transfer function and the output node uses the ‘logsig’ transfer function. The ‘Levenberg-Marquardt’ method is used for training the BP neural network, which could give better performance than the batch training for large and non-stationary data sets. Standard Matlab toolboxes are used for the calculations of the BP neural network.





**Fig. 7** ROC curve for each class

To get a stable comparison result, ten fold cross validation method is used for testing. For BP Neural network model the mean error is 0.1331 mm and the mean square error is 0.0337 mm<sup>2</sup>. It is clear that the SVM model's predictive ability is better than that of BP NN because it adapt to the little sample problem and can avoid the local extreme.

## 7 Conclusion

In this paper, the SVM based modeling method was used to describe welding deviation. The conclusions are drawn as follows.

1. The modeling method can meet the criteria of seam tracking in rotating arc NGW.
2. SVM is proved to be a highly effective classification tool because of its structural risk minimization principle, which minimizes an upper bound of the generalization error rather than the training error. This eventually leads to better generalization than neural networks, which implement the empirical risk minimization (ERM) principle and do not converge to global solutions.
3. With the continuous development and advancement of the SVM theory and practice research, the applications in welding process based on SVM will be increasingly prominent.

**Acknowledgements** The authors would like to thank the financial support from the National Natural Science Foundation of China (No 51005107), Natural Science Foundation of Jiangsu Province (No. BK2011509), Specialized Research Fund for the Doctoral Program of Higher Education (20133220110001), the Qing Lan Project of Jiangsu province for outstanding young teachers and technology innovation team.

## References

1. Kim GH, Na SJ (2001) A study of an arc sensor model for gas metal arc welding with rotating arc Part 2: Simulation of an arc sensor in mechanically rotating gas metal arc welding. *Proc Inst Mech Eng B* 215(9):1281–1288
2. Vapnik VN (2000) *The nature of statistical learning theory*. Springer, New York
3. Zhou B, Liu YS (2008) Adaptive control for laser welding process based on support vector machines. *Autom Instrum* 07:31–34
4. Qu M, Ma YZ (2007) Research of CO<sub>2</sub> welding shield gas flux classifier based on SVM. *Electr Weld Mach* (04):68–70, 73
5. Yuan-xiang L, Xiao-guang Z, Ding G (2006) Defects recognition based on support vector machine within radiographic testing weld. *Coal Mine Mach* 05:773–776
6. Fu-hua S (2008) Friction welding technological parameter optimization based on LSSVM and AFSA. *Trans China Weld Inst* (12):104–108+118
7. Chi L (2011) Review of support vector machine and its applications in welding process. *Electr Weld Mach* 10:42–45
8. Wang JY, Ren YS, Yang F, Guo HB (2007) Novel rotation arc system for narrow gap MAG welding. *Sci Technol Weld Join* 12(6):505–507
9. Li WH, Sun DD, Yang F, Wang JY, Ren YS (2011) A new type of welding deviation extraction algorithm based on rotating arc sensor for narrow gap MAG welding. *Mater Sci Technol* 19(6):48–52
10. Zhao C, Zhang H, Zhang X, Zhang R, Luan F, Liu M, Hu Z, Fan B (2006) Prediction of milk/plasma drug concentration (M/P) ratio using support vector machine (SVM) method. *Pharm Res* 23(1):41–48
11. Hsu CW, Chang CC, Lin CJ (2003) *A practical guide to support vector classification*. Department of Computer Science, National Taiwan University
12. Guo N, Zhang J, Han Y, Zhang L, Yuan X (2012) Effects of welding parameters on metal transfer process in rotating arc narrow gap horizontal GMAW

# Dynamics Modeling and Analysis of a Type of High Frequency 6-DOF Parallel Platform

Qi-Tao Huang, Zheng-Mao Ye and Zhi-zhong Tong

**Abstract** To break the frequency band restricts caused by the transverse vibration of the actuators, a new type of hydraulically driven 6-DOF parallel platform with higher frequency band is proposed. This study presents the kinematics and dynamics of this type of 6-DOF parallel platform. Following the theoretical description of the kinematics and dynamics, a multi rigid body dynamic model is established with the Kane's method according to a real platform which is under construction. The simulation results are shown that this platform is qualified to high frequency applications.

## 1 Introduction

Since 1965, the 6-DOF parallel manipulator was proposed by British engineer D. Stewart in his paper and was applied in the flight simulator [1]. This type of parallel structure mechanisms are widely used as motion simulator, vibration isolator, manipulator etc. [2] But these applications are all confined in low frequency band (up to about 25 Hz), especially for the heavy load hydraulic driven parallel platforms. Heavy load parallel platforms usually adopt hydraulic cylinders as the actuators and cylinders are always slender due to the platforms' work space. One of the main restricts is the transverse vibration of the hydraulic driven cylinders. S. Uzny has taken the hydraulic cylinder which fixed elastically on both ends into account, and researched the transverse vibration of the hydraulic driven cylinder [3]. L. Tomski also has carried out the theoretical and numerical research into the stability and free vibrations of a hydraulic cylinder subjected to Euler's load [4]. Some useful results are presented but the results confined in single cylinder.

The hydraulically driven parallel manipulator is suitable for the large load situations due to its high stiffness and great carrying capacity. And those cylinders

---

Q.-T. Huang (✉) · Z.-M. Ye · Z. Tong  
Department of Mechanical Engineering, Harbin Institute of Technology, Harbin, China  
e-mail: huangqitao@hit.edu.cn

used are usually single rod slender due to the platforms' structure. However, if the natural frequencies and modes of the transverse vibration of the hydraulic driven cylinders occur in the frequency band of the parallel manipulator, it will cause seriously problem. To avoid this problem and expand the frequency band of the parallel manipulator, a new type of 6-DOF parallel platform is proposed [5].

The analysis of the kinematics and dynamics are the basis of recognize and control of a mechanism. For the Stewart parallel manipulator, Fichter analyzed the dynamics with the inertial forces of the kinematic chains neglected [6]. B. Dasgupta solved the inverse dynamics of Stewart Platform applying Newton-Euler equations [7]. A. Codourey established the dynamics model of Stewart Platform using the virtual work principle and Lagrange's equation [8]. Merlet has proposed a type of parallel platform structure [9]. Yan Jin had ever research the partially decoupled 6-DOF parallel manipulator with the actuators vertical to the base [10].

This paper proposes a more general 6-DOF parallel manipulator to avoid the traverse vibration of the actuators in order to enhance the frequency band. The dynamics model of this type of mechanism is established by Kane's method.

## 2 Structure Description and Kinematics

### 2.1 Structure Description and Coordinates

The schematic view of the new type of 6-DOF parallel manipulator's structure and its coordinates (There is no strict mapping relationship between the two pictures) is shown in Fig. 1. As shown in the Fig. 1,  $B_iC_i$  ( $i = 1 \dots 6$ , similarly herein after) represents the actuating hydraulic cylinder, which is fixed on the lower platform at point  $B_i$ , so the orientation of the vector  $B_iC_i$  is settled. Through reducing the

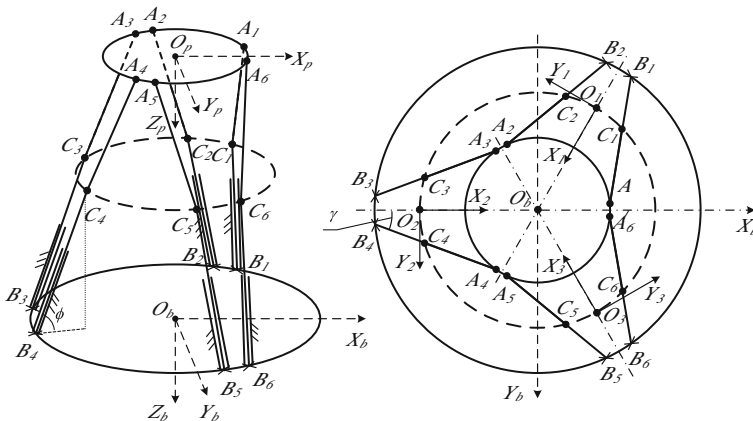


Fig. 1 Schematic view of the high frequency 6-DOF parallel manipulator

moving part of the actuators, the effects of the transverse vibration of the cylinders will be reduced. And  $A_iC_i$  represents the linkages; it is connected to the moving platform by a spherical joint at point  $A_i$ , and is connected to the end of the cylinder's piston rod by another spherical joint at point  $C_i$ .

All the six kinematics chain have the same parameters, i.e. the six linkages are exactly the same. As shown in Fig. 1b that the moving platform ( $A_i$ ) and the fixed ground ( $B_i$ ) are symmetrically and reversely placed. In the kinematics chains, the hydraulic cylinders are used as actuators to driven the moving platform. Totally 8 structure parameters are needed to completely determine the structure of this type of parallel manipulator, and they are given in Table 1.

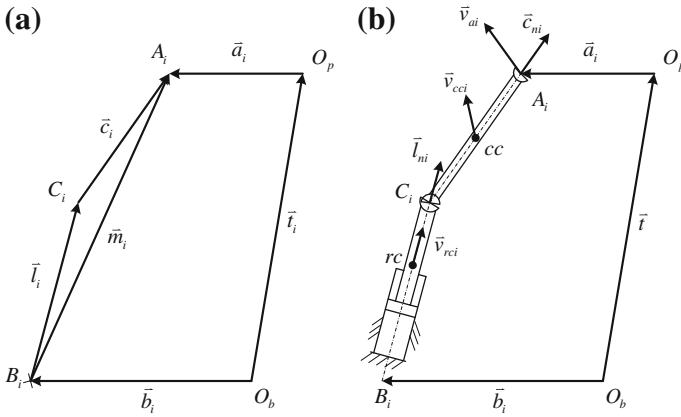
The degree of freedom of this parallel manipulator can be derived from the Kutzbach- Glübler formulation. And the DOF of this manipulator is 6.

Take the center point  $O_p$  of the upper gimbal circle as the origin, the end-effectors' coordinate  $O_p-X_pY_pZ_p$  can be established, and it's fixed on the moving platform. Similarly, the ground coordinate  $O_b-X_bY_bZ_b$  can be established of which the origin is the center point of the lower gimbal circle. As shown in Fig. 1. Now the position of a point, the velocity or acceleration of a part can be described as a vector in these two coordinates. In particular, a vector in the end-effectors' coordinate will have a superscript p referring to this frame. For example, the position of the upper gimbal point can be described as the vector  $a_i^p$  in the end-effector coordinate, and in the ground coordinate it will be described as  $a_i$ . Similarly,  $b_i$  represents the position of the lower platform around the momentary Z, Y, X axes of the end-effector coordinate. And in the sequence of 3-2-1, the rotation matrix which maps a vector of the end-effector coordinate into the ground coordinate is defined as  $R$ .

In order to describe the vector of the hydraulic cylinders which are fixed on the lower platform, it is necessary to establish a actuator coordinate for each cylinder, and it can be marked as  $B_i - X_iY_iZ_i$ , as shown in Fig. 1b. Then the unit vector of each hydraulic cylinder can be marked as  $l_{ni}^B$  in the corresponding actuator coordinate, and in the sequence of 3-2-1, the rotation matrix which maps a vector of each actuator coordinate into the ground coordinate is defined as  $R_{B_i}$ , then the unit vector of each cylinder can be described as  $l_{ni} = R_{B_i}l_{ni}^B$  in the ground coordinate.

**Table 1** The 6-DOF parallel manipulator's structure parameters

Variable	Description
$r_a$	Upper gimbal radius
$r_b$	Lower gimbal radius
$d_a$	Upper gimbal spacing
$d_b$	Lower gimbal spacing
$\phi$	Angle between actuator and lower gimbal plane
$c$	Linkage length
$l_0$	Initial actuator length
$\gamma$	Angle between the projection of actuator on the lower gimbal plane and the graduation line of the lower gimbals



**Fig. 2** Schematic view of a kinematic chain. **a** Relationship of position vectors, **b** relationship of velocity vectors

### 2.2 Kinematics Analysis

For conveniently and clearly describing the kinematics of this manipulator, it is better to take a single kinematic chain into observation, and Fig. 2 shows the schematic view of a kinematic chain. Note that the vector  $\vec{m}_i$  in Fig. 2a doesn't represent any real part of the manipulator, it is just a intermediate variable.

As shown in Fig. 2a, the vector  $\vec{m}_i$  can be described by

$$\vec{m}_i = \vec{t} + \mathbf{R}\vec{a}_i^p - \vec{b}_i \tag{1}$$

And then the vector  $\vec{c}_i$  which represents the linkage can be derived as

$$\vec{c}_i = \vec{m}_i - \vec{l}_i \tag{2}$$

in which  $\vec{l}_i$  represents the vector of the cylinder, and  $\vec{l}_i = l_i \vec{l}_{ni}$ ,  $l_i$  describes the length of the cylinder. Notice that the length of the linkage is a constant, so

$$c_i^2 = c^2 \tag{3}$$

now replace  $\vec{c}_i$  in Eq. (3) with Eq. (2), and a quadratic equation with regard to the length of the cylinder, which is

$$l_i^2 - 2(\vec{m}_i \cdot \vec{l}_{ni})l_i + |\vec{m}_i|^2 - c^2 = 0 \tag{4}$$

solve this equation, and abandon the solution which does not meet the real architecture of the manipulator, the length of the cylinder can derived as follows

$$l_i = (\mathbf{m}_i \cdot \mathbf{l}_{ni}) - \sqrt{(\mathbf{m}_i \cdot \mathbf{l}_{ni})^2 - |\mathbf{m}_i|^2 + c^2} \tag{5}$$

Till now, the vector  $\mathbf{l}_i$  and the vector  $\mathbf{c}_i$  can be completely determined.

Figure 2b shows the relationship of the velocity vectors in a kinematic chain. As calculating the velocities, a condition should be noticed that the generalized velocity of the moving platform is known as  $\dot{\mathbf{q}} = [\dot{\mathbf{t}}, \boldsymbol{\omega}]^T$ , in which  $[\dot{x}, \dot{y}, \dot{z}]^T = \dot{\mathbf{t}}$  is the end-effector coordinate's translation velocity in the ground coordinate, and  $\boldsymbol{\omega} = [\omega_x, \omega_y, \omega_z]^T$  is the angular velocity of the end-effector coordinate in the ground coordinate, which can be derived from Euler equation and is a function of  $\psi, \theta, \varphi$ .

Choosing point  $O_p$  as the base point, the velocity of the upper gimbal point  $A_i$  can be described as

$$\mathbf{v}_{ai} = \dot{\mathbf{t}} + \boldsymbol{\omega} \times \mathbf{R}\mathbf{a}_i^p \tag{6}$$

which can also be expressed as a matrix equation that is

$$\mathbf{v}_{ai} = \mathbf{J}_{ai,q}\dot{\mathbf{q}} \tag{7}$$

$\mathbf{J}_{ai,q}$  is the jacobian that translates the generalized velocity of the moving platform into the velocity of the upper gimbal point.

As shown in Fig. 2b, assume that the c.o.g. of the piston rod is point  $rc$ , and the c.o.g. of the linkage is point  $cc$ . Assume that the linkage is prismatic, then point  $cc$  is at the geometric center of the linkage. As the orientation of the cylinder is stationary, the translation velocity of the actuator is the same as the velocity of point  $rc$ . This relationship can be expressed by the equation below

$$\mathbf{v}_{rci} = \dot{l}_i \mathbf{l}_{ni} \tag{8}$$

$\dot{l}_i$  is the translation speed of the actuator. According to the velocity projection theorem, the projection of the actuator translation speed on the linkage equals to the projection of the upper gimbal point velocity on the linkage, which leads to the equation below

$$\mathbf{c}_{ni}^T \mathbf{v}_{ai} = \mathbf{c}_{ni}^T (\dot{l}_i \mathbf{l}_{ni}) \tag{9}$$

Solve Eq. (9), and the translation speed of the actuator is

$$\dot{l}_i = \frac{\mathbf{c}_{ni}^T \mathbf{v}_{ai}}{\mathbf{c}_{ni}^T \mathbf{l}_{ni}} \tag{10}$$

considering Eq. (6), Eq. (10) can be described as

$$\dot{l}_i = \frac{1}{\mathbf{c}_{ni}^T \mathbf{I}_{ni}} \left[ \mathbf{c}_{ni}^T, (\mathbf{R} \mathbf{a}_i^p \times \mathbf{c}_{ni})^T \right] \dot{\mathbf{q}} \quad (11)$$

According to Eq. (11), a matrix equation for all the six kinematic chains can be defined as

$$\dot{\mathbf{L}} = \left[ \mathbf{C}_n^T, (\mathbf{R} \mathbf{A}^p \times \mathbf{C}_n)^T \right] \dot{\mathbf{q}} = \mathbf{J}_{lq} \dot{\mathbf{q}} \quad (12)$$

with the definition that

$$\dot{\mathbf{L}} = [\dot{l}_1, \dot{l}_2, \dots, \dot{l}_6], \mathbf{C}_n = \left[ \frac{\mathbf{c}_{n1}}{\mathbf{c}_{n1}^T \mathbf{I}_{n1}}, \frac{\mathbf{c}_{n2}}{\mathbf{c}_{n2}^T \mathbf{I}_{n2}}, \dots, \frac{\mathbf{c}_{n6}}{\mathbf{c}_{n6}^T \mathbf{I}_{n6}} \right], \mathbf{A}^p = [\mathbf{a}_1^p, \mathbf{a}_2^p, \dots, \mathbf{a}_6^p]$$

And is the jacobian between the actuator translation speed vector and the generalized velocity of the moving platform.

The angular velocity of the linkage is going to be calculated next. According to the knowledge of analytical mechanics, the angular velocity of a rigid body is constant wherever the base point is. When point  $C_i$  is chosen as the base point, the velocity of the upper gimbal point  $A_i$  will be described as

$$\mathbf{v}_{ai} = \dot{l}_i \mathbf{I}_{ni} + \boldsymbol{\omega}_{ci} \times \mathbf{c}_i \quad (13)$$

replace  $\dot{l}_i$  with Eq. (10), the angular velocity of the linkage can be obtained,

$$\boldsymbol{\omega}_{ci} = \frac{1}{c} \mathbf{c}_{ni} \times \left( \mathbf{I} - \frac{\mathbf{I}_{ni} \mathbf{c}_{ni}^T}{\mathbf{c}_{ni}^T \mathbf{I}_{ni}} \right) \mathbf{v}_{ai} \quad (14)$$

which,  $\mathbf{I}$  is a 3-order unit matrix (similarly hereinafter). With the introduction of the notation  $\mathbf{P}_{lci} = \mathbf{I} - \frac{\mathbf{I}_{ni} \mathbf{c}_{ni}^T}{\mathbf{c}_{ni}^T \mathbf{I}_{ni}}$ , Eq. (14) can be reordered into a matrix equation,

$$\boldsymbol{\omega}_{ci} = \mathbf{C}_{ti} \mathbf{P}_{lci} \mathbf{v}_{ai} = \mathbf{J}_{oi,a} \mathbf{v}_{ai} \quad (15)$$

in which  $\mathbf{C}_{ti}$  is a skew symmetric matrix constituted by the elements of the vector  $\frac{\mathbf{c}_{ni}}{c}$ , and it has property:  $\mathbf{C}_{ti}^T = -\mathbf{C}_{ti}$ .  $\mathbf{J}_{oi,a}$  is the jacobian between the velocity of the upper gimbal point and the angular velocity of the linkage.

With matrix  $\mathbf{P}_{lci}$ , Eq. (8) can be rewritten as

$$\mathbf{v}_{rci} = (\mathbf{I} - \mathbf{P}_{lci}) \mathbf{v}_{ai} = \mathbf{J}_{ri,a} \mathbf{v}_{ai} \quad (16)$$

which  $\mathbf{J}_{ri,a}$  is the jacobian between the velocity of the upper gimbal point and the c.o.g. velocity of the piston rod.



Chosen point  $C_i$  as the base point, the c.o.g. velocity of the linkage is

$$\mathbf{v}_{cci} = \mathbf{v}_{ai} - \boldsymbol{\omega}_{ci} \times \frac{c}{2} \mathbf{c}_{ni} \quad (17)$$

replace  $\boldsymbol{\omega}_{ci}$  with Eq. (14), reorder Eq. (17) into

$$\mathbf{v}_{cci} = \left( \mathbf{I} - \frac{1}{2} \mathbf{P}_{lci} \right) \mathbf{v}_{ai} = \mathbf{J}_{ci,a} \mathbf{v}_{ai} \quad (18)$$

which  $\mathbf{J}_{ci,a}$  is the jacobian between the velocity of the upper gimbal point and the c.o.g. velocity of the linkage.

By differentiating Eq. (6), the acceleration of the upper gimbal point  $A_i$  can be calculated,

$$\begin{aligned} \dot{\mathbf{v}}_{ai} &= \ddot{\mathbf{i}} + \dot{\boldsymbol{\omega}} \times \mathbf{R} \mathbf{a}_i^p + \boldsymbol{\omega} \times (\boldsymbol{\omega} \times \mathbf{R} \mathbf{a}_i^p) \\ &= \mathbf{J}_{ai,q} \ddot{\mathbf{q}} - |\boldsymbol{\omega}|^2 \mathbf{P}_\omega \mathbf{a}_i \end{aligned} \quad (19)$$

$\mathbf{P}_\omega = \mathbf{I} - \boldsymbol{\omega}_n \boldsymbol{\omega}_n^T$  is the projection matrix.

Similarly, the angular acceleration of the linkage, the c.o.g. acceleration of the linkage and the c.o.g. acceleration of the piston rod can be derived by differentiating Eqs. (14), (18) and (16).

$$\dot{\boldsymbol{\omega}}_{ci} = \mathbf{C}_{ti} (\dot{\mathbf{P}}_{lci} \mathbf{v}_{ai} + \mathbf{P}_{lci} \dot{\mathbf{v}}_{ai}) \quad (20)$$

$$\dot{\mathbf{v}}_{cci} = \dot{\mathbf{J}}_{ci,a} \mathbf{v}_{ai} + \mathbf{J}_{ci,a} \dot{\mathbf{v}}_{ai} \quad (21)$$

$$\dot{\mathbf{v}}_{rci} = \dot{\mathbf{J}}_{ri,a} \mathbf{v}_{ai} + \mathbf{J}_{ri,a} \dot{\mathbf{v}}_{ai} \quad (22)$$

The kinematics of this type of parallel manipulator and the motion relationship of deferent parts of this mechanism is established.

### 3 Dynamics Modeling

Depending on whether the inertial forces of the actuators and the linkages are taken into account, the dynamics of the parallel manipulator divided into single-body dynamics or multi-body dynamics. And on the assumption that parts of the mechanism which constitute the manipulator are rigid bodies.

When it comes to the situation where the mass of the moving platform and the load is much larger than that of the actuators and the linkages so that the inertial forces of the actuators and the linkages can be neglected, the dynamics of the manipulator will be simplified as single-body dynamics.

The drive force that is generated by the actuator can be denoted as  $f_{ci}$ . As the inertial force of the linkage is ignored, it can be considered as a two-force member, and the force it outputs will be denoted as  $f_{ai}$ . In the ideal case, the power that is transmitted by the linkage is always conserved, which can be easily described by the equation below

$$f_{ci} \cdot \dot{l}_i = f_{ai} \cdot v_c \quad (23)$$

where  $v_c = \mathbf{c}_{ni}^T (\dot{l}_i \mathbf{l}_{ni})$  is the axial translation speed of the linkage. The force that the linkage outputs can be easily derived by solving Eq. (23), which is

$$\mathbf{f}_{ai} = \frac{f_{ci}}{\mathbf{c}_{ni}^T \mathbf{l}_{ni}} \mathbf{c}_{ni} \quad (24)$$

With Newton's law, the translational motion of the moving platform can be described as

$$\mathbf{C}_n \mathbf{f}_c + m_p \mathbf{g} = m_p \ddot{\mathbf{t}} \quad (25)$$

where  $\mathbf{f}_c = [f_{c1}, f_{c2}, \dots, f_{c6}]^T$  is the drive force vector of the actuators,  $m_p$  is the mass of the moving platform and  $\mathbf{g}$  is the acceleration of gravity which is a vector.

And with Euler equation, the rotational motion is described by

$$[\mathbf{R}^P \times \mathbf{C}_n] \mathbf{f}_c = \mathbf{I}_b \dot{\boldsymbol{\omega}} + \boldsymbol{\omega} \times \mathbf{I}_b \boldsymbol{\omega} \quad (26)$$

where  $\mathbf{I}_b = \mathbf{R} \mathbf{I}_p \mathbf{R}^T$ , and  $\mathbf{I}_p$  is the inertia matrix of the moving platform in the end-effectors' coordinate. Combine these two equations; the single-body dynamic model of the manipulator is derived,

$$\begin{bmatrix} \mathbf{C}_n \\ \mathbf{R}^P \times \mathbf{C}_n \end{bmatrix} \mathbf{f}_c = \begin{bmatrix} m_p \mathbf{I} & 0 \\ 0 & \mathbf{I}_b \end{bmatrix} \begin{bmatrix} \ddot{\mathbf{t}} \\ \dot{\boldsymbol{\omega}} \end{bmatrix} + \begin{bmatrix} 0 & 0 \\ 0 & \boldsymbol{\Omega} \mathbf{I}_b \end{bmatrix} \begin{bmatrix} \dot{\mathbf{t}} \\ \boldsymbol{\omega} \end{bmatrix} - \begin{bmatrix} m_p \mathbf{g} \\ 0 \end{bmatrix} \quad (27)$$

where  $\boldsymbol{\Omega}$  is a skew symmetric matrix constituted by the elements of the vector  $\boldsymbol{\omega}$ . In short, Eq. (27) is rewritten as

$$\mathbf{J}_{\text{iq}}^T \mathbf{f}_c = \mathbf{M}_p \ddot{\mathbf{q}} + \mathbf{C}_p \dot{\mathbf{q}} - \mathbf{G}_p \quad (28)$$

in which

$$\begin{aligned} \mathbf{M}_p &= \begin{bmatrix} m_p \mathbf{I} & 0 \\ 0 & \mathbf{I}_b \end{bmatrix} && \text{the mass matrix} \\ \mathbf{C}_p &= \begin{bmatrix} 0 & 0 \\ 0 & \boldsymbol{\Omega} \mathbf{I}_b \end{bmatrix} && \text{the coriolis/centripetal effect matrix} \\ \mathbf{G}_p &= \begin{bmatrix} m_p \mathbf{g} \\ 0 \end{bmatrix} && \text{gravity matrix} \end{aligned}$$

However, when it comes to the situation where the mass of the moving platform and the load is not that large, and the inertial forces of the actuators and the linkages can't be neglected, the dynamics of the manipulator will be considered as multi-body dynamics. The inertial forces of the actuators can be split up in two parts: the gravitational forces and the translational inertial forces. And the inertial forces of the linkages can be split up in three parts: the gravitational forces, the translational inertial forces and the rotational inertial forces. These forces will first be projected on the upper gimbal points, and then any force generated at this point can be easily projected at the generalized platform velocities using jacobian  $\mathbf{J}_{ai,q}$ . And at the generalized platform velocities, Kane's method will be applied to establish the multi-body dynamics of the manipulator.

Assume that the masses of the linkage and the piston rod are  $m_c$  and  $m_r$ . The gravitational forces are easily projected on the upper gimbal point,

$$\mathbf{G}_{ci}^a = \mathbf{J}_{ci,a}^T m_c \mathbf{g} \quad (29)$$

$$\mathbf{G}_{ri}^a = \mathbf{J}_{ri,a}^T m_r \mathbf{g} \quad (30)$$

The translational inertial forces generated by the mass at the c.o.g. of the linkage and the piston rod are easily projected at the upper gimbal point,

$$\mathbf{f}_{ci}^a = \mathbf{J}_{ci,a}^T m_c \dot{\mathbf{v}}_{cci} \quad (31)$$

$$\mathbf{f}_{ri}^a = \mathbf{J}_{ri,a}^T m_r \dot{\mathbf{v}}_{rci} \quad (32)$$

By rewriting  $\dot{\mathbf{v}}_{cci}$  and  $\dot{\mathbf{v}}_{rci}$  as a function of  $\dot{\mathbf{v}}_{ai}$  using Eq. (21) and Eq. (22), these two Eqs. (21) and (22) are rewritten as

$$\mathbf{f}_{ci}^a = \mathbf{J}_{ci,a}^T m_c (\dot{\mathbf{J}}_{ci,a} \mathbf{v}_{ai} + \mathbf{J}_{ci,a} \dot{\mathbf{v}}_{ai}) = \mathbf{M}_{ci} \dot{\mathbf{v}}_{ai} + \mathbf{C}_{ci} \mathbf{v}_{ai} \quad (33)$$

$$\mathbf{f}_{ri}^a = \mathbf{J}_{ri,a}^T m_r (\dot{\mathbf{J}}_{ri,a} \mathbf{v}_{ai} + \mathbf{J}_{ri,a} \dot{\mathbf{v}}_{ai}) = \mathbf{M}_{ri} \dot{\mathbf{v}}_{ai} + \mathbf{C}_{ri} \mathbf{v}_{ai} \quad (34)$$

Assuming that the inertia of the linkage around an axis which passes through the c.o.g. of the linkage and is orthogonal to its axial direction is  $i_c$ , then the rotational inertial force generated by the inertia of the linkage is projected at the upper gimbals point,

$$\mathbf{f}_{ici}^a = \mathbf{J}_{oi,a}^T i_c \dot{\boldsymbol{\omega}}_{ci} \quad (35)$$

replace  $\dot{\boldsymbol{\omega}}_{ci}$  with  $\dot{\mathbf{v}}_{ai}$  by using Eq. (20) and rewrite Eq. (35), the result is

$$\mathbf{f}_{ici}^a = \mathbf{J}_{oi,a}^T i_c \mathbf{C}_{ti} (\dot{\mathbf{P}}_{lci} \mathbf{v}_{ai} + \mathbf{P}_{lci} \dot{\mathbf{v}}_{ai}) = \mathbf{M}_{ici} \dot{\mathbf{v}}_{ai} + \mathbf{C}_{ici} \mathbf{v}_{ai} \quad (36)$$

The generalized inertial force of the system along the generalized platform velocities can be derived by summing all the inertial forces of the six kinematic chains as well as the moving platform and projecting them to the generalized platform velocities. And that is

$$\mathbf{f}^* = \sum_{i=1}^6 \mathbf{J}_{ai,q}^T (\mathbf{f}_{ci}^a + \mathbf{f}_{ri}^a + \mathbf{f}_{ici}^a) + \mathbf{M}_p \ddot{\mathbf{q}} + \mathbf{C}_p \dot{\mathbf{q}} \quad (37)$$

The generalized drive force of the system along the generalized platform velocities consists of the projected drive forces of the actuators and gravitational forces of the parts at the generalized platform velocities. It is described as

$$\mathbf{f} = \mathbf{J}_{lq}^T \mathbf{f}_c + \sum_{i=1}^6 \mathbf{J}_{ai,q}^T (\mathbf{G}_{ci}^a + \mathbf{G}_{ri}^a) + \mathbf{G}_p \quad (38)$$

According to Kane's method, the multi-body dynamics of the manipulator is derived,

$$\mathbf{J}_{lq}^T \mathbf{f}_c = \mathbf{M}_s \ddot{\mathbf{q}} + \mathbf{C}_s - \mathbf{G}_s \quad (39)$$

where  $\mathbf{M}_s$ ,  $\mathbf{C}_s$  and  $\mathbf{G}_s$  are given as below,

$$\begin{aligned} \mathbf{M}_s &= \mathbf{M}_p + \sum_{i=1}^6 \mathbf{J}_{ai,q}^T (\mathbf{M}_{ci} + \mathbf{M}_{ri} + \mathbf{M}_{ici}) \mathbf{J}_{ai,q} \\ \mathbf{C}_s &= \mathbf{C}_p \dot{\mathbf{q}} + \sum_{i=1}^6 \mathbf{J}_{ai,q}^T [(\mathbf{C}_{ci} + \mathbf{C}_{ri} + \mathbf{C}_{ici}) \mathbf{J}_{ai,q} \dot{\mathbf{q}} \\ &\quad - (\mathbf{M}_{ci} + \mathbf{M}_{ri} + \mathbf{M}_{ici}) |\boldsymbol{\omega}|^2 \mathbf{P}_{\omega} \mathbf{a}_i] \\ \mathbf{G}_s &= \mathbf{G}_p + \sum_{i=1}^6 \mathbf{J}_{ai,q}^T (\mathbf{G}_{ci}^a + \mathbf{G}_{ri}^a) \end{aligned}$$

## 4 Simulation Results

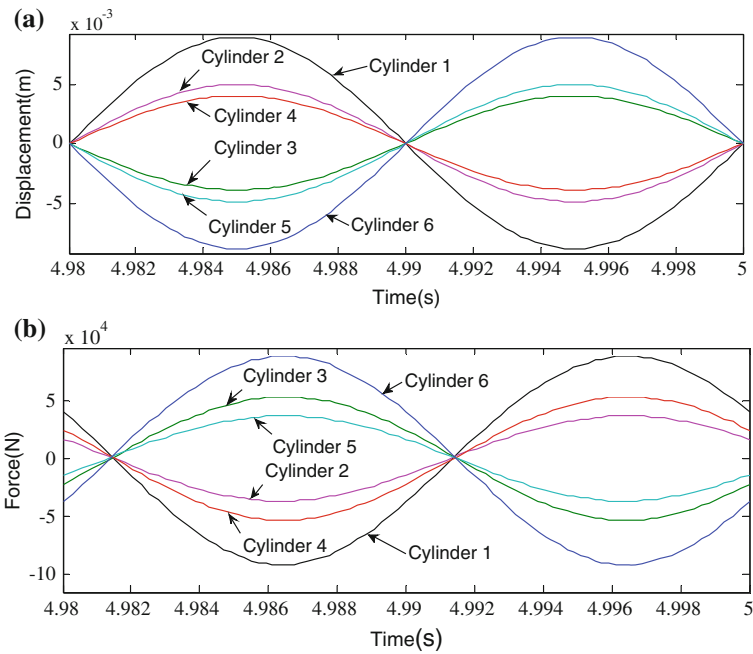
The multi rigid body dynamics model of this type parallel mechanism established by Simulink according to the formulations derived in the parts 3, the displacements and driving forces of the actuators can be calculated, which could be pavements for the optimization and real-time control of this type of manipulators.

The structure parameters of the 6-DOF platform are given in Table 2, and the displacements and driving forces of the actuators are shown from Figs. 3, 4, 5, and 6.

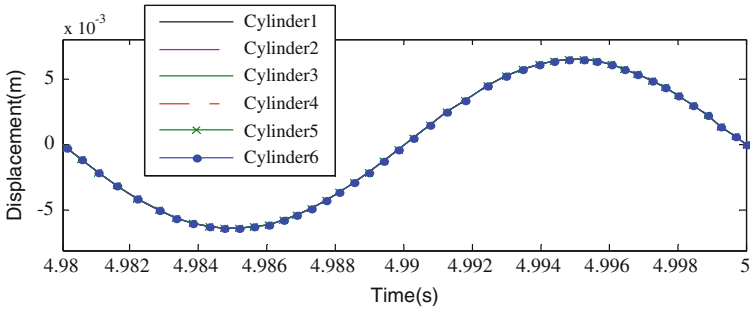
**Table 2** The structure parameters of the 6-DOF platform

Variable	Value
$r_a$	0.75 m
$r_b$	1.3 m
$d_a$	0.26 m
$d_b$	0.35 m
$\phi$	$60^\circ$
$\gamma$	$26.375^\circ$
$c$	0.8 m
$l_0$	0.5 m
$s$	0.2 m
$d$	0.1 m
$m_r$	20 kg
$m_p$	100 kg
$m_c$	15 kg
$i_c$	$1.6 \text{ kg m}^2$

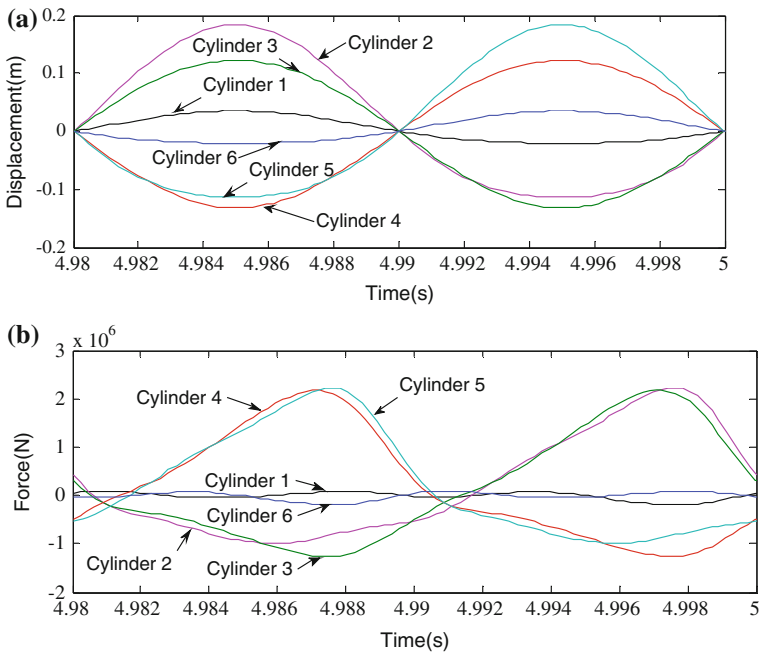
$s$  is the stroke of the cylinder, and  $d$  is the diameter of the piston



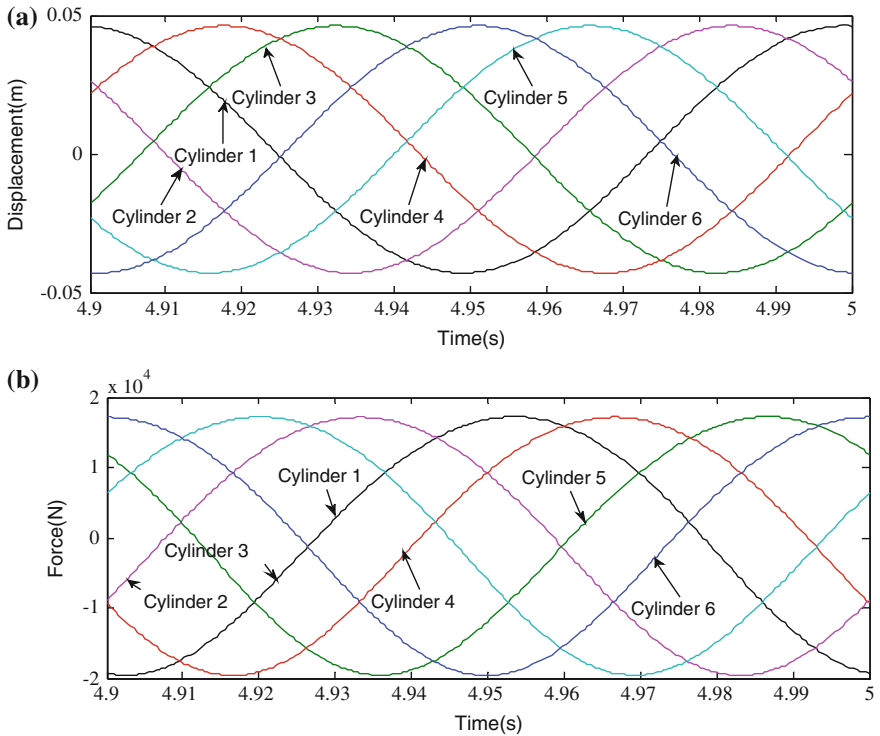
**Fig. 3** Translation along X axis with movement  $0.01 \text{ m} \cdot \sin(2\pi \cdot 50t)$ . **a** Displacement curves, **b** force curves



**Fig. 4** Translation along Z axis with movement  $0.01 \text{ m} \cdot \sin(2\pi \cdot 50t)$



**Fig. 5** Rotation around X axis with movement  $20^\circ \cdot \sin(2\pi \cdot 50t)$ . **a** Displacement curves, **b** force curves



**Fig. 6** Movement around Z axis on a circle with radius of 0.05 m. **a** Displacement curves, **b** force curves

## 5 Conclusion

The kinematics of the newly proposed hydraulically driven 6-PSS parallel manipulator was analyzed, and the velocity and acceleration relationship between different parts of the manipulator was derived as well as the Jacobians. To deriving the multi-rigid-body dynamics, Kane's method was applied which avoided a lot of differential operations, and thus the dynamics is concise and could be easily realized in the computer. According to the multi-rigid-body dynamics derived, the Simulink model was established. The displacement and driving force of the actuators under different movements were derived, this could be the useful base for the optimization and real-time control of this type of parallel mechanism.

**Acknowledgement** This research has been supported by National Natural Science Foundation of China, Research Project No. 51105094.

## References

1. Stewart D (1965) A platform with 6 degrees of freedom. In: Proceedings of the institution of mechanical engineers, 180(Part 1, 15):371–386
2. Dasgupta B, Mruthyunjaya TS (2000) The Stewart platform manipulator: a review. *Mech Mach Theory* 35:15–40
3. Uzny S (2009) Free vibrations and stability of hydraulic cylinder fixed elastically on both ends. In: Proceeding of application of math and mechanical, vol 93, pp 303–304
4. Tomski L, Uzny S (2011) A hydraulic cylinder subjected to Euler's load in aspect of the stability and free vibrations taking into account discrete elastic elements. *Arch Civil Mech Eng* 6(3):769–785
5. Tan Q (2012) Research of high frequency 6-DOF parallel platform. Mater Thesis, Harbin Institute of Technology, 2012.09
6. Fichter EF (1986) A Stewart platform based manipulator general theory and practical construction. *Int J Robot Res* 5(2):157–182
7. Dasgupta B, Mruthyunjaya TS (1998) Closed form dynamic equations of the general Stewart platform through the Newton-Euler approach. *Mech Mach Theory* 33(7):993–1012
8. Codourey A (1998) Dynamic modeling of parallel robots for computed-torque control implementation. *Int J Robot Res* 17(12):1325–1336
9. Merlet JP (1991) Articulated device, for use in particular in robotics. U.S. Patent 5,053,687, 1991-10-1
10. Yan J, Chen IM, Yang G (2009) Kinematic design of a family of 6-DOF partially decoupled parallel manipulators. *Mech Mach Theory* (44):912–922



# The Application of Robotic Welding in the Shipbuilding

Hua-Bin Chen, Tao Lin and Shan-Ben Chen

**Abstract** Welding is the most critical, expensive and time consuming procedure among the whole shipbuilding manufacturing process. Welding automation and intelligence play an important role in the modern shipbuilding industry. Arc welding robot can be ideal for the shipbuilding to increase productive efficiency and improve the working conditions. However, traditional “teach-playback” robot lack of intelligence on the assembly variation, welding deformation and the plate of machining errors. And the paper developed an off-line programming system for the inner bottom hull, which was implemented and successfully used in the shipbuilding. Firstly, we focus on the CAD model building of the inner bottom hull that can be described as geometry information. Secondly, we present a suitable offline programming and seam path planning method, which can generate robot program automatically. Finally, in combination with the touch and arc sensor, a novel arc welding robotic system is set up. Experiments on the inner bottom hull are conducted, and the fillet weld size can meet the requirements on the shipbuilding quality standards.

## 1 Introduction

The shipbuilding industry is steadily advancing by introducing robots to its work fields for increases in productivity and improvements in working conditions. Traditionally, the shipbuilding industry has relied on the labor of a large pool of skilled workers, who faced the prospect of long hours and demanding tasks such as welding, cutting and painting to get large vessels launched. In the recent years, with the development of electronic technique and computer technology, robots and robotic technologies are now mature enough to release welder from hard manual work [1]. And, how to apply commercial robotic system properly to meet the

---

H.-B. Chen (✉) · T. Lin · S.-B. Chen  
School of Materials Science and Engineering, Shanghai Jiao Tong University,  
Shanghai 200240, China  
e-mail: hbchen@sjtu.edu.cn

production purpose in the shipyard is a key research topic for shipbuilding engineers.

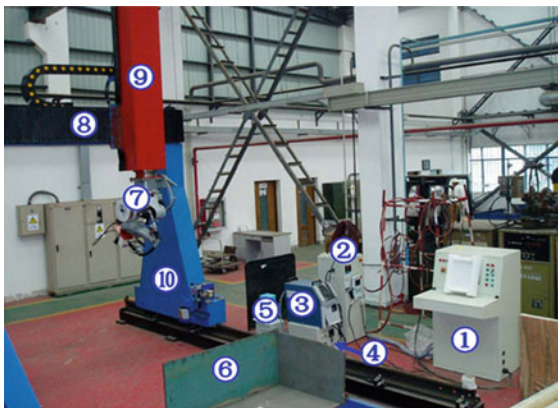
It is well known that welding is the most crucial, expensive, and time-consuming process among the shipbuilding process. Therefore, arc welding robot applications will yield a large productivity improvement in hull assembly welding [2]. Currently, robot programming through the conventional teaching process is still a tedious and time-consuming task, which requires more skills and expertise [3]. Currently, Offline programming (OLP) technology, which is based on the 3D model of the complete robot work cell, is becoming more popular. In contrast to the traditional “teach-playback” method, OLP has more strength on programming complex systems and efficient for production with large volumes [4]. For most of the past few decades, CAD-based systems have been proposed to assist operator in the robot programming process. In order to improve the intuitiveness and flexibility of OLP task, researchers combine the prior knowledge of real world and CAD model together. Typically, it introduced the sensor-assisted technology to the path planning and automatic programming [5, 6]. Ahn [7] proposed the offline automatic teaching method to use vision information. The operator can teach the desired locations according to the environmental vision information in OLP directly. Solvang et al. [8] also presented a vision based programming methodology by identifying a path drawn onto the workpiece. Takarics and Szemes [9] attempted to a new way to determine the trajectory for welding robots based on the stereo vision. It can determine the welding path in the space and to give the welding trajectory of the robot using two fixed cameras [10]. In Ref. [5], the author presents a CAD-based system to program a robot from a 3D CAD environment, allowing users to generate robot programs through human-robot interface platform. Kim presents a method to generate three-dimensional robot working paths off-line based on CAD data in an automatic adhesive spray system for shoe outsoles and uppers [11]. This research do much for increasing productivity in shoe manufacturing as a core work of a robotic adhesive spray system. Pires et al. [4] presented a CAD interface capable of adding in the programming process of welding applications, which enable pre-program is so easy to simulate and adjust the position and orientation by extracting welding definition from the CAD file.

Although a variety of research has been done in the area of CAD-based robot planning and automatic generation programming [12], how to apply above mentioned technology properly to meet the production purpose in the shipyard is a difficult research topic. In this study, a new arc welding robotic system is proposed for the inner bottom hull in the shipbuilding. We develop a offline programming system of inner bottom hull provides robot calibration, inner bottom hull CAD model acquisition, fillet weld path planning, and automatic program generation. Ultimately, we hope that it can be applied for the shipbuilding process to liberate much more labor.

## 2 Robotic Arc Welding System Set Up

The robotic arc welding system mainly includes PLC control-cabinet, MH6 robot, NX100 controller, multiple axis gantry system, teach pendant, digital welding power, wire cutter device, arc tracking sensor and inner bottom, see Fig. 1. The whole welding steps can be strictly controlled by a sequential process. The robot could not enter into the inner bottom before the gantry dropping out completely. At beginning, the multiple axis gantry system dropped out the welding zone before accurate assembling of the inner bottom. In our developed off-line programming system, we call this task-level programming. In this step, it is important to transform an off-line CAD model into a robot program with further error correction. On the one hand, it can eliminate the assembling error through the touch sensor function. Considering the welding deformation, on the other hand, the method uses the seam arc welding sensor to accommodate the inconsistencies of the work piece during welding process.

Before doing all the welding tasks, it enables the robot to return to the home positions. First of all, the standard-program is finished using the off-line programming. In this session, the job program is transformed to the robot controller. Given the variation of the size and shape in the inner bottom, the initial welding position and key welding points of the seam path would be revised during the welding process. Among them, the off-line programming included four parts: the acquisition of geometric model, robot calibration, seam path planning in robotic welding and generation of the tasks file. In this system, PLC-based controller process is a process control system which generated and transfer control instruction for the servo system. Considering the safety and flexibility of motion structure, PLC system has two control modes which consisted of logical and illogical type. Thus the operator could manually control each motion structure separately. Finally, the system had the function of fault alarm detection in IPC (Industrial Personal Computer)-PLC



- ① PLC control-cabinet
- ② DX100 controller
- ③ Digital welding power
- ④ Arc tracking sensor
- ⑤ Transformer
- ⑥ Base
- ⑦ Robot
- ⑧ Beam trail
- ⑨ Lifting mechanism
- ⑩ Gantry

Fig. 1 Arc welding robot system of inner bottom

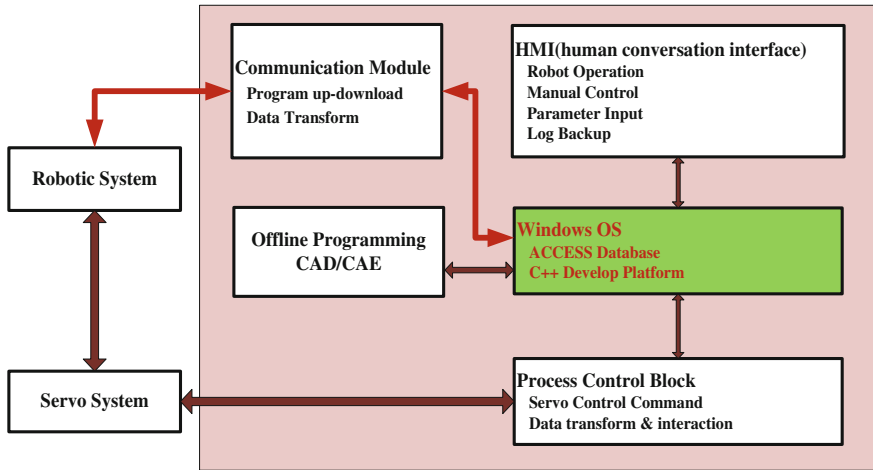


Fig. 2 The flow chart of the inner bottom welding software system structure

communication through the inspection of response of PLC. Figure 2 depicts the whole software flow chart of the inner bottom arc welding robotic system.

### 3 Weld Path Planning and Automatic Robot Program Generation

In this paper, the study concerned offline programming, seam path planning and welding based on the analog work piece of the inner bottom hull. Actually there are critical problems about the coordinate transform, where the position system of the robot is a key issue on the CAD model. Aimed at inner bottom hull, a simple rectangle was described as geometry information. In consideration of the special requirements of weld path planning for the inner bottom hull, it should be inserted two points, i.e. initial and end welding point. So we can proceed to read from the DXF files, it can be realized to extract and save the graphic information. The graphic elements sample after pre-processing was shown in Fig. 3.

Aside from the basic DXF information mentioned above, weld arrangement and path planning are continued to be processed by the storage DXF information.

The sub-assembly is separated to stringers and floor plate, so large number of fillet weld need to be conducted. For the single inner bottom, it included four flat fillet seams and vertical fillet seams. The robot was mounted on the gantry beam, as well as the installing orientation was parallel to the trail. Figure 3 shows the coordinate correlation between the inner bottom frame and 6-axis Cartesian robotic manipulator. {R} denotes the base coordinate system affixed to the base of the robot. {W} denotes the fixed world coordinate system attached to the trail.

**Fig. 3** The graphic element sample of the inner bottom hull

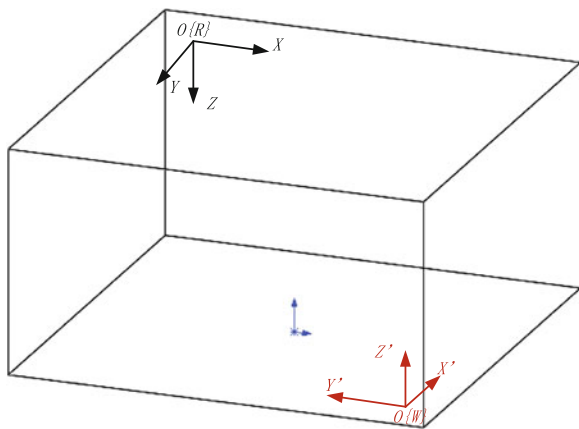
```

LWPOLYLINE 1
PolyLinePointsNum: 4
PLPoint 1: 0.0 , 0.0
PLPoint 2: 1536.0 , 0.0
PLPoint 3: 1536.0 , 1500.0
PLPoint 4: 0.0 , 1500.0

.....
LWPOLYLINE 2
PolyLinePointsNum: 4
PLPoint 1: 0.0 , 2000.0
PLPoint 2: 1536.0 , 2000.0
PLPoint 3: 1536.0 , 2816.0
PLPoint 4: 0.0 , 2816.0
    
```

Since the robot home position located just above the inner bottom frame, it could be set the initial position  $(\frac{L}{2}, \frac{W}{2}, H_0)$  of the 6-axis robot. From Fig. 4 it is apparent that the matrix of the inner bottom and 6-axis robot frame is assumed orthogonal. In reality, however, this is not completely orthogonal. In the following installation, the robot deviations was up to 2–3°. To take this into account, the 6-axis robot has turned around World z axis with a rotation of  $\theta$ . On this point, the following task planning would be involved. In this case, the welding process was separated two parts: positive orientation and negative orientation. When the robot is located at “positive orientation”, the translation matrix from {R} to {W} is provided by the following Eq. (1)

**Fig. 4** The coordinate of inner bottom frame and 6-axis robot



$$\begin{bmatrix} 0 & -1 & 0 & \frac{W}{2} \\ -1 & 0 & 0 & \frac{L}{2} \\ 0 & 0 & -1 & \frac{H_0}{2} \\ 0 & 0 & 0 & 1 \end{bmatrix} \begin{bmatrix} x_0 \\ y_0 \\ z_0 \\ 1 \end{bmatrix} = \begin{bmatrix} \frac{W}{2} - y_0 \\ \frac{L}{2} - x_0 \\ \frac{H_0}{2} - z_0 \\ 1 \end{bmatrix} \tag{1}$$

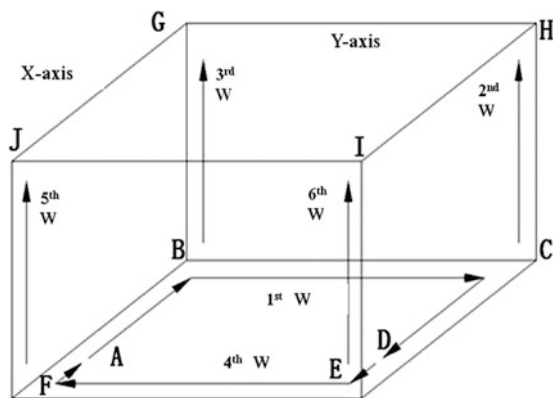
Another situation is when the 6-axis turned around z axis with a rotation  $-180^\circ$ . The primary reason for this is the limitation of the welding accessibility. Thus, the equation could be transformed to

$$T_W^R = \begin{bmatrix} 0 & 1 & 0 & \frac{W}{2} \\ 1 & 0 & 0 & \frac{L}{2} \\ 0 & 0 & -1 & \frac{H_0}{2} \\ 0 & 0 & 0 & 1 \end{bmatrix} \tag{2}$$

Motion planning is a main problem in a given environment. It should be stated as finding a trajectory for a robot, such that the robot can move along this trajectory from its initial weld position to the ending weld position without any colliding with any obstacles in three dimensions. In this case, the longitudinal girders and brackets are formed “#” structure in the inner bottom hull. Accordingly, there are a large number of fillet welds needs to be welded in the shipbuilding. For the single “#” structure, it’s composed of four flat fillet welds and vertical fillet welds, see Fig. 5. The whole welding task was separated into two parts: the first planning path is flat fillet weld along  $A \rightarrow B \rightarrow C \rightarrow D$  direction and  $C \rightarrow H$ ,  $B \rightarrow G$  vertical fillet welds. The second planning path is  $D \rightarrow E \rightarrow F \rightarrow A$  flat fillet welds and  $F \rightarrow J$ ,  $E \rightarrow I$  vertical fillet welds.

The reason for using asymmetry path planning method was to improve the welding quality of the angular point of the inner bottom hull. From the Fig. 5, it can

Fig. 5 The task planning of the inner bottom hull



be seen that the  $A \rightarrow B \rightarrow C \rightarrow D$  and  $D \rightarrow E \rightarrow F \rightarrow A$  welding path planning were conducted at one time. In addition, the posture of the TCP (Torch Center Point) was not considered in the above-mentioned section during welding process. However, the TCP should be rotated  $90^\circ$  when the welding torch was at the corner of the inner bottom hull. Moreover, the posture of the welding torch needed to be adjusted according to the practical work piece.

In order to increase the welding efficiency of the inner bottom hull and decrease the positioning error between a real work piece and its simulation, arc welding robot system were performed as Fig. 6. In this system, it included several functional modules: robot calibration, CAD model acquisition, welding procedure specification setup, off-line programming generation, robot simulation and task management. In this case, the real positioning error could be adjusted according to the assembled condition as shown in bottom picture of in Fig. 6. Also, the arc sensor is used to calibrate the welding torch offset during welding process. To reduce the affect of the assembling deviation, especially positioning deviation after tack welding, touch sensor was applied to the recognition of the welding initial position,

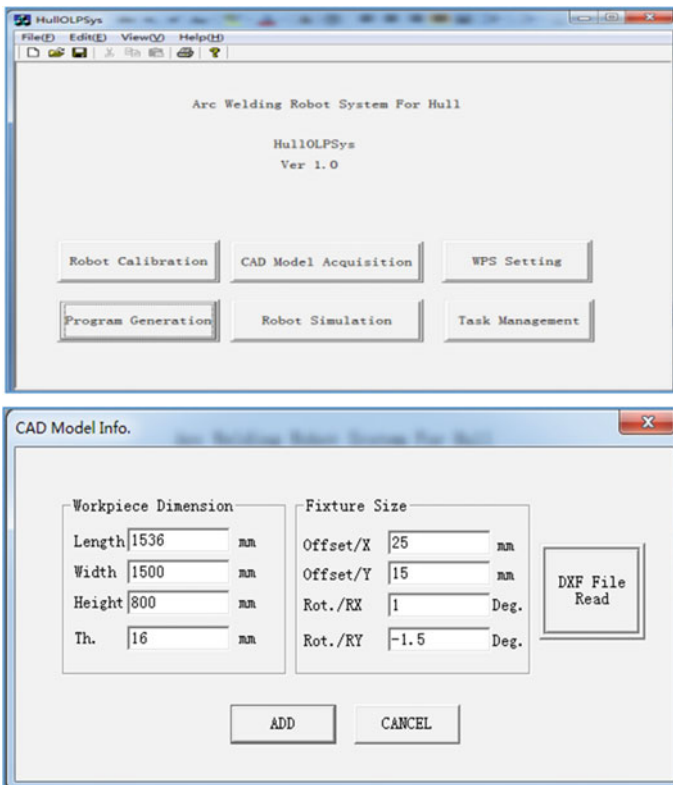


Fig. 6 Inner bottom hull offline programming software system

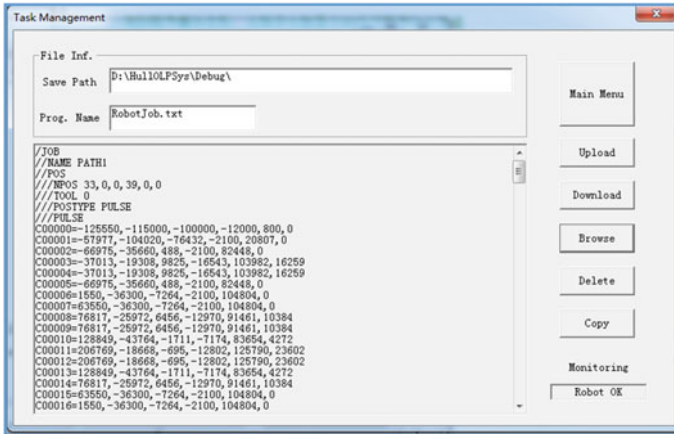


Fig. 7 A snippet of a robot program generated

which can ensure the location and posture accuracy of the welding torch. Therefore it could be avoided torch collision. Returning to the off-line programming module, by clicking CAD acquisition button, the operator could select a certain work piece to convert into a robot program. Second, if the jigs have translation and rotation relative to the X or Y axis of the robot coordinate system, it was needed to correct. Finally, the generated robot program can be simulated and tested. The results would be presented and discussed in the following section.

In the next of this section, the software system could automatically generate robot programs with the information extracted from CAD drawings. Figure 7 illustrates the generation of the robot programs for Motoman controller. The snippet of a robot program generated for Motoman robot shows the seam path planning in combination with the specific point correction of the JBI file. Finally, it is important to note that after generating a robot program, the robot can communicate with computers or other equipment via serial RS232 port or Ethernet. The generated code could be downloaded to the controller smoothly. And for this application interface makes the convenience between the user and the robot controller. Before the welding task, the user can browse the JBI file in the main computer.

### 4 Experiments and Results

The CAD-based arc welding robotic system presented in this paper was designed to perform the welding task of inner bottom hull in shipbuilding, as seen in the left picture of Fig. 8. In the experiment, robot arc welding programs from a CAD model of the cell in which the seam paths described in the form of DXF Point, DXFLine and DXFPolyline. Additionally, the value of the tool center point (TCP) and orientation of the weld torch on the workpiece are also obtained from the software



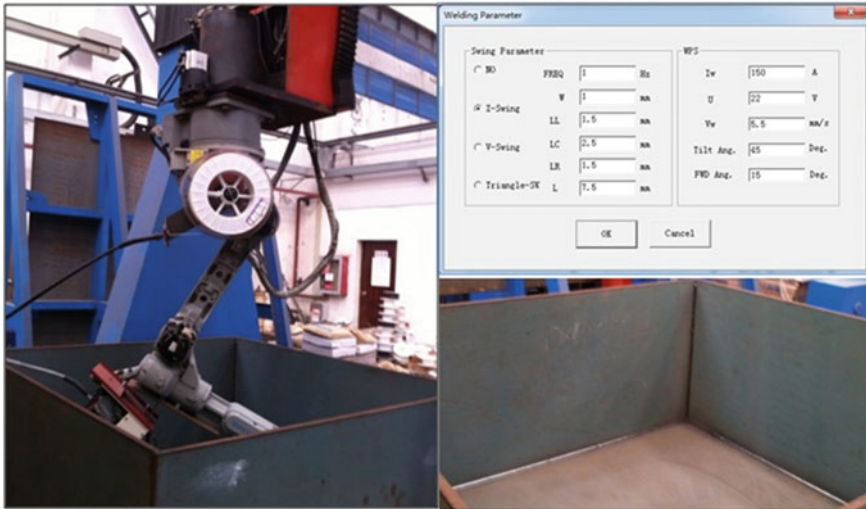


Fig. 8 Arc welding robotic system for inner bottom hull and appearance of fillet weld

system. The experiment demonstrated the reliability and robustness of the proposed CAD-based arc welding robotic system. No matter if is CAD model acquisition or seam path planning, robot program generation or download JBI files, it can be performed successfully without various geometry size workpiece. Through a lot of experiments, the position and orientation of the weld torch could meet the requirements. Also, the algorithm and software are developed that enable all the specific weld point accessibility throughout the robot's entire workspace.

This proposed system was also applied to the hull curved plate of the sub-assembly. After the running of the weld task, the flat fillet and vertical seam were straight, good weld appearance with smooth weld metal was shown in the right picture of Fig. 8. Additionally, the fillet weld size could meet the requirements on the shipbuilding quality standards.

There are still some aspects of this arc welding robotic system for the hull for improvement in our future work. On the one hand, the algorithm to generate robot program, it should be more robust through the vision sensor. This is because that the vision sensor can help to handle the assembly deviation and machine errors in a quick way. On the other hand, hull assembly is the most complex, the development of the highly compatible offline programming software still face difficulties.

## 5 Conclusion

A novel arc welding robotic system in shipbuilding has been studied and tested. The developed offline programming system of inner bottom hull provides robot calibration, inner bottom hull CAD model acquisition, fillet weld path planning, and automatic program generation. Finally, we carried out appropriate verification tests for inner bottom hull on this platform. In combination with the touch and arc sensor, the current path generation from CAD model was revised and compensated further. Through the running of the weld task, the flat fillet and vertical seam were straight, good weld appearance with smooth weld metal. Moreover, the fillet weld size could meet the requirements on the shipbuilding quality standards. Using this system, it has laid the good foundation for future process experiments and application.

**Acknowledgements** This research has been supported by the National Development and Reform Commission Major Project. We wish to thank Chao Zhan and Bojian Zhao for their assistance on experiments and software.

## References

1. Kim C-S, Hong K-S, Han Y-S (2006) Off-line programming, virtual reality simulation and open architecture, industrial robotics: Programming, simulation and applicant. Low Kin Huat, Germany
2. Nagao Y, Urabe H, Honda F, Kawabata J (2000) Development of a panel welding robot system for subassembly in shipbuilding utilizing a two-dimensional CAD system. *Adv Robot* 14(5):333–336
3. Neto P, Pires JN, Moreira AP (2010) CAD-based off-line robot programming. In: *Robotic automation and mechatronics (RAM), 2010 IEEE conference*, pp 516–521
4. Pires JN, Godinho T, Ferreira P (2004) CAD interface for automatic robot welding programming. *Ind Robot Int J* 31(1):71–76
5. Mitsi S, Bouzakis KD, Mansour G, Sagris D, Maliaris G (2005) Off-line programming of an industrial robot for manufacturing. *Int J Adv Manuf Technol* 26(3):262–267
6. Ghosh BK, Xiao D, Xi N, Tam TJ (1996) Multisensor-based robotic manipulation in an un-calibrated manufacturing work cell. *J Franklin Inst* 336:237–255
7. Ahn CK, Lee Mc (2000) An off-line automatic teaching by vision information for robotic assembly task. In: *26th Annual conference of the IEEE, 2000, vol 3*, pp 2171–2176
8. Solvang B, Sziebig G, Korondi P (2008) Robot programming in machining operations. *Robot manipulators*, Marco Ceccarelli
9. Takarics B, Szemes PT (2008) Superflexible welding robot based on the intelligent space concept. In: *7th International symposium of Hungarian researchers on computational intelligence*, pp 791–796
10. Yeasin M, Chaudhuri S (2000) Toward automatic programming: learning human skill from visual data. *IEEE Trans Syst Man Cybern Part B* 30(1):180–185
11. Kim JY (2004) CAD-Based automated robot programming in adhesive spray systems for shoe outsoles and uppers. *J Robot Syst* 21(11):625–634
12. Pan Z, Polden J, Larkin N et al (2010) Recent progress on programming methods for industrial robots. In: *1st International symposium on and 2010 6th German conference on robotics (ROBOTIK)*, pp 1–8

# The Microstructure and Properties of S32750 Multipass Welds

Hua Huang, Jing-Hui Jin and Zhong-Ping Ding

**Abstract** Factors of welding duplex stainless steel S32750 were analysed in this article. The welding parameters were determined in the test. The results show that, with a higher heat input, strictly control of interpass temperature, and using welding wire containing stable austenite elements, reasonable proportion of the two phases could be got in duplex phase stainless steel S32750, while the harmful intermetallic phase was prevented to get.

## 1 Foreword

Duplex phase stainless steel has the advantages of both austenitic stainless steel and ferritic stainless steel, such as excellent toughness, weldability, high strength and good corrosion resistance. It is widely used in engineering of petroleum, chemical, marine. As a typical third generation of duplex phase stainless steel, S32750 has good resistance to pitting corrosion and stress corrosion cracking. With the excellent mechanical properties and PREN > 40, S32750 is suitable for harsh media conditions [1].

The material of seawater inlet pipes was made of S32750 in a power plant. This article did the research about the microstructure and properties of S32750 multipass welds according to the requirements of Chinese standards, and determined the parameters for the welding on site.

## 2 Main Properties of Material

S32750 contains high Cr elements. The welding wire is ER2594. Their chemical composition requirements in ASME are shown in Table 1, and the mechanical properties of S32750 are shown in Table 2.

---

H. Huang (✉) · J.-H. Jin · Z.-P. Ding  
China Nuclear Power Engineering Co., Ltd, Shenzhen, People's Republic of China  
e-mail: hh1983@126.com

**Table 1** Chemical composition of base metal and welding wire (wt%)

	C	Mn	P	S	Si	Ni	Cr	Mo	N	Cu
S32750	0.030	1.2	0.035	0.020	0.8	6.0–8.0	24.0–26.0	3.0–5.0	0.24–0.32	0.5
ER2594	0.030	2.5	0.030	0.020	1.0	8.0–10.5	24.0–27.0	2.5–4.5	0.20–0.30	1.5

**Table 2** The mechanical properties of S3275

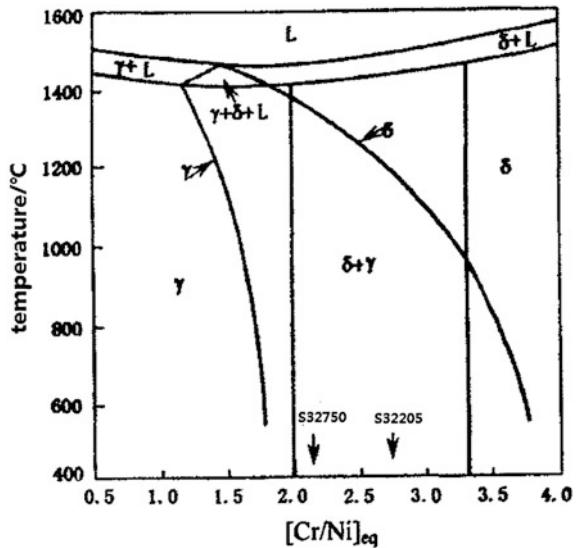
Material	$\sigma_b$ /MPa	$\sigma_{0.2}$ /MPa	Elongation/%	Hardness/HB
S32750	800	550	15	310

### 3 Factors of the Welding Process

For welding of super duplex phase stainless steel, the most prominent problem was how to ensure corrosion resistance and low temperature impact properties of welds. The phase proportion of welds and the intermetallic compounds was a key factor to affect the corrosion resistance and low temperature impact properties.

According to Cr, Ni equivalent weight formula in WRC-1992,  $[Cr]_{eq} = \%Cr + \%Mo + 0.7 \times \%Nb$ ,  $[Ni]_{eq} = \%Ni + 35 \times \%C + 20 \times \%N + 0.25 \times \%Cu$ . The Fe–C–Ni phase diagram was shown in Fig. 1. For the phase diagram, all the phase are complete ferrite when the steel liquid solidified, and this ferrite phase can be retained until the temperature reach ferrite solubility curve. Next only to the lower temperature, part of the ferrite was transformed into austenite.

**Fig. 1** The Fe–Cr–Ni phase diagram



With decreasing temperature of weld pool, the cooling process after solidification was a fast unbalance  $\delta \rightarrow \gamma$  process. If the cooling rate was too fast, with low  $\delta \rightarrow \gamma$  conversion,  $\delta$  phase became more while  $\gamma$  phase became less in the weld metal; Conversely, if the cooling rate was slow with heat input, it would make more  $\delta \rightarrow \gamma$  transformation, and enough  $\gamma$  phase could be obtained, but it also led to get coarse grains,  $\sigma$  phase and precipitation of secondary austenite ( $\gamma_2$ ), which would reduce the corrosion resistance and toughness of welds [2, 3].

The subsequent weld bead had a heat effect to the front layer in multipass welding. Ferrite further transforms into austenite in the weld metal, and austenite become dominant in the two-phase structure. The high temperature zone of heat affected zone (HTHAZ), which was adjacent to the weld, will bear a secondary heat cycle. So after subsequent cooling, HTHAZ will get more austenite phase, and the microstructure and properties of welds will be significant improved [2]. It was noteworthy that surface layer of HTHAZ was not subjected to the second heat cycle, so this HTHAZ could not often get the two satisfactory phases ( $\gamma$  phase only reached 20–30 %). It was recommended in some literatures [2], a surplus weld would be applied to surface weld. After the surface layer bear the second heat cycle, the surplus weld would be removed by grinding. If it was very difficult to do the surplus weld, the layer which will contact with working medium should be welded first, and the layer which will not contact with working medium should be welded in the final step.

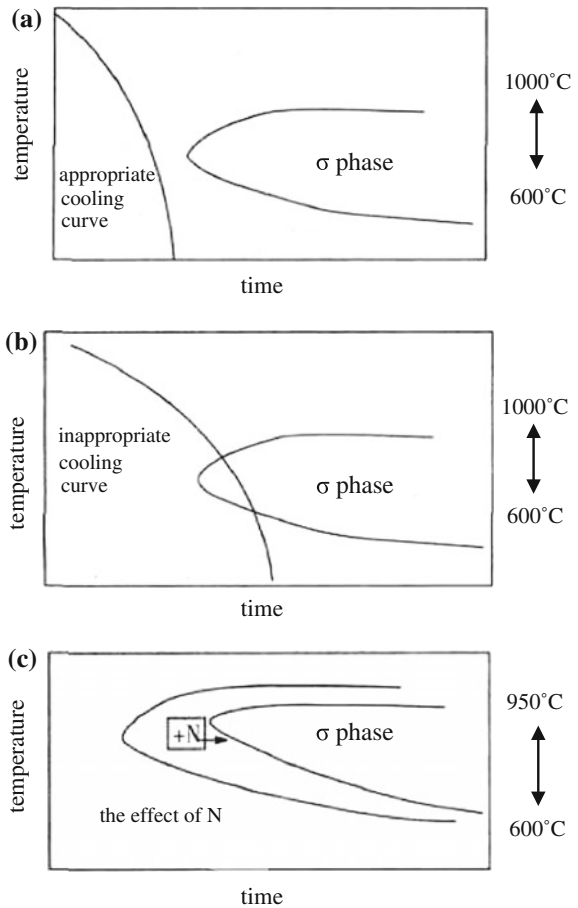
Most research [1, 4–6] suggest that, interpass temperature of duplex phase stainless steel should be controlled below 150 °C. That ensured to form a reasonable proportion of the weld phase, and reduce intermetallic phases.

According to the research for formation and increase of austenite, the effect of N was far greater than Ni. At high temperatures, N also has better ability of stabilizing austenite than Ni. After welding, a single ferrite phase can be prevented to form by the element of N. The curve of  $\sigma$  phase formation was shifted to the right by the element of N, so the cooling time was sufficient to ensure no formation of  $\sigma$  phase, as shown in Fig. 2. For the role of N, many studies suggest to add 2–3 % of nitrogen to protective gas. But even in Sweden, which was experienced in the welding of duplex phase stainless steel, these mixed gas was not widely used. For the operation and effect [7], adding nitrogen to protective gas will accelerate the loss of tungsten electrode, made the arc unstable to cause splashing, and increase the tendency to pores. If the content of N element in the welding material was enough, by improving the quality of gas protection to minimize the loss of N [5], pure argon could be directly used as the protective gas.

## 4 The Welding Process

The base metal of welding test was  $\phi 610 \times 9.53$  mm pipe. The groove form and welding sequence was shown in Figs. 3 and 4. Before welding, the groove and around 25 mm of the groove was polished until metallic luster could be saw.

**Fig. 2** Relationship of  $\sigma$  phase formation between the cooling curve and the element of N. **a** The  $\sigma$  phase was not formed. **b** The  $\sigma$  phase was formed. **c** The curve of  $\sigma$  phase formation was shifted to the right by the element of N



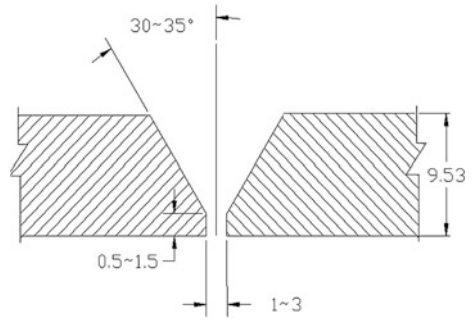
ER2594 welding wire was used for TIG welding. The specification of ER2594 was  $\phi$  2.4 mm. The swing method of weld wire was zigzag.

The back side of first welding layer was protected by a purity of 99.99 % argon until the third welding layer was finished. The flow of 99.99 % argon for back side was 6–15 L/min. The interpass temperature was controlled below 150 °C. The welding parameters were shown in Table 3.

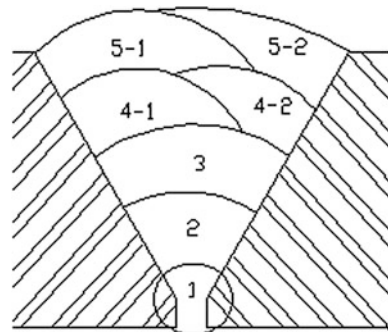
## 5 Test Methods and Results

The weld specimen was assessed by following items.

**Fig. 3** The groove of well



**Fig. 4** The welding sequence



**Table 3** The welding parameters

The number of welding layer	Polarity	Welding current (A)	Voltage (V)	Welding speed (mm/min)	Argon flow of welding torch (L/min)
1-3	DCSP	65-120	9-12	60-80	6-12
4-5	DCSP	70-120	9-12	8-90	6-12

### 5.1 Appearance and Penetration Test

No undercut, porosity, cracks were found on the surface of welded joint. According to JB/T4730.5 standard, the penetration test was done to welded joint, and the result was Class I.

### 5.2 Radiographic Examination

According to DL/T821 standard, radiographic examination was done to welded joint, and the result was Class I.

### 5.3 Tensile Test

Tensile specimens were machined according to GB/T2651 standard. The result was shown in Table 4. The tensile strength of each sample was higher than the lower limit tensile strength of the base metal S32750.

### 5.4 Bending Test

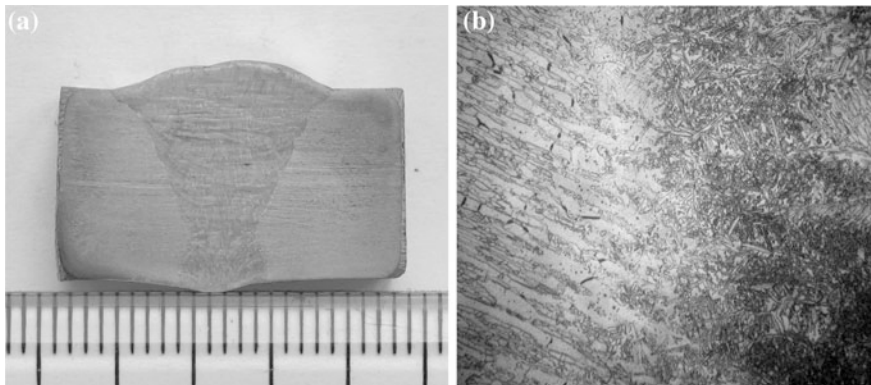
Bend specimens were machined according to GB/T2649 standard and GB/T2653 standard. Six bend specimens should be made according to DL/T1117 standard: Two specimens for face bending, two specimens for back bending, and four specimens for side bending. All bending test were qualified.

### 5.5 Metallography

According to DL/T884 standard, metallographic specimen was made. Macroscopic and microscopic photos were shown in Fig. 5.

**Table 4** The tensile strength result

The number of tensile specimen	Tensile strength $\sigma_b$ /MPa	Fracture position
1#	858	Base metal
2#	853	Weld joint



**Fig. 5** Metallography. **a** Macroscopic photo  $\times 3.5$ . **b** Microscopic photo  $\times 200$



Austenitic and ferritic structure was found in heat affected zone and welds. No microcrack was found.

### 5.6 Hardness Testing

According to GB/T2654 standard, hardness testing was carried out in weld joints, heat affected zone, and base metal. Every row of different region had three separate dent point, as it was shown in Fig. 6. The test results were shown in Table 5.

According to DL1117 standard, if the content of nickel was above 3 % and steel without heat treatment, the hardness value should be less than or equal to 450HV. The welding joint met the requirements of hardness value in the test.

### 5.7 The Test of Ferrite Content

According to GB/T1954 standard by using magnetic method, ferrite content in five areas of the welds was respectively 38.8, 42.6, 37.6, 39.7, and 40.5 %, with an average of 39.8 %.

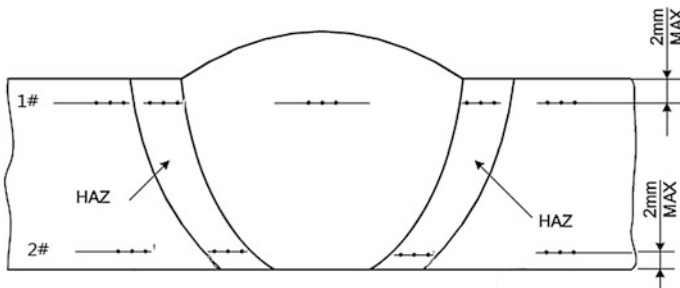


Fig. 6 Location of dent point for hardness testing

Table 5 Hardness value

The number of tensile specimen	Hardness value of base metal/HV	Hardness value of heat affected zone/HV	Hardness value of welds/HV
1#	297, 297, 297, 306, 306, 302	299, 302, 302, 290, 297, 306	270, 270, 283
2#	292, 292, 297, 292, 292, 287	302, 302, 306, 322, 311, 306	306, 311, 302

## 6 Analysis of Test Results

Lower limit of the tensile strength for S32750 was 795 MPa. Although the fracture position of 2# specimen was located in the weld area, the tensile strength was higher than 795 MPa, which was still within the qualified scope. The result of radiographic examination and penetration test were both Class I. The surface of bend specimen was without cracks.

The hardness values of the weld near the covering layer were slightly lower than the hardness values of backing layer. The subsequent weld bead had a heat effect to the front layer in multipass welding, and ferrite further transforms into austenite in the weld metal. So the ferrite of covering layer was relatively more than the one of backing layer, which led the hardness value of former was low.

Austenitic and ferritic structure was found in heat affected zone and welds. The average of ferrite content was 39.8 %, meeting the requirement of single phase who does not exceed 65 %.

## 7 Conclusion

1. With a higher heat input, strictly control of interpass temperature, and using welding wire containing stable austenite elements, reasonable proportion of the two phases could be got in duplex phase stainless steel S32750, while the harmful intermetallic phase was prevented to get.
2. The welding parameters were determined: By using TIG welding, the back side of first welding layer was protected by a purity of 99.99 % argon until the third welding layer was finished. The flow of argon for back side was 6–15 L/min. The interpass temperature was controlled below 150 °C. The voltage was 9–12 V, and argon flow of welding torch was 6–12 L/min. The welding current of first to third layer was 65–120 A, while the welding speed was 60–80 mm/min. The welding current of fourth to fifth layer was 70–120 A, while the welding speed was 80–90 mm/min.

20 seawater inlet pipes were welded with above parameters, and the qualified rate of penetration test and radiographic examination was 100 %, which also confirmed the correctness of the welding parameters.

## References

1. Liu Y (2007) The confirmation about welding technology between S32750 (SAF2507) super duplex stainless steel tube and tube-sheet. *Mod Weld* 12:34–36
2. Yanli S (2007) Influence of welding technology on properties of 2205 dual phase stainless steel. *Weld Joining* 6:47–51

3. Lihua Gong (2010) Corrosion resistance of super duplex stainless steel welded joint. *Trans China Weld Inst* 31(7):59–63
4. Cang Wang (2011) Discussion on S32750 super duplex stainless steel welding technology. *Machinist Metal Forming* 62(8):54–56
5. Qiang Li (2011) Argon arc welding. *Pet Chem Constr* 33(1):48–50
6. Li W (2012) Welding of UNS S32750 super duplex stainless steel for seawater desalination plant. *Modern Weld* 5:33–38
7. Qiang Li (2012) The manufacture technology of super duplex stainless steel thin wall storage. *Pet Chem Constr* 34(4):70–74

# Microstructure, Mechanical Properties of Welded Joints of F22 and F91

Min-Li Ma and Xi-Zhang Chen

**Abstract** This paper introduces the welding producers of F22 and F91 which is used in high pressure forged steel valves inside hydrogenation unit, and also presents the tensile test, bend test, hardness test, impact test and microstructure observation of the weld joints. The experimental results are as follows: the microstructure of welds is acicular ferrite; the weld tensile strength is higher than that of base metal F22; tensile specimen fracture in the side of base metal F22 which strength is relatively lower; the impact absorbed energy is higher than the EU PED standard 27 J; welded joints are well adapted to harsh working environment.

## 1 Introduction

Due to the successful development of high pressure forged steel valves used for hydrogenation unit in china, F22 steel and F91 steel which can bear high temperature and high pressure have been widely used in recent years. F22 steel is a kind of low alloy steel which produced by quenched and tempering. It has good mechanical properties and corrosion properties due to the fine distribution of molybdenum carbides and amount of chromium [1]. F91 steel is a kind of heat-resistant steel which microstructure is tempered martensite, it has many advantages such as high allowable stress, high persistent strength, high fatigue strength, high ability of creep, high corrosion resistance and oxidation resistance [2]. The maximum service temperature of F91 steel reaches to 650 °C. It has been

---

M.-L. Ma  
Nantong Vocational University, Nantong 226007, China

X.-Z. Chen (✉)  
College of Mechanical and Electrical Engineering, Wenzhou University,  
Wenzhou 325035, China  
e-mail: chenxizhang@wzu.edu.cn

widely used in high temperature and high pressure parts for the advantage of excellent high temperature performance [3].

Figure 1 shows a forged steel brake valve produced by a company from Nantong, the valve body and valve seat are made of F22 and F91 forging steel, respectively. Because of the relative more concentration of alloying elements and the relative bigger performance differences between these two steels, welding defects such as cold and hot cracks often appear in the welding process of valve body and valve seat. This experiment adopted the flux cored arc welding (FCAW) for welding the F22 and F91 steel, did the mechanical properties such as tensile, bending, impact and hardness test for welded joints, and also did the analysis of the microstructure and fracture morphology of welding seam and heat affected zone. We researched the influence from welding materials and weld heat input to joint microstructures, mechanical properties and impact toughness of weld zone. The results lay the foundation of dissimilar steel welding between F22 and F91 steel and provide a fine technical support for the high pressure forged steel valves which used for hydrogenation unit.

## 2 Experimental Materials and Methods

Experimental welding base metals are forging steel plates of F22 and F91 steel, the thickness are 40 mm, supply status are tempered sorbite (Figs. 2 and 3); welding materials are low alloy steel flux-cored wires E91T1-B3C with the diameter of 1.2 mm; Table 1 shows the chemical composition and mechanical properties of F22 steel, F91 steel and deposited metal of flux-cored wires E91T1-B3C.

The welding equipment is YD-350GR3 CO<sub>2</sub> gas shielded welder produced by Tangshan Panasonic industrial machinery co. Ltd.; the size of welding procedure test plates is 350 mm (direction of weld bead) × 150 mm (direction of rolling) × 40 mm, as shown in Fig. 4, the joint type is butt joint, the groove type is Y. This experiment employed the multi-layer and multi-pass welding. Figure 5 shows the specific welding sequence.

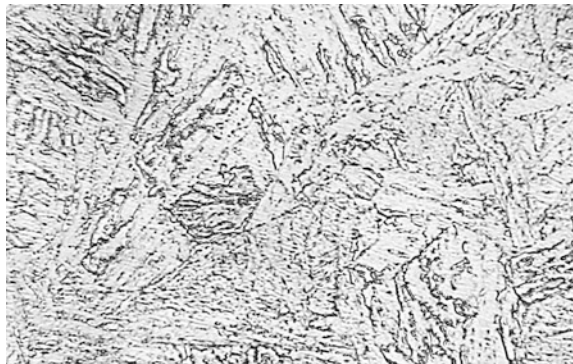
The Y-groove cracking sensitivity test was conducted according to GB/T4675.1 Method of Y-groove cracking test. The size of welding procedure test plates is 200 mm (direction of weld bead) × 75 mm (direction of rolling) × 8 mm (thickness). The length of the test weld is 80 mm, the groove type is inclined Y, the foot height is half of the thickness. The length of constraint welds on both sides is 60 mm, the groove type is X and the foot height is half of the thickness. The constraint welds (double sided welding) and the test weld were all welded by using solid wire WH80-G. Table 2 shows the process parameters of Y-groove cracking test, without heat treatment after welding. Dye penetrant inspection were used to inspect surface cracks and root cracks after 48 h, mechanical processing and polishing corrosion were used to inspect section cracks.

The experiments and inspections were conducted according to EN15614 Specification and qualification of welding procedures for metallic materials—

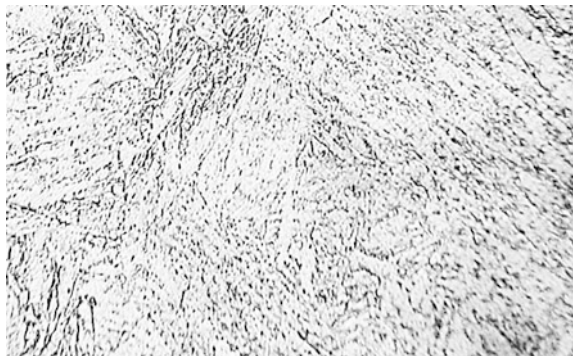
**Fig. 1** A forged steel brake valve produced by a company from Nantong, China



**Fig. 2** Microstructures of the base metal F22



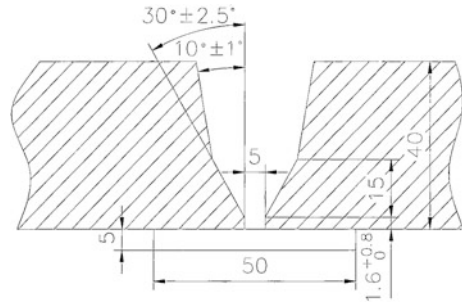
**Fig. 3** Microstructures of the base metal F91



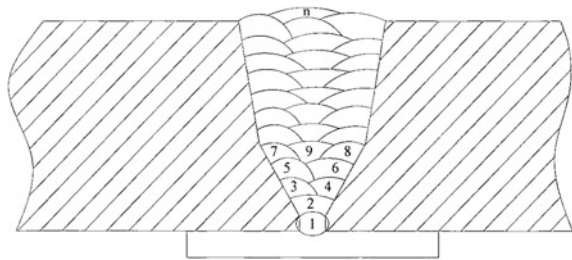
**Table 1** The mass fraction and mechanical properties of F22 steel, F91 steel and deposited metal of flux-cored wires E91T1-B3C

Materials	C	Mn	P	S	Si	Cu	Cr	Ni	Mo	ReI/MPa	Rm/MPa	$\delta$ (%)	$\psi$ (%)
F22	0.13	0.36	0.007	0.009	0.23	–	2.15	–	0.93	435	372	23	48
F91	0.10	0.41	0.01	0.004	0.31	–	8.24	0.38	0.87	712	569	25	71
E91T1-B3C	0.052	0.86	0.015	–	0.28	0.02	2.14	0.47	0.977	655	725	17	

**Fig. 4** The joint type and groove type



**Fig. 5** The welding sequence



**Table 2** Welding parameters

Welding layers	Welding method	Filler metal		Current		Voltage range (V)	Welding speed (mm/s)
		Class	Diameter	Polar	Current (A)		
Root	FCAW	E91T1-B3C	Φ1.2	DCRP	160–200	20–28	3.0–6.0
Filler	FCAW	E91T1-B3C	Φ1.2	DCRP	180–230	20–28	3.0–6.0
Cover	FCAW	E91T1-B3C	Φ1.2	DCRP	180–230	20–28	3.0–6.0

Welding procedure test—Part 1: Arc and gas welding of steels and arc welding of nickel and nickel alloys. Table 3 shows the content and species of our experiment.

The specimens were cut from the qualified parts according to EN15614 after passing non-destructive testing.

The appearance inspections were done to specimens according to EN970.

The radiographic testing was conducted according to ASTM IX Qualification Standard for Welding and Brazing Procedures, Welders, Brazers, and Welding and Brazing Operators. The specimens were detected by using flaw detector XCF-3005Q referring to EN1435. Agfa films were used; osmosis grade was A; Tube voltage was 290 kV; the distance from specimen to film was 700 mm and the exposure time is 7 min.



**Table 3** The content and species of the experiment

Experimental species	Appearance inspection	Radiographic testing	Surface cracks detection	Transverse tensile	Transverse bending
Experimental content	100 %	100 %	100 %	2 specimens	4 specimens
Experimental species	Impact test	Hardness test	Low multiples metallographic test		High-expansion metallographic test
Experimental content	2 groups	1 specimen	1 specimen		Not required

Surface cracks detection was conducted according to ISO03452. HD-RS penetrant, HD-BX cleaner and HD-EV imaging agent were used in the experiment, the penetration time should be greater than or equal to 10 min under the temperature conditions between 10 and 50 °C. Observation should be done in 7–30 min later after applying imaging agent.

Then producing metallographic specimens, the specimens size of base metal was 15 mm × 20 mm × 10 mm which were cut in 1/4 thickness of the 40 mm thick steel plate and far away from the weld. The specimen size of welded joints was 20 mm (perpendicular to the weld) × 20 mm × 40 mm, contained the areas of base metal, heat affect zone and weld, weld was located in the center of the specimen. After being grinded, polished and corroded by 4 % nital for 4 s, specimens were placed in the field emission scanning electron microscope JSM-7001F for observing the microstructure morphology. Impact toughness test was conducted by using pendulum impact testing machine JBC-300B according to GB/T2650-2008, the specimen size was 55 mm × 10 mm × 5 mm, the V-notch of weld impact specimen was located in the center of weld, the V-notch of heat affected zone impact test specimen was located in the heat affected zone (1.5 mm far from the surface of weld fusion line), the gap plane was perpendicular to the surface of the specimen, the groove depth was 2 mm, the test temperature was 20, 0, −20, and −40 °C respectively. Cold bending test were conducted according to GB/T2653-2008 Bend test methods on welded joints, surface bending and back bending test were conducted on hydraulic universal testing machine WE-300A. Tension test at room temperature was conducted according to GB/T2651-2008 Tension test method on welded joints, the test plate size was 55 mm × 350 mm × 8 mm, the tensile fracture was observed by using scanning electron microscope JSM-7001F, the SEM photos of fracture morphology was photographed by using electronic scanner PHILIP-XL30. Specimens after metallographic observation were selected for microhardness test; the test was conducted according to GB/T2654-2008 Hardness test methods on welded joints, the load and hold time was 0.5 N and 20 s, respectively. As shown in Fig. 2 position 1 (2 mm distance from the upper surface), microhardness test was conducted in every 0.3 mm from one side of the base metal through weld to the other side; and then the same test was conducted in position 2 (2 mm distance from the lower surface).

### 3 Experimental Results and Analysis

#### 3.1 Appearance Inspection

Table 4 shows the results of specimen appearance inspection; defects of the quality grade can permissible limits for class B according to EN25817. The height of weld should be not less than the surface of base metal, weld and base metal should be smooth transition. When the weld is lower than the base metal, the bearing cross-sectional area will be reduced and the strength will be weakened. But when the weld is much higher than the base metal, the cross-sectional mutation will easily cause the stress concentration. Excess weld metal can in theory improve the bearing ability of the weld cross-section, but it will cause the stress concentration and the falling of fatigue life when the excess weld is too large. Practice has proved that excess weld does not have much effect on strengthening the joint

Crack is the most harmful one of welding defects; it is caused by the local fracture of materials. Bearing area is significantly reduced when cracks appear. Sharp gap is formed in the crack tip and became the area of stress concentration; the crack tip is easy to extend leading to destruction. Therefore, cracks must not be allowed to exist in the boiler and pressure vessel.

The edges and corners of dregs are likely to lead to stress concentration; it will become fatigue source under the cyclic loading. Dregs are mainly come from the electrode coating and the flux slag. It is necessary but often being overlooked to clean the dregs on the surface. When I worked for product inspection in a manufacturing enterprise, I found that an organic heat carrier furnace did not appear any abnormal situation such as leakage in the beginning of the hydrostatic test. When checked the fillet weld that connects the smoke tube and the boiler shell, it was found that there were dregs on the weld surface, and then we asked workers to clear the dregs. Works felt that there was fine water injected to hand in the clean process. Water jet out could not be observed by naked eyes without any other inspection tools. It was found that a very fine water beam jetted out and presented a faint light

**Table 4** Appearance inspection results of welding specimen

Inspection items		Excess weld metal	Back excess height	Weld width	Crack	Lack of fusion	Lack of penetration	
Result	10459 specimens	8–1.5 mm	No	About 30 mm	No	No	No	
	10460 specimens	1.2–2 mm	No	About 30 mm	No	No	No	
Inspection items		Misalignment	Undercut	Tungsten inclusion	Dregs	Root concavity	Overlap	Back concavity
Result	10459 specimens	No	No	No	No	No	No	No
	10460 specimens	No	No	No	No	No	No	No

by using a flashlight. It was obviously found the water leakage after cleaning up the dregs. If the other defects were failed to check out caused by not completely clear the exterior surface of the equipment, potential safety hazard will exist when the equipment is put into operation, especially for the equipment which hold flammable or toxic medium.

Porosity will also reduce the strength of welding structure. The main reason is that the defects reduce the bearing sectional area of welding structure and cause stress concentration in the edges of the defects. In the high stress concentration area, the stress concentration may lead to craze in the edges of porosity and gradually extend to cracks. The stress concentration will become more serious.

Undercut not only thinning the base metal, but also forming geometric discontinuity between weld and base metal, forming stress concentration, making the reduction of weld strength. It is often caused by large welding current however the electrode moves too fast. Undercut can be polished to a smooth transition in order to eliminate the stress concentration if the thickness of base metal could meet the strength requirement.

For the pressure vessel, undercut must not be existed on weld surface of vessels made of steel which standard tensile strength lower limit is greater than 540 MPa, Cr–Mo low alloy steel, stainless steel and vessels which welding joint coefficient is 1. Undercut on weld surface of other vessels should not be longer than 0.5 mm; continuous length should not be greater than 100 mm and the overall length on both sides of the weld should not be exceed 10 % of the weld length.

For the steam boiler, undercut must not be existed in longitudinal seam, girth seam and butt seam of the shell cover or tube sheet in the boiler shell, tank and header. The depth of undercut in other welds should not be greater than 0.5 mm; the overall length on both sides of the pipe weld should not be exceed 20 % of the pipe perimeter and should no be greater than 40 mm.

### ***3.2 Radiographic Testing***

The inspection results of specimens 10459 and 10460 are grade 1. Therefore, they can be received.

### ***3.3 Surface Crack Detection***

Mechanical property test and sampling method were conducted according to ASTM A370-12 Standard Test Methods and Definitions for Mechanical Testing of Steel Products.

### 3.4 Tensile Test

The tensile test equipment is a computer screen explicit hydraulic universal testing machine WEW-1000B; Fig. 6 shows the processing size of the specimen. Table 5 shows the tensile test parameters and results. Results are as follows: the tensile strength of welded joint is more than 550 MPa, which satisfies the tensile strength requirement of base metal F22. Tensile specimen fractured in the base metal F22 which strength was relatively lower.

### 3.5 Bending Test

Both bending test and tensile test devices are the same, Fig. 7 shows the processing size of the specimen. Table 6 shows the results of 180° lateral bending test. The results of 180° lateral bending test are qualified.

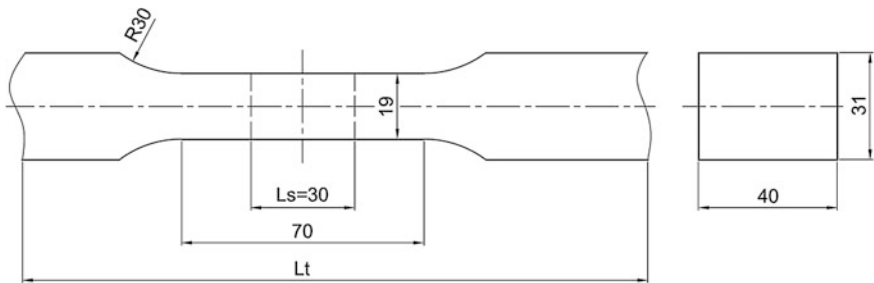


Fig. 6 The processing size of tensile test specimen

Table 5 The tensile test parameters and results

	Tensile strength/N/mm <sup>2</sup>	The nature and location of destroy
10460-1	560	Base metal (F22)
10460-2	550	Base metal (F22)

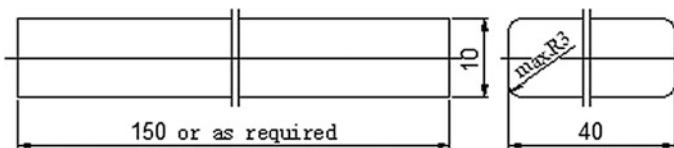


Fig. 7 The processing size of bending test specimen

**Table 6** The results of 180° lateral bending test

Specimen no.	Quantity	Result	Specimen no.	Quantity	Result
10460-3	1	Qualified	10460-5	1	Qualified
10460-4	1	Qualified	10460-6	1	Qualified

The results of tensile test and bending test show that the strength of welded joint is higher than base metal, the toughness of welded joint is much better and the performance of weld is high.

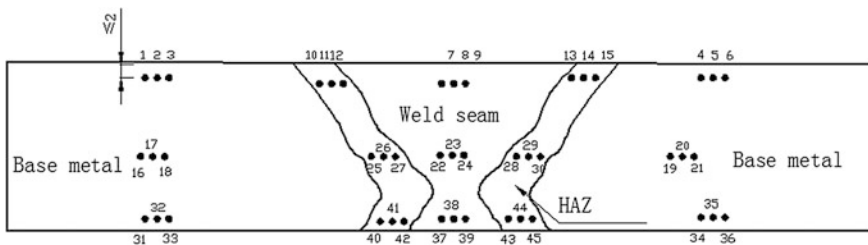
### 3.6 Hardness Test

The hardness test equipment is a Vickers hardness tester HVS-50. Figure 8 shows the measuring points distribution of hardness test; the scale of test force is HV10; the results are shown in Table 7.

As shown in the above experiment, the average hardness of weld metal layer is 226.9HV. The average hardness of base metal F22 and HAZ are 231.8HV and 243.1HV, respectively. The average hardness of base metal F91 and HAZ are

**Table 7** The results of hardness test

	Base material						Welding line			HAZ					
Measuring points	1	2	3	4	5	6	7	8	9	10	11	12	13	14	15
Hardness	237	228	234	243	238	234	228	238	228	253	242	251	263	268	266
Measuring points	16	17	18	19	20	21	22	23	24	25	26	27	28	29	30
Hardness	235	227	233	242	239	247	232	223	216	241	246	249	256	260	247
Measuring points	31	32	33	34	35	36	37	38	39	40	41	42	43	44	45
Hardness	231	232	229	234	238	236	221	221	235	239	235	232	238	247	242



**Fig. 8** The measuring points distribution of hardness test

239.0HV and 254.1HV, respectively. For the weld center, although the hardness is overall decline, because of the further proliferation of element in both sides of the weld, near weld area on both sides of base metal has a high hardness than the base metal F22 and F91; it also ensures the strength of the weld area. It reaches an agreement with the results of the tensile test and the bending test.

### 3.7 Impact Test

The impact test equipment is an ultra-low temperature automatic impact testing machine JBD-300D, Fig. 9 shows the location and processing size of the specimen, the impact position is the weld area of welded joint. Table 8 shows the impact test parameters and results.

The results are as follows: the impact absorbing energy of welded joint reached to 72.3 J when the specimen was impacted in 24 °C, much higher than the EU PED standard 27 J; The impact absorbing energy of welded joint was 27.7 J in -15 °C, satisfied the EU PED standard 27 J.

The results show that the toughness of weld joint can meet the requirement of the EU PED standard.

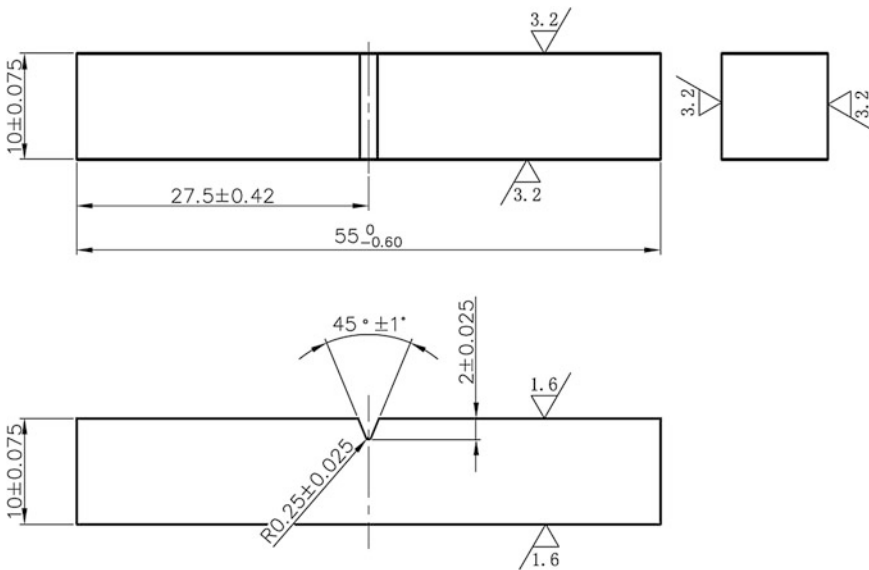


Fig. 9 The location and processing size of the specimen

**Table 8** The results of impact test

Specimen no.	Test temperature (°C)	Impact value (J)
10460-1	24	79
10460-2	24	74
10460-3	24	64
10460-4	-15	28
10460-5	-15	28
10460-6	-15	27

## 4 Microstructure Analysis

The microstructures of the weld center, the fusion line by the side of F22 steel and the fusion line by the side of F91 steel were observed by using digital metallographic microscope. The results are shown in Figs. 10, 11 and 12, the results meet the requirement of NB/T47014, NB/T47015, NB/T47016-2011 Welding procedure qualification for pressure equipment.

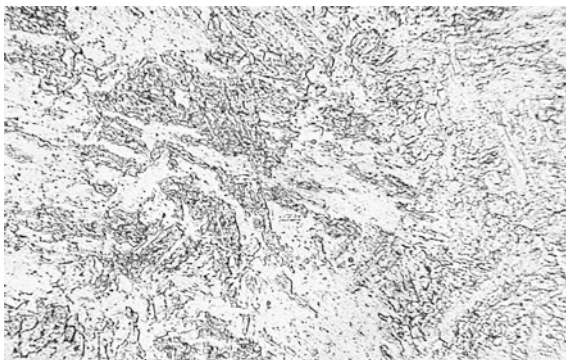
It can be seen that the microstructures of weld center are mainly acicular ferrite, a tiny amount of spheroidal pearlite and divorced pearlite; grains are fine and evenly distributed. The white substrate in the fusion line by the side of F22 steel is ferrite; the small dot objects are all carbide, and the grain size is fine. The white substrate in the fusion line by the side of F91 steel is ferrite; most of the pearlite is nodulized, and the grain size is fine.

The above results show that the welding procedures is rational; the welding parameters are suitable and the welding organization is preferable.

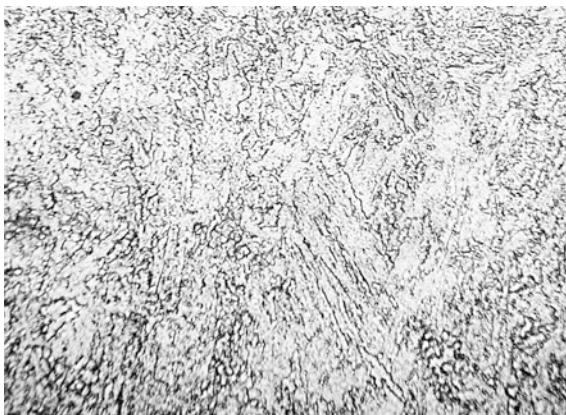
**Fig. 10** 400× Aqueous solution of ferric chloride (the weld center)



**Fig. 11** 500× Aqueous solution of ferric chloride (the fusion line by the side of F22 steel)



**Fig. 12** 500× Aqueous solution of ferric chloride (the fusion line by the side of F91 steel)



## 5 Conclusion

The welding procedures of dissimilar steel F22 and F91 has been applied in products shown in Fig. 1; these products have been used in petrochemical enterprises of CHINA, AMERICA and SPAIN, etc. In the past two years, quality problems such as early failure did not appear in welded joints; the weld quality is reliable enough to adapt to the bad working environment of high pressure hydrogenation valves.

## References

1. Fallahmohammadi E, Bolzoni F, Fumagalli G et al (2014) Hydrogen diffusion into three metallurgical microstructures of a C–Mn X65 and low alloy F22 sour service steel pipelines. *Int J Hydrogen Energy* 39(25):13300–13313



2. Wang FS, Chen SJ, Gao Z (2008) Effect of melting point depressant elements on the microstructures and properties of T91 steel transient liquid-phase bonding joint. *Electric Weld Mach* 38(11):18–21
3. Shen XF (2013) Stress rupture performance and microstructure variation for welded joint of F91 steel made by hot wire NG-TIG. Shanghai Jiao Tong University

# Enhanced Active Control of Metal Transfer in GMAW

Jun Xiao, Shu-Jun Chen, Guang-Jun Zhang and Yu-Ming Zhang

**Abstract** An optimized current waveform is proposed in this study to first excite enhanced droplet oscillation and then utilize it to enhance the droplet detachment. The excitation is intentionally generated by reducing the current from a peak level, referred to as the exciting peak, to the base level. Another peak level, referred to as the detaching peak, is then applied after a time interval called the detaching phase delay to synchronize the detaching action with the beneficial droplet momentum as a phase match such that the droplet detachment is enhanced by the beneficial momentum. The active metal transfer control utilizing the enhanced droplet oscillation, referred to as the enhanced active metal transfer control, is further systematically studied in this paper. Experimental research shows that the minimum detaching peak current in the enhanced active metal transfer control is not only remarkably lower than the spray transition current, but also significantly lower than that of the original active control process.

## 1 Introduction

Pulsed gas metal arc welding (GMAW-P) produces drop spray transfer at a wide range of average current lower than the spray transition current by applying a pulsed current waveform [1, 2], however, the peak current still must be higher than the spray transition current [3–5]. The active metal transfer control by utilizing an

---

J. Xiao · S.-J. Chen (✉)

The Welding Research Institute, Beijing University of Technology, Beijing, China  
e-mail: sjchen@bjut.edu.cn

G.-J. Zhang

The State Key Lab of Advanced Welding and Joining, Harbin Institute of Technology, Harbin, China

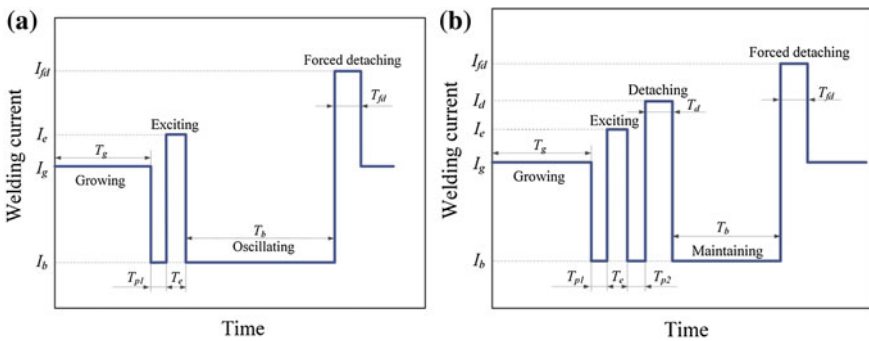
Y.-M. Zhang

The Institute for Sustainable Manufacturing and Department of Electrical and Computer Engineering, University of Kentucky, Lexington, KY, USA

excited droplet oscillation is an innovative method to achieve robust drop spray transfer in GMAW-P with reduced peak current lower than the spray transition current [6, 7]. As an evolution to the original active control, an optimized current waveform was proposed to achieve stronger droplet oscillation at lower currents [8]. As shown in Fig. 1a, the droplet grows during the growing period, and gets elongated during the exciting pulse. At the falling edge of the exciting pulse the droplet springs back to the wire tip and starts to oscillate. It is the droplet downward momentum that can be synchronized with a detaching peak to enhance the droplet detachment, thereby, the detaching peak current can be reduced to be lower than the spray transition current. The synchronization between the droplet downward motion and detaching pulse, referred to as the phase match, is prerequisite for effective utilization of the beneficial droplet momentum. The active metal transfer utilizing such enhanced droplet oscillation is studied in this paper to reveal its advantage in reducing the detaching peak current.

## 2 Approach

Two current waveforms are used to conduct the experiments: (1) the one shown in Fig. 1a, denoted as Wave1; (2) the one inheriting from Wave1 by inserting a relatively low detaching pulse with a detaching phase delay, denoted as Wave2 and as shown in Fig. 1b. Wave1 allows fully observation of the enhanced droplet oscillation to measure key variables such as the optimal detaching phase delay and the oscillation frequency. For Wave2, it will be used to conduct the resultant enhanced active metal transfer control experiments. In all the experiments below, the following parameters are fixed:  $I_g = 80$  A,  $T_g = 20$  ms;  $I_b = 30$  A,  $T_{p1} = 2$  ms,  $I_{fd} = 175$  A,  $T_{fd} = 5$  ms. Thus the initial droplet diameter before the exciting pulse in all the experiments is controlled to be 1.2 mm approximately. The following terminologies are defined: (1) The moment when the excited droplet reaches its



**Fig. 1** Waveform for enhanced droplet oscillation and detachment **a** for enhanced oscillation **b** for active metal transfer control

maximum elongation is referred to as the elongation peak moment; (2) The moment when the droplet changes its moving direction from upward (toward the wire) into downward (away from the wire) is referred to as the oscillation reversing moment; (3) The time interval between the end of the exciting pulse and the start of the detaching pulse is referred to as the detaching phase delay, denoted as  $T_{p2}$ , which determines the phase match. Further, if the detaching pulse starts exactly at the reversing moment, the resultant detaching phase delay is referred to as the optimal detaching phase delay, denoted as  $T_{p2}^*$ , and the oscillation can be fully utilized.

### 3 Experimental Setup

Figure 2 shows the experimental system including the welding cell, data acquisition system, high-speed camera and the controllers. The power source works in constant current mode. The arc length is controlled to be stable by regulating the wire feed speed based on arc voltage feedback. An embedded controller is designed to compute the current output waveform and adjust the wire feed speed. The data acquisition system and high-speed camera are triggered by the same 5 V TTL signal, thus the recording of the actual current waveform and metal transfer are synchronized. The recording frequency is set at 5000 Hz. All the welding experiments are conducted as bead-on-plate welding with 3 mm/s travel speed and 15 L/min pure argon shielding gas. The base metal is mild steel; the wire is ER70S-6 with 0.8 mm diameter; and the distance from the contact tip to the workpiece is set at 12 mm. If not otherwise specified, the arc length in the experiments is approximately 6 mm.

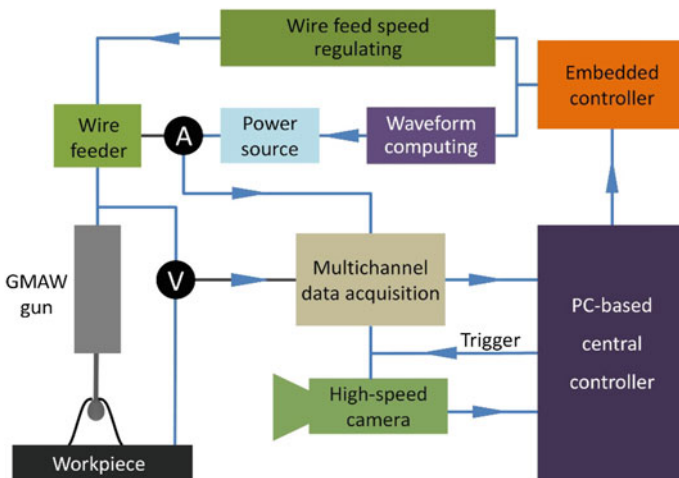


Fig. 2 Sketch of experimental system

### 4 Effect of Exciting Parameters

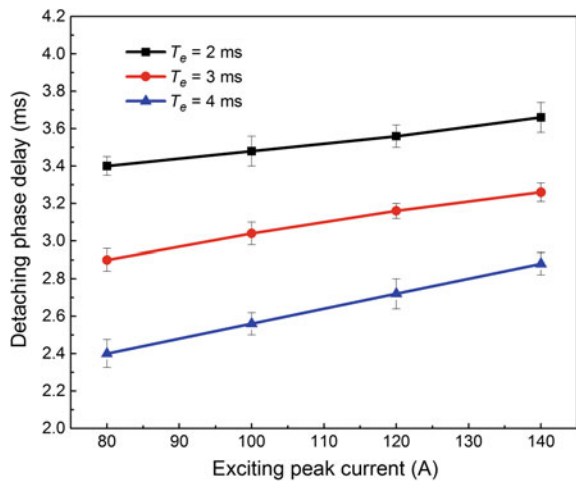
Experiments 1–12 using Wave1 are conducted to study the effect of the exciting parameters on the optimal detaching phase delay. A complete metal transfer cycle being studied here includes four sub-stages: droplet growing, exciting, oscillating and forced detaching. The varying parameters are listed in Table 1.

It can be seen from Fig. 3 that  $T_{p2}^*$  increases with  $I_e$ . Because the initial droplet mass at the exciting end moment slightly increases with the exciting peak current. However, with the same  $I_e$ , the  $T_{p2}^*$  decreases when  $T_e$  from 2 to 4 ms, even though the initial droplet mass under a longer exciting peak duration is slightly greater. That is caused by the phase offset between the exciting end moment and elongation

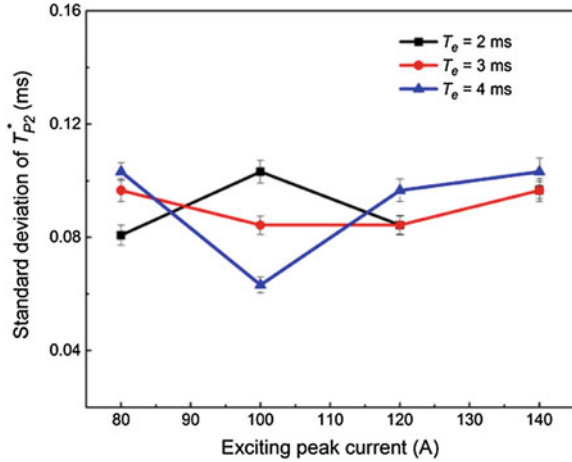
**Table 1** Exciting parameters in experiments 1–12

No.	$I_e$ (A)	$T_e$ (ms)
1	140	4
2	140	3
3	140	2
4	120	4
5	120	3
6	120	2
7	100	4
8	100	3
9	100	2
10	80	4
11	80	3
12	80	2

**Fig. 3**  $T_{p2}^*$  measured from experiment 1–12



**Fig. 4** Standard deviation of  $T_{p2}^*$  in experiment 1–12



peak moment, which means the initial phase of the oscillation is significantly affected by the exciting peak duration. Also the three lines in Fig. 3 are approximately parallel, indicating that the phase offset is mainly determined by the exciting peak duration but almost independent to the exciting peak current. Figure 4 shows that the standard deviations of  $T_{p2}^*$  in experiments 1–12 are all sufficiently small. The maximum standard deviation is only approximately 0.1 ms. Such a low fluctuating level suggests sufficient robustness of  $T_{p2}^*$  under given current waveform parameters.

## 5 Minimization of Detaching Peak Current

The minimization study will be conducted by experiments using Wave2 with optimal detaching phase delays obtained from experiment 1–12. For each used exciting peak current ( $T_e$  fixed at 3 ms), the metal transfer under different detaching current and duration are analyzed, and thus the minimum detaching peak currents under different exciting parameters are determined and shown in Fig. 5. The typical metal transfer in the enhanced active metal transfer control is shown in Figs. 6 and 7. It can be seen from frame 2–4 of these two figures, the droplets are effectively elongated by the exciting pulses, and the detaching pulses are then applied right after the droplets start to move away from the wire tips; therefore the oscillation is fully utilized and the droplets are detached at low currents.

It can be seen from Fig. 5 that the minimum detaching current 120 in the enhanced active metal transfer is significantly lower than the transition current 165 A. For only 4 ms detaching peak duration, the detaching peak current needed in conventional GMAW-P (single pulse) to detach droplets at the same size increases

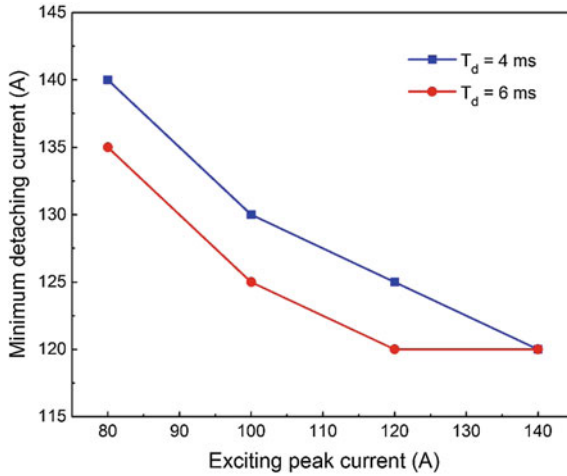


Fig. 5 Minimum detaching current under different exciting peak current

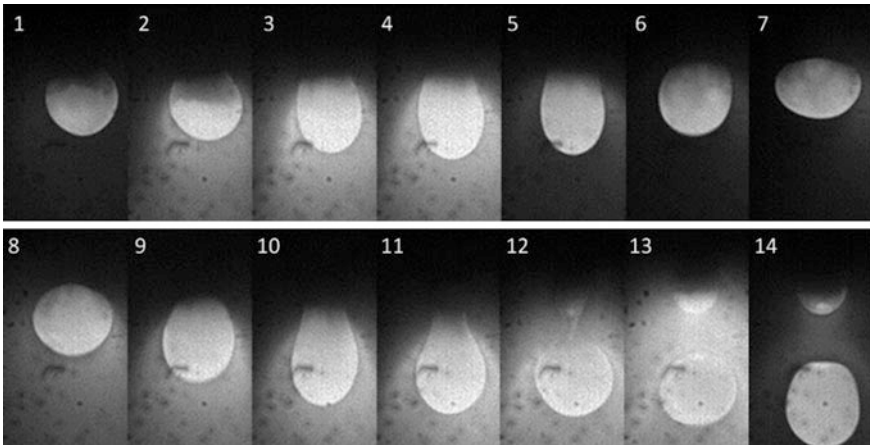
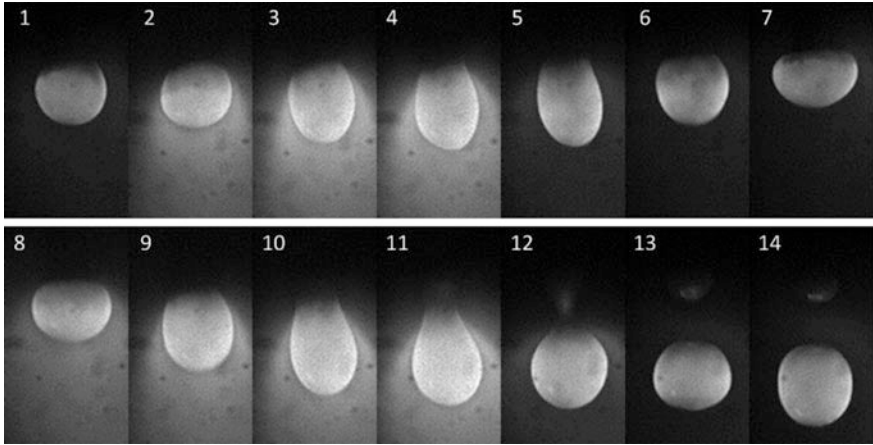


Fig. 6 Droplet oscillation and detachment in enhanced active metal transfer control.  $I_e = 120$  A,  $T_e = 3$  ms,  $I_d = 120$  A,  $T_d = 6$  ms, 1 ms per frame

to over 180 A; however, in the enhanced active control, it is only 125 A. In the original active control process, the minimum detaching peak current is determined to be 145 A. It also can be seen from Fig. 5 that the minimum detaching current in the enhanced active metal transfer control decreases as the exciting peak current increases. However, such decrease becomes less significant as the exciting peak current increases and eventually stops. The selection of the exciting peak current should be based on the resultant reduction in the minimum detaching peak current such that the greater of the exciting peak current and corresponding minimum detaching current be minimal.



**Fig. 7** Droplet oscillation and detachment in enhanced active metal transfer control.  $I_e = 120$  A,  $T_e = 3$  ms,  $I_d = 125$  A,  $T_d = 4$  ms, 1 ms per frame

## 6 Conclusion

Active metal transfer control utilizing the enhanced droplet oscillation is systematically studied in this paper. The effect of the exciting parameters on the optimal detaching phase delay is examined. A series experiments have been conducted to determine the lower limit of the detaching current using the optimal detaching phase delays. The main conclusions are summarized below:

1. Given other waveform parameters, the optimal detaching phase delay decreases as the exciting peak duration increases because the initial phase of the excited oscillation changes with the exciting peak duration.
2. The minimum detaching current to achieve stable drop spray transfer in the enhanced active metal transfer is determined to be significantly lower than that in conventional GMAW-P. The advantage of the enhanced active metal transfer control is thus clearly confirmed.

## References

1. Sadler H (1999) A look at the fundamentals of gas arc metal welding. *Welding J* 78(5):45–50
2. Allum CJ (1985) Welding technology data: pulsed MIG welding. *Welding Metal Fabrication* 53:24–30
3. Thomsen JS (2006) Control of pulsed gas metal arc welding. *Int J Model Ident Control* 1 (2):115–125
4. Kim YS, Eagar TW (1993) Metal transfer in pulsed current gas metal arc welding. *Welding J* 72 (7):279s–287s



5. Amin M (1983) Pulse current parameters for arc stability and controlled metal transfer in arc welding. *Metal Constr* 15:272–278
6. Zhang YM, Ligu E, Kovacevic R (1998) Active metal transfer control by monitoring excited droplet oscillation. *Welding J* 77(9):388s–395s
7. Zhang YM, Ligu E (1999) Method and system for gas metal arc welding. U.S. Patent #6,008,470
8. Xiao J, Zhang GJ, Zhang YM et al (2013) Active droplet oscillation excited by optimized waveform. *Welding J* 92(7):205s–217s

# Research on Reconstruction of Weld Pool Surface Based on Shape from Shading During Robot Aluminum Alloy Pulse GTAW

Jiyong Zhong, Chengdong Yang, Yanling Xu, Huabin Chen  
and Shanben Chen

**Abstract** In the interest of controlling the weld bead formation quality during robot aluminum alloy gas tungsten arc welding (GTAW) process, it's necessary to monitor the shape and surface height information of the weld pool in real-time, which can indicate the penetration and formation. This paper presents an algorithm of shape from shading (SFS) based on single image for weld pool surface reconstruction. Two classic SFS algorithms are analyzed with the results of reconstruction from the synthetic half sphere image. Based on the Zheng and Chellapa algorithm, this paper proposes some measures for the improvement, such as smoothing process, strengthening the boundary constraints, using the known characteristics of the object surface and weighting error functions. And the improved algorithm is used to reconstruct the aluminum alloy weld pool surface during the robot pulse GTAW process. The result shows that the algorithm can successfully reconstruct the weld pool surface with effectiveness and accuracy and the computation of the surface height can be applied in real-time.

## 1 Introduction

In practical welding, deformation, variable heat radiation, variable gap and mismatch often influence the formation of weld bead. Human welders adjust the welding parameters to ensure the weld quality with their eyes to be the delicate visual sensors. Robots with only teaching and playback function or welding equipments with constant parameter configuration are unable to overcome these disturbances and changes encountered in mass production, so it has been difficult to meet the high welding quality requirements. Especially in the time of pursuit of high quality and efficiency,

---

J. Zhong · C. Yang · Y. Xu · H. Chen · S. Chen (✉)  
School of Materials Science and Engineering, Shanghai Jiao Tong University,  
Shanghai, China  
e-mail: sbchen@sjtu.edu.cn

welding automation and intelligent has become the trend, so the requirement of real time control of weld is very urgent [1]. Therefore development of sensory technology of dynamic weld pool characteristics acquisition and intelligent control has been a hotspot and difficulty in welding research [2–5].

For sheet weld formation control, welding process sensing mainly refers to the detection of the controlled parameter, which is always backside width of the weld bead. In practical welding, it's always unreachable for the backside monitoring, so people often detect the weld pool front characteristics information to indirectly reflect backside width of the weld bead. Visual sensor uses CCD devices to acquire the welding process images in the wave rang of visible light. The sensor system does not contact with welding loop, and do the monitoring job without affecting the welding process, and can provide a wealth of information, such as the type of the joint, the weld pool shape, arc shape etc. According to the imaging light source whether the auxiliary light source or self light source of the welding region, direct visual sensor system can be divided into active and passive two categories [6]. Based on the image characteristics information acquired by visual sensing system, visual monitoring system can be divided into two-dimensional and three-dimensional two methods. With respect to the 2D information, the 3D information of weld pool has more advantage in revealing weld pool surface shape and weld formation. As everyone knows, weld pool surface fallen height and weld reinforcement can better reflect the appearance of backside weld bead.

Seinivasan et al. [7] designed a 3D visual sensor of structure light to detect the sinking height of the weld pool surface. The point light source produced by laser generator turns into a line light source through a cylindrical lens, and illustrate upper the groove to form laser stripe corresponding to the shape of the groove with intersection with workpiece. The stripe image is processed by computer to calculate the position of the center of groove, groove width and deformation of the stripe. This way easily affected by welding arc light and the detection is located in the pool rear solidified, which will bring a certain lag for penetration control.

In order to obtain 3D information of weld pool surface, Kovacevic et al. [8], Kovacevic and Zhang [9] designed a suit of weld pool visual detection system, which is consist of strong pulse laser grid multi structure light strip and high-speed electronic shutter camera. The electronic shutter of camera synchronizes the laser pulse frequency. In the laser pulse duration, the laser energy density is far stronger than the arc energy density, and all intensity of laser is far stronger than the arc intensity, which can effectively restrain the arc interference and help to get clear reflectance image of weld pool surface. Then the height of weld pool surface can be calculated out. However the detection system has complicated structure that is often not suitable to some certain welding condition.

Zhao et al. [3] researched the visual sensor for low carbon steel pulse GTAW. He first used the way of shape from shading in 3D computer vision to obtain weld pool surface height information. With deep analysis of the characteristics of low carbon steel butt welding, he put forward the general reflectance map model matched actual imaging conditions and a basic algorithm for solving equation. Due to characteristics of the actual weld pool image, surface smooth constraints, boundary

conditions and the gray weighted adjustment are introduced to acquire 3D information of weld pool surface based on single weld pool image. Li et al. [10] obtained the aluminum alloy weld pool surface height information based on SFS. However the calculation time is too long to apply on the real-time information acquirement in welding process.

Hence the present work attempts to develop the algorithm of SFS for the acquirement of weld pool surface height in aluminum alloy pulse GTAW process. The algorithm will have enough effectiveness and accuracy to be applied to the real-time information acquirement in welding process.

## 2 Experiment System

### 2.1 Experimental Apparatus

The robot pulse GTAW system is nonlinear, multivariable and suffers the external disturbance. Hence, the control system must have high reliability and respond quickly. And to achieve automation of the process we need to develop the sensors and control technologies. The system for sensing and controlling the weld bead is shown in Fig. 1.

The experimental apparatus consists of five parts: the computer, the interface circuit box, the robotic system, the weld power supply, and the vision sensor. The computer for main control is equipped with a DH-CG400 image acquisition card

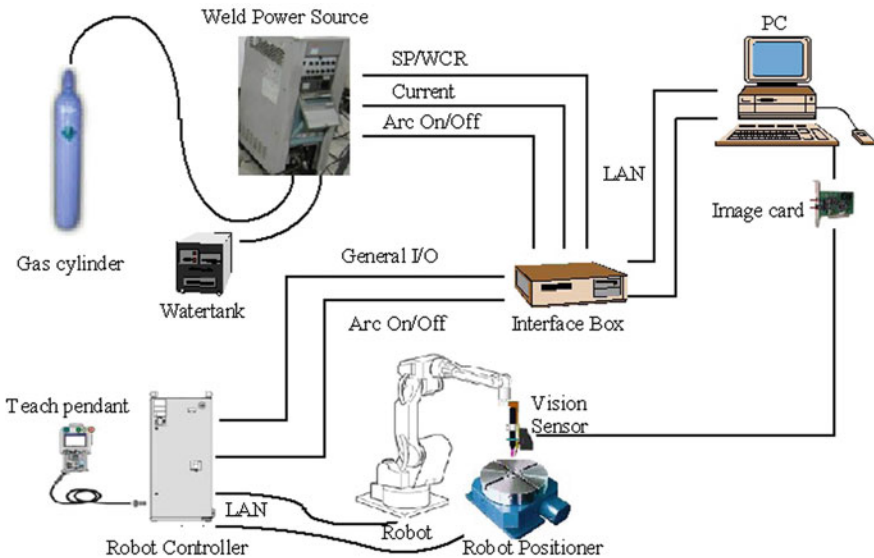
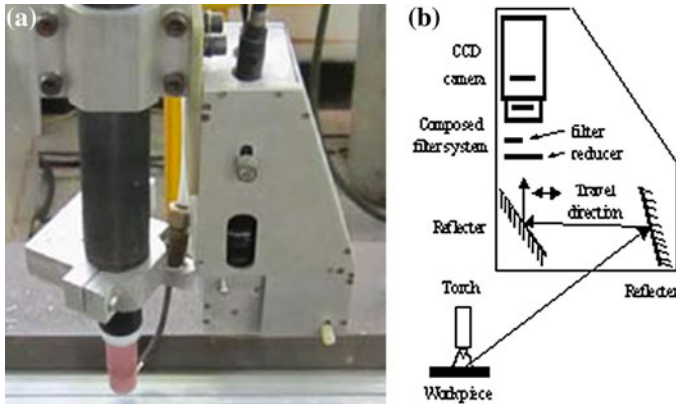


Fig. 1 System architecture of robot GTAW

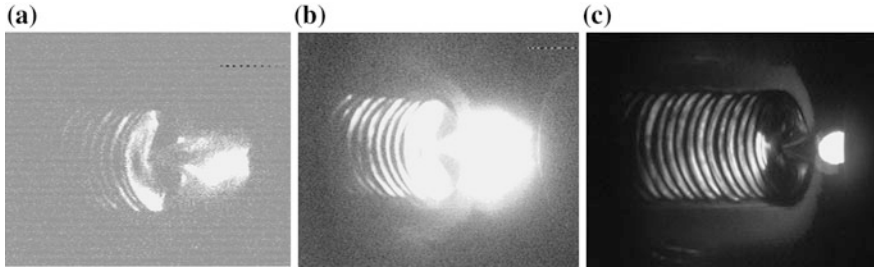


**Fig. 2** The vision sensor device. **a** The actual sensor; **b** the sensor structure

and a 4-CH 12-bit multi-function PCI Express DAQ card, which is respectively applied to obtain the images and data samples and to run the program. The interface circuit box was designed to keep the robot encoder and the computer from the high frequency interference and intense current. The robotic system consists of a six degree of freedom robot, a robot controller and a two axis manipulator. A dual inverter arc welding power source which is OTC AVP500 and a CM-271 wire feeder make up the weld power supply. The vision sensor which is shown in Fig. 2 includes a CCD camera and some optical filters.

## 2.2 Capturing the Weld Pool Image in Real-Time

In robotic welding automation, obtaining a clear weld pool image is the most important prerequisite for the control of the weld process. It will directly affect the weld formation quality and control precision in follow-up welding process. In this paper, a clear weld pool image will be helpful to reconstruct the weld pool surface and to get the precise reinforcement of weld seam. The main issue of using the passive visual sensor needed to be solved is to reduce the influence of arc light so that to get the details of the weld pool. Xu et al. [11] detected the distribution of arc spectrum for aluminum alloy during pulse GTAW. And He tested out the spectrum of wave pass of filter and dimmer glasses. That research helps this paper to choose the right filter and dimmer glasses with proper peak transmittance and center wavelength. Different combination of the filter and dimmer glasses can get images with different quality. Figure 3a is the image of weld pool with only two pieces of dimmers. The dimmers can reduce most of the arc light and the pool radiation. The pool radiation is much weaker than the arc light, consequently when the arc light is reduced successfully the clarity of the pool will be sacrificed, which adds the difficulty of acquiring the details of the pool. Figure 3b is the image of weld pool with



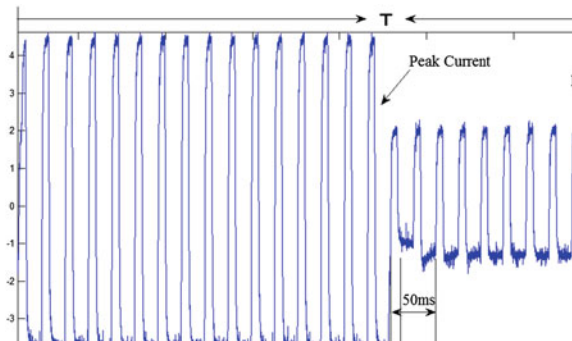
**Fig. 3** The images of weld pool with different filters, **a** with dimmer glasses; **b** with filter glasses; **c** with filter-dimmer glasses

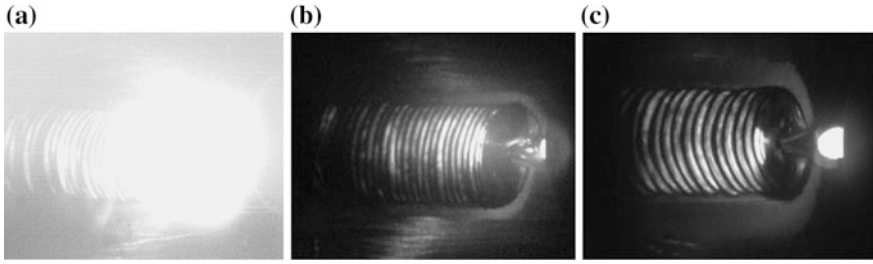
only two pieces of filter glasses. The filter glasses only allow the arc light with wavelength at about  $660 \pm 10$  nm get through. Without the attenuation of dimmers the arc light is still too dazzling. With the combination of one piece of filter glass and dimmer glass this paper get the clear image of weld pool which is shown at Fig. 3c.

Figure 4 is the waveform of the pulse alternating current for the aluminum GTAW in one pulse, which contains base current and peak current. During the welding process, the peak current causes the arc light much stronger than the current at the base value. Even if images obtained at a different time of the base current get differences.

As can be seen from Fig. 5a, the image got at peak current shows that the arc is so strong that the weld puddle is covered by the brightness. As the base current is much smaller than the peak current, the arc was stable and weak enough for the clear images. When the current alternates from peak to base, the arc is not stable. It's better to delay enough time to capture an image so that to avoid to get a dim image, which is shown at Fig. 5b. But too much time to delay will affect the efficiency of image processing. After a lot of experiments, this paper finds out that 50 ms delay after the alternation is the best time to capture the image. So the right way to get clear images of weld pool during robotic pulse GTAW process is to use a composite filter-dimmer with two dimmer glasses and one narrow-band filter, and to capture images 50 ms delay after the alternation which alternates the current from peak to base.

**Fig. 4** The welding current of one pulse





**Fig. 5** The images taken at different time, **a** at peak current; **b** 10 ms delay at base current; **c** 50 ms delay at base current

### 3 Establishment of Pool Surface Illumination Model Based on SFS

Shape from shading (SFS) is one of the key technologies in computer vision three-dimensional shape recovery. Its mission is to recover the parameters of the surface points' relative height and the normal surface direction from a gradual variation of shading in the single image. In computer vision, SFS realization consists of two processes. First, describe the brightness of the image as a geometrical function of the actual object's surface, which is the imaging model of the actual object's surface. Then, reconstruct the surface at a given imaging model. Thus the accuracy of SFS will depend on the appropriate imaging model that is able to determine the relationship between surface shape and brightness, and a good numerical algorithm which can reconstruct the surface shape from a given image.

Actually, the brightness of the image surface points will be affected by many factors, such as the light source, the surface material properties and shape, the position and other parameters of the camera. To solve the problem quickly and precisely, SFS conventional methods carry out the following assumptions. (1) The light source is a point source at infinity. (2) Lambertian Surface Model for the reflection model. (3) The imaging geometrical relationship is orthogonal projection. Then the surface point's brightness  $E$  is affected only by the cosine of the source incidence angle  $\theta_i$ , where  $E = \cos \theta_i$ . In terms of the camera coordinate system as the reference, the height of the surface is expressed as  $z = z(x, y)$ . The surface normal direction can be indicated by each point's surface normal vector  $n = (n_1, n_2, n_3)$  and the surface gradient  $(p, q)$ , or surface slant angle  $\gamma$  and tilt angle  $\tau$ .

Model can be expressed as

$$E(x, y) = \frac{(1 + pp_s + qq_s)}{(1 + p^2 + q^2)^{1/2}(1 + p_s^2 + q_s^2)^{1/2}} = R(p, q) \quad (1)$$

where  $(-p_s, -q_s, 1)$  represents direction of light source,  $E(x, y)$  is normalized value of image brightness, and  $R(p, q)$  is the reflection function.

Generally, the SFS problem determined only by that model is pathological. So to eliminate the morbid and to establish appropriate regularization model, there must be restrictions upon the surface shape. According to the different ways to establish regularization model, the existing SFS algorithms can be divided into a minimum value method, evolution method, local analytical method and linearization method. Because of the request of harsh conditions, the last three methods are not suitable for the reconstruction of welding pool image. Therefore, this paper will focus on analysis and research of the minimum value method.

### 3.1 Weld Pool Surface Illumination Model

Equation 1 gives the general illumination model. However, combined with the weld pool image sensing characteristics of the experiment system, the general illumination can be simplified further. The actual weld pool image sensing has the following characteristics

1. As can be seen from Fig. 5c, arc shrinks to a spherical and can be assumed as a point light source with the same intensity in all directions.
2. The effect of distance from the light source to the weld pool surface on image brightness can be neglected because of these reasons, small area of the weld pool surface, small differences of every surface point distance from the arc, strong arc light.
3. In the sensing system, the relative position between CCD, arc and weld pool is fixed. Then in the equation, vectors  $i$ ,  $v$ ,  $h$  are the functions of the weld pool surface vector  $n$ .

Then the weld pool surface illumination model is

$$\begin{aligned}
 E &= R(p, q) = R(n) \\
 &= \begin{cases} \eta(v^T n_z)^4 (\beta_d(i^T n) + \beta_s \frac{\exp\{-k[\cos^{-1}(\frac{h^T n}{(i^T n)(v^T n)}]\})}{(i^T n)(v^T n)}) + b, & (i^T n) \geq 0 \\ 0, & \text{otherwise} \end{cases} \quad (2)
 \end{aligned}$$

where  $n = (-p, -q, 1)$ ,  $\eta = g \frac{I_0}{r^2}$  is the illumination coefficient, which is relevant with the light source intensity and the gain of CCD.

### 3.2 Improved Algorithm

This paper takes the following measures in the process of the solution based on Zheng and Chellapa algorithm.



1. Smoothing process

Before calculation, smoothing process is used on the input image (only for the actual image). The smoothing process is to filter and remove the influence of high frequency noise on the solving process.

2. Strengthen the boundary constraint

Before the reconstruction, extract the edge of the object in the image, with a dark background for the region beyond the boundaries (set the gray value as zero).

3. Using the known characteristics of object surface

In SFS algorithm, if the known characteristics conditions of object surface are substituted in the process of calculation, the accuracy of calculation results can be improved well. The known characteristics of object surface contains the absolute height of some characteristic points (maxima, minima) on the surface, edge height, self shading boundary or shading boundary position, or some geometric characteristics of surface, such as central symmetry, bilateral symmetry and contour distribution, and so on. All of them can be used as constraints in the process of solution.

4. Weight error function

Define error cost function the overall brightness error. Seen from the surface height calculation results of single image, when the normal direction is similar with the light source direction, the height calculation gets biggest error, which is caused by the local height nonlinearity of the reflectance map equation. At the same time, the image gray value corresponding to the surface is the maximum, so we can introduce the brightness weighted factors to adjust the proportion of the error in whole brightness. The weighted factor is introduced into the brightness error cost function

$$E1 = W(I) \cdot [I(x, y) - R(p, q)]^2 \quad (3)$$

As the reflectance map equation corresponding to the surface with big gray value has strong nonlinearity, we need weaken its action in the error cost function. When the gray value is less than 150, the weighted factor is set the maximum 1.0. That is because in the way of shape from shading, the pixels with lower gray value contain accurate and rich information of surface height. The gray value weighted factor is described as follows.

$$W(I) = \begin{cases} e^{-(I-150)^2/5000}, & I \geq 150 \\ 1.0, & otherwise \end{cases} \quad (4)$$

The above brightness error weighted factor  $W$  is introduced to the Zheng and Chellapa functional expression Eq. (2) to get following equation

$$\iint F(p, q, Z) dx dy$$

$$\begin{aligned}
 F = & W[I(x, y) - R(p, q)]^2 \\
 & + [I_x(x, y) - R_p(p, q)p_x - R_q(p, q)q_x]^2 \\
 & + [I_y(x, y) - R_p(p, q)p_y - R_q(p, q)q_y]^2 \\
 & + \mu[(p - Z_x)^2 + (q - Z_y)^2]
 \end{aligned} \tag{5}$$

where,

$R(p, q)$	image illumination equation
$(p, q)$	gradient of the surface to be calculated
$I(x, y)$	gray value of the surface
$[I(x, y) - R(p, q)]^2$	brightness error
$[I_x(x, y) - R_p(p, q)p_x - R_q(p, q)q_x]^2$	gradient error
$+ [I_y(x, y) - R_p(p, q)p_y - R_q(p, q)q_y]^2$	
$[(p - Z_x)^2 + (q - Z_y)^2]$	integrability constraint
$W$	Weighted factor of brightness error
$\mu$	integrability factor

Compared to Horn algorithm, this constraint has the advantages of avoiding that smooth constraint makes the surface too smooth and difficult to adjust the smooth factor.

To solve the solution, specific calculation steps are as follows.

- Step 1. Initialize imaging model parameters ( $\tau, \gamma$ ).
- Step 2. Standardize the input image, generate images with different resolutions. The minimum size of image is 32 \* 32 pixels, and  $(p_0, q_0, z_0) = 0$ .
- Step 3. Update  $(p, q, z)$ .  
Condition judgment: if the solution is stable or the number of iterations reaches the maximum number which is set before, then go on to Step 4, or continue Step 3.
- Step 4. Enlarge image size, and use the last results to get the initial value of last layer by interpolation, and obtain the image with this layer resolution. Then turn to Step 3, until calculate to the layer with highest resolution.

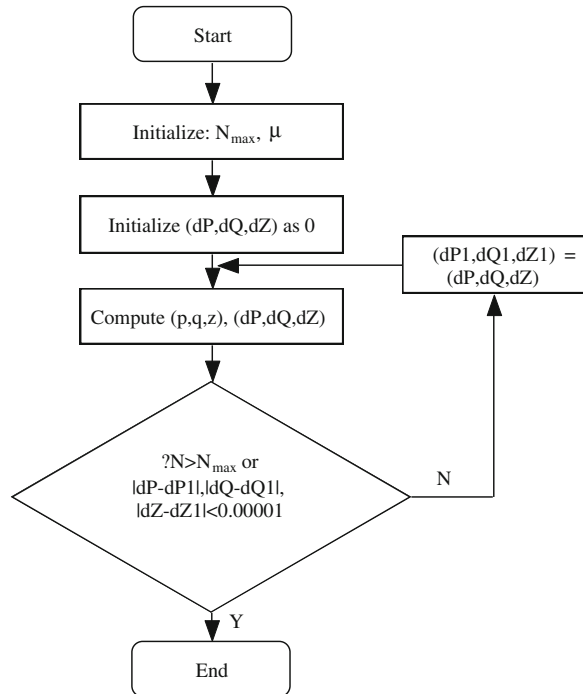
Firstly initialize imaging model parameters. Then standardize the input image to keep the gray value of image in the range of 0–1, and generate images with different resolutions. The image with lowest resolution is first calculated, and  $(p_0, q_0, z_0)$  is initialized as zero. Solve equations to get the solution of this layer. Enlarge image size, and use the last results to get the initial value of last layer by interpolation, and obtain the image with this layer resolution. Continue the calculation till the layer with highest resolution. In the iterative computation of the lowest resolution layer introduce into the absolute height, edge height, self shading boundary or shielding

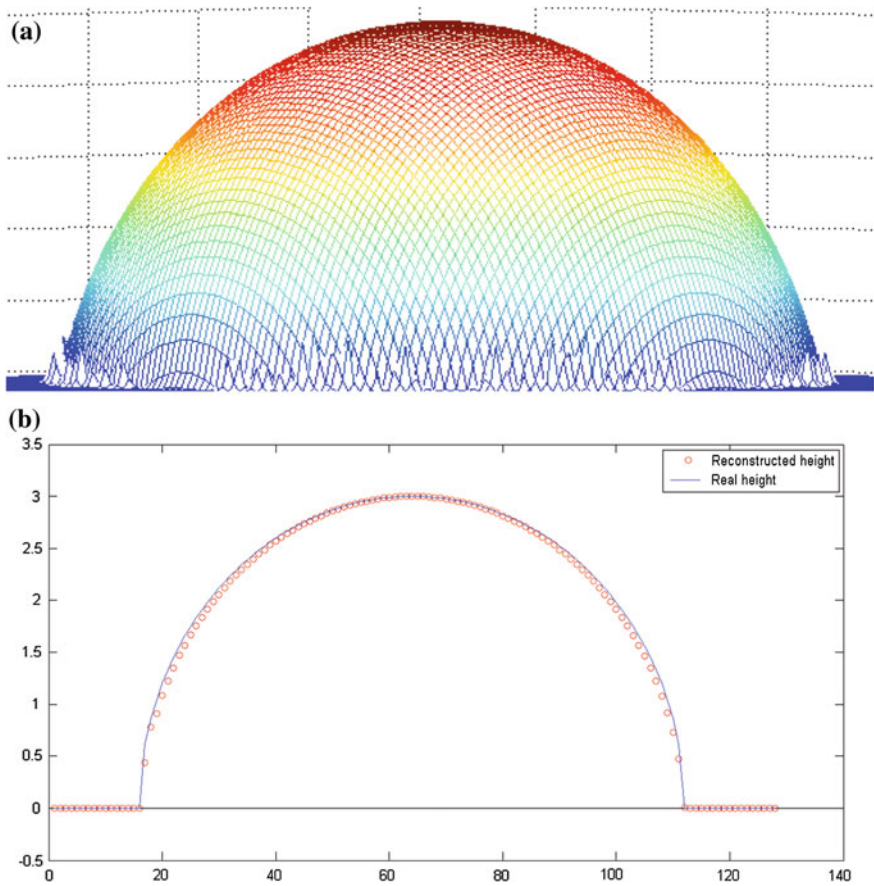
boundary position of some typical points (maxima, minima), or some surface geometry feature, such as center symmetry, bilateral symmetry and contour distribution etc., which are the prior knowledge of the object surface to guide the solving process.

The iterative computation process under every kind of resolution is shown in Fig. 6. In the figure,  $N_{max}$  is the biggest iteration number, which is set as 300 in this paper.  $(dP, dQ, dZ)$  is the increment sum of every pixel  $(p, q, z)$  of the image in this iteration. And  $(dP1, dQ1, dZ1)$  is the increment sum of every pixel  $(p, q, z)$  of the image of last iteration. As the weighted coefficient  $\mu$  is fixed to be 1 in this paper.

In order to verify the effectiveness of the improved algorithm, this paper uses the synthesized image as input image, and sets the light source direction as  $(135^\circ, -135^\circ)$ . Figure 7a is the reconstruction of the synthesized half sphere calculated by the improved algorithm. Figure 7 shows that the improved algorithm calculation has a good closeness to the real solution. And the improved algorithm improves the smoothness of Zheng and Chellapa algorithm. In order to further verify the accuracy of this algorithm, this paper cuts the synthesized and reconstructed half sphere along with the direction of light source to get a group of points, and compare the height of those points. As is shown in Fig. 7b, the height errors of those points are very small, and the mean error is about 0.0723. The results indicate that the

**Fig. 6** Flowchart of the iteration computation process





**Fig. 7** Calculation result of the improved algorithm. **a** Reconstructed height map by the improved algorithm; **b** height compare along with the direction of light source

improved algorithm can well reconstruct the object surface and has good accuracy. So this paper will use this algorithm to reconstruct the surface of weld pool in the welding process.

#### 4 Reconstruction of Weld Pool Surface from a Single Image

According to the weld pool surface imaging illumination equation, 3D reconstruction of pool image is calculated based on the above improved algorithm, and then the weld pool surface height is extracted. Three dimensional reconstruction of the weld pool surface process is as follows.

1. Initialize the imaging illumination model parameters  $(\eta, b, k, \rho_s, \rho_d, n_s, n_c, n_z)$ .
2. Preprocess the weld pool image, including noise reduction, image enhancement, wire stain clearance and segmentation of the pool target.
3. Standardize the input image. That is normalizing the image data.
4. SFS calculation. Introduce into the known characteristics of the weld pool surface during the calculation. (a) Incident light direction vector is  $(0, 0, 1)$ . (b) The workpiece surface height is 0. (c) The contour of the weld pool surface along the welding direction is approximately symmetrical.
5. Coordinate conversion. The coordinate of the object calculated from the above steps of SFS is the camera coordinate. In order to facilitate the extraction of the weld pool surface height, the coordinate needs to be converted to the workpiece coordinate. Set the camera coordinate system and the workpiece coordinate system respectively as  $O\text{-}XYZ$  and  $o\text{-}xyz$ . The workpiece coordinate system take the weld pool center (the point on the workpiece surface right below the tungsten pole) as the origin, the welding direction as X axis, the direction perpendicular to the surface of the workpiece as Z axis. Then the conversion relationship between the two coordinate systems is

$$(X, Y, Z, 1) = (x, y, z, 1)TM \tag{6}$$

where,  $T$  and  $M$  respectively is shift transformation matrix and rotation transformation matrix.

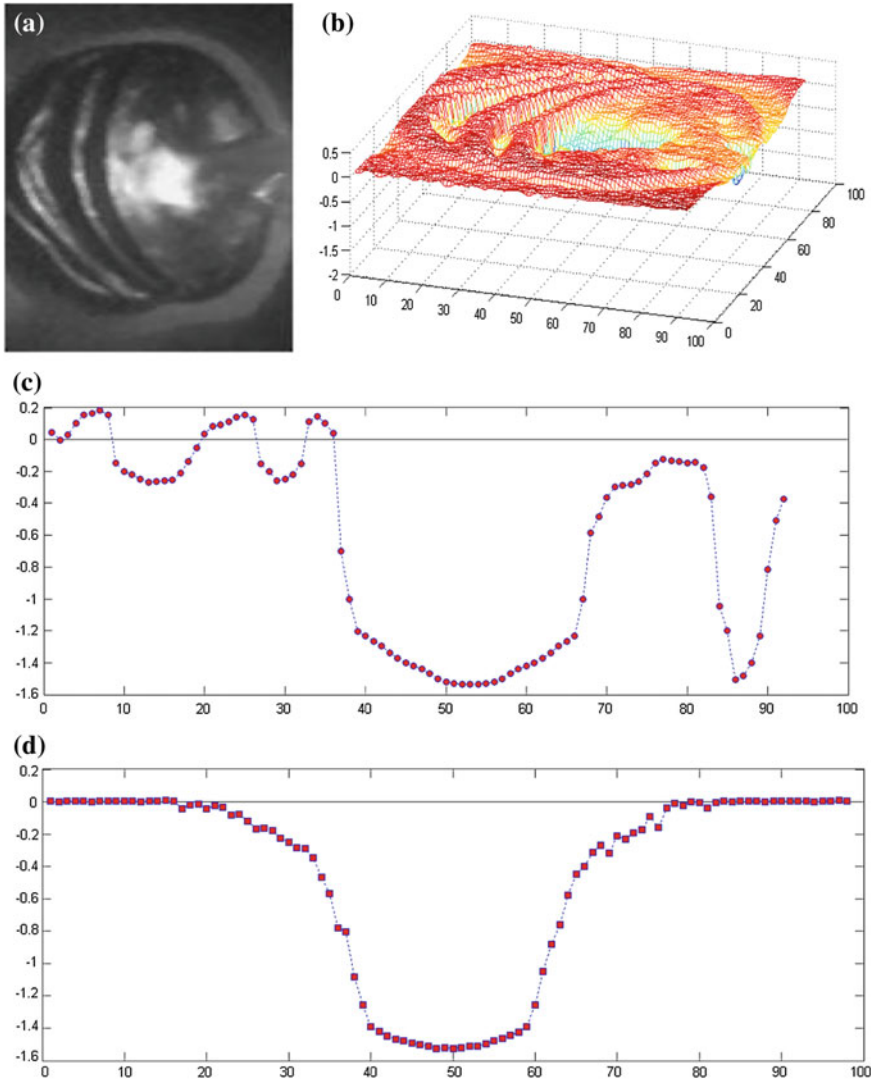
$$T = \begin{pmatrix} 1 & 0 & 0 & 0 \\ 0 & 1 & 0 & 0 \\ 0 & 0 & 1 & 0 \\ -x_T & -y_T & -z_T & 1 \end{pmatrix} \tag{7}$$

$$M = \begin{pmatrix} \cos \varphi \cos \psi - \cos \varphi \cos \psi \cos \theta & -\cos \varphi \cos \psi - \cos \varphi \cos \psi \cos \theta & \sin \psi \sin \theta & 0 \\ \sin \varphi \sin \psi + \sin \varphi \cos \psi \cos \theta & -\sin \varphi \sin \psi + \cos \varphi \cos \psi \cos \theta & -\cos \psi \sin \theta & 0 \\ \sin \varphi \sin \theta & \cos \varphi \sin \theta & \cos \theta & 0 \\ 0 & 0 & 0 & 1 \end{pmatrix} \tag{8}$$

where,  $\theta$ ,  $\psi$  and  $\varphi$  are the Euler angles between axes of the two coordinate systems (nutation angle, precession angle and rotation angle).

6. Output the results.

Figure 8 shows the weld pool image, the surface reconstruction results calculated by the improved SFS algorithm, the heights along x-axis and y-axis going through the pool centre of the reconstructed surface. The calculation reconstructed the weld pool surface correctly and got the height information precisely. Total calculation process cost less than 84 ms and that indicated the SFS reconstruction can meet the requirements of the real-time processing during welding process.



**Fig. 8** SFS calculation results of the weld pool surface. **a** The input image; **b** 3D reconstructed surface; **c** the heights along x-axis going through the centre of the reconstructed surface; **d** the heights along y-axis going through the centre of the reconstructed surface

## 5 Conclusions

In this paper an algorithm of shape from shading based on single image is presented. This paper proposes some measures to improve the algorithm, such as smoothing process, strengthening the boundary constraints, using the known

characteristics of the object surface and weighting error functions. This algorithm successfully reconstructs the aluminum alloy pulse GTAW weld pool surface based on the pool image and calculates out the height of the weld pool surface. The computation results indicate that this algorithm has good effectiveness and accuracy, and lays the foundation for the real-time control of three-dimensional weld pool information in welding process.

**Acknowledgments** This work is supported by the National Natural Science Foundation of China under the Grant No. 51405298, 61374071 and the NDRC of China, under the Grant No. HT[2012] 2144.

## References

1. Ward P (2001) Improving productivity with robotic welding. *Welding J* 80(8):52–54
2. Wikle HC (2001) Infrared sensing techniques for penetration depth control of the submerged arc welding process. *J Mater Process Technol* 113(6):228–233
3. Zhao DB, Chen SB, Wu L (2001) Intelligent control for the shape of the weld pool in pulsed GTAW with filler metal. *Welding J* 80(11):253–260
4. Kannatey-Asibu E (1997) Milestone developments in welding and joining processes. *ASME J Manuf Sci Eng* 119(11):801–810
5. Zhao DB, Chen SB, Wu L (2001) Intelligent control for the shape of the weld pool in pulsed GTAW with filler metal. *Welding J* 80(11):253–260
6. Kin JW, Na SJ (1991) A study on an arc sensor for gas metal arc welding of horizontal fillets. *Welding J* 70(8):216–221
7. Seinivasan V, Han YK, Ong SH (1993) Image reconstruction by a Hopfield network. *Image Vision Comput* 11(5):278–282
8. Kovacevic R, Zhang YM, Li L (1996) Monitoring of weld penetration based on weld pool geometrical appearance. *Welding J* 75(10):317–328
9. Kovacevic R, Zhang YM (1997) Real-time image processing for monitoring of free weld pool surface. *J Manuf Sci Eng* 119(5):161–169
10. Li LP, Yang XQ, Zhang FY, Lin T (2011) Research on surface recover of aluminum alloy PGTAW pool Based on SFS. In: *Robotic welding, intelligence and automation*. LNEE, vol 88, pp 307–314
11. Xu YL, Yu HW, Zhong JY, Lin T, Chen SB (2012) Real-time seam tracking control technology during welding robot GTAW process based on passive vision sensor. *J Mater Process Technol* 212(8):1654–1662

**Part IV**  
**Intelligent Control and Its Applications**  
**in Engineering**



# The Development of a Low Cost Autonomous Robotic Arc Welding System

Mitchell Dinham and Gu Fang

**Abstract** A significant challenge for robotic welding to be widely adopted is the time taken to program robot paths for new parts. While computer vision can be used to detect and locate weld joints, due to the large number of possible joint configurations, work piece materials and environmental impacts such as lighting conditions, autonomous weld joint detection and localisation remains a significant challenge. This paper introduces an autonomous robotic arc welding system that is capable of detecting realistic weld joints and calculating their position in the robot workspace with minimal human interaction. The proposed method is capable of detecting and localising butt and fillet weld joints regardless of base material, surface finish or imperfections. The welding results show that the proposed method is capable of producing high quality weld paths suitable for industrial applications.

## 1 Introduction

At present, robotic welders are generally programmed by human operators using teach and playback methods. It can take considerable amounts of time to program and commission new jobs. This makes robotic welding unsuitable for low to medium volume manufacturing, as it is often quicker to weld the parts manually. Furthermore, teach and playback programming requires highly repeatable parts with tight tolerances and expensive tooling to hold them in place. This can be justified in mass production; however the expense of designing new jigs and tooling as well as the costs associated with the lost production time for reprogramming makes the investment in robotic welding unjustifiable for low to medium volume production runs in small to medium size enterprises (SME's).

---

M. Dinham (✉) · G. Fang  
School of Computing, Engineering and Mathematics, University of Western Sydney,  
Sydney, Australia  
e-mail: Mitchell.dinham@gmail.com

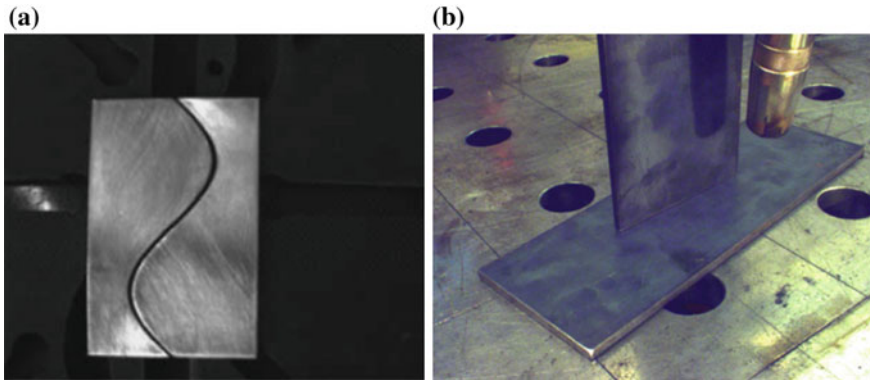
To make the benefits of robotic welding a viable option for these applications, it must become more flexible. The systems should be quickly and easily adapted to new parts. To achieve this, the system would be required to automatically recognise the weld joints and accurately locate their positions in the robot's workspace. Computer vision systems can be used to detect the weld joints and provide a path to the robot to weld them automatically. The autonomous system must also be versatile and robust to cope with the varying environmental and operational conditions of welding workshops. For a computer vision system these environmental effects can include poor lighting conditions and imperfect work pieces that may be covered in rust, mill scale and scratches. The system would also have to be versatile to cope with a variety of joint configurations, surface finishes and base material such as paint, steel and aluminium which will affect contrast of the weld joint and increase or decrease the effects of reflections.

Since 2008, the University of Western Sydney and Lincoln Electric Australia have undertaken extensive research with the goal of developing an autonomous robotic arc welding system. The aim of the project was to develop new computer vision methods for the reliable and accurate detection and localisation of butt and fillet weld joints in an industrial welding environment. These methods were verified through experimentation on an industrial robot in a typical workshop environment. This paper summarises the key research breakthroughs and publications of the project [1–3]. This paper is organised as follows: Sect. 2 presents related work in the area of vision based seam identification and localisation. Section 3 details the methodology used to develop the autonomous robot arc welding system with the experimental results given in Sect. 4. The conclusions are then given in Sect. 5.

## 2 Related Work

There are currently no commercial weld joint detection methods capable of identifying weld joints without human operator involvement. In industry, current state of the art implementations of flexible robotic welding include vision systems such as the Fanuc's iR Vision [4] and ServoRobot [5]. These are simple "look" and "shift" solutions. They are used to identify a pre-taught weld joint and then "shift" the manually pre-programmed path to accommodate any offsets in position. Offline simulation programs such as the Fanuc's WeldPro [6] and ABB's robot studio [7] can reduce setup time, however they still require significant human operator interaction and the programs taught in a virtual world will inevitably need to be "touched-up" when applied in the real world due to physical differences between the CAD model and the physical system layout.

Much of the research for weld joint detection has focused on Gas Tungsten Arc Welding (GTAW) of aluminium for butt weld joints [8–10]. From a computer



**Fig. 1** a Weld Joint in [10] and b the fillet weld joint used in the proposed method

vision stand point, the high contrast between the bright aluminium work pieces and a dark background simplifies binary image segmentation. By comparison, there has been limited work published on the detection of weld joints for Gas Metal Arc Welding (GMAW) of ferrous materials. The detection of weld joints for steel work pieces present unique challenges for computer vision. In a welding environment almost everything is made of steel including the work bench. This makes image segmentation more difficult for GMAW than GTAW as the work piece and the bench may be similar shades of grey. Furthermore, unlike butt-weld joints, fillet welds provide increased complexity. The thinner weld joint gaps and low contrast between the steel work pieces can make joint detection difficult. An example of the types of weld joints featured in literature are shown in Fig. 1a with a comparison to the fillet weld joints our system aimed to solve shown in Fig. 1b.

If the welding joint can be found in the image plane, the 2D pixel co-ordinates can be transformed into 3D real world co-ordinates for robot path planning using triangulation via stereo vision. To perform triangulation it is required to find the same point in two or more images. Finding two or more matching points requires a process known as image matching. Weld joints do not contain unique feature points and can be considered as a repetitive texture. Similar to weld joint detection, stereo matching cannot be reliably solved with traditional methods due to the nature of the welding environment.

In general image processing technology has been developed for many years with many algorithms available for particular applications. However these applications are specific to a certain problem in image processing [11]. For welding, image processing is difficult and requires the development of specialised algorithms. To date there is no method that is capable of solving the requirements for autonomous robotic welding.

### 3 Methodology

#### 3.1 System Description

The autonomous robotic arc welding system described in this paper uses an eye-in-hand stereo vision system. An eye-in-hand stereo vision system allows the cameras to be manoeuvred using the robot to get an unobstructed view of the weld joint. Their compact size also allows for better access to a wider range of welding positions. Although stereo vision can be achieved using a single moving camera, dual cameras allow for efficient image capture of the weld joint as the robot does not have to be moved multiple times. The calibration of the robot, and eye-in-hand stereo vision cameras can be achieved using the low cost method in [1]. This particular calibration method allows for sub-millimetre accuracy in determining weld joints in the robot workspace.

The system is shown in Fig. 2a. The setup consisted of a Fanuc ArcMate 100iC, a 6 axis industrial robot with a repeatability of  $\pm 0.08$  mm. It is fitted with a welding torch and Lincoln Electric PowerWave welding power source. The stereo vision system consisted of two off the shelf uEye USB colour CCD cameras (resolution  $1280 \times 1024$ ). The cameras are attached to the welding torch as shown in Fig. 1b. The work bench is an industrial grade Demmeler welding bench. The cost of the camera hardware was approximately US\$5000. Compared to existing commercial packages such as ServoRobot US\$50,000 or US\$13,000 for the laser/camera system in [12], the proposed method is much more affordable to SME's from a cost standpoint.

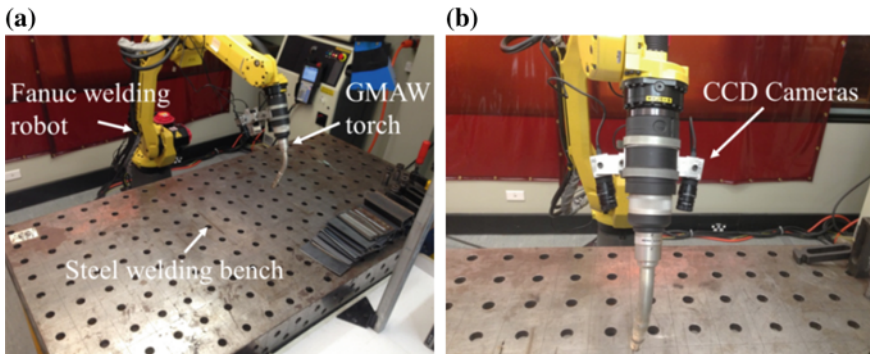


Fig. 2 a System overview and b Stereo CCD cameras

### 3.2 Weld Joint Detection

There are many papers published on the detection of butt welds; however there are no widely accepted and mature methods for fillet weld joint detection. Therefore in order to develop an autonomous robotic arc welding system, a new weld joint detection method was developed to adaptively detect fillet weld joints of any shape without prior knowledge of the shape or position of the joint in the image [2]. The proposed method can detect the weld joint in work pieces regardless of base material, surface finish or surface imperfections such as heavy scratching, rust, mill scale.

The proposed method introduces a new adaptive line growing algorithm to detect the welding joints. The method is based the assumption that the weld seam is darker than the surface of the work pieces either side of the joint. The method analyses the entire image from a global perspective without the need for user defined search windows. An overview of the detection process is shown in Fig. 3. The main steps include capturing stereo images of the work piece 3(a) and then

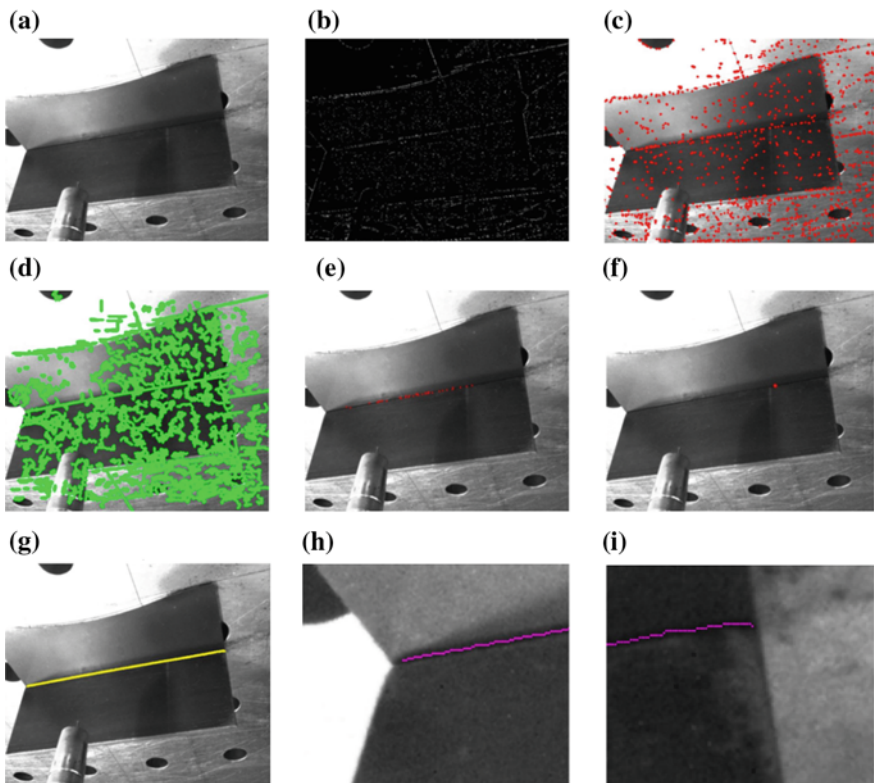


Fig. 3 Adaptive line growing method for weld joint detection

converting them to binary edge images where initial seed locations are determined by eroding each edge segment to a single pixel 3(b). Each seed represents the possible location of the weld joint in the image 3c. Each initial seed location is grown outward using the new line growing method to find possible weld seams 3 (d). Based on growth properties of the initial seeds, they can be categorised as either part of the seam or not 3(e). The final seed pixel is then selected from analysing the local neighbourhood of each of the remaining seeds 3(f). The final seam line is then grown along the weld joint until the ends of the joint are reached 3(g–i).

### ***3.3 Weld Joint Localisation***

Stereo vision can be used to calculate the 3D co-ordinates of the weld joint. This can be achieved using triangulation through stereo matching. Due to the challenges of the welding environment, stereo matching is not a trivial process. Typically the image regions around the weld joints can be considered featureless as the weld joint is a uniform groove between two metal components. They also have uniform texture due to monotone steel surfaces which are mostly grey in colour. The reflections off the steel surfaces together with ambient lighting conditions greatly affect the contrast and pixel intensity between the left and right camera views.

If the weld joint is extracted as a feature in both the left and right views, then finding the matching points is simplified by using the intersection of the epipolar line with the weld seam. This method has an additional benefit that it does not require rectified images, which not only simplifies the matching process but reduces the computation time. It is also independent of pixel intensity comparisons. This method of stereo matching is fairly trivial when the epipolar line and seam line intersect at only one point. However this condition cannot always be met in practice. For example, when matching points on a curved weld joint, the seam line and the epipolar line can be tangential; this will result in multiple seam line points intersecting with the epipolar line. Another example is when the epipolar line and the seam line intersect in more than one location. Therefore additional matching criteria are needed.

The problem of multiple intersections is addressed using known information about the workspace and camera position to estimate the correct match based on the weld joint real world co-ordinates. The seam line is detected in the left and right images using the algorithm described previously [2], then using the seam line co-ordinates in the left image as reference, a set of matching pixels in the right image can be estimated by finding the intersection between the epipolar line and the seam line in the right image. The correct match is estimated using three steps: (i) calculate the reprojection error of the reference point using the calculated 3D co-ordinates; (ii) introduce a height threshold, i.e., for an incorrect match, the error in the calculated height is likely to be excessive. If we know the height of the table and the height that the image is taken from, then the height of the weld joint must be between the two; (iii) compare the calculated height with the height of the previous

waypoint(s). If we choose reference points in the left image that are 20 pixels apart, then the change in height between consecutive weld joint way points in the real world is to be small.

The first step in the matching process is to select the reference points from the seam line in the left image. The reference points are chosen close to each other. Industrial robots are programmed to follow a weld path given the start and end points as well as intermediate waypoints. The intermediate waypoints are calculated by dividing the seam line into equal spaced points at 20 pixel intervals.

For a calibrated stereo vision system, the epipolar line  $L_e$  in the right image can be calculated by

$$L_e = F[u_L \ v_L \ 1]^T \tag{1}$$

where  $F$  is the fundamental matrix and  $[u_L \ v_L \ 1]$  are the homogenous pixel co-ordinates of the reference pixel in the left image and  $T$  is the matrix transpose. All seam line pixels that are within the intersection radius  $R$  of the epipolar line and seam line are then calculated using

$$M_P = \begin{cases} S_R(u_R, v_R) & |L_{er} - S_R(u_R, v_R)| \leq R \\ null & otherwise \end{cases} \tag{2}$$

where  $M_P$  is an array containing all the putative matching pixels in the right image,  $S_R$  is the seam line in the right image containing pixel co-ordinates  $(u_R, v_R)$ . An example is shown in Fig. 4.

If the epipolar line intersects the seam line once, then the correct match is found using the reprojection error. This is achieved by calculating the 3D position for all matches and then using these to estimate the co-ordinates of the corresponding reference pixel in the left image. The pixel with the smallest reprojection error is considered to be the correct match and is given by

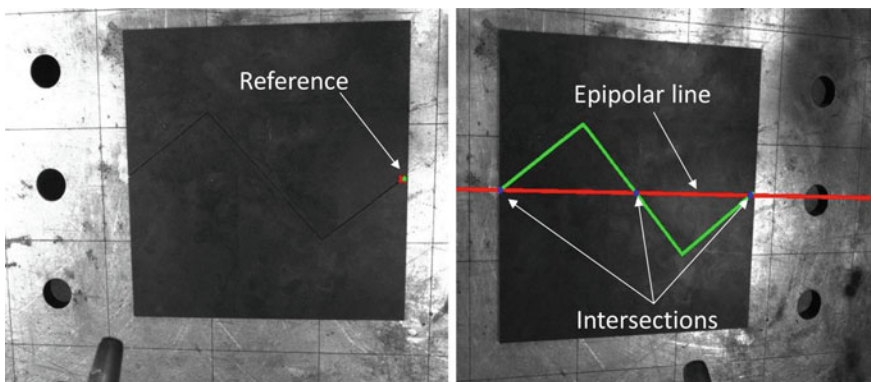


Fig. 4 Multiple intersection example



$$w_{PL}[u_{PL} \ v_{PL} \ 1]^T = \mathbf{P}_{CL}[X_{WP} \ Y_{WP} \ Z_{WP} \ 1]^T \quad (3)$$

where  $(X_{WP}, Y_{WP}, Z_{WP})$  are the 3D co-ordinates calculated using the reference pixels  $(u_{REF}, v_{REF})$  in the left image and the initial matches in the right image  $M_P$ ,  $\mathbf{P}_{CL}$  is the left camera projection matrix and  $(u_{PL}, v_{PL})$  are the estimated co-ordinates for the reference pixel based on the initial matches. Therefore for the single intersection scenario the matching pixels in the right image  $(u_{match\_r}, v_{match\_r})$  are calculated by finding the reprojected estimate with the smallest distance from the reference pixel such that

$$\left\{ (u_{match\_r}, v_{match\_r}) \in M_P \mid M_P(u_R, v_R) = \arg \min_i ((u_{PLi}, v_{PLi}) - (u_{REF}, v_{REF})) \right\} \quad (4)$$

For non-trivial scenario of multiple intersections, Eq. (4) will not have a unique solution. Therefore using pixel co-ordinates alone will result in the likelihood of a false match. If points are incorrectly matched, then the calculated heights will usually be some unrealistic value. Since the height of the table is known, and the height of the cameras are known, then the height of the correct match must lie somewhere between the two. Secondly, if the waypoints are chosen to be close to each other, then we can compare the calculated heights with the height of the previous correct match.

$$M_P(u_R, v_R) = \begin{cases} S_R(u_R, v_R) & [Z_{WP(u_R, v_R)} \leq Z_{max}] \vee [Z_{WP(u_R, v_R)} \geq Z_{table}] \vee [(Z_{WP(u_R, v_R)} - Z_{(match\_r-1)}) \leq Z_T] \\ null & otherwise \end{cases} \quad (5)$$

where  $Z_{camera}$  is the height of the camera,  $Z_{table}$  is height of the table and  $Z_T$  is height change threshold between the current seam line points  $Z_{WP(u_R, v_R)}$  and the previously matched seam line point  $Z_{(match\_r-1)}$ . This will narrow the initial matches down to a set of possible matches around one of the intersection points between the bipolar line and seam line. From there the correct match can be found using (4).

## 4 Results

Experiments were conducted using a GMAW Pulse waveform with a CTWD of 18 and 0.9 mm diameter welding wire. The wire feed speed, voltage and travel speeds for each case study were set manually based on recommended settings by the manufacturer. The robot path was entered manually into the robot controller using the calculated co-ordinates obtained from the proposed localisation method. The 3D Cartesian error for weld joint localisation in the robots base co-ordinate frame was found to be within  $\pm 1$  mm for all case studies.



The welding results are shown in Figs. 5 and 6. The image captured from the left camera for three cases are shown in Fig. 5a, with the detected weld seam in Fig. 5b and the welded result in Fig. 5c. Close ups of each work piece are given in Fig. 6a–c which demonstrate the accuracy of the weld joint detection and localisation method. Welding characteristics such as penetration and bead shape are not considered in this paper.

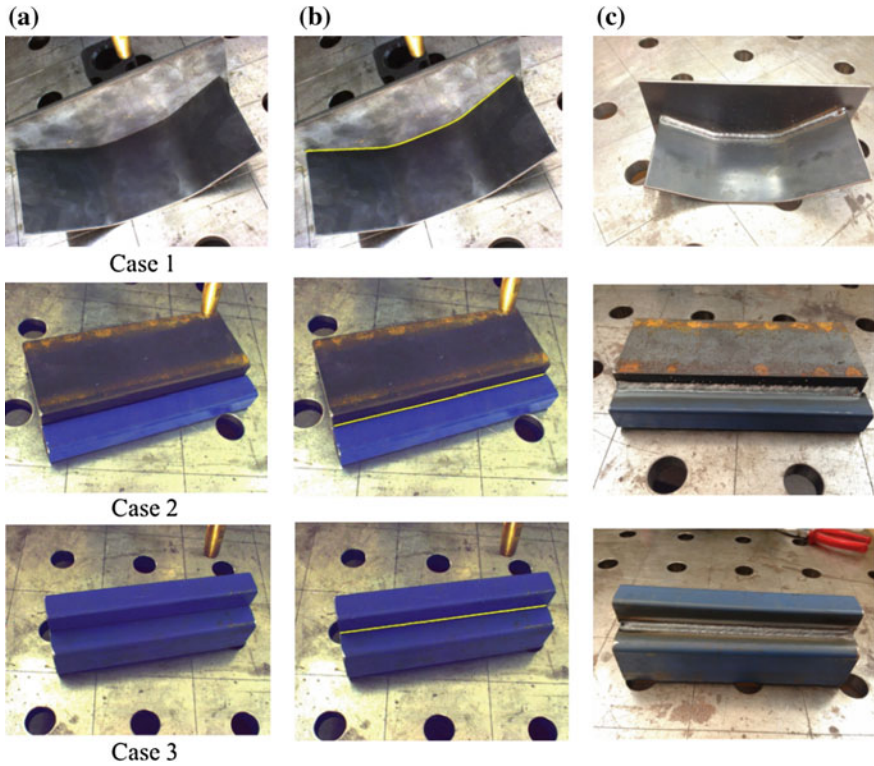


Fig. 5 a Image captured from the left camera. b Detected weld seam and c Welded results

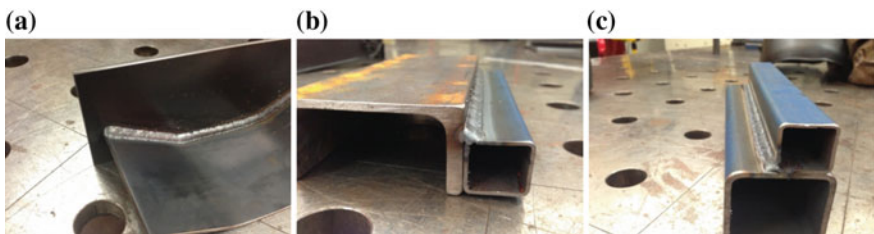


Fig. 6 Close ups of Welds a Case 1, b Case 2 and c Case 3

## 5 Conclusion

The results show that accurate weld joint detection has been achieved. They also demonstrate the proposed weld joint detection methods ability to detect and locate the weld joint regardless of joint geometry, surface finish or surface condition of the work piece such as rust or scratches. Based on extensive experimental testing, the proposed robotic arc welding system can provide the required the flexibility to reduce costs for both programming labour and hardware investment. Therefore the research and development provided by this project can advance the wider use of robotic welders in SME's.

**Acknowledgement** This work is supported by the Australian Research Council under project ID LP0991108 and the Lincoln Electric Company Australia.

## References

1. Dinham M, Fang G (2010) Simultaneous calibration method of a stereo vision system and a welding robot. In: IEEE international conference on robotics and biomimetics (ROBIO), pp 1452–1456
2. Dinham M, Fang G (2013) Detection of fillet weld joints using an adaptive line growing algorithm for robotic arc welding. *J Robotics Comput Integr Manuf* 30:229–243
3. Dinham M, Fang G (2013) Autonomous weld seam detection and localisation using eye-in-hand stereo vision for robotic arc welding. *J Robot Comput Integr Manuf* 29:288–301
4. Fanuc, iRVision Setup and Operations Manual A-86843EN/01. Rochester Hills, Michigan 48309-3253: FANUC Robotics America Corporation, 2007
5. ServoRobot (2013) Seam Finding, Seam Tracking and Adaptive Control. Available: <http://www.servorobot.com/en/manufacturing-solutions/seam-finding-tracking-adaptive-control.html>. 5 May 2013
6. Fanuc (2013) ROBOGUIDE-WeldPRO. Available: <http://www.fanurobotics.com/Products/vision-software/ROBOGUIDE-simulation-software.aspx>. 5 May 2013
7. ABB (2013) RobotStudio. Available: <http://www.abb.com/product/seitp327/78fb236cae7e605dc1256f1e002a892c.aspx>. 5 May 2013
8. Xu Y, Yu H, Zhong J, Lin T, Chen S (2012) Real-time seam tracking control technology during welding robot GTAW process based on passive vision sensor. *J Mater Process Technol* 212:1654–1662
9. Chen SB, Lv N (2014) Research evolution on intelligentized technologies for arc welding process. *J Manuf Process* 16:109–122
10. Chen SB, Chen XZ, Qui T, Li JQ (2005) Acquisition of weld seam dimensional position information for arc welding robot based on vision computing. *J Intell Rob Syst* 43:77–97
11. Chen X, Chen SB, Lin T, Lei Y (2006) Practical method to locate the initial weld position using visual technology. *Int J Adv Manuf Technol* 30:663–668
12. Michalosa G, Makrisa S, Eytanb A, Matthaiakisa S, Chryssolourisa G (2012) Robot path correction using stereo vision system. In: 45th CIRP conference on manufacturing systems 2012, pp 352–357

# Multi-pass Route Planning for Thick Steel Plate Using Laser Welding with Filler Wire

Tian-Yu Huang, Li-Wen Fan, Yi-Ning Bao, Hao Shi and Ke Zhang

**Abstract** Laser welding with filler wire, performed by welding robots, provides high stability and efficiency for welding thick plates used in shipbuilding, electrical engineering and nuclear industry. The route planning methodology is of central importance in this process. Firstly, build a welding system suitable for thick plate laser building with filler wire. Then, establish a strategy on the principle that the cross section areas of the welding beads are equal under same welding parameters, parallelogram/trapezoid method is applied to plan the layers, number of beads for each layer, and the concrete position for each bead before the welding for both V-shape and trapezoid grooves. Auto-planning and visualization are achieved by programming. Furthermore, a specially designed method for welding capping layer, concerning the coverage of the edges of the groove, is introduced to perfect the joint quality. Finally, experimental test shows the effectiveness of this planning philosophy in laser welding with filler wire of thick plate. Testing results highly agree with the planning with only slight differences in both normal and capping layers. High quality leveling interface and fusion can be realized after filler passes based on the multi-pass route planning.

## 1 Introduction

Laser welding process is now much used for different kinds of industry like aviation, navigation as a high-energy beam welding process due to its stable and focusing energy input and high productivity [1]. Compared to conventional welding process, its higher heating and cooling rate can cause less distortion thus providing a more satisfied work [2, 3]. On the other hand, laser beam is highly concentrated beam, which can meet the need for industrial sustainable processes and systems [4].

---

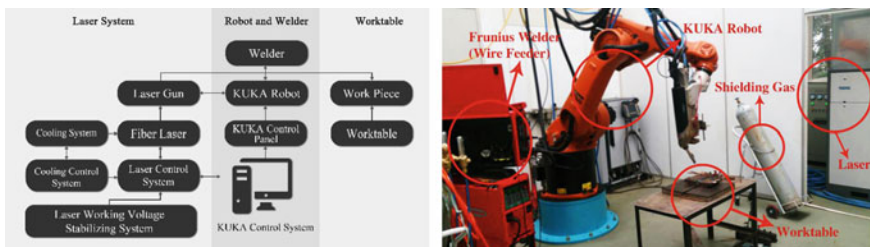
T.-Y. Huang · L.-W. Fan · Y.-N. Bao · H. Shi · K. Zhang (✉)  
Shanghai Key Laboratory of Materials Laser Processing and Modification,  
Shanghai Jiao Tong University (SJTU), Shanghai 200240, People's Republic of China  
e-mail: zhangke@sjtu.edu.cn

Welding with continuous filling wire is a common practice for fusion welding process and route planning is associated with the laser welding with filling wire [5]. Thick plate structures adopt conventional methods such as manual and semi-automatic welding, which are very complicated and of low productivity [6]. To improve the automatic welding technique, research on multi-pass route planning for thick steel plate planning makes great significance and it develops a new automatic welding method [7]. In this research, for a stable performance and convenience for route planning, the process parameters like welding speed, filling rate and welding power are fixed to get a fixed weld bead model [8, 9]. After getting the welding parameters, automatic welding will come true through the route planning. Near the end of fill welding, the top layer of the weld groove may no longer be well defined [10]. This research will also give an appropriate solution to the planning of the capping layer.

## 2 Laser Welding with Filler Wire: System and Methodology

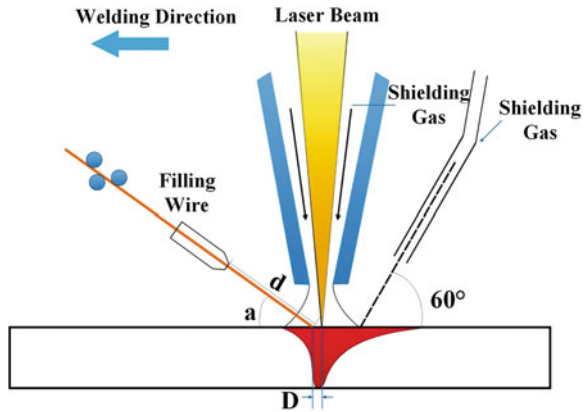
Figure 1 shows the framework of the laser welding with filler wire system, which mainly includes a KUKA robot, a fiber laser system, a welder and a worktable. The IPG-10000 fiber laser, which maximum power can be up to 10 kW, and a Fronius welder, being in charge of feeding filler wire, are loaded on the KUKA 60HA robot. To satisfy the high assembly accuracy required by robot welding, a worktable equipped with a fixture is designed to grip the work piece. Shielding gas is applied through a gas cylinder during the process of welding.

The process of laser welding with filler wire is illustrated as Fig. 2. A molten pool is formed under laser-matrix reaction. The filling wire is fed into the leading end of the pool. Meanwhile, the protective gas of Argon is applied externally in consideration of eliminating inclusions and bubbles. Three parameters have major impact on the morphology of welding bead: welding speed, laser power and feeding speed. Preview study [3] has shown the relationship between geometric parameters of a bead and welding parameters, which indicates that under given welding



**Fig. 1** Laser welding with filler wire system

**Fig. 2** Laser welding with filler wire



parameters, the area of the bead is fixed and possible to be predicted. In the study of multi-pass route planning, a basic assumption is that welding parameters are unchanging, namely the area of every single bead is constant.

### 3 Multi-pass Route Planning Algorithm

#### 3.1 Coordinate System

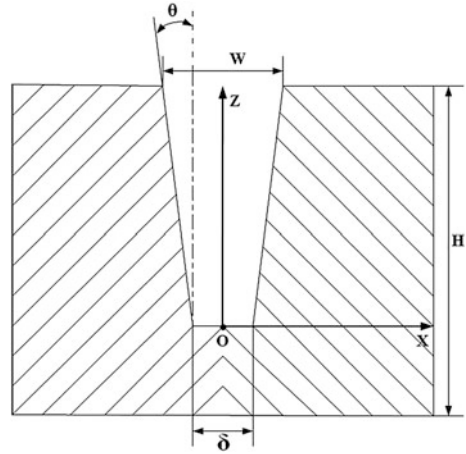
Before route planning, it is necessary to measure the parameters of the grooves:  $H$  (the height of the groove),  $\theta$  (the angle of the groove),  $\delta$  (the bottom width of the groove),  $W$  (the upper width of the groove). Then we can establish the coordinate system.

Figure 3 shows the coordinate system defined in the trapezoid grooves. The original point is at the midpoint of the groove bottom. The X-axis is parallel to the width of groove, the Y-axis is parallel to the length of groove and the Z-axis crosses over the original and is vertical to the back surface of groove.

#### 3.2 Route Planning

In the process of thick steel plate welding, it has been mentioned that the cross section areas of the welding beads under same welding parameters are equal. For simplicity, the welding beads in route planning can be considered as parallelograms and trapezoids. It is required to measure the cross section area of welding beads under the same parameters through surface welding. Then, two parameters of welding beads shall be measured:  $l$  (the bottom width of the bead),  $S$  (the cross section area of welding bead). The  $l_i$  (the bottom width of the  $i$  layer) has a

**Fig. 3** Schematic diagram of the groove



relationship with  $l$  that can calculate the number of welding beads of every layer,  $m$ , through the following formula:

$$m = \left\lceil \frac{l_i}{l} \right\rceil + 1 \tag{1}$$

Generally, welding sequence can be divided into two categories, one is welding from one side to the other side, another is welding from sides to the middle. The latter category is usually adopted for its good fusion. For beads located in the same layer, each bead has the same Z direction offset. However, the beads in the different layer have different Z direction offsets. The offset in Z direction is expressed as the following formula:

$$\Delta Z = \frac{-l_i + \sqrt{l_i^2 + 4 \tan \theta \sum_{i=1}^n m_i S}}{2 \tan \theta} \tag{2}$$

$m_i$  is the number of welding beads of the  $i$  layer.

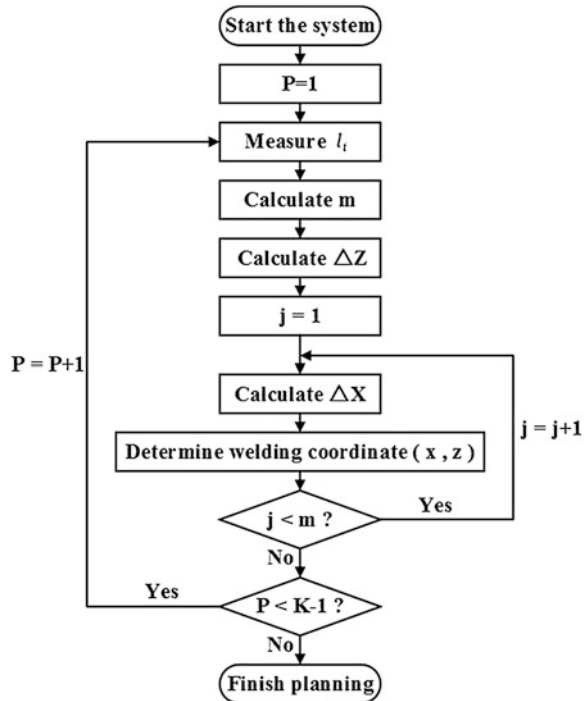
When more than one beads are in a layer, offsets in X direction for the welding gun are necessary, which is:

$$\Delta X = \frac{m_i - 1 - 2(j - 1)}{2m_i} (l_i + 2\Delta Z \cdot \tan \theta) \tag{3}$$

$j$  is the ordinal number of the bead of layer ( $j = 1, 2 \dots m$ ).

On the basis of the work of route planning, the number of layers and beads will be successfully calculated. Assuming that the total number of layers is  $K$ . This process of planning for thick steel plate welding can be demonstrated in Fig. 4.

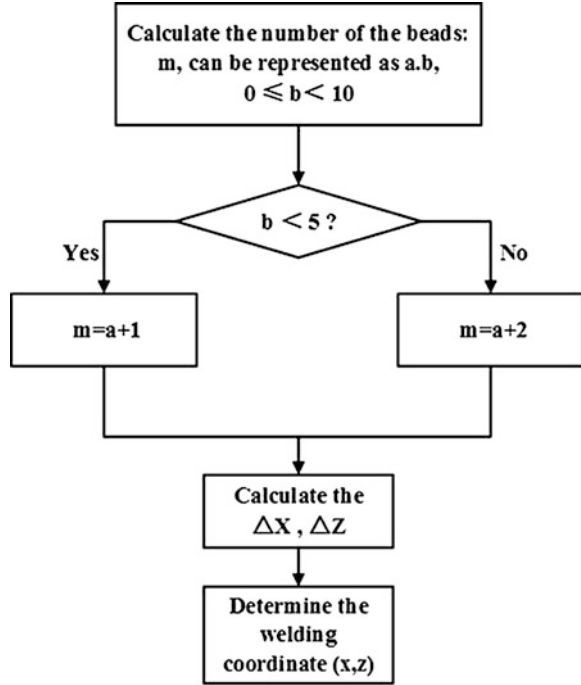
**Fig. 4** Process of route planning



### 3.3 Capping Planning

Capping layer is the last layer filled in the groove. This step is important since it is closely related to the joint quality both mechanically and morphologically. The filler wire cannot fill all the vacancy of the groove under conventional route planning, which will lead to notches causing stress concentration. So not only does capping fill in the vacancy of the groove, but also it needs to connect the surface of two plates so that compensation is needed. The morphology of the filled groove should be sector shaped, that is to say, the surface is slightly convex, covering over the matrix surface. Since the cross section area of each bead is fixed, the core principle of the compensation is to add one or more beads to the last layer to feed more wire, thus increasing the total area of the filling layer. As the increase of area, the height of this layer will rise due to the fixed width of the layer to be filled. In this way, a larger connected area between the wire and the matrix can eliminate notches and improve the mechanical performance. In this part of route planning, two situations are proposed due to different parameters.

**Fig. 5** process of capping planning



First, the approximated number of beads can be calculated by the equation:

$$m = \frac{l_i}{l} \quad (4)$$

Generally  $m$  is not an integer. In that case  $m$  is round to the nearest tenth. So it can be represented as the general format “ $a + b/10$ ”. Both  $a$  and  $b$  are positive integers and  $b$  should be no more than 9. The number  $b$  is taken as the criterion to decide how much beads are required to compensate the vacancy: If  $0 \leq b < 5$ , one more bead is added to the last layer, the total bead number of capping layer  $m$  should be  $a + 1$ , while if  $5 \leq b < 10$ , two beads are added for compensation, the number  $m$  will become  $a + 2$ . Thus, the exact number of bead to weld will be defined. Then substitute the value of  $m$  into the formula (2) and (3) to calculate  $\Delta X$  and  $\Delta Z$  (Fig. 5).

### 3.4 Programming and Visualization

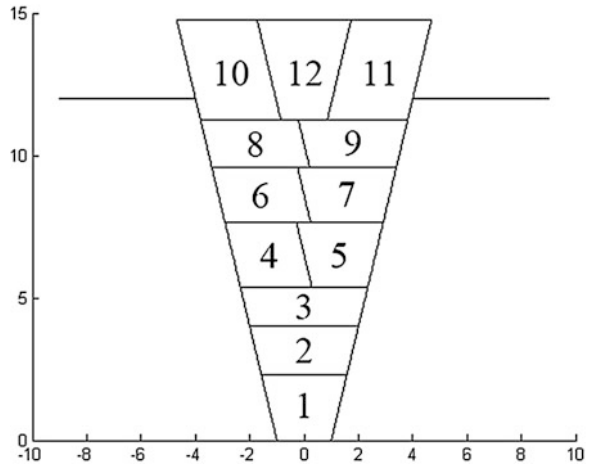
Combining the strategy of route and capping planning, Both Matlab and KUKA robot program is developed to perform the calculation and visualization of the welding plan. The function of the Matlab program is to input appropriate parameters (groove and bead size) for outputting a table including detailed information of each bead, e.g. its layer number, its coordinate and the predicted height of the bead



(calculated by dividing the area of the parallelogram by its width). Visualization is achieved with these data. The output result format is shown in Fig. 6 and Table 2 under the input listed in Table 1.

The KUKA program, coded via OrangeEdit, is able to do the planning and transform the result into movement commands of robot, through which laser welding with filler wire can be accomplished automatically.

**Fig. 6** Visualization of the planning



**Table 1** Input data for the example

Groove	H/mm	$\theta$ (cotangent)	$\delta$ /mm
	12	4	2
Bead	Area/mm <sup>2</sup>		Width/mm
	6		4

**Table 2** Output offsets for each bead planned

Layer No.	Bead No.	Bead height	X coordinate	Z coordinate
1	1	2.32	0.00	0.00
2	1	1.68	0.00	2.32
3	1	1.38	0.00	4.00
4	2	2.28	1.46	5.38
4	2	2.28	-1.46	5.38
5	2	1.90	1.70	7.66
5	2	1.90	-1.70	7.66
6	2	1.67	1.90	9.56
6	2	1.67	-1.90	9.56
7	3	2.03	3.13	12.73
7	3	2.03	0.00	12.73
7	3	2.03	-3.13	12.73

### 4 Experiment and Discussion

Two plates in the thickness of 15.5 mm constituting a trapezoid groove were welded to testify the planning theory proposed above. Due to thermal deformation in backing welding, the groove size is measured after the backing welding. The geometric information of the groove are listed in Table 3.

The welding parameters and the size of the bead accordingly are listed in Table 4.

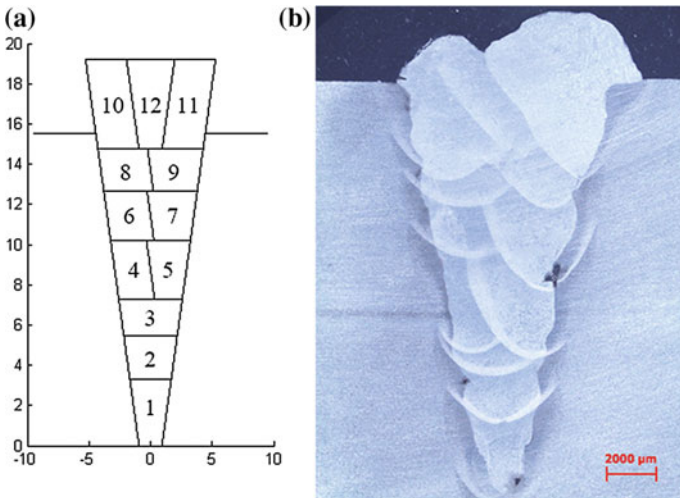
Figure 7 shows the comparison between the route plan and the welded joint. It reveals that the welding result approximately agree with the plan, with good interfacial fusion and almost no inclusion or bubble. Few voids appear in first few passes along the edges of groove, which can be attributed to the instability of the

**Table 3** Groove size

$\delta$ /mm	W/mm	H/mm	$\theta$ /°
1.863	8.874	15.525	12.75

**Table 4** Welding parameters and bead size

Welding parameters	Welding velocity (m/min)	Laser power (kW)	Feeding velocity (m/min)
	0.5	4	4
Bead size	Area/mm <sup>2</sup>	Width/mm	Height/mm
	8.535	4.6	2.921



**Fig. 7** Experiment result: **a** Visualized plan by Matlab. **b** Welding joint under the plan

feeding of filler wire and shielding gas, and deviation of laser spot and wire. The capping layer is accord with what is expected, covering the edges and filled the groove completely.

## 5 Conclusion

This research investigated multi-pass route planning for thick steel plate using laser welding with filling wire. A 15.5 mm thick plate is welded to testify the planning theory. The major findings are listed as follows: (1) Build a system based on KUKA robot for laser welding with filling wire which can be applied to thick plate welding. (2) Establish a strategy for multi-pass route planning for thick plate on the basis of constant welding parameters and parallelogram and trapezoid simplification. A software has been programmed to plan and visualize thick plate planning automatically given appropriate parameters. (3) Propose the principle of capping layer planning to improve the quality of the welding joint (4) Prove the effectiveness of the strategy by experimental test of welding a thick steel plate, with good fusion and no bubble or inclusion.

**Acknowledgement** This article is conducted with the program “The key technologies of ultra-narrow gap laser welding of thick plates and intelligent equipment,” which is finally supported by the special development of key technologies and equipment of Shanghai, in China. The project number is ZB-ZBYZ-03-11-0485, and is also supported by National Undergraduate Innovative Test Program in China under the Grant No. 201410248030.

## References

1. Caiazzo F, Alfieri V, Corrado G, Cardaropoli F, Sergi V (2013) Investigation and optimization of laser welding of Ti–6Al–4V titanium alloy plates. *J Manuf Sci Eng* 135(061012):1–8
2. Klemens P (1976) Heat balance and flow conditions for electron beam and laser welding. *J Appl Phys* 47:2165–2174
3. Shi H, Zhang K, Xu Z, Huang T, Fan L, Bao W (2014) Applying statistical models optimize the process of multi-pass narrow-gap laser welding with filler wire. *Int J Adv Manuf Technol* 75:279–291
4. Suthakar T, Balasubramanian K, Sankaranarayanan K (2012) Multi objective optimization of laser welding process parameters by desirability approach of design of experiments. In: ASME 2012 international mechanical engineering congress and exposition, american society of mechanical engineers, pp 1921–1929
5. Sun Z, Salminen A (1997) Current status of laser welding with wire feed. *Mater Manuf Processes* 12:759–777
6. Yang C, Zhang H, Zhong J, Chen Y, Chen S (2014) The effect of DSAW on preheating temperature in welding thick plate of high-strength low-alloy steel. *Int J Adv Manuf Technol* 71:421–428
7. Yang CD, Huang H, Zhang H, Chen Y, Chen SB (2012) Multi-pass route planning for thick plate of low alloy high strength steel by double-sided double arc welding. *Adv Mater Res* 590:28–34

8. Benyounis K, Olabi A (2008) Optimization of different welding processes using statistical and numerical approaches—A reference guide. *Adv Eng Softw* 39:483–496
9. El-Batahgy A-M (1997) Effect of laser welding parameters on fusion zone shape and solidification structure of austenitic stainless steels. *Mater Lett* 32:155–163
10. Moon H-S, Kim YB, Beattie RJ (2006) Multi sensor data fusion for improving performance and reliability of fully automatic welding system. *Int J Adv Manuf Technol* 28:286–293

# Study of Mechanism and Kinetic About Low Frequency Piezoelectric Motor

Rui Wang, Shu-Chen Yang, Xiao-Yang Jiao and Xiao-Tao Li

**Abstract** This paper presents a new type of tilting low frequency piezoelectric motor which can satisfy the need of small size and high torque for precise instrument. The driven mechanism of the motor is studied and the dynamic model of the motor is established. Based on the need of experimental research, the prototype is manufactured. In addition, the experimental test of the prototype, namely, the impact of input frequency on output speed and torque, is conducted, which shows that for the new type of low frequency piezoelectric-motor the optimal work performance is achieved, when input frequency is 290 Hz.

## 1 Introduction

Compared with the piezoelectric ultrasonic motor, the low frequency piezoelectric motor is a new kind of piezoelectric drive motor working at low frequency. On the drive pattern, the low frequency piezoelectric motor is similar to the current contact ultrasonic motor, that is, by the frictional force produced between stator and rotor of the motor, the vibration of the piezoelectric vibrator is transferred into the driving force that drives the rotor. However, the driving frequency of low frequency piezoelectric motor is much lower than that of the contact ultrasonic piezoelectric motor, so that the problem that the contact ultrasonic piezoelectric motor must be equipped with

---

R. Wang (✉) · S.-C. Yang  
Jilin Teachers' Institute of Engineering Technology, Changchun, China  
e-mail: wrcat@126.com

S.-C. Yang  
e-mail: 397641519@qq.com

X.-Y. Jiao · X.-T. Li  
Jilin University, Changchun, China  
e-mail: ljiaoxiaoyang@163.com

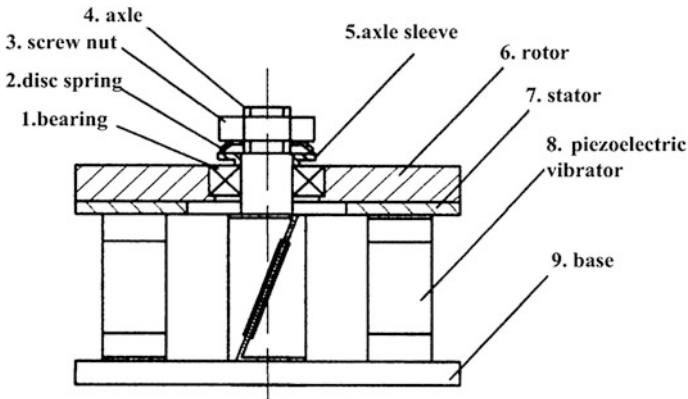
X.-T. Li  
e-mail: lixiaotao@jlu.edu.cn

high frequency drive power supply is solved. In addition, the piezoelectric motor has the merits of compact structure, high precision transmission, anti-electromagnetic interference and so on, therefore, it is widely applied in the precision instruments. Scholars abroad have studied piezoelectric motor long time ago, for example, Williams and Brown applied for the patent of piezoelectric motor in 1942, from then on, piezoelectric motors [1] have been successively developed by the German Siemens company and Matsushita company, the American IBM company, the Japan canon company and so on. The research of piezoelectric motor in China started relatively late. In the 1990s, Professor Jiwei Jiao and others from Dalian University of Technology developed a kind of vibration feeder using double piezoelectric wafer [2, 3]; Professor Yuming Du cooperating with colleagues obtained the design thought and method based on the low frequency of piezoelectric vibrator, in the view of the design method of feeder [4]; In 2005, Chunyue Lu and others studied and developed a piezoelectric motor with clutch coupling [5]. Also, in the research field of low frequency piezoelectric drive technology, study of piezoelectric vibrating motor in order to reduce driving frequency is carried out by many scholars abroad in recent years, however, its working frequency is several thousand Hz or so [6–8]. At present, due to the vibration frequency of piezoelectric motor studied by scholars at home and abroad is generally larger than several thousand Hz and its drive needs to be equipped with high-frequency electric source, thus, it has characteristics of high cost, large volume and complex method of application, therefore, its practical application is limited.

This paper presents a new type of piezoelectric motor driven by low frequency power supply, that is, it is driven by vibration between 30 Hz and 300 Hz, instead of ultrasonic vibration. Compared with ultrasonic piezoelectric motor, it has many merits, such as, small noise, high torque, the ability to form a continuous rotary motion and work in frequently-used power supply (50 Hz) and so on, thus, it has good practical application prospect. In this paper, the drive capability and drive mechanism of low frequency piezoelectric motor are studied and the dynamic model of driving structure is established. In addition, the prototype is manufactured and the experimental research of input and output performance is carried out.

## **2 The Structure and Driving Mechanism of Low Frequency Piezoelectric Motor**

As shown in Fig. 1, the structure of low frequency piezoelectric motor is mainly composed of rotor, stator, disc spring, Z-shaped piezoelectric vibrator, base and so on. Piezoelectric vibrator is the driving source of low frequency piezoelectric motor, which is uniformly arranged along the circumferential direction of pedestal, at 90° and the upper and lower end face are respectively fixed to the stator and the base. Because of the inverse piezoelectric effect of piezoelectric materials, when applied with appropriate alternating voltage, the piezoelectric vibrator produces double vibrations harmony with the supply frequency. It is because the piezoelectric vibrator is fixed to the stator and the base that when the piezoelectric vibrator



**Fig. 1** Low frequency piezoelectric motor structure diagram

produces flexural vibration, it is forced to make small torsional deformation, thus, the bending torsional vibration of piezoelectric vibrator is achieved.

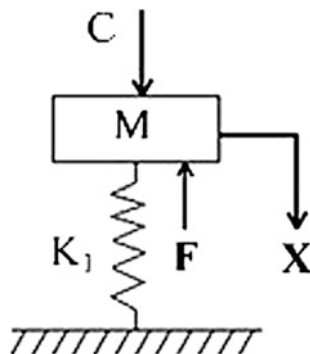
The bending torsional vibration of piezoelectric vibrator drives the stator to produce slant reciprocal rectilinear motion. The rotor is fixed to the base by bearing 1, disc spring 2, axle 4 and screw nut 3, thus, the rotor has free rotational motion, but its vertical displacement relative to the base is limited. Adjusting screw nut 3, an appropriate pre-tightening force  $C$  is applied to the rotor. When the piezoelectric vibrator drives the stator oblique upward movement, the pressure  $N$  between the stator and the rotor increases gradually, the frictional force  $f$  between the stator and the rotor increasing gradually, as well. When the friction force  $f$  exceeds the critical value  $f_c$ , the rotor is forced to move upward obliquely with it; when the piezoelectric vibrator starts to do downward bend torsion movement, the piezoelectric vibrator drive the stator to do downward twist motion, however, because of the inertia effect of the motor, the motor will continue oblique upward movement with a certain displacement  $\delta$ , thus, the motor separates from the stator and the frictional force  $f$  between the stator and the rotor is less than the critical value  $f_c$ , that is, the motor can't be driven to move down diagonally with the stator. In this way, in the process of bending torsional vibration of the piezoelectric vibrator (generally a vibration period), the motor makes a tiny rotary movement. If piezoelectric vibrator vibrates continuously, the continuous rotation of the piezoelectric motor rotor is achieved.

### 3 Establishment of the Dynamic Analysis Model

#### 3.1 Force Analysis of Motor in Vertical Direction

When the contact force exists between the stator and motor of the piezoelectric motor, that is, the braced force of the leaf spring at the bottom is not equal to the gravity of the stator and center shaft, pressure will exist between the stator and the

**Fig. 2** Low frequency of piezoelectric motor vibration model



motor. Assume that the value of the pressure is  $C$  and its direction is vertically downward. Periodic exciting force  $F(t)$  was applied to the motor by the stator. In the first half period of motion, the motor moves, which is driven by the stator and the vibration model of this system is shown in Fig. 2; the disc spring, as part of the motor, works as a spring. On this occasion, the damp of this system is generally small, which can be neglected. Therefore, this system can be seen as a second order linear undamped spring mass system.

The differential equation of this system can be expressed as Eq. 1

$$m\ddot{x} + kx + C = F(t) = F(t) \sin \omega t \tag{1}$$

Under the condition of single degree of freedom, the solution of differential equation of forced oscillation is composed of two parts, that is, the general solution  $x_1$  and the particular solution  $x_2$ , that is,  $x = x_1 + x_2$ .

Generally, when the damp is fairly small, the general solution  $x_1$  is the solution of homogeneous equation of free vibration. Therefore, only in the primary stage of the movement of this system, does the general solution  $x_1$  have practical significance. In the differential equation of this system, only the particular solution  $x_2$ , that is, the steady-state solution has practical significance.

Since the motivation  $F(t)$  is simple harmonic vibration, supposed that the particular solution is

$$x_2 = X \sin(\omega t + \varphi) + C_1 \tag{2}$$

where  $x$  is amplitude;  $\varphi$  is phase angle;  $C_1$  is constant.

Substitute Eq. 2 into Eq. 1 and the solution is obtained and systemized as

$$X = \frac{F/k}{1 - (\omega/\omega_n)^2} \tag{3}$$

$$C_1 = -C/K \tag{4}$$



$$\omega_n = \sqrt{k/m} \quad (5)$$

The particular solution is expressed as

$$x = x_2 = \frac{F/k}{1 - (\omega/\omega_n)^2} \sin \omega t - C/K \quad (6)$$

From the analysis above, it can be seen that, generally, for the tilting low-frequency piezoelectric motor, the forced oscillation of the motor in simple harmonic vibration belongs to simple harmonic vibration, its frequency of vibration equal to excitation frequency. If the stiffness value of the spring at the bottom is equal to the excitation frequency of the stator, namely,

$$m\ddot{x} + kx + c = 0 \quad (7)$$

Its general solution is

$$x(t) = A_1 \cos \omega_n t + A_2 \sin \omega_n t + c' \quad (8)$$

The resonant frequency is expressed as

$$\omega_n = \sqrt{k/m} \quad (9)$$

From the formula above, it can be seen that when the excitation frequency of piezoelectric vibrator is equal to the resonant frequency of this system, the normal rotation movement of the rotor will be achieved.

### 3.2 Force Analysis of Rotation Movement of the Rotor

The Piezoelectric vibrator, simulated by alternating current, can be seen as doing simple harmonic motion, the simple harmonic motion of the rotor expresses as

$$S = A \sin \omega t \quad (10)$$

where A is amplitude of vibration;  $\omega$  is frequency of vibration; t is time of vibration.

When the rotor is applied with periodic impact force, that is,  $F = P \cdot \sin \omega t$ , of the stator and the restoring force of the spring at the bottom, the differential equation can be expressed as:

$$m\ddot{y} + ky + f + mg - p \sin \omega t \sin \theta = 0 \quad (11)$$

where f is pulling force provided by spring at the bottom; k is the stiffness coefficient of spring at the bottom.

When the item of Eq. 11 on the left is less than zero, the rotor of the system can be thrown up; when the item of Eq. 11 on the left is equal to zero, the rotor will be at the critical state of being thrown up; when the item of Eq. 11 on the left is larger than zero, The rotor will not be thrown up.

During the movement of the rotor, driven by the stator, the stress of the rotor in y direction is expressed as

$$N = m\ddot{y} + ky + f + mg - p \sin \omega t \sin \theta \tag{12}$$

The stress of the rotor in x direction is expressed as

$$P \sin \omega t \cos \theta - \mu N > 0 \tag{13}$$

At this moment, the rotor will rotate in the positive direction.

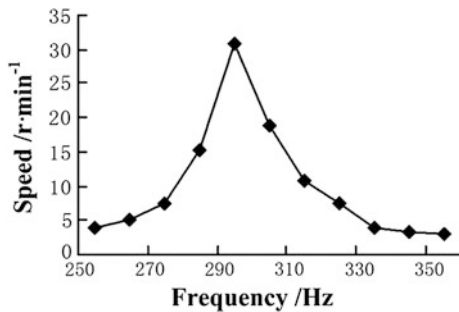
## 4 Experimental Analysis

Through the prototype test of the manufactured low frequency piezoelectric motor, the impact of input frequency of the low frequency piezoelectric motor on output speed and torque and the impact of input voltage of the motor on output speed and torque.

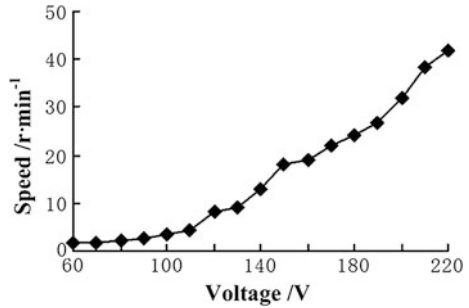
### 4.1 The Relationship of Frequency and Speed

Figure 3 shows the relation curve of output speed changing with input frequency, when the input voltage of the low frequency piezoelectric motor is 180 V. Adjusting the input frequency, when the frequency is up to 200 Hz, the rotor starts to move slightly. When the frequency increases to 250 Hz, the rotor speed is 4.2 r/min. After then, the rotor speed will be measured once if the frequency

**Fig. 3** Low frequency piezoelectric motor speed changing with frequency relations



**Fig. 4** Low frequency piezoelectric motor speed vary with voltage



increases 10 Hz. It can be seen that when the input frequency is up to 290 Hz, the rotor speed gets the maximum 30.7 r/min; when the input frequency exceeds 290 Hz, the rotor speed decreases sharply. The conclusion of this experiment is that resonant frequency of the low frequency piezoelectric motor is 290 Hz.

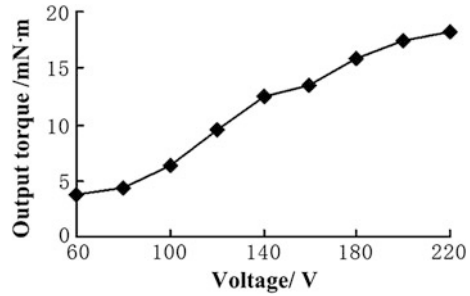
## 4.2 The Relationship of Voltage and Speed

Figure 4 shows the relation curve of output speed changing with input voltage, when the input frequency of the low frequency piezoelectric motor is 290 Hz (the resonant frequency). When the input voltage is up to 60 V, the rotor starts to move slowly. The rotor speed will be measured once if the voltage increases 10 Hz, the input voltage adjusted from 60 to 220 V. It can be seen that the output speed increases with the increase of input voltage. When the voltage is between 60 and 100 V, the rotor speed increases gently; when the voltage exceeds 100 V, the rotor speed increases distinctly and when the voltage is up to 220 V, namely, the power frequency voltage, the maximum rotor speed is 41.6 r/min.

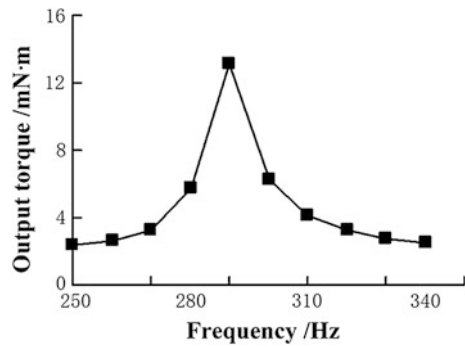
## 4.3 The Relationship of Voltage and Output Torque

Figure 5 shows the relation curve of output torque of the rotor changing with input voltage, when the input frequency of the low frequency piezoelectric motor is 290 Hz (the resonant frequency). The output torque increases with the increase of input voltage. When the input voltage is less than 60 V, the torque is quite small; when the voltage is between 60 and 140 V, the output torque increases sharply with the increase of input voltage; however, when the input voltage exceeds 140 V, the output torque increases slightly. When the input voltage is 220 V, the maximum torque is 18.3 mN m.

**Fig. 5** Low frequency piezoelectric motor torque vary with voltage



**Fig. 6** Low frequency piezoelectric motor torque vary with frequency relations



#### ***4.4 The Relationship of Frequency and Output Torque***

Figure 6 shows the relation curve of output torque of the rotor changing with input frequency, when the input voltage of the low frequency piezoelectric motor is 180 V. From the experiment, it can be seen that when the input frequency is 288.3 Hz, the maximum torque of the rotor is 13.1 mN m. It shows that the rotor with load is almost coincident with the resonant frequency without load.

### **5 Conclusion**

Through the experiment study and analysis above, it can be seen that

1. The rotor vibration of the low frequency piezoelectric motor can be seen as simple harmonic vibration in the vertical direction, the vibration frequency equal to the excitation frequency applied to piezoelectric vibrator.
2. The continuous rotation of the low frequency piezoelectric motor rotor is determined by the pre-tightening force  $F_C$  between rotor and stator and the driving force of piezoelectric vibrator. The pre-tightening force  $F_C$  can't be too

small and the driving force of piezoelectric vibrator can't be too large, otherwise, the stator can't make the rotor rotate continuously.

3. The low frequency piezoelectric motor can make the rotor rotate continuously in low frequency with certain output torque. When the input frequency is resonant frequency, the optimal output speed and torque are achieved; when input frequency is a fixed value, the output speed and torque of the low frequency piezoelectric motor will increase with the increase of the input voltage.

## References

1. Ueha T, Yang Z, Zheng X (1998) Theory and application of ultrasonic motor. Shanghai Science and Technology Press
2. Jiao Q, Cui W, Sun B, He C (2001) Develop of piezoelectric vibration feeder. *Sensor Technol* 20(4):23–26
3. Jiao Q, Cui W, Sun B (2001) Intelligent drive power supply of small piezoelectric vibration feeder. *Comput Autom Meas Control* 9(3):52–57
4. Du Y, Guan Z, Wu D (1999) Technology of reverse of the piezoelectric vibrating feeder. *Mech Des* 16(4):18–20
5. Lu C, Zhao C (2005) The design of piezoelectric motor driven by clutch coupling. *Piezoelectrics Acoustooptics* 27(1):24–26
6. Lamberti N, Iula A, Pappalardo M (1998) A piezoelectric motor using flexural vibration of a thin piezoelectric membrane. *IEEE Trans Ultrason Ferroelectr Freq Control* 45(1):23–29
7. Ueha S, Tomikawa Y, Kurosawa M, Nakamura K (1993) Ultrasonic motor theory and application. Claredon Press, Oxford
8. Kurosa M, Nakamura K, Okamoto T, Ueha S (1989) An ultrasonic motor using bending vibration of a short cylinder. *IEEE Trans Ultrason Ferroelectr Freq Control* 36:668–674

# Microstructures and Mechanical Properties of 30CrMnSiA Steel Joints Welded by Vacuum Electron Beam

Shan-Lin Wang, Shan-Ben Chen, Xing Li and Li-Peng Wan

**Abstract** The 30CrMnSiA plate with 2 mm thickness which is applied extensively in aerospace industry was welded by vacuum electron beam, and the microstructures and mechanical properties of joint were investigated. The results indicate that a well-formed joint can be fabricated by vacuum electron beam with various welding parameters. Due to intensive heat and rapid cooling rate, the typical lath martensite is formed in fusion zone and the grains in the narrow heat affected zone are grown greatly. The microhardness and tensile strength of joint exceed to 600 Hv and 1400 MPa, respectively, which are extensively higher than that of basic metal. The fracture is occurred in the heat affected zone during tensile experiment.

## 1 Introduction

Due to higher hardness, penetration and specific strength, 30CrMnSiA steel presents excellent complex mechanical properties, resulting in the usage as welded constructions such as blade in high pressure blower, high strength structural parts in air plane served in the condition with oscillating load. The shielded metal-arc welding (SMAW), CO<sub>2</sub> gas metal-arc welding (GMAW), and so on are usually applied for the joint of 30CrMnSiA steel, however, the severe distortion and cold crack are usually occurred. Therefore, the parts welded by SMAW or GMAW are difficult to

---

S.-L. Wang (✉) · S.-B. Chen

Intelligentized Robotic Welding Technology Laboratory, Shanghai Jiao Tong University,  
Shanghai 200240, China  
e-mail: slwang70518@nchu.edu.cn

S.-L. Wang · X. Li

School of Aeronautic Manufacturing Engineering, Nanchang Hangkong University,  
Nanchang 330063, China

L.-P. Wan

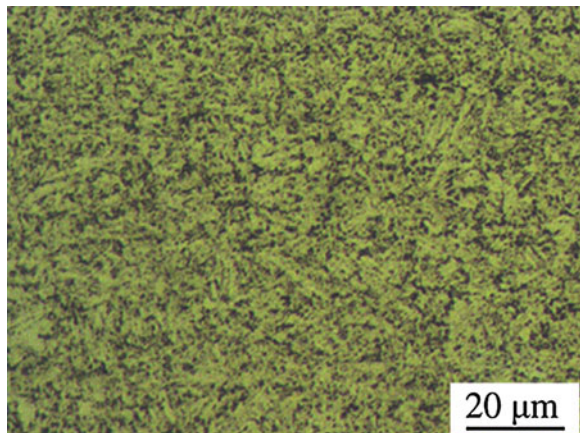
AVIC Jiangxi Hongdou Aviation Industry Group Corporation Limited,  
Nanchang 330024, China

apply in aerospace products requiring high tensile strength [1–4]. The cold metal transfer technology, pre-roll-assisted welding, etc. are reported to improve strength and crack resistance of joint [5–7]. While the tensile strength and crack resistance of the joint can be improved when they are welded by pulsed metal argon-arc welding, plasma arc welding, and vacuum electron beam which exhibit high heat density, resulting from the fine grains formed in fusion zone and a narrow heat affected zones [8, 9]. Since the parts of 30CrMnSiA steel are welded scarcely in aerospace industry, and the microstructure and mechanical properties of the joints are reported rarely. Therefore, providing experimental proof for the welding application of vacuum electron beam in 30CrMnSiA steel, in this study, the effect of welding parameters on microstructures and mechanical properties of the joints are explored.

## 2 Experimental

The butt joints of the 30CrMnSiA steel plate with the size of 300 mm × 100 mm × 2 mm were welded by vacuum electron beam, which is a medium-carbon quenching and tempering steel, consisted of sorbites and some ferrites, as shown in Fig. 1. During welding process, the accelerating voltage was 150 kV, the beam current was 4–13 mA, the welding velocity was 5 mm/s, and other parameters are listed in Table 1. In order to avoid the entrance of metal steam and ion into chamber of electron beam generator, the central axis of electron beam generator was deviated a 3° angle with the vertical direction of welds surface during welding processes. The microhardness along cross section of joint was measured by 401MVD hardness test machine, the hold time is 10 s, and load force is 1.96 N. The tensile test specimen was made according to the standard of metallic materials-tensile testing (GB/T 2652-2008) at ambient temperature, and the tensile strength was measured by Instron 4200IX testing machine at a strain rate of  $1 \times 10^{-4}$  m/s. The fracture morphologies were observed by SEM.

**Fig. 1** Microstructure of basic metal

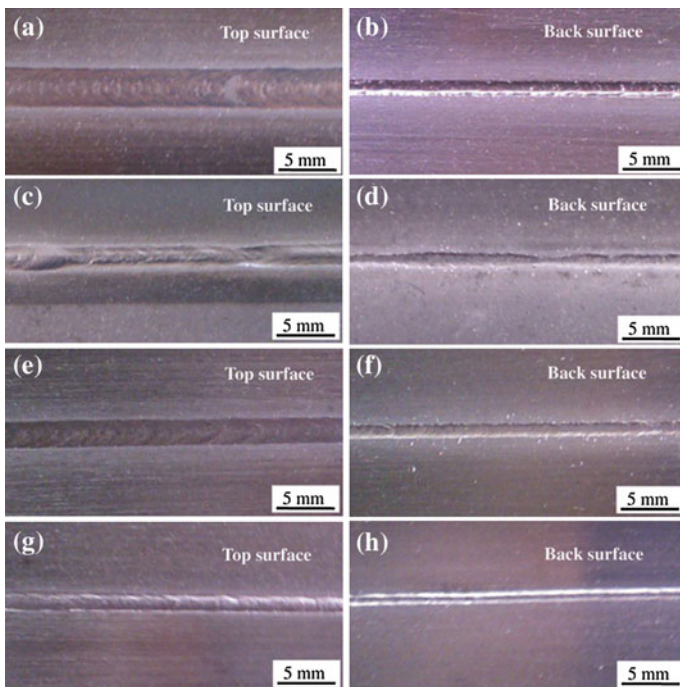


**Table 1** The welding parameters of vacuum electron beam

No.	EB focus distance/mm	EB focus current/mA	Welding voltage/kV	Welding current/mA	Scanning waveform	Welding velocity/mm s <sup>-1</sup>
1#	AA400	2290 (27 mA)	150	4	×0.3 F50 Hz cycle	5
2#	AA400	2290 (27 mA)	150	10	×0.5 F200 Hz cycle	10
3#	AA400	2290 (27 mA)	150	10	×0.5 F5000 Hz square wave	10
4#	AA400	2290 (27 mA)	150	13	×0.5 F200 Hz cycle	25

### 3 Results and Discussions

Figure 2 shows the surface shape of four joints welded with different parameters. The smooth surfaces and ripples are obvious, and no lack of fusion, incomplete penetration, undercutting and weld flash, etc. can be observed, except for the some shallow cavities on the top surface for the 2# joint. With decrease of heat input, the weld width at cross section also reduces. The weld width is near 5 mm using the weld parameters of welding current 4 A, welding velocity 5 mm/s and a cycle



**Fig. 2** Surface shape of four joints welded with different parameters: **a** and **b** 1#, **c** and **d** 2#, **e** and **f** 3#, **g** and **h** 4#

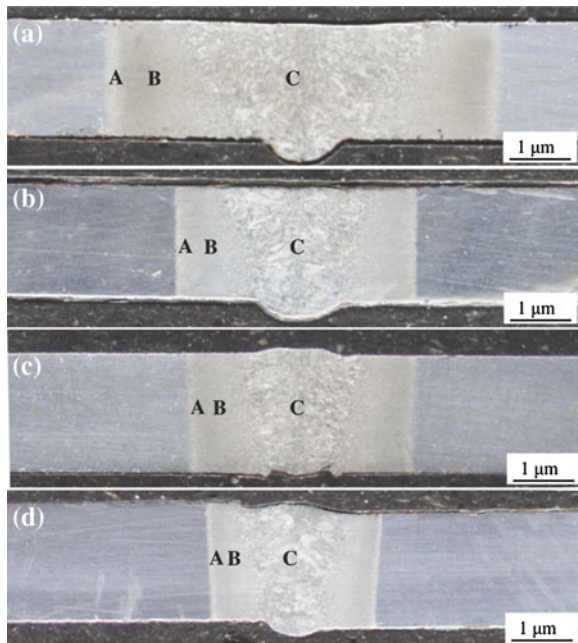


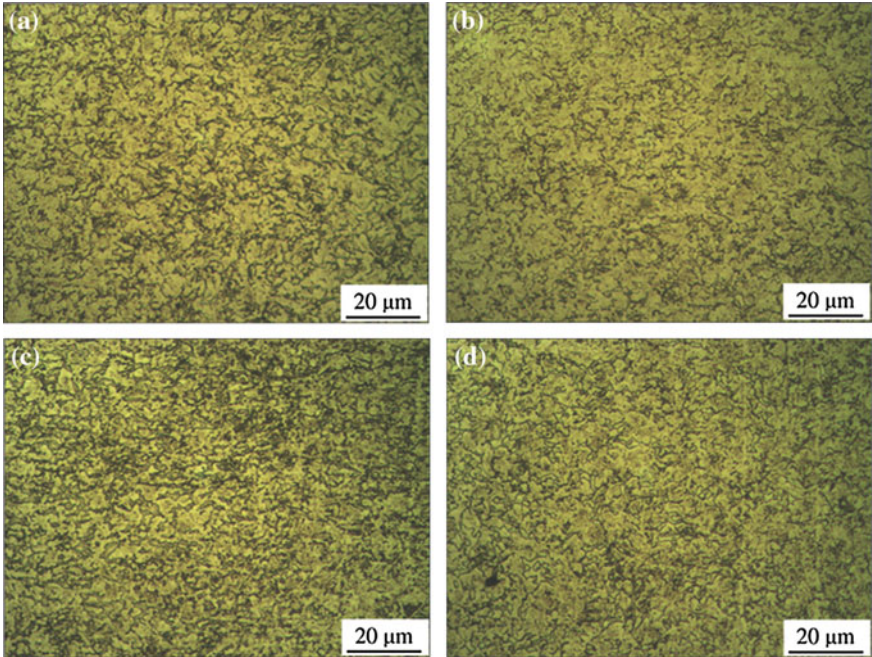
scanning waveform with 0.3 mm in radius and 50 Hz frequency, while the weld width decrease to 2 mm with welding current 13 A, welding velocity 25 mm/s and a cycle scanning waveform with 0.5 mm in radius and 200 Hz frequency, as shown in Fig. 3.

Figure 4 shows the microstructures of heat affected zone as marked with 'A' in Fig. 3. It is a typical pearlite that is composite of granular ferrite and flake carbide. Since the temperature of this zone is lower than that of  $Ac_1$ , the austenite transformation can't be developed, while the dispersal carbide will grow with the carbon diffusion in the high temperature, and then forms the flake carbide. Though the heat input is different with the four weld processes, the temperature should be similar in this zone, so the size of pearlite is similar, as shown in Fig. 3.

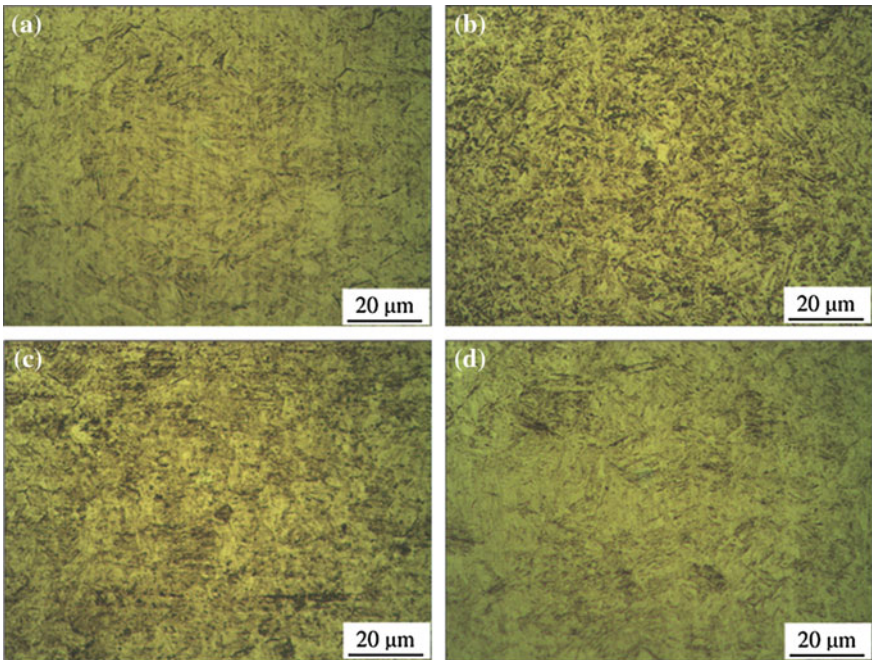
Figure 5 shows the microstructure of heat affected zone as marked with 'B' in Fig. 3, which are attained with different weld processes. During vacuum electron beam welding process, due to the high and concentrated heat input, though the width of heated affect zone is lower than that with traditional arc fusion welding, the temperature is still higher than that of  $Ac_3$  in 'B' zone, so the sorbite will transform into austenite, however, as the short holding time of the temperature higher than  $Ac_3$ , the austenite does not coarsening sharply. During cooling, the austenite will transform into martensite, as shown in Fig. 5d, and the cooling rate increases with the decrease of heat input, resulting in the increase of martensite. When the heat

**Fig. 3** Cross section morphologies of four joints: a 1#, b 2#, c 3#, d 4#





**Fig. 4** Microstructures of heat affected zone for all joints: **a** 1#, **b** 2#, **c** 3#, **d** 4#

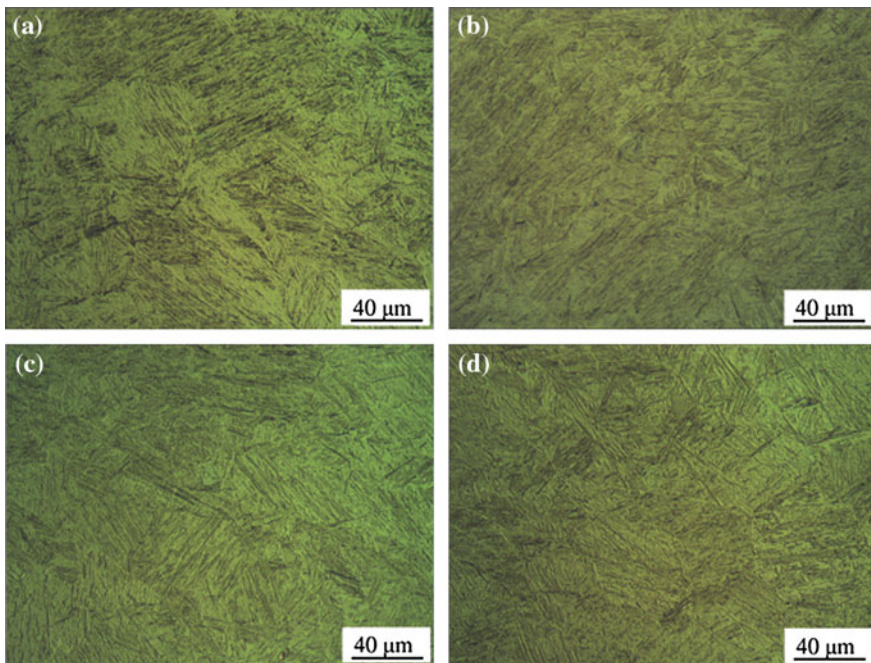


**Fig. 5** Microstructures of heat affected zone for all joints: **a** 1#, **b** 2#, **c** 3#, **d** 4#

input increases, the temperature also increase in heat affected zone. Therefore, the cooling rate will decrease during cooling, promoting that one part of austenite transforms into martensite, one part transforms into bainite and another are not transformed, and forms retained austenite [10], as shown Fig. 5a–c.

The microstructures of fusion zone marked with ‘C’ in Fig. 3 are shown in Fig. 6. It is obvious that the coarse lath martensite is formed in the fusion zone though the heat input is different. Owing to the concentrated heat input, the peak temperature in fusion zone is very high, while the  $A_{c3}$  is only 800 °C for 30CrMnSiA steel, so austenite will coarsen in initial stage during cooling, and then the coarse austenite transforms martensite with the temperature decreasing. Moreover, with the increasing of cooling rate as the lower heat input, the lath martensite is more coarsening, as shown in Fig. 6.

Figure 7 is microhardness distribution of joints, which is tested along cross section with the weld center as original point. The microhardness exceeds 600 Hv, near double higher than that of basic metal. Moreover, the microhardness in heat affected zone increase gradually from basic metal side to fusion line, and no lower value than that of basic metal is measured in this zone. As decrease of heat input,



**Fig. 6** Microstructures of fusion zone for four joints: **a** 1#, **b** 2#, **c** 3#, **d** 4#



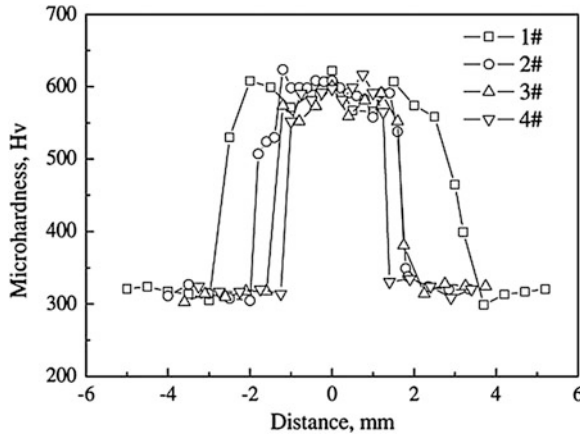
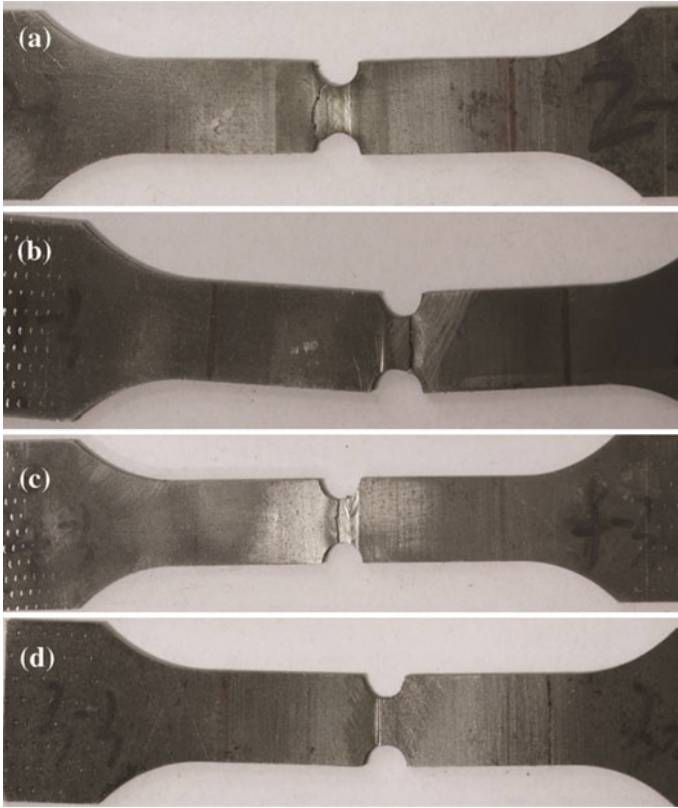


Fig. 7 Microhardness along horizontal central line in cross section of four joints

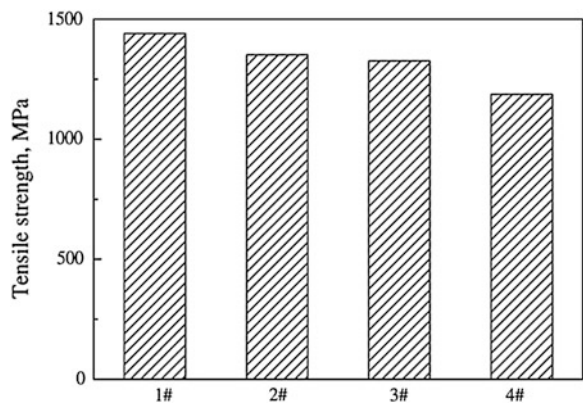
the width of heat affected zone is also decreased, and the tendency is matching with that as shown in Fig. 3. The maximum hardness value is similar for the four joint. Though different heat input for the four joints, the microstructure in fusion zone is lath martensite, so the effect of heat input on microhardness is not sharp. The microstructures in heat affected zone are composed of martensite, bainite and retained austenite, and the grains are not coarsened obviously, therefore, no softening is not occurred near basic metal.

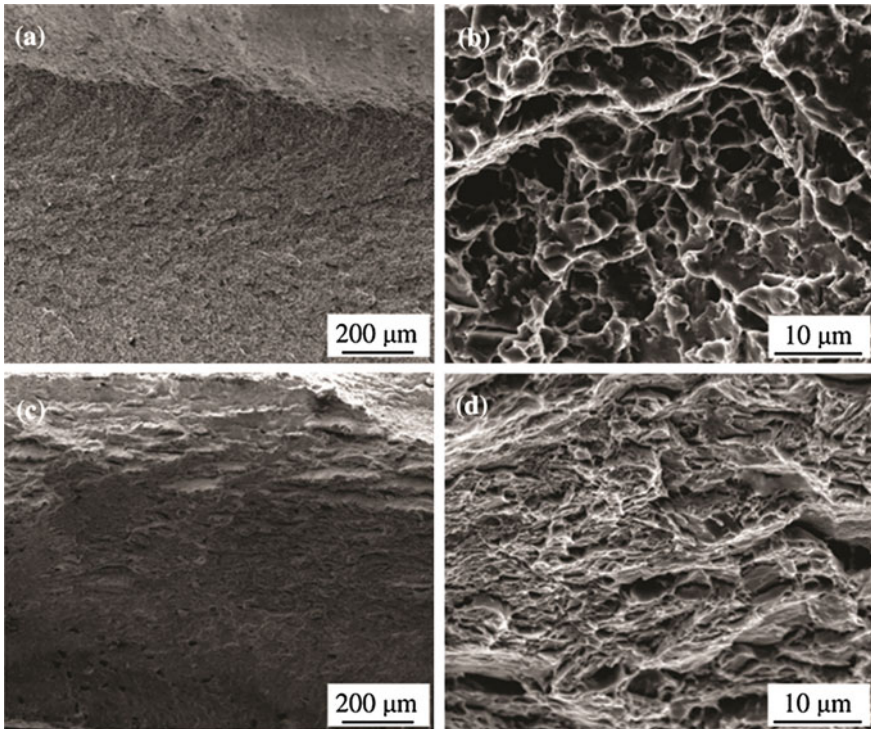
In order to measure the tensile strength of welds, a half cycle with a radius of 0.3 mm is cut at the weld center line in ether side of standard tensile specimen. The fracture of four joints welded with different heat input is shown in Fig. 8. It can be seen that a fracture is developed in heat affected zone for all specimens. The maximum tensile strength exceed 1400 MPa for 1# joint, and as decrease of heat input, the tensile strength also decrease, while the minimum tensile strength also exceeds 1200 MPa for 4# joint, which is most higher than that of basic metal of 1000 MPa, as shown in Fig. 9. As the excellent weldability for 30CrMnSiA steel, no defects are formed in the joints, and the martensite with high tensile strength and hardness also presents some ductility, as shown in Fig. 10a, where the uniform dimples can be developed in the fracture. Therefore, the excellent tensile strength can be obtained for this joint. However, as decrease of heat input, the cooling rate increases, leading to the microstructural non-uniformity more and more apparently since the lower diffusion velocity of alloying elements in heat affected zone, and the martensite is more and more coarsening, so the tensile strength and ductility of joint reduces gradually [11], and a cleavage fracture occurs for 4# joint as shown in Fig. 10b.



**Fig. 8** Fractural images of joints after tensile strength test: **a** 1#, **b** 2#, **c** 3#, **d** 4#

**Fig. 9** Tensile strength of four joints





**Fig. 10** Fracture morphologies of joints

## 4 Conclusion

1. The excellent formation and no defects joint can be attained for 30CrMnSiA steel welded by vacuum electron beam welding. The lath martensite is formed in fusion zone and the microstructure of heat affected zone is consisted of martensite, bainite and some retained austenite.
2. The tensile strength of joint exceeds 1400 MPa and is most superior basic metal. No softening occurs in the joints and the fracture always is developed in heat affected zone.

## References

1. Du H, He X (2013) Micro-crack analysis on TIG weld of missile 30CrMnSi shell. *Aeronaut Manuf Technol* 13:11–116
2. Han J, Chi Y (2004) Narrow gap submerged arc welding for major Diametral shell made of BHW-35. *Press Vessel Technol* 21(3):32–35

3. Yang J, Huang L, Zhang Y (2011) Mechanism of cold welding cracks in 30CrMnSi steel joints welded by TIG method. *Trans China Weld Inst* 32(12):13–17
4. Zhang S, Zhang H (2013) Study on laser welding technology of T-joints of 30CrMnSi steel. *Hot Working Technol* 42(7):199–200
5. Jiang X, He P, Feng J (2007) Microstructure characteristics of CuSi3 cladding on 30CrMnSi steel with cold metal transfer technology. *Trans China Weld Inst* 28(2):47–51
6. Liu DB, Yang JG, Pan HB (2012) Controlling delayed cracks in welded joints of MCQTT steel by welding with trailing impacting and rolling. *China Weld* 21(2):33–37
7. Wang J, Cao J, Feng JC (2010) Microstructure and mechanical performance of depositing CuSi<sub>3</sub> Cu alloy onto 30CrMnSi steel plate by the novel consumable and non-consumable electrodes indirect arc welding. *Mater Des* 31:2253–2258
8. Pang H, Zhang Z (2012) Analysis of crack near fusion line for 35CrMnSi steel welded by vacuum electron beam. *Nondestr Inspection* 36(4):36–38
9. Chen G, Zhang B, Wang Z (2011) Vacuum electron beam welding of 35CrMnSi steel. *Trans China Weld Inst* 32(9):33–38
10. Xie R, Li L, Chen F (2009) Microstructure and mechanical properties of 35CrMnSi steel welded by vacuum electron beam. *Weld Technol* 38(1):6–8
11. Yan S, Liu J, Zhang H (2010) Research on laser welding of 30CrMnSi steel. *Acta Armamentarii* 31(7):30–37

# Key Technologies and Automation System for Large-Scale Aerospace Component Welding

Yirong Zou, Baohua Chang, Li Wang, Jiluan Pan and Dong Du

**Abstract** The welding of large-scale structures is a challenging issue for automatic welding robots and systems. We present the technologies and the implementation of system for the automatic welding of complex large-scale structures. Numerical simulation technology for calculating the welding distortion and the residual stress is applied for the optimization of the welding process. The on-line sensing technology is proposed for the control of welding torch motion. The implementation of the automatic welding system is presented in a case study on the welding of the launcher fuel tank.

## 1 Introduction

Technologies of welding automation are gathering more and more attentions as the development of shipbuilding, civil construction, automobile manufacturing, and aerospace manufacturing, etc. The welding of large-scale structures which possess complex configuration is a challenging issue for automatic welding robots and systems. The difficulty of large-scale component welding can be described in the following three aspects:

- The complexity of the welding trajectory requires the synchronized control of the torch motion and the welding parameters. Difficulty arises when the seam to be welded takes the shape of a space curve. The combined planning of both the welding pose and the welding parameters should be implemented in the programming of the automatic welding system. Also, the scale and the weight of the structure requires large operation range and robust mechanical performance of the actuating part of the system.

---

Y. Zou · B. Chang · L. Wang · J. Pan · D. Du (✉)  
Department of Mechanical Engineering, Key Laboratory for Advanced Materials  
Processing Technology, Ministry of Education, Tsinghua University, Beijing 100084,  
People's Republic of China  
e-mail: dudong@tsinghua.edu.cn



- Tremendous heat input during the welding process causes directly the problem of distortion of large-scale structure, especially for the welding of large components with small thickness, which is one of major challenges in aerospace manufacturing. Welding distortion may bring difficulties to the automatic welding process. Jigs and fixtures need to be used in order to minimize the welding distortion. Residual stress and distortion exist after removing the jigs and fixtures.
- The clamp positioning error and the distortion generated during the welding process both can give rise to the deviation of the planned welding path to the desired trajectory. Real-time sensing technology for on-line feedback control should be implemented. High adaptability is required.

Industrial robots are widely used in the welding of large components with complex structure. Using the offline robot programming method, the welding robot or the automatic welding system can repeat the pre-planned welding trajectory with precision. However, the “teach-and-playback” method is time-consuming and hardly flexible [1]. Machine vision has been introduced to the domain of welding automation for several years. A typical early installation was at Volvo Flygmotor in 1987. A visual sensing system has been applied to the welding of the square section tube that formed the exhaust cone for Ariane 5 rocket motor [2]. An accuracy of 0.1 mm has been achieved. The welding of complex structure has been drawing the attentions of researchers and engineers. A binocular method for weld detection has been proposed to recognize the starting point of the weld in unstructured environment [3]. A laser scanning method has been studied to solve the problem of welding trajectory auto-planning [4]. However, the drawbacks of the existing methods [3–7] include: although using general industrial robots provides convenience to the trajectory programming, the operation range is limited by the robot size; the visual sensing methods are not designed for the recognition of the weld seam which has an width of less than 0.5 mm; the compromise between the sensing range and the accuracy needs to be taken into consideration.

The aim of this paper is to provide a brief introduction of key technologies and the system implementation. The remaining part of the paper proceeds as follows: Sect. 2 describes the numerical simulation technology for calculating the welding distortion and the residual stress, in order to optimize the design of the welding process. Section 3 presents the on-line sensing technology for the control of welding torch motion. Section 4 analyzes the implementation of the automatic welding system via a case study on the welding of the launcher fuel tank. Finally, the conclusions give a brief summary on the whole study.

## **2 Numerical Simulation Technology for Process Optimization**

The petal-shaped pieces are important components of launcher fuel tank. They experience highly inhomogeneous thermomechanical process during the welding process. Significant residual distortion and even cracks can be induced by high

thermal stress. Various factors, including the welding parameters and the welding sequence, may influence the conditions of stress and distortion during and after the welding process. For better product quality, the welding procedure should be analyzed and improved.

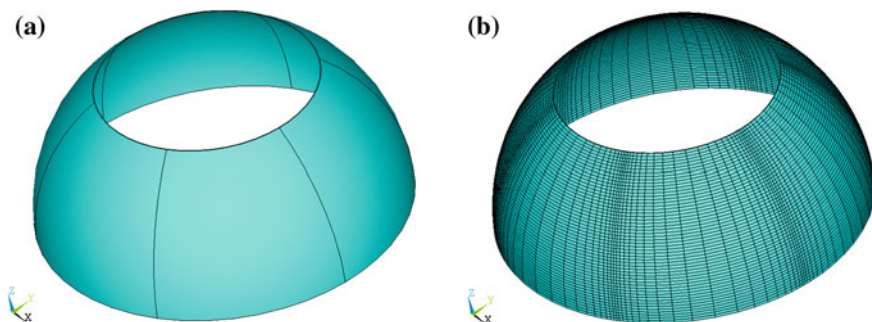
The numerical simulation technology provides a cost-effective and accurate alternative to the actual tests for the optimization of the welding procedure. In this section, the finite element software ANSYS is used for the numerical simulation of the petal unit welding. The optimal welding parameters and weld sequence are determined for controlling the residual stress and the welding distortion within the limit of the design requirements.

## 2.1 Establishment of Computational Model

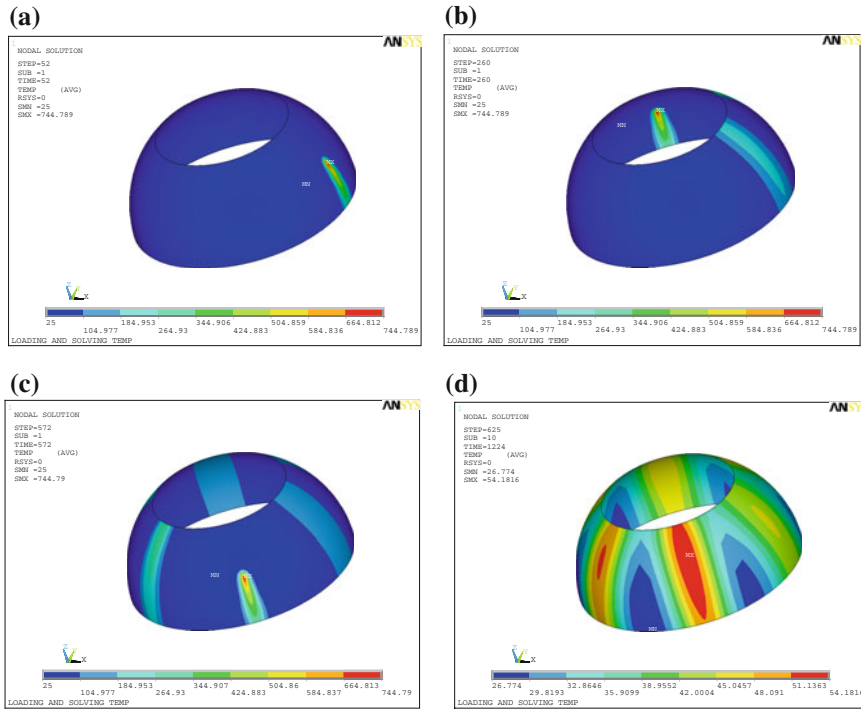
The unit consists of six petal-shaped LY19 aluminum alloy pieces, with a bottom diameter of 2250 mm, a height of 900 mm and a thickness of 3 mm. The geometrical model is established as shown in Fig. 1a. Figure 1b shows the 3D finite element mesh. In the weld region, finer elements are employed due to the high gradients of temperature, stress and strain. The minimum element is  $2\text{ mm} \times 2\text{ mm} \times 3\text{ mm}$ . The whole mesh consists of 63,600 elements and 129,600 nodes.

## 2.2 Results of Simulation

Based on the thermo-elastoplastic finite element model that has been established, the temperature field, stress and strain fields, in addition to the distortion of the welding process can be calculated. The computational results are presented as following.



**Fig. 1** Geometric model and its mesh division. **a** Geometrical model of the petal unit, **b** finite element mesh



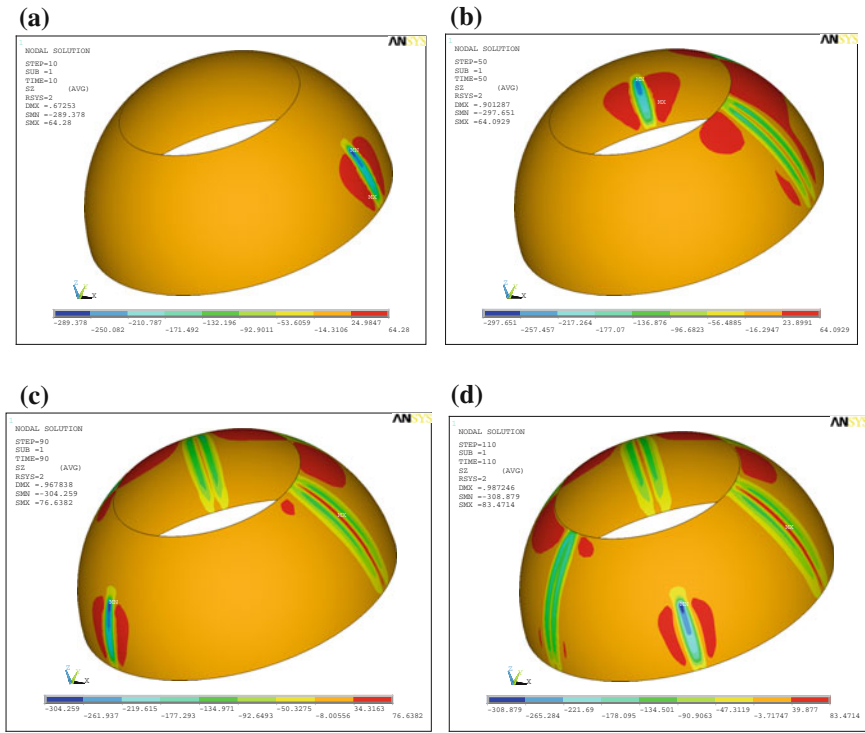
**Fig. 2** Evolution of the temperature field. **a** Arc at the middle of the first weld, **b** arc at the middle of the third weld, **c** arc at the middle of the sixth weld, **d** during the post-welding cooling

### 2.2.1 Temperature Field

Figure 2 shows the temperature distribution in the petal-unit at different time of the welding process. The welding arc is considered as the heat source, and the positions of high temperature zone coincide with the position of the welding arc. The temperature decreases as the arc passed by. The temperature distribution and its evolution history obtained by thermal analysis are used as to define the body load for the mechanical analysis that follows. The distribution and the evolution of stress, strain, distortion and temperature of the welding process are thus determined.

### 2.2.2 Stress Field

The distribution of longitudinal stress in the petal unit evolves during the welding process, as shown in Fig. 3. The position where the heat source exists experiences high compressive stress due to the thermal expansion, while the neighboring region experiences tensile stress. During the stage of cooling, the stress inside the weld seam turns to tensile stress, due to the compressive plastic strain generated in the weld zone and its neighborhood.



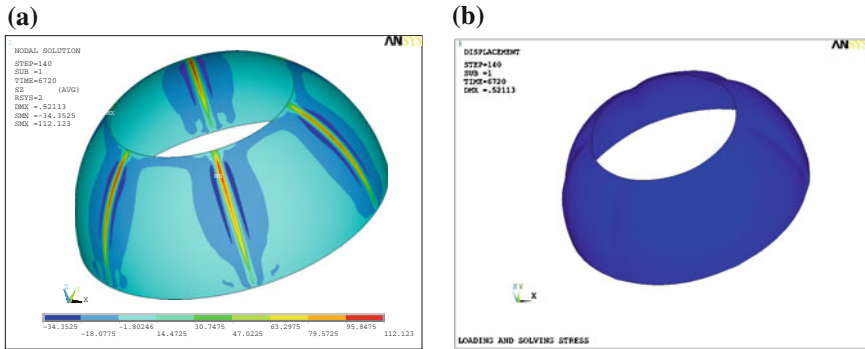
**Fig. 3** Distributions of the longitudinal stress at different welding time. **a** Arc at the middle of the first weld, **b** arc at the middle of the third weld, **c** arc at the middle of the fifth weld, **d** arc at the middle of the sixth weld

### 2.2.3 Residual Stress and Distortion

The longitudinal residual stress and the distortion of the petal unit after cooling to ambient temperature and removing the jigs and fixtures are simulated, as illustrated in Fig. 4. Tensile residual stress exists inside the weld zone, while the compressive residual stress exists near the weld zone. The upper part of the petal-shaped piece has larger tensile residual stress than the lower part. The distortion mainly occurs near the weld. The shrinkage distortion results in difficulty in the detaching of the unit from the fixture after the welding is completed.

## 3 Sensing Technologies for Trajectory Control

During the welding process, the preplanning of the path may become inadapive under the condition that deviation may occur between the preplanned trajectory and the real position of the weld seam. It is necessary to apply on-line sensing



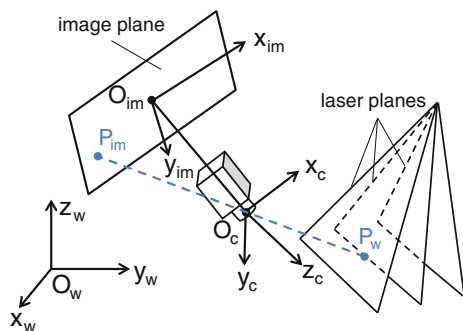
**Fig. 4** Residual stress and distortion. **a** Longitudinal residual stress, **b** residual welding distortion

technology for trajectory control, in the purpose of ensuring the accuracy of the welding position and the welding pose for every instance of the welding process. Two major problems are to be solved: (a) the deviation caused by clamp positioning error should be eliminated by trajectory adjustment before the welding starts; (b) the offset of the welding torch should be detected and serves as the feedback for the seam tracking control. The following technologies are implemented to provide solutions to the existing problems.

### 3.1 In Situ Rapid Adjustment of Trajectory

The position of the weld seam can be deviated by the clamp positioning error, welding distortion and other factors. Thus, if the welding proceeds along the pre-planned trajectory without correction, the welding quality cannot be ensured, even server defaults may occur. An in situ technology for rapid adjustment of trajectory needs to be applied. The proposed technology involves a visual sensing system including a multi-linear structured light source and a camera. The mathematical model of the system is illustrated in Fig. 5. The transform between the

**Fig. 5** Mathematical model of on-line visual sensing for adjustment of preplanned path



camera coordinate frame ( $O_C X_C Y_C Z_C$ ), the world coordinate frame ( $O_W X_W Y_W Z_W$ ) and the image coordinate frame ( $O_I X_I Y_I$ ) can be established by a calibration step. The calibrated system allows rapid calculation of the desired welding trajectory in the world coordinate frame. Each point on any one of the laser stripes satisfies Eqs. (1)–(3), where  $x_{im}, y_{im}$  represent the pixel coordinates in the image coordinate frame,  $x_c, y_c, z_c$  represent the coordinates in the camera coordinate frame,  $x_w, y_w, z_w$  represent the coordinates in the world coordinate frame,  $j$  represents the index of the laser planes. Parameters including  $f_x, f_y, u_0, v_0, R, T$  are the calibrated variables determined in the calibration of the camera. The position of projected laser stripes can be localized in the world coordinate frame. The surface of the work pieces is then determined, leading to precise positioning of the weld seam in the world coordinate frame. The effectiveness and the accuracy of the proposed technology has been verified through experiments of welding trajectory detection. A weld seam which takes the form of a space curve is used in the experiments. The seam detected by the visual sensing technology and the measurement by robot teaching are compared with each other. Figure 6 shows one pair of the detected trajectory and the measured one in the world coordinate frame. The average error between the two curves is calculated for the estimation of the sensing accuracy.

$$\begin{bmatrix} f_x & 0 & u_0 \\ 0 & f_y & v_0 \\ 0 & 0 & 1 \end{bmatrix} \begin{bmatrix} x_c/z_c \\ y_c/z_c \\ 1 \end{bmatrix} = \begin{bmatrix} x_{im} \\ y_{im} \\ 1 \end{bmatrix} \quad (1)$$

$$[R_i \quad T_i] \begin{bmatrix} x_w \\ y_w \\ z_w \\ 1 \end{bmatrix} = \begin{bmatrix} x_c \\ y_c \\ z_c \end{bmatrix} \quad (2)$$

$$a_j x_{cj} + b_j y_{cj} + c_j z_{cj} = 1, \quad j = 1, 2, 3, \dots, m \quad (3)$$

With the rapid trajectory adjustment technology, the welding path can be automatically adjusted to adapt arbitrary change of the position of the weld seam. The visual sensing technology can help to re-plan the welding path, which can significantly reduce the deviation to less than 1 mm. The remaining deviation between the re-planned path and the true position of the seam should be taken into account during the process of welding. A seam tracking technology in real time needs to be applied.

### 3.2 On-Line Seam Tracking and Pose Detecting

For on-line seam tracking, the visual sensing of the weld seam offset to the welding torch is of great necessity. The welding of thin large-scale structure involves square groove with the width of gap which is less than 0.5 mm. It is difficult for the widely

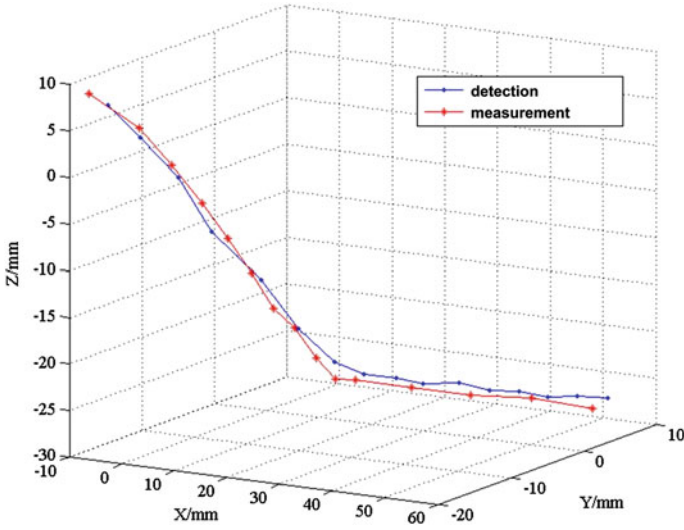


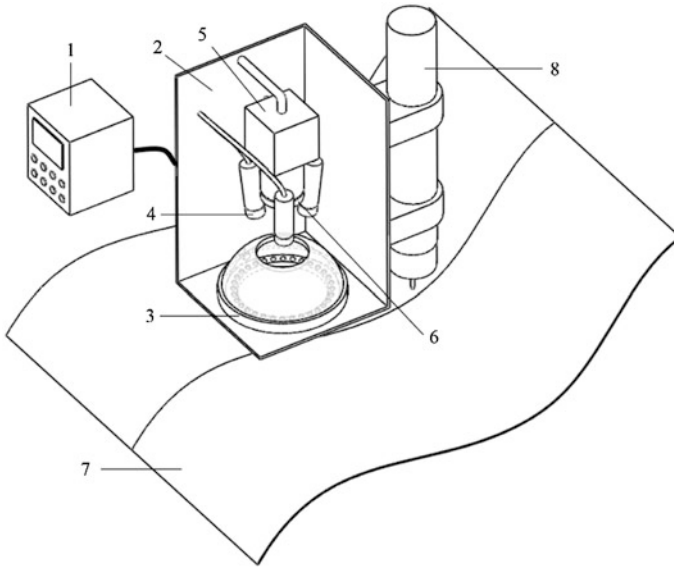
Fig. 6 Trajectory adjustment: welding paths before and after adjustment

industrialized structured light method (single or triple line) to detect the position and the size of the square groove with high accuracy. The proposed technology involves a visual sensing system including auxiliary illumination, a pose-detection aperture and a camera. The auxiliary illumination is provided by a spherical light source which consists of the LED array and the reflecting inner surface of a spherical enclosure. Figure 7 illustrates the design of the system. Figure 8 shows the simulated intensity distribution in a distance of 150 mm provided by the spherical light source. The light emitted onto the visual field have approximately homogeneous intensity. The detection of weld seam can reach an accuracy of 0.03 mm with a high resolution camera through the image processing method.

The pose-detection aperture consists of three laser point light sources, also shown in Fig. 7. The aperture provides a three-point pattern of laser projected on to the surface of the work piece. The image of the laser pattern is captured by the camera and processed for the calculation of the relative pose of the welding torch, which is fixed to the pose-detection aperture as well as the camera. The equation of the plane can be determined in the coordinate frame of the camera, by solving the combination of Eqs. (4)–(8), where  $f_1, f_2$  are the transform function between the image coordinate frame and the camera coordinate frame,  $X_i$  represents the points on the laser propagation direction of the  $i$ th laser point light source,  $S_i$  is the unit vector of the laser propagation vector.

$$A_i = [X_{i,0} + t_{i,1}(u_i, v_i) \cdot S_i + t_{i,2}(u_i, v_i) \cdot V_i(u_i, v_i)]/2 \tag{4}$$

$$V_i(u_i, v_i) = [f_1(u_i, v_i), f_2(u_i, v_i), 1]^T \tag{5}$$



**Fig. 7** Design of the system for seam and pose detection. 1 Control module, 2 sensor enclosure, 3 spherical light resource, 4 laser array, 5 camera, 6 filter, 7 work piece, 8 welding torch

$$t_{i,1}(u_i, v_i) = \frac{-[\mathbf{X}_{i,0}^T \mathbf{V}_i(u_i, v_i)][\mathbf{S}_i^T \mathbf{V}_i(u_i, v_i)] + [\mathbf{X}_{i,0}^T \mathbf{S}_i][\mathbf{V}_i^T(u_i, v_i) \mathbf{V}_i(u_i, v_i)]}{[\mathbf{S}_i^T \mathbf{V}_i(u_i, v_i)]^2 - [\mathbf{S}_i^T \mathbf{S}_i][\mathbf{V}_i^T(u_i, v_i) \mathbf{V}_i(u_i, v_i)]} \quad (6)$$

$$t_{i,2}(u_i, v_i) = \frac{-[\mathbf{X}_{i,0}^T \mathbf{V}_i(u_i, v_i)][\mathbf{S}_i^T \mathbf{S}_i] + [\mathbf{X}_{i,0}^T \mathbf{S}_i][\mathbf{S}_i^T \mathbf{V}_i(u_i, v_i)]}{[\mathbf{S}_i^T \mathbf{V}_i(u_i, v_i)]^2 - [\mathbf{S}_i^T \mathbf{S}_i][\mathbf{V}_i^T(u_i, v_i) \mathbf{V}_i(u_i, v_i)]} \quad (7)$$

$$\mathbf{A}_i^T \boldsymbol{\alpha} = 1 \quad (8)$$

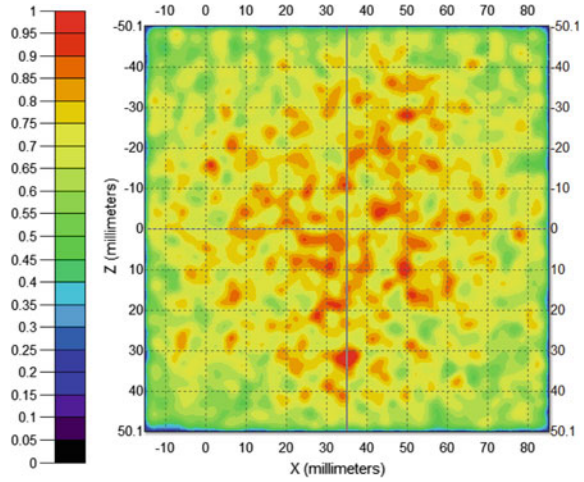
## 4 System Implementation: Case Study on Launcher Fuel Tank Welding

The launcher fuel tank welding is a challenging task in the aeronautic manufacturing. High welding quality is required. The welding parameters, including the welding voltage and current, the welding pose, the travel speed and the wire feed rate, should be strictly controlled and synchronized to the motion of the welding torch. The welding process should be optimized. The accurate trajectory programming and the adaptive on-line adjustment should be applied.

The numerical computation indicates how the process parameters influence the residual stress and the distortion. Based on the analysis of the simulation results, the



**Fig. 8** Simulated intensity distribution of the integrating sphere light source



welding process is optimized to achieve high quality of the petal unit welding. The time-consuming experimentations on the welding procedure specification are avoided. It is economical and efficient to obtain optimal procedure parameters by simulation instead of procedure test.

A robotic system of automatic welding is implemented and specialized for the ellipse weld seam of the fuel tank for the launcher. The actuating part of the robotic system consists of a two-axis positioner, an actuator for X-axis motion and an actuator for Y-axis motion, illustrated in Fig. 9. The kinematics of the robotic system is modeled by Eqs. (9)–(11), where  $a$  and  $b$  represent separately the length of the major and the minor axis of the ellipse,  $e$  represents the distance between the center of the ellipse and the rotating center of the two-axis positioner,  $\alpha$  represents the rotating angle,  $V_3$  represents the horizontal velocity of the welding torch,  $V_h$  represents the vertical velocity of the welding torch. In the described case, the welding velocity is required to be constant during the whole process, supposed that the velocity equals  $C$ .

The evolution of the kinematics of the actuating system is determined by solving the equation group. The results are illustrated in Fig. 10.  $V_w$  represents the welding velocity,  $\omega_c$  represents the angular velocity of the positioner,  $V_A$  represents the linear velocity of the welding point,  $V_2$  represents the horizontal component of  $V_A$ ,  $Ltx$  represents the horizontal displacement of the welding torch,  $Lty$  represents the vertical displacement of the welding torch,  $Lw$  represents the length of the weld. The trajectory is pre-programmed using the numerical solution. Kinematic parameterizations of typical points on the trajectory are presented in Table 1. Other components of the robotic system include the in situ trajectory detecting system, the on-line seam tracking and pose detection system, the arc length control system and the high performance TIG welding aperture.

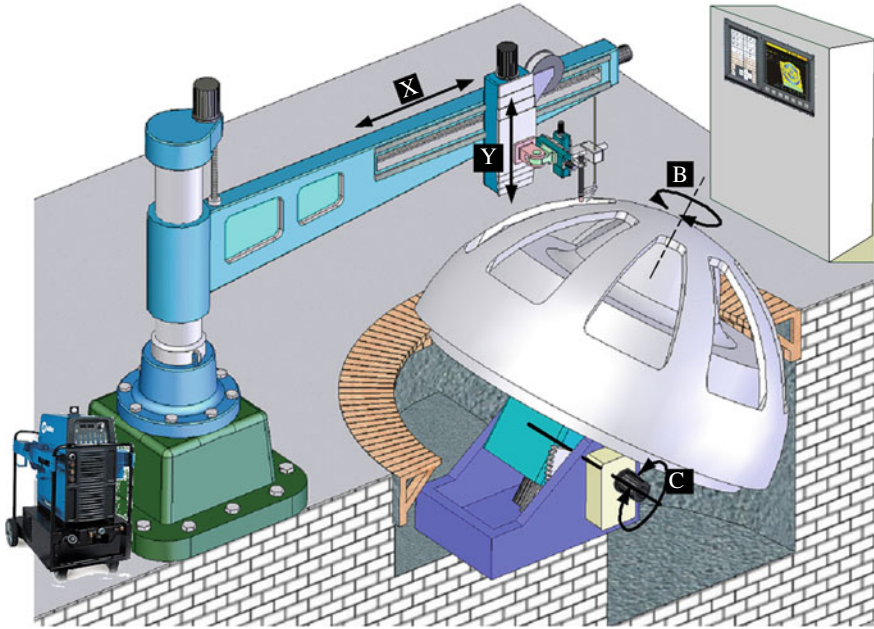


Fig. 9 System configuration for automatic welding of launcher fuel tank

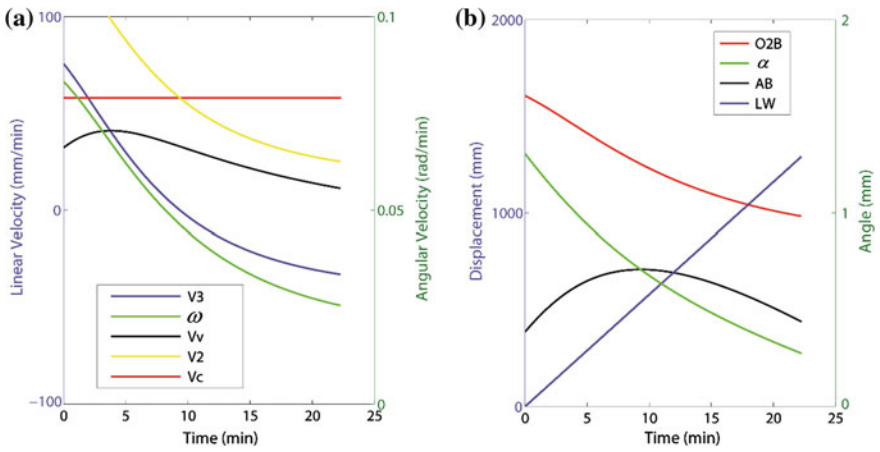


Fig. 10 System kinematics as functions of time. **a** Linear and angular velocities, **b** displacement and angle

**Table 1** Numerical results of system kinematics of typical points

Point index	Welding speed C (mm/min)	Time (min)	Kinematics					
			V3 (mm/min)	Vh (mm/min)	ωc (°/min)	Ltx (mm)	Lty (mm)	α (rad)
0001	300	0.001	390.825	166.510	0.430	387.138	1606.077	1.306
0100	300	0.121	363.702	181.086	0.419	432.526	1585.144	1.255
0200	300	0.247	333.336	193.078	0.406	476.137	1561.704	1.203
0300	300	0.376	300.537	202.173	0.391	517.172	1536.079	1.152
0400	300	0.511	265.884	208.297	0.375	555.286	1508.412	1.100
0500	300	0.651	229.964	211.455	0.358	590.125	1478.863	1.048
0600	300	0.799	193.359	211.728	0.341	621.318	1447.609	0.997
0700	300	0.955	156.631	209.266	0.323	648.477	1414.848	0.945
0800	300	1.119	120.306	204.282	0.304	671.197	1380.800	0.894
0900	300	1.294	84.865	197.040	0.286	689.053	1345.704	0.842
1000	300	1.480	50.733	187.843	0.268	701.602	1309.822	0.791
1200	300	1.894	-12.217	164.922	0.233	708.923	1236.865	0.687
1400	300	2.372	-66.444	138.239	0.201	689.364	1164.507	0.584
1600	300	2.927	-110.898	110.315	0.173	639.293	1095.712	0.481
1800	300	3.571	-145.427	83.118	0.150	555.966	1033.778	0.378
1900	300	3.927	-159.105	70.197	0.140	501.512	1006.474	0.326
1950	300	4.115	-165.087	63.945	0.136	471.150	993.930	0.301
1990	300	4.268	-169.473	59.047	0.133	445.400	984.474	0.280
2000	300	4.304	-170.412	57.957	0.132	439.431	982.421	0.275

$$V_3 = \left[ \sqrt{\frac{a^4 \cdot \tan^2 \alpha}{b^2 + a^2 \cdot \tan^2 \alpha} + \left( \sqrt{b^2 - \frac{a^2 b^2 \cdot \tan^2 \alpha}{b^2 + a^2 \cdot \tan^2 \alpha}} + e \right)^2} \cdot \sin \left( \arctan \frac{b^2 - a^2 + e\sqrt{b^2 + a^2 \cdot \tan^2 \alpha}}{(a^2 \cdot \tan \alpha) + (b^2 + e\sqrt{b^2 + a^2 \cdot \tan^2 \alpha}) \cdot \cot \alpha} \right) \right] \tag{9}$$

$$V_h = \left[ \sqrt{\frac{a^4 \cdot \tan^2 \alpha}{b^2 + a^2 \cdot \tan^2 \alpha} + \left( \sqrt{b^2 - \frac{a^2 b^2 \cdot \tan^2 \alpha}{b^2 + a^2 \cdot \tan^2 \alpha}} + e \right)^2} \cdot \cos \left( \arctan \frac{b^2 - a^2 + e\sqrt{b^2 + a^2 \cdot \tan^2 \alpha}}{(a^2 \cdot \tan \alpha) + (b^2 + e\sqrt{b^2 + a^2 \cdot \tan^2 \alpha}) \cdot \cot \alpha} \right) \right] \tag{10}$$

$$\begin{aligned}
& \left[ \frac{a^4 \cdot \tan^2 \alpha}{b^2 + a^2 \cdot \tan^2 \alpha} + \left( \sqrt{b^2 - \frac{a^2 \cdot b^2 \cdot \tan^2 \alpha}{b^2 + a^2 \cdot \tan^2 \alpha} + e} \right)^2 \right. \\
& \quad \cdot \sin \left( \arctan \frac{b^2 - a^2 + e\sqrt{b^2 + a^2 \cdot \tan^2 \alpha}}{(a^2 \cdot \tan^2 \alpha) + (b^2 + e\sqrt{b^2 + a^2 \cdot \tan^2 \alpha}) \cdot \cot \alpha} \right) \left. \right] \\
& + \sqrt{\frac{a^4 \cdot \tan^2 \alpha}{b^2 + a^2 \cdot \tan^2 \alpha} + \left( \sqrt{b^2 - \frac{a^2 b^2 \cdot \tan^2 \alpha}{b^2 + a^2 \cdot \tan^2 \alpha} + e} \right)^2} \cdot \frac{d\alpha}{dt} \\
& \cdot \cos \left( \arctan \frac{b^2 - a^2 + e\sqrt{b^2 + a^2 \cdot \tan^2 \alpha}}{(a^2 \cdot \tan^2 \alpha) + (b^2 + e\sqrt{b^2 + a^2 \cdot \tan^2 \alpha}) \cdot \cot \alpha} \right) = C
\end{aligned} \tag{11}$$

## 5 Conclusions

This paper has presented the technologies and the implementation of system for the automatic welding of complex large-scale structures. The performance has been investigated and discussed. The simulation of the welding distortion and the residual stress plays an important role in designing and optimizing the welding process. Distortion and residual stress are preferred to be minimized. The welding process is designed based on the result of the numerical simulation. Before the welding starts, the in situ weld seam detection technology has been applied for the adjustment of the programmed welding trajectory. The miss-positioning of the welding torch can be reduced to less than 1 mm. Higher accuracy has then been achieved by the application of the on-line seam tracking and pose detection technology during the welding process. An accuracy of 0.03 mm has been achieved for the detection of weld seam. An automatic welding system specialized for the ellipse seam of the launcher fuel tank has been implemented.

**Acknowledgment** This work is supported by the National Natural Science Foundation of China under Grant Number 51375257.

## References

1. Pan Z, Polden J, Larkin N et al (2011) Automated offline programming for robotic welding system with high degree of freedoms. In: Wu Y (ed) Advances in computer, communication, control and automation. LNEE, vol 121, pp 685–692
2. Wilson M (2002) The role of seam tracking in robotic welding and bonding. Ind Robot 29 (2):132–137

3. Chen SB, Chen XZ, Qiu T (2005) Acquisition of weld seam dimensional position information for arc welding robot based on vision computing. *J Intell Rob Syst* 43:77–97
4. Tsai MJ, Lee HW, Ann NJ (2011) Machine vision based path planning for a robotic golf club head welding system. *Robot Comput Integr Manuf* 27:843–849
5. Wu B, Xue T, Zhang T, Ye SH (2010) A novel method for round steel measurement with a multi-line structured light vision sensor. *Meas Sci Technol* 21(2):025204
6. Hoffman A, Albertazzi A, Santos JC et al (2006) A stereoscopic endoscopic optical system for measurement of the 3D weld geometry of pipes—concepts and preliminary results. In: *Proceedings of OMAE2006, 25th international conference on offshore mechanics and arctic engineering*, Hamburg, Germany, 4–9 June 2006
7. Kim CH, Choi TY, Lee JJ et al (2008) Intelligent vision sensor for the robotic laser. In: *Welding 6th IEEE international conference on industrial informatics*

# Research of a Linear Switched Reluctance Motor

Xiao-Yue Liang, Su Wang and Xin-Gang Miao

**Abstract** It completely designs a sort of Linear Switched Reluctance Motor and states a research of high speed working Linear Motor. Through the designing of the specific parameters and the building of actual stereo model and the FEMM stimulation of electromagnetism, the result of stimulation can prove the accuracy of the calculation. Furthermore, the comprehensive outcome verifies the capability of high speed Linear Motor to be reality and its expanding developing space.

## 1 Introduction

Nowadays as the traditional electric machine develops much more mature, the research of Linear motor already has a sort of basement. The idea of translating the traditional electric machine could take advantage of saving the median transmission devices. As the development of electromagnetism catapult, the linear motor has been made several applications. The US has excogitated the linear motor applied on catapulting device.

## 2 Research of the Linear Switched Reluctance Motor

### 2.1 Linear Switched Reluctance Motor

Linear Switched Reluctance Motor (LSRM), it is different from the traditional linear machine which depend on the first and second coil to produce magnetic field and traction by interaction. It obeys the theory of flux closing along the largest

---

X.-Y. Liang (✉) · S. Wang · X.-G. Miao  
Beijing Engineering Research Center for Construction Safety, Beijing University of Civil Engineering and Architecture, Beijing 100044, China  
e-mail: 09292011@bjtu.edu.cn

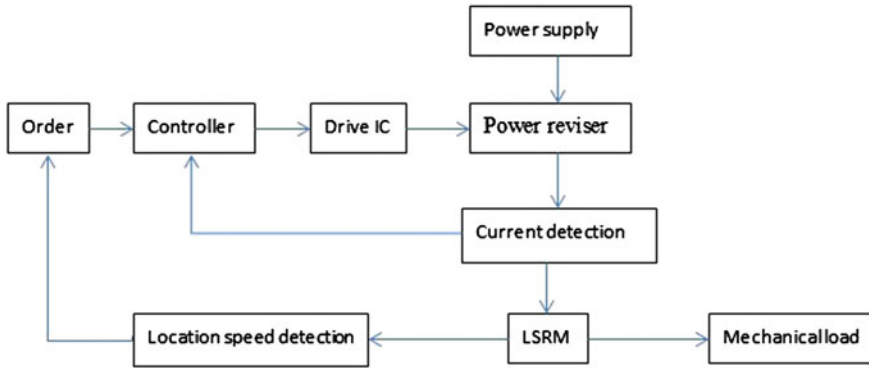


Fig. 1 Structure of LSRM

permeability route while produces magnetic force to drive the machine. LSRM has more phase, meanwhile it has less step pitch. It is in favor of reducing the pulsation of moment.

LSRM is mainly constituted of the motor itself, the power reviser, controller, test device of position, as in Fig. 1. The power reviser can provide power directly to the machine. It has to match the requirement of power transmission of the machine. The test device of position will deliver the detected position of the machine to the controller so the controller can manage the transmission speed and position.

## 2.2 The Design of LSRM

### 2.2.1 The Design of Motion Science

The motion of Linear motion is similar to the catapult device. The magnetic force is in direct proportion of the square of current. To produce enough push in the catapult device, it has to ensure certain current input. The magnetic force  $F$  can be confirmed by formula (1),

$$F = \frac{1}{2} L' I^2 \tag{1}$$

$$a = F/m \tag{2}$$

in formula (2):  $m$  is the mass of the moved object. Velocity of the object after  $t$  time is:

$$V_2 = V_1 + at = V_1 + \frac{F}{m}t = V_1 + \frac{L'I^2t}{2m} \tag{3}$$

the accelerate is:

$$a_a = \frac{v_m}{t_a} = \frac{7.9}{0.125} = 63.2 \text{ m/s}^2$$

the temporary resultant force can be calculated as:

$$F_a = M \cdot a_a = 1 \cdot 63.2 = 63.2 \text{ N}$$

the accelerate in the period of speed cut:

$$a_d = -63.2 \text{ m/s}^2$$

the temporary resultant force is:

$$F_d = -63.2 \text{ N}$$

### 2.2.2 The Parameter Design of LSRM [1]

It designs a 12/8 poles LSRM, its construction of winding is as Fig. 2.

The rate of LSRM:  $P = F_a v_m = 63.2 \times 7.9 = 499.28 \text{ W}$ .

Suppose that RSRM has a stator's polar angle  $\beta_s = 30^\circ = 0.5236 \text{ rad}$  and a rotor's polar angle  $\beta_r = 36^\circ = 0.6283 \text{ rad}$ . After the accurate debugging of parameter, the constant is:  $k_e = 0.4$ ,  $k_d = 1$ ,  $k_2 = 0.7$ ,  $B_g = 1.1215$ ,  $A_{sp} = 23886.5$  and  $k = 0.6545$ . The aperture can be calculated as:

$$D = \sqrt{\frac{P\pi}{60 k_e k_d k_1 k_2 k B_g A_{sp} v_m}} = 33.29 \text{ mm}$$

The RSRM's thickness of steel stick is:  $L = k_d = 0.6545 \times 33.29 = 21.79 \text{ mm}$ .

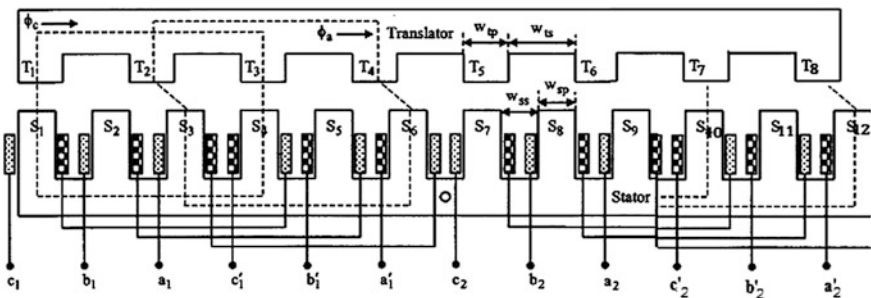


Fig. 2 LSRM's construction of winding



The groove width can be calculated as:  $C = (D\beta_s/2) = 21.72$  mm.

Hypothetically  $D_0 = 70$  mm, then the pole height of the stator can be calculated as:

$$H_s = \frac{D_0}{2} - \frac{D}{2} - C = \frac{70}{2} - \frac{33.29}{2} - 8.72 \approx 25 \text{ mm}$$

The back board of the rotor:

$$C_{ry} = \left(\frac{D}{2}\right) \beta_r = \left(\frac{33.29}{2}\right) \frac{36 \times \pi}{180} = 10.46 \text{ mm}$$

The pole height of rotor is:

$$h_r = (D/2) - g - C_{ry} = (33.29/2) - 0.3 - 10.46 \approx 6.2 \text{ mm}$$

Based on the calculation of  $C_{ry}$  and  $h_r$ , above can gain the size of aperture:

$$D = (h_r + C_{ry} + g) \times 2 = (6.2 + 10.46 + 0.3) \times 2 = 34 \text{ mm}$$

The magnetic density in the air gap is:

$$H_g = \frac{B_g}{\mu_0} = \frac{1.1215}{4\pi \times 10^{-7}} = 892461.3 \text{ A/m}$$

Based on maximum current  $i = 10.42$  A,

$$T_{ph} = \frac{H_g \times 2 \times g}{i} \approx 210$$

Suppose the current density  $J = 6$  A/mm<sup>2</sup> the conductor cross-section is:

$$a_c = \frac{i}{J\sqrt{m}} = \left(85 / 6\sqrt{3}\right) = 0.8179 \text{ mm}^2$$

AWG #18 is the general coil material of RSRM, the cross-section is 0.871 mm<sup>2</sup>. So far, it completes the design of RSRM. Then it come the design of transmission to LSRM.

The period of LSRM is:

$$N_{SC} = \frac{L_t}{\pi D} = \frac{4.8}{\pi \times 33.29 \times 10^{-3}} = 46$$

The stator pole is:

$$n = N_s N_{SC} = \frac{L_t}{\pi D} = 276$$

The stator width is:

$$w_{sp} = \frac{A_s}{L} = \left(\frac{D}{2}\right)\beta = \frac{33.29 \times 30\pi}{2 \times 180} = 8 \times 7 \text{ mm}$$

The stator groove width is:

$$w_{ss} = \frac{(\pi D - N_m w_{sp})}{N_m} = \frac{(\pi \times 33.29 - 6 \times 8.7)}{6} = 21.7 \text{ mm}$$

The rotor pole is:

$$\omega_{tp} = C_{ry} = 10.46 \text{ mm}$$

The rotor groove width is:

$$w_{ts} = \frac{(\pi D - N_t w_{tp})}{N_t} = \left(\frac{\pi \times 33.29 - 4 \times 10.46}{4}\right) = 15.69 \text{ mm}$$

The rotor length is:

$$L_{tr} = 8\omega_{tp} + 8\omega_{ts} = 209.2 \text{ mm}$$

The coil diameter is:

$$d_c = \sqrt{\frac{4a_c}{\pi}} = \sqrt{\frac{4 \times 0.817}{\pi}} = 1.02 \text{ mm}$$

Supposing that  $\omega = 5$  and the number of vertical windings is:

$$N_v = F_f \left(\frac{h_s - \omega}{d_c}\right) = 0.7 \frac{(25 - 5)}{1.02} = 13.73 \approx 14$$

$F_f = 0.7$  in the formula above.

The number of horizon windings is:

$$N_h = \frac{T_{ph}}{2N_v} = \frac{210}{2 \times 14} = 7.5 \approx 8$$

The area of the coil is:

$$2 \frac{a_c N_h N_c}{F_f} = 261.44 \text{ mm}^2$$

$H_s, H_g, H_r, H_{ry}$  are respectively the magnetic field strength of the stator pole, stator back board, rotor pole and rotor back board.

Magnetic flux in the air gap is:

$$B_g = \frac{B_s A_s \mu_o}{P_g g} = \frac{1.2881 \times 0.002 \times 0.005 4\pi \times 10^7}{1.5081 \times 10^6 \times 0.001} = 1.0733 \text{ T}$$

Single phase magnetic conductivity when rotor right above the groove is:

$$P_{gu} = \mu_o L \omega (2 \times 1.3229 + 2 \left( \frac{h_s}{\omega_{ss}} - \frac{2}{\pi} + \frac{g}{\omega_{ss}} \right) + \frac{\omega_{sp}}{2(g + h_r)})$$

The inductor when rotor right above the groove is:

$$L_U = 2 \left( \frac{T_{ph}}{2} \right)^2 P_{gu} = 2 \left( \frac{210}{2} \right)^2 \times 3.5799 \times 10^7 = 7.8936 \text{ Mh}$$

In the modeling research, the magnetic conductivity when rotor is right above the groove is:

$$P_{gu} = 3.5799 \times 10^7 \text{ Wb/A}$$

The model finally is figured out as a 50 cm machine, which has the maximum velocity of 7.9 m/s and accelerate time of 1.125 s. Obviously the result is much better than traditional linear machine.

### 3 Stereo Modeling Research

#### 3.1 Solidworks Stereo Model

As the rotor shown in Fig. 3, eight poles rotor are mainly pressing by steel sticks. The single steel stick is used to test the position of the rotor. The rotor has wheels beneath and the assist board on the top [2].

#### 3.2 Finite Element Stimulation [3]

It used traditional finite element stimulation software FEMM to verify the magnetic field of LSRM [4]. The result proved the theory parameter research in part one. Finite element is an effective magnetic field count method. Based on that, the passage analyses magnetic field different rotor position at it's working condition, which is shown in Fig. 4.

The stimulation shows that the minimum magnetic field comes when the rotor is right above groove, meanwhile the maximum magnetic field comes when the rotor is right above stator.

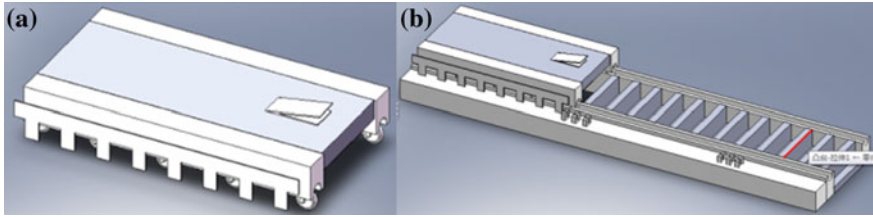


Fig. 3 a Rotor model. b LSRM model

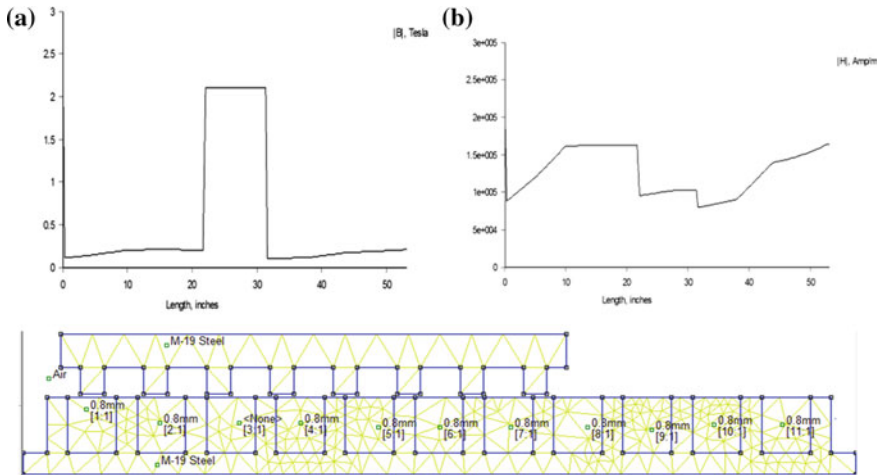


Fig. 4 Finite element analysis. a Finite element stimulation. b H-L curve B-L curve

## 4 The Advantages of Linear Motor

### 4.1 Superiority of LSRM

LSRM has flexible adjust method, many adjustable parameter and large radiation area [5]. As a result, it is unnecessary to add low temperature cooling devices. In the same time, it has the easily controllable f-v property. The outstanding speed regulation and robustness can adapt to different load and improve stability of the system. It uses power converter to power-up the LSRM in order to reach better power saving and improve efficiency. On the account of the complexity of LSRM magnetic circuit and the low efficiency at low speed, this linear motor hasn't been applied in reality yet.

## 4.2 Speed Optimization

To use the linear motor as the carrier of robot arms or scanner meanwhile the stability controlling of its velocity, accelerate and position can adjust its parameters. It use the theory of state space to optimize the motor speed.

## 5 Conclusion

In the paper, it expatiates a high speed linear motor model, research of a 12/8 poles LSR0 M. As the application direction of linear motor expands, high speed and optimal control will be a development tendency in the future. Linear motor will be used much more in machine tools, magnetic catapult, linear motion etc. On account of higher speed than other motors, LSRM can combine traditional numerical control machine tool to gain higher processing speed.

## References

1. Krishnan R, Arumugan R, Lindsay JF (1988) Design procedure for switched-reluctance motors. *IEEE Trans Ind Appl* 24:456–461
2. Lawrenson P (1983) Switched-reluctance motor drives. *Electron Power* 29(2):144–147
3. Fochmann M, Kiesewetter D, Sadrieh A (2010) The biased effect of aggregated and disaggregated income taxation on investment decisions, FEMM working paper Nr. 25, December 2010
4. Bae H-K, Lee B-S, Vijayraghavan P, Krishnan R (1999) Linear switched reluctance motor: converter and control. In: Conference Record of the 1999 IEEE-IAS Annual Meeting, vol 1. Phoenix, AZ, Oct 1999, pp 547–554
5. Boldea I, Nasar SA (1997) Linear electric actuators and generators. Cambridge University Press, Cambridge, pp 163–178

# The Stone Carving Reproduction for the Reservation of Chinese Ancient Architectures

Zhuo Liu, Xin-Gang Miao and Su Wang

**Abstract** Chinese ancient architectures as a kind of historical and cultural heritage, witness the splendid history of civilization and the wisdom of our ancestors. However, they encounter the inevitable embarrassment situation because of accelerating of urbanization. Currently ancient architectures, more or less are suffering from some natural or man-made destruction, therefore, the protection of ancient architectures is particularly important. The preservation and reproduction for carved stone which as an essential part of ancient architectures, has become an attractive topic. But because the process for reproduction of carved stone, can't be an integrated system. The process become cumbersome, slow and inefficient. This paper presents a method that using modern means such as three-dimensional reverse system combined with robot carving technology to deal with this problem.

## 1 Introduction

Chinese ancient architecture is very special in global architecture. It's famous for its cultural value and historical heritage. Especially the biggest feature of ancient architecture is the use of carved stone and wood carving. As for the preservation and reproduction of carved stone and wood carving, the significant question is how to reserve the value of art and history.

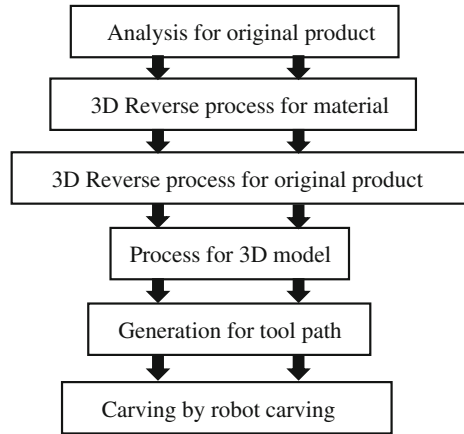
The combination of the traditional process and 3D Reverse Process technology method, used in the preservation and reproduction of carved stone and wood carving, can dispose the problems that reserve the value of art and history, at the same time get the products efficiently. Originally, through these processes, we can understand the initial of Chinese ancient architecture more deeply.

---

Z. Liu (✉) · X.-G. Miao · S. Wang

Beijing University of Civil Engineering and Architecture, Beijing Engineering Research Center of Monitoring for Construction Safety, Beijing 100044, China  
e-mail: 670411163@qq.com

**Fig. 1** System for reproduction of stone carving

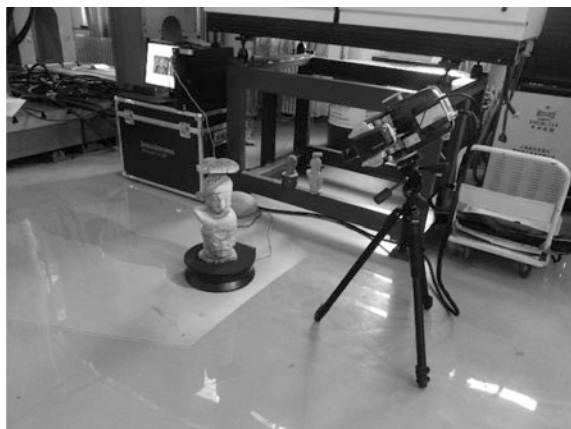


As Fig. 1, this paper presents a new perspective that designs a systematical process to deal with this question by using 3D reverse and robot carving technology.

## 2 Application

One of the key procedures for reproduction of stone carving is the extraction and analysis of the 3D data from the original product. The using of 3D reverse technology can speed up the process of data acquiring and 3D structured light scanner can make this process more efficient. As Fig. 2, this paper used the 3D structured light scanner from breuckmann of Germany.

**Fig. 2** 3D structured light scanner



## 2.1 3D Reverse Process for Material

Because of the high accuracy and stability, 3D Reverse Technology is widely used in designation and products for aviation and aerospace fields, animation or game.

The traditional method for reproduction always waste more material because of neglecting the preprocessing of material targeted. During the process of carving, the 3D reverse preprocessing for the material can save the resource efficiently and it can smooth the process at the same time. Point cloud data extraction process is shown in Fig. 3.

After extract the point cloud data, it is necessary to dispose the useless point, the noise, etc. These procedures include patching holes, noise reduction, deleting redundant surface, model simplifying. The reason why simplify the model is to accelerate the entire process. The result of processing shown in the Fig. 4.

## 2.2 3D Reverse Process for Original Product

Certainly, the process for original product is important as well because the purpose of reproduction is to make the product seemed as the original one. The result of process based on the material shown as Fig. 5.

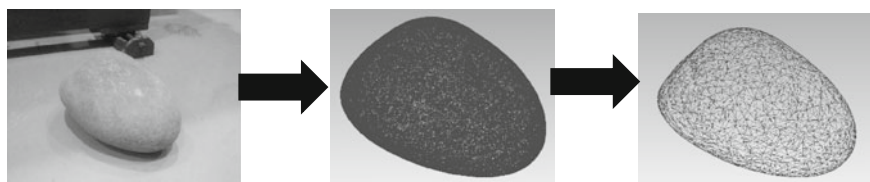
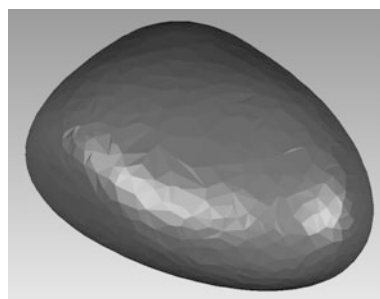


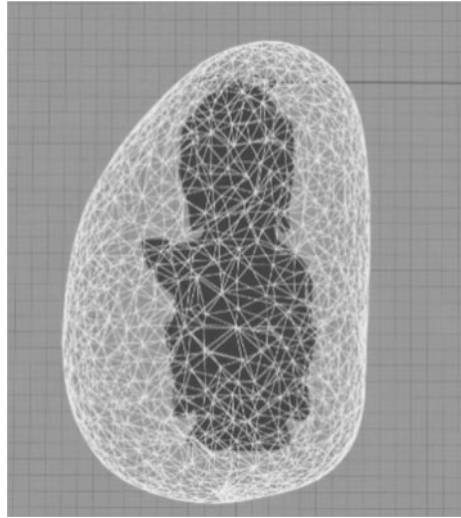
Fig. 3 Point cloud data extraction process

Fig. 4 The result of processing





**Fig. 5** The result of process based on the material



### 3 The Definition of Point Cloud Surface

This paper apply to the definition of point cloud surface during the experiment and seemed the definition of point cloud surface as an important part to research. In  $R^n$  space,  $P = \{P_i \in R^n\}$  express a  $n - 1$  dimension Closed surface space. Define  $f: R^n \rightarrow R$  as zero level set of the surface, namely:  $S_p = f^{-1}(0)$ .

Resume a point  $x$  on the surface,  $c(x)$  is Center of mass,  $n(x)$  is its distance field of approximated gradient, the main definition is:

1. When the normal direction of  $x$  is predictable, define the Local centroid  $x \in R^n$ , shown as equal (1):

$$C(x) = \frac{\sum_i \theta(\|x - P_i\|) P_i}{\sum_i \theta(\|x - P_i\|)} \tag{1}$$

$\theta$  is weighting function, namely compactly supported function. Generally, this function can be defined by piecewise polynomial, shown as equal (2):

$$\theta(r) = \begin{cases} (1 - \frac{r}{h})^4 (\frac{4r}{h} + 1) & 0 \leq r \leq h \\ 0 & r > h \end{cases} \tag{2}$$

$h$  is the control parameter, it can be used to control the function of scale.

2. Because the normal direction of  $x$  is predictable, The method of vector field definition is varied, The definition of different function corresponds to different solutions. Using distance function, the normal can be defined by calculating the local normal direction to the weighted centroid distance, shown as equal (3):

$$n(x) = \frac{\sum_i \theta(\|x - P_i\|)n_i}{\sum_i \theta(\|x - P_i\|)} \tag{3}$$

This is only the way we define the point cloud surface, as for the disposal of point cloud we used Hermit surface model.

## 4 The Application of Robot Carving System

### 4.1 General Structure

The robot system is four axis space structure: X, Y, Z and the rotating platform the axis of rotation A. The rotation axis A is used to accomplish the 3D carving. During the process of 3D carving, the scale of rotation axis A is 0°–360°. The designation of rotating platform is the key part of 3D carving. Vacuum adsorption platform is used to the outside of robot carving system, axis Y is gantry mode movement, the robot install on the gantry beam. The carving machine is on the end of robot. Combined the robot and gantry, a variety of complex tasks can be solved.

Because the industrial auxiliary robot installed on the gantry, the gantry must have enough static stiffness and dynamic stiffness. Compared with normal CNC machine, the static stiffness and dynamic stiffness should be increased by more than 50 % at least. The General structure shown as Fig. 6.

### 4.2 Introduction of Robot

MOTOMAN-MH50 robot is Vertical joint structures which has axis S, L, Y, R, B, T. This kind of structure, which is more flexible and efficient, can deal with complex tasks. The robot shown as Fig. 7.

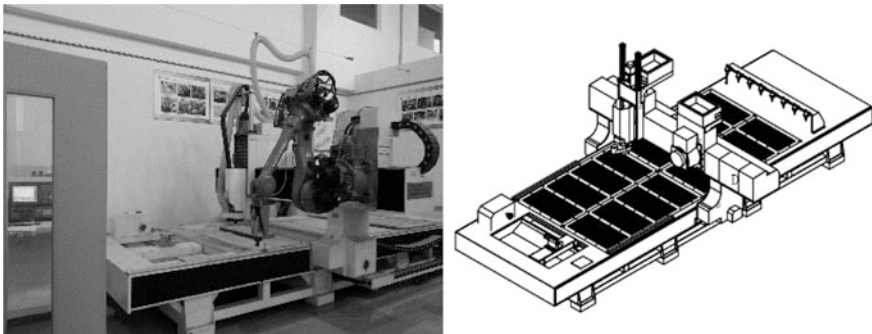
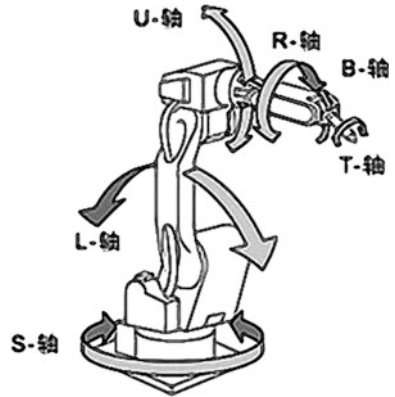


Fig. 6 The general structure

Fig. 7 The robot



Using the model which is processed can generate the tool path and through robot carving system the product can be reproduced perfectly.

## 5 Conclusion

Chinese ancient architectures as the heritage of art and culture, should be protected as possible. Stone carving, as a crucial part, should be paid more attention. This paper present a new perspective to reproduce carved stone systematically. Three-dimensional reverse system combined with robotic carving technology finished the reproduction efficiently.

## References

1. Zhang J, Wang S, Miao X-G (2013) Industrial robot-assisted precision CNC wood processing system. *Dev Innov Mach Electr Prod* 26(3):24–26
2. Foley J et al (2000) Getting there: the ten top problems left. *IEEE Comp Graphics Appl* 20 (1):66–68
3. Huang H (2006) CNC engraving system developed based on digital image processing. Southwest Jiaotong University, Chengdu
4. Shum H, Kang SI (2000) A review of image-based rendering techniques. In: *Proceedings of IEEE/SPIE visual communications and image processing*, Perth, Australia, 2000, pp 12–13
5. Amenta N, Choi S, Dey TK, Leekha N (2002) A simple algorithm for homeomorphic surface reconstruction. *Int J Comput Geom Appl* 12(1–2):125–141
6. Jin C-L (2012) *The 3D point cloud key algorithm of complex curved surface reconstruction*. Shanghai University, Shanghai
7. Kumar GS, Kalra PK, Dhande SG (2004) Curve and surface reconstruction from point: an approach based on self-organizing maps. *Appl Soft Comput* 5(1):55–66

# Research and Analysis of Architectural Construction Safety Dynamic Infrasound Network System Based on Acoustic Vector Sensor

Hui-Chao Xu, Su Wang and Bao-Jun Zhao

**Abstract** This paper introduces the research of ACSDINS (Architectural Construction Safety Dynamic Infrasound Network System) based on the analysis of research background and research situation in building safety monitoring. The system adopted acoustic vector sensor as the main equipment to achieve the signal acquisition and chose steel model as the monitoring object. Experimental and analytical results demonstrated the feasibility of ACSDINS. It has broad application prospects and important practical significance in the field of safety monitoring.

## 1 Introduction

Recently, with the application of steel in the building industry and the development of steel structures, people increasingly focus on the performance of building structure which, therefore, increasing the amount of researches on the aspect of test deformation of steel structure. Solid materials like steel structure are easy to make inside changes of structure under complicated conditions like under the outside stress. However, the changes of solid materials after survived from some forces are quite few, which are not possible to tell through the exam of the inside structure.

Hence, for the tiny changes, people can use mechanical wave produced during the steel structural changes, which is similar to the transmit of acoustic wave, to observe the situations in steel structure changes through collection, management, analysis of acoustic waves, as well as carrying on analysis and conduction to realize the problems live inside the structure in order to process effective protection and

---

H.-C. Xu (✉) · S. Wang

School of Mechanical Engineering and Automation, BeiHang University,  
Beijing 100191, China  
e-mail: gezi\_xuhuichao@126.com

S. Wang · B.-J. Zhao

Beijing Engineering Research Center of Monitoring for Construction Safety,  
Beijing University of Civil Engineering and Architecture, Beijing 100044, China

consolidation to ensure the safety of building and avoid accidents and damages result from some safety problems in the structure.

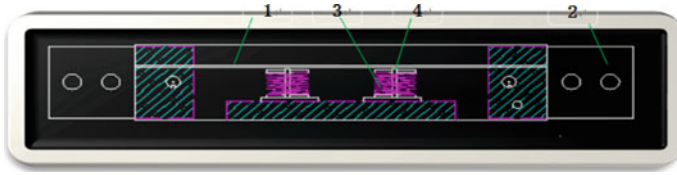
ACSDINS (Architectural Construction Safety Dynamic Infrasound Network System) adopted non-destructive sensing technology and used physical principles of resonance film to detect the micro-displacement, thereby continuous monitoring the force and deformation of various types of steel in different environments [1]. Through the applications of ACSDINS, it can achieve the functions of real-time online monitoring, data analysis, and risk and early-warning for a number of steel structures which have high security requirements. That can make us discover the security risks in time, and take the necessary measures to remove potential hazards to avoid sudden accidents. The model of ACSDINS consists of three main parts. It is steel structure dynamic infrasound square, infrasound information acquisition and processing platform, the man-machine interface. As the composite function of the polybasic dynamic infrasound roles in any mechanical pole of the steel structure, its strength and rigidity of mechanical pole would occur with quick response and physical changes. So the dynamic infrasound monitoring system is a special apparatus of measurement test and on-line monitoring and analysis.

## **2 Dynamic Infrasound Detection Technology**

The application of Infrasound detection technology in complex steel structures are solid infrasound field of study, or is to study the mechanical vibration generated by the mechanical kinetic energy from the power source of direct or indirect role in the complex steel structure [2–4]. The vibration is the radiant point of solid infrasound. Infrasound propagated in complex steel structure, and its propagation speed, transmission distance, spectral characteristics and wave type conversion have a direct and close correlation with the physical properties of complex steel structure.

### ***2.1 The Application of Infrasound Detection Technology in Steel Structure***

The main equipment of architectural safety infrasound detection program is the infrasound detection system. The infrasound propagated in complex steel structure is seemed as information carriers to do physical field detection analysis, calibration and positioning of the dynamic properties of steel target objects in any wave surfaces [5, 6]. It includes the calibration and measurement of internal stress field and strain gradient, micro-displacement and macro-displacement, flow of energy and torque, far infrasound load and high infrasound load, mechanical strength and stiffness, mechanical fatigue damage and destruction and free resonance and forced vibration of the infrasound wave surface in physical field. It also includes dynamic field of measurement on the target surface and properties of infrasound calibration.



1 - vector film; 2 - baseline block; 3 - coil; 4 - core

**Fig. 1** Internal structure diagram of acoustic vector sensor

## 2.2 Acoustic Vector Sensor

Differential resistive sensors and vibrating wire sensors have become increasingly unable to meet the requirements of sensitivity and response speed in modern monitoring system. ACSDINS adopted acoustic vector sensor as the main equipment to achieve the signal acquisition. The main internal components of acoustic vector sensor are divided into four parts: vector film, baseline block, coil and core. Internal structure diagram of acoustic vector sensor is shown in Fig. 1.

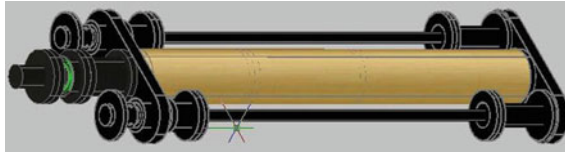
Fastened the acoustic vector sensor with mechanical steel rods tightly, they could generate deformation together when external force is applied. As force acting on the baseline block, the sensor is deformed and the vector film will also be deformed at the same time. So the coil cut the magnetic field lines that the internal magnetic field changes, and induced electromotive force. Therefore, the acoustic signals are converted into electrical signal. Energy transfer mainly comes from the baseline block sampling, so it is featured with high reliability and stability.

## 3 Architectural Construction Safety Dynamic Infrasonic Network System Model

The model of ACSDINS consists of three main parts. It is steel structure dynamic infrasonic square, infrasonic information acquisition and processing platform, the man-machine interface. As the composite function of the polybasic dynamic infrasonic roles in any mechanical pole of the steel structure, its strength and rigidity of mechanical pole would occur with quick response and physical changes. That is to say that dynamic infrasonic role in the mechanical pole of steel structure and causes the mechanical strength and rigidity changing. Thus the dynamic infrasonic monitoring system is a special apparatus of measurement test and on-line monitoring and analysis.

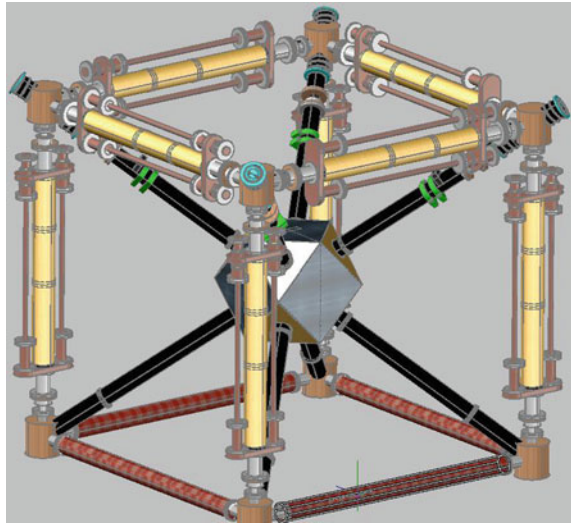
### 3.1 Steel Structure Dynamic Infrasonic Square

Define Steel structure dynamic infrasonic square is the most basic bottom part. One end of vector film in Infrasonic vector film sensors are installed on the steel



**Fig. 2** One-dimensional infrasound channel design

**Fig. 3** Multi-dimensional infrasound channel design



structure fixed reference side; the other end is fixed to the movable sampling end. So the tension of vector film is facilitating to adjustment. Summing the one-dimensional infrasound into a multi-dimensional infrasound applied in the system.

One-dimensional and multi-dimensional infrasound channel design is shown in Figs. 2 and 3. Resonance frequency selection device and harmonic drive are used to detect the vector film. The circuit connects to its outputs end. Infrasound vector film sensors work closely with related tooling components and they are installed on the position to be monitored of the mechanical pole of steel structure. Then connect vector film infrasound sensor output with front-end amplifier module input; connect front-end amplifier module output with opt coupler input.

### ***3.2 Infrasound Information Acquisition and Processing Platform***

Data acquisition system is an independent single-loop monitoring system and mainly composed of two-dimensional solid infrasound sonar sensor, current transducer, signal analysis processor and communication interface. Its acquisition

of mechanical and acoustic micro-change signal from buildings or other facilities is transmitted into a standard signal through current transmitter. Then input to signal analysis processor to calculate a standard measurement.

The section of infrasound information acquisition and processing platform connects opt coupler module output and serial digital acquisition module parallel input; the serial digital acquisition module parallel output connect with the pre-processing signal acquisition computer parallel input through parallel data bus; connect the preprocessing signal acquisition computer serial output with data processing and analysis computer serial input to form the serial data flow transmission between preprocessing signal acquisition computer and data processing and analysis data processing and analysis computer so as to make the data flow send out through the window of the preprocessing signal acquisition computer can be safely transmitted to the data processing and analysis computer input. Data processing and analysis computer is connected with the LCD screen to ensure smooth data flow.

### **3.3 Units Man–Machine Interface**

Man–machine interface makes the real-time online data that calculated by the infrasound information acquisition and processing platform display on the screen. At the same time, signal analysis and measurement processor outputs signal. Signal is incorporated into the field data bus through the communication module. Then it is sent to the central data processing system.

Central data processing system consists of IPC and various types of signal expansion and the control module. On the one hand, it can complete sets of multi-loop signal processing and computing and send the signal and data to the master monitoring system in central control room through the field bus. On the other hand, it accepts and analyzes the field signals and instruction of the central control room, and then outputs a corresponding control signal. It can directly control the field or control room signal light or alarm devices, and can also control the start and stop switch, to ensure that the facilities operate in the range of security force.

In conclusion, the three parts of the model is steel structure dynamic infrasound square, infrasound information acquisition and processing platform, the man–machine interface. Hence, Fig. 4 shows the structure of overall system.

## **4 Experiment and Analysis**

In order to verify the accuracy, reliability and validity of the dynamic infrasound monitoring system, a large number of experiments based on ACSDINS model have been done.



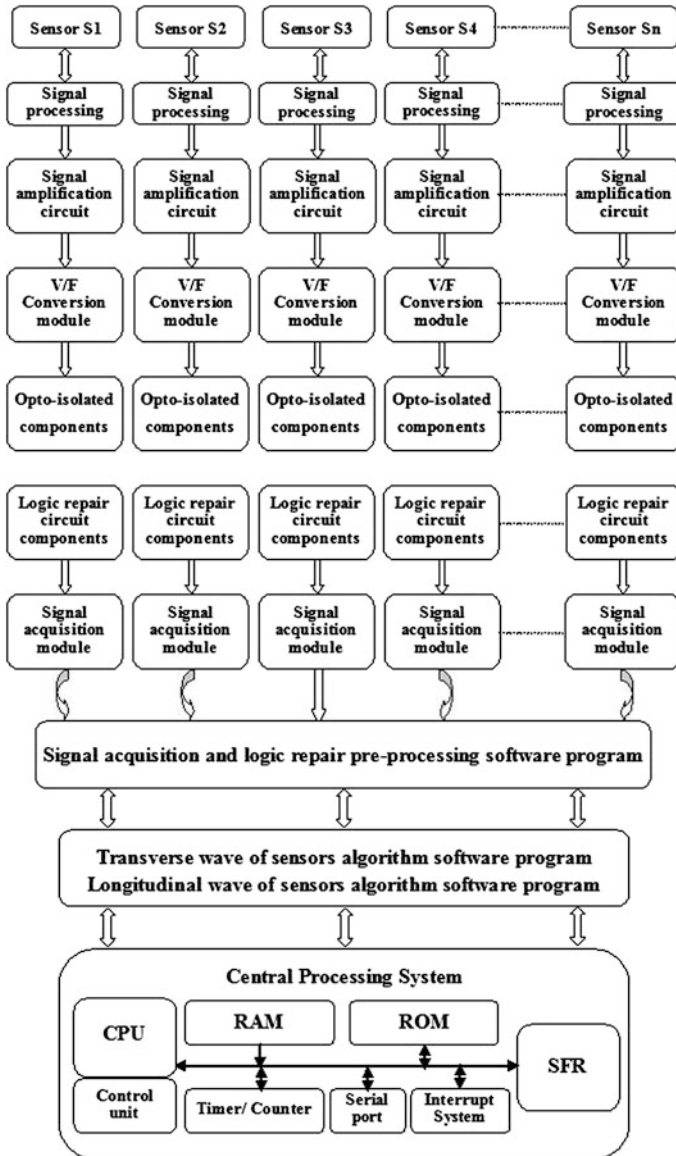


Fig. 4 The structure of overall system

### 4.1 System Experiment

In the experiments, the system detected the strength and rigidity of mechanical pole of steel structure through line monitoring and early warning analysis. As an example, the perception trend of the sensor is shown in Figs. 5 and 6. The system



Fig. 5 The perception trend on longitudinal wave



Fig. 6 The perception trend on transverse wave

has a higher selectivity vector and can effectively filter out various types of acoustic interference. A large number of accumulation and analysis were done on the monitoring data.

This system is suitable for temperature, vibration, centripetal force, nuclear radiation and electromagnetic interference and other adverse working conditions. With self-test and zero automatic correction function, the system is easy to install and maintain. Due to simple man-machine interaction, professionals and non-professionals can easily use the system.

## 4.2 System Analysis

After lots of long time experiments, preliminary estimates of the monitoring data show that: for the changes of tensile and compressive stress, transverse wave sensor is about 4–6 % of the power source, while longitudinal wave sensor is about 11–13 %. Experiments and analytical results show that ACSDINS is featured with speed response, accurate detection and analysis, and anti-interference ability. The results of the force and strain analysis were accurate and small errors.

## 5 Conclusion

A method of autonomous seam acquisition and tracking with passive vision for arc welding robot is proposed. By means of obtaining the weld seam information of anterior seam in the welding direction and generating corresponding seam coordinates, the robot can track the weld seam and finish the whole weld task with PD controller.

**Acknowledgment** I would like to express my gratitude to all those who helped me during the writing of this thesis. My deepest gratitude goes first and foremost to Beijing Construction Safety Engineering Technology Research Center. Without its support, this thesis could not have reached its present form.

## References

1. 许会超 (2012) 声波信号在钢结构安全监测中的应用研究. 北京:北京建筑工程学院
2. Mutschlecner PJ, Whitaker RW (2003) Infrasonic observations of earthquakes. Infrasound Workshop. San Diego, USA
3. Imriyas K, Pheng LS, Lin, TA (2007) A decision support system for predicting accident risks in building projects. *Archit Sci Rev* 50(2):149–162
4. Wang L-Y, Wang Q-S (2009) The Application of nondestructive testing techniques in the construction steel structure industry. In: *Sci-tech information development and economy*

5. Wang S, Xiong E (2008) A theoretical research on magnetic nondestructive testing of steel structures. *Sci Pap Online*
6. Hua J, Li M, Zhang J (2009) Fundamental modeling issues on benchmark structure for structural health monitoring. *Sci China Ser E: Technol Sci*

# Design and Optimization of Magnetic Wheel for Wall Climbing Robot

Zheng-Yi Xu, Ke Zhang, Xiao-Peng Zhu and Hao Shi

**Abstract** To satisfy the requirements on payload and surface adaptability of wall climbing robot working on ship hull, a kind of magnetic wheel with optimized adhesive ability is designed. A numerical computation model for accurately computing the 3D magnetic field is developed by using finite element method. Force requirements under various surface conditions are studied and dimensions of the wheel are optimized. Prototype results show that the wheel achieved desirable adhesive ability with decent weight, which can provide adhering force over 1100 N on ship hull per wheel, and satisfies engineering requirements under all considered conditions in the design of robot.

## 1 Introduction

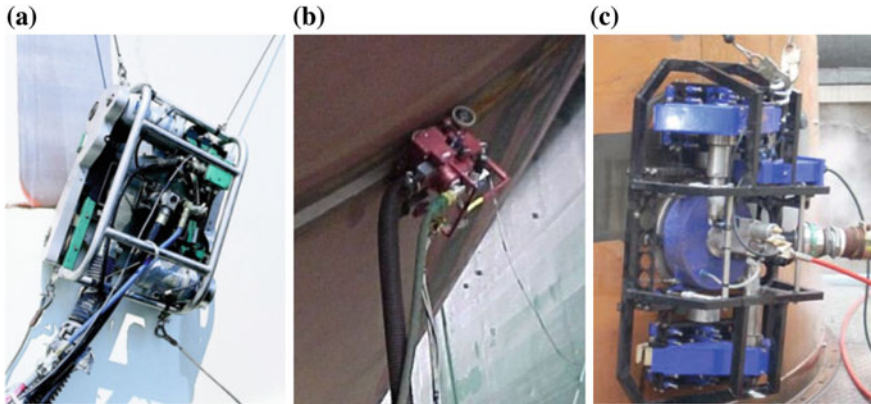
In the ship building industry, many procedures are performed on ship hulls including the removal of rust, the stripping of coatings and corrosion, the cleaning of weld seams, non-destructive testing and inspecting, and so on. Traditionally, these operations are done manually by staff on aerial working platforms: the tasks are intense, tedious, and potentially dangerous. A ship hull could be over 30 m high, with a surface area exceeding 20,000 m<sup>2</sup> [1], and could include a variety of surface features such as: obstacles, high curvature, weld seams, and so on.

Based on these conditions above, we proposed to develop a wall-climbing robot system to climb up the hull and do these operations instead of manual operation.

There're already some cases that robots are used in surface projects of ship hulls or iron tanks [1–6].

---

Z.-Y. Xu · K. Zhang (✉) · X.-P. Zhu · H. Shi  
Shanghai Key Laboratory of Materials Laser Processing and Modification,  
School of Materials Science and Engineering, Shanghai Jiao Tong University,  
Dong Chuan Road, No. 800, Shanghai 200240, China  
e-mail: zhangke@sjtu.edu.cn



**Fig. 1** Surface cleaning robots already in application. **a** HydroCAT. **b** VAL-250. **c** M250

Flow Water Jet developed a robot system called HydroCAT as Fig. 1a, to do surface cleaning job with ultra-high pressure (UHP) water jet equipment [3]. Its adhesion force is provided by vacuum suction.

Another instance is VAL-250, as Fig. 1b, which was designed by Urakami Research Company, under the request from Samsung heavy industries [4]. Different with HydroCAT, it uses grit-blasting device as the surface process solution, which costs less compare to UHP blasting. But its adhering method is also vacuum suction.

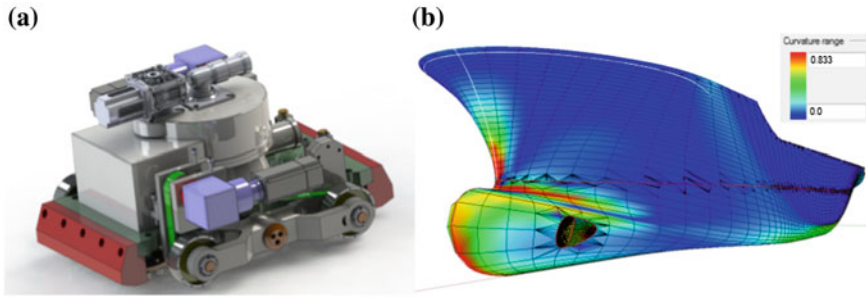
Differently, Magnetic Crawler M250 [5], as Fig. 1c, which is a product of Jetstream GmbH, uses magnetic force as its adhering solution as its name. Magnets are mounted on the chassis to apply magnet force. These magnets do not directly contact the surface but with a constant small gap, between 2 and 10 mm, to keep the chassis adhering. A problem worth to be concerned is the magnetic force varies too much and even hinders robot's locomotion against curvature. In a similar design [7], same problem is also posed. As designed force of 2300 N, the magnets generate 1300–3470 N as curvature radius changes from 1.5 to  $-1.5$  m.

Some low payload robots [8, 9] just simply put magnets on their caterpillars. As only magnets on both ends will functioning as adhering force during locomotion, but all magnets on surface do hindering when the robots are steering, these robots' steering abilities are not well enough.

## 2 Magnetostatic Model for Wheel

### 2.1 Requirements of Payload and Working Condition

Our design embodies a four-wheeled structure as shown in Fig. 2a. With moderate wheel spacing it could efficiently balance stability and mobility. A set of grit-blasting devices with recycling functions is applied as the working unit rather



**Fig. 2** Robot concept and working surface. **a** Grit blasting robot design. **b** Ship hull curvature

than a UHP device: this costs less and will not cause as much pollution. However, the shortcoming of the chosen grit-blasting method is that its payload requirement is relatively high. For this reason, how to design the wheel structure and how much force they should apply became key foci for this study.

The total mass of our robot will be controlled under 40 kg and it can carry 80 kg extra payload.

Also, as shown in Fig. 2b, by analyzing the geometry data on 3D-model of ship hull, we decided the minimum curvature radius our robot can meet as 1.2 m (or maximum curvature as  $0.833 \text{ m}^{-1}$ ). Except the red zones at the both ends of hull, all other surfaces can meet that standard. On the other hand, a typical weld-seam model we defined with 20 mm width and 5–8 mm height. The robot should cross the weld seam safely by any direction: either parallel, perpendicular or just one sided. Influences of the surface conditions to magnetic force will be studied.

## 2.2 Wheel Structure

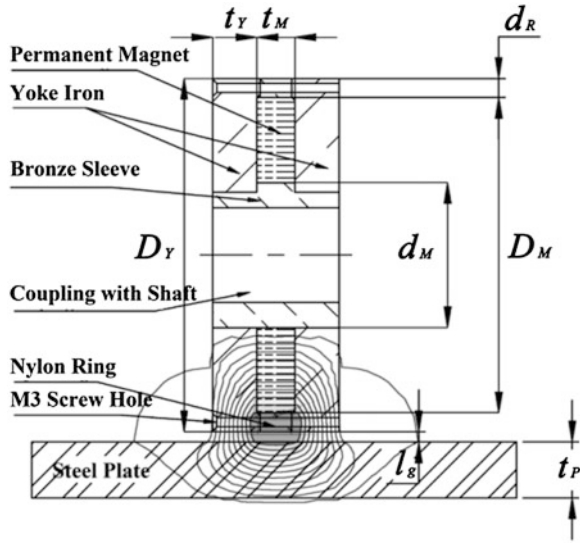
As shown in Fig. 3, the wheel is with a N38H NdFeB magnet which is axial magnetized in the middle and two soft irons as yokes at both sides. The diameter of yoke iron is slightly bigger than the magnet, so the magnet do not contact with the adhered surface directly. All the three pieces are fixed on a bronze sleeve, adapting with rotating shaft. The wheel will be directly contacting the surface at any time, which means the thickness of air gap is low, stable and predictable.

Some important dimensions are also shown in Fig. 3, such as DM: out diameter of magnet; dM: inner diameter of magnet; dR: differences between yoke iron radius and magnet radius; tY: thickness of yoke and tM: thickness of magnet. Additionally, about the working condition, lg represents the length of non-ferromagnetic gap and tP as the thickness of adhered plate.

In magnetostatic solution, virtual displacement method [10] could be used to calculate magnetic force. Introducing Maxwell's Force Tensor [11], magnetic force could be written as:



**Fig. 3** Magnetic wheel design in section view



$$F = \oint_S \left[ \frac{1}{\mu_0} (\mathbf{B} \cdot \hat{n}) \mathbf{B} - \frac{1}{2\mu_0} B^2 \hat{n} \right] dS \tag{1}$$

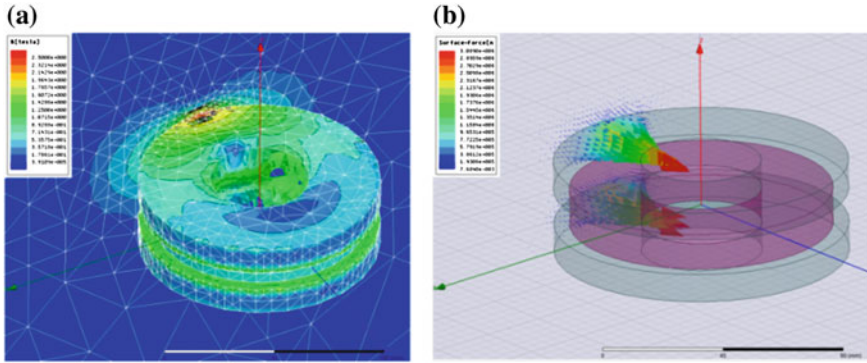
Here S refers to a close surface that we select for integration and F refers the magnetic force applied on it. And  $\mu_0$  refers to magnetic permeability of vacuum; B refers to magnetic induction intensity and  $\hat{n}$  refers the unit vector on the closed interface which integrates on.

In our study, ANSYS Maxwell is chosen as the finite element (FE) solution environment. By setting up the FE model, we need to build up the wheel’s geometry and apply meshes to them, definite materials and set boundary conditions [12], then magnetostatic field could be solved and so as magnetic force. As depicted in Fig. 4a, the scalar of magnetic induction intensity over the wheel body and hull surface. And as depicted in Fig. 4b, the force distribution on hull surface could be portrayed intuitively.

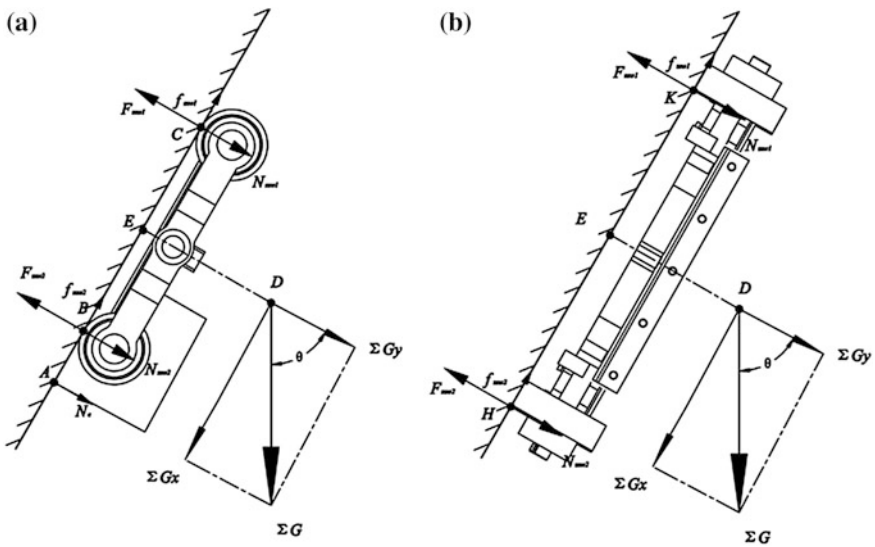
### 3 Analysis, Optimization and Discussion

#### 3.1 Static Analysis

A static model is built to analysis how much force is needed in this design. As depicted in Fig. 5, ship hull is simplified as a plane with a tilt angle, which scope is  $\theta \in [0, \pi/2]$ , corresponding the situations from bottom-up to vertical surface. The total payload is simplified as a single force applied on point D. And we consider



**Fig. 4** Results of FE simulation. **a** Mapping of magnetic induction intensity. **b** Magnetic force distribution



**Fig. 5** Static analysis of both crawling direction. **a** Static model on longitude direction. **b** Static model on latitude direction

two conditions of the direction of the robot, as shown in Fig. 5, called longitude direction and latitude direction.

In longitude crawling direction, it faces such possible failure cases:

- (1) Peeling off: this failure refers to not enough normal force is generated for adhering.
- (2) Sliding down: this refers to not enough static friction force is generated to preserve static equilibrium.

- (3) Rolling down: this refers to the critical state that upper part would peel off while lower part still adhering because the moment produced by payload.

For case (1) and (2), we can build equations of force balance at critical state:

$$\begin{cases} 2F_{mw1} + 2F_{mw2} = \sum G_y + 2N_{m1} + 2N_{m2} \\ \sum G_x = 2\sum f = 2\mu N_{m1} + 2\mu N_{m2} \end{cases} \quad (2)$$

By self-lock function supplied by motors, influences of rolling friction force can be ignored. So  $\mu$  here refers to its sliding friction coefficient. We can build an equation that minimum magnet force needed as:

$$F_{mw\min} = \frac{\sum G}{4} \left( \cos \theta + \frac{1}{\mu} \sin \theta \right) \quad (3)$$

For case (3), an anti-topple structure is mounted downside, which changed the possible rolling pivot from point B to point A. By lengthening arms of forces, it can help generating greater magnetic force torques to prevent robot from rolling down. An equation of critical torque state could be built:

$$2F_{mw1}l_{AC} + 2F_{mw2}l_{AB} - 2N_{mw1}l_{AC} - 2N_{mw2}l_{AB} - \sum G_y l_{AE} - \sum G_x l_{DE} = 0 \quad (4)$$

In critical state, as the normal force on all contacts expect rolling pivot come to zero, we can build an equation that minimum magnet force needed as:

$$F_{mw\min} = \frac{\sum G}{4} \left( \cos \theta + \frac{2l_{DE}}{2l_{AB} + l_{BC}} \sin \theta \right) \quad (5)$$

By introducing actual parameters, as  $\sum G = 120$  kg,  $\mu = 0.5$ ,  $l_{AB} = 0.105$  m,  $l_{BC} = 0.37$  m,  $l_{DE} = 0.36$  m, we can plot the minimum magnet force needed by  $\theta$ . Also we can reach solutions in similar way for the latitude position, with  $l_{HK} = 0.412$  m. In intermediate directions, requirements are between them.

As a conclusion, the minimum requirement of magnetic force for each wheel is  $F_{mw\min} = 657.40$  N.

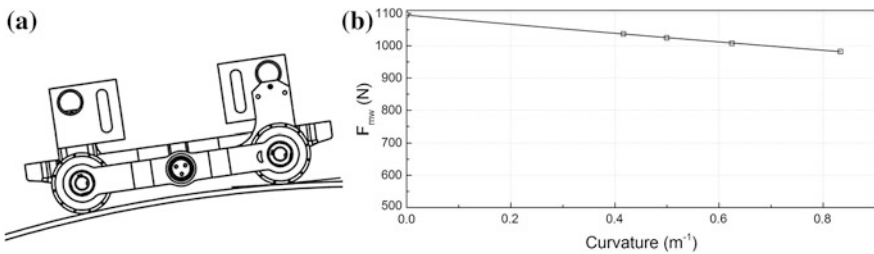
### 3.2 Evaluations on Practical Working Condition

The result above is under the condition that approximates the hull as a flat plane. But in practical working condition, there're still some factors to influence magnetic force the wheel can afford. So magnetic force the wheel should offer must be with a reasonable design margin.

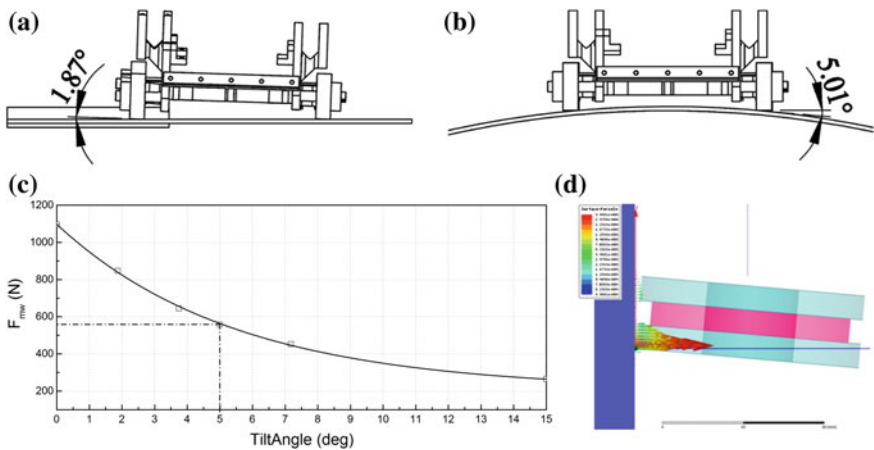
To evaluate these influences, we built corresponding FE model and environment, to compare its magnetic force in various situations with plane condition. Then the margin will be decided accordingly.

**Curvature Evaluation** As depicted in Fig. 6, this situation appears typically in longitude direction. The curvature slightly changes magnetic force, when it comes to the largest value of  $0.833 \text{ m}^{-1}$ , magnetic force will remain 89.61 % of plane case.

**Tilt Evaluation** A tilting condition means not the both sides of one wheel can perfectly fit the hull. There're two occasions that cause the status. As depicted in Fig. 7a, a height difference between left and right chassis will cause imperfect contacting. With such height difference up to 30 mm, the tilt angle will be  $1.87^\circ$  max. And as depicted in Fig. 7b, which is typical in latitude direction of chassis, high curvature will cause imperfect contact. Such tilt angle will be as high as  $5.01^\circ$  in extreme condition. That angle will cause 49.16 % loss of magnetic force, as shown in Fig. 7c, d.



**Fig. 6** Magnetic force variance with curvature changes. **a** Schema of surface curvature. **b** Magnetic force variance with curvature (longitude)



**Fig. 7** Tilt angle cases and evaluation. **a** Schema of height difference case. **b** Schema of curvature caused case. **c** Magnetic force variance with tilt angle. **d** Magnetic force distribution at  $5.01^\circ$  tilt angle

Although this influence is explicit, but to ship hull structure, a curvature that high only appears on low height when external payload is actually much lower than the upper limit of 120 kg. By such fact, it will not affect the requirement of magnetic force obviously.

**Weld Seam Crossing Evaluation** Actually, we can treat this situation as a variation of curvature issue. When wheel is on top of a weld seam, it is equivalent as on a small section of curved surface with small curvature radius. The influence is instantaneous but also should be evaluated.

The seams on ship hull are normally with width of 20 mm and height of 5–8 mm. By placing the wheel on top of seam model, the simulate result is shown in Fig. 8. Magnetic force decreases to 66.91 % by the height of 8 mm.

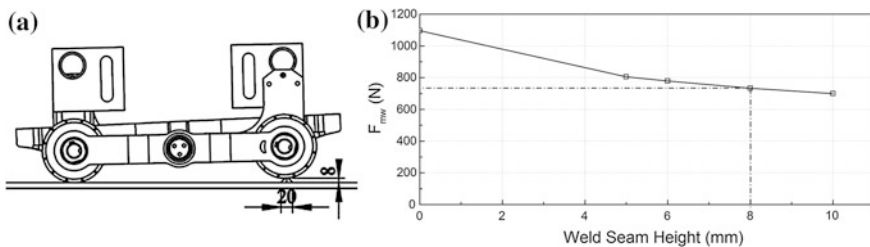
**Design Margin of Magnetic Force** By evaluations above, about 66.91 % of magnet force on plane will meet the requirement of 657.40 N. So the final requirement is 982.40 N, which approximately as 1000 N, will be the standard for wheel optimization.

### 3.3 Optimization

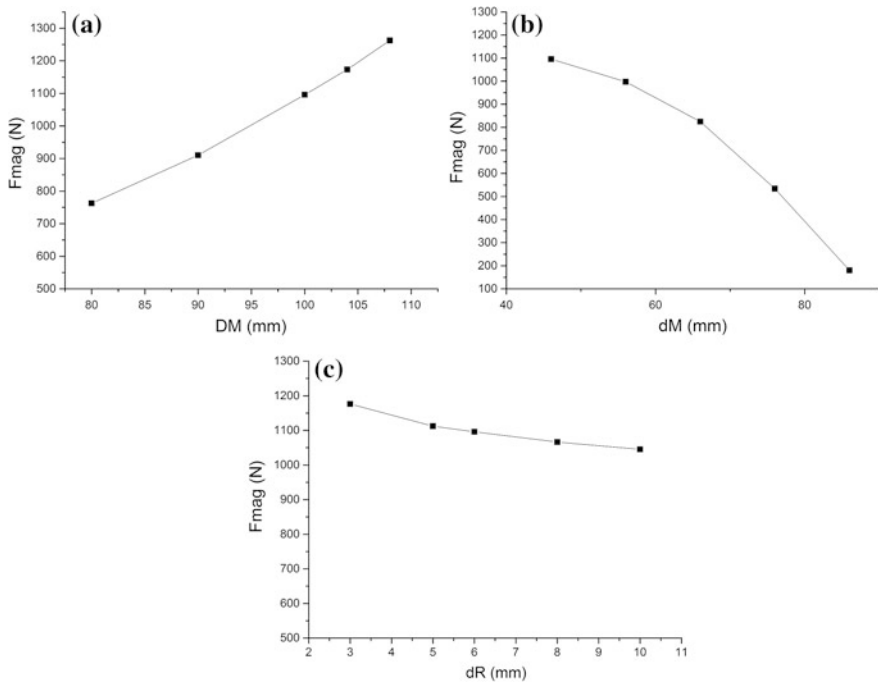
As working condition,  $l_g$  is defined as 0.5 mm, which is a decent estimate with ample allowance;  $t_P$  is set as 20 mm, a typical thickness of ship hull, which will not be the bottleneck of magnetic force. Main optimization goal is  $F_{mag}$ , refers to the magnetic force of a wheel. Two other responses are defined as references, as  $m$ : mass of whole structure and  $R$ : defined by  $F_{mag}/mg$ , to show the efficiency every mass of the wheel could provide.

**Optimization on Diameters** By Eq. (1), we can recognize that relationships between  $F_{mag}$  with  $dM$ ; also  $F_{mag}$  with  $DM$  are monotonously. By fix other parameters and change these factors individually, the result of magnet force is shown in Fig. 9a, b.

At last,  $dM$  is chosen at the engineering minimum as 46 mm and  $DM$  was chosen at 100 mm, by which we can have enough space to optimization other parameters and keep magnet force over 1000 N.



**Fig. 8** Weld seam crossing case and evaluation. **a** Schema of weld seam crossing. **b** Magnetic force variance with seam height



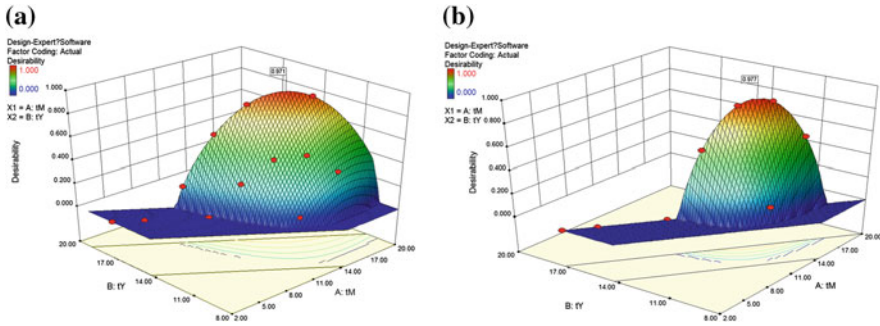
**Fig. 9** Diameters' influences on magnetic force. **a** DM influences. **b** dM influences. **c** dR influences

And about dR in Fig. 9c, as it slightly lengthens the magnet circuit, it has a relatively small effect on magnet force though it's also monotonous. Considering M3 screw holes are bored beside the edge of yoke iron to help positioning, dR is decided as 6 mm.

**Optimization on Thicknesses** With an upper limit on total thickness, tM and tY constraint with each other. We use response-surface research to optimization the best distribution of tM and tY. By planning 14 parameter combinations and simulate, a best solution is optimized under our constraint.

We set two gauges of total thickness. To guarantee the safety factor in our design, we set the upper limit of total thickness as 40 mm in the first gauge. As shown in Fig. 10a, the sheared zone represents the limit of total thickness. And to the surface graph, the blue planar part refers to the lower limit of magnetic force as 1000 N. The higher point shows more desirability to our optimize goal. At the peak of the surface, the recommended distribution is tM = 14.36 mm, tY = 12.82 mm. When  $F_{mag}$  predicted is as high as 1348.55 N, which is also proved by simulation. Simultaneously R reached 59.74.

Another gauge considers more about the mass. Due to the weight of robot is strictly controlled; we set the other gauge as 36 mm by total thickness. In this

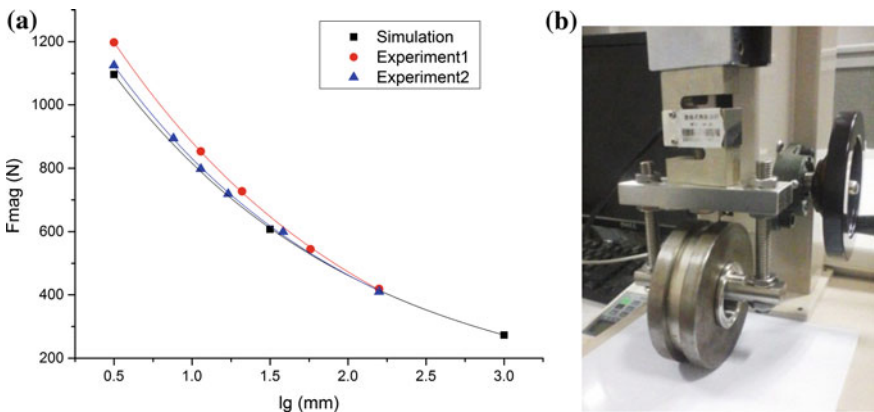


**Fig. 10** Optimization on thicknesses. **a** Desirability evaluation under 40 mm total thickness. **b** Desirability evaluation under 36 mm total thickness

situation, the recommended distribution is  $tM = 13.09$  mm,  $tY = 11.46$  mm, when  $F_{mag} = 1155.52$  N and  $R = 56.69$ , with the mass per wheel is controlled to 2 kg. The result is shown in Fig. 10b.

### 4 Prototype and Implementation

At last, we choose the second gauge for prototyping. And for engineering convenience, the final parameters are decided by the nearest integers, as  $tM = 12$  mm,  $tY = 12$  mm. Plus with  $DM = 100$  mm,  $dM = 46$  mm and  $dR = 6$  mm. The magnet force is tested by varying gap length  $l_g$ , from 0.5 to 3.0 mm. By comparing with result of simulation, as shown in Fig. 11, magnetic force simulated is



**Fig. 11** Comparing magnetic force of prototype and corresponding FE model. **a** Prototype versus simulation. **b** Prototype and experiment equipment

1095.9 N, and the actual value is over 1125.4 N, the validity and accuracy of FE model and optimization result is proved, which also satisfies our requirements.

## 5 Conclusion

In this study, by using FE method, a numerical magnetostatic model for the magnet wheel is built, which proves a reliable reference for parameters optimization. And the dimensions of magnet wheel are optimized, referencing theoretical models and working condition evaluations. Prototype of wheel is also made, proving the correctness and accuracy of FE model, as magnetic force per wheel could reach 1100 N under 0.5 mm air gap.

In next step, the optimized wheels will be assembled into the main assembly of robot prototype, in order to validate their further performance in working condition.

## References

1. Ross B, Bares J, Fromme C (2003) A semi-autonomous robot for stripping paint from large vessels. *Int J Robot Res* 22(7–8):617–626
2. Bar-Cohen Y, Bao X, Dolgin BP, Marzwell NI (2001) Residue detection for real-time removal of paint from metallic surfaces. In: 6th annual international symposium on NDE for health monitoring and diagnostics. International society for optics and photonics. pp 115–120
3. Echt A, Dunn KH, Mickelsen RL (2000) Automated abrasive blasting equipment for use on steel structures. *Appl Occup Environ Hyg* 15(10):713–720
4. V-ROBO brochure, Urakami Research Company, pp 12, 13
5. Jetstream Hochdruck-Lösungen GmbH, <http://www.jetstream-germany.com/en/products/crawler>
6. Iborra A, Pastor JA, Alonso D, Alvarez B, Ortiz FJ, Navarro PJ, Suardiaz J (2010) A cost-effective robotic solution for the cleaning of ships' hulls. *Robotica* 28(03):453–464
7. Gui ZC, Chen Q, Sun ZG, Zhang WZ, Liu K (2006) Optimization of permanent-magnetic adhesion device for wall-climbing robot. *Diangong Jishu Xuebao Trans China Electrotechnical Soc* 21(11):40–46
8. Xu Z, Ma P (2002) A wall-climbing robot for labelling scale of oil tank's volume. *Robotica* 20(02):209–212
9. Schoeneich P, Rochat F, Nguyen OTD, Moser R, Mondada F (2011) TRIPILLAR: a miniature magnetic caterpillar climbing robot with plane transition ability. *Robotica* 29(07):1075–1081
10. Demarest KR (1998) *Engineering electromagnetics*. Prentice Hall, New York, pp 206–209
11. Ida N, Bastos JP (1997) *Electromagnetics and calculation of fields*. In: Mittra R (ed), vol 2, Springer, New York, pp 182–189
12. Jin J (2002) *The finite element method in electromagnetics*. Wiley, Hoboken, pp 184, 185



# Improved Cold Crack Resistance of Q690 Steel Weldments Using Double-Sided Arc Welding

Cheng-dong Yang, Yu-xi Chen and Shan-ben Chen

**Abstract** A new technology of double sided double arc welding (DSAW) in which gas metal arc welding (GMAW) is employed for root welding and filler passes of Q690 thick plate was proposed in this paper. Numerical simulation has been used to study the cold crack resistance of Q690 steel weldments. The critical stress ( $\sigma_{cr}$ ) in DSAW without preheating is 514.49 MPa, while in conventional welding with 100 °C preheating temperature, it is 378.21 MPa. The higher critical stress implies that the samples in DSAW without preheating have lower cold crack sensitivity than those in conventional welding with 100 °C preheating temperature. DSAW can improve the cold crack resistance of Q690 with lower preheating temperature or even without preheating.

## 1 Introduction

High-strength low-alloy steel has been widely used in shipbuilding, high pressure vessels, nuclear engineering, heavy-duty machinery and ocean engineering for its high strength and good toughness. However, the sensitivity to cold crack of this material requires preheating treatment before welding to prevent the formation of cold cracks. Unfortunately, the process of preheating may lead to many problems such as softening of the welding structure, increasing the cost of welding and reducing production efficiency [1]. Currently, these thick plate structures adopt conventional methods such as manual and semi-automatic arc welding, which are very complicated and of low productivity. The process of conventional welding technology is presented as follows: preheating, gas metal arc welding (GMAW) on one side, then back chipping via carbon arc air gouging, polishing, magnetic particle examination, preheating again, GMAW on the other side and post-heating. It is well

---

C. Yang · Y. Chen · S. Chen (✉)  
School of Materials Science and Engineering, Shanghai Jiao Tong University,  
Shanghai, China  
e-mail: cdyang@sjtu.edu.cn

know that industry robot has been applied largely in welding for its high accuracy and efficiency [2–7]. To solve these problems, a technology of DSAW in which GMAW is employed for root welding and filler passes. The process of DSAW presented first by Zhang et al. [8], used one power supply and two torches: normally a plasma arc welding torch on one side of the plate and a plasma arc or gas tungsten arc welding torch on the other side. Special welding fixtures are required to provide access to both sides of the plate during welding. The arc is struck between the two torches. The plates to be welded are grounded and not part of the electric welding circuit. To date, for the advantages of DSAW, it has been widely used in welding Al alloy [9–13] and some applications in stainless steel [14] and Mg alloy [15].

To control the welding parameters on each side of the plate respectively by a DSAW system with only one welding power is not possible. To this end, the DSAW system with two powers was presented. In this paper, experiments have been conducted to investigate the thermal characteristics in DSAW. Simultaneously, numerical simulation has been used to predict the transient temperatures. In addition, theoretical analysis have been done to investigate the effect of DSAW on cold crack resistance in welding thick plate of Q690 steel.

## 2 DSAW Experiment

The system of DSAW is shown in Figs. 1 and 2. It mainly consists of two robots (a KUKA robot and an ABB robot), a central controller, a coordinated control center, two welding powers, a worktable and a vision sensor. The communication between

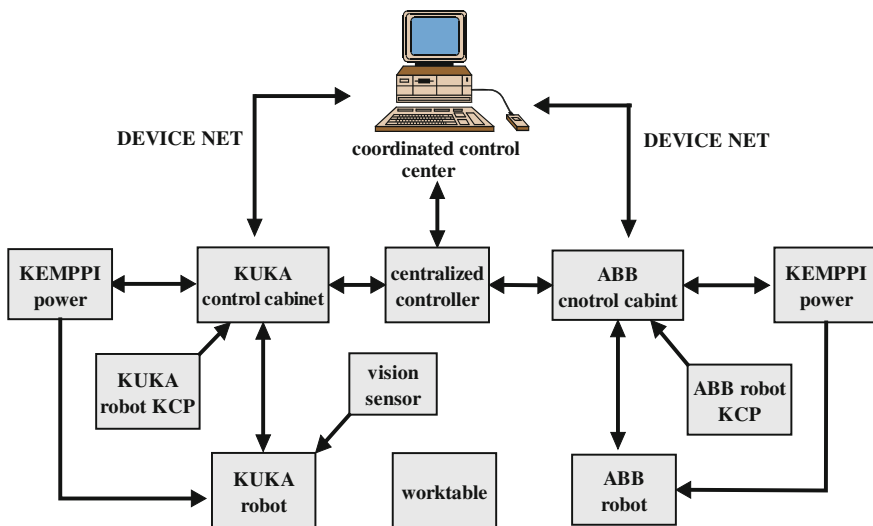


Fig. 1 System of DSAW

**Fig. 2** Experimental system



**Table 1** Chemical constitution of low alloy high strength steel (wt%)

Element	C	Si	Mn	P	S	Ni	Cu	Cr	Nb	Mo	V
Content	0.10	0.280	1.29	0.008	0.0005	1.177	0.020	0.518	0.018	0.579	0.002

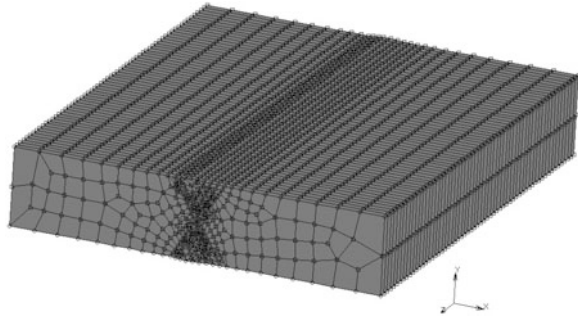
welding powers and two robots is implemented by Device Net. The central controller administers the arc on and arc off. Vision sensor in the system is used for initial welding position guiding, multi pass path planning and correcting. Due to the rigid assembly accuracy demanded by robot welding, a worktable has been ad hoc designed in this system with the functions of location, quick fixation and providing external restrictions to alleviate the welding deformation.

The plate with a symmetric double V groove is 50 mm in thickness, 160 mm in width, and 250 mm in length, and the gap width is 4 mm. The distance between fore torch and rear torch is kept fixed at 30 mm. With the purpose of verifying the results which calculated by the numerical simulation, thermocouples have been used to measure the actual temperature during welding. Welding parameters used in the experiment are as follows: the welding speed is 30 cm min<sup>-1</sup>, the welding voltage is 19.5 V, the welding current is 135 A and the flow rate of shielding gas is 20 L min<sup>-1</sup>. The chemical constitution of low alloy high strength steel in this experiment has been shown in Table 1.

### 3 Finite Element Model

In this section, the three-dimensional model was established by using the numerical simulation software MARC.MSC. Figure 3 shows the finite element model used in the welded butt joint plate. The whole model is made up of 17,160 elements and 19,337 nodes. Considering that the temperature gradient of welded zone is very

**Fig. 3** Three-dimensional finite element model



high, the mesh in weld and heat affected zone is dense, whereas the mesh far away from the weld is sparse. The element size around the weld region is 2 mm in the welding and thickness direction. The initial condition is an ambient temperature of 20 °C. The X axis is the width direction of the plate, the Y axis is the thickness direction, and the Z axis is the welding direction of the plate in Fig. 3. This paper adopts the double ellipsoid heat source model proposed by Goldak [16]. Physical and mechanical properties are determined by considering the characteristics of temperature dependence.

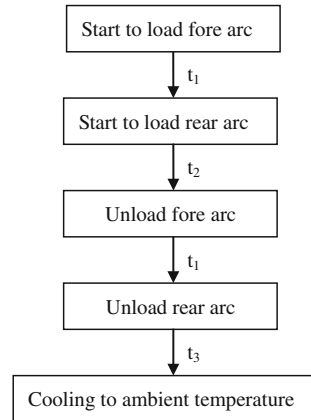
The low alloy high strength steel with 0.1 % carbon has been adopted in this paper. Under the condition of ambient temperature, Poisson's ratio is 0.285, the density is 7.8 kg m<sup>-3</sup>, and the melting point is 1450 °C. The thermodynamic property of the material [17]: the specific heat is 434 J kg<sup>-1</sup> °C<sup>-1</sup>, the yield strength is 850 MPa, the heat conductivity is 30.7k °C/W m<sup>-1</sup>, the thermal expansion coefficient is 1.06 × 10<sup>-5</sup> °C<sup>-1</sup>, and the Young's modulus is 2.08 × 10<sup>5</sup> MPa under room temperature. The heat transfer near the weld molten pool zone is mainly dominated by heat radiation, while in the further place surface heat exchange dominates. Considering the common effects of radiation and surface heat exchange, the formula of compound heat conduction coefficient is shown below [18].

$$h = \frac{\varepsilon_{em}\sigma_{bol}\left((T + 273)^4 - (T_{amb} + 273)^4\right)}{(T - T_{amb})} + h_{con} \quad (1)$$

where  $h$  is the compound heat conduction,  $\varepsilon_{em}$  is the radiation coefficient,  $h_{con}$  is the convection coefficient,  $\sigma_{bol}$  is the Stefan–Boltzmann constant,  $T$  is the temperature variable, and  $T_{amb}$  is the surrounding temperature.

The process of root welding in double-sided double arc is shown in Fig. 4. The effect of DSAW on temperature field is investigated. Arc distance variant is set as  $d$ , which means the fore torch is ahead of the rear torch by an arc distance of  $d$  during root welding. Both torches have the same welding speed. The fore arc is loaded first, then after  $t_1$ (s) the rear arc is actuated. Both torches go along together in the weld direction for a period of time  $t_2$ (s) before the unloading of the fore arc. Whereafter the rear arc goes alone for another period of time  $t_1$ (s) until it is finally

**Fig. 4** Root welding loading sequence



unloaded and the work-piece starts to be naturally cooled in the air.  $t_3$  is the time needed for the work-piece to be cooled from its average temperature to the surrounding temperature. According to the arc distance  $d$  and welding speed  $v$ , the foregoing time  $t_1$  is expressed as follows.

$$t_1 = \frac{d}{v} \tag{2}$$

$t_2$  is described as:

$$t_2 = \frac{L - d}{v} \tag{3}$$

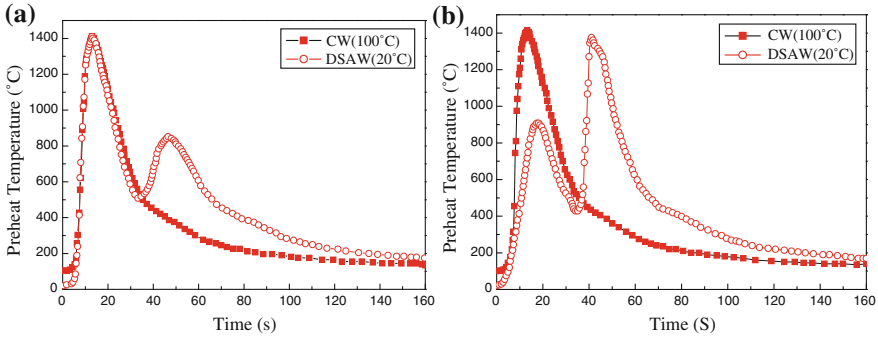
where  $L$  is the length of the plate (mm),  $v$  is the welding speed ( $\text{mm s}^{-1}$ ).

It can be determined quantitatively when the arc distance is known. This time mainly related to the material’s heat release coefficient and the ambient temperature.

## 4 Results and Discussions

### 4.1 Thermal Analysis

The thermal cycle curves of conventional welding (CW) with 100 °C preheating temperature and DSAW without preheating are shown in Fig. 5. The thermal cycle curve of CW shows only one peak, while two peaks appears on that of DSAW. Another apparent difference is the DSAW has slower cooling rate compared to CW. The fore arc provides the rear pass with a preheat action, leading to the first peak of DSAW in Fig. 5b. Meanwhile the rear arc provides the fore pass with a second thermal cycle, and this thermal cycle induces the second peak of DSAW in Fig. 5a.



**Fig. 5** The thermal cycle curves of CW and DSAW. **a** Fore pass. **b** Rear pass

The mutual interaction of preheating by fore arc and post-heating by rear arc can reduce the temperature gradient and make the cooling rate of DSAW small.

The actual transient temperatures have been measured by thermocouples, and the curve clearly indicates that the calculated temperatures agree with that of the experimental temperature both in fore pass and rear pass.

Table 2 shows the cooling parameters under different welding methods and various preheating temperatures. Cooling parameters play a greatly important role in welding microstructure and properties, especially the parameters of  $t_{8/5}$  and  $t_{8/3}$ .  $t_{8/5}$  and  $t_{8/3}$  is the time for the welded zone to be cooled from  $A_{r3}$  (800 °C) to the most unstable temperature of austenite (500 °C) and to the temperature (300 °C) that the martensite begins to transform respectively. Comparing the CW and DSAW, Table 2 obviously reveals that  $t_{8/5}$  and  $t_{8/3}$  are larger in DSAW. Under the different preheating conditions: non-preheating, 50 and 100 °C preheating respectively in DSAW,  $t_{8/5}$  and  $t_{8/3}$  increase with the preheating temperature rising,  $t_{8/5}$  increases in a slow speed, while  $t_{8/3}$  has a relatively faster rate. Quick cooling rate prevents the diffusible hydrogen from escaping from welded and heat affected zones, and causes the formation of hardened structure as well. The residual diffusible hydrogen remained in the welded zone will induce cold cracks. But if the cooling rate is extremely slow, the welded zone and heat affected zone will maintain in high temperature for longer time, thus the structure of upper bainite and M-A component may appear in welding heat affected zone which will influence

**Table 2** Cooling parameters

Welding method	Preheating temperature T (°C)	Fore pass		Fear pass	
		$t_{8/5}$ (s)	$t_{8/3}$ (s)	$t_{8/5}$ (s)	$t_{8/3}$ (s)
CW	100	9.4	32.4	8.7	31.8
DSAW	100	15.1	55.1	15.3	56.3
DSAW	50	14.0	46.4	14.2	47.5
DSAW	20	12.9	40.6	13.1	42.3

the strength of welding heat affected zone. So a reasonable  $t_{8/5}$  and  $t_{8/3}$  are very necessary to guarantee the welding quality of low alloy high strength steel. When CW with 100 °C preheating temperature is chosen, the  $t_{8/5}$  is only 9.4 s. It means the martensite which has transformed from austenite in heat affected zone does not have enough time to finish self tempering, therefore it is not decomposed completely, result in decreasing the impact toughness of fusion zone. If the way of DSAW is selected, the time which it takes to cool from 500 to 300 °C is twice as that needed by CW under the same preheating temperature. Cooling process slows down in the range of temperature from 400 to 200 °C wherein martensite has been transformed. This provides the function of self tempering for martensite in heat affected zone, which can decrease the content of diffusible hydrogen in welded zone and heat affected zone, alleviate cold crack sensitivity and improve the crack resistance.

The most obvious phenomenon in Table 2 is that the  $t_{8/5}$  and  $t_{8/3}$  under non-preheating condition in DSAW is longer than in CW with 100 °C preheating temperature. For the function that the fore pass preheating and the rear pass post-heating reduce the temperature gradient, the cooling rate in DSAW without preheating is lower than that in CW with 100 °C preheating temperature, and diffusible hydrogen has more time to escape from welded and heat affected zones. The escape of diffusible hydrogen contributes to improving the crack resistance, alleviating the cold crack. It means the DSAW without preheating has better property in cold crack resistance than CW with 100 °C preheating temperature.

## 4.2 Cold Crack Sensitivity Analysis

The mechanism of cold crack generation in welding high strength steel is that the quenched steel is subject to the invasion and induction of hydrogen, which causes embrittlement and cracks under the influence of restraint stress. The higher critical stress ( $\sigma_{cr}$ ) of the sample, the better cold crack resistance it will get. The higher critical stress ( $\sigma_{cr}$ ) is closely related to lower content of hydrogen and the longer time of  $t_{8/5}$  and  $t_{100}$ . The formula is shown as follows [19].

$$\sigma_{cr} = (86.3 - 211p_{cm} - 28.2\lg([H] + 1) + 2.73t_{8/5} + 9.7 \times 10^{-3}t_{100}) \times 9.8 \quad (4)$$

where  $[H]$  is the content of diffusible hydrogen in deposited metal (ml/100 g),  $p_{cm}$  is the carbon equivalent of alloying element,  $t_{100}$  is the time that it takes welded zone to cool from peak temperature to 100 °C.

$$P_{cm} = C + \frac{Si}{30} + \frac{Mn + Cu + Cr}{20} + \frac{Mo}{15} + \frac{V}{10} + \frac{Ni}{60} + 5B \quad (5)$$

Combining formula (5) and the chemical constitution of low alloy high strength steel shows in Table 1,  $p_{cm} = 0.259\%$  can be calculated.

$H_{R100}$  is the residual diffusible hydrogen content when the welded zone of HSLA (high strength low alloy) steels is cooled down to 100 °C.  $H_{R100}$  has more important effect on cold crack sensitivity than the initial hydrogen content  $H_0$  in the deposited metal [20]. Based on Fick diffusion law, when welded zone is cooled to 100 °C, the expression of residual diffusible hydrogen is shown as follows:

$$H_{R100} = \frac{8}{\pi} H_0 \exp\left(-\frac{\pi^2 M}{4\bar{h}_w}\right) \quad (6)$$

$H_0$  is the initial content of hydrogen when weld is solidified (ml/100 g). This study applies ultra-low hydrogen wire, thus the initial hydrogen content is 3.4 ml/100 g.  $\bar{h}_w$  is the average bead thickness (mm), and  $M$  is the diffusion factor of hydrogen (mm<sup>2</sup>).

$$\bar{h}_w = \frac{\pi v_1 d^2 a_H}{4v_2 w} \quad (7)$$

where  $v_1$  is the wire feed rate,  $d$  is the wire diameter,  $v_2$  is the welding speed,  $w$  is the weave range, and  $a_H$  is the deposition coefficient. The  $\bar{h}_w = 5$  mm can be calculated.

$$M = (183.7 + 2.543t_{200} - 2.298t_{250} + 3.551t_{100} + 14.47t_{300}) \times 10^{-3} \quad (8)$$

According to formula (8) and the characteristic parameters of CW and DSAW shown in Table 3,  $M_{CW} = 1.582$  mm<sup>2</sup> (conventional welding with 100 °C preheating temperature),  $M_{DSAW} = 2.21$  mm<sup>2</sup> (DSAW without preheating) can be readily obtained.

The calculated result reveals that  $H_{R100} = 2.91$  (DSAW without preheating),  $H_{R100} = 3.97$  (conventional welding with 100 °C preheating temperature),  $t_{8/5}$  in DSAW without preheating and CW with 100 °C preheating temperature is 12.9 and 9.4 s respectively,  $t_{100} = 212$  (DSAW without preheating),  $t_{100} = 193$  (CW with 100 °C preheating temperature), then the critical stress ( $\sigma_{cr}$ ) can be calculated,  $\sigma_{cr} = 514.49$  MPa (DSAW without preheating),  $\sigma_{cr} = 378.21$  MPa (CW with 100 °C preheating temperature). The higher the critical stress ( $\sigma_{cr}$ ), the better property of cold crack resistance the DSAW has. The calculated results demonstrate clearly that  $\sigma_{cr}$  in DSAW without preheating is higher than  $\sigma_{cr}$  in CW with 100 °C preheating temperature, which indicates that DSAW without preheating has better property of cold crack resistance than CW with 100 °C preheating temperature.

**Table 3** Characteristic parameters of CW and DSAW

Welding method	Preheating temperature (°C)	$t_{100}$ (s)	$t_{200}$ (s)	$t_{250}$ (s)	$t_{300}$ (s)
CW	100	193	76	57	45
DSAW	20	212	122	97	82



## 5 Conclusions

The effect of double-sided double arc welding on preheating temperature in welding thick plate of low alloy high strength steel has been discussed, and the major findings are summarized as follows.

- (1) A new technology of DSAW in which GMAW is employed for backing welding and filler passes was proposed.
- (2) The critical stress ( $\sigma_{cr}$ ) in DSAW without preheating is 514.49 MPa, while the critical stress in conventional welding with 100 °C preheating temperature is 378.21 MPa. The higher critical stress implies the lower cold crack sensitivity.
- (3) DSAW can improve the cold crack resistance of Q690 weldments with lower preheating temperature or even without preheating.

**Acknowledgment** This work is supported by the National Natural Science Foundation of China under the Grant No. 61374071 and the NDRC of China, under the Grant No. HT[2012]2144.

## References

1. Mohandas T, Madhusuda RG, Satish KB (1999) Heat-affected zone softening in high-strength low-alloy steels. *J Mater Process Technol* 88(1):284–294
2. Ye Z, Fang G, Chen SB, Zou JJ (2013) Passive vision based seam tracking system for pulse-MAG welding. *Int J Adv Manuf Technol* 67(9–12):1987–1996
3. Xu YL, Zhong JY, Ding MY, Chen HB, Chen SB (2013) The acquisition and processing of real-time information for height tracking of robotic GTAW process by arc sensor. *Int J Adv Manuf Technol* 65(5–8):1031–1043
4. Xu PQ, Xu GX, Tang XH, Yao S (2008) A visual seam tracking system for robotic arc welding. *Int J Adv Manuf Technol* 37(1–2):70–75
5. Shen HY, Wu J, Lin T, Chen SB (2008) Arc welding robot system with seam tracking and weld pool control based on passive vision. *Int J Adv Manuf Technol* 39(7–8):669–678
6. Ma HB, Wei SC, Sheng ZX (2010) Robot weld seam tracking method based on passive vision for thin plate closed-gap butt welding. *Int J Adv Manuf Technol* 48(9–12):945–953
7. Fronthaler H, Croonen G, Biber J, Heber M, Ruther M (2013) An online quality assessment framework for automated welding processes. *Int J Adv Manuf Technol*. doi:10.1007/s00170-013-4964-3
8. Zhang YM, Zhang SB (1998) Double-sided arc welding increases weld joint penetration. *Weld J* 77(6):57–62
9. Zhang YM, Zhang SB (1999) Welding aluminum alloy 6061 with the opposing dual-torch GTAW process. *Weld J* 78(6):202–206
10. Zhang YM, Pan C, Male AT (2000) Improved microstructure and properties of 6061 aluminum alloy weldments using a double-sided arc welding process. *Metall Mater Trans A* 31(10):2537–2543
11. Kwon Y, Weckman DC (2008) Double sided arc welding of AA5182 aluminium alloy sheet. *Sci Technol Weld Join* 13(6):485–495
12. Moulton JA, Weckman DC (2010) Double-sided arc welding of AA5182-O aluminum sheet for tailor welded blank applications. *Weld J* 89(1):11–23

13. Zhao YB, Lei ZL, Chen YB, Tao W (2011) A comparative study of laser-arc double-sided welding and double-sided arc welding of 6 mm 5A06 aluminium alloy. *Mater Des* 32 (4):2165–2171
14. Zhang YM, Pan C, Male AT (2001) Welding of austenitic stainless steel using double sided arc welding process. *Mater Sci Technol* 17(10):1280–1284
15. Chowdhury SM, Chen DL, Bhole SD, Cao X, Powidajko E, Weckman DC, Zhou Y (2010) Tensile properties and strain-hardening behavior of double-sided arc welded and friction stir welded AZ31B magnesium alloy. *Mater Sci Eng, A* 527(12):2951–2961
16. Goldak J, Chakravarti A, Bibby M (1984) A new finite element model for welding heat sources. *Metall Mater Trans B* 15(2):299–305
17. Hu JF, Yang JG, Fang HY, Li GM, Zhang Y (2006) Numerical simulation on temperature and stress fields of welding with weaving. *Sci Technol Weld Joining* 11(3):358–365
18. Abid M, Siddique M (2005) Numerical simulation to study the effect of tack welds and root gap on welding deformations and residual stresses of a pipe-flange joint. *Int J Press Ves Pip* 82(11):860–871
19. Yuriok N, Suzuki H (1990) Hydrogen assisted cracking in C-Mn and low alloy steel weldment. *Int Mater Rev* 35(4):217–249
20. Zhang WY (2011) *Welding metallurgy: principle*. China Machine Press. Beijing, pp 11–12